Information [illegible] A. P. Style Manual)

Manuscripts

Send manuscripts to S. A. [illegible], Brookhaven National Laboratory, Upton, Long Island, New York.

Each article submitted will be [illegible] of (a) textual material, i.e., all [illegible] to be set in type, and (b) [illegible] graphs from which zinc etchings [illegible] tones will be made. Textual material [illegible] of an abstract, the body of the [illegible] material, references, and figure [illegible] this material must be in English [illegible] (except mathematical expressions) [illegible] with wide margins (for editorial [illegible] the printer) on a durable, white paper [illegible] letter size. The original copy, [illegible] should be submitted.

For general style, spellings, [illegible] form, recent issues of this journal [illegible] consulted.

The prime requisite is that the [illegible] clear to the typesetter, who is not [illegible] nor a mathematician.

Abstracts

An abstract must accompany [illegible] It should be adequate as an index [illegible] mary. As an index, it should [illegible] major and minor, concerning what [illegible] tion is presented. As a summary [illegible] the conclusions of the article [illegible] results of general interest.

Mathematical Expressions

All but the simplest mathematical [illegible] should be carefully printed in [illegible] to distinguish between capital and [illegible] Indicate clearly superscripts and [illegible] inverted carets and carets, [illegible] complicated superscripts and [illegible] repetition of a complicated exponential [illegible] senting it by some convenient [illegible] the margin Greek letters and [illegible] Use fractional exponents instead [illegible] Use the solidus (/) for fractions [illegible] will save vertical space.

References

References should appear [illegible] bered consecutively, and arranged [illegible]

[1] A. B. Smith, Phys. Rev. 41, 883 [illegible]
[2] H. Lamb, *Hydrodynamics* (Cambridge, England, 1940), sixth [illegible]

Tables

All but the simplest tabular [illegible] should be organized in tabular form [illegible] as a [illegible] of the running text. Tables may be typed [illegible] on sheets separate from the running text, [illegible] indications in the margin of the running text [illegible] where the table is to be inserted. Each table must [illegible] have a caption which will make the data in the [illegible] table intelligible without reference to the text. Avoid complicated column headings; if necessary, use symbols which are explained in the [illegible] caption.

Figures

Wherever possible figures should be planned for the width of a column of the *Physical Review* (3 inches). A convenient reduction ratio is about 2:1 or 3:1. The original drawings or photographs should therefore be in general about 6 to 9 inches wide and the lettering and symbols should be large enough on the original that when reduced [illegible] will not be less than about $\frac{1}{16}$ in. (~1.5 mm). If the reduction is 3:1, the original lettering should be not less than $\frac{1}{16}$ in. high.

The process of making zinc etchings or copper halftones is a black and white photographic one. Therefore line drawings must be in *India ink* on white paper or tracing cloth. Coordinate paper is not acceptable but if used must be blue lined and the coordinate lines which are to show must be inked over.

Photographs should have maximum black and white contrast.

Plan figures to use space efficiently. Avoid wasting space, particularly at the top or bottom.

Identify on the black or other suitable place on the original drawing or photograph with [illegible] author's name and the figure number. Figures should be numbered consecutively and their approximate position indicated in the margin of the [illegible] running text. Figure captions should be typed and included with the manuscript (but as part of the figure).

Avoid round and oval photographs.

Alterations

Take great care that each manuscript is typographically accurate. A limited number of alterations in proof are unavoidable, but the cost of making extensive alterations after the article has been set in type will be charged to the author.

Send all correspondence concerning papers in the process of publication should be addressed to the Publication Manager, American Institute of Physics, 57 East 55 Street, New York 22, New York.

THE
PHYSICAL REVIEW

A journal of experimental and theoretical physics established by E. L. Nichols in 1893

SECOND SERIES, VOL. 94, NO. 1 APRIL 1, 1954

Positive Point-to-Plane Corona Studies in Air*

M. MENES† AND L. H. FISHER
Department of Physics, College of Engineering, New York University, University Heights, New York, New York
(Received November 13, 1953)

Formative time lags for the development of the positive point-to-plane corona in dry air were measured oscillographically at pressures ranging from atmospheric to a few centimeters of Hg. Studies with a photomultiplier tube show that the observed formative lags are associated with a filamentary streamer type of corona. These corona formative lags are of the order of 10^{-7} sec even near threshold and vary much more slowly with overvoltage than do uniform field formative lags in air. The results indicate that no long buildup process is associated with the formation of the filamentary streamer type of corona in air, and in particular rule out any cathode secondary mechanism from playing a role in the formation. Near atmospheric pressure, with the experimental conditions used, the corona formative time lags were often too short to be resolved from the statistical scatter; when resolvable they were found to be too long to be ascribed solely to a single transit time of the initiating electron avalanche across the high field region of the gap. The results therefore do not preclude a fast buildup process in the gas preceding streamer formation.

Threshold measurements on both impulse and dc corona indicate that the steady glow type of corona has a different threshold than the streamer type. No formative lag data on the steady glow corona were obtained.

I. INTRODUCTION

THE clarification of the physical processes active in the positive and negative point-to-plane corona in air (and in other gases) has been carried out in recent years by Loeb and by workers in his laboratory. In particular, one of the important processes occurring in the positive corona is believed to be active in the uniform field breakdown in air near atmospheric pressure. The present study was undertaken to investigate this point.

Earlier studies of the positive point corona in air have shown it to consist of two basic forms: a glow about the point, or thin filamentary streamers extending from the point.[1–5] The glow about the point may be associated with either a steady gap current (steady glow corona) or with a fluctuating current (burst pulse glow corona). The filamentary streamers[6] are associated with a gap current and a luminosity that rise in a very short time (10^{-7} sec).[7] These filamentary streamers have been explained by the streamer mechanism.[1–3,8,9] The streamer mechanism is described as a very rapid extension of ionization from the head of an electron avalanche by means of photons in the short ultraviolet. These photons liberate electrons in the gas and the latter form secondary electron avalanches. A strong distortion of the gap field by the space charge of the initial avalanche is invoked to enhance the electron multiplication of the secondary avalanches, and to guide the propagation of the discharge along a well defined channel. In the positive corona, filamentary streamers on their way to the cathode reach a region of such low electric field that their progress is inhibited.

* Supported by the U. S. Office of Naval Research and the Research Corporation. For preliminary reports of this work see M. Menes, Phys. Rev. **82**, 569 (1951) and M. Menes and L. H. Fisher, Phys. Rev. **84**, 1075 (1951); **86**, 134 (1952).

† Now at Westinghouse Research Laboratories, East Pittsburgh, Pennsylvania.

[1] A. F. Kip, Phys. Rev. **54**, 139 (1938); **55**, 549 (1939).
[2] G. W. Trichel, Phys. Rev. **55**, 382 (1939).
[3] L. B. Loeb and A. F. Kip, J. Appl. Phys. **10**, 142 (1939).
[4] D. B. Moore and W. N. English, J. Appl. Phys. **20**, 370 (1949).
[5] H. W. Bandel, Phys. Rev. **84**, 92 (1951).

[6] The filamentary streamers discussed here and studied in this experiment are the first streamers which appear in a corona gap when the voltage is raised. Under certain conditions, such as short gap lengths or low pressures, the first filamentary streamers to appear may cross the gap causing breakdown.
[7] W. N. English, Phys. Rev. **77**, 850 (1950).
[8] We designate the luminous filaments observed in the positive point corona as "filamentary streamers" and the mechanism postulated to explain them as the "streamer mechanism" or simply streamer.
[9] L. B. Loeb, *Fundamental Processes of Electrical Discharge in Gases* (John Wiley and Sons, Inc., New York, 1939), p. 527.

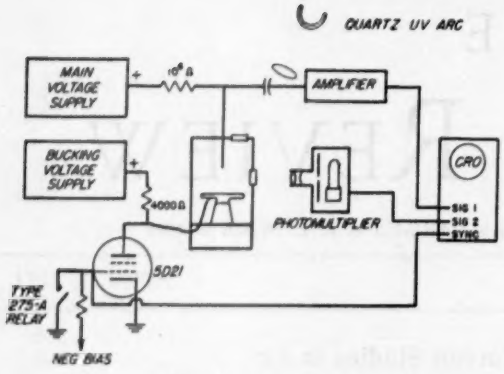

FIG. 1. Block diagram of apparatus.

Loeb[9] suggested that a similar filamentary streamer develops in the uniform field breakdown, and that due to the uniformity of the field the filamentary streamer reaches the cathode and leads to breakdown.[10] Raether[11] came to almost identical conclusions from a study of cloud track pictures of incomplete breakdowns in uniform fields.

One of the principal features of the description of the uniform field breakdown by the streamer mechanism is that it explains the extremely rapid breakdowns (10^{-7} sec and less) observed with overvolted gaps. However, recent experiments with very slightly overvolted plane parallel gaps in air have revealed formative time lags of the order of 10^{-5} and even 10^{-4} sec.[12] These formative time lags are much too long to be in accord with a breakdown theory in which a filamentary streamer follows the first electron avalanche. A modification of the theory seems necessary at low overvoltages wherein a filamentary streamer occurs only after an adequate space charge has been built up after many successive electron crossings. The experimental data indicate that this buildup takes place through a Townsend type of discharge involving photoemission of electrons at the cathode as a secondary mechanism.[13]

Similar formative time lag measurements with impulse voltages very close to threshold were undertaken for the positive corona to see whether the corona discharge near threshold is also preceded by a long buildup time. These studies were carried out to determine what processes are active in the formation of the positive point corona discharge, and in particular to ascertain the role of the streamer mechanism in this discharge.

II. APPARATUS AND EXPERIMENTAL PROCEDURE

The corona gap consisted of a plane circular brass cathode of 11-cm diameter with a polished tungsten needle forming the positive point. Points having radii of curvature of 0.007, 0.02, and 0.03 cm were used with electrode separations of 0.5, 1.0, and 1.5 cm. The gap was enclosed in a cylindrical brass chamber of 14-cm diameter and 12-cm length. A quartz window permitted irradiation of the cathode with ultraviolet light and a second window was used for observation of the discharge. The air admitted to the chamber was dried chemically and passed over a liquid air trap. Pressures of 700, 500, 300, 200, 100, 50, and 30 mm of Hg were used with each gap geometry, the chamber being evacuated and refilled for each pressure.

The measurement of formative time lags was carried out by suddenly applying a voltage to the corona gap, and measuring oscillographically the time lag of the resulting corona current pulses. Continuous ultraviolet illumination of the cathode provided initiating electrons. Measurements of gap current *vs* voltage were made with steady applied voltages up to threshold for all gap geometries and pressures for three intensities of ultraviolet illumination. The light emitted by the discharge under both dc and impulse conditions was observed visually, and oscillographically by means of a photomultiplier tube so arranged that it could "see" any desired part of the gap.

A block diagram of the system is shown in Fig. 1. Because of difficulty involved in switching the full required gap voltage, use was made of an approach voltage. The main voltage was obtained from a power supply with a stability of one part in 5000. This main voltage is sufficient to cause a discharge, the discharge being prevented from occurring by a positive bucking voltage applied to the cathode. The discharge is initiated when the bucking voltage is suddenly shorted out. The dynamic drop of the switching tube (type 5D21) depends on the value of the bucking voltage. This dynamic drop was measured oscillographically and found to be 55 (±15 volts) for the generally used bucking voltage of 1000 volts. However, the time lag data show that this dynamic drop is reproducible to within three volts. The time to switch from the approach voltage (difference voltage) to within five volts of the final voltage was observed to be of the order of 0.03 microsecond.

The current pulses resulting from the corona discharge were amplified, delayed by 0.3 microsecond and displayed on an oscilloscope whose sweep was triggered by the switching tube. The switching tube also couples a small voltage pulse to the amplifier through the capacity of the gap. This pulse served as a time reference mark

[10] For a detailed description of the method by which the streamer leads to breakdown, see L. B. Loeb and J. M. Meek, *The Mechanism of the Electric Spark* (Stanford University Press, Stanford, 1941), p. 39.

[11] H. Raether, Arch. Elektrotech. **34**, 49 (1940); Z. Physik **117**, 375, 524 (1941); Ergeb. exakt. Naturw. **22**, 73 (1949).

[12] L. H. Fisher and B. Bederson, Phys. Rev. **81**, 109 (1951). The existence of long formative lags in uniform field breakdown of air has been confirmed by H. W. Bandel, Washington Gaseous Electronics Conference, October, 1953 (unpublished).

[13] G. A. Kachickas and L. H. Fisher, Phys. Rev. **88**, 878 (1952). See also F. Llewellyn Jones and A. B. Parker, Proc. Roy. Soc. (London) **A213**, 185 (1952).

from which the time lags of the discharge were measured. The over-all rise time of the amplifier circuit was 0.03 microsecond, and the full gain was of the order of 10^4. This permitted current pulses as small as 10^{-6} amp to be observed across an input resistor of 1000 ohms.

Several runs with a bucking voltage of 500 instead of 1000 volts were carried out; after correction for the slightly different switching tube drop, both the threshold and the time lags were in good agreement with those obtained with the full bucking voltage.

III. EXPERIMENTAL RESULTS AND DISCUSSION

Threshold voltages were obtained for both the dc and impulse positive point corona. The dc threshold (sometimes called the onset voltage) is defined as the lowest voltage at which a steady corona discharge with

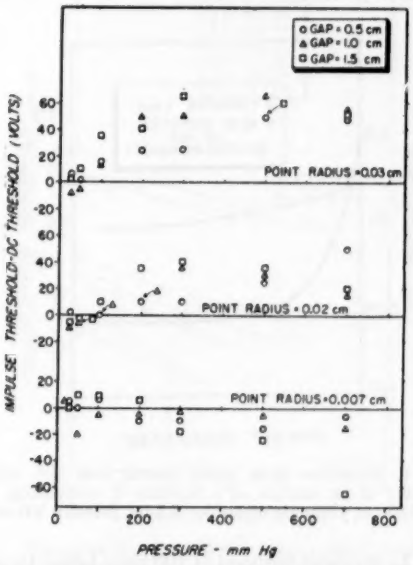
GAP = 0.5 cm
GAP = 1.0 cm
GAP = 1.5 cm
POINT RADIUS = 0.03 cm
POINT RADIUS = 0.02 cm
POINT RADIUS = 0.007 cm
IMPULSE THRESHOLD-DC THRESHOLD (VOLTS)
PRESSURE - mm Hg

FIG. 2. Voltage difference between the impulse and dc thresholds as a function of pressure for various gap geometries.

constant current maintains itself in the absence of ultraviolet illumination of the cathode. With strong ultraviolet illumination the current-voltage curves are continuous throughout the whole voltage region studied and no sharp threshold is observed. In order to determine the dc threshold, very slight ultraviolet illumination was used to initiate the corona. With such low ultraviolet illumination, there is a region of some ten to twenty volts below the dc threshold where the corona current fluctuates. Because it is difficult to establish a sharp demarcation between this region of fluctuating corona (burst pulse corona) and the region of steady corona, there is an estimated uncertainty of at most five volts in the dc threshold.[14]

[14] Bandel (see reference 5) has also observed this difficulty in determining the dc positive corona threshold in air.

The impulse threshold was taken as the lowest impulse voltage at which discharge pulses could be seen on the oscilloscope. As already mentioned, the absolute accuracy of the impulse voltage is of the order of ± 15 volts. The dc and impulse thresholds were often found to differ by as much as 60 volts; this is in excess of any known experimental error. This difference is plotted in Fig. 2 as a function of pressure for all gaps studied. As may be seen, neither threshold is consistently higher than the other.

A study of the impulse corona with the photomultiplier indicates that the discharge which causes the gap current pulses observed on the oscilloscope is of the filamentary streamer type; visual observation of the steady corona shows it to consist of a glow about the point. It thus appears that the dc and impulse thresholds as determined in this experiment are the threshold voltages for the steady glow corona and the filamentary streamer type of corona, respectively.

The question remains as to why nothing was observed on the oscilloscope for impulse voltages higher than the glow corona threshold but lower than the filamentary streamer threshold. The glow-corona gap current near threshold ranged from 2×10^{-7} to 5×10^{-7} amp. If the discharge current pulses due to the glow corona under impulse conditions are of the same magnitude, they might easily have passed unnoticed due to the inadequate sensitivity of the amplifier.

A typical set of dc current-voltage curves for one gap geometry (point radius 0.03 cm, electrode separation 1.5 cm) and various pressures is shown in Fig. 3. For simplicity, curves for only the highest value of illumination used are shown. Figure 4 is a detailed plot in the region just below threshold of the 500-mm case of Fig. 3 for the three values of ultraviolet intensity.

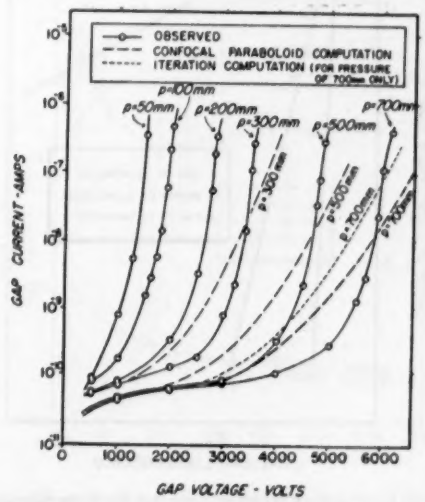

FIG. 3. Observed and computed dc current-voltage curves for one gap geometry and a range of pressures. Point radius 0.03 cm, electrode separation 1.5 cm.

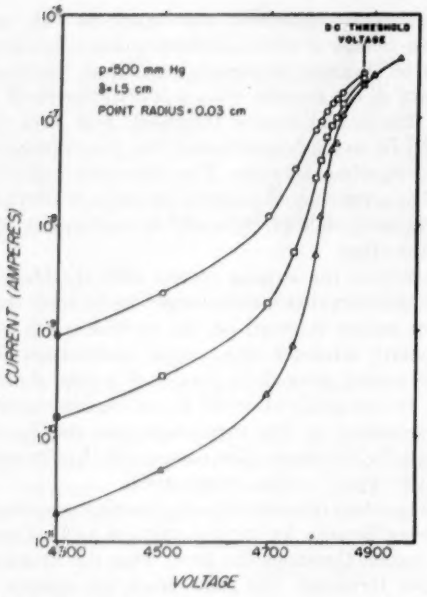

FIG. 4. Detailed plot of current-voltage curves of the 500-mm case of Fig. 3 for three values of ultraviolet intensity.

Also shown in Fig. 3 are computed current-voltage curves for pressures of 700, 500, and 300 mm Hg. These computed curves were obtained by using the field along the axis in conjunction with values of the first Townsend coefficient in air as given by Sanders.[15] For all but one of the computed curves the field was calculated approximately by regarding the gap as composed of two confocal paraboloids; the remaining computed curve is for 700-mm Hg and was obtained from gap fields calculated by an interation method given by Loeb, Parker, Dodd, and English.[16]

Comparison of the observed gap currents with the computed gap currents show three main features which were found in all cases studied:

(a) In the voltage region from 1000 volts below threshold to about 100 volts below threshold, the observed gas multiplication is much less than the computed electron multiplication. This may be due to the attachment of electrons to oxygen molecules or to the inapplicability of the Townsend ionization function in nonuniform fields.[17]

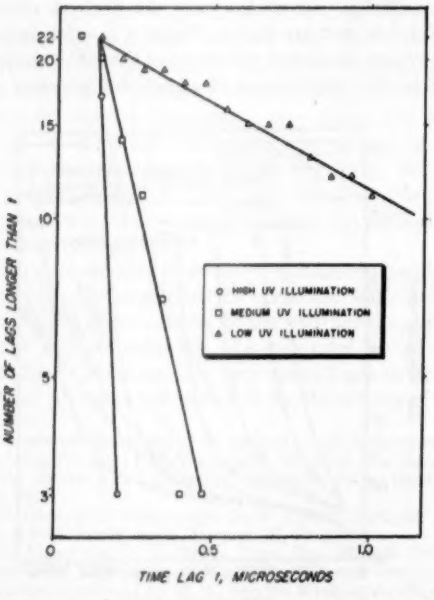

FIG. 5. Laue plots of observed time lags for three intensities of ultraviolet illumination at a fixed overvoltage of 0.18 percent. Point radius 0.03 cm, electrode separation 1.0 cm, pressure 200 mm Hg. Each of the curves is for a total of 22 observations.

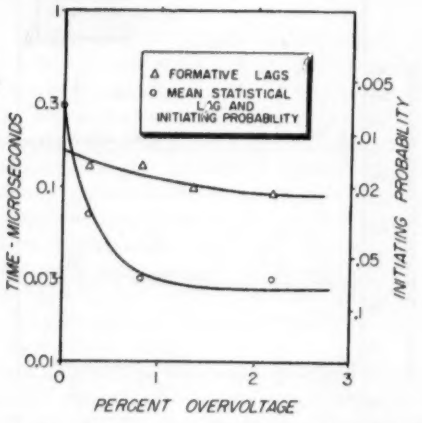

FIG. 6. Formative time, mean scatter time and initiating probability of an electron as a function of overvoltage. Point radius 0.03 cm, electrode separation 1.5 cm, pressure 300 mm Hg.

(b) In the neighborhood of 100 volts below threshold there is a sudden upswing in the observed gap current. This upswing is much sharper than could be expected from the shape of the computed curve, and must thus be attributed to a secondary mechanism.

(c) In the vicinity of the threshold voltage, the current-voltage curve becomes less steep and tends to

[15] F. H. Sanders, Phys. Rev. **41**, 667 (1932). When necessary, at the very high field strengths, use was made of the ionization coefficient for nitrogen as measured by D. Q. Posin, Phys. Rev. Rev. **50**, 650 (1936).

[16] Loeb, Parker, Dodd, and English, Rev. Sci. Instr. **21**, 42 (1950).

[17] Difficulty has been encountered in the use of the first Townsend coefficient in nonuniform fields. This has been studied in hydrogen by L. H. Fisher and G. L. Weissler, Phys. Rev. **66**, 95 (1944), by P. L. Morton, Phys. Rev. **70**, 358 (1946), and in hydrogen and air by G. W. Johnson, Phys. Rev. **73**, 284 (1948). These experiments show that in nonuniform fields, more ionization is produced than is calculated from Townsend's ionization function except for one case in air. At this time, it does not seem possible to decide why our calculated curves are above the observed ones.

flatten out and the gap current is no longer proportional to the primary current emitted from the cathode. This limiting effect is generally attributed to the positive ion space charge in the gap.

Repeated time-lag measurements for a given geometry, pressure, and overvoltage gave a scatter; this scatter decreased with increasing ultraviolet light and increasing overvoltage. Because of the scatter, twenty five measurements of the time lag were made at each setting. Although an analysis by means of Laue plots[18] for various intensities of illumination showed the scatter to be due to the random appearance of initiating electrons, it was not considered desirable because of possible space charge effects to increase the ultraviolet intensity to eliminate the scatter. A typical Laue plot

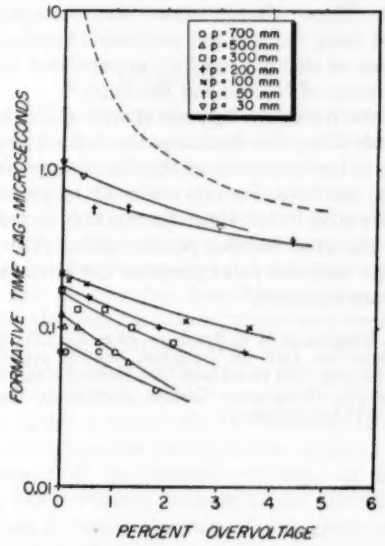

FIG. 7. Formative time lags of the positive point corona as a function of overvoltage for one gap (point radius 0.03 cm, electrode separation 1.5 cm) and a range of pressures. Also shown by the dashed line are formative lags as found by Fisher and Bederson (see reference 12) for a plane parallel gap of one centimeter in air.

for three illuminations under otherwise identical conditions (point radius 0.03 cm, gap length 1.0 cm, pressure 200 mm Hg) is shown in Fig. 5. The formative time lags were obtained from the intercepts of the Laue plots.

Comparison of the mean scatter time of the observed lags with the initial photoelectric current emitted from the cathode makes possible an estimate of the probability which a single electron has of initiating a filamentary streamer. Figure 6 shows the formative time lag, the mean scatter time, and the initiating probability as a function of overvoltage for one gap geometry (point radius 0.03 cm, electrode separation 1.5 cm) at a pressure of 300 mm of Hg. The initiating probabilities

[18] M. von Laue, Ann. Physik **76**, 261 (1925).

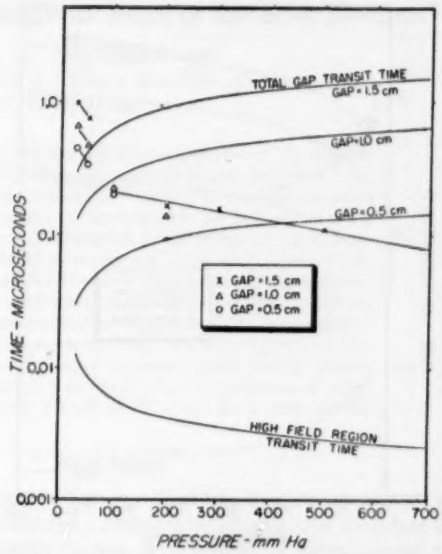
TOTAL GAP TRANSIT TIME
GAP = 1.5 cm
GAP = 1.0 cm
GAP = 0.5 cm
x GAP = 1.5 cm
Δ GAP = 1.0 cm
o GAP = 0.5 cm
HIGH FIELD REGION TRANSIT TIME
TIME - MICROSECONDS
PRESSURE - mm Hg

FIG. 8. Threshold formative lags of the positive point corona as a function of pressure for a point radius of 0.03 cm and electrode separations of 0.5, 1.0, and 1.5 cm. Also shown are computed electron transit times at threshold for the whole gap and for the high field region of the gap.

for an electron at other gap geometries and pressures fall in the same general range.

Formative time lags for one gap geometry (point radius 0.03 cm, electrode separation 1.5 cm) are shown in Fig. 7, where they are plotted as a function of

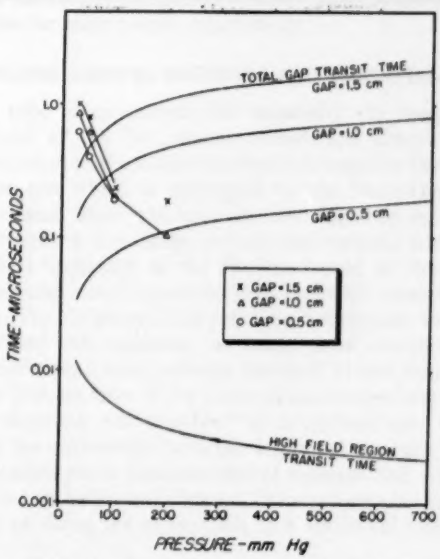
TOTAL GAP TRANSIT TIME
GAP = 1.5 cm
GAP = 1.0 cm
GAP = 0.5 cm
x GAP = 1.5 cm
Δ GAP = 1.0 cm
o GAP = 0.5 cm
HIGH FIELD REGION TRANSIT TIME
TIME - MICROSECONDS
PRESSURE - mm Hg

FIG. 9. Threshold formative lags of the positive point corona as a function of pressure for a point radius of 0.02 cm and electrode separations of 0.5, 1.0, and 1.5 cm. Also shown are computed electron transit times at threshold for the whole gap and for the high field region of the gap.

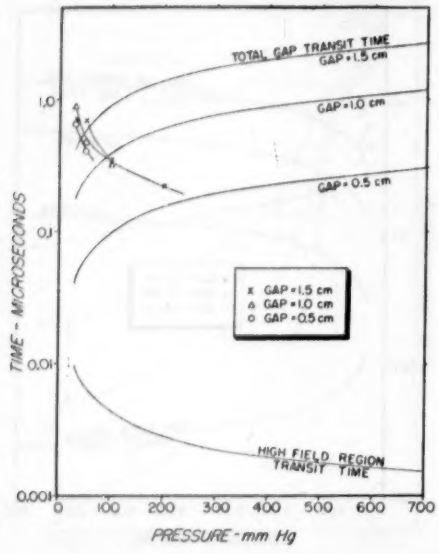

FIG. 10. Threshold formative lags of the positive point corona as a function of pressure for a point radius of 0.007 cm and electrode separations of 0.5, 1.0, and 1.5 cm. Also shown are computed electron transit times at threshold for the whole gap and for the high field region of the gap.

percent overvoltage. This particular gap geometry was the only one for which formative time lags were obtained at all pressures. For the other gaps, formative lags were obtained only at the lower pressures; at pressures near atmospheric the statistical scatter was generally so large that it masked the formative lag. It was, however, possible to set an upper limit to the formative lag from the shape of the statistical distribution; this limit is of the order of 0.1 microsecond.

Also plotted in Fig. 7 for comparison purposes are the formative lags for a plane parallel gap of one centimeter in air as given by Fisher and Bederson.[12] The corona formative lags do not become longer and longer as threshold is approached (the plane parallel gap formative lags do show this behavior), but tend toward a definite limiting value at threshold. These threshold formative lags for the various gap geometries are shown plotted as a function of pressure in Figs. 8, 9, and 10. Also plotted in these figures are electron transit times, both for the whole gap, and for the region of the gap where electron multiplication is appreciable (field strength to pressure ratio greater than 30 v/cm mm Hg). These transit times were computed at threshold using the confocal paraboloid approximation and values of electron mobility extrapolated from the measurements of Nielsen and Bradbury.[19]

Since the formative lags are shorter than the total gap transit time, this eliminates the cathode as playing any role in the formation of the filamentary streamer. However, the formative lags are much longer than the high field region transit time. There is thus an indication that an ionization buildup process taking place wholly in the gas near the point precedes the formation of a filamentary streamer.[20]

[19] R. A. Nielsen and N. E. Bradbury, Phys. Rev. **51**, 69 (1937).

[20] Evidence for such an ionization buildup preceding the streamer has also been found with photomultiplier techniques by M. R. Amin, Washington Gaseous Electronics Conference, October, 1953 (unpublished).

An Experimental Measurement of the Gyromagnetic Ratio of the Free Electron*

W. H. Louisell,† R. W. Pidd, and H. R. Crane
Harrison M. Randall Laboratory of Physics, University of Michigan, Ann Arbor, Michigan

(Received December 23, 1953)

The gyromagnetic ratio of the free electron is measured by a method which is an extension of the classical double-scattering experiment. A magnetic field is interposed between the first and second scattering foils, whose direction is parallel to the path followed by the electrons. The electron spins precess in the magnetic field, resulting in a rotation of the plane of maximum asymmetry, as observed after the second scattering event. In the experiment reported, the rotation is approximately 1800 degrees. In the motion of the electron between the two scatterers the small lateral component of velocity gives rise to a "cyclotron" motion whose frequency is, theoretically, the same as the spin precession frequency to within about one part in a thousand. The cyclotron motion, therefore, furnishes a convenient reference frequency, but it also introduces problems in that it causes the asymmetries which have their origin in geometrical misalignment, finite aperture, etc., to follow the rotation of the spin asymmetry. By comparing all measurements made with the foils of high atomic number with measurements made with an aluminum foil of equal scattering power, and by further precautionary procedures and cross checks, the spin asymmetry is separated from asymmetries of other origin. The result, for 420-kev electrons and gold scatterers, is $g=2.00\pm0.01$. Plans for a more precise measurement are mentioned.

INTRODUCTION

WHILE many experiments of great precision are available for the determination of the magnetic moment and the gyromagnetic ratio for the electron when bound in an atom, no such fortunate situation exists in regard to the measurement of these properties for the free electron. In fact, it has been only within recent years that the existence of a magnetic moment in the free electron has been demonstrated experimentally, although, of course, there were very strong theoretical reasons for believing that it was present. No experiment, prior to the one to be reported in this paper, has yielded a quantitative value for the moment, except in order of magnitude. Over the past half-dozen years a new interest in the problem of making a precise measurement of the magnetic moment of the free electron has developed, because of the discovery that in the case of bound electrons, the magnetic moment differs from the Bohr magneton by about one part in a thousand. The anomaly, which first made its appearance as a slight discrepancy between experimental and theoretical values in certain energy levels in atoms,[1–3] is now firmly and accurately established.[4–6] The theory, which connects the discrepancy with a correction to the magnetic moment of the electron,[7] has been worked out in detail.[8–10] While it is expected that the same correction will be found to apply to the magnetic moment of the free electron, it is by no means to be considered as a foregone conclusion, and therefore there is interest in the development of experimental techniques which will be capable of the required precision. All of the existing methods and proposals for measuring the magnetic moment or the g factor for the free electron should, therefore, be reappraised as to whether or not they have the inherent capability of attaining a precision of at least one part in a thousand, since this has become the important region, theoretically. In this paper we shall make this examination briefly, and shall then present the results of an experiment which, although it does not attain the accuracy mentioned, at least constitutes an opening wedge and furnishes possibilities for more precise experiments.

EXPERIMENTAL METHODS AND PROPOSALS

A type of experiment for measuring the magnetic moment of the free electron which has always had prominence in the literature, but in a negative fashion, is the one which is analogous to the Stern-Gerlach experiment. Bohr[11] pointed out that since in such an experiment a knowledge of both the moment and the classical trajectory of the electron would be implied, the scheme would encounter difficulties for reasons expressed by the uncertainty principle. Subsequent writers presented this argument as being more sweeping in character than was, perhaps, justified. It was taken to mean that no form of the Stern-Gerlach experiment for free electrons, was possible.[12] It is realized now that, while the uncertainty principle argument does preclude the simultaneous measurement of moment and trajectory for an individual electron, there remains the possibility of doing the experiment in a statistical fashion,

* This work was supported by the U. S. Atomic Energy Commission.

† Now at Bell Telephone Laboratories, Murray Hill, New Jersey.

[1] Nafe, Nelson, and Rabi, Phys. Rev. 71, 914 (1947).
[2] W. E. Lamb and R. C. Retherford, Phys. Rev. 72, 241 (1947).
[3] P. Kusch and H. M. Foley, Phys. Rev. 72, 1256 (1947).
[4] J. E. Nafe and E. B. Nelson, Phys. Rev. 73, 718 (1948).
[5] P. Kusch and H. M. Foley, Phys. Rev. 74, 250 (1948).
[6] Koenig, Prodell, and Kusch, Phys. Rev. 88, 191 (1952).
[7] G. Breit, Phys. Rev. 72, 984 (1947).
[8] J. Schwinger, Phys. Rev. 73, 416 (1948).
[9] J. Schwinger, Phys. Rev. 76, 790 (1949).
[10] R. Karpus and N. Kroll, Phys. Rev. 77, 536 (1950).
[11] See W. Pauli, *Handbuch der Physik* (J. Springer, Berlin, 1933), Vol. 24, Part 1, p. 242.
[12] For example, see N. F. Mott and H. S. W. Massey, *Theory of Atomic Collisions* (Oxford University Press, London, 1949), pp. 65, 69, 74.

that is, by sending a large number of electrons through the apparatus and by attempting to use the detailed line shape to reveal the effects of the magnetic moment. The thing which the uncertainty principle argument does show to be inescapable is that the displacement, or splitting, of the line that one would be seeking to find would be smaller than the line breadth. While the extraction of information from the shape of a line has been done successfully in many instances, such an attack appears particularly unpromising in connection with the electron moment problem. Its solution could at most give an indication of the presence of the moment, and it would certainly not give the 0.1 percent accuracy which is now sought, for comparison with the recent theory.

The other experiment which is well known, and which is the only one to date which has given positive results, is the double-scattering experiment. This method depends upon the fact, shown theoretically by Mott[13] in 1929, that a beam of electrons undergoing single nuclear scattering is partially polarized in a direction normal to the plane defined by the incident beam and the scattered direction. A second scattering process exhibits an aximuthal asymmetry in intensity, if measured in the same plane. It is not possible to state here the set of conditions for which the asymmetry is expected to be a maximum, because calculations have been made only for one angle of scattering: 90 degrees. The asymmetry increases monotonically with Z but has a maximum with respect to energy. For 90-degree scattering and for $Z=80$ the optimum energy is about 150 kev, and the asymmetry 13 percent. Attempts to observe this asymmetry experimentally have been made over a long period of time,[14–19] and the results of the later experiments[17–19] show beyond doubt that an asymmetry of about the predicted magnitude exists. They are not quantitative experiments, however, in the sense of measuring the magnetic moment.

Another line of attack is based upon the magnetic resonance method and has given rise to proposals for experiments in two somewhat different forms. In both forms polarized electrons are trapped in stable orbits in a magnetic field. A radio-frequency perturbing field is then applied, and the frequency which destroys the polarization is determined. From the frequency which destroys the polarization, and the strength of the magnetic field, the value of the gyromagnetic ratio is obtained. The two methods differ in the way in which the electrons are polarized, prior to trapping, and in the way in which the presence or absence of polarization is determined after the application of the perturbing field. In the first method, electrons with an extremely sharp low-energy cutoff are sorted as to spin state by being allowed to encounter a very carefully adjusted potential hill, in the process of entering the part of the field in which they are to be trapped. Ideally, those with one spin orientation will pass and be trapped, while those with the opposite spin orientation will be rejected. Analysis, after the application of the perturbing rf, consists, again, in the sorting action of the potential hill in the process of letting the electrons escape from the trapping field. Since the sorting depends upon the exceedingly small difference which results from the spin interacting with the magnetic field, the experiment demands carefully determined electron energies and precise control of fields and potentials. An experiment along these lines was tried, without positive results, by Dicke,[20] and another one, differing in details, is now being prepared by Bloch.[21] The other form of the reso. nance method, proposed by Tolhoek,[22] but so far not tried, uses high-energy electrons, and employs double scattering as the means of polarization and analysis. The trapping procedure, with the application of the perturbing rf field, takes place between the first and second scattering events.

It should be remarked, in connection with both the proposals which involve resonance, that since the required perturbing frequency is almost identical to the cyclotron frequency, the strong coupling to the cyclotron motion might introduce serious difficulties. In order to achieve the accuracy of about one part in 10^5, which seems to be the ultimate goal of all such experiments, the motion would have to persist for the order of 10^5 cyclotron revolutions, and during this time considerable energy might be transferred from the perturbing field to the cyclotron motion. Nevertheless, the magnetic resonance methods just described are the only ones, with the exception of the proposed extension[23] of our own experiment, which have the inherent possibility of giving really quantitative results, that is, results of sufficient accuracy to reveal the correction to the electron moment.

A number of schemes have been suggested or tried which are based in one way or another upon use of aligned atoms. A very early attempt, by Myers and Cox,[24] to demonstrate polarization in an electron beam was a double-scattering experiment using magnetized iron foils as the scatterers. Fues and Hellman[25] proposed an experiment in which the polarized electrons were to be obtained by letting ultraviolet light act upon the beam of neutral, aligned atoms produced by a Stern-Gerlach apparatus. Analysis was to be accomplished by allowing the electrons to be recaptured by oriented ions, similarly derived from a Stern-Gerlach beam. The same

[13] N. F. Mott, Proc. Roy. Soc. (London) **A124**, 425 (1929).
[14] E. G. Dymond, Proc. Roy. Soc. (London) **A145**, 657 (1934).
[15] H. Richter, Ann. Physik **28**, 533 (1937).
[16] K. Kikuchi, Proc. Math. Phys. Soc. Japan **22**, 805 (1940).
[17] Shull, Chase, and Myers, Phys. Rev. **63**, 29 (1943).
[18] K. Shinohara and N. Ryu, J. Phys. Soc. Japan **5**, 119 (1950).
[19] E. Trounson and J. A. Simpson, Phys. Rev. **63**, 55 (1943).
[20] R. H. Dicke (private communication).
[21] F. Bloch, Physica **19**, 821 (1953).
[22] H. A. Tolhoek and S. R. DeGroot, Physica **17**, 17 (1951).
[23] Crane, Pidd, and Louisell, Phys. Rev. **91**, 475 (1953).
[24] F. E. Myers and R. T. Cox, Phys. Rev. **34**, 1067 (1929).
[25] E. Fues and H. Hellman, Physik. Z. **31**, 465 (1930).

authors[25] have suggested that photoelectrons, ejected from the aligned atoms of a magnetized iron foil, might be polarized. The analysis of polarization through the measurement of the transmission or scattering of the electron beam by magnetized iron foil has been proposed, and was, in fact, used, in the experiment of Myers and Cox.

Finally, there are several suggestions for means of obtaining polarized electrons which have not been developed at all, but which might be worthy of further consideration. It appears that it is feasible to align nuclei in a strong magnetic field at near absolute zero temperature. Beta rays emitted from nuclei so aligned might be polarized,[26] provided the kind of nuclear transition were properly chosen. Also in connection with beta disintegration, there is a possibility which does not require the prealignment of the nuclei. Where a beta ray is followed by a gamma ray, the spin orientation of the beta ray could be expected to be correlated with the directions of emission of the beta ray and gamma ray, provided, again, that a nucleus having favorable type of transition were selected for observation. The possibility of finding cases in the photoelectric effect in which the polarization of the photoelectron is correlated with the polarization of the incident light should be worth investigating.

ROTATION OF THE PLANE OF POLARIZATION IN THE DOUBLE-SCATTERING EXPERIMENT

The extension of the double-scattering experiment which we have introduced[23,27] is to interpose between the first and second scatterers a magnetic field, parallel to the path between the scatterers. This causes the electron to precess, and rotates the plane of polarization so that the plane of maximum asymmetry after the second scattering no longer coincides with the plane of the first scattering. By measuring the angle of rotation and knowing the magnetic field, the electron energy, and the distance, the gyromagnetic ratio for the electron may be found. If the magnetic field is intense enough and the path long enough to produce many revolutions of the plane of polarization, the measurement may be quite precise. The precision with which the plane of polarization may be ascertained is independent of the number of revolutions it has made between the scatterers. Therefore, the relative precision improves in direct proportion to the number of revolutions.

In the experiment to be reported here, five revolutions of the plane of polarization were produced, and the probable error in the resulting value for the g factor was $\pm\frac{1}{2}$ percent. Had it been possible to have more revolutions, the g factor could have been determined to a correspondingly greater accuracy, without the necessity of any greater absolute precision in the determination of the plane of polarization.

FIG. 1. The "cyclotron" or "beta-ray spectrometer" motion, shown for one focal length and for four initial directions of the lateral component of velocity. Left: looking along the magnetic field direction. Right: side views of the same paths. The arrows on one of the paths indicate the precession of the spin direction.

A fact which has a dominating influence upon the design of the experiment is that the orbital rotation frequency or "cyclotron frequency" of the electron in the magnetic field differs from the frequency of precession of the spin direction by the higher-order correction terms only, or by about one part in a thousand. The two frequencies are

$$\nu_c = eH/2\pi mc,$$
$$\nu_s = (eH/4\pi mc)g,$$

where

$$g = 2(1+\alpha/2\pi+\cdots).$$

The relativistic change in mass enters in the same way in the two equations. It has been shown that the above equation for the spin precession frequency (with g set equal to 2 exactly) results alike from semiclassical considerations and from Dirac theory.[28] Since one part in a thousand lies beyond the degree of precision of the present experiment, we must proceed on the assumption that the cyclotron and spin rotations are not separable, and we may use semiclassical concepts to describe the motion.

The cyclotron motion results only from the lateral component of momentum of the electron relative to the solenoid axis and so depends upon the finite angular spread which is admitted by the system of diaphragms. We are familiar with this motion, of course, in the solenoid type of beta-ray spectrometer. A diagram showing the motion, with the spin direction indicated by small arrows on one of the paths, and with the cyclotron motion exaggerated, is given in Fig. 1. The first consequence of the motion described, as far as this experiment is concerned, is the fact that all asymmetries in the beam, whether they are associated with the spin or not, rotate around together. Therefore, the mere fact that an asymmetry is observed which has the expected angle of rotation does not in itself prove that a polarization effect is being observed. The fact that it is a rotation of polarization that is being observed has, then, to be proved in other ways.

The second consequence of the type of motion we are concerned with is the fact that the beam comes to a focus at the end of each length corresponding to a cyclotron revolution. This means that the size and structure of the spot incident upon the analyzer foil,

[26] H. A. Tolhoek and S. R. DeGroot, Physica **17**, 81 (1951).
[27] Louisell, Pidd, and Crane, Phys. Rev. **91**, 475 (1953).
[28] K. M. Case and H. Mendlowitz, Phys. Rev. **91**, 475 (1953).

or its defining diaphragm, changes periodically, as the total angle of rotation is increased. This raises problems in comparing directly the results for different total angles of precession, unless they differ by an integral number of revolutions.

Neither of the above two consequences of the cyclotron motion is in any way fatal to the method, but nevertheless, the precautions and cross checks which have to be made on their account constitute a major part of the effort of the experiment.

All of the results of the cyclotron motion are not bad. The beta-ray spectrometer type focusing, which comes with the cyclotron motion, is of vital importance in preserving the intensity of the beam. The entire beam which is admitted to the system by the diaphragms at the polarizer end of the solenoid is transmitted to the analyzer, regardless of the distance. Without this advantage, the experiment would not have been possible. Also, the fact that the spin precession and cyclotron frequencies are so nearly the same contains an advantage in that, experimentally, the one can be measured directly with reference to the other, and the resulting value of the g factor, therefore, does not depend upon accurate measurements of the magnetic field and the electron energy.

APPARATUS

The general layout of the experiment is shown by the schematic diagram in Fig. 2. With this as a guide, the various components of the apparatus will be described, and the important problems in the design of the system will be discussed.

Electron Accelerator

The electron beam was obtained from the injector system of the Michigan synchrotron. This was a 3-gap accelerator tube, powered by a Cockroft Walton type condenser-rectifier voltage multiplier. The electron beam from this apparatus had 420-kev energy, regulated to ± 0.8 kev. The electron moment experiment was set up alongside the synchrotron, and the electron beam was borrowed nightly. The change-over was made simply by deflecting the beam, by means of a small magnet, into a side pipe which led to the electron moment apparatus, and by making a minor circuit change to render the beam continuous rather than pulsed. The necessity of using the synchrotron injector in the form in which it existed, with a minimum of disturbance to the synchrotron program, is what dictated the value of the electron energy, 420 kev, which was used in the electron moment experiment. We call attention to the reason for the choice because, as is well known, 420 kev is considerably above the energy which should theoretically give the maximum asymmetry in the double-scattering experiment.

Solenoid

The magnetic field between the scatterers was provided by solenoid consisting of a single layer of $\frac{1}{4}$-in. copper tubing wound on a 6-in. brass tube, 30 ft long. The current was furnished by a motor generator and was maintained constant to 0.1 percent by means of an electronic regulator circuit. The resistance of the coil was about 1 ohm, and the current used in the experiments to be reported was about 58 amp. Cooling was

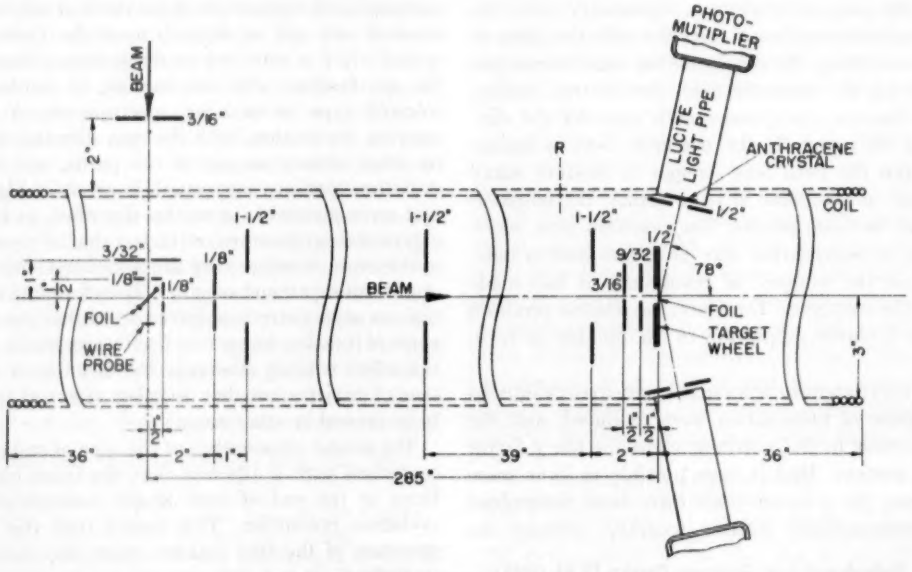

FIG. 2. Schematic diagram of the apparatus.

accomplished by water flowing through the copper tubing.

Earth's Magnetic Field Compensating Coils

The earth's magnetic field was compensated by a set of four rectangular coils, each 1 ft×30 ft, mounted outside the solenoid in such a way that the wires made the edges of a 1-×1-×30-ft rectangular parallelopiped. Each coil contained 20 turns and the currents used were the order of 1 amp, supplied from storage batteries.

Scattering Foils

The first scattering foil (polarizer) was supported in a ring of $\frac{1}{2}$-in. inside diameter. Its plane was at 45 degrees to both the incident beam and the solenoid axis, and it was in the transmission position. Gold foil (0.135 mg/cm^2) was always used for the polarizer. At times it was removed so that measurements of the intensity of scattering from the edges of the ring could be made. The analyzer foil was mounted so that the beam was incident normally upon it. The foil holder in this case was multiple, consisting of a disk with four apertures, one open and the others covered by foils of gold, 0.135 mg/cm^2, silver, 0.23 mg/cm^2, and aluminum, 0.67 mg/cm^2. The disk could be rotated from outside the vacuum, so that rapid changes from one to another could be made for intercomparison.

There can be no doubt that the foils were thin enough so that true single scattering was obtained. For the gold foil, considering normal incidence, the angle for which $\pi p^2 nt = 1$ is approximately 2 degrees. (p is the classical impact radius, n is the number of atoms per cc, and t is the thickness of the foil.) According to Wenzel's criterion, it is only necessary that the scattering angle (90° and 78° in our case) be several times the angle for which $\pi p^2 nt = 1$. The silver and aluminum foils were about the same, with respect to the criterion. While the foils were much thinner than necessary from the standpoint of insuring single scattering, they were thick enough to give an adequate counting rate after the two scattering processes, and the thicknesses were chosen mainly for the latter consideration. The counting rate at each of the scintillation counters was about 100/sec. This was obtained with a current of approximately one microampere incident upon the polarizer foil. The ratio is consistent with the value obtained using single-scattering theory and the apertures in the apparatus.

Counters

Two scintillation counters were used to detect the electrons scattered from the analyzer. Each consisted of a No. 5819 photomultiplier, a Lucite light pipe 4 in. long, and an anthracene crystal. The anthracene crystal, 5 mm thick, was about flush with the inner surface of the solenoid coil so the window of the No. 5819 was about 4 in. outside the coil. The problem here, of course, was to reduce the magnetic field in the photomultiplier, by a combination of magnetic shielding and separation by the light pipe, to a value small enough so that it would not influence the measurements. Each photomultiplier was enclosed in an iron pipe of $\frac{3}{8}$-in. wall thickness. In addition a laminated iron shield of 10 layers of 0.014-in. sheet iron was built up around the iron pipe. It was found that this amount of shielding, plus the separation provided by the light pipe, gave the required isolation. The test applied was to make the scintillation counter count by means of a gamma-ray source, and then to compare its counting rates with and without current in the solenoid.

The circuits consisted of two parallel channels, each comprising a linear amplifier, pulse-height discriminator (integral type), and scaler.

Rotation of the Counter Assembly

The entire analyzer end of the apparatus, consisting of about the last $3\frac{1}{2}$ ft of the solenoid, and including the analyzer foil assembly, diaphragms, and the two opposed scintillation counters, could be rotated about the axis of the solenoid to allow the measurement of the asymmetry in the scattered intensity throughout the 360 degrees of angle about the solenoid axis. The location of the rotating joint is indicated at R in Fig. 2.

Diaphragm System

The important geometrical features of the apparatus, with the locations and diameters of the diaphragms, are shown in Fig. 2. The diaphragm outside the solenoid, which defines the entering beam, is actually above the plane of the drawing, since the entering beam bends downward in going from the edge of the solenoid to the center, across the magnetic field. The systems of small diaphragms close to the polarizer and analyzer foils serve to define a small area in the center of each foil which electrons can strike, and to prevent electrons from being scattered from the foil holders. The real aperture of the system, which we call γ, the maximum angle an electron path can make with the solenoid axis, is fixed by a $1\frac{1}{2}$-in. diameter diaphragm located at the last antinode ($\frac{1}{2}$ focal length) before the analyzer foil. When the magnetic field is set so as to give five focal lengths between polarizer and analyzer, γ is 2.25 degrees. For a given value of γ the required size and position of the diaphragm are, clearly, dependent upon the magnetic field. However, in the experiments that were carried out the field was varied through only a small range (cyclotron rotations of 1781, 1814, and 1847 degrees). A single compromise position for the diaphragm was used which maintained γ constant to within 10 percent.

Shielding

The fact that over 24 ft of distance separated the analyzer foil and counters from the polarizer and the

electron source greatly simplified the shielding problem. The two ends of the solenoid were in different rooms, separated by a concrete wall 3 ft thick. In addition, a patch of lead ½ in. thick was placed on the wall to shadow the counters from the radiation originating in the electron accelerator. The signal-to-background ratio, which will be explained later, was approximately 10 to 1.

ALIGNMENT, ADJUSTMENT, AND PRELIMINARY TESTS

Alignment

The diaphragms defining the beam incident upon the polarizing foil were aligned by using the wire probe, shown in Fig. 2. By this means the transmitted beam was located and made to fall upon the center of the foil. Because of the bending of the beam by the magnetic field, the alignment had to be adjusted for each value of the field. The diaphragms between foils were aligned by optical means. A filament was placed at the position of the polarizer foil, and the holes in the diaphragms were reduced to pinholes by means of annular fillers. The actual alignment was then done by eye.

The preliminary alignment of the magnetic field was done as follows. A small electron gun, giving a beam of about 1000-ev energy was placed on the solenoid axis at the position of the polarizing foil and a fluorescent screen was placed at the position of the analyzer foil. At this low electron energy the spot on the fluorescent screen was essentially the same size as the source, and the beam followed quite exactly the magnetic lines of force. The currents in the four correcting coils were simply adjusted until the spot fell in the center of the analyzing foil. This test showed that the centers of the two foils were on the same line of force; it did not show that the line of force was a straight line. The experiment was not highly sensitive to the latter consideration, since the defining diaphragms were located near the two ends only. The solenoid and correcting coils were mechanically straight, and it was assumed that the field was sufficiently straight.

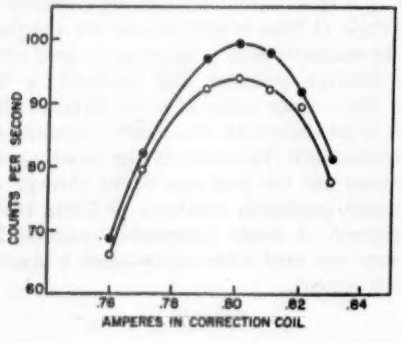

FIG. 3. Typical plot used for centering the beam on the analyzer foil. Circles and dots refer to the two counters. Cyclotron rotation, 1814 degrees.

The final alignment was made by using the 420-kev doubly scattered beam itself. By making a plot of the counting rates in the two counters while the beam was slowly moved by means of one of the pairs of earth's field correcting coils, the setting giving the maximum current at the analyzer foil could easily be found. Individual plots of this kind were made for the vertical and horizontal directions, after the apparatus had been otherwise aligned for each value of magnetic field. One of the plots is shown in Fig. 3.

As expected, the maxima were sharper when the focal spot was small (near a focal condition) than when it was off focus. There was, however, no difficulty in setting the correction coils for the maxima at any of the three values of magnetic field used.

Preliminary Tests of the Counting System

An important method by which background was reduced was the use of a pulse-height discriminator, which, as far as possible, admitted only those pulses due to electrons which had not suffered energy losses. To determine how well this could be done, two tests of the system were made. In the first, the 0.66-Mev internal conversion line of Cs^{137} was resolved. The Cs source was mounted on a thin Zapon film which was then coated with a thin aluminum layer. Runs were made with one counter, at a series of discriminator biases, and a differential curve obtained by applying the subtraction process to the data. The other test was the resolution of the 420-kev peak due to the electrons from the accelerator, elastically scattered. In obtaining the curves one counting channel was kept at fixed gain and discriminator setting in order to take account of variations in beam current, while a bias *vs* counting rate curve was run on the other channel. The experiment was then repeated with the channels interchanged. The results, for the Cs^{137} and the 420-kev electrons, are shown in Fig. 4. The discriminator bias for each channel was set to operate, during the electron polarization experiments, at a value corresponding to the point of maximum slope on the left side of the peak in the figure.

Magnetic Field Calibrations

As mentioned earlier, the value of the g factor may be obtained from a direct comparison of the rotation of the plane of polarization and the cyclotron rotation, without the necessity for precise measurements of the magnetic field (which would have to be averaged over the path) or of the energy of the electron beam. This method was adopted, and a means had to be devised for measuring the number of cyclotron revolutions as a function of the current in the solenoid.

The intensity of the beam reaching the analyzer end of the solenoid was large enough so that a spot was easily observed visually on a fluorescent screen. The

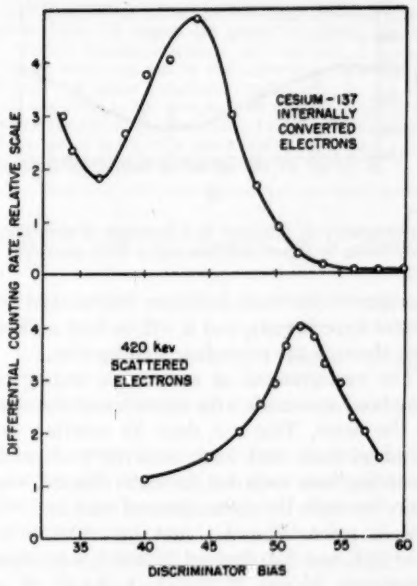

FIG. 4. Discriminator curves after differentiation. The abscissa scales of the two curves are not directly comparable, because the amplifier gains were not the same.

analyzer foil holder and the small defining diaphragms were removed, and the fluorescent screen was placed on the solenoid axis at a position $3\frac{1}{16}$ in. from the analyzer foil position toward the polarizer. When focused, the image spot was not sensibly larger than the object. The object in this case was the actual source of scattered electrons, which was (when projected onto the plane normal to the solenoid axis) a spot $\frac{3}{32}$ in. in diameter. The accuracy of the method may be estimated from the geometry of the system. The observations were made with the fifth focus on the fluorescent screen, and with an aperture angle γ of 2.25 degrees. Under these conditions it can be shown by simple geometry that the spot diameter changes by approximately $\frac{1}{4}$ in., or about twice the diameter of the focused image, for each 1 percent change in solenoid current. The measurements made were therefore estimated to be accurate ± 0.5 percent. The result of a number of determinations of the focal condition, after correction for the length factor mentioned above, was that 57.45 ± 0.30 amp corresponded to five cyclotron revolutions between the two scattering foils.

Bending at Entry and Exit

The beam from the accelerator, before striking the polarizer, has to travel at right angles to the magnetic field in the solenoid, a distance equal to the radius of the solenoid. This produces a change in direction of about 17 degrees. There is a more gradual bending of the beam outside the solenoid, and in the opposite sense. The direction of incidence of the beam at the polarizer target was measured by means of the slit system and the wire probe. A series of measurements gave a mean of 12.5 ± 1 deg with respect to the horizontal, at 57.9 amperes in the solenoid.

The bending of the electron paths between the analyzer foil and the counter windows takes place entirely within the uniform field of the solenoid so the angle can be calculated more accurately than it can be measured. The central path is a helical arc whose chord extends from the center of the analyzer foil to the center of the counter window, the latter being $2\frac{1}{2}$ in. from the solenoid axis. The angle between the counter axis and the direction of emergence of this path from the analyzer foil is 8.7 degrees at 57.9-amp current in the solenoid.

ASYMMETRIES NOT ASSOCIATED WITH SPIN AND THEIR ELIMINATION FROM THE DATA

As mentioned earlier, certain sources of asymmetry having nothing to do with the polarization effect are inherent in the experiment, and present a problem especially because they follow the polarization asymmetry as it rotates around. In this section the origins of these asymmetries will be pointed out, and the methods of dealing with them will be described.

There is only one cause of asymmetry, other than polarization, which does not have its origin in instrumental alignment or adjustment. It is the one which is the result of the nonlinearity in the relation between the scattering cross section and angle, and the finite aperture. Consider the typical double-scattering geometry sketched in Fig. 5. Four paths, AC', AD', BC, and BD lead to the counters. Because of the small differences in scattering angles, due to the finite aperture, BD contributes the most and AD' the least. AC' and BC are intermediate and contribute equally, because they differ only by the order in which the two scattering angles occur. However, the contribution of BD and AD' is not equal to that of AC plus BC because of the nonlinearity of the relation between scattering cross section and angle. Thus an asymmetry is produced which depends upon the angle γ. An integration over a circular aperture gives an asymmetry (ratio of intensities at C and D) of $1+2\gamma^2$. For $\gamma = 2.25°$, which is the value it had in the experiment, the asymmetry is 0.3 percent. The sense of the asymmetry is opposite to that produced by polarization.

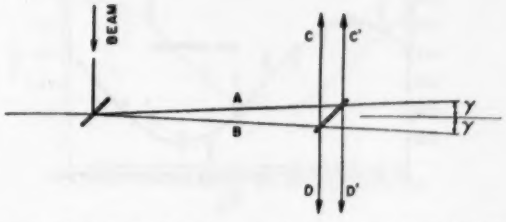

FIG. 5. The introduction of a nonspin asymmetry in the double-scattering experiment by a finite aperture.

A somewhat related way in which asymmetry may be produced has to do with misalignment of the diaphragm system. Applying the argument of the above paragraph it is clear that if there is any misalignment which makes the maximum angle admitted greater for, say, the A path than for the B path, an asymmetry at the counters will be produced. The more holes the beam has to pass through, the greater is the chance for such an effect. For this reason, it was considered important to avoid overdetermining the aperture by using more diaphragms than necessary, and to locate the diaphragms only near the two ends of the system.

A strong asymmetry is expected to come from the difference in response of the two counter channels. A somewhat different aperture at the scintillation crystal may be responsible for a small part of this, but in the main it is due to differences in the photomultiplier tubes, amplifiers, and pulse-height discriminators. Before measurements were made, the counting rates in the two channels were balanced to within about 5 percent by the use of the Cs^{137} source, and by means of the scattered electrons themselves.

The multiplicity of ways in which spurious asymmetries enter into the experiment would render extremely tedious, as well as risky, any attempt to keep the apparatus in delicate enough adjustment so that the spin asymmetry would stand out above the other asymmetries, in an absolute sense. A far more reliable way of dealing with the spurious asymmetries is to obtain and use, as far as possible, only ratios and not

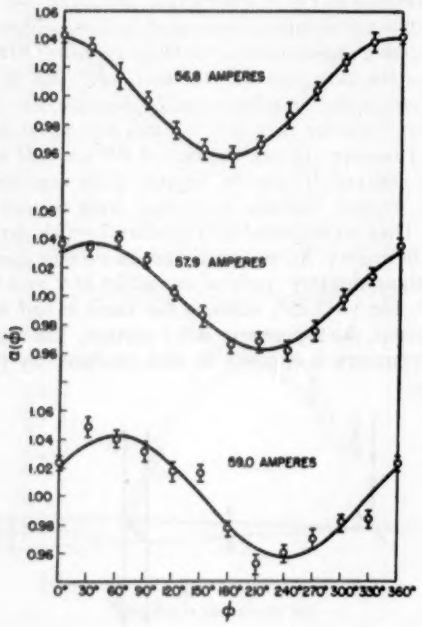

FIG. 6. Asymmetry in intensity as a function of direction, after scattering by a gold polarizer and a gold analyzer.

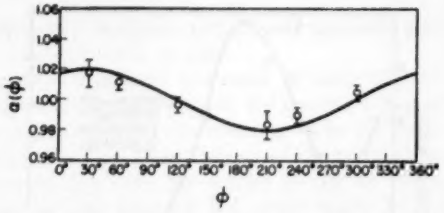

FIG. 7. Asymmetry in intensity as a function of direction, after scattering by a gold polarizer and a silver analyzer.

absolute quantities. Such a scheme was worked out for the present experiments, and it will be best understood by going through the procedure step by step.

(1) The measurement at each angle setting of the counting head was made with and without the analyzer foil in the beam. This was done by rotating the foil holder wheel back and forth between two positions. The counting rate recorded for each channel was the difference between the rates obtained with and without the foil in place. The net rate for channel 1 was $R_1(\phi)-r_1(\phi)$, and for channel 2, which was diametrically opposite, it was $R_2(\phi+\pi)-r_2(\phi+\pi)$, R and r standing for the rates with and without the foil, and the subscript identifying the channel. Changes in background associated with the position of the head were in this way eliminated. The counting rates without the foil were approximately 10 percent of those with the foil.

(2) The pair of measurements (with and without foil) at each setting of the head was repeated, with the head rotated 180 degrees. Two asymmetries were thus obtained:

$$K_1=\frac{R_1(\phi)-r_1(\phi)}{R_2(\phi+\pi)-r_2(\phi+\pi)},$$

and

$$K_2=\frac{R_2(\phi)-r_2(\phi)}{R_1(\phi+\pi)-r_1(\phi+\pi)},$$

in which the background count was eliminated. These two measurements allowed the counter asymmetry to be eliminated, giving

$$N(\phi)=[K_1(\phi)K_2(\phi)]^{\frac{1}{2}}$$

as the apparent asymmetry. The validity of this way of eliminating the counter channel asymmetry was checked by evaluating $[K_1(\phi)/K_2(\phi)]^{\frac{1}{2}}$, the counter asymmetry, for all angles. It was found to be independent of angle to within the expected statistical fluctuation.

(3) The procedures described in 1 and 2 above were repeated, substituting an aluminum foil of equivalent scattering power for the gold foil, in the analyzer position. (Gold was used as the polarizer in all cases.) The aluminum analyzer was expected to give the asymmetries associated with diaphragm and beam misalignment and finite aperture, in approximately the same degree as they were given by the gold, but it was

TABLE I. Experimental results for the three different values of the magnetic field. All angles are given in degrees. ϕ_c is the cyclotron rotation between scatterers, ϕ_d is the sum of the angles of deflection at entry and exit to the solenoid field, B and β are the amplitude and phase constants, respectively, in the cosine wave which was fitted to the data by least squares, ϕ_s is the angle through which the asymmetry was rotated relative to the direction of the beam before entry into the solenoid field, and g is the gyromagnetic ratio, which is $2(\phi_s-\phi_d)/\phi_c$.

ϕ_c	ϕ_d	B	β	ϕ_s	g
1781 ±9	20.8 ±2	0.041	7±4	1807 ±4	2.00±0.01
1814 ±9	21.2 ±2	0.037	33±5	1833 ±5	2.00±0.01
1847 ±9	21.6 ±2	0.042	60±4	1860 ±4	1.99±0.01

expected to give only about one-tenth of the polarization asymmetry given by the gold. The use of aluminum as a reference was the way in which effects of these asymmetries were eliminated. The value for the true asymmetry due to polarization was then obtained as

$$\alpha(\phi)=N_{Au}(\phi)/N_{Al}(\phi).$$

To indicate the magnitude of the correction introduced by normalizing to $N_{Al}(\phi)$ it may be stated that the amplitude of $N_{Al}(\phi)$ was about the same as that of $N_{Au}(\phi)$ and that its phase was different. An actual plot of $N_{Al}(\phi)$ will be given in the section on results.

(4) Finally, a set of measurements was made with a foil of intermediate atomic number, to determine whether the asymmetry attributed to polarization changed in the expected way with the atomic number.

MEASUREMENTS AND RESULTS

The program of measurement had to be limited to a small number of different sets of conditions for two reasons: (1) The amount of work involved in lining up the beam and making check runs was considerable, and had to be repeated for each new set of conditions. (2) The beta-ray-spectrometer type of focusing caused the size of the spot at the analyzing end, and consequently the current, which passed through the defining diaphragm, to vary rapidly with magnetic field. For these reasons the experimental effort was concentrated on just three settings, one being approximately at the focus corresponding to five cyclotron revolutions (1814°) and a setting on either side of the focus (1781° and 1847°). In all, approximately 1000 runs were made, each consisting of about 4000 counts in each channel, and each for a particular foil, angle, and field. In all of the measurements the polarizer foil was gold. Measurements with gold and with silver as the analyzer foil were made. In all measurements the analyzer foil was alternated with the aluminum foil and the blank hole for comparison and elimination of background count, as described earlier.

The results for the gold analyzer are plotted in Fig. 6. In Table I the angles of rotation due to the Lorentz forces—the cyclotron rotation and the deflections at entry and exit to the solenoid—as experimentally determined at the three values of field are given as ϕ_c and ϕ_d. A wave of the form $[1-B\cos(\phi-\beta)]$ representing the best fit by the least-squares method was determined. B and β are given in the table. The total observed angle of rotation of the polarization direction, ϕ_s, and finally the value of the gyromagnetic ratio, g, which is merely $2(\phi_s-\phi_d)/\phi_c$, are given. The consistency of the result over the range of approximately 60 degrees in angle indicates that the number of whole revolutions, i.e., 5, was the correct number.

The results for the silver analyzer are shown in Fig. 7. Since the purpose of this part of the experiment was only to check the dependence of magnitude of the asymmetry upon atomic number, measurements were made at fewer angles than in the case of the gold analyzer, and the results were not used in the determination of the g factor. The magnitude of the asymmetry was approximately one-half that obtained with the gold analyzer, a ratio consistent with the theoretical expectation, which is Z_{Ag}/Z_{Au} or 47/79.

As a check on possible asymmetry due to geometrical misalignment or to the finite aperture, a series of measurements was made using a defining diaphragm one-half the diameter of the one used in the main series of measurements. The analyzer was gold, and all conditions other than the aperture were the same as those applying to the middle curve in Fig. 6. The reduction of the aperture produced no effect, other than a reduction in counting rate. The results are plotted in Fig. 8, and the points from the middle curve of Fig. 6 are included for comparison.

In Fig. 9 are plotted (open circles) the values of $N_{Al}(\phi)$ which were obtained in the experiment on gold at 57.9 amp and which were used for the normalization of the values given in the middle curve of Fig. 6. The solid dots give the values of $N_{Al}(\phi)$ obtained with the reduced aperture ($=1.12°$). The plots of $N_{Al}(\phi)$ are presented because of their important bearing upon the reliability of the final results.

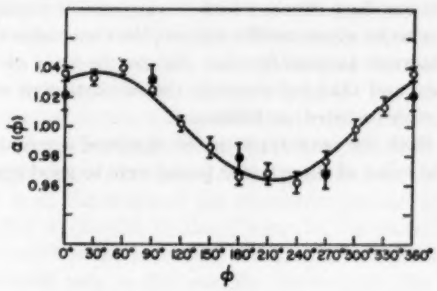

FIG. 8. Results obtained with reduced aperture (solid dots) compared with those obtained with full aperture (open circles).

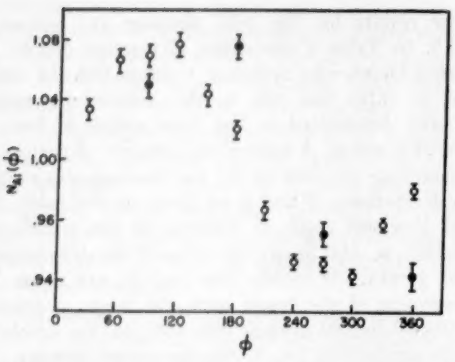

FIG. 9. The asymmetry obtained with the aluminum analyzer, i.e., the normalizing factor. Open circles: values used in the computation of the middle curve of Fig. 6. Solid dots: values used in the computation of the reduced aperture asymmetry in Fig. 8.

DISCUSSION OF RESULTS

The results presented in the foregoing section establish beyond doubt the practicality of observing and measuring the precession of the spin of the free electron in a magnetic field. The design of the experiment is such that the recognized asymmetries which are not associated with the spin precession are in principle eliminated, and the results of the two auxiliary experiments which it was possible to perform (change of Z and change of aperture) confirmed the belief that such asymmetries were in fact eliminated. The standard deviation given with the experimental value for g was composed of the standard deviations estimated for (a) the determination of the phase of the asymmetry β, (b) the measurement of the number of cyclotron revolutions, and (c) the angles of bending at entry and exit to the solenoid. It was not possible to include an estimate of the error introduced by a residual nonspin asymmetry, if it existed, in spite of the methods used to eliminate it. Such a residual would introduce into the asymmetry an additional cosine term of a different phase and amplitude. Since there is no formal way in which such a term can be estimated, the conviction that it does not exist in an important degree can be gotten only from a critical consideration of the design of the experiment, and the auxiliary checks which it was possible to make.

The checks whose results support the conclusion that the observed asymmetry was due to the spin of the electron, and that the errors in the measurement were small, may be listed, as follows.

(1) Both the magnitude of the observed asymmetry and the value of the g factor found were in good agreement with those predicted by theory. This double agreement constituted, in a sense, a cross check.

(2) When an analyzer foil of intermediate atomic number was substituted for the gold foil, the magnitude of the asymmetry decreased by the expected amount.

(3) A change in the aperture of the diaphragm system produced no essential change in either the amplitude of the asymmetry or the value of g.

(4) Measurements taken on different days, after realignment and adjustment of the apparatus gave results which agreed with one another, within the expected statistical limits.

(5) The individual asymmetries obtained for the gold analyzer and for the aluminum analyzer were quite far wrong in both phase and amplitude (see Fig. 9), but when they were divided, one by the other, the result was very close to the theoretical expectation, both in phase and amplitude. This greatly decreased the likelihood that the observed "spin" asymmetry was just a manifestation of the cyclotron rotation.

The amplitude of the asymmetry in the double-scattering experiment is defined by Mott as δ, where the ratio of the intensities in opposite directions in the line of maximum asymmetry is $(1+\delta)/(1-\delta)$. Calculations which give δ as a function of energy have been made by Mott and others[29] but none are available for angles of scattering other than 90°. For gold polarizer and analyzer, at 420 kev and for both scattering angles 90°, δ is expected to be 0.05. The experimental value of B in Table I is the asymmetry for gold-gold normalized to gold-aluminum. Since, theoretically, the latter is about 10 percent of the former, we may estimate δ_{Au} as 1.1 B or 0.044. The scattering angles used in the experiment were 90° and 78°, which would be expected to give a value for δ somewhat smaller than 0.05. The agreement is, therefore, well within the limits of the available theoretical predictions.

The precision of which the present method is capable is not sufficient to reveal the correction to the g factor, which is about one part in a thousand. An extension of the experiment, in which the electrons will be trapped in a magnetic field and in which spin will precess through at least 10^4 revolutions, is now under way. This should make possible a determination of the g factor to one part in about 10^5.

The authors are indebted to Professor K. M. Case for many discussions of the theoretical aspects of the problem, to Mr. H. A. Westrick and Mr. O. E. Haas for the instrument work, and to Mr. T. LaRocca for assistance in operating the apparatus.

[29] For curves of δ *vs* energy, see H. A. Tolhoek and S. R. DeGroot, Physica 17, 1 (1951).

The Problem of Multiple Scattering

E. P. WIGNER
Palmer Physical Laboratory, Princeton University, Princeton, New Jersey
(Received November 16, 1953)

Multiple scattering can be regarded as a succession of elementary events. The distribution function for the particles which have gone through $n+1$ elementary events is the convolution of two functions. The first of these expresses the scattering law; the second one is the distribution function for particles which have gone through n events. It is well known that such convolutions can be calculated very easily by means of Fourier transforms if the elementary event is the traversal of a free path in an arbitrary direction. In this case, the Fourier transform of the convolution is the product of the Fourier transforms of the convolvents. In the case of more general scattering laws, integrals over products of the distribution function, and of represensations of the group which leaves the scattering law invariant, play the same role which the Fourier transforms play in the aforementioned case. From the present point of view, the exponential in the Fourier transform is a representation of the displacement group. It is shown that one can solve several problems of multiple scattering on the basis of the above observation. These problems include the scattering of a point particle without change of energy but an arbitrary angular distribution, and several more involved problems.

INTRODUCTION

GROSJEAN[1] has given, by direct calculation, a solution of the problem of multiple scattering in an infinite medium. The reason for taking up the same problem again is that the method of calculation to be presented is somewhat more transparent and also applicable to a wider range of problems. It is based on the symmetry of the problem considered and uses the theory of group representations.

By multiple scattering we mean a succession of "elementary events" which change the state of the system and which are statistically independent of each other. In the theory of multiple scattering, the elementary event is, in general, a collision and the subsequent traversal of a free path. It changes the state of the system from the one in which it is before a collision to the state in which it is before the next one. The statistical independence of elementary events will be guaranteed if the description of the state of the system is complete, i.e., if it extends to all the parameters. In many cases, this is not necessary. Thus, if one is interested only in the velocity distribution after a certain number of collisions, and if the medium in which the particle moves is homogeneous and extends over all space, one can suppress the position coordinates in the description of the state and consider, as elementary events, the changes in the velocity vector caused by the subsequent collisions. It is clear that the statistical independence of subsequent elementary events is preserved under the conditions specified even though the description of the state is incomplete in this case. The same holds in the case of spherically symmetric scattering with respect to the direction of the velocity if one is interested only in the density distribution of the particles, irrespective of the direction of their velocities. In the most important case of multiple scattering, in which a complete specification of the state of the system is necessary, the elementary act can contain, just as well, a free path with a *subsequent* collision. In this case, the elementary event changes the state from the one *after* a collision to the state *after* the next collision.

The condition under which we can give an explicit solution of the problem is as follows. (1) The probability that an elementary event changes the state in a certain way is invariant under a group G. (2) Every state of the system is obtainable from a single fixed state by the operations of the group G. In the case of multiple scattering in an infinite homogeneous and isotropic medium, the group G contains all rotations and displacements in space, i.e., is the Euclidean group. The conditions of homogeneity and isotropy of the scattering medium express the fact that the scattering law, i.e., the law of the elementary event, is invariant under G. If the moving particle has no structure and does not change its energy as a result of the collisions, its state is completely characterized by its position and the direction of its velocity. Hence, every state of the particle can be obtained from a standard one by a displacement and a rotation, i.e., by an element of G. As standard state one can choose, for instance, the one in which the particle is at the origin of the coordinate system and its velocity is parallel to the Z axis. In the second case mentioned in the preceding paragraph, in which one is interested only in the velocity distribution, the scattering law will have the symmetry of the rotation group and G will be this group. If the collision does not

[1] C. C. Grosjean, dissertation, Columbia University, 1951 (unpublished). This thesis also has rather extensive references to earlier literature. Among earlier papers, those of W. Bothe [Z. Physik **54**, 161 (1929)] and of S. Goudsmit and J. L. Saunderson [Phys. Rev. **54**, 773 (1939) and **58**, 36 (1940)] anticipate most nearly Grosjean's results. The last article solves, in particular, the same problem which is treated by Eqs. (16) of the present note. Grosjean's article goes further than these by being able to give a rigorous expression for the probability of a given displacement, not only for the probability of a given deflection. This corresponds to Eqs. (17) of the present note. For later developments of Grosjean's method, see also C. C. Grosjean, Koninkl. Vlaam. Acad. Wetenschap. Letter en Shone Kunsten België Jaarboek **13**, No. 36 (1951) and Physica **19**, 29 (1953).

change the energy of the moving particle, its state is given by the direction of the velocity vector and any such direction can be obtained from a standard one by rotation, i.e., by an element of G. Hence, our method will be applicable to both these cases and a similar discussion shows that it is applicable also in the last case mentioned above,—that of spherically symmetric scattering if the particle again does not change its energy in the course of the collisions. Further and more general examples will be given later.

EQUATIONS OF MULTIPLE SCATTERING

A.

Even though the method of solution to be adopted will be essentially the same in all cases to be considered, it seems worth while to distinguish two cases at this point. In the first case, there is only one group element which carries the standard state e of the particle into a given state s. In this case, the group element in question can be denoted by s itself, the unit element e corresponding to the standard state. This is the situation if the particle is restricted to move in a plane, no matter whether its "state" has to be characterized only by the direction of its velocity, or by this direction and the position of the particle. Let us denote in this case the probability distribution (per unit volume element of the invariant group space) after n elementary events by $f_n(s)$. The volume element is simply $d\varphi$, with φ the angle between direction of the velocity and the standard direction, if one excludes the consideration of the position of the particle. It is $d\varphi dxdy$, with x and y the rectangular coordinates of the particle, if one is interested also in the probability of the position of the particle. If the energy also changes in the course of collisions, it becomes a fourth parameter of s and the volume element will depend on the energy dependence of the law of scattering.

The probability that an elementary event change the state s into a unit volume element at t will be denoted by $P(s,t)$. The invariance of this probability under the operations of the group means that for every group element u

$$P(s,t)=P(us,ut). \tag{1}$$

This equation already uses our assumption that there is a correspondance between states and the elements of the group which leaves the law of the elementary event invariant. Writing, in particular, $u=s^{-1}$ in (1), one obtains

$$P(s,t)=P(e,s^{-1}t)=P(s^{-1}t). \tag{1a}$$

This equation expresses the fact that the scattering law remains the same no matter whether one uses e or s as the basic state. The probability distribution $f_{n+1}(t)$ is given therefore by

$$f_{n+1}(t)=\int f_n(s)P(s,t)ds=\int f_n(s)P(s^{-1}t)ds, \tag{2}$$

where ds signifies the invariant group integration. (Right and left invariant group integrals are identical in all the groups to be considered.) It is very natural that the probability distribution after $n+1$ collisions be given by the convolution of the probability distribution after n collisions and the scattering law.

Because of the somewhat abstract nature of the derivation of (2), it may be worth while to illustrate it on the aforementioned examples. If, in two-dimensional scattering, the position of the particle is suppressed, the group G is simply the group of rotations in two dimensions and can be characterized by an angle φ. The state (φ_0) of the particle is obtained from the standard state, with the velocity directed parallel to the X axis, by a rotation with φ_0; i.e., it is the state in which the velocity includes an angle φ_0 with the X axis. If t and s in (2) are characterized by the angles φ and φ_0 this equation becomes

$$f_{n+1}(\varphi)=\int f_n(\varphi_0)P(\varphi-\varphi_0)d\varphi_0, \tag{3}$$

since the angle which characterizes the group element $s^{-1}t$ becomes $\varphi-\varphi_0$. According to its definition,

$$P(\varphi')=\sigma(\varphi')/\sigma, \tag{3a}$$

where $\sigma=\int\sigma(\varphi')d\varphi'$ is the total cross section. Hence, (3) gives the usual way to calculate the angular distributions successively.

If one wishes to obtain the spatial distribution of the particle as well as its velocity, the group G becomes the group of motions in two dimensions. It can be characterized by a displacement by x, y and a rotation by φ (the latter preceding the former). The group element,

$$s=\begin{Vmatrix}\cos\varphi_0 & -\sin\varphi_0 & x_0\\ \sin\varphi_0 & \cos\varphi_0 & y_0\\ 0 & 0 & 1\end{Vmatrix}=\begin{Vmatrix}1 & 0 & x_0\\ 0 & 1 & y_0\\ 0 & 0 & 1\end{Vmatrix}\cdot\begin{Vmatrix}\cos\varphi_0 & -\sin\varphi_0 & 0\\ \sin\varphi_0 & \cos\varphi_0 & 0\\ 0 & 0 & 1\end{Vmatrix},$$

characterizes the state in which the particle is at x_0, y_0 and the direction of the velocity includes an angle φ_0 with the X axis. A direct method to obtain P in terms of the cross section will be given in the section Calculation of $P(s,t)$. In the present case we wish to verify only *a posteriori* that (2) gives the well-known equation (3e) if

$$P(x',y',\varphi')=\sigma(\varphi')r^{-1}e^{-\sigma r}\delta(\psi-\varphi'), \tag{3b}$$

where r and ψ are abbreviations for the polar coordinates of $x'=r\cos\psi$ and $y'=r\sin\psi$. The δ function in (3b) expresses the fact that the displacement is always in the direction of the velocity. For the verification of (2), let us denote the parameters of the group element s by x_0, y_0, φ_0, those of t by x, y, φ; the parameters of $s^{-1}t$

then become

$$x'=(x-x_0)\cos\varphi_0+(y-y_0)\sin\varphi_0,$$
$$y'=-(x-x_0)\sin\varphi_0+(y-y_0)\cos\varphi_0, \qquad (3c)$$
$$\varphi'=\varphi-\varphi_0.$$

The polar coordinates of x', y' are r and $\psi=\alpha-\varphi_0$, where r and α are polar coordinates for $x-x_0=r\cos\alpha$, $y-y_0=r\sin\alpha$. Hence

$$P(x',y',\varphi')=\sigma(\varphi-\varphi_0)r^{-1}e^{-\sigma r}\delta(\alpha-\varphi),$$

and with the invariant volume element for ds given above, (2) becomes

$$f_{n+1}(x,y,\varphi)=\int\int\int dx_0dy_0d\varphi_0f_n(x_0,y_0,\varphi_0)$$
$$\times\sigma(\varphi-\varphi_0)r^{-1}e^{-\sigma r}\delta(\alpha-\varphi). \qquad (3d)$$

This becomes the well-known equation,

$$f_{n+1}(x,y,\varphi)=\int\int\int drd\alpha d\varphi_0f_n(x_0,y_0,\varphi_0)$$
$$\times\sigma(\varphi-\varphi_0)e^{-\sigma r}\delta(\alpha-\varphi)$$
$$=\int\int dr\,r\varphi_0f_n(x-r\cos\varphi,\ y-r\sin\varphi,\ \varphi_0)$$
$$\times\sigma(\varphi-\varphi_0)e^{-\sigma r}, \qquad (3e)$$

if one replaces the integration variables x_0, y_0 by r and α and carries out the integration over α. It may be arguable that the well-known (3e) is simpler than (2) but we shall see that (2) suggests more directly a method of solution than does (3e).

B.

The preceding calculation applies in the case in which G has only one element which transforms the standard state e into a given state s. This is not true if, for instance, a particle without structure moves in three- rather than two-dimensional space. The reason therefore is that there are rotations—those about the direction of the velocity in the standard state—which leave the standard state unchanged. The rest of the present section contains a discussion of the group theoretic description of the state and of the scattering law. While the former discussion is essential, the discussion following (5a) is not necessary if one is interested only in using the present method. The result of this discussion is (9) which becomes evident at any rate if one calculates P explicitly.

Let us denote the number of parameters which characterize the states by n_1, the number of parameters of the group G by n. There will be then an $n-n_1$ parametric subgroup E, the elements of which carry the standard state $\mathcal{S}$ into itself:

$$e_1\mathcal{S}=\mathcal{S} \text{ if } e_1 \text{ contained in } E. \qquad (4)$$

Two group elements, s and s', will carry $\mathcal{S}$ into the same state $\mathcal{S}$ if

$$\mathcal{S}=s\mathcal{S}=s'\mathcal{S}; \quad \mathcal{S}=s^{-1}s'\mathcal{S}. \qquad (4a)$$

$s^{-1}s'$ is an element of the subgroup E, i.e., if s and s' are in the same left coset of E. One can say that in the more general case now considered the left cosets of E correspond to the different states of the particle rather than the group elements themselves.

We shall see that expressions of the form (2) are very easily evaluated and we wish to define, therefore, also in the present case a probability function $f(s)$, depending on the group elements rather than on left cosets. This $f(s)$, if integrated over the elements of the cosets which correspond to a set of states, will give the probability of the states of the set. In order to express this analytically, it is useful to introduce two types of parameters, ζ and ϵ, for the group G. There are n_1 parameters ζ and they have the same value for all elements of a left coset and serve to distinguish these cosets, i.e., to characterize the states of the particle. There are $n-n_1$ parameters ϵ and they distinguish the various elements of the left cosets. One can choose, for instance, the parameters ζ and ϵ in such a way that the element with parameters ζ and ϵ become

$$s(\zeta,\epsilon)=s(\zeta,0)e(\epsilon), \qquad (4b)$$

where $e(\epsilon)$ are the elements of the subgroup E and $s(\zeta,0)$ is a continuous function of $\mathcal{S}(\zeta)$. If we denote the probability of the states $\mathcal{S}(\zeta)$ per unit range of ζ by $F(\zeta)$, we shall demand of $f(s)$

$$F(\zeta)=\int f(s)g(\zeta,\epsilon)d\epsilon, \qquad (5)$$

where the integration over ϵ is to be extended over the subgroup E, $g(\zeta,\epsilon)$ is the weight factor which makes $g(\zeta,\epsilon)d\zeta d\epsilon$ the invariant integral, and s is the group element with the parameters ζ, ϵ. This equation expresses the postulate that the integral of f over a coset give the probability of the state to which the coset corresponds.

Clearly, (5) does not determine $f(s)$ completely and we can further postulate that it have the same value for each element of a coset, i.e., be a constant along the path of integration of (5)

$$f(s)=f(se_1) \text{ if } e_1 \text{ contained in } E. \qquad (5a)$$

All our probability functions shall have the property (5a).

In a similar way, we shall try to replace the transition probability $P(\mathcal{S}_1,\mathcal{S}_2)=P(\zeta_1,\zeta_2)$ by a function $P(s,t)$ of the group elements s,t. This has to be done in such a way that if

$$F_{n+1}(\zeta_2)=\int F_n(\zeta_1)P(\zeta_1,\zeta_2)d\zeta_1, \qquad (6)$$

and if F_n and f_n correspond to each other in the sense of (5), (5a), then

$$f_{n+1}(s_2)=\int f_n(s_1)P(s_1,s_2)ds_1 \tag{6a}$$

also correspond to F_{n+1} in the same sense, no matter what the functional form of F_n is. Since f_{n+1}, as a probability function, will have to satisfy (5a), we can conclude at once that

$$P(s_1,s_2)=P(s_1,s_2e_2) \text{ if } e_2 \text{ contained in } E. \tag{7a}$$

Expressing now both F in (6) by the corresponding f, we find

$$\int f_{n+1}(s_2)g(\zeta_2,\epsilon_2)d\epsilon_2=\int\int f_n(s_1)g(\zeta_1,\epsilon_1)P(\zeta_1,\zeta_2)d\epsilon_1 d\zeta_1$$

$$=\int f_n(s_1)P(\zeta_1,\zeta_2)ds_1,$$

where s_2 and s_1 are the group elements with the parameters ζ_2,ϵ_2 and ζ_1,ϵ_1, respectively, and the second line follows from the definition of $g(\zeta,\epsilon)d\zeta d\epsilon$ as the invariant group integral. The condition that the f_{n+1} obtained from (6) satisfy (6a) is, therefore,

$$\int ds_1\int f_n(s_1)P(s_1,s_2)g(\zeta_2,\epsilon_2)d\epsilon_2=\int ds_1 f_n(s_1)P(\zeta_1,\zeta_2).$$

Since f_n is not an arbitrary function of s_1 but satisfies (5a), the last equation does not fully determine $P(s_1,s_2)$ and we are free to let it depend on ϵ_1 in an arbitrary fashion. The simplest choice is

$$\int P(s_1,s_2)g(\zeta_2,\epsilon_2)d\epsilon_2=P(\zeta_1,\zeta_2), \tag{7}$$

according to which we have, in addition to (7a),

$$P(se_1,s_2)=P(s_1,s_2) \text{ if } e_1 \text{ contained in } E. \tag{7b}$$

According to (7a) and (7b), $P(s_1,s_2)=P(s_1',s_2')$ if s_1 and s_1' are in the same left coset of E and the same holds of s_2, s_2'. This is indeed the most natural convention; it renders all quantities $f(s)$, $P(s,t)$ functions only of the ζ parameters of their (group element) variables. It follows that $P(s_1,s_2)$ can be taken out of the integral sign of (7) and this equation, together with (7a), (7b), completely determines $P(s_1,s_2)$ once $P(\zeta_1,\zeta_2)$ is given.

The invariance of the law governing the elementary event can be expressed in the following way. Let us assume that the distribution will be given by $f_{n+1}(s_2)$ if it was $f_n(s_1)$ one event before. Then if the distribution is $h_n(s_1)=f_n(us_1)$, it will go over into $h_{n+1}(s_2)=f_{n+1}(us_2)$ after another event. This will hold for every group element u. One easily verifies that the h satisfy (5a) if the f do. Expressing the above condition analytically, one finds that

$$f_{n+1}(us_2)=h_{n+1}(s_2)=\int h_n(s_1)P(s_1,s_2)ds_1$$

$$=\int f_n(us_1)P(s_1,s_2)ds_1 \tag{8}$$

must be a consequence of

$$f_{n+1}(t)=\int f_n(s)P(s,t)ds. \tag{8a}$$

Since ds_1 indicates the invariant group integration, one can replace in (8) us_1 by s. Writing, furthermore, t for us_2, (8) goes over into

$$f_{n+1}(t)=\int f_n(s)P(u^{-1}s,u^{-1}t)ds, \tag{8b}$$

and this will be a consequence of (8a) if

$$\int f_n(s)P(s,t)ds=\int f_n(s)P(u^{-1}s,u^{-1}t)ds. \tag{8c}$$

Writing out the integration in terms of ζ,ϵ,

$$\int f_n(\zeta)P(s,t)g(\zeta,\epsilon)d\zeta d\epsilon$$

$$=\int f_n(\zeta)P(u^{-1}s,u^{-1}t)g(\zeta,\epsilon)d\zeta d\epsilon,$$

where s is the group element with the parameters ζ,ϵ. Since the last equation must hold for all f_n,

$$P(s,t)\int g(\zeta,\epsilon)d\epsilon=P(u^{-1}s,u^{-1}t)\int g(\zeta,\epsilon)d\epsilon. \tag{8d}$$

Both $P(s,t)$ and $P(u^{-1}s,u^{-1}t)$ could be placed before the integral sign because they are independent of ϵ. Setting then $u=s$, one again obtains (1a) for P and also obtains, from (6a), the same Eq. (2) which holds in the case in which there is only one group element which transforms the standard state into a given state. The only difference between the two cases is, therefore, the additional condition (5a) on the distribution functions, and the conditions (7a), (7b) on $P(s,t)$, which must be satisfied in order to make (2) valid also if there are group elements which leave the standard state unchanged and hence all the elements of a left coset transform the standard state into the same state. It is worth noting that (7a), (7b) give

$$P(e_1se_2)=P(s) \text{ for } e_1,\ e_2 \text{ contained in } E. \tag{9}$$

Hence, P depends in general on even fewer independent variables than f. The example of the following section will illustrate this point.

CALCULATION OF $P(s,t)$

In the case of the motion of a particle in two-dimensional space without energy change, we obtained the expressions (3a), (3b) for P by inspection; insertion of these expressions into (2) gave the relatively simple and well-known equations for multiple scattering for this case and thus verified (3a) and (3b) *a posteriori*. We shall not follow this procedure in the case of the scattering of a particle in three-dimensional space without energy change, principally because the explicit form of the equation of multiple scattering in three dimensions [i.e., the analog of (3e)] is very complicated. In fact, one of the simplifications which the method here presented introduces is the avoiding of these explicit equations and the possibility of evaluating (2) without writing down this equation in any other form. In order to use and interpret the solution, it is necessary, however, to express $P(s,t)$ in terms of the quantities commonly used (i.e., the differential cross section) and to establish the connection between the $f_n(s)$ and the commonly used angular distribution $F(\Omega)$. These connections are given, in principle, by (7), (7a), (7b), and by (5), (5a) but the corresponding relation will be explicitly evaluated now for the aforementioned case, i.e., scattering of a particle without change of energy under disregard of its position. It will be given also for the case in which the position of the particle is considered also.

The group G in the first case is the three-dimensional rotation group. As standard state, we choose the one in which the velocity is parallel to the Z axis. The subgroup E which leaves the standard state invariant consists of the rotations about Z. It is reasonable to choose the polar angles φ, ϑ of the velocity direction as the variables ζ describing the state. Equation (4b) then becomes

$$s(\varphi,\vartheta,\epsilon)=s(\varphi,\vartheta,0)Z(\epsilon), \tag{10}$$

where $Z(\epsilon)$ is a rotation by ϵ about the Z axis and we can choose for $s(\varphi,\vartheta,0)$ any rotation which turns the Z axis into the φ, ϑ direction. If we choose

$$s(\varphi,\vartheta,0)=Z(\varphi)X(\vartheta), \tag{10a}$$

the angles φ, ϑ, ϵ become the Eulerian parameters of the group elements. The distribution function f will depend, by (5a), only on φ and ϑ and we have, by (5) for the probability of a unit range in φ and ϑ:

$$F(\varphi,\vartheta)=\int_0^{2\pi} f(\varphi,\vartheta)\sin\vartheta d\epsilon=2\pi f(\varphi,\vartheta)\sin\vartheta, \tag{10b}$$

$\sin\vartheta d\varphi d\vartheta d\epsilon$ being the invariant volume element expressed in terms of Eulerian parameters.

According to (9), the function $P(s)$ depends only on the parameter ϑ—the simplicity of this condition is a consequence of (10a), i.e., of the use of Eulerian parameters to describe the group elements. A similar simplification can be accomplished, however, also in most other cases by choosing three sets of parameters ζ_1, ζ_2, ϵ defined by the equation

$$s(\zeta_1,\zeta_2,\epsilon)=e(\zeta_1)s(\zeta_2)e(\epsilon), \tag{11}$$

where $e(\zeta_1)$ and $e(\epsilon)$ cover the subgroup E and the $s(\zeta_2)$ are so chosen that all elements of the group are obtained by letting ζ_2 vary over a suitable domain.

Since $P(s,t)$ depends only on $s^{-1}t$, it is sufficient to determine $P(e,t)=P(t)$ where e is the unit element. We then have, from (7),

$$\int_0^{2\pi} P(\vartheta)\sin\vartheta d\epsilon=\sigma(\vartheta)\sin\vartheta/\sigma. \tag{10c}$$

Since we have set $s_1=e$ the right side represents the probability that an elementary event change the velocity, originally parallel to Z, into a velocity at ϑ, φ within unit range of $d\vartheta$ and $d\varphi$. Since the differential cross section $\sigma(\vartheta)$ is usually defined per unit solid angle, the probability of the transition to unit $d\vartheta d\varphi$ range becomes $\sigma(\vartheta)\sin\vartheta$. It is an obvious consequence of the spherical symmetry of the problem that this probability is independent of φ. This does not give an additional condition, however, because the symmetry of $P(s)$ is fully described already in (9).

Summarizing, we have

$$f(s)=f(\varphi,\vartheta,\epsilon)=(2\pi\sin\vartheta)^{-1}F(\varphi,\vartheta), \tag{12}$$

$$P(s)=P(\varphi,\vartheta,\epsilon)=(2\pi)^{-1}\sigma(\vartheta)/\sigma. \tag{12a}$$

It may be useful to repeat that $F(\varphi,\vartheta)$ is not the probability per unit solid angle but per unit $d\varphi d\vartheta$ interval. No $\sin^{-1}\vartheta$ appears in the expression for $f(s)$ if F is given in terms of the distribution function per unit solid angle.

The expressions for the case in which one wishes to consider not only the direction of the velocity but also the position of the particle can be derived with equal ease. The group G for this case is the group of motions in three dimensions (Euclidean group) defined in the same fashion as the group of motions in two dimensions was. The distribution function $F(x,y,z,\varphi,\vartheta)$ depends on the position of the particle as well as the direction of its velocity. The group elements depend on six parameters: the Eulerian angles $\varphi,\vartheta,\epsilon$ of the rotation, and the three components x,y,z of the subsequent displacement. The subgroup E contains only the rotations about Z; it is the same group as in the preceding example. The connection between the group theoretic f and the usual F is, in complete analogy to (12)

$$f(s)=f(x,y,z,\varphi,\vartheta,\epsilon)=(2\pi\sin\vartheta)^{-1}F(x,y,z,\varphi,\vartheta). \tag{13}$$

The form of $P(s)$ is simpler if we consider as fundamental process the traversal of a free path and a subsequent collision (i.e., if we adopt the second point of view of the Introduction). The probability of the tran-

sition from the standard state into unit interval at the state $s=(x,y,z,\varphi,\vartheta)$ then becomes $\delta(x)\delta(y)e^{-\sigma z}\sigma(\vartheta)\sin\vartheta$. Hence, application of (7) to the case $s_1=e$, $s_3=s$ gives

$$P(s)\int \sin\vartheta d\epsilon=\delta(x)\delta(y)e^{-\sigma z}\sigma(\vartheta)\sin\vartheta$$

or

$$P(s)=P(x,y,z,\varphi,\vartheta,\epsilon)=(2\pi)^{-1}\sigma(\vartheta)e^{-\sigma z}\delta(x)\delta(y). \quad (13a)$$

One convinces oneself easily that this expression satisfies (9).

The above expressions could have been foreseen without the detailed derivation given above. In fact, the numerical factors in (12) to (13a) need not be known for actual calculations since the successively calculated distribution functions can easily be normalized *a posteriori*.

EVALUATION OF THE EXPRESSION (2)

The reason that (2) can be evaluated particularly simply if s and t are elements of a group is that the group integral of the product of the convolute and the matrix of a representation is the product of two matrices which are obtained from the convolvents in a similar fashion. In fact, we obtain from $D(s)D(u)=D(su)$:

$$\int f_{n+1}(t)D(t)dt=\int\int f_n(s)P(s^{-1}t)D(t)dsdt$$

$$=\int\int f_n(s)P(u)D(su)dsdu$$

$$=\int f_n(s)D(s)ds\cdot\int P(u)D(u)du. \quad (14)$$

The second line is obtained by substituting $t=su$ and noting the invariance of the group integral with respect to such a substitution.[3] Since $D(s)$ is, in general, a matrix, all expressions in (14) are matrices, with the number of dimensions of D. Written out in more detail, (13) reads

$$\int f_{n+1}(s)D(s)_{\lambda\lambda}dt$$

$$=\sum_\mu\int f_n(s)D(s)_{\nu\mu}ds\int P(s)D(s)_{\mu\lambda}ds. \quad (14a)$$

This equation holds no matter whether the representation D is reducible or irreducible. If D is the regular representation, one is led back to (2); the simplest results are obtained if D is irreducible. If (14) holds for a function f_{n+1} and all irreducible representations, this f_{n+1} satisfies (2).

[3] Equation (14) must have been known already to G. Frobenius.

It follows from the above that

$$\int f_n(s)D(s)ds=\Phi^{(n)}=\Phi^{(0)}\Pi^n;$$

$$\Pi=\int P(s)D(s)ds. \quad (14b)$$

Again, the Φ and Π are matrices with as many dimensions as D. The evaluation of (14b) is often made very much easier by the fact that f_0 and P satisfy (5a) and (9), i.e., actually do not depend on all the group variables. In particular, if one assumes the representations in the form in which the matrices corresponding to elements of E are in the reduced form, only those $\int f_0(s)D(s)_{\lambda\nu}ds$ will be different from zero in which ν corresponds to a unit representation of E and both μ and ν must correspond to such representations if $\int P(s)D(s)_{\mu\nu}ds$ is to be finite.

In the first case discussed in the last section, it follows either from (9) or more directly from (12a), that assuming the customary form of the irreducible representations[3] only the 0,0 element of $\Pi(l)$ is different from zero. One has

$$\Pi(l)_{\nu\mu}=\int P(s)D^{(l)}(s)_{\nu\mu}ds$$

$$=\int_0^{2\pi}\int_0^{\pi}\int_0^{2\pi}\frac{\sigma(\vartheta)}{2\pi\sigma}e^{i\nu\varphi}d^{(l)}{}_{\nu\mu}(\vartheta)e^{i\mu\epsilon}d\varphi\sin\vartheta d\vartheta d\epsilon$$

$$=(2\pi/\sigma)\delta_{\nu 0}\delta_{\mu 0}\int_0^{\pi}\sigma(\vartheta)d_{00}{}^{(l)}(\vartheta)\sin\vartheta d\vartheta. \quad (15)$$

Hence, in all powers of the "matrix" $\Pi(l)$ only the 0–0 element is different from zero and this is the corresponding power of (15). Similarly, it follows from (5a), or more directly from (12), that only the 0 column of

$$\Phi^{(n)}(l)=\int f_n(s)D^{(l)}(s)ds \quad (15a)$$

contains elements which are different from 0. This is, of course, consistent with (14b) and (15).

Let us consider, for instance, the angular distribution obtained by means of Born's first approximation, for Rutherford scattering on a shielded nucleus. For a potential proportional to $r^{-1}e^{-\alpha r}$ the angular distribution becomes, with $\beta=\alpha^2/2k^2$, where k is the wave number of the particle,

$$\frac{\sigma(\vartheta)}{\sigma}=\frac{\beta(2+\beta)}{4\pi(1+\beta-\cos\vartheta)^2}. \quad (16)$$

[3] See, e.g., E. P. Wigner, *Gruppentheorie und ihre Anwendung* (Friedr. Vieweg, Braunschweig, 1931), Chap. XV.

In order to evaluate the integral (15), it is most convenient to write $\cos\vartheta = x$ and to use d_{00} in the form

$$d_{00}^{(l)}(\vartheta) = P^l(\vartheta) = \frac{1}{2^l l!}\frac{d^l(x^2-1)^l}{dx^l}. \tag{16a}$$

This gives for $\Pi(l)_{00}$ (we shall omit the indices 0 for convenience)

$$\Pi(l) = 2\pi\int_{-1}^{1}\frac{\beta(2+\beta)}{4\pi(1+\beta-x)^2}\frac{1}{2^l l!}\frac{d^l(x^2-1)^l}{dx^l}dx$$

$$= \frac{\beta(2+\beta)}{2^{l+1}l!}\int_{-1}^{1}\frac{(l+1)!(1-x^2)^l}{(1+\beta-x)^{l+2}}dx. \tag{16b}$$

The second line is obtained by l-fold partial integration. For $l=0$, this gives (as always) $\Pi(0)=1$ for $l=1$,

$$\Pi(1) = 1+\beta-\tfrac{1}{2}\beta(2+\beta)\ln(2+\beta)/\beta. \tag{16c}$$

This is the forward bias after one collision; after n collisions the forward bias in the nth power of this. (16c) has been obtained already in the earlier articles of reference 1.

Let us consider, as a second example, the motion of a particle without energy change in two-dimensional space. The unitary irreducible representations of the corresponding group—the Euclidean group of the plane—are infinite-dimensional and can be characterized by a continuous variable k:

$$D^{(k)}(r,\psi,\varphi)_{m'm} = e^{im'\psi}J_{m'-m}(kr)e^{im(\varphi-\psi)}. \tag{17}$$

The notation is the same as in (3b): the group element (r,ψ,φ) is given by the matrix of the equation preceding (3b) if one sets therein $x=r\cos\psi$, $y=r\sin\psi$, $\varphi_0=\varphi$. The very simple derivation of (16) is given in the Appendix.[4] J_n is the Bessel function of order n. We define again

$$\Pi(k)_{m'm} = \int P(s)D^{(k)}(s)_{m'm}ds$$

$$= \int\sigma(\varphi)r^{-1}e^{-\sigma r}\delta(\psi-\varphi)e^{im'\psi}J_{m'-m}(kr)$$
$$\times e^{im(\varphi-\psi)}rdrd\psi d\varphi; \tag{17a}$$

the $P(s)$ was taken from (3b). The integration over ψ can be carried out at once, and one obtains

$$\Pi(k)_{m'm} = \int_0^{2\pi}\sigma(\varphi)e^{im'\varphi}d\varphi\int_0^{\infty}e^{-\sigma r}J_{m'-m}(kr)dr$$

$$= \frac{\sigma_{m'}}{(k^2+\sigma^2)^{\frac{1}{2}}}\xi^{m'-m}, \tag{17b}$$

where

$$\sigma_m = \int_0^{2\pi}\sigma(\varphi)e^{im\varphi}d\varphi; \quad \xi = \frac{\sigma}{k} - \left(1+\frac{\sigma^2}{k^2}\right)^{\frac{1}{2}}. \tag{17c}$$

[4] For representations of similar groups, see also E. Inonu and E. P. Wigner, Nuovo cimento 9, 705 (1952).

One sees that $\Pi(k)$ is again of rank 1. One easily proves by induction that

$$[\Pi(k)]^{n+1} = \frac{[2\pi\sigma(0)]^n}{[\sigma^2+k^2]^{\frac{1}{2}n}}\Pi(k), \tag{17d}$$

where $\sigma(0)$ is the differential cross section in the forward direction:

$$2\pi\sigma(0) = \sum\sigma_m. \tag{17e}$$

It would have been possible, of course, to transform (17) in such a way that, similar to (15), only one element of the $\Pi(k)$ matrix would have been different from zero. However, the rather arbitrarily chosen form of (17) has caused no difficulty.

In order to obtain the expansion matrices $\Phi^{(n)}(k)$ of f_n from those of $[\Pi(k)]^n$, we have to multiply the matrix expanding f_0 with $[\Pi(k)]^n$. If the particle is, originally, in the standard state, its expansion matrices are all unit matrices and $\Phi^{(n)}(k)=[\Pi(k)]^n$. Hence, these matrices play a role similar to that of the source solution of diffusion equations. In order to return, from the Φ, to the distribution function f, one has to invert equations of the form (15a). This is a trivial matter if the group is closed and can be done easily also for the representations (17) by means of well-known expansion formulas for Bessel and trigonometric functions. The problem of inverting Eqs. (15a) for not closed groups has been attacked recently in a rather general form by Harish-Chandra and by Segal.[5] In many cases, such as dealt with in Eqs. (16), the expansion matrices have more immediate physical significance than the distribution function f itself.

CALCULATION OF TOTAL DENSITY FUNCTIONS

In many cases one is interested in the total distribution of all particles, irrespective of the number of elementary events they have passed through. Usually, this will be finite only if the elementary process can lead to absorption.

If the probability of absorption $1-\gamma$ is independent of the state of the particle before the elementary event, the total distribution function will be

$$f = \sum\gamma^n f_n. \tag{18}$$

The corresponding momentum matrix becomes

$$\Phi(l) = \int f(s)D^{(l)}(s)ds = \sum\gamma^n\Phi^{(n)}(l)$$

$$= \Phi^{(0)}(l)\sum\gamma^n\Pi(l)^n = \Phi_0(l)[1-\gamma\Pi(l)]^{-1}. \tag{18a}$$

The right side of (18a) can be written down at once in all cases considered in the preceding sections.

[5] I. E. Segal, Ann. Math. 52, 272 (1950) and Harish-Chandra, Proc. Natl. Acad. Sci. U.S. 37, 813 (1951).

APPLICABILITY OF THE METHOD

It has been realized already by Grosjean that one can successively evaluate the distribution functions for multiple scattering, if one wishes to take the energy changes into account, most easily if the probability of a certain fractional change in energy is only a function of the scattering angle. This is the case for elastic scattering on atoms at rest. It seems natural to ask, therefore, whether the calculations presented above, if applied to a larger than the Euclidean group, could be given a physical interpretation. We shall not try to solve this problem in general but point only to the simplest generalization of the Euclidean group, that formed by the matrices

$$s=\begin{Vmatrix} cr & \mathfrak{a} \\ 0 & 1 \end{Vmatrix}. \tag{19}$$

In (19), r is a real orthogonal matrix, $\mathfrak{a}$ is a real vector, $c>0$. For $c=1$, the s form the Euclidean group; dropping this restriction increases the number of group parameters by 1. Clearly, c will be connected in some way with the velocity of the particle.

The condition of invariance means that the transition probability from s_1 to s_2 be equal, for all u, to the transition probability from us_1 to us_2. It is enough to demand this for a set of u from which all group elements can be obtained by multiplication. We choose the following u:

$$u_1=\begin{Vmatrix} 1 & \mathfrak{a} \\ 0 & 1 \end{Vmatrix}, \quad u_2=\begin{Vmatrix} r & 0 \\ 0 & 1 \end{Vmatrix}, \quad u_3=\begin{Vmatrix} c1 & 0 \\ 0 & 1 \end{Vmatrix}. \tag{19a}$$

The above condition, applied to $u=u_1$ shows that the transition probability from the state $(c_1,r_1,\mathfrak{a}_1)$ to $(c_2,r_2,\mathfrak{a}_2)$ is equal to the transition probability from $(c_1, r_1, \mathfrak{a}_1+\mathfrak{a})$ to $(c_2, r_2, \mathfrak{a}_2+\mathfrak{a})$. This shows that $\mathfrak{a}$ plays the role of the position vector of the particle, or is proportional to the position vector. The invariance condition is also satisfied with respect to u_2 if r continues to describe the direction of the velocity of the particle. Application to u_3 gives, finally, that the transition probabilities

$$(c_1,r_1,\mathfrak{a}_1)\to(c_2,r_2,\mathfrak{a}_2) \text{ and } (cc_1,r_1,c\mathfrak{a}_1)\to(cc_2,r_2,c\mathfrak{a}_2) \tag{19b}$$

are equal for all c. In other words, the probability of a path of length $|c(\mathfrak{a}_1-\mathfrak{a}_2)|$ at the value cc_1 of the first parameter is as great as the probability of the path $|\mathfrak{a}_1-\mathfrak{a}_2|$ at the value c_1 of the first parameter. Expressed still differently, the mean free path is proportional to the first parameter. For the first parameter itself, the change from c_1 to c_2 is as probable as from cc_1 to cc_2. The simplest interpretation of this is that

$$c=Cv^n; \tag{19c}$$

that is, c, and hence also the mean free path, is proportional to the n'th power of the velocity where $n\neq 0$ but can be arbitrary otherwise. Together with the preceding conditions, condition (19b) then stipulates that the angular distribution of the scattering be independent of the velocity and that the probability of a certain fractional change in energy depend only on the change in the direction of the velocity.

It seems likely that many other multiple scattering distributions can be calculated accurately, many others approximately, following the procedure outlined above. So far, no case has been encountered in which the calculation of the nth power of Π, or of the reciprocal in (18a), would have been at all difficult. On the other hand, it does not appear to be possible to use the rotation (or Euclidean) group to calculate the multiple scattering of a particle with spin, by using the variable ϵ of (12) to describe the spin's motion. It seems that a more powerful method is needed to overcome the difficulties of this problem.

APPENDIX

The irreducible representations of the group of motions in two dimensions can most easily be given in the Hilbert space of functions $f(\alpha)$ the variable α of which is restricted to the interval $0\leq\alpha<2\pi$. The operators $P_s=P_{r,\psi,\varphi}$ of the representation in this space are defined by

$$\begin{aligned} P_s f(\alpha)=P_{r,\psi,\varphi}f(\alpha)&=e^{-ik(r\cos\psi\cos\alpha+r\sin\psi\sin\alpha)}f(\alpha-\varphi)\\ &=e^{-ikr\cos(\psi-\alpha)}f(\alpha-\varphi). \end{aligned} \tag{A1}$$

The group element s is a rotation by φ about the origin, followed by a displacement with a vector the polar coordinates of which are r and ψ. Borrowing concepts from quantum mechanics, one can say that f describes states in which the absolute value of the momentum is k but the direction of the momentum is variable and given by α. Rotation of this state by φ replaces α by $\alpha-\varphi$; displacement by the vector $r\cos\psi$, $r\sin\psi$ multiplies it with the exponential in (A1). The magnitude of k characterizes the representation; it can assume any positive value.

One can write (A1) also in the form

$$P_s f(\alpha)=\int \Delta^{(k)}(r,\psi,\varphi)_{\alpha\alpha'}f(\alpha')d\alpha', \tag{A2}$$

with a singular representation matrix:

$$\Delta^{(k)}(r,\psi,\varphi)_{\alpha\alpha'}=e^{-ikr\cos(\psi-\alpha)}\delta(\alpha-\varphi,\alpha'), \tag{A2a}$$

and the calculation of the text can be carried out also using this form of $\Delta^{(k)}$. The form of $D^{(k)}$ given in the text is obtained by using, instead of $f(\alpha)$, its Fourier expansion:

$$f(\alpha)=\sum_m f_m e^{-im\alpha}. \tag{A3}$$

Substitution of this into (A1) gives

$$P_{r,\psi,\varphi}\sum_m f_m e^{-im\alpha}=\sum_m e^{-ikr\cos(\psi-\alpha)}e^{im(\varphi-\alpha)}f_m$$

$$=\sum_{mm'}D^{(k)}(r,\psi,\varphi)_{m'm}f_m e^{-im'\alpha}, \quad \text{(A4)}$$

where

$$D^{(k)}(r,\psi,\varphi)_{m'm}=(2\pi)^{-1}\int_0^{2\pi}e^{-ikr\cos(\psi-\alpha)}e^{im(\varphi-\alpha)}e^{im'\alpha}d\alpha$$

$$=(2\pi)^{-1}\int_0^{2\pi}e^{-ikr\cos\beta-i(m'-m)\beta}d\beta \times e^{i(m'-m)\psi+im\varphi}. \quad \text{(A5)}$$

Because of

$$J_n(z)=(2\pi)^{-1}i^{-n}\int_0^{2\pi}e^{-iz\cos\beta-in\beta}d\beta, \quad \text{(A5a)}$$

this differs from the expression given in the text only by the factor $i^{m'-m}$ which can be eliminated by a similarity transformation. It is worth noting that the transition from (17b) to (17c), i.e., the evaluation of the second integral of (17b), can be best carried out using the form (A5a) for J.

A similar calculation is possible also in the three-dimensional case but it is more laborious and will not be given here. It is, essentially, contained in the Appendix to Grosjean's last article.

PHYSICAL REVIEW VOLUME 94, NUMBER 1 APRIL 1, 1954

Calculated Values of the Parameters of Noble Gas Discharges

WALTER J. GRAHAM AND ARTHUR J. RUHLIG
Naval Research Laboratory, Washington, D. C.
(Received December 14, 1953)

Molar properties of gaseous discharges are determined by the transport cross section which is expressible in terms of the phase shifts defined in electron-atom scattering theory.

$\sigma_t(v)$ was calculated for helium, neon, and argon using values of phase shifts η_0 to η_8 derived by Westin from existing scattering data. Druyvesteyn distribution functions were calculated for E/p from 0.1 to 1.0. Average values were then calculated for collision frequency, drift velocity, diffusion coefficient, and average energy.

Also, collision frequency and elastic energy loss were calculated using Maxwell distributions for kT_e up to 10 ev. These calculations are particularly useful at very low energy, where extrapolation of phase shifts is more reliable than of the experimental data. Values of σ_t are compared with those of Barbiere (taken from direct scattering data); values of drift velocity are somewhat lower than Nielsen's data.

I. INTRODUCTION

THE theory of gas discharges reduces essentially to a study of the various types of collisions which take place among the electrons, atoms, and ions. In many practical cases where the average electron energy is low, the properties of the discharge are determined primarily by the differential cross section $\sigma(k,\vartheta)$ for elastic scattering of an electron by an atom. Here k is the electron wave number, and ϑ the angle through which the electron is deviated.

The ordinary total cross section[1] $\sigma(k)$ is defined by

$$\sigma(k)=\int_0^{\pi}\sigma(k,\vartheta)2\pi\sin\vartheta d\vartheta. \quad (1)$$

In gas discharges, however, since the energy lost by an electron in an elastic collision depends on ϑ, a more important quantity is the transport cross section $\sigma_t(k)$ defined by

$$\sigma_t(k)=\int_0^{\pi}\sigma(k,\vartheta)(1-\cos\vartheta)2\pi\sin\vartheta d\vartheta. \quad (2)$$

(This quantity is also referred to as the diffusion or momentum transfer cross section.) From collision theory, these two cross sections can be expressed[2] in terms of the phase shifts η_n introduced by the atom in the partial waves associated with successive units of angular momentum of the incident electron about the center of the atom:

$$\sigma(k)=\frac{4\pi}{k^2}\sum_{n=0}^{\infty}(2n+1)\sin^2\eta_n, \quad (3)$$

$$\sigma_t(k)=\frac{4\pi}{k^2}\sum_{n=0}^{\infty}(n+1)\sin^2(\eta_n-\eta_{n+1}). \quad (4)$$

Most of the molar properties of the electrons in a discharge, such as drift velocity, diffusion coefficient, etc., are given by some function of σ_t and k, averaged over a distribution function which in turn involves σ_t. Hence, a knowledge of the phase shifts η_n permits calculation of σ_t and this, in turn, enables one to derive the

[1] N. F. Mott and H. S. W. Massey, *Theory of Atomic Collisions* (Oxford University Press, London, 1949), Chap. 2.

[2] H. S. W. Massey and C. B. O. Mohr, Proc. Roy. Soc. (London) A144, 434 (1933).

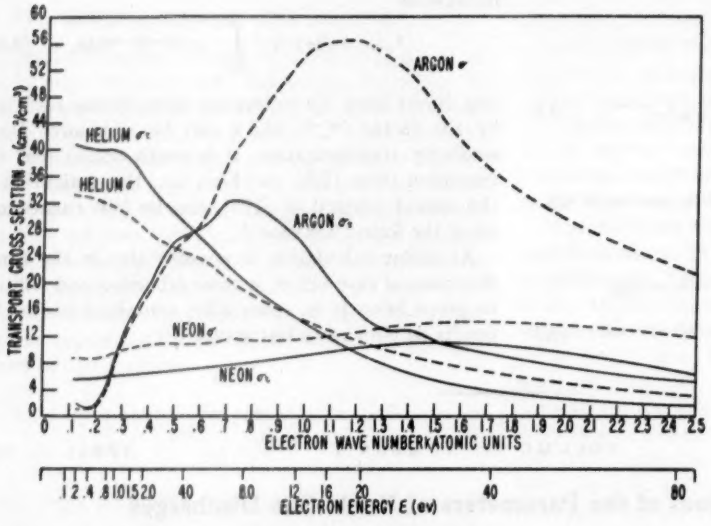

FIG. 1. Transport cross section σ_t as function of electron wave number k, as calculated from phase shifts. The dotted curves are the ordinary total cross sections, σ. Values given refer to pressure of 1 mm Hg, and temperature of 0°C.

various discharge parameters if the distribution function is known. Theoretical calculation of the phase shifts is very difficult, especially at low energies where the Born approximation fails and exchange effects are not negligible. A calculation of σ_t directly from the experimental angular scattering data is possible, but unfortunately scattering experiments become difficult at electron energies of a few ev or less.

II. METHOD OF CALCULATION

Westin[3] in 1946 derived a self-consistent set of phase shifts from experimental data. Voss[4] had shown that mathematical conditions were imposed on the angular scattering distribution curves such that, given an arbitrary angular curve, one could not necessarily reproduce it by some suitable choice of phase shifts. He showed further that the experimental data of Ramsauer and Kollath[5] in argon did not adequately satisfy these consistency conditions for electron energy less than 2 ev or greater than 6 ev. Westin made a thorough compilation of all experimental scattering data available for helium, neon, and argon, and with the aid of a specially-built electromechanical device carried out extensive trial-and-error calculations to find a set of phase shifts best fitting the experimental data.

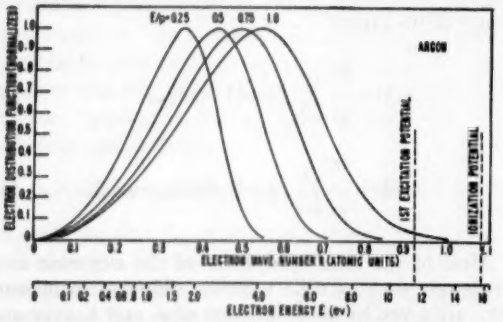

FIG. 2. Generalized Druyvesteyn distribution functions in argon for several values of E/p(volts/cm per mm Hg). Calculations were made using transport cross sections derived from phase shifts.

Values of $\sigma(k)$ and $\sigma_t(k)$ have been calculated for helium, neon, and argon, using Eqs. (3) and (4) and the table of phase shifts given by Westin. His data cover a range of k from 0.2 to 5.0 atomic units. The results are shown in Fig. 1. (All cross sections calculated in this paper are for 0°C. and 1 mm Hg.) The deviation of σ_t from σ is obviously quite marked. Barbiere[6] calculated σ_t directly from the Ramsauer-Kollath scattering data. His values agree almost exactly for neon. For helium they are about 40 percent lower at 2 ev and agree at about 10 ev; and in argon the disagreement is more pronounced, Barbiere's values being about 30 percent lower at low energy and about 100 percent larger at 12.5 volts. The above comparisons are understandable, since the composite scattering data used by Westin for argon deviated appreciably from the Ramsauer-Kollath data, while in helium and neon the difference was much smaller.

These calculated values of σ and σ_t should have particular significance at low energy, because the phase shifts can be extrapolated toward zero energy more reliably than the scattering data. This is true because the scattering theory imposes the restriction that each phase shift equals a multiple of π at k equal to zero. To assign a theoretical value to the cross section at zero

[3] S. Westin, Kgl. Norske Videnskab. Selskab. Forh. No. 2 (1946).
[4] W. Voss, Z. Physik **83**, 581 (1933).
[5] C. Ramsauer and R. Kollath, Ann. Physik **9**, 756 (1931); **10**, 143 (1931); **12**, 837 (1932).
[6] D. Barbiere, Phys. Rev. **84**, 653 (1951).

energy one needs to know the slope of the phase-shift curve.

III. RESULTS FOR DRUYVESTEYN DISTRIBUTION

The velocity distribution function $f(\mathbf{r},\mathbf{v},t)$ for electrons in a gas discharge is given by a solution[7] of the Boltzmann transport equation,

$$\frac{\partial f}{\partial t}=\nabla_v\cdot\frac{e}{m}\mathbf{E}f-\nabla_r\cdot\mathbf{v}f+\frac{\partial f}{\partial t}\Big]_{\text{coll.}}, \tag{5}$$

where ∇_v and ∇_r are the gradient operators in velocity and coordinate space, respectively. In the case of a small uniform dc field E, the solution can be given in the form

$$f=f_0+\frac{\mathbf{v}}{v}\cdot\mathbf{f}_1, \tag{6}$$

where the subscripts refer to a Legendre polynomial expansion in velocity space. By substituting into Eq. (5), and considering only elastic collisions, one obtains the generalized Druyvesteyn distribution for the symmetric part,

$$f_0=A\exp\left(\frac{-3m^2}{M(eE)^2}\int_0^v\sigma_t^2v^3dv\right). \tag{7}$$

Calculations of f_0 have been made for E/p from 0.1 to 2.0 volts/cm per mm Hg in helium, neon, and argon. An example of the influence of the field on the distribution function in argon is shown in Fig. 2. As indicated by the curves, an E/p of much more than 1.0 would indicate an appreciable number of electrons with enough energy to cause inelastic impacts.

The asymmetric term in Eq. (6) can be expressed in terms of f_0 as follows:

$$\mathbf{f}_1=\frac{e}{m}\mathbf{E}\frac{1}{v\sigma_t}\frac{\partial f_0}{\partial v}+\frac{1}{\sigma_t}\nabla_rf_0. \tag{8}$$

The drift velocity $\bar{v}$ for a field E in the x direction is given simply by v_x averaged over $f(\mathbf{r},\mathbf{v})$. By taking $\langle v_xv_y\rangle_{Av}=\langle v_xv_z\rangle_{Av}=0$ and $\langle v_xv_x\rangle_{Av}=\frac{1}{3}v^2$ and using the first term on the right in Eq. (8), one obtains

$$\bar{v}=\frac{4\pi m^2}{NMeE}\int_0^\infty v^5\sigma_tf_0dv, \tag{9}$$

where

$$N=\int_0^\infty f(\mathbf{r},\mathbf{v})d\mathbf{r}d\mathbf{v}.$$

Similarly, by averaging the diffusion current over $f(\mathbf{r},\mathbf{v})$ and using the second term on the right of Eq. (8), one gets for the average diffusion coefficient

$$\bar{D}=\frac{4\pi}{3N}\int_0^\infty\frac{v^3}{\sigma_t}f_0dv. \tag{10}$$

[7] Morse, Allis, and Lamar, Phys. Rev. 48, 412 (1935).

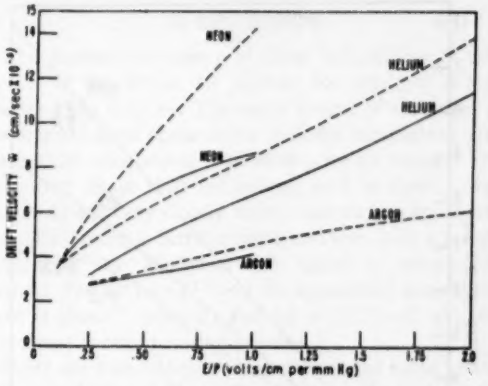

FIG. 3. Drift velocity $\bar{v}$ as a function of E/p. The solid curves are values calculated using phase shifts; the dotted curves are averages taken from Nielsen's experimental data.

By using the above equations and replacing the normalizing factor N by the close approximation $N\cong 4\pi\int_0^\infty f_0v^2dv$, the parameters $\bar{v}$ and $\bar{D}$ were calculated for E/p from 0.1 to 1.0 in the three gases. Drift velocity curves are shown in Fig. 3, where the dotted curves are taken from Nielsen's measurements[8] using the electron shutter method. His data are probably the best available. The marked discrepancy in neon is largely due to the fact that for values of E/p greater than 0.25, an appreciable fraction of electrons will have an energy exceeding the excitation and ionization potentials (because of the small cross section for neon). Hence, the distribution function derived assuming only elastic impacts is not very reliable. It might be noted that a theoretical curve of Allen[9] for neon, taking inelastic collisions into account, would lie about half-way between the calculated curve and Nielsen's

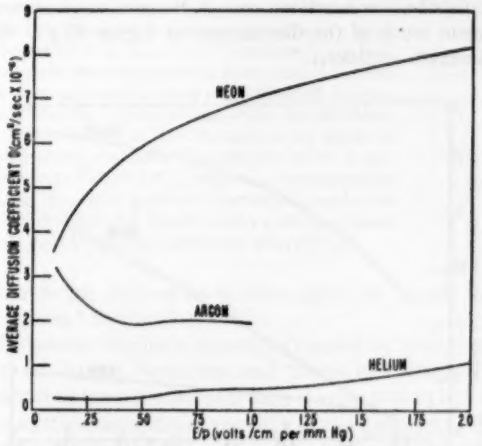

FIG. 4. Average diffusion coefficient $\bar{D}$, for electrons in helium, neon, and argon, as a function of E/p.

[8] R. Nielsen, Phys. Rev. 50, 950 (1936).
[9] H. Allen, Phys. Rev. 52, 707 (1937).

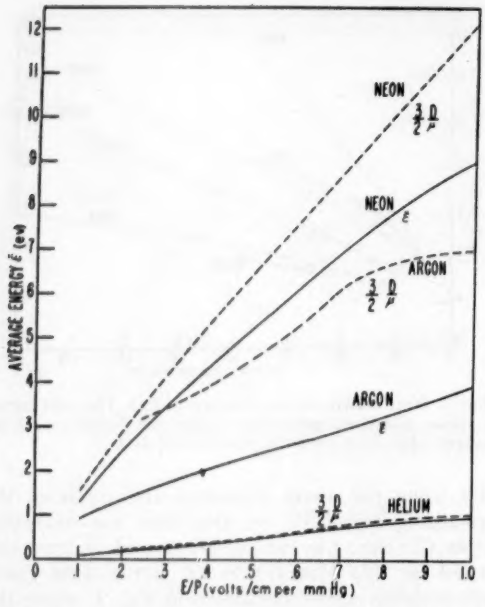

FIG. 5. Average energy of electrons ϵ as a function of E/p, averaging over the generalized Druyvesteyn distribution function. The dotted curves represent average energy as defined by the Einstein relation, where D is the diffusion coefficient and μ the mobility.

curve in Fig. 3. Diffusion coefficient curves are shown in Fig. 4.

The average energy was calculated directly by averaging $\frac{1}{2}mv^2$. It was then compared with the average energy associated with temperature defined by the Einstein relation between mobility and diffusion constant. The results are shown in Fig. 5. The differences arise because the cross sections are not constant, and the distribution functions are not Maxwellian; however, in neon much of the discrepancy at higher E/p is due to inelastic collisions.

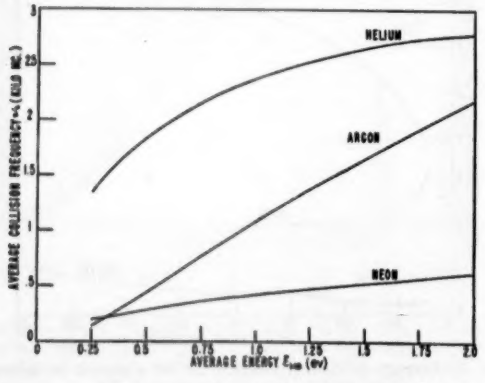

FIG. 6. Average transport collision frequency as a function of average energy assuming a Maxwell-Boltzmann distribution and using transport cross sections derived from phase shifts.

IV. RESULTS FOR MAXWELL DISTRIBUTION

In addition to the above calculations using the Druyvesteyn distribution, a calculation was made of the average transport collision frequency, $\nu_t = v\sigma_t$, averaging over a Maxwell-Boltzmann distribution of various average energies $\bar{\epsilon}_{MB}$ from 0.25 to 2.0 ev. The results are shown in Fig. 6.

Calculations also were made of the average rate of energy loss in elastic collisions, using a Maxwell-Boltzmann distribution for both the electrons and atoms. One can show that the energy loss $\Delta\epsilon$ by an

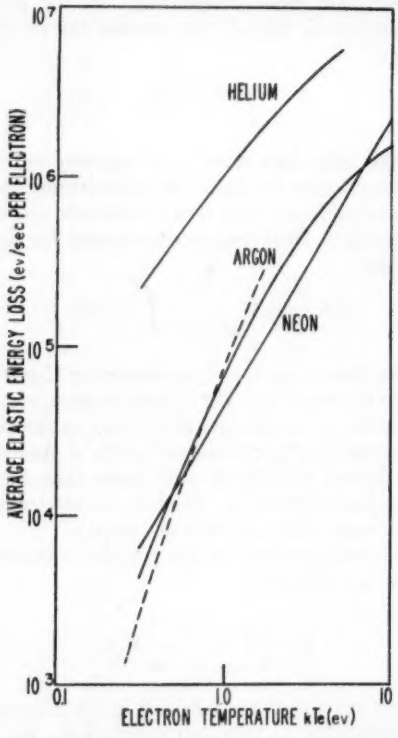

FIG. 7. Average elastic energy loss per electron as a function of electron temperature assuming a Maxwell-Boltzmann distribution for electrons and atoms, and using transport cross sections derived from phase shifts. The dotted curve represents a calculation made by Kenty using the Compton formula and Ramsauer-Kollath cross sections in argon.

electron on elastic collision is given by

$$\Delta\epsilon = \mu_0 \mathbf{V}_0 \cdot (\mathbf{v} - \mathbf{v}'), \tag{11}$$

where $\mu_0 = mM/(m+M)$; $\mathbf{V}_0$ is the velocity of the center of mass, and $\mathbf{v}$ and $\mathbf{v}'$ are the relative velocities before and after impact. This can be reduced to

$$\Delta\epsilon = \mu_0(1-\cos\vartheta)(\mathbf{V}_0 \cdot \mathbf{v}). \tag{12}$$

The rate of energy loss P for a given electron is then

$$P = v\sigma\Delta\epsilon = v\sigma\mu_0(\mathbf{V}_0 \cdot \mathbf{v}), \tag{13}$$

and the average rate of energy loss $\bar{P}$ is then

$$\bar{P}=\frac{1}{N_a N_e}\int_0^\infty\int_0^\infty d\mathbf{V}dv v\sigma_{tm}(\mathbf{V}_0\cdot\mathbf{v})F_e(v)F_a(V), \quad (14)$$

where $F_e(v)$,N_e and $F_a(V)$,N_a refer to electrons and atoms, respectively.

Values of $\bar{P}$ are shown in Fig. 7, the temperature of the gas atoms being taken as 293°K. The dotted curve is one calculated by Kenty,[10] using the Compton formula,[11] and total cross-section data of Ramsauer and Kollath. He assumed a Maxwell-Boltzmann distribution for the electrons, neglecting the motion of the gas atoms. He also measured the loss experimentally, over a limited range of electron temperature from 0.84 ev to 1.29 ev. His calculated values differed from his experiment by a few percent at the lower temperature and by about 20 percent at the higher temperature. If one makes the comparison using the values of elastic loss per electron derived from the phase-shifts, the agreement is better than 6 percent over the range of Kenty's experimental values.

[10] Kenty, Easley, and Barnes, J. Appl. Phys. **22**, 1006 (1951).
[11] K. T. Compton, Phys. Rev. **22**, 333 (1923).

V. DISCUSSION

The probable accuracy of these calculations is estimated to be within 10 percent for electron energy greater than 0.15 ev. The main source of error lies in the original set of phase shifts. A direct comparison with theoretical calculations is possible only for helium. The zero-order phase shift for helium used in these calculations agrees very closely with a calculation by Morse and Allis[12] using a Hartree field, and also with a recent calculation by Moiseiwitsch[13] using a variational method. For $k<1.0$ (13.5 ev) the agreement among the three is about 1 percent; and for $k<2.5$($\sim$85 ev) the agreement is better than 6 percent.

There are two features of significance in these phase shift calculations. First, the extrapolation of phase shifts to energies less than 1 or 2 ev is probably more reliable than extrapolation of the direct scattering data. Second, the transport cross sections constitute a central set of data from which many discharge parameters can be calculated; thus, if experimental agreement is established for several parameters, then one can more confidently extend the calculations to parameters which are not easily measured accurately.

[12] P. M. Morse and W. P. Allis, Phys. Rev. **44**, 269 (1933).
[13] B. L. Moiseiwitsch, Proc. Roy. Soc. (London) **A219**, 102 (1953).

PHYSICAL REVIEW VOLUME 94, NUMBER 1 APRIL 1, 1954

Ionic Conductivity of Impure Polar Crystals*

A. B. LIDIARD†
Department of Physics, University of Illinois, Urbana, Illinois
(Received October 28, 1953)

Experimental determinations of the ionic conductivity of impure or "doped" alkali halide crystals are often used to find the mobility of the cation vacancies. For this purpose it is important to know to what extent the vacancies and the impurity ions have associated together to form neutral "complexes," which do not contribute to the conductivity. Previous interpretations of the experimental data have relied largely on the law of mass action to give the degree of association, but have neglected the long-range Coulomb interactions between the unassociated impurity ions and vacancies. The effect of these interactions on the calculated degree of association and upon the dc conductivity is examined in this paper. The interactions are shown to be significant even in systems containing impurities in concentrations of no more than one part in 10^4. A new analysis of the results obtained by Etzel and Maurer for the system $NaCl+CdCl_2$, leads to a binding energy of about 0.35 ev for the cadmium ion-vacancy complex. The mobility of the sodium ion vacancy is found to be about 30 percent larger, at all temperatures, than was inferred by Etzel and Maurer, using a simpler theory to interpret the data. The activation energy for the vacancy motion remains however at about 0.9 ev.

I. INTRODUCTION

THE ionic conductivity of polar crystals has in recent years engaged the attention of many investigators. The earlier work, mainly on pure crystals, has been reviewed by Mott and Gurney[1] and by Seitz.[2] More recent reviews have been given by Jacobs and Tompkins,[3] and by Jost.[4]

In general the ionic current is carried by the migration of lattice vacancies and interstitial ions. The analysis of the experimental data is complicated by the temperature dependence not only of the numbers of the various carriers but also of their mobilities. Thus the

* This work was supported by the U. S. Office of Naval Research.
† Present address: Department of Physics, University of California, Berkeley 4, California.
[1] N. F. Mott and R. W. Gurney, *Electronic Processes in Ionic Crystals* (Oxford University Press, Oxford, 1948), Chap. II.
[2] F. Seitz, *The Modern Theory of Solids* (McGraw-Hill Book Company, Inc., New York, 1940), Chap. XV.
[3] P. W. M. Jacobs and F. C. Tompkins, Quart. Revs. London **6**, 238 (1952).
[4] W. Jost, *Diffusion in Solids, Liquids, Gases* (Academic Press, New York, 1952), Chap. IV.

contribution of a particular carrier to the conductivity is limited both by the thermal energy needed to create it and by the energy barriers which prevent its free migration once it is formed. Uncertainties in the values of these energies limit the usefulness of the theory of conduction in the general ionic crystal.[5] Particular substances may however present simplified situations. Thus in AgBr, the ionic current is carried only by the interstitial silver ions and by the silver ion vacancies. The alkali halides are an even simpler example. Here interstitial ions do not occur to any appreciable extent and, at least for temperatures less than about 400°C,[6] the cation vacancies alone carry the current. But the situation can be refined further. Consider, for example, the solution of small amounts of $CdCl_2$ in NaCl. The Cd^{++} ions enter the Na^+ lattice substitutionally, but owing to their double charge there must also be introduced an equal number of Na^+ vacancies in order to maintain electrical neutrality. Since the number of thermally produced vacancies is very small, it only needs an impurity content of one part in 10^4 to keep the number of vacancies quite independent of temperature. Hence, by considering a "doped" alkali halide crystal we have a system with only one type of current carrier, the latter being present in known constant amount. The same situation can be obtained in the silver halides, although here much larger additions[7] of the divalent ion are required (about 1 percent).

It might appear that we have now so simplified the system as to make it of no further theoretical interest and of experimental interest only in so far as it enables a simple direct measure of the cation vacancy's mobility. That this is not so is because of the effective negative charge $(-e)$ carried by the cation vacancy and the effective positive charge $(+e)$ of the divalent impurity ions. Now charges of the same kind repel one another, and unlike charges attract, so that at the absolute zero of temperature the lowest-energy state of the system will be one in which each impurity ion has a cation vacancy attached to it in the nearest neighboring position.[8] Such a pair is spoken of as a "complex." At higher temperatures some of these attachments will be broken, and the thermodynamic state at a temperature T can be described by giving the number of complexes which remain. Now the complexes have no net charge and so do not contribute to the conductivity. In the interpretation of conductivity data it is therefore important to know the number of complexes present, particularly as a function of the impurity concentration. The law of mass action has been used for this purpose by several workers.[9–11] At any given temperature let there by n complexes present; if the total number of impurity ions is N_i there will be N_i-n unassociated vacancies, and the law of mass action states that

$$\frac{N_+ n}{(N_i-n)^2}=K(T), \tag{1}$$

where $K(T)$ is a function only of the temperature. The number of solvent cations is denoted by N_+. Equation (1) enables us to calculate the variation in the degree of association n/N_i, i.e., the variation in the conductivity, as we alter the concentration N_i/N_+ of the impurity. It was on this basis that Etzel and Maurer[11] analyzed their experimental data on the system $NaCl+CdCl_2$.

However, by requiring $K(T)$ to be independent of N_i we are implicitly neglecting the interactions between unassociated impurity ions and vacancies. As far as we are aware they have not yet been taken into account in the present connection,[12] although an indication of their possible importance has been obtained by Teltow.[10] He analyzed his data on $AgBr+CdBr_2$ both on the basis of an association described by (1) and also on the assumption that the vacancies and impurity ions formed an unassociated (strong) Debye-Hückel electrolyte. At impurity concentrations of less than one percent the data could be fitted reasonably well on either basis, although for larger concentrations it was apparent that some combination of the two assumptions was necessary We therefore propose to retain the idea of associated complexes, but in addition to treat the unassociated vacancies and impurity ions as forming a Debye-Hückel electrolyte in which the neutral complexes are immersed. It is of general interest to study the effect of neglecting the long range interactions among the unassociated charges and in the present paper we shall discuss this question with the aid of a simple model in which they are taken to be Coulombic at all distances. Although the calculations of Reitz and Gammel[13] for the system $NaCl+CdCl_2$ show that this is unlikely to be accurate at distances as small as the nearest neighbor separation, it does not seem probable that this error will materially affect our general conclusions about the influence of the

[5] General equations giving the number of vacancies and interstitial ions, of both kinds, have been derived by R. H. Fowler and E. A. Guggenheim, *Statistical Thermodynamics* (Cambridge University Press, Cambridge, 1939), Chap. XIII.

[6] See Table XV of reference 2.

[7] The conductivity of AgCl and AgBr containing lead and cadmium ions has been studied by E. Koch and C. Wagner, Z. physik. Chem. **B38**, 295 (1937) and by J. Teltow, Ann. Physik, **5**, 63 (1949).

[8] This is, of course, the nearest neighboring position on the cation sublattice. Since the anion sublattice plays no active role in our considerations we shall speak of the cation sublattice simply as the lattice. Thus in NaCl the "lattice" is of face-centered cubic type.

[9] O. Stasiw and J. Teltow, Ann. Physik **1**, 261 (1947).

[10] J. Teltow, Ann. Physik **5**, 71 (1949).

[11] H. W. Etzel and R. J. Maurer, J. Chem. Phys. **18**, 1003 (1950).

[12] J. Frenkel [*Kinetic Theory of Liquids* (Clarendon Press, Oxford, 1946), p. 36 ff.], considering the thermal production of anion and cation vacancies in the pure salt, had earlier shown how these long range interactions would lead to a space change in the surface regions of the crystal. See also a recent paper by K. Lehovec [J. Chem. Phys. **21**, 1123 (1953)].

[13] J. R. Reitz and J. L. Gammel, J. Chem. Phys. **19**, 894 (1951). These calculations have since been extended by F. Bassani and F. G. Fumi who have calculated association energies between vacancies and Cd, Ca, and Sr impurity ions in both NaCl and KCl [Nuovo cimento (to be published)]. I am very grateful to Professor Fumi for informing me of their results prior to publication.

interaction.[14] The assumption that the interaction is purely Coulombic has the practical advantage of leading to a set of equations containing a minimum of unknown parameters. Our aim is thus not so much to account in detail for one special system as to see those effects of the long-range forces between the unassociated charges which are common to all systems. In the next section we obtain equations showing the influence of these forces on the degree of association into complexes, as a function of temperature and impurity content. Numerical results giving n/N_i as a function of T for various molar concentrations between 10^{-4} and 10^{-2} are exhibited graphically. In Sec. III we apply these results to the derivation of the steady dc conductivity. We show that departures from the simple association theory[11] may well be detectable even at impurity concentrations as low as a few parts in 10^4. A fresh analysis of the experimental data obtained by Etzel and Maurer (in Sec. IV) bears out this deduction. In the course of this analysis we obtain a value of 0.35 ev for the binding energy of the Cd^{++}: vacancy complex in NaCl. The activation energy for vacancy diffusion in NaCl deduced by Etzel and Maurer to be 0.9 ev is unaltered, although we find that the mobility is some 30 percent larger than is predicted by their Eq. (18). In subsequent papers we shall apply these calculations to a discussion of diffusion and of the ac conductivity and dielectric loss.

II. DEGREE OF ASSOCIATION INTO COMPLEXES

Our problem in this section is the calculation of the degree of association between the impurity ions and the cation vacancies. As explained in the introduction we shall take the potential energy of two such "charges" separated by a distance r to be,

$$V(r)=\pm\frac{e^2}{\epsilon r}. \tag{2}$$

The positive sign is taken when the "charges" are the same and the negative sign when they are different; ϵ is the static dielectric constant of the pure solvent salt. We may proceed therefore by considering the Helmholtz free energy F of an alkali halide crystal, which is perfect except for the presence in the cation sublattice of N_i divalent impurity ions and N_i vacancies, interacting with one another according to Eq. (2). It may be assumed that F can be written as the sum of two parts: (1) a configurational term directly dependent on the presence of the impurities and (2) a vibrational term which is independent of the arrangement of the impurities in the lattice. (That the vibrational contribution to the free energy is independent of the arrangements of the impurity ions and vacancies can easily be justified as a first approximation.) In calculating the degree of association we then need not consider the second term at all. When in the following we speak of the free energy, we shall in fact mean only the configurational free energy, since this is all we shall need.

We shall suppose that of the N_i impurity ions and N_i vacancies which are distributed among the cation lattice sites, n are paired together into complexes. Each complex has z distinguishable orientations since the vacancy can be at any one of the z nearest neighboring positions to the impurity ion. The complexes have no net charge and we shall be justified in neglecting their small dipolar interactions with one another and with the unassociated charges. If now the impurity content is *sufficiently low for us also to neglect the mutual interactions of the unassociated charges* if follows immediately that the configurational free energy is

$$F_0\cong -kT\ln\left\{\frac{z^n\prod_{s=0}^{n}(N_+ +2N_i-2s)}{n!}\cdot\frac{(N_+ +2(N_i-n))!}{N_+!(N_i-n)!(N_i-n)!}\right\}-\frac{ne^2}{\epsilon r_0}. \tag{3}$$

The first term is the entropy term, the expression inside the braces being the product of the number of distinguishable ways of placing the n complexes on the lattice and the number of ways of arranging the remaining N_i-n impurity ions and N_i-n vacancies. The second term in the expression (3) is the energy of association, calculated by substituting the nearest neighbor separation, r_0 into Eq. (2). We can now obtain the equilibrium number of complexes by minimizing F_0 with respect to n. Using Stirling's theorem and the condition $N_i/N_+\ll 1$ we find

$$\frac{N_+ n}{(N_i-n)^2}=z\exp\left(\frac{e^2}{\epsilon r_0 kT}\right). \tag{4}$$

This is equivalent to the mass action formula (1), although (4) gives an explicit form for the temperature dependence of the equilibrium constant. If we rewrite (4), in terms of the molar concentration,

$$c=N_i/N_+, \tag{5}$$

and the degree of association,

$$p=n/N_+, \tag{6}$$

we get

$$p=1-\frac{1}{y}[-1+(1+2y)^{\frac{1}{2}}], \tag{7}$$

where

$$y=\exp\left[\frac{T_0}{T}+\ln(2zc)\right]. \tag{8}$$

[14] We would draw attention to the theory of liquid electrolyte solutions which has achieved great success, even though it neglects specific non-Coulombic interaction forces between ions close to one another. See, for example, H. Falkenhagen, *Electrolytes* (Oxford University Press, Oxford, 1934).

Here T_0, equal to $e^2/\epsilon r_0 k$, is the binding energy in units of Boltzmann's constant. We note that to derive (7) and (8) it is not necessary to make any assumption about the source of the binding energy. In Fig. 1 we show p as a function of T/T_0 for three different concentrations.

We now have to consider how these results are modified when the interactions between the unassociated ions and vacancies are not sufficiently small as to be negligible. The necessary modification in expression (3) can be obtained from the theory of electrolyte solutions, since our system of unassociated ions and vacancies is equivalent to a solution of a binary electrolyte in a medium of dielectric constant ϵ. The fact that our "ions" can only occupy discrete lattice positions whereas the ions in a solution can move around continuously, is not likely to be significant at the small concentrations occurring in this problem. For, at these concentrations, the average separation between charges will be much larger than the lattice spacing, and the discreteness of the allowed positions will be unimportant. We shall therefore describe the effects of the Coulomb interactions between the unassociated impurity ions and vacancies by means of the equations of the Debye-Hückel theory of electrolytes.[15] In applying these equations, we have to be careful not to allow an impurity ion and a vacancy to approach closer than the next nearest neighboring distance r_1, since if they approached as close as the nearest neighboring distance they would be considered as a complex and therefore not part of our unassociated "electrolyte." We shall therefore take the ionic radius parameter of the electrolyte theories to be r_1. We are now in a position to write down the additional free energy F_{el} due to interactions, which must be added to F_0 to get the total configurational free energy. From Eq. (913.1) of reference 5 we have:

$$F_{el}=\frac{-2(N_i-n)e^2}{3\epsilon}\cdot\kappa\tau(\kappa r_1). \tag{9}$$

where κ, the Debye-Hückel screening constant, is given by

$$\kappa^2=\frac{8\pi(N_i-n)e^2}{VekT}, \tag{10}$$

and

$$\tau(x)=\frac{3}{x^3}\left\{\ln(1+x)-x+\frac{x^2}{2}\right\}. \tag{11}$$

In Eq. (10) V is the volume of the crystal. We can now find the equilibrium value of n, the number of complexes by minimizing the sum of F_0 and F_{el} with respect to n. In place of (4) we get

$$\frac{nN_+}{(N_i-n)^2}=z\exp\left\{\frac{1}{kT}\left[\frac{e^2}{\epsilon r_0}-\frac{1}{2}\left(\frac{2e^2}{\epsilon}\right)^{\frac{1}{2}}\times\left(\frac{4\pi(N_i-n)}{VkT}\right)^{\frac{1}{2}}\cdot\frac{1}{1+\kappa r_1}\right]\right\}. \tag{12}$$

This equation is essentially the same as one derived by Bjerrum[16] in his theory of ionic association in electrolyte solutions. His definition of association is, however, more general than the association into complexes which we have used. In the language of our problem, it includes impurity vacancy pairs farther apart than nearest neighbors. The extension of our calculations in this manner is considered in the final section.

Equation (12) can be derived in a more intuitive way starting from (4), if we notice that the additional term in the exponential is merely the average potential energy of an unassociated vacancy in its surrounding Debye-Hückel charge cloud [see, for example, Eq. (911, 10) of reference 5]. The total expression in the square brackets is therefore the effective energy of excitation for a vacancy going from the associated to the unassociated state.

In order to obtain numerical results from Eq. (12) we have to make assumptions about the nature of the lattice, so that r_0 and r_1 may be related to one another and to V. Let us consider the NaCl-type lattice; here the cation sub-lattice is face-centered cubic, so that $z=12$, $r_1/r_0=\sqrt{2}$, and $V=2N_+a^3$, where a is the anion-cation separation equal to $r_0/\sqrt{2}$. With this assumption

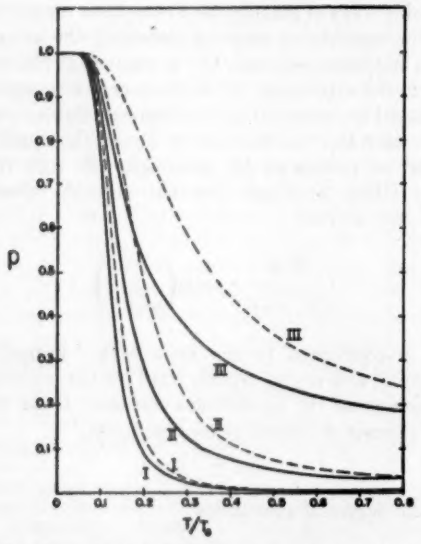

FIG. 1. Curves showing the degree of association p as a function of the reduced temperature T/T_0 at three different concentrations; I, $c=10^{-4}$; II, $c=10^{-3}$; III, $c=10^{-2}$. The dashed lines have been obtained from Eqs. (7) and (8); the full lines were calculated from Eq. (13).

[15] For a complete account see the reference cited in footnote 14. However for the purpose of this section it is more convenient to refer to Chapter IX of reference 5, particularly Secs. 904 through 914.

[16] N. Bjerrum, Kgl. Danske Videnskab. Selskab., Mat.-fys. Medd. 7, No. 9, (1926). See also Sec. 924 of reference 5.

of a face-centered cubic lattice, Eq. (12) can be rewritten as

$$\frac{p}{(1-p)^2}=\exp\left[\frac{T_0}{T}+\ln(12c)-\frac{2(2\pi\sqrt{2})^{\frac{1}{2}}(T_0/T)^{\frac{1}{2}}[(1-p)c]^{\frac{1}{2}}}{\{1+4(\pi\sqrt{2})^{\frac{1}{2}}[(1-p)cT_0/T]^{\frac{1}{2}}\}}\right]. \quad (13)$$

For $c\leqslant 10^{-3}$ it was found convenient to solve (13) by successive approximations using the pairs of equations [see (7) and (8)]:

$$p^{(j+1)}=1-\frac{1}{y^{(j)}}[-1+(1+2y^{(j)})^{\frac{1}{2}}], \quad (14)$$

and

$$y^{(j)}=\exp\left[\frac{T_0}{T}+\ln(24c)-\frac{2(2\pi\sqrt{2})^{\frac{1}{2}}(T_0/T)^{\frac{1}{2}}[(1-p^{(j)})c]^{\frac{1}{2}}}{\{1+4(\pi\sqrt{2})^{\frac{1}{2}}[(1-p^{(j)})cT_0/T]^{\frac{1}{2}}\}}\right], \quad (15)$$

and starting with $y^{(0)}$ given by (8). For concentrations greater than 10^{-3} this process requires more than three iterations, and it is more convenient to rearrange (13) to give T/T_0 as a function of p. Thus,

$$\left(\frac{T}{T_0}\right)^{\frac{1}{2}}\ln\left(\frac{p}{12c(1-p)^2}\right)+\left(\frac{T}{T_0}\right)\cdot 4(\pi\sqrt{2})^{\frac{1}{2}}(1-p)^{\frac{1}{2}}c^{\frac{1}{2}}\ln\left(\frac{p}{12c(1-p)^2}\right)-\left(\frac{T}{T_0}\right)^{\frac{1}{2}}+(1-p)^{\frac{1}{2}}c^{\frac{1}{2}}(\pi\sqrt{2})^{\frac{1}{2}}(2\sqrt{2}-4)=0. \quad (16)$$

In Fig. 1 we show the solutions of (13) for concentrations 10^{-2}, 10^{-3}, and 10^{-4} and for comparison we also show the corresponding solutions of (7) and (8). (Results have also been obtained for a number of other concentrations; details will be supplied on request.) We notice that the effect of the Coulomb interactions is to hasten the decay of p with increasing T, and that this effect is more pronounced the greater the impurity content. Even so the transition is not especially sharp; for example, since T_0 is of the order of several thousand degrees a system containing 1 percent of impurity would have to be raised many hundreds of degrees in order to reduce the degree of association from 90 percent to 40 percent. In the normal region of experimentation on ionic conductivity the degree of association is thus an appreciable fraction of unity. The gradualness of the transition also means that any thermal effects due to the dissociation of complexes will be very slight. Thus there will be an additional specific heat which may be calculated from (3) and (9) by using the formula

$$C_v=-Td^2(F_0+F_{el})/dT^2. \quad (17)$$

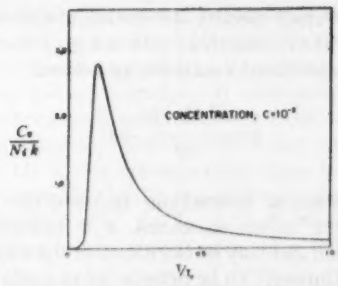

FIG. 2. The configurational specific heat, in units of the gas constant per gm-mole of impurity, as a function of the reduced temperature, T/T_0; impurity concentration, 10^{-2} mole per mole.

This is shown as a function of T in Fig. 2 for a lattice of the NaCl type and an impurity concentration of 10^{-2}. The apparent sudden rise of C_v from zero to nearly 0.03 R per gram-mole probably requires several hundred degrees to occur. This combined with the small height of the peak makes it seem quite impossible that the transition could be observed experimentally in this way. Nevertheless Dr. H. Kanzaki at the University of Tokyo in a private communication to the author, has reported the occurrence of a small λ-type anomaly in the specific heat of AgCl+1 percent $CdCl_2$ at 310°C which is not present in pure AgCl. He also reports a similar peak in the specific heat of AgBr+1 percent $CdBr_2$, occurring at about 130°C, but whose precise shape depends on the heat treatment which the specimen has undergone. As explained later in Sec. V, even our Eq. (13) probably underestimates the sharpness of the transition in real systems, and it is at least *possible* that the decomposition of the complexes could be detected thermally by measurements such as those which Kanzaki has made.

III. THE STEADY DC CONDUCTIVITY

As in the last section we can ignore the small dipolar interactions between the complexes and the unassociated impurity ions and vacancies. Furthermore, the complexes being neutral, we may forget them in this section since we shall only be concerned with the conductivity in the presence of a constant applied field E.[17] The unassociated impurity ions have no mobility *by themselves*,[18] so that they too make no direct contribution to the conductivity. They are however of indirect importance in that they form part of the Debye-Hückel

[17] This is only permissible for fields for which Ohm's law is obeyed. At higher fields the equilibrium number of complexes depends on E; see L. Onsager, J. Chem. Phys. 2, 599 (1934).

[18] This does not imply that the impurity ions are permanently fixed at their positions in the lattice. An impurity ion may move whenever there is an adjacent vacancy into which it can jump, although not otherwise. In other words at any instant only the associated impurity ions are mobile, but since the equilibrium existing in the numbers of associated and unassociated impurity ions is a dynamical equilibrium, *every* impurity ion before long gets its chance to move. Hence it is legitimate to assume a thermodynamic equilibrium distribution of impurity ions, even though they make no direct contribution to the conductivity.

atmosphere which hinders the motion of the vacancies. We express the conductivity σ in terms of the mobility u of the unassociated vacancies, as follows:

$$\sigma=\frac{N_i(1-p)}{V}\cdot eu. \tag{18}$$

In the absence of interactions between the impurity ions and the cation vacancies, u is independent of concentration and may be calculated in the way used by Mott and Gurney.[1] To be definite let us again take the face-centered cubic lattice; we then find that

$$u=4a^2ew_0/kT, \tag{19}$$

in which w_0 is the field free probability that a vacancy will jump to one particular neighboring position in unit time. This probability w_0 is a quantity explicitly independent of the impurity concentration. We may write it in terms of a frequency factor ν and a barrier height U as

$$w_0=\nu e^{-U/kT}, \tag{20}$$

(see Seitz, reference 2, particularly Sec. 122). In general this restriction is perhaps too naive, for we must expect that the introduction into the lattice of foreign ions and their accompanying vacancies will give rise to distortions such as to alter the barrier height U. This point has not received much attention so far,[19] but at least for the system $NaCl+CdCl_2$ to which we shall apply these equations the distortion at the limit of solubility is too small to be observable (private communication from Professor H. Pick). In deriving Eq. (19) it has been assumed that the field acting to make the vacancy jump preferentially in one direction, is the macroscopic internal electric field E ("pipe" field), and not a Lorentz internal field depending on the polarization of the crystal. The reasons for regarding this as a good approximation are contained in Sec. 5 in Chapter 1, reference 1.

At impurity concentrations where the Coulomb forces become important Eq. (19) for the mobility is not sufficient. The long-range interactions lead to the same relaxation effects as occur in the electrolyte solutions.[20] The tendency of a vacancy to be held back by its "atmosphere" of impurity ions requires us to multiply (19) by some factor $f<1$, in order to get the true mobility for substitution into (18). The theory of Onsager,[21] gives

$$f_0=1-\frac{e^2\kappa}{3\epsilon kT(2+\sqrt{2})}. \tag{21}$$

Here we have dropped the electrophoretic term, which has meaning in a liquid where the ions can drag the solvent along with them, but no meaning in connection with our crystal. The factor (21) has been previously used in the present connection by Teltow.[10] However, the formula (21) omits to take account of the closest distance of approach of the ions. Fortunately the electrolyte theory has been recently extended by Pitts,[22] and in place of (21) we shall take

$$f=1-\frac{e^2\kappa}{3\epsilon kT(\sqrt{2}+1)(1+\kappa r_1)(\sqrt{2}+\kappa r_1)}. \tag{22}$$

We may substitute for κ in terms of p, c, and T, so that for our face-centered cubic lattice, (22) becomes

$$f=1-\frac{2(2\pi\sqrt{2})^{\frac{1}{2}}}{3(\sqrt{2}+1)}\cdot\frac{c^{\frac{1}{2}}(1-p)^{\frac{1}{2}}(T_0/T)^{\frac{1}{2}}}{(1+\kappa r_1)(\sqrt{2}+\kappa r_1)}, \tag{23}$$

with

$$\kappa r_1=2\kappa a=4(\pi\sqrt{2})^{\frac{1}{2}}c^{\frac{1}{2}}(1-p)^{\frac{1}{2}}(T_0/T)^{\frac{1}{2}}. \tag{24}$$

Collecting together (18), (19), and (23), we obtain as the expression for the ionic conductivity:

$$\sigma=\frac{2e^2w_0}{akT}\cdot c(1-p)\times\left[1-\frac{2(2\pi\sqrt{2})^{\frac{1}{2}}}{3(\sqrt{2}+1)}\cdot\frac{c^{\frac{1}{2}}(1-p)^{\frac{1}{2}}(T_0/T)^{\frac{1}{2}}}{(1+\kappa r_1)(\sqrt{2}+\kappa r_1)}\right], \tag{25}$$

in which p is the solution of (13). The simple association theory as expressed by Eqs. (7), (8), (18), and (19) leads to a conductivity σ' given by

$$\sigma'=\frac{2e^2w_0}{akT}c(1-p^{(0)}). \tag{26}$$

If we abbreviate $2e^2w_0/akT$ by $1/\alpha$, we may write (26) with the aid of (7) and (8) as

$$c=\alpha\sigma'+12e^{T_0/T}(\alpha\sigma')^2. \tag{27}$$

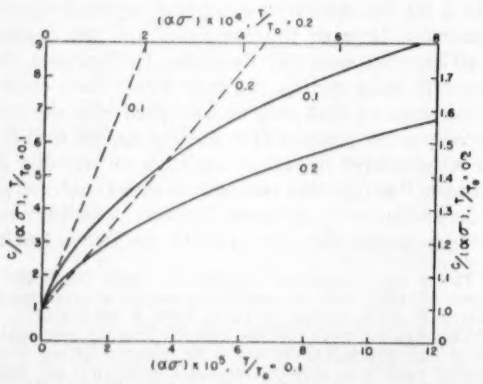

FIG. 3. Curves of $c/\alpha\sigma$ against $\alpha\sigma$ showing the difference between the simple association theory (dashed lines) and the theory presented here (full lines). The numbers on the curves are the corresponding values of T/T_0.

[19] The theory of a similar problem in metals has been given by A. W. Overhauser, Phys. Rev. 90, 393 (1953).

[20] See Chap. IX of reference 14, or alternatively H. S. Harned and B. B. Owen, *The Physical Chemistry of Electrolyte Solutions* (Reinhold Publishing Company, New York, 1950), second edition, Chaps. 2 and 4.

[21] L. Onsager, Physik. Z. 28, 286 (1927), Eq. (45).

[22] E. Pitts, Proc. Roy. Soc. (London) A217, 43 (1953).

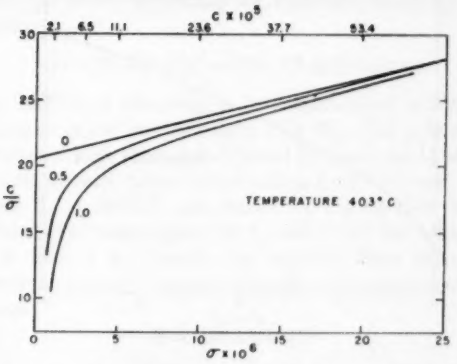

FIG. 4. Curves showing the effect of "background" impurity on plots of c/σ against σ (σ in ohm^{-1} cm^{-1}). The straight line corresponds to Eq. (29), as used by Etzel and Maurer to describe experimental results for the system NaCl+$CdCl_2$. The numbers on the curves are the concentrations c_0, of background impurity in units of 10^{-5}.

The conductivity σ given by (25) does not satisfy any such simple relation. We can see from (27) that a plot of $c/\alpha\sigma'$ against $\alpha\sigma'$ will give us a straight line. On the other hand, from Fig. 3 it is quite clear that the curves of $c/\alpha\sigma$ against $\alpha\sigma$ are only approximately straight lines at the higher concentrations; at lower concentrations the curvature increases and, in fact, as c and thus σ tend to zero the gradient $d(c/\alpha\sigma)/d(\alpha\sigma)$ diverges as c^{-1}. We also notice from Fig. 3 that the curves of $c/\alpha\sigma$ against $\alpha\sigma$ bear no simple relation to the particular straight lines corresponding to (27), i.e., their gradients cannot be simply related to the corresponding values of $\exp(T_0/T)$.

Before proceeding to study the experimental results in the light of Eq. (25), we must first draw attention to the effects of having a small constant background of impurity cations in the lattice, in addition to the much greater number deliberately added. This is the situation existing in practice since no crystal can be obtained absolutely pure. Suppose then that in addition to the concentration c of divalent impurity purposely added, there was also, unknown to us, an amount c_0 already present. Then taking Eq. (27) as an adequate relation between the conductivity σ and the total concentration $c+c_0$ of cation vacancies, we would have

$$c/\sigma = -c_0/\sigma + \alpha + 12\alpha^2 e^{T_0/T}\sigma. \tag{28}$$

A plot of c/σ against σ would then be a straight line only at concentrations $c \gg c_0$. As c and therefore σ decreased, the curve would bend increasingly downwards as shown in Fig. 4. Such a curvature would entirely mask the smaller effects of the long range interactions between the unassociated impurity ions and vacancies. Fortunately this difficulty is easily overcome; the experimental results may be corrected by adding to c, a value of c_0 inferred from the conductivity of a "pure" crystal in its "structure-sensitive" or low-temperature region.[1,2]

In the next section we shall consider the experimental data collected by Etzel and Maurer[11] for the system of NaCl+$CdCl_2$. As suggested by the theory, we analyze the plots of $(c+c_0)/\sigma$ against σ at various temperatures. (This has been made possible by Dr. Etzel's courtesy in supplying us with numerical data not contained in reference 11). Other systems which have been studied experimentally, but which we shall not consider here, include KCl+$CaCl_2$, $BaCl_2$, $SrCl_2$,[33] NaCl+$CaCl_2$,[34] and the silver halide systems referred to above.

IV. THE DATA OF ETZEL AND MAURER

In Table I we give the experimental values of σ and c as obtained[11] for the system of NaCl+$CdCl_2$ at four different temperatures. By a least-squares method Etzel and Maurer fitted these data directly to a parabolic equation of the type (27) resulting from the simple association theory, i.e.,

$$c = F\sigma + L\sigma^2. \tag{29}$$

The values which they deduced for F and L were given in Table III of their paper, and it appears from their Fig. 3 that the fit is very good. However, as suggested by the results of the last section, we have plotted $(c+c_0)/\sigma$ against σ at the four temperatures of Table I (Fig. 5). For c_0 we have taken the value 0.45×10^{-5}, corresponding to 10^{17} vacancies per cc in the "pure" NaCl as found by Etzel and Maurer.[11] That this is a reasonably good value may be checked by plotting σ against c from Table I; the negative intercept on the c axis is c_0. (It is nevertheless rather unsatisfactory that there is so much scattering of the experimental points in view of the importance of the c_0 correction, but we note that we can argue that c_0 cannot be *greater* than 0.45×10^{-5}.) Looking at Fig. 5 we see definite evidence at all four temperatures of that gentle curvature in the c/σ *versus* σ lines which Fig. 3 indicates should result from the Coulomb interactions of the unassociated ions and vacancies. But if this really is the case, F and L cannot have the significance they would appear to have from a comparison of (29) with (27); thus for example

TABLE I. Experimental values for the electrical conductivity of the system NaCl+$CdCl_2$ at 403°C, 344°C, 295°C, and 256°C as a function of the molar concentration of $CdCl_2$.

Concentration, $c\times10^5$	Conductivity (ohm^{-1} cm^{-1}), $\times10^6$ at 403°C	344°C	295°C	256°C
66.3[a]	24 200	6200	1440	360
38.75[a]	14 500	3900	950	242
19.0	8600	2230	565	147
8.8	4400	1170	300	81
5.0	3200	860	215	58
5.1	2580	680	173	46
3.6	2380	610	156	41
1	1080	290	73	19
0	220	64	17	5

[a] Mean of two values.

[33] H. Kelting and H. Witt, Z. Physik. 126, 697 (1949).
[34] C. Bean, thesis, University of Illinois, 1952 (unpublished).

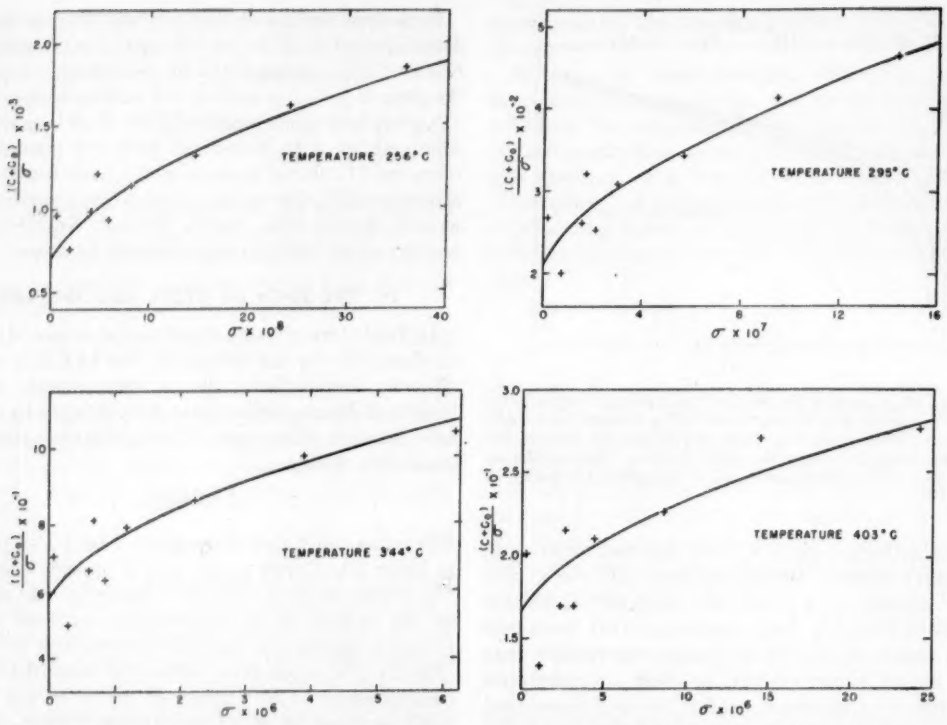

FIG. 5. The experimental data for NaCl+$CdCl_2$ given in Table I as represented by plots of $(c+c_0)/\sigma$ against σ (σ in ohm^{-1} cm^{-1}). For c_0 we have taken 0.45×10^{-4} as indicated in the text. The theoretical curves are obtained from Eq. (25) by taking $T_0=3900°K$ and w_0 as given by (19) and (30).

L/F^2 is not 12 exp(T_0/T) and cannot be used to find the binding energy of the Cd^{++}: vacancy complex as Etzel and Maurer attempted to do. We therefore propose a new analysis of the data of Table I based on Eq. (25). This is complicated by our not knowing either T_0 which is a constant or w_0 which is a function of temperature.

We shall not give the details of the derivation of these unknowns but only a summary of the method. Firstly we draw a set of smooth curves (not marked) through the points shown in Fig. 5 and from these we obtain, at each temperature, the values of the conductivity σ, corresponding to selected values of the concentration, $c+c_0$. (The highest concentration we used was 5×10^{-4}, i.e., below the highest concentration studied experimentally.) We aim first to derive T_0; we therefore eliminate the factor w_0 by calculating the ratio $\sigma/\sigma(5\times10^{-4})$ at each of the selected concentrations. This ratio equals $\alpha\sigma/\alpha\sigma(5\times10^{-4})$ which by (25) depends only on c, which we know, and T/T_0 which we do not know. By graphical interpolation we can now obtain, at each concentration, a set of values of T/T_0 corresponding to the four experimental temperatures. We average these to get just one set, from which knowing the experimental temperatures we derive a set of (four) values for T_0. Despite the many uncertainties, the four values which we obtained in this way showed no systematic variation with temperature and none differed by more than 7 percent from the mean. This mean value was 3900°K, corresponding to a binding energy for the complex of 0.34 ev. This may be compared with the theoretical value of 0.44 ev calculated by Reitz and Gammel.[13]

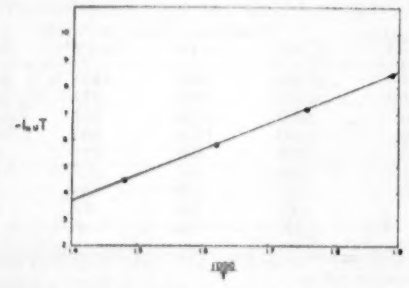

FIG. 6. The temperature dependence of the limiting mobility, u, in cm^2/volt sec; see Eqs. (19) and (30).

Having determined T_0, a direct comparison of the experimental σ *versus* c curves with the corresponding theoretical $\alpha\sigma$ *versus* c curves now gives α at each of the four temperatures. Knowing α we can calculate the limiting vacancy mobility u, in the absence of interactions [Eq. (19)]. In Fig. 6 we plot $\ln(uT)$ against $1/T$.

The four points appearing there are well fitted by the equation

$$uT = 21{,}200 \exp(-9750/T) \text{ cm}^2/\text{volt sec.} \quad (30)$$

The coefficient occurring in the exponential, which we interpret as the barrier height U in Eq. (20) is in close agreement with the value obtained by Etzel and Maurer. The theoretical curves which follow from (25) and (30) when T_0 is 3900°K are shown in Fig. 5. We have verified that these values for T_0 and U are not affected more than a few percent by starting from different "smooth curves" drawn through the experimental points.

V. CONCLUSION

We conclude with a note on the shortcomings of our theory. If we calculate T_0 from Eq. (2), it comes out to be about 7000°K for NaCl, i.e., almost twice the value we get by a direct comparison with experiment. One may therefore question the usefulness of comparing our simple model with real systems in which the impurity ion-vacancy interactions depart so appreciably from (2) at short distances. Now in our model, T_0 fixes both the binding energy of the complex and the magnitude of the interactions at large separations. Hence, by choosing T_0 so that kT_0 is the real binding energy of the complex, we alter the scale of the interactions at large distances, making them too small in this case. Therefore, as we have applied our theory, it underestimates the effect of the long-range interactions among impurity ions and vacancies. This defect can be corrected by taking explicit account of the non-Coulombic interaction between a vacancy and an impurity ion. This non-Coulombic part will only be significant at small separations, but it is not sufficient to suppose it is important only when the pair forms a complex. If it were, we would simply repeat the above calculations, replacing the binding energy $e^2/\epsilon a\sqrt{2}$ everywhere by its correct value. If we did this for the system $NaCl+CdCl_2$ and used the complex binding energy calculated by Reitz and Gammel,[13] namely, 0.44 ev, we should be employing a model in which the binding energy of a complex was less than that of a pair at the next nearest neighbor separation. The calculations can be extended therefore only when we first know the non-Coulombic part of the interaction energy at all the separations where it is not negligible. We may then proceed with the statistics of the problem by extending the definition of association so as to include all those pairs with an appreciable non-Coulombic interaction. We would, in fact, be dealing with an assembly of complexes some of which would be in their ground state while others would be in excited states.

This raises the question of the legitimacy of the idea of excited complexes; or rather, since a little reflection convinces us of the arbitrariness of the idea of association, the question is really at *what* separation ought we to draw the distinction between an unassociated pair and an associated pair. This question has been fully discussed by Fuoss,[25] for electrolyte solutions. He concludes that it is legitimate to divide the ions into two classes—those that are associated and those that are unassociated—provided the dividing distance is taken to be in the region of

$$q = e^2/2\epsilon kT. \quad (31)$$

The predicted properties of the solution are nevertheless insensitive to the exact distance which is chosen. For the temperatures of interest in connection with our problem, this implies that it makes very little difference whether we take the limiting separation to be $2a$ or $10a$. We have verified this directly for our simple model by treating pairs up to eighth neighbors (at $4a$) as associated. In regard to future calculations, which include the non-Coulombic interactions, we can therefore say that there is no point in taking the concept of association further than is necessary to include the significant non-Coulombic terms.

ACKNOWLEDGMENTS

It is a pleasure to record my thanks to Professor Seitz for suggesting this field of study and for his interest and encouragement. I would also like to thank Dr. Etzel and Dr. Pitts for sending me unpublished results and Mr. F. Booth of Kings College, London, for his comments on the manuscript. Finally, thanks are due Mrs. Jean Kellom for carrying out the numerical work.

[25] R. M. Fuoss, Trans. Faraday Soc. **30**, 967 (1934). For discussions of the effects of the dipolar interactions, which we have neglected, see R. M. Fuoss and C. A. Kraus, J. Am. Chem. Soc. **55**, 476, 1019, 2387 (1933), and R. M. Fuoss, J. Am. Chem. Soc. **56**, 1027 (1934).

Polaron Self-Energy and Bloch-Nordsieck Method

K. S. SINGWI AND B. M. UDGAONKAR
Tata Institute of Fundamental Research, Bombay, India

(Received July 27, 1953; revised manuscript received January 4, 1954)

By using the Bloch-Nordsieck method the self-energy of a polaron has been investigated in two limiting cases: (i) when the polaron velocity is low, i.e., $mv^2<\hbar\omega$, and (ii) when the velocity is high, i.e., $mv^2>\hbar\omega$. In case (i), this method gives results which are no better than those obtained by the use of the customary second-order perturbation theory, when the coupling constant is large. The contribution of the phonons of large momenta, if not more, is at least as much as that of the phonons of low momenta. However, in case (ii), we hope that our results are more satisfactory in view of the fact that the assumptions of the B−N method are better justified. In this case the self-energy is found to vary inversely as the velocity.

1. INTRODUCTION

RECENTLY Lee and collaborators[1,2] have investigated the motion of slow electrons in polar crystals by use of a method equivalent to Tomonaga's method of intermediate coupling. Now an essential assumption in the method of Tomonaga is that there is no correlation in the emission of successive virtual phonons by the electron. The recoil of the electron during the emission or absorption of a phonon would, however, introduce such a correlation. In applying the method the above authors hope that the variational method has taken this correlation into account, even though the wave function is chosen under the assumption of no correlation. This hope seems to be justified by the improved results obtained by these authors. However, it is not obvious whether the improvement in the results is due to the averaging effect of the variational procedure or to the fact that most of the important phonon momenta are sufficiently small for the the electron-recoil to be really negligible. In order to decide this question and also to study the motion of a fast electron, in which case the method of Lee *et al.*[2] breaks down, we have used in the present paper the Bloch-Nordsieck method. This method assumes the electron-recoil to be negligible but does not assume the coupling constant to be small. In the case of an electron with $mv^2\sim\hbar\omega$, or lower velocities, the method gives results which are not better than those obtained by the use of the second-order perturbation theory. We thus see that the B-N method is not superior to the perturbation method in such problems where the coupling constant is not small. This conclusion is further corroborated by the fact that the electron-lattice interaction energy in metals, calculated by Bardeen[3] and one of us (K.S.S.[4]) earlier by using the B-N method, is also of the same order as the perturbation-theoretical result (see Appendix). The inadequacy of the B-N method has to be attributed to the increased importance of virtual quanta of large momenta when the coupling constant is large. However, in the limiting case of high velocities, where the assumptions of this method are better justified, we expect to get more satisfactory results. In this case, we find that the self-energy of a polaron varies inversely as the velocity, a result which one should expect on physical grounds.

[1] T-D. Lee and D. Pines, Phys. Rev. 88, 960 (1952).
[2] Lee, Low, and Pines, Phys. Rev. 90, 297 (1953). We are thankful to these authors for making their paper available to us prior to publication.
[3] J. Bardeen, Revs. Modern Phys. 23, 268 (1951).
[4] K. S. Singwi, Phys. Rev. 87, 1044 (1952).

2. METHOD OF CALCULATION

Following Fröhlich, Pelzer, and Zienau,[5] we take the Hamiltonian as

$$H=\sum_k\frac{1}{2}\left(M\omega^2X_k^2+\frac{Y_k^2}{M}\right)+\frac{4\pi e}{\sqrt{V}}\sum_k\frac{1}{k}\left(X_k\sin\mathbf{k}\cdot\mathbf{r}+\frac{Y_k}{M\omega}\cos\mathbf{k}\cdot\mathbf{r}\right)+\frac{p^2}{2m},\quad(1)$$

where X_k and Y_k are canonical variables describing the lattice vibrations and therefore satisfying $[X_k,Y_{k'}]=i\hbar\delta_{kk'}$; ω is the frequency of the longitudinal optical vibrational mode of the lattice vibrations.[6] $\mathbf{r}$, $\mathbf{p}$ and m are the position and momentum vectors and the mass, respectively, of the electron; V is the volume of the crystal and M is given by[5]

$$\frac{1}{M\omega^2}=\frac{1}{4\pi}\left(\frac{1}{n^2}-\frac{1}{\epsilon}\right),\quad(2)$$

where n and ϵ are the optical refractive index and the static dielectric constant of the medium respectively.

Assuming the electron recoil to be small so that the difference,

$$\mathbf{P}=\mathbf{p}-m\mathbf{v},$$

between the actual electron momentum at any time and its average value $m\mathbf{v}$ is a small vector, we write (neglecting $P^2/2m$)

$$\frac{p^2}{2m}=\frac{(\mathbf{P}+m\mathbf{v})^2}{2m}\simeq\mathbf{P}\cdot\mathbf{v}+\tfrac{1}{2}mv^2=(\mathbf{p}-m\mathbf{v})\cdot\mathbf{v}+\tfrac{1}{2}mv^2$$
$$=\mathbf{p}\cdot\mathbf{v}-\tfrac{1}{2}mv^2.$$

[5] Fröhlich, Pelzer, and Zienau, Phil. Mag. 41, 221 (1950).
[6] We have assumed ω to be constant, which is not quite correct, This assumption would particularly break down when the masses of the two ions are nearly equal, e.g., in a crystal of KCl.

We also write

$$Q_k=\left(\frac{M\omega}{\hbar}\right)^{\frac{1}{4}}X_k,\quad P_k=\frac{Y_k}{(M\omega\hbar)^{\frac{1}{4}}},\quad\text{and}\quad A=\frac{4\pi e}{\sqrt{V}}\left(\frac{\hbar}{M\omega}\right)^{\frac{1}{4}}.$$

Then

$$[Q_k,P_{k'}]=\frac{1}{\hbar}[X_k,Y_{k'}]=i\delta_{kk'};\tag{3}$$

and the Hamiltonian becomes

$$H=\mathbf{p}\cdot\mathbf{v}-\tfrac{1}{2}mv^2+\tfrac{1}{2}\textstyle\sum_k(P_k^2+Q_k^2)\hbar\omega +A\textstyle\sum_k k^{-1}(Q_k\sin\mathbf{k}\cdot\mathbf{r}+P_k\cos\mathbf{k}\cdot\mathbf{r}).\tag{4}$$

Following Bloch and Nordsieck, we now make the canonical transformation:

$$Q_k=Q_k'+\sigma_k\sin(\mathbf{k}\cdot\mathbf{r});\quad P_k=P_k'+\sigma_k\cos(\mathbf{k}\cdot\mathbf{r});\quad \mathbf{r}=\mathbf{r}';\tag{5}$$
$$\mathbf{p}=\mathbf{p}'-\textstyle\sum_k\hbar\mathbf{k}\sigma_k[P_k'\cos\mathbf{k}\cdot\mathbf{r}+Q_k'\sin\mathbf{k}\cdot\mathbf{r}+\tfrac{1}{2}\sigma_k];$$

with

$$\sigma_k=-\frac{A}{\hbar k(\omega-\mathbf{v}\cdot\mathbf{k})}.\tag{6}$$

Then the transformed Hamiltonian is

$$H'=\mathbf{p}'\cdot\mathbf{v}-\frac{mv^2}{2}+\tfrac{1}{2}\textstyle\sum_k(P_k'^2+Q_k'^2)\hbar\omega -\frac{1}{2\hbar}\sum_k\frac{A^2}{(\omega-\mathbf{v}\cdot\mathbf{k})k^2}.\tag{7}$$

This is just the Hamiltonian of an electron and the lattice field without interaction, diminished by $|\Delta E|$, where

$$\Delta E=-\frac{A^2}{2\hbar}\sum_k\frac{1}{k^2(\omega-\mathbf{v}\cdot\mathbf{k})}.\tag{8}$$

This, therefore, is the depression in the energy of the electron brought about by its interaction with the lattice polarization.

In order to evaluate ΔE, we replace the sum over k by an integration:

$$\sum_k\rightarrow\frac{V}{(2\pi)^3}\int d^3k.$$

Then, using (3), we get

$$\begin{aligned}\Delta E&=-\frac{VA^2}{2\hbar(2\pi)^3}\int\frac{d^3k}{k^2(\omega-\mathbf{v}\cdot\mathbf{k})}\\&=-\frac{VA^2}{8\pi^2\hbar}\int_0^{k_0}\int_0^{\pi}\frac{\sin\theta d\theta dk}{(\omega-vk\cos\theta)}\\&=-\frac{VA^2}{8\pi^2\hbar v}\int_0^{k_0}\frac{dk}{k}\log\frac{vk+\omega}{|vk-\omega|}\\&=-\frac{2e^2}{M\omega v}\int_0^{k_0}\frac{dk}{k}\log\frac{vk+\omega}{|vk-\omega|}.\end{aligned}\tag{9}$$

The upper limit in this integral would ordinarily be the Debye cutoff $k_{\max}^D\sim 2^{\frac{1}{2}}\pi/a$, where a is the lattice constant. However, since we are using the Bloch-Nordsieck method and neglecting the recoil, the phonon-momenta $|\hbar k|$ have to be much smaller than the electron momentum $|mv|$. We, therefore, have to use the smaller of the two quantities $mv/\hbar$ and $k_{\max}^D$ as the upper limit. For electron energies comparable with the phonon-energy $\hbar\omega$, it can readily be seen that $mv/\hbar<k_{\max}^D$, so that the proper limit is $mv/\hbar$. (Actually, for the recoil to be really negligible, k_0 should be considerably smaller than $mv/\hbar$. $mv/\hbar$ would be the most favorable value.) With this upper limit, we shall evaluate (9) in two limiting cases: (i) small velocities ($mv^2<\hbar\omega$) and (ii) large velocities ($mv^2>\hbar\omega$).

Case I. Low Velocities

If $vk<\omega$, and since $k_0=mv/\hbar$, $mv^2<\hbar\omega$, we can expand the logarithm in (9) as a power series and get

$$\begin{aligned}\Delta E&=-\frac{4e^2}{M\omega v}\int_0^{mv/\hbar}dk\left[\frac{v}{\omega}+\frac{1}{3}\left(\frac{v}{\omega}\right)^3k^2+\cdots\right]\\&=-\frac{4e^2}{M\omega v}\left[\frac{mv^2}{\hbar\omega}+\frac{1}{9}\left(\frac{mv^2}{\hbar\omega}\right)^3+\cdots\right].\end{aligned}\tag{10}$$

If $mv^2\ll\hbar\omega$, we may retain only the first term in (10) and then the expression for ΔE reduces to

$$\Delta E=-\frac{2}{\pi}\left(\frac{mv^2/2}{\hbar\omega}\right)^{\frac{1}{4}}\alpha\hbar\omega,\quad\text{for } mv^2\ll\hbar\omega,\tag{11}$$

where α is the coupling constant given by[5]

$$\alpha=\frac{e^2}{2\hbar c}\left(\frac{2mc^2}{\hbar\omega}\right)^{\frac{1}{2}}\left(\frac{1}{n^2}-\frac{1}{\epsilon}\right).\tag{12}$$

Case II. High Velocities

If $k_0>\omega/v$ or $mv^2>\hbar\omega$, we have

$$\begin{aligned}&\int_0^{k_0}\frac{dk}{k}\log\frac{\omega+vk}{|\omega-vk|}\\&=\int_0^{\omega/v}\frac{dk}{k}\log\frac{\omega+vk}{\omega-vk}+\int_{\omega/v}^{k_0}\frac{dk}{k}\log\frac{\omega+vk}{vk-\omega}\\&=2\int_0^{\omega/v}\left[\frac{v}{\omega}+\frac{1}{3}\left(\frac{v}{\omega}\right)^3k^2+\cdots\right]dk\\&\quad+2\int_{\omega/v}^{k_0}\left[\left(\frac{\omega}{v}\right)\frac{1}{k^2}+\frac{1}{3}\left(\frac{\omega}{v}\right)^3\frac{1}{k^4}+\cdots\right]dk\\&=4\left[1+\frac{1}{3^2}+\frac{1}{5^2}+\cdots\right]-2\left[\frac{\hbar\omega}{mv^2}+\frac{1}{9}\left(\frac{\hbar\omega}{mv^2}\right)^3+\cdots\right]\\&=\frac{\pi^2}{2}-2\left[\frac{\hbar\omega}{mv^2}+\frac{1}{9}\left(\frac{\hbar\omega}{mv^2}\right)^3+\cdots\right].\end{aligned}\tag{13}$$

For $mv^2 \gg \hbar\omega$, this gives $\pi^2/2$, so that

$$\Delta E \sim -\frac{\pi}{4}\left(\frac{\hbar\omega}{mv^2/2}\right)^{\frac{1}{2}} \cdot \alpha\hbar\omega, \quad \text{for } mv^2 \gg \hbar\omega. \tag{14}$$

If $mv^2 \sim \hbar\omega$, (10) or (13) gives

$$\Delta E \sim -\frac{\pi\sqrt{2}}{8}\alpha\hbar\omega = -0.56\alpha\hbar\omega, \tag{15a}$$

$$= -0.09 \text{ ev}, \tag{15b}$$

for $\omega = 4.8 \times 10^{13}$ sec^{-1} and $\alpha = 5.2$ (for NaCl crystal); whereas the one-phonon approximation of Fröhlich *et al.*[5] gives

$$\Delta E = -\alpha^2\hbar\omega = -0.09 \text{ ev}. \tag{16}$$

Thus the two values (15b) and (16) are the same. This agreement, however, is purely accidental as is shown by the fact that the two formulas for ΔE have completely different dependence on the coupling constant α, and agree only when $\alpha = 5.2$. On the other hand, the more accurate value calculated by Lee *et al.*[2] is

$$\Delta E = -\alpha\hbar\omega = -0.16 \text{ ev}. \tag{17}$$

3. DISCUSSION

We thus see that for $mv^2 \sim \hbar\omega$, the self-energy given by the B-N method is the same as that obtained from the one-phonon approximation, and that ΔE varies directly as the velocity for small velocities [Eq. (11)], vanishing when v tends to zero. The calculation of Lee *et al.* shows, however, that for low velocities ΔE has a constant value $-\alpha\hbar\omega$. In this region, therefore, our method is very inaccurate. On the other hand, in the case of high velocities, where the assumption of the neglect of the electron recoil is better justified, we expect the result (14) to be more reliable. In this case we see from (14) that $\Delta E \propto 1/v$. (14) can be rewritten as

$$\Delta E = -\frac{\pi}{4}\left(\frac{1}{n^2} - \frac{1}{\epsilon}\right)\frac{e^2\omega}{v}, \tag{18}$$

by using (12). It is interesting to note that the interaction energy estimated classically by Fröhlich *et al.*[5] is the same as (18) except for the factor $\pi/4$ which replaces the factor $\frac{1}{2}$ in their expression [Eq. (1.3), p. 223, reference 5].

It has often been thought that since the B-N method does not involve an expansion in powers of the coupling constant, it should give results better than the perturbation theory for intermediate and higher values of the coupling constant.[7] In this method the momenta of the quanta involved are assumed to be small (so that the electron-recoil may be neglected) and it is this assumption that is responsible for poor results. In fact, if we compare our ΔE, as given by (15a), with that obtained by Lee *et al.*[1,3] we find that it is half their value. And since our method neglects the contribution of high-momentum phonons we may safely conclude that at least, if not more, half the contribution to ΔE comes from phonons of large momenta.

This conclusion is further corroborated by the results obtained by one of us (K.S.S.) and Bardeen[3,4] earlier in the application of the B-N method to the electron-lattice interaction in metals. There, too, the result obtained by using the B-N method is of the same order as the result obtained earlier by Fröhlich[8] from the second-order perturbation theory. (See Appendix.)

The range of applicability of the B-N method is therefore considerably limited. The intermediate coupling method of Tomonaga also neglects the effect of correlation between quanta introduced by the electron recoil. The fact that it gives better results than the B-N method in spite of this assumption shows that the average effect of the recoil is taken into account in an indirect way by the variational procedure employed in the method. The B-N method has no such adjustable parameters that could be varied, and, therefore, fails to compensate for the neglected recoil.

Our thanks are due to Professor H. J. Bhabha for his kind interest in this work. Thanks are also due Professor R. E. Peierls for many interesting discussions which the authors had while they were visiting Birmingham.

APPENDIX

In an earlier paper, hereafter referred to as I, the mutual interaction of two electrons as a result of the exchange of phonons was calculated by one of us (K.S.S.) using the Bloch-Nordsieck method. In paper I the method of evaluating the summation (I.5) was incorrect, and, therefore, we have here reperformed the integration[9] and find that the magnitude of the interaction is of the same order as the result of the customary perturbation theory, depending, of course, on the limit chosen for the maximum of the phonon wave number.

The interaction between two electrons [see paper I, Eq. (5)] is given by

$$U(r_1 - r_2) = \Re A \nabla_{r_1}^2 \sum_q \frac{s^2 \exp[i\mathbf{q}\cdot(\mathbf{r}_1 - \mathbf{r}_2)]}{s^2q^2 - (\mathbf{v}\cdot\mathbf{q})^2}. \tag{A.1}$$

$\Re$ means that we have to take the real part of the expression, and the suffix r_1 denotes that the derivative is with respect to r_1; v is the electron velocity, and s is the sound velocity. A is a constant.

[7] In fact, this method has been applied to meson-nucleon systems by several authors. But there too it cannot improve upon the perturbation method [see Takeda, Tanikawa, and Taniuti, Progr. Theoret. Phys. (Japan) 6, 994 (1951)].

[8] H. Fröhlich, Phys. Rev. 79, 845 (1950).

[9] We are thankful to Professor R. E. Peierls for suggesting that the integral should be re-evaluated.

If electron 2 is moving along the z axis, $r_2=vt$, and (1) becomes

$$U(r_1-r_2)=\Re A s^2\nabla_{r_1}^2\sum_q \frac{\exp\{i[q_x x_1+q_y y_1+q_z(z_1-vt)]\}}{s^2(q_x^2+q_y^2)+q_z^2(s^2-v^2)}. \tag{A.2}$$

If we take cylindrical coordinates $q_\perp$, q_z, and θ, and replace the summation by an integral, (A.2) becomes

$$U(r_1-r_2)=\Re A s^2\frac{V}{(2\pi)^3}\nabla_{r_1}^2\int d\theta dq_z q_\perp dq_\perp \times\frac{\exp\{i(\mathbf{q}_\perp\cdot\mathbf{r}_\perp)+iq_z(z_1-vt)\}}{s^2q_\perp^2-q_z^2(v^2-s^2)}. \tag{A.3}$$

Now

$$\int_0^{2\pi}\exp(i\mathbf{q}_\perp\cdot\mathbf{r}_\perp)d\theta=\int_0^{2\pi}\exp(iq_\perp r_\perp\cos\theta)d\theta =2\pi J_0(q_\perp r_\perp), \tag{A.4}$$

and

$$\int_{-\infty}^{\infty}\frac{\exp[iq_z(z_1-vt)]}{s^2q_\perp^2-q_z^2(v^2-s^2)}dq_z =-\frac{1}{v^2-s^2}\int_{-\infty}^{\infty}\frac{\exp[iq_z(z_1-vt)]}{q_z^2-\beta^2q_\perp^2}dq_z \tag{A.5}$$

$$=\frac{\pi}{\beta q_\perp(v^2-s^2)}\sin[\beta q_\perp|z_1-vt|], \tag{A.6}$$

where we have taken the principal value of the integral in (A.5) and where

$$\beta^2=s^2/(v^2-s^2).$$

In taking the principal value of the above integral, we have essentially used a symmetric combination of advanced and retarded potentials, corresponding to a symmetric double wake about the position of the electron. In the absence of any definite model, a condition which may give rise to superconductivity, it appears reasonable to take the principal value. However, if the general wake picture as visualized in I has anything to do with superconductivity, then integration will have to be carried out with the boundary condition[10] that the wake be found behind the electron. This boundary condition corresponds to using the retarded potential only and can be easily imposed by a suitable choice of the contour. If this is done the interaction energy is twice that given by (A.8).

[10] This fact was pointed out to us by Dr. Pines.

Introducing (A.4) and (A.6) into (A.3) we get

$$U(r_1-r_2)=\Re\frac{AV\beta}{4\pi}\nabla_{r_1}^2\int_0^\infty dq_\perp\sin[\beta q_\perp|z_1-vt|]J_0(q_\perp r_\perp)$$

$$=\frac{AV\beta}{4\pi}\nabla_{r_1}^2\int_0^\infty dq_\perp\sin[\beta q_\perp|z|]J_0(q_\perp r_\perp)$$

$$=\frac{AV\beta}{4\pi}\nabla_{r_1}^2\begin{cases}(\beta^2z^2-r_\perp^2)^{-\frac{1}{2}} & \text{if } |\beta z|>r_\perp\\ 0 & \text{if } |\beta z|<r_\perp\\ \infty & \text{if } |\beta z|=r_\perp,\end{cases} \tag{A.7}$$

where

$$\mathbf{r}=\mathbf{r}_1-\mathbf{r}_2 \quad\text{and}\quad z=z_1-z_2.$$

The interaction energy given by (A.7) is singular on the sound cone and vanishes outside it. An electron, therefore, interacts only with electrons within its sound-cone; and since the solid angle of this is β^2, it interacts only with a fraction β^2 of the electrons surrounding it. To calculate the average interaction energy per electron, we have therefore, to multiply (A.7) by β^2. Again, since for a given value of z, $U(r)$ is minimum when $r_\perp=0$, we might expect the electrons to arrange themselves in chains directed along the direction of motion. To get an estimate of the average interaction energy we may neglect $r_\perp$ and find that

$$U(r)\simeq\frac{AV}{2\pi\beta^2r^3}.^{11} \tag{A.8}$$

To get $\bar{U}$, the average interaction energy per electron, we have to multiply (A.8) by β^2 as pointed out above. It is seen from (A.8) that the magnitude of $\bar{U}(r)$ depends critically on the value of r chosen. The uncertainty relation, however, sets a lower limit to the value of r, which is given by

$$r_{\min}\cdot\Delta p\gtrsim\hbar,$$

where Δp is the uncertainty in the electron momentum. Therefore,

$$r_{\min}\gtrsim\frac{\hbar}{\Delta p}.$$

But Δp cannot exceed $\hbar q_{\max}$, the maximum momentum of the phonons with which the electron interacts. Hence

$$r_{\min}>1/q_{\max}.$$

[11] We are grateful to Dr. M. J. Buckinham for drawing our attention to the factor β^2 missing in Eq. (9) of I. The sign in Eq. (I.9) was incorrect. It is + and not −. The force between electrons is thus repulsive. An electron outside the wake of another electron will not therefore be able to enter it, whereas one inside will be drawn to the axis of the wake, thus giving rise to several chains.

The value of $\bar{U}(r_{\min})$ is, therefore, very sensitive to the value chosen for $q_{\max}$. For the Bloch-Nordsieck method to be applicable, we may suppose $q_{\max} < (1/20) \times$ Debye cutoff, i.e., $q_{\max} \leqslant 5 \times 10^6$. Then $r_{\min} = 2 \times 10^{-7}$. This gives

$$\bar{U}(r_{\min}) \approx 10^{-2} \text{ ev},$$

which is the same as that given by Fröhlich using the second-order perturbation theory. It should be clearly understood that the above choice of $q_{\max}$ is entirely arbitrary and there is nothing in the B-N method to guide us in this respect except that the momenta of the phonons have to be much less than those of the electrons with which they interact.

PHYSICAL REVIEW VOLUME 94, NUMBER 1 APRIL 1, 1954

Piezoresistance Effect in Germanium and Silicon

CHARLES S. SMITH
Bell Telephone Laboratories, Murray Hill, New Jersey
(Received December 30, 1953)

Uniaxial tension causes a change of resistivity in silicon and germanium of both *n* and *p* types. The complete tensor piezoresistance has been determined experimentally for these materials and expressed in terms of the pressure coefficient of resistivity and two simple shear coefficients. One of the shear coefficients for each of the materials is exceptionally large and cannot be explained in terms of previously known mechanisms. A possible microscopic mechanism proposed by C. Herring which could account for one large shear constant is discussed. This so called electron transfer effect arises in the structure of the energy bands of these semiconductors, and piezoresistance may therefore give important direct experimental information about this structure.

INTRODUCTION

THE effect of pure hydrostatic pressure on resistance has been extensively studied, notably by Bridgman, who also made the first piezoresistance measurements[1] known to us on several polycrystalline metals. Bridgman has also outlined the formal nature of the piezoresistance effect in single crystals[2] and applied this analysis to the measurements of Allen[3] on bismuth. Cookson[4] later corrected the original outline by Bridgman. Allen has reported single crystal tension coefficients in addition for tin,[5] antimony,[6] and zinc and cadmium.[7] The present observations[8] for germanium and silicon are apparently the first for cubic crystals and the first giving the complete tensor.

The change in resistance caused by stress induced dimensional changes is small and may be corrected for, allowing any remaining effect to be expressed as a change in resistivity ρ. The resistivity may be stress dependent through either the mobility or the number of the charge carriers. The effect of stress on the mobility of the charge carriers has been observed for many materials. For example, values of $d \ln\rho / d \ln v$ running from two to six are reported for pressure experiments;[9] these values agree fairly well for a number of metals with a simple calculation[9] of the change of mobility produced by the change in the amplitude of thermal vibrations with volume v,

$$(d \ln\rho / d \ln v) = (2\alpha v_0 / \chi_0 C_v), \tag{1}$$

where α is the thermal expansion coefficient, χ the compressibility, and C_v the specific heat. For silicon and germanium the calculated values of this quantity are 1.4 and 1.7.

In semiconductors the stress may be expected to change the number of charge carriers. The stress X causes a volume change δv which in turn causes a change δE_g in the energy gap between the valence and conduction bands. The number of carriers and hence the resistivity therefore change. For germanium at 300°K $\delta E_g = -4.0 d \ln v$ (electron volts),[10] and for intrinsic germanium this means that $d \ln\rho_i / d \ln v = -77$. This volume-energy gap effect can be shown to be roughly proportional to $(\rho/\rho_i)^2$; the observations reported below were carried out at values of $(\rho/\rho_i)^2$ where the energy gap effect is detectable but small.

The piezoresistance results for germanium and silicon which are reported here have been expressed in terms of the pressure coefficient of resistivity and two simple shear coefficients. One of the shear coefficients for each of the materials is exceptionally large and cannot be

[1] P. W. Bridgman, Proc. Am. Acad. Arts Sci. **60**, 423 (1925).
[2] P. W. Bridgman, Phys. Rev. **42**, 858 (1932).
[3] Mildred Allen, Phys. Rev. **42**, 848 (1932).
[4] J. W. Cookson, Phys. Rev. **47**, 194 (1935).
[5] Mildred Allen, Phys. Rev. **52**, 1246 (1937).
[6] Mildred Allen, Phys. Rev. **43**, 569 (1933).
[7] Mildred Allen, Phys. Rev. **49**, 248 (1936).
[8] The large tension effects were noticed in these laboratories by J. R. Haynes. The stress sensitive drift mobility observed by Lawrence in *n* germanium is probably the same effect. R. Lawrence, Phys. Rev. **89**, 1295 (1953).
[9] N. F. Mott and H. Jones, *The Theory of the Properties of Metals and Alloys* (Oxford University Press, London, 1936), p. 271.
[10] J. H. Taylor, Phys. Rev. **80**, 919 (1950).

explained in terms of these previously known mechanisms. The mobility mechanism appears to be too small to account for the magnitude of the large shear coefficient, and the energy gap effect gives zero contribution to both shear coefficients. Thus the explanation of the salient feature of the present work must be sought in an essentially new mechanism.

EXPERIMENTAL

As shown in the Appendix it is necessary to make three experimental measurements of at least two types in order to determine the complete piezoresistance in germanium and silicon. The essential features of the arrangements which have been used are shown in Fig. 1. Uniaxial tensile stress X was applied to single crystal rods by hanging a weight on a string, and the IR drop was measured. The two crystal orientations shown in the figure were used in combination with the two electrode configurations shown, yielding the necessary three measurements of two types. The extra measurement was made for a few specimens as an internal check.

Procedure

The IR drop across the potential electrodes was read by a type-K potentiometer. The stress induced difference potential δV was indicated directly in microvolts on the output meter of a Type-9835A Leeds and Northrup dc amplifier.

The observational procedure was to load the specimen, balance the potentiometer at a convenient meter reading, lift the weight and replace it, observing the throw of the output meter δV, and then to repeat the process for the next load. The potential change δV was found to reverse with the sign of the stress, to show no detectable hysteresis, and to be linear with load in the range employed.

The fast response of the indicating instrument made it possible to make the observations in spite of small drifts caused by ambient temperature changes. The electrical observations were all made at *constant current* supplied from a 300-volt, 300 000-ohm source. The potentials V ranged all the way from a few millivolts to a few volts for the different electrode arrangements and resistivity values studied. Loads ranging from 0.1 to 1 kg were applied, corresponding to stress levels from 10^7 to 10^8 dyne cm^{-2}. In the constant current case $\delta V/V=\delta R/R$; values of this quantity ran from 10^{-5} to 10^{-3} for different specimens.

Materials and Specimen Preparation

The starting materials were single crystals of As-doped n-type germanium and Ga-doped p-Ge and silicon crystals which were grown n or p from selected raw material. The crystals were oriented on an x-ray goniometer. The individual specimens A, B, C, D (Fig. 1), of a given nominal resistivity value were cut

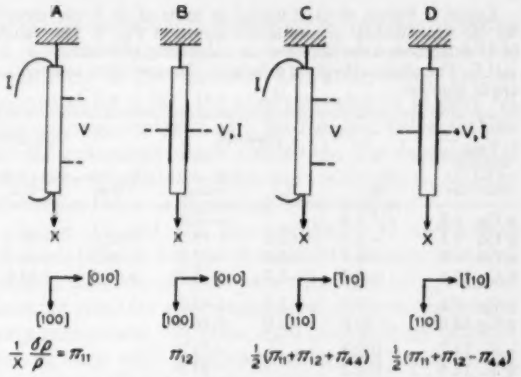

FIG. 1. Schematic diagram showing the stress system, the crystallographic orientations and the electrode structures which have been used. Arrangements A and C are designated as longitudinal in the text; B and D are called transverse.

from adjacent slices to hold the resistivity variation within the group to 10 percent. The specimen ends were waxed into small grips with sealing wax in the transverse cases (B, D), or rhodium plated and soldered in the longitudinal cases (A, C). The grips were aligned manually with only small difficulties from misalignment as noted below. The long transverse electrodes were rhodium and copper plated.

Corrections

The directly observed quantity in the present experiments is $(1/X)(\delta R/R)$, which must be corrected for dimensional changes to yield $(1/X)(\delta\rho/\rho)$ by adding for the several cases as follows:

$$\text{(A)}, -(S_{11}-2S_{12}); \quad \text{(C)}, -(\tfrac{1}{2}S_{44}-S_{12});$$
$$\text{(B)}, +S_{11}; \quad \text{(D)}, +(\tfrac{1}{2}S_{44}+S_{12}).$$

The elastic compliances S_{ij} are well known for silicon and germanium.[11]

The transverse measurements are then subject to another correction which arises because the current lines are not straight at the ends of the electrodes. Such a correction would not be necessary if the medium were isotropic in resistivity under stress. An approximate correction has been worked out by H. Suhl of these laboratories and is

$$\Pi_T=\Pi_T(\text{obs})+\frac{\omega}{2\Pi l}(\Pi_T-\Pi_L), \qquad (2)$$

where the Π's are $(1/X)\delta\rho/\rho$, L and T stand for longitudinal and transverse, ω is the width of the specimen, and l the length of the transverse electrode. This correction is nearly negligible for the reported results for arrangement B. It amounts to around 10 percent for the reported values of arrangement D and its uncertainty becomes significant. Arrangement D, how-

[11] E. M. Conwell, Proc. Inst. Radio Engrs. 40, 1327 (1952).

TABLE I. Values of $(1/X)(\delta\rho/\rho)$ in units of 10^{-12} cm^2 dyne^{-1} for the experimental arrangements shown in Fig. 1. The values of D calculated were obtained by combining observation A, B, and C. The observations are adiabatic. The specimen resistivities are in ohm-cm.

Type, material, and resistivity	Observed A	Observed B	Observed C	Observed D	Calculated D
	Π_{11}	Π_{12}	$\frac{1}{2}(\Pi_{11}+\Pi_{12}+\Pi_{44})$	$\frac{1}{2}(\Pi_{11}+\Pi_{12}-\Pi_{44})$	$\frac{1}{2}(\Pi_{11}+\Pi_{12}-\Pi_{44})$
n Ge 1.5	−2.3		−71.8		
n Ge 5.7	−2.7	−3.9	−71.7	+62.0	+65.1
n Ge 9.9	−4.7	−5.0	−73.8	+66.2	+64.1
n Ge 16.6	−5.2	−5.5	−74.7	+67.9	+64.0
p Ge 1.1	−3.7	+3.2	+48.1		
p Ge 15.0	−10.6	+5.0	+46.5		
n Si 11.7	−102.2		−31.2		
n Si 18.6	−102.2		−31.0		
p Si 7.8	+6.6	−1.1	+71.8		
p Si 22.7	+6.5		+71.9		

ever, has been used only as an internal check of the derived coefficients. The combined results omit this observation.

Precision and Errors

By the nature of the apparatus the electrical precision was constant at something better than one percent in δV for all specimens except those where a combination of two out of three things obtained: low resistivity, transverse electrodes, or small piezoresistance.

The crystallographic orientations of the final rods were within 20 minutes of the nominal values in all cases. This accuracy of alignment is quite satisfactory because the piezoresistance effect, although highly anisotropic, varies as the square of the error angle at the orientations used.

The transverse measurements are generally of less precision than the longitudinal simply because V is small. Moreover, a rectifying contact on such specimens will give a spurious reading arising in the energy gap effect.[12] The procedure which has been adopted is to test all transverse specimens for rectification, keeping only those which showed linear V–I curves. Thus, for example, the transverse scheme failed entirely for n Si, and the necessary third observation was obtained by an isothermal pressure measurement.

The longitudinal results for n Ge and some of those for p Ge were obtained with rods to which the potential electrodes were directly applied by rhodium plating. All the silicon and most of the p Ge measurements were obtained with "bridges" which are rods with integral semiconductor side arms. Contacts could be made to the side arms which are well outside the stress field, thus eliminating any question of stress induced electrode effects. In several cases rod specimens were checked against bridge specimens with excellent agreement.

Certain specimens showed slight piezoresistance nonlinearity in the initial mounting, but this nonlinearity was removed in all cases by straightening the mount or remounting. Another indication that these small effects were caused by poor alignment of grips and sample was the inconsistency of the magnitude and sign of this nonlinearity. The origin of the nonlinearity has not been tracked down but there are several ways in which nonuniform or biaxial stress plus tensor piezoresistance could account for it.

[12] Hall, Bardeen, and Pearson, Phys. Rev. 84, 129 (1951).

Conditions

The piezoresistance was observed with the specimen in a thermally lagged and reasonably light tight enclosure. The room temperature results were either obtained at 25±1°C or a short extrapolation was made to that temperature. The low-temperature results were obtained by mounting the specimen in a dewar flask over boiling liquid N_2.

The resistivity values which have been studied were chosen to be below the point where minority carrier conduction is important and above the point where impurity scattering becomes significant.

The present observations are considered to be adiabatic rather than isothermal. The measured thermal time constant of the specimens in their measurement environment was about 15 seconds, while the time constant of the amplifier was 0.6 second. The difference between the isothermal and adiabatic values is small in any case, roughly 0.5×10^{-12} cm^2 dyne^{-1}.

RESULTS

Table I shows the end product of the foregoing procedures; the entries in that table are termed observations. The tensor nature of the piezoresistance effect is outlined in the appendix where it is shown how the observations A, B, and C may be expressed in terms of the elements Π_{11}, Π_{12}, and Π_{44} of the pertinent fourth rank tensor. It is more interesting, however, to quote the results in the form of three other constants which are combinations of the actual tensor elements.

In the case of cubic crystals there are three combinations of the elastic constants C_{ij}, namely $(C_{11}+2C_{12})/3$, C_{44} and $(C_{11}-C_{12})/2$ which relate crystallographically simple stresses to the corresponding strains and which have been termed fundamental elastic constants. For germanium and silicon there are three similar combinations of piezoresistance coefficients $\Pi_{11}+2\Pi_{12}$, Π_{44}, and $\Pi_{11}-\Pi_{12}$. The combination $\Pi_{11}+2\Pi_{12}$ is the negative of the pressure coefficient. The shear coefficients Π_{44} and $\Pi_{11}-\Pi_{12}$ give the transverse electric field which develops when an appropriate shear stress is applied, but it is simpler to consider their meaning directly in terms of hypothetical modifications of the present experiments C and A, respectively. The coefficient Π_{44} would give directly $(1/X)(\delta\rho/\rho)$ in arrangement C if, in addition to the longitudinal tensile stress X, an equal transverse compression were also applied. The two stresses effectively change the angle between

two [100] type directions. The coefficient $\Pi_{11}-\Pi_{12}$ bears the same relation to arrangement A, the stresses changing the angle between two orthogonal [110] directions. These constants are listed in Table II.

The shear constants Π_{44} and $\Pi_{11}-\Pi_{12}$ have the same adiabatic and isothermal values. The adiabatic pressure coefficient is listed as directly determined from the observations. The isothermal pressure coefficients were obtained by applying the appropriate correction, using for the temperature coefficients of resistance the values given by conventional mobility-temperature laws except for the 16.6 ohm-cm n Ge sample where the negative temperature coefficient of resistance was measured. Values of the isothermal pressure coefficient determined by Bridgman for several samples of n and p Ge have been included in Table II for comparison. The latter have been corrected slightly for dimensional changes.

TABLE II. Values of the derived piezoresistance coefficients in units of 10^{-12} cm^2 dyne^{-1}. Resistivities are in ohm-cm.

Type, material, and resistivity	Π_{44}	$\Pi_{11}-\Pi_{12}$	$-\frac{1}{P}\frac{\delta\rho}{\rho}=\Pi_{11}+2\Pi_{12}$ Adiabatic	Isothermal
n Ge 1.5	−138.1	+ 1.0	(− 8.7)[a]	− 7.0
n Ge 4.2[b]				− 8.3
n Ge 5.7	−136.8	+ 1.2	−10.5	− 8.8
n Ge 8.4[b]				− 9.8
n Ge 9.9	−137.9	+ 0.3	−14.7	−13.0
n Ge 16.6	−138.7	+ 0.3	−16.2	−17.9
n Ge 18.5[b]				−27.1
p Ge 0.9–3.3[c]				+ 2.5
p Ge 1.1	+ 96.7	− 6.9	+ 2.7	+ 5.2
p Ge 15.0	+ 98.6	− 15.6	− 0.6	+ 1.9
n Si 11.7	− 13.6	−155.6	+ 4.6	+ 5.7[d]
p Si 7.8	+138.1	+ 7.7	+ 4.4	+ 6.0

[a] This value extrapolated from n Ge 5.7 and n Ge 9.9.
[b] P. W. Bridgman (see reference 13) and by letter. Values are from the initial pressure effect.
[c] P. W. Bridgman (see reference 13). There were six specimens in this resistivity range, five of which were consistent at the value shown and one of which showed zero pressure effect.
[d] Measured directly.

The elastoresistance coefficients defined in the appendix relate the fractional resistivity change to the strain and have the advantage of putting all the coefficients for all the materials on a comparable strain basis. Simple combinations of these have meanings similar to those for the fundamental piezoresistance coefficients. In particular $(m_{11}+2m_{12})/3=d\ln\rho/d\ln v$ is the volume dilation coefficient. The shear constant m_{44} gives $(1/e)(\delta\rho/\rho)$ in arrangement C when the longitudinal strain $e/2$ and the transverse strain $-e/2$ are imposed. The shear constant $(m_{1.}-m_{12})/2$ is similarly related to arrangement A. These fundamental elastoresistance coefficients are listed in Table III.

DISCUSSION OF THE RESULTS

The coefficients presented in Table II or in Table III are of both signs and show a wide range of magnitudes reflecting the very high anisotropy of the piezoresistance in these cubic materials. A convenient measure of the anisotropy is the quantity $\Pi_{44}/\frac{1}{2}(\Pi_{11}-\Pi_{12})$ (or its reciprocal for n Si); the smallest value of 14 here for this quantity contrasts with the frequent value of three for the equivalent elastic anisotropy. The fundamental constants separate the large and small effects, and the discussion below is divided up accordingly.

Tables II and III list essentially 12 coefficients (four materials×3 types of constant). It may be noted initially that four of these vary with resistivity, *viz.*, the pressure effect for n germanium and all three coefficients for p germanium. The other eight constants are believed not to vary with resistivity within the experimental uncertainty. This conclusion must be reached for silicon by inspection of Table I, where the important longitudinal observations show such marked independence of resistivity that the difficult third observation was made only for the lower resistivity value. It is hardly conceivable that Π_{12} and Π_{44} should *both* vary in just such a way as to keep $\frac{1}{2}(\Pi_{11}+\Pi_{12}+\Pi_{44})$ constant.

The Pressure Effect

Values of the isothermal $\Pi_{11}+2\Pi_{12}$ in Table II are convenient to consider first because several values directly determined by Bridgman[13] for n germanium are available for comparison. Inspection of the combined total of seven measured values show that they vary smoothly with resistivity. Closer inspection shows that $\Pi_{11}+2\Pi_{12}$ is linear with the resistivity squared and the resistivity variation is therefore assigned entirely to the energy gap effect as discussed in the introduction. The slope of the ρ^2 plot is correct for this mechanism. The energy gap effect may then be extrapolated out allowing one to deduce a value of the pressure coefficient which describes the effect of pressure on *lattice* mobility alone without the complication of a change in charge carrier number.

For p-type germanium the sign of $\Pi_{11}+2\Pi_{12}$ agrees with that determined by Bridgman at low resistivity, but the magnitude does not. No reason for this discrepancy has been discovered, our own measurements

TABLE III. Values of the dimensionless elastoresistance constants. Resistivities are in ohm-cm.

Type, material, and resistivity	m_{44}	$\frac{m_{11}-m_{12}}{2}$	$\frac{d\ln\rho}{d\ln v}=\frac{m_{11}+m_{12}}{3}$ Adiabatic	Isothermal
n Ge 1.5	− 93.0	+ 0.4	− 6.6	− 5.3
n Ge 5.7	− 92.0	+ 0.5	− 8.0	− 6.8
n Ge 9.9	− 92.8	+ 0.1	−11.1	− 9.8
n Ge 16.6	− 93.4	+ 0.1	−12.3	−13.6
p Ge 1.1	+ 65.1	− 2.8	+ 2.0	+ 3.9
p Ge 15.0	+ 66.5	− 6.3	− 0.5	+ 1.4
n Si 11.7	− 10.8	−79.5	+ 4.6	+ 5.7
p Si 7.8	+110.0	+ 3.9	+ 4.4	+ 6.0

[13] P. W. Bridgman, Proc. Am. Acad. Arts Sci. 82, 71 (1953).

having been repeated with other specimens as were Bridgman's. In any case upon intercomparing the present low- and high-resistivity pressure coefficients the effect of the energy gap is again apparent, the change in coefficient being, correctly, in the same direction as for n-type germanium. The magnitude of the resistivity dependence is also very roughly correct, but the point need not be belabored when only two data are available. The fact that the pressure effect in both types of silicon is apparently independent of resistivity (again see Table I) would seem to imply zero energy gap effect at room temperature and at these resistivities.

The values of $(m_{11}+2m_{12})/3=d\ln\rho/d\ln v$ for silicon and at the lowest resistivity in germanium then describe the effect of a volume change on the mobility. Such values may be compared in sign and magnitude with those given by Eq. (1) which basically describes the effect of volume dilation on the amplitude of the thermal waves and hence on mobility. The values shown in Table II have the normal positive sign given by Eq. (1) except for n germanium which is anomalous. The same quantity for Li, Ca, and Sr has anomalous sign. Frank has suggested that the negative sign in Li results from a decrease with volume of the effective mass of the electrons.[9]

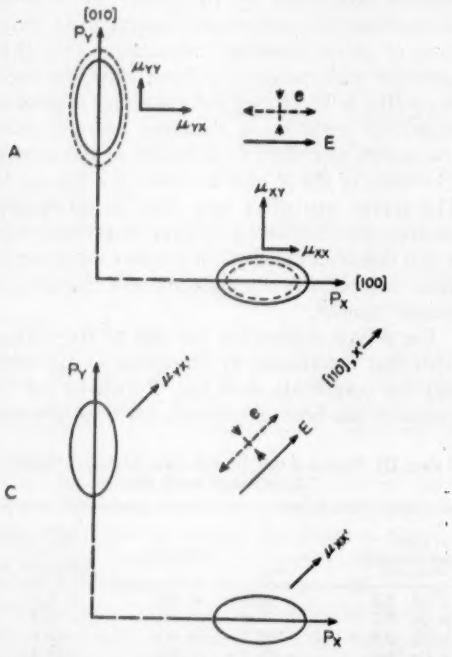

FIG. 2. Schematic diagram of probable constant energy surfaces in momentum space for n Si. The electrons are located in six energy valleys at the centers of the constant energy ellipses which are shown greatly enlarged. The effect of stress on the two valley energies shown is indicated by the dotted ellipsoids. The mobilities of the several groups of charge carriers in various directions are roughly indicated by the arrows. The diagrams correspond to the two experimental arrangements A and C of Fig. 1.

The assumptions underlying Eq. (1) are valid only at temperatures above the characteristic temperature. This condition is not met by silicon and only barely by germanium so that magnitudes may be compared only as to order. For p germanium the experimental value of $(m_{11}+2m_{12})/3$ is somewhere between two and five compared with the calculated value of 1.7. Both types of silicon give about 4.5 compared with the calculated 1.4. Thus Eq. (1) gives at least the right order of magnitude for these three coefficients.

The Small Shear Coefficient

For each of the materials studied one of the shear constants is large and one is small. The small ones are $(m_{11}-m_{12})/2$ for n Ge (zero within the experimental uncertainty), p Ge (-2.8 to -6.3) and p Si ($+3.9$). The coefficient m_{44} is small for n Si (-10.8). The resistivity dependence of $(m_{11}-m_{12})/2$ for p Ge is certainly real. These values for the small shear coefficient are also of the order of magnitude of what one would expect from the shear analog of Eq. (1). It thus seems unprofitable to look for a more detailed mechanism than that of the effect of strain in general on the thermal wave amplitude in the case of three volume dilation coefficients and all four of the smaller shear coefficients.

The Large Shear Coefficient

The shear coefficient m_{44} is large for n Ge (-93), p Ge ($\sim+66$), and p Si ($+110$). The coefficient $(m_{11}-m_{12})/2$ is, on the other hand, the large one for n Si (-80). The variation with resistivity of m_{44} in the case of p Ge is small but is nevertheless felt to be real. The fact that the sign of the large effect is the same as that of the charge carriers is at worst useful as a mnemonic.

The large shear coefficients are at least one order of magnitude larger than one would expect from the effect of strain on the amplitude of the thermal waves. It is evident that an explanation of these large coefficients must be sought in an essentially different mechanism. One such new mechanism which can account for large shear coefficients is described below.

ELECTRON TRANSFER MECHANISM

C. Herring of these laboratories has suggested such an effect based on current theoretical ideas of the structure of the energy bands in these materials.[14] The suggested effect is quite capable of producing a large shear coefficient and automatically predicts the high anisotropy which the experiment shows. The mechanism in the form which will be outlined applies particularly to n Si and p Ge. We state in advance that there is

[14] F. Herman, Phys. Rev. 88, 1210 (1952); F. Herman and J. Callaway, Phys. Rev. 89, 518 (1953).

agreement with theory for n Si but disagreement for p Ge.

The structure of the constant energy surfaces in n Si is at present thought to be as indicated in Fig. 2. These surfaces consist of ellipsoids of revolution located on the cube axes in momentum space, the six-ellipsoid picture.[15] The electrons are located in the energy minima which means that there are six groups of them centered at the ellipsoid centers. Because the surfaces are ellipsoidal the effective mass of an electron in a given group is anisotropic. Hence, the mobility associated with a group is anisotropic although the overall mobility is not. The energy value at a minimum will furthermore be sensitive to a normal strain component in the direction of the minimum.

Figure 2 corresponds to experimental arrangement A except that the simple strain system defining $(m_{11}-m_{12})/2$ is indicated rather than the tensile stress X. The electric field and the current are in the [100] direction. In the absence of strain the two energy valleys shown are equally populated with electrons, but the two groups of electrons have different mobilities in the [100] direction. When the strain system is applied, the two energy minima shift in opposite directions indicated by the shift of a given constant energy surface from the full to the dashed positions. There are then two effects of roughly comparable importance: (a) the electrons transfer from the x valley to the lower-energy y valley, and (b) the probability of an electron being scattered from a y valley into an x valley is decreased. In the strained state there are then more electrons that have high mobility and fewer electrons of low mobility in the field direction. Hence $\delta\rho/\rho$ and $(m_{11}-m_{12})/2$ are negative and finite for the situation assumed in Fig. 2. The experimental value for this constant in n Si is negative and large.

The sign of the electron transfer effect is changed by (a) making the ellipsoids oblate rather than prolate or (b) by reversing the direction of the energy shift. The present measurements eliminate two of the four possible combinations but cannot distinguish between the remaining two. Figure 2 has merely been drawn to be consistent with the experimental result for n Si. The order of magnitude of the effect is determined by the ellipsoid axial ratio and by a factor $\Delta E/kT$, where ΔE is the energy shift per unit strain. The experimental result of -80 for $(m_{11}-m_{12})/2$ for n Si requires ΔE to be of the order of several electron volts, which is reasonable.

The electron transfer mechanism furthermore predicts a zero contribution to the m_{44} coefficient for the six ellipsoid picture. This fact is shown by Fig. 2 which corresponds with experimental arrangement C except again for the strain. The mobilities of the x and y groups of electrons are the same in the [110] direction and the strain shifts the energy of the two valleys the same, i.e., not at all. In both essential respects the mechanism will give zero effect. This is reflected in the low value of m_{44} for n Si.

In using Fig. 2 the ellipsoids in the z direction have been ignored. The *strain* systems considered do not affect these energy valleys and so for small strains their electron population will not be changed. This statement does not hold for the *stress* system imposed in arrangement C, Fig. 1. The moderately high value of observation C for n Si reflects the presence of the z ellipsoids.

The same argument can be carried through for other arrangements of ellipsoids consistent with cubic symmetry although such arrangements are not suggested by the energy band calculations. In particular, arrangements of eight [111] ellipsoids and 12 [110] ellipsoids have been considered. The eight [111] ellipsoid picture predicts a definite m_{44} contribution and a zero $(m_{11}-m_{12})/2$ contribution roughly corresponding to the experimental results for n and p Ge and p Si. The 12 [110] ellipsoid picture predicts that both shear constants will be finite, of the same sign, and that $m_{44}>(m_{11}-m_{12})/2$. The predicted [110] electron transfer anisotropy is not large, however, in disagreement with all the present results.

The situation relating the electron transfer mechanism plus ellipsoid picture to the present piezoresistance results may be summarized simply. *If ellipsoids are present and if the electron transfer mechanism is the principal one operating, then the ellipsoids must be located on* [100] *axes for* n Si *and on* [111] *axes for the other three types of material.*

In the case of p germanium the above qualified conclusion of [111] ellipsoids does not agree with the energy band calculations which suggest that [111] ellipsoids are unlikely. There are, also, several other types of experiment which will not be discussed but which favor the six [100] ellipsoid picture for p germanium. The existence of another or an additional mechanism must be considered seriously therefore. The strain may produce a change of resistance through its action on the phonons, on the electrons, and on the coupling between them. As has been pointed out above, the strain-phonon effect can account for small piezoresistance coefficients. The electron transfer effect is one possible action of strain on the electrons. The possibility of another strain-electron or of a strain-coupling action remains for p germanium.

There are indeed two indications in the present experiments that p germanium is different from the other materials. The shear constants show a definite resistivity dependence in contrast to the other materials, and the temperature dependence of the piezoresistance in p Ge is different from the others. Preliminary measurement of the temperature dependence of the large shear coefficient has been carried out from 300 to 200°K. For this purpose only the specimen A or C giving the large observation was used. The temperature

[15] W. Shockley, Phys. Rev. **90**, 491 (1953).

curves were fitted to the equation $\Pi = AT^{-b}$ at 300 and 200°K. The values of b are 0.8 for n Ge, 1.1 for p Ge, 0.7 for n Si, and 0.6 for p Si. These two facts suggest that an additional mechanism is operating in p germanium.

The discussion of the electron transfer mechanism has been made in terms of ellipsoidal constant energy surfaces for the sake of definiteness. It should be pointed out that all that is really required for the mechanism is that the energy surfaces be nonspherical at the location of the charge carriers. The ellipsoid picture is not particularly indicated by the energy band calculations for n Ge and p Si but, other nonspherical energy surfaces could equally well produce the electron transfer effect and consequently highly anisotropic piezoresistance. The present results would then show, again assuming the electron transfer mechanism, that the charge carriers are located principally in [111] directions in momentum space for n germanium and p silicon.

ACKNOWLEDGMENT

The author is grateful for the opportunity of spending a year at Bell Telephone Laboratories on leave of absence from Case Institute of Technology. In this work he has had help and advice from his colleagues J. A. Hornbeck, J. R. Haynes, G. L. Pearson, W. L. Bond, T. S. Benedict, W. P. Mason, and W. Shockley in addition to those named in the text. He is indebted to W. Augustyniak for excellent technical assistance.

APPENDIX

Cubic Piezoresistance Coefficients

The change of resistivity is a symmetrical second rank tensor as is the stress. The tensor connecting the two is therefore of fourth rank, and the piezoresistance effect is strictly analogous to the piezooptical effect[4] with the resistivity replacing the dielectric constant. For germanium and silicon three coefficients are required to specify completely the piezoresistance property. In this section we make the necessary definitions and show how the fundamental piezoresistance and elastoresistance coefficients of the text may be computed from the observations. The restriction of a cubic crystal is imposed immediately on the resistivity. Crystal symmetry conditions are used later to restrict the conclusion of three piezoresistance constants to the cubic crystal classes T_d, O, and O_h, four constants being required for the other two cubic classes T and T_h. For convenience the same matrix notation as has been used relatively recently for the piezooptical effect[16] will be used here.

The starting point of the analysis is

$$E = \rho J, \tag{3}$$

where E is the electric field, J the current density and ρ a three by three symmetrical matrix[17] in the general case of a triclinic crystal and arbitrary reference axes. For a cubic crystal and arbitrary axes the ρ matrix reduces to a scalar, but it is convenient here to continue thinking of it as a matrix. If a change in ρ occurs because of stress, one may write for the *special case of constant current density*, which applies in the present experiments,

$$\delta E = (\delta\rho) J; \tag{4}$$

δE is now the change in electric field, a vector, and $(\delta\rho)$ is again a three-by-three symmetrical matrix. For a cubic crystal it is convenient to divide through by the scalar resistivity, giving

$$\delta E = \Delta J, \tag{5}$$

and then to write out explicitly:

$$\begin{aligned} \delta E_1/\rho &= \Delta_{11}J_1 + \Delta_{12}J_2 + \Delta_{13}J_3, \\ \delta E_2/\rho &= \Delta_{12}J_1 + \Delta_{22}J_2 + \Delta_{23}J_3, \\ \delta E_3/\rho &= \Delta_{13}J_1 + \Delta_{23}J_2 + \Delta_{33}J_3, \end{aligned} \tag{6}$$

where $\Delta_{ij} = (\delta\rho)_{ij}/\rho$. The nondiagonal terms are not necessarily zero, nor are the diagonal terms equal in a general frame of reference in a cubic crystal. The quantity Δ relating a vector δE to a vector J transforms just like the stress or the dielectric constant but not like the conventional strain. The diagonal terms in Δ giving the change in field along the corresponding current density component are in a crude sense analogous to an elastic normal strain; the nondiagonal terms give the change in field (the field which develops in the cubic case) normal to a given current density component, and may be thought of as electrical shear strains.

The matrix Δ may be written as a six element column matrix using the descending sequence Δ_{11}, Δ_{22}, Δ_{33}, Δ_{23}, Δ_{31}, Δ_{12}, and the stress X may be similarly written. The connection between Δ and X may be written for a cubic crystal using *general reference axes* as

$$\Delta = \Pi X, \tag{7}$$

where Π is a six-by-six matrix of piezoresistance constants. This matrix is not quite symmetrical even for the cubic case and not at all symmetrical for a triclinic crystal in the generalized version of Eq. (7). If now the cubic axes [100], [010], and [001] are chosen as reference axes and the symmetry of any one of the cubic crystal classes T_d, O, or O_h is used it can be shown that Π reduces to

$$\Pi = \begin{bmatrix} \Pi_{11} & \Pi_{12} & \Pi_{12} & 0 & 0 & 0 \\ \Pi_{12} & \Pi_{11} & \Pi_{12} & 0 & 0 & 0 \\ \Pi_{12} & \Pi_{12} & \Pi_{11} & 0 & 0 & 0 \\ 0 & 0 & 0 & \Pi_{44} & 0 & 0 \\ 0 & 0 & 0 & 0 & \Pi_{44} & 0 \\ 0 & 0 & 0 & 0 & 0 & \Pi_{44} \end{bmatrix}. \tag{8}$$

Germanium and silicon belong to crystal class O_h.

[16] W. L. Bond, Bell System Tech. J. 22, 1 (1943).

[17] For a good discussion see W. Boas and J. K. MacKenzie in *Progress in Metal Physics* (Interscience Publishers, Inc., New York, 1950), Vol. 2, p. 93.

Experimental arrangements A and B make use of just this array of coefficients. In both arrangements $X_{11}=X$ and all other stresses are zero. The electrode arrangement of A measures Δ_{11} and that of B measures Δ_{22}; thus for A, $\Pi_{11}=\Delta_{11}/X_{11}$, and for B, $\Pi_{12}=\Delta_{22}/X_{11}$ are directly measured.

The choice of axes in arrangements C and D permits Π_{44} to be determined in a simple but indirect way. For the reference axes [110], [$\bar{1}$10], [001] the transformation of Eq. (8) gives for arrangement C, $\frac{1}{2}(\Pi_{11}+\Pi_{12}+\Pi_{44})=\Delta_{11}/X_{11}$ and for D, $\frac{1}{2}(\Pi_{11}+\Pi_{12}-\Pi_{44})=\Delta_{22}/X_{11}$. Thus all three piezoresistance coefficients can be determined using A, B, and C, with D left over as a check on internal consistency. Table I shows that the agreement between the observed D and the value calculated from A, B, C is reasonable in view of the approximate correction applied to D.

The necessary third observation cannot be obtained by making another longitudinal measurement in a third crystallographic direction. The general longitudinal effect is given by $\Pi_{11}'=\Pi_{11}-2\Pi\Gamma$, where $\Pi=\Pi_{11}-\Pi_{12}-\Pi_{44}$ and Γ is an orientation function. Only Π_{11} and the combination Π can be determined by longitudinal measurements alone, and thus the third measurement must be of a different type. The transverse observation B serves this purpose.

The equations reducing the observations to the fundamental piezoresistance coefficients defined in the text are then,

$$\begin{aligned}\Pi_{11}+2\Pi_{12}&=A+2B,\\ \Pi_{44}&=2C-A-B,\\ \Pi_{11}-\Pi_{12}&=A-B,\end{aligned}\tag{9}$$

where A, B, and C refer to the numbers given in Table I.

A set of elastoresistance coefficients also can be deduced from the present results. The change-in-resistivity matrix Δ can be related to the strain e by the elastoresistance coefficients m,

$$\Delta=me,\tag{10}$$

where the strain e is, to be explicit, the six-element column matrix of terms $\partial u/\partial x$, $\partial v/\partial y$, $\partial w/\partial z$, $[(\partial v/\partial z)+(\partial w/\partial y)]$, $[(\partial w/\partial x)+(\partial u/\partial z)]$, $[(\partial u/\partial y)+(\partial v/\partial x)]$, where u, v, w are the displacements of a point with coordinates x, y, z. Since we have for the relation between stress and strain,

$$X=Ce,\tag{11}$$

where C is the elastic constant matrix, it follows, using Eq. (7) that

$$m=\Pi C.\tag{12}$$

The fundamental strain coefficients are quickly given by the aid of this last relation and a little algebra as

$$\begin{aligned}\tfrac{1}{3}(m_{11}+2m_{12})&=(\Pi_{11}+2\Pi_{12})(C_{11}+2C_{12})/3,\\ m_{44}&=\Pi_{44}C_{44},\\ \tfrac{1}{2}(m_{11}-m_{12})&=(\Pi_{11}-\Pi_{12})(C_{11}-C_{12})/2.\end{aligned}\tag{13}$$

The Magnetic Susceptibility of Nd Metal*

J. F. ELLIOTT,† S. LEGVOLD, AND F. H. SPEDDING
Institute for Atomic Research and Department of Physics, Iowa State College, Ames, Iowa
(Received August 10, 1953; revised manuscript received January 4, 1954)

The magnetic susceptibility of neodymium metal has been measured over the temperature range of 20.4°K–300°K. The metal was found to obey a Curie-Weiss law above 145°K with a paramagnetic Curie point of −16°K and an effective moment of 3.68 Bohr magnetons. Near 145°K there appears to be a change in slope of the curve of $1/\chi$ *vs* T. From 145°K to 31.5°K the metal again obeys a Curie-Weiss law with a paramagnetic Curie point of about 1°K and an effective moment of 3.35 Bohr magnetons. The low-field susceptibility at 20.4°K is much larger than predicted by the low-temperature Curie-Weiss law, and the susceptibility has a definite field dependence.

I. INTRODUCTION

THE magnetic susceptibility of neodymium has been measured previously by Klemm and Bommer,[1] and by Trombe.[2] The measurements of Klemm and Bommer showed the metal to obey the Curie-Weiss law over the temperature range of 90°K–292°K, with an effective moment of 3.65 Bohr magnetons. Trombe's measurements over the temperature range of 77°K–297°K showed a discontinuity in slope of the plot of $1/\chi$ *vs* T in the neighborhood of 110°K. Above 110°K the effective moment was found to be 3.59 Bohr magnetons, and below 110°K the effective moment was 2.08 Bohr magnetons.

II. EXPERIMENTAL PROCEDURE AND RESULTS

The metal used in this study was prepared by methods previously reported.[3,4] The spectrographic analysis of the metal showed it contained the following impurities: Ca, detectable but less than 400 parts per million (ppm); Mg, detectable but less than 200 ppm; Si, detectable but less than 200 ppm; Pr, not detected with limit of detection of 800 ppm; Fe, not detected with limit of detection of 50 ppm.

TABLE I. The magnetic susceptibility per gram of neodymium.

T°K	$\chi_g \times 10^6$	$1/\chi_g \times 10^{-4}$
20.4	707.4	0.141
31.5	348.7	0.287
44.0	248.6	0.402
65.3	167.4	0.598
84.0	126.1	0.793
89.0	120.5	0.829
119.7	88.87	1.125
157.7	68.07	1.469
199.8	54.60	1.832
238.5	46.05	2.172
287.7	39.01	2.563
297.5	37.68	2.660

The susceptibility measurements were made using the Gouy method. The sample was 25.15 cm long, 0.434 cm in diameter, and weighed 25.627 grams.

The magnetic field was calibrated with a proton resonance flux meter for three different magnitudes of field strength: 4000, 7000, and 12 000 oersteds. Most of the data were taken in applied fields in the neighborhood of 12 000 oersteds. However, at 20.4°K, 83°K, and at room temperature, measurements were made at all three fields to investigate the field dependence of the susceptibility.

The cryogenic apparatus used in the measurements employed a temperature-controlled helium gas stream flowing past the sample and was the same as that used in previous work.[5] The temperature difference between the two ends of the sample was less than one degree for all measurements. The cryogenic apparatus was used throughout except at 20.4°K and at room temperature where the sample was immersed directly in a liquid bath.

Temperatures were measured with copper-constantan thermocouples calibrated against a platinum resistance thermometer which had been calibrated by the Bureau of Standards.

The susceptibility of neodymium in a field of about 12 000 oersteds at various temperatures is shown in Table I. Figure 1 is a plot of the inverse of the susceptibility from Table I as a function of the absolute temperature. The plot seems to consist of two straight lines intersecting at about 145°K. Of interest also is the fact that the susceptibility at 20.4°K is much larger than would be predicted from the behavior in the temperature range from 31.5°K to 145°K.

Above 145°K, the indicated effective moment is 3.68 Bohr magnetons, and the indicated paramagnetic Curie point is about −16°K. Below 145°K the indicated effective moment is 3.35 Bohr magnetons and the paramagnetic Curie point is about 1°K. The molar Curie constants for the two ranges are 1.695°K/mole

* Contribution No. 295 from the Institute for Atomic Research and Department of Physics, Iowa State College, Ames, Iowa. Work was performed in the Ames Laboratory of the Atomic Energy Commission.
† Now at General Electric, Syracuse, New York.
[1] W. Klemm and H. Bommer, Z. anorg. u. allgem. chem. **241**, 264 (1939).
[2] F. Trombe, Ann. phys. **7**, 383 (1937).
[3] F. H. Spedding *et al.*, J. Am. Chem. Soc. **69**, 2777, 2786, 2812 (1947).
[4] F. H. Spedding and A. H. Daane, J. Am. Chem. Soc. **74**, 2783 (1952).
[5] Elliott, Legvold, and Spedding, Phys. Rev. **91**, 28–30 (1953).

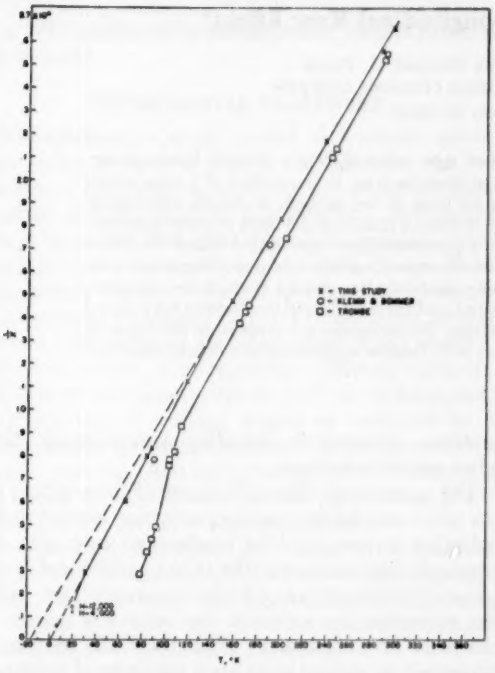

FIG. 1. The reciprocal of the magnetic susceptibility of neodymium metal as a function of temperature. The field was 12 000 oersteds except for the 20.4°K points where two values at different fields are shown.

and 1.396°K/mole, respectively. The effective moment calculated by Van Vleck[6] for the trivalent neodymium ion in 3.68 Bohr magnetons. Our data have not been corrected for the diamagnetism of the core nor for the paramagnetism of the conduction electrons.

The susceptibility at room temperature and at 82°K was found to be slightly field-dependent, being about one percent higher in a field of 4000 oersteds than in a field of 12 000 oersteds. This difference we believe to be outside the experimental error which we believe did not exceed 0.5 percent. At 20.4°K, the susceptibility was found to have a marked field-dependence; the susceptibility decreased with increasing fields. The values of the susceptibility per gram at 20.4°K in fields of about 4000, 7000, and 12 000 oersteds were $(793.3 \pm 1.5)\times 10^{-6}$, $(746.9\pm 0.3)\times 10^{-6}$, and $(707.4\pm 0.7)\times 10^{-6}$, respectively.

It appears from the data at 20.4°K that the weak-field susceptibility does not follow the Curie-Weiss law which apparently holds immediately above 30°K. In seeking an explanation for this anomalous temperature dependence of the weak-field susceptibility, it should be noted that there is an observed specific-heat anomaly[7] near 20.4°K, to which the magnetic behavior may be related. This specific heat anomaly has been described as conceivably arising from the crystal field splitting of the $4f$ electron energy states with a consequent redistribution of electrons among the split levels as the temperature is changed. In order to have a magnetic anomaly at temperatures where such transitions occur, it is only necessary to make the plausible assumption that the different states have different magnetic moments.

The field dependence of the susceptibility at 20.4°K is such as to indicate an approach to saturation, the susceptibility decreasing in increasing fields. This may conceivably be attributed to the expected field dependence of the susceptibility at low temperatures predicted by the complete Brillouin function, including possibly an internal field corresponding to $\theta = 1$°K and including the split states described above in the discussion of the temperature dependence of the weak-field susceptibility.

The electrical resistivity[8] and the Hall effect[9] of neodymium also indicate that the metal has some anomalous properties near hydrogen temperatures. The latter particularly indicates that the magnetic moment of the metal is increasing rapidly near this temperature.

The authors wish to express their thanks to Jack Powell for preparing the rare earth salts and to A. H. Daane, Richard Barton, and David Dennison for preparing the metal samples.

[6] J. H. Van Vleck, *Electric and Magnetic Susceptibilities* (Oxford University Press, London, 1932).

[7] Parkinson, Simon, and Spedding, Proc. Roy. Soc. (London) **207**, 137 (1951).

[8] James, Legvold, and Spedding, Phys. Rev. **88**, 1092 (1952).

[9] Kevane, Legvold, and Spedding, Phys. Rev. **91**, 1372 (1953).

Magnetic Domains by the Longitudinal Kerr Effect*

CHARLES A. FOWLER, JR., AND EDWARD M. FRYER
Department of Physics, Pomona College, Claremont, California
(Received November 20, 1953)

Rotation of the polarization plane of obliquely incident light reflected from a polished ferromagnetic surface is successfully employed to reveal the antiparallel domains lying in the surface of a large single crystal of silicon iron. This Kerr magneto-optic effect is the basis of two methods of domain observation which are described in detail: (1) the optical probe method in which a small, focused beam of plane polarized light scans the crystal surface before being reflected into a photomultiplier tube located behind the Nicol prism analyzer, and (2) the photographic method in which the crystal surface is broadly illuminated with polarized light and the reflected beam is photographically recorded after passage through the analyzer. The truly saturated character of the domains is demonstrated, and the directions of the domains are assigned without ambiguity. Domain wall movement and Barkhausen discontinuities are revealed in photographs taken as the crystal is subjected to a changing magnetizing field. Possible applications and limitations of the method are discussed.

INTRODUCTION

THE domain structure of single ferromagnetic crystals has been vividly demonstrated by several investigators using the powder-pattern technique, and a great deal of information has been obtained concerning the behavior of surface domains under various conditions of pressure, tension, and applied magnetic fields.[1] In that technique the colloidal particles become strongly concentrated at regions of the surface where the magnetic field gradient is large. This may occur at the Bloch walls separating domains in the case of flux closure configuration (all domains parallel to the surface), and also in cases where flux closure does not exist and domains come to an abrupt end at the crystal surface. Thus the boundaries of the surface domains are clearly outlined. The direction of magnetization in each domain is not usually determined, but Williams and his collaborators[2] have managed to infer it by means of a clever "scratch technique" combined with a study of wall movement with applied field. It has been noted that the powder-pattern method becomes difficult to apply to crystals with low anisotropy.

This investigation was undertaken with a view to establishing an alternative method for revealing domain structure that would complement the powder-pattern method. In the several cases of the Kerr magneto-optic effect, the rotation of the plane of polarization of reflected light has a magnitude and a sense that depend upon the amount and direction, respectively, of the magnetization at the surface.[3] Since domains are regions of saturated magnetization, the possibility exists that adjacent domains will be revealed in contrasting intensity when they are illuminated with plane polarized light and observed by reflection through a suitably oriented analyzer, if the problems inherent in detecting a microscopic Kerr effect can be overcome.

The macroscopic Kerr effects are of three types: (1) the polar case having the magnetization normal to the reflecting surface, (2) the longitudinal case with the magnetization vector parallel to the surface and in the plane of incidence, and (3) the transverse case where the magnetization vector in the surface is normal to the plane of incidence. In all of these, the rotation is dependent in various ways upon the angle of incidence, the direction of light vibration, and the wavelength of the light, and is accompanied by an added circular component which is generally weak and becomes negligibly small for incident light vibrations parallel or perpendicular to the plane of incidence. For saturated iron the value of the rotation for the normal polar case is about 20 minutes; for the longitudinal case it is zero at normal incidence and reaches a maximum of about 5 minutes at 60° incidence; for the transverse effect the rotation is about the same as for the longitudinal case. The available data are not too meaningful, however, since they were obtained for different samples and often without mention of the intensity of magnetization or the wavelength of the light employed.[3]

The normal polar effect with its relatively large rotation offers the best chance for successful observation of domains, and the most likely surface having the required antiparallel normal domains is a basal plane of hexagonal cobalt cut normal to the single axis of easy magnetization. Employing a special metallographic microscope, Williams, Wood, and Foster[4] succeeded in photographing the mottled domain structure typical of such a cobalt surface.

For surfaces having no normal component of magnetization, such as the prism faces of the cobalt crystal or the three principal planes of a cubic iron crystal, the longitudinal or transverse effects must be employed. By using the longitudinal Kerr effect at 60° incidence, we were able to detect photoelectrically and photographically the several antiparallel domains

* Supported by the U. S. Office of Naval Research.
[1] R. M. Bozorth, *Ferromagnetism* (D. Van Nostrand Company, Inc., New York, 1951), pp. 532–538.
[2] Williams, Bozorth, and Shockley, Phys. Rev. **75**, 155 (1949).
[3] *International Critical Tables* (McGraw-Hill Book Company, Inc., New York, 1929), first edition, Vol. VI, p. 435.
[4] Williams, Foster, and Wood, Phys. Rev. **82**, 119 (1951).

in a (100) surface of a demagnetized single crystal of silicon iron.[5]

EXPERIMENTAL PROCEDURE

The specimen, a single crystal of 4 percent silicon iron, grown and cut by Mr. J. G. Walker of the Bell Telephone Laboratories, was used for all of the work reported in this paper. It is primarily a rectangular slab, 1.7×1.4×0.3 cm, with edges parallel to the cubic axes, the two large surfaces being (100) planes. However, certain corners and edges had been cut obliquely to reveal such planes as (110), (111), etc., thus leaving the two (100) surfaces, on which most of our observations were made, with somewhat different contours. The crystal was electropolished until the surfaces were relatively free of working strains as indicated by a disappearance of the maze pattern. The powder patterns then showed the (100) surface srtucture to consist of a number of domains always parallel to the long [010] edge when the specimen was demagnetized.

In order to control the magnetization, the crystal was simply laid flat on one surface of a closed magnetic circuit, where the stray field was sufficient to magnetize the crystal to saturation when the magnetizing current reached about 100 ma. ($H \approx 5$ oersted.)

The Optical Probe Method

Success in observing the domain structure was first achieved by scanning across the (100) face in the [001] direction with a small polarized light-probe and recording photoelectrically the intensity of the reflected light after passage through a nearly crossed analyzer. Adjacent antiparallel domains, rotating the polarization plane slightly to right or left, respectively, cause the intensity transmitted through the analyzer to increase or decrease accordingly. The setup is shown schematically in Fig. 1, where a 60° incidence was chosen to give the maximum Kerr rotation. The source is an AH4 General Electric mercury arc whose operation on 60-cycle ac permits simple amplification of the modulated signal. The short-focus probe lens L_1 forms a diminished image of the small source-aperture upon the crystal surface after which the light is rendered parallel by a second lens L_2. Both the polarizer and the analyzer are good quality Nicol prisms of 17-mm aperture. The signal, received by a 1P21 photomultiplier tube, is suitably amplified and recorded on a recording potentiometer. In practice we have found that satisfactory results can be obtained with the incident electric vector either parallel or perpendicular to the plane of incidence; however, ambiguity with the transverse Kerr effect is avoided by polarizing the electric vector perpendicular to the incidence plane, for which direction the transverse effect is zero.

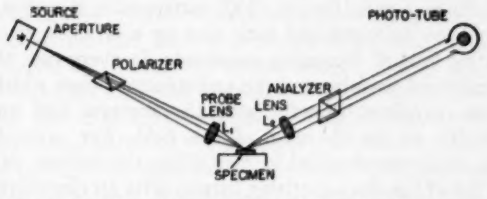

FIG. 1. Experimental arrangement for observing domains by scanning with a polarized optical probe.

By magnetizing the crystal to saturation first in one direction and then the reverse, the intensity of the light reaching the photocell can be made to differ by as much as 20 percent when the analyzer is set at approximately 1° from extinction and the very critical optical system is in perfect alignment. A signal (Kerr reversal)-to-noise ratio of about 100 has been achieved, allowing detection of polarization rotations as small as 10 seconds.

To permit scanning, the motion of the magnet and its specimen is controlled by a micrometer screw, and this is coupled through matched Selsyns to the chart movement of the recording potentiometer. Such a scan across the demagnetized crystal does not give directly the "square-wave" curve typical of antiparallel domain configuration for the same reason that a scan across the saturated specimen does not yield a constant signal. Plane polarized light, reflected obliquely at a metal surface and examined through a nearly crossed analyzer, is an arrangement utilized by metallographers to accentuate every surface irregularity. Thus in this case, the minute pits, scratches, and imperfections cause the curve of the saturation scan to fluctuate strongly, but the *difference* between the magnetically saturated and the demagnetized scans reveals the domains as expected. Figure 2 shows a typical corrected curve.

The Photographic Method

The photographic setup, which is quickly obtained by changing a few components in the optical probe arrangement, is illustrated schematically in Fig. 3. A condensing lens is introduced and the probe lens is

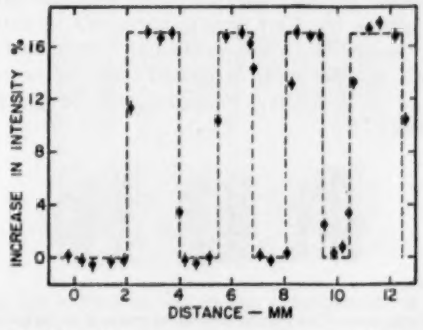

FIG. 2. Plot of a scan across the (100) surface of the crystal with a 0.5-mm probe. The ordinate is percentage increase of the light transmitted through the analyzer as the demagnetized crystal is magnetized to saturation.

[5] C. A. Fowler, Jr., and E. M. Fryer, Phys. Rev. 86, 426 (1952).

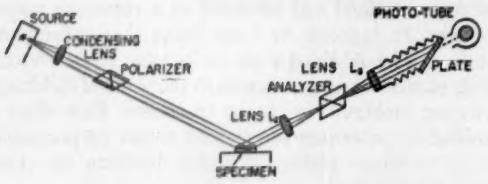

FIG. 3. Experimental arrangement used for photographing the domains of the silicon iron crystal.

removed so that the incident beam is essentially parallel. The lens L_2 and a second positive lens L_3, separated by essentially the sum of their focal lengths, constitute a compound camera objective which is focused on the crystal surface. Inasmuch as the object surface is oblique to the camera axis, the image plane is tilted at an angle that depends upon the orientation of the object plane and upon the linear magnification. For the unit magnification we have employed with the silicon iron specimen, the film holder is tilted at the same angle as the crystal surface. The analyzer is located at the point where the beam is most constricted, assuring maximum passage of light. The photocell, employed in this case as a monitor for checking the conditions for photographing domains, is shown in position behind the camera.

With this apparatus and using Eastman Contrast Process Ortho film, we obtained photographs of the domains in the silicon iron specimen with a 2-minute exposure when the illumination was unfiltered light from the mercury arc.[5] Our earliest photographs were noticeably fuzzy and unsharp at the domain edges. This can be attributed to the large local variations of intensity, mentioned in the previous section, which often exceed the contrast between adjacent domains. We have managed to circumvent this difficulty by a technique that is equivalent to correcting the scan curve. A film positive is made from a negative of the crystal magnetized to saturation. This "reversed flat" is carefully superposed on the domain photograph negative and a print made from the combined pair, thus tending to cancel the undesirable local fluctuations while leaving the Kerr domain variations. A detailed description of this "noise-reduction" technique and the limit to which it can be pushed when sufficient care is taken in balancing exposures will be published elsewhere.[6]

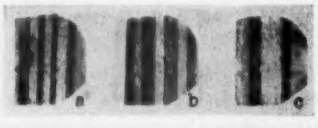

FIG. 4. Three different domain configurations of the demagnetized specimen. The crystal was demagnetized in each case by a 60-cycle alternating field of decreasing amplitude, but the duration of the demagnetizing process decreased from (a) to (b) to (c).

[6] Fowler and Fryer, J. Opt. Soc. Am. 44, 256 (1954).

RESULTS

It should be remarked at the outset that it is possible visually to see the domains and watch them disappear as the specimen is magnetized to saturation, provided that the observer adapts his eyes to the dark. However, because of the low over-all intensity, visual observation is very unreliable.

Direction and Saturation of Domains

Photographs, supplemented by information from the photocell monitor, allow an unambiguous interpretation of a surface domain configuration and its changes. For example, the magnetization vector of a longitudinally oriented domain clearly has a direction that depends upon whether the domain in the photograph is light or dark. That the magnetization in a domain is truly saturated, as theoretically pictured, is demonstrated since it is observed that the optical probe when

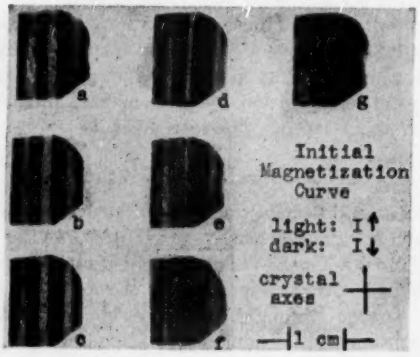

FIG. 5. Photographs of the domain behavior in the (100) surface as the applied field is increased from zero to a value sufficient to produce saturation. The field is zero in (a), whereas increasing values of H (toward the bottom of the page) are applied in (b) to (g).

located anywhere within a favorably oriented domain of the demagnetized specimen gives no change in the signal when a parallel saturation field is applied.

Demagnetized Configurations

Magnetization and subsequent demagnetization of the sample generally result in similar but not identical domain patterns. Figure 4 includes three different configurations in the top (100) surface after the crystal has been demagnetized each time by a 60 cycle alternating field of decreasing amplitude. In every case the number of domains and the uniformity of their widths were correlated directly with the slowness and uniformity of the decrease of the field. For example, Fig. 4(a) was obtained by controlling the uniform rate of fall of the demagnetizing current with an electrolytic resistor, requiring 5 minutes for the 200 ma to reduce to zero, while 4(b) and 4(c) were demagnetized with increasing speed.

Initial Magnetization Curve

A series of photographs, taken as the crystal, originally demagnetized, was subjected to a gradually increasing field, is shown in Fig. 5. The monitor indicated that the magnetization process consists of several sudden discrete changes in the magnetization (Barkhausen jumps) separated by periods of stability. Each of the photographs shown was taken immediately following such a jump. Close examination of the pictures reveals the typical sporadic movement of the domain walls as the magnetization of the crystal increases in this discontinuous manner.

Hysteresis

Figure 6 shows photographs taken as the specimen was carried through half of a hysteresis loop, that is, from saturation in one direction (a) to saturation in the opposite direction (j). After applying a saturation field, no change occurred in the pattern as the field was reduced to zero until it reached a value of about 3 oersteds in the opposite direction, at which point a dagger-like domain appeared (b) and continued to grow with increasing field until it covered the entire crystal surface in the saturated condition (j). All such series of photographs that we have taken have shown similar but not identical behavior. Both the monitor response and the photographs themselves again indicate the sporadic, Barkhausen wall motion.

Domain Closure

The configuration of the domains inside a crystal and their behavior under changing conditions of field, stress, or temperature can be studied only in terms of the surface domains. We have made a start on this problem by examining the top and bottom (100) faces of the crystal for several cases of zero or near zero magnetization (see Fig. 7). None of the pictures taken of this specimen shows any evidence of 90° closure domains in the [001] direction, which suggests an unusual reluctance to magnetization in that direction. A direct check of this peculiar anisotropy by rotating the crystal 90° and applying a longitudinal magnetizing field in the [001] direction showed no Kerr rotation for fields as high as 15 oersteds. Quite apparently an anisotropy leading to a strong preference for magnetization in the [010] direction was acquired during the process of growing this crystal or its subsequent annealing. The pairs of top and bottom photographs of Fig. 7 were obtained by turning the crystal bottom side up about a transverse axis. The close match of the stripes, dark with dark and light with light, strongly suggests that flux-closure paths for the unmagnetized state run along the top face and back along the bottom. Unfortunately those edge faces of the specimen that had not been cut oblique to the two (100) surfaces were rough or scarred to a point that precluded satisfactory photographs to show closure domains along the [100] direction at the ends. However, one photograph of one of the side faces, although of very poor quality, indicated that only two layers of domains are involved in the demagnetized specimen.

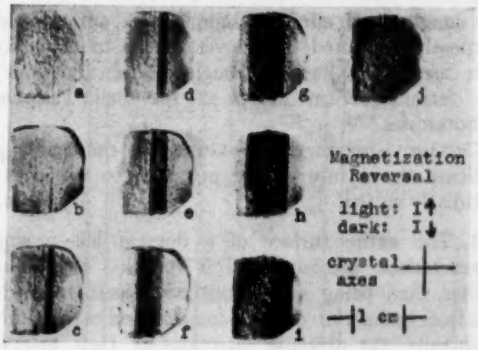

FIG. 6. Photographs of the domain behavior in the (100) surface as a strong external field, toward the top of the page in (a), is reduced to zero and then increased to saturation value in the opposite direction, (j).

A much more interesting problem is the behavior of the domains throughout the crystal as it is taken through a magnetization curve or a hysteresis cycle. Here our observations have been impeded by the unsatisfactory method of applying the magnetizing field, for with the magnetizing setup described above, it is impossible to examine more than one face without changing the field on the specimen. We have now designed a completely new magnet which permits observation of every side of the specimen without any change of the magnetizing field, and we are proceeding with the study of a crystal cut into a true rectangular slab with all edges along ⟨100⟩ directions and all faces satisfactorily polished.

CONCLUSION

The Kerr magneto-optic method is one which can complement the powder pattern method in many problems of domain investigation. In order to establish

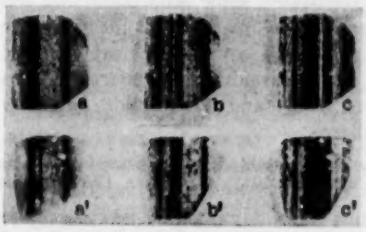

FIG. 7. Corresponding domain configurations in the top and bottom (100) surfaces of the crystal. The magnetization of the dark domains is toward the bottom of the page, and the crystal was turned from the top side (a,b,c) to the bottom (a',b',c') about a horizontal, transverse axis. The close match of dark with dark and light with light in a,a' and approximate matches in b,b' and c,c' suggest flux-closure paths.

the longitudinal effect technique, the authors have purposely restricted their investigation to the silicon iron case, so well known through the beautiful work of the ferromagnetism group at the Bell Telephone Laboratories.[2,7,8]

Certain advantageous features of the technique indicate the nature of the problems to which it is peculiarly suited.

1. The entire surface of a domain has a single characteristic intensity and is revealed as a whole rather than being merely outlined; furthermore the relative intensities of the domains indicate without ambiguity the absolute directions of their magnetization.

2. The magnitude of the magnetization at any point on a specimen is subject to rapid quantitative measurement through the optical probe technique.

3. Although a properly polished, strain-free surface is required just as with the powder technique, the need for repolishing between observations is of course completely eliminated.

4. The method is not affected by either high or low temperatures as long as the surface is preserved, so that the study of domain behavior at interesting transition points becomes a distinct possibility.

5. Since the method is by its very nature a dynamic one, certain problems concerning domain dynamics can be undertaken.

There is some question as to how suitable the method will be for studying the truly microscopic domains of polycrystalline samples. The answer probably lies in the degree to which surface imperfections in the image can be eliminated by the photographic "noise-reduction" technique.

We wish to thank H. J. Williams and R. M. Bozorth of the Bell Telephone Laboratories for the loan of the silicon iron crystal and for valuable discussions concerning the investigation. We are also indebted to Dr. Burton Henke of Pomona College for several helpful suggestions.

[7] H. J. Williams and W. Shockley, Phys. Rev. 75, 178 (1949).
[8] Williams, Shockley, and Kittel, Phys. Rev. 80, 1090 (1950).

PHYSICAL REVIEW VOLUME 94, NUMBER 1 APRIL 1, 1954

The Electrical Conductance of Pressed Powders, in Particular of Zinc Oxide*

J. C. M. BRENTANO AND COLMAN GOLDBERG†
Northwestern University, Evanston, Illinois

(Received September 14, 1953; revised manuscript received December 8, 1953)

The electrical conductance of a pressed semiconducting material in powder form, representing a multiboundary semiconductor, is investigated. Experiments are described in which the dc conductance of the powder pressed between parallel plates in an evacuated chamber is determined for different pressures and temperatures. A model based on the change of the energy gaps with pressure is developed which accounts for the phenomena observed. Transient changes of conductance with time are observed for which only tentative explanations are suggested. Most of the experimental work refers to zinc oxide.

I. INTRODUCTION

EXTENSIVE work has been done on the electrical properties of powdered and sintered materials. Recently Hausner[1] examined the properties of sintered powders containing some semiconducting constituent. Miller[2] and Hahn[3] made a detailed investigation of sintered zinc oxide powder, whereas Davis[4] examined powders of semiconductive materials, in particular aluminum oxide and zinc oxide pressed between parallel plates.

The work on sintered materials, particularly the work of Miller and his associates, showed the effect of internal grain boundaries; sintering imposes, however, certain conditions on the material resulting from the heating process which, according to the nature and pressure of the gas in which sintering takes place, produces a chemical modification of the grain surface.

The method used by Davis of compressing the powder avoids these chemical changes. Some of his results, however, are not readily accounted for in terms of a general theory. The present investigation was undertaken with the purpose of examining more closely the conditions which arise when pressing a semiconducting powder.

Kantorowicz[5] has investigated the change of electrical conductance of pressed metal powders and has shown that the conductance or reciprocal of resistance

* This work is the subject of the doctoral dissertation (Northwestern University, 1951) of Colman Goldberg and is there presented in greater detail.
† 1950–1951 Milwaukee Gas Specialty Company Fellow; now with Westinghouse Research Laboratories, East Pittsburgh, Pennsylvania.
[1] H. H. Hausner, Electronics 21(1), 138 (1948).
[2] P. H. Miller, Phys. Rev. 60, 890 (1941).
[3] E. E. Hahn, J. Appl. Phys. 22, 855 (1951).
[4] D. H. Davis, doctoral dissertation (Northwestern University, Evanston, 1951); J. C. M. Brentano and D. H. Davis, Phys. Rev. 79, 216 (1950).
[5] O. Kantorowicz, Metallwirtschaft 10, 45 (1931); Ann. Physik 12, 1 1933.

can be expressed by a relation:

$$1/R=G=c_1(p_m)^{\frac{1}{2}}+c_2, \qquad (1)$$

where p_m is the pressure and c_1 and c_2 are constants depending on the elastic properties of the metal.

Holm[6] has given a theoretical derivation of (1). He considers that the current flow through a compressed powder is constricted at the contact points of the powder particles. This accounts for the high resistance of the powder. With increasing pressure the contact areas between the particles become large and the resistance is thus reduced.

Recently Bridgman[7] measured the resistance of semiconducting powders for hydrostatic pressures up to 50 000 kg/cm². For zinc oxide he finds that at 25°C and at 100°C the resistance decreases with increasing pressure, whereas at 200°C the resistance increases with increasing pressure.

For tellurium Bardeen[8] has drawn attention to the relationship between the change of conductivity and the change of the energy gap between bands with hydrostatic pressure. Taylor[9] has shown that the energy gap for germanium is increased by applying hydrostatic pressure.

Gyulai and his co-workers[10] have investigated the effect of pressure on the electrical conductivity of rock salt. This work has been discussed and interpreted by Seitz;[11] it will not be discussed further here.

Davis experimented with pressed semiconducting oxides, in particular with aluminum oxide and zinc oxide. He reports that in a general way the conductance of the powder increases with pressure. He further finds that the dc conductance is time dependent in the sense that any sudden change of pressure produces a transient increase in conductance followed by a gradual decrease. He also observed that a reversal of the applied potential is accompanied by a transient increase of conductance.

II. EXPERIMENTAL PROCEDURE

Since most of the work of Davis was done with Al_2O_3, which ordinarily possesses a high resistivity and is hygroscopic, it was thought that his results may be largely due to surface effects of an electrolytic or ionic nature due either to moisture or to a gas film leading to surface conductivity of the type advocated by Cabrera and Mott.[12] In order to minimize such effects, in particular that of moisture, we made our measurements while the powder was in a vacuum. The apparatus used is as follows.

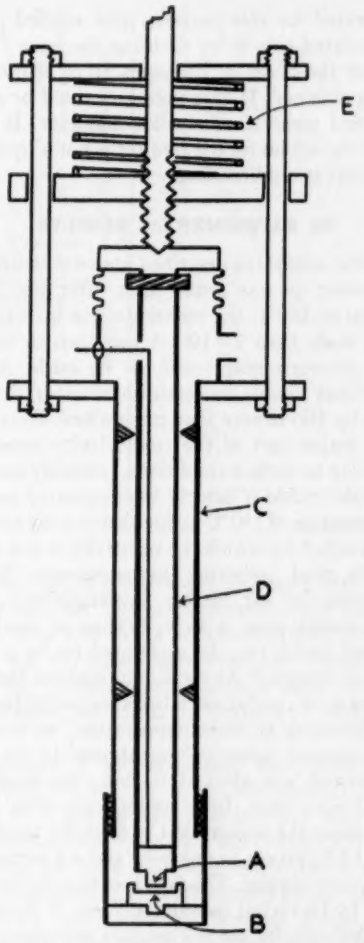

FIG. 1. Schematic diagram of the vacuum chamber for pressing powders.

The powder is placed as a layer between the plates A and B (Fig. 1) which are the end plates to an outer tube C and an inner tubular stem D connected by sylphon bellows, so as to form a vacuum-tight enclosure which could be evacuated or filled with a gas to any pressure desired. Plate A is insulated and the electrical connection to the outside is made through a glass-metal seal. The leakage resistance between the outer grounded plate B and the inner plate A was over 10 000 megohms. The lower part of the instrument could be immersed in a bath and maintained at a fixed temperature. The force f between A and B was obtained by means of a screw acting through the intermediary of a spring; the purpose of the spring E being to secure a steady force which would not appreciably be affected by "settling" of the powder or by differences in the thermal expansion of C and D. The compression of the spring gave a ready means for measuring the acting force; the spring

[6] R. Holm, *Electrical Contacts* (H. Gebers, Stockholm, 1946).
[7] P. W. Bridgman, Proc. Am. Acad. Arts Sci. **79**, 125 (1951).
[8] J. Bardeen, Phys. Rev. **71**, 717 (1949).
[9] J. H. Taylor, Phys. Rev. **80**, 919 (1950).
[10] Z. Gyulai and D. Hartley, Z. Physik. **51**, 379 (1928); Z. Gyulai, Z. Physik **78**, 830 (1932); Z. Gyulai and J. Boros, Z. Physik **96**, 355 (1935).
[11] F. Seitz, Phys. Rev. **80**, 238 (1950).
[12] N. Cabrera and N. F. Mott, Repts. Progr. Phys. **12**, 163 (1949); N. F. Mott, Trans. Faraday Soc. **43**, 429 (1947).

was calibrated for this purpose. The applied pressure p_m is calculated simply by dividing the force f by A_m, the area of the plate A. Pressures up to 38 000 lb/in.^{2} have been attained. Higher pressures could be attained with an end piece A of smaller diameter. It will be seen that the action on the powder is not a hydrostatic pressure, but is unidirectional.

III. EXPERIMENTAL RESULTS

Using the apparatus described above with aluminum oxide powder it was found that after one hour of evacuation at 150°C the resistance was increased by a factor of more than 1×10^4; it was then so high that accurate measurements could not be made. Although we were thus unable to establish whether the effects observed by Davis were then maintained, it was shown that the major part of the conductivity observed by him was due to surface conditions, probably moisture.[13]

When zinc oxide is held in the evacuated apparatus at a temperature of 150°C in due time a quasi-stationary state is reached for which the resistivity is not too high to permit good resistance measurements. ZnO was thus chosen for all further investigations. In this quasi-stationary state a slow increase of conductance is observed which may be accounted for by a gradual removal of oxygen.[14] At room temperature the rate of this increase of conductance becomes negligible.

Experimenting at room temperature, we found that when a constant potential was applied to the powder and a current was allowed to flow, the conductance decreased with time. In a typical case with 15 volts applied across the compressed powder the conductance decreased 1.8 percent in one hour and 4.4 percent when 100 volts were applied. This is in the sense of the changes observed by Davis but considerably less. If the potential was applied only for the few seconds necessary to make the measurement the conductance remained constant during the time between the measurements. Davis further observed that when a current had been flowing through the powder under the action of an external emf on removal of this emf a current would flow in a direction opposite to that of the original current. This transient was not observed by us, although the apparatus was sensitive enough to detect 0.06 percent of the original current. Thus the transients observed by Davis for a powder held at constant pressure were greatly reduced by the treatment described above, which leads us to believe that these transients were due to surface phenomena which are removed by evacuation and heat treatment.

The effect of changes of pressure on the conductance of zinc oxide may be summarized as follows. (a) When the pressure on the sample is changed there is a sudden change in conductance followed by a slow decrease in conductance, the conductance becoming constant after approximately two hours. (b) At low pressures when the pressure is increased there is a sudden increase of conductance followed by the slow decrease described in (a). The net result of these changes, while at low pressures, is that an increase in pressure causes an increase in conductance. (c) At higher pressures, when the pressure is increased, there is a sudden decrease of conductance followed by the slow conductance decay described in (a). (d) From (b) and (c) it follows that there is a pressure for which the conductance is a maximum. It is found that when the temperature is lowered this maximum occurs at a lower pressure. (e) At pressures above that of the conductance maximum the logarithm of conductance is proportional to the pressure (Fig. 2). The constant of proportionality (the slope of the straight line of Fig. 2) is inversely proportional to P_m. P_m is defined as the maximum pressure that has been applied in the history of the sample in question.

IV. INTERPRETATION OF EXPERIMENTAL RESULTS

We have defined a pressure $P_m=f/A_m$, where f is the force acting on a piston of area A_m. The subscript "m" being used to indicate that we are referring to quantities that are measurable. Actually P_m has no meaning on a microscale. The powder consists of an agglomeration of particles with interstices so that the force f is not being applied to the area A_m, but to a much smaller area a which is the sum of the contact areas for any cross section of the powder. The actual pressure at any particular contact will then depend on its area, its orientation, and the total contact area in the cross section of the contact in question. We introduce the symbol p to represent an average value of this quantity which comprises also a term for the average orientation of the contact areas. The definition of symbols can be summarized by the relation

$$f=p_mA_m=pa. \tag{2}$$

The area a and the pressure p are not measurable quantities. They have physical meaning on a microscale and as used here represent averages only.

According to Holm, the actual contact area a increases as the pressure p_m is increased. This increase is rapid at low pressures, it becomes slower with increasing pressure so that a may be considered to be

[13] It should be noted that preliminary experiments in which we examined under a protective oil seal Al_2O_3 powder that had been heated in a partial vacuum to 130°C showed reduced conductivity, but all the relaxation phenomena reported by Davis. The low conductivity in vacuum referred to above is only reached gradually in the course of an hour, indicating that the surface conductivity, whatever its nature, is not readily removed. A residual effect of this kind may play a part in some of the phenomena reported for ZnO further on.

[14] Zinc oxide is an excess or donor semiconductor with a stoichiometric excess of zinc, which can alter with the oxygen pressure of the surrounding gas. This can be attributed to removal of oxygen from the lattice or, according to H. Fritsche [Z. Physik 133, 422 (1952)], to removal of interstitial oxygen. Whichever the nature of the process, it is temperature dependent and very slow at room temperature, which conditions are in agreement with our findings.

approximately constant in the range of higher pressures. [See Eq. (1).] Because of this variation of a with p_m, it can be seen from Eq. (2) that $\partial p/\partial p_m$ is small at low pressures, becoming larger and practically constant as the pressure increases.

For the higher compression rates used the densities of the powder approximated the density values of zinc oxide given in the literature within the limits of error. We did not determine the particle size distribution, so that the actual size of the interspaces was not known.

For a semiconductor we express the conductance as

$$G=G_0e^{-\epsilon/kT}. \tag{3}$$

We use this classical approximation commonly adopted when ϵ is large compared with kT. From experiments reported further on, the slope of $\ln\epsilon$ *versus* $1/kT$ gave $\epsilon\sim 0.2$ ev for the powders examined by us, which seems to justify the approximation made. For small activation energies an intrinsic conduction term should be added. In our case the activation energy ϵ is half the energy distance between the impurity levels and the conduction band, G_0 depends on the physical dimensions of the sample and includes the geometry of the constrictions. G_0 increases rapidly with pressure for low pressures and becomes approximately constant for high pressures.

The condition for a conductance maximum [Sec. III (*d*)] can be seen from Eq. (3) to be

$$\partial G_0/\partial p_m=(G_0/kT)(\partial\epsilon/\partial p)(\partial p/\partial p_m). \tag{4}$$

Since $\partial G_0/\partial p_m$ and $\partial p/\partial p_m$ are always positive, the maximum requires a positive $\partial\epsilon/\partial p_m$. In the way of a rough check we determined the sign of $\partial\epsilon/\partial p_m$ by measuring ϵ at different pressures. The ϵ values were derived from measuring the conductance over a range of temperatures. The averaged values were $\epsilon=0.209$ ev for 1200 psi and $\epsilon=0.240$ ev for 10490 psi. The evaluation showed $\partial\epsilon/\partial p_m$ to be positive and of approximately the right magnitude to account for the phenomena observed. It will be noted that $\partial\epsilon/\partial p_m$ is not the same as $\partial\epsilon/\partial p$, which is the quantity with a more direct physical meaning. Unfortunately, $\partial\epsilon/\partial p$ cannot be measured directly, and we are forced to deal with $\partial\epsilon/\partial p_m$; it can, however, readily be seen that the two quantities have the same sign. A positive $\partial\epsilon/\partial p$ means that the gap between the impurity levels, and the conduction band is enlarged as the pressure is increased. Positive values are known to exist. For the particular case of zinc oxide Bridgman reports that ϵ increases with pressure at 200°C and decreases with pressure at 0°C and 100°C. In comparing this with our findings, we must consider that the change of ϵ with pressure depends on impurities, but more important, that our p does not refer to hydrostatic pressure, but to a unidirectional stress and that the lattice deformation differs from that produced by hydrostatic pressure.

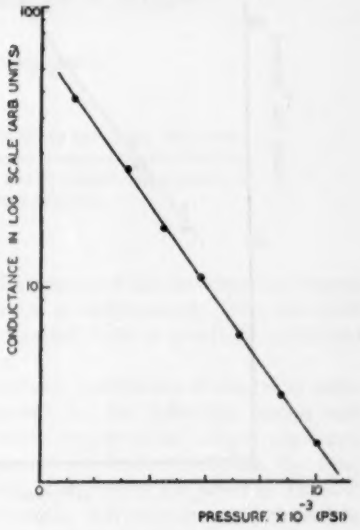

FIG. 2. Conductance in logarithmic scale *versus* pressure, for high pressures.

Since $\partial G_0/\partial p_m$ is positive and decreases with pressure while $\partial p/\partial p_m$ for higher pressures tends towards a constant value and $\partial\epsilon/\partial p$ is little sensitive to pressure changes, Eq. (4) shows that when the temperature is lowered the conductance maximum must occur at a lower pressure, which is in agreement with (*d*) of Sec. III.

The pressure p on the contact area cannot be increased indefinitely. At a certain critical pressure bruising or cracking of particles will occur. This critical pressure will vary with the configuration of the surrounding particles and with the particle size. We introduce the symbol p^* as an average or representative quantity for the maximum pressure which can be applied before breakage of the particle occurs. If the acting pressure on the powder is increased to a value greater than any previously attained pressure the pressure at some contact areas will reach the value for which bruising or crushing of particles occurs and an irreversible increase of the contact area takes place until the contact cross section has increased to a value for which $p=p^*$. If we designate by P_m the maximum acting pressure that has ever been applied to the powder, then

$$p^*a=P_mA_m, \tag{5}$$

and a, the average contact area, is then a function of P_m.

For $p_m<P_m$ in the high pressure range, for which G_0 may be considered as constant:

$$\ln G=\ln G_0-\epsilon/kT, \tag{6}$$

and substituting

$$\epsilon(p_m)=\epsilon_0+\frac{\partial\epsilon}{\partial p}\frac{\partial p}{\partial p_m}p_m, \tag{7}$$

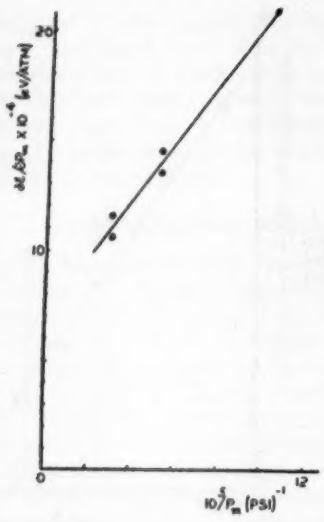

FIG. 3. $\partial\epsilon/\partial p_m$ versus $1/P_m$.

we find:

$$\ln G = \ln G_0 - \frac{\epsilon_0}{kT} - \frac{1}{kT}\frac{\partial\epsilon}{\partial p}\frac{\partial p}{\partial p_m}p_m. \tag{8}$$

From Eq. (2) and Eq. (5), it follows that for the high pressure range

$$\partial p/\partial p_m = A_m/a = p^*/P_m; \tag{9}$$

so that we can write:

$$\ln G = \text{const} - \frac{1}{kT}\frac{\partial\epsilon}{\partial p}\frac{p^*}{P_m}p_m. \tag{10}$$

Equation (10) agrees with the experimental result in Sec. III (*e*), in particular with the finding that the constant of proportionality between the logarithm of conductance and pressure is inversely proportional to P_m. Figure 3 shows some of the values of $\partial\epsilon/\partial p_m$ obtained for different values of P_m plotted against $1/P_m$.

The above accounts for most of the experimental findings reported in Sec. III, with exception of the transients which are more difficult to explain. These transients probably result from the superposition of several effects.

The decrease in conductance observed with a constant potential applied to the powder kept at a fixed pressure may be due to residual moisture or to ionic surface conductivity of the type discussed by Mott and Cabrera, to which reference has been made. Such ionic surface conduction would produce phenomena in the nature of electrolytic polarization. Electronic space charges also could play a part. Miller observed some transients with sintered ZnO, the constitution of which, however, differs from that of a powder, and Bridgman observed some at 200°C.

Davis[4] observed that when rock salt crystals were placed under increasing stress a transient increase of current occurred just below the stress for which shattering took place. Pierucci[15] observed a similar effect when cleaving crystals. The transient increase of conductance, which accompanies a change of pressure, may be related to effects of this type. Pierucci interprets his results by assuming that whenever a regrouping of the lattice configuration takes place, some electrons are temporarily lifted into the conduction band before taking their final positions. A general reshuffle of the lattices and grain boundaries will also give rise to a reshuffle of the configuration of space charges.

We do not have a sufficient amount of data available to attempt to give a definite explanation of the transients observed.

V. CONCLUSIONS

The phenomena which we have reported seem to be related to microquantities which we cannot observe in detail, but only interpret in their effect on observable macroscopic quantities. E.g., a significant quantity is $\partial\epsilon/\partial p$, where p is the stress at the contact area. This p is not equivalent to the quantity p_m nor to the hydrostatic pressure applied by Bridgman. Further, the value of ϵ is depending on the impurity content and is thus affected by heat treatment, so that it is likely to vary for different specimens.

Because of this uncertainty we feel that the work reported here is not so much a contribution to the study of the effect of compression on the semiconducting properties of zinc oxide as it is to the study of what happens to a semiconducting powder when it is compressed. This may be of interest to anyone desiring to study the electrical properties of materials that are not obtainable as single crystals but as powders only.

[15] M. Pierucci, Nuovo cimento **6**, 78 (1949).

Effect of Elastic Strain on the Electrical Resistance of Metals

G. C. KUCZYNSKI
Metallurgy Department, University of Notre Dame, Notre Dame, Indiana
(Received November 16, 1953)

The strain coefficients of electrical resistivity of some eighteen metals and alloys have been determined experimentally. It has been shown that for most metals the free electron theory accounts qualitatively for the observed effects. In the case of bismuth and antimony, the discussion of the possible deformation of the Brillouin zones of these metals with strain seems to explain their abnormal behavior.

THE phenomenon of the change of the electric resistance of metallic wires with elastic strain was first investigated by Lord Kelvin[1] in 1856 and his pupil Tomlinson.[2] Their research was followed by that of Donaldson and Wilson,[3] Smith,[4] Bridgman,[5–7] Rolnick,[8] Allen,[9] and others. Most recently an excellent study was published by Druyvesteyn,[10] who measured the variation of electrical resistivity of metals with elastic deformation in different crystallographic directions. The phenomenon is today utilized in the operation of electrical-resistance strain gauges.[11]

The change in electrical resistance due to strain is partly due to the geometrical changes taking place in the deformed body and partly due to physical changes within the metal itself. In the case of a metallic wire stretched longitudinally, these two factors enter the following equation:

$$\frac{dR}{Rd\epsilon}=(1+2\mu)+\frac{d\rho}{\rho d\epsilon}, \qquad (1)$$

where R is the total resistance of the wire, ρ its specific resistivity, ϵ the strain, and μ Poisson's ratio. $dR/Rd\epsilon$ could be called the coefficient of strain sensitivity of resistance, or gauge factor, and $d\rho/\rho d\epsilon$ the strain coefficient of specific resistivity. The first term on the right side of Eq. (1) represents the purely geometrical effect of the deformation and the second, the physical one. In this paper we shall discuss only the effect of elastic strains upon the specific resistivity of metals and alloys.

EXPERIMENTAL RESULTS

A number of wires of pure metals and alloys were tested in the apparatus specially built for the purpose and described elsewhere.[12] The wire was stretched by the lever action of a beam and the increments of length were measured with a cathetometer. The electrical resistance was measured with a carefully calibrated Wheatstone bridge.

The strain sensitivity coefficients of electrical resistivity were measured for the following metals and alloys: copper, nickel, copper-nickel alloys, platinum, aluminum, tungsten, molybdenum, tantalum, tin, iron, cobalt, and bismuth. The results are listed in Table I. Data on bismuth-lead, bismuth-tin, and bismuth-selenium alloys have been published previously.[13]

TABLE I. Strain coefficients of resistivity of metallic wires of various diameters.

Material	Wire diameter (cm)	$\frac{d\rho}{\rho d\epsilon}$	Remarks
Cu	25.80×10^{-3}	1.60	Annealed
	12.85	1.55	Annealed
	5.48	1.20	Annealed
	2.61	0.90	Annealed
	1.06	0.90	Annealed
Ni	12.06	− 8.82 to − 9.82	Grade A ann.
	2.22	− 3.95 to − 7.12	Grade A ann.
	23.80	− 2.95	As drawn
	12.00	− 3.22 to − 5.62	As drawn
	2.51	− 2.12 to − 2.92	As drawn
	25.30	−11.62 to −12.62	Mond nickel
	2.69	− 8.82	Annealed
Al	25.00	1.40	Annealed
Pt	12.67	2.60	Annealed
	2.41	2.22	Annealed
Fe	22.62	0.44	Annealed
Co	14.50	0.84	Annealed
Mo	12.45	0.80	As received
Ta	12.42	1.30	As received
W	12.95	1.16	As received
	1.42	1.16	As received
Sn	31.80	3.34	Extruded
Bi	29.20	−11.36	Extr. and ann.
	7.70	−11.16	Extr. and ann.
Cu-Ni (Atom % Ni)			
1.08	25.30	1.54	Annealed
	2.54	0.43	Annealed
11.50	25.80	0.70	Annealed
	2.69	0.80	Annealed
45.00	25.60	0.30	Annealed
72.00	25.60	− 0.19	Annealed
	2.64	− 0.19	Annealed
96.00	25.30	−10.82 to −11.62	Annealed
98.30	25.50	−13.06	Annealed
99.50	25.50	−13.62	Annealed
	2.64	− 8.12	Annealed

[1] W. Thompson, Trans. Roy. Soc. (London) **146**, 649 (1856).
[2] H. Tomlinson, Trans. Roy. Soc. (London) **174**, 1 (1883).
[3] J. A. Donaldson and R. Wilson, Proc. Roy. Soc. (London) **27**, 18 (1907).
[4] N. F. Smith, Phys. Rev. **28**, 107, 429 (1909).
[5] P. W. Bridgman, Proc. Am. Acad. Arts Sci. **57**, 39 (1922).
[6] P. W. Bridgman, Proc. Am. Acad. Arts Sci. **59**, 117 (1923).
[7] P. W. Bridgman, Proc. Am. Acad. Arts Sci. **60**, 423 (1925).
[8] H. Rolnick, Phys. Rev. **36**, 506 (1930).
[9] M. Allen, Phys. Rev. **42**, 848 (1942).
[10] M. J. Druyvesteyn, Physica **17**, 748 (1951).
[11] A. V. deForest, Instruments **15**, 112 (1942).
[12] J. T. Norton and G. C. Kuczynski, Instruments **21**, 328 (1948).
[13] G. C. Kuczynski and J. T. Norton, J. Appl. Phys. **19**, 683 (1948).

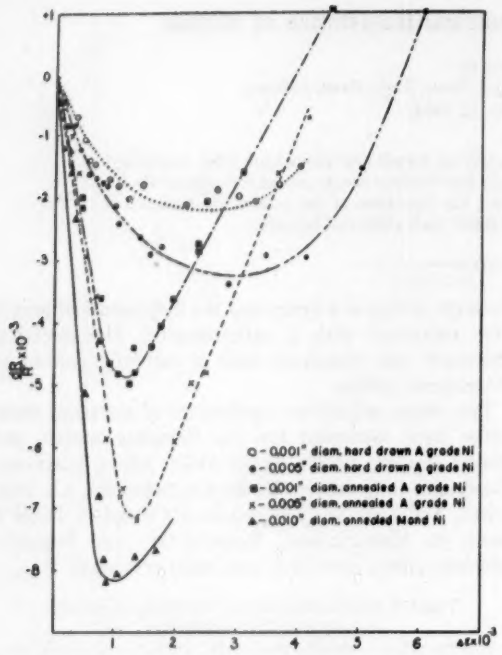
○ - 0.001" diam. hard drawn A grade Ni
● - 0.005" diam. hard drawn A grade Ni
⊞ - 0.001" diam. annealed A grade Ni
x - 0.005" diam. annealed A grade Ni
▲ - 0.010" diam. annealed Mond Ni

FIG. 1. Fractional change of electrical resistance for various nickel samples as a function of the strain increment $\Delta\epsilon$.

A study of the Table I reveals that: (a) Most metals and alloys investigated have rather low and positive strain coefficients of electrical resistivity. (b) Notable exceptions to this rule are Ni and Bi and some Ni and Bi alloys.[13] (c) The strain sensitivity decreases with the wire diameter. It should be noted that this effect is not geometrical but due to the cystallographic anistropy of the factor $d\rho/\rho d\epsilon$.[10] (d) The results listed in Table I are in fair agreement with those obtained by other investigators, as can be seen in Table II.

In addition it has been observed that, beyond the yield point, the values of $d\rho/\rho d\epsilon$ decreased greatly for all metals. In the case of Ni, even within the elastic limit, a notable change of $d\rho/\rho d\epsilon$ has been observed. In Fig. 1, dR/R for Ni is plotted against increments of strain $\Delta\epsilon$. The curves seem to reach a minimum at a certain value of $\Delta\epsilon$ and subsequently the coefficient becomes positive with an ultimate value of about 3.0. Similar behavior was observed by McKeehan.[14] Also a hysteresis effect below the elastic limit of Ni has been observed and is shown in Fig. 2.

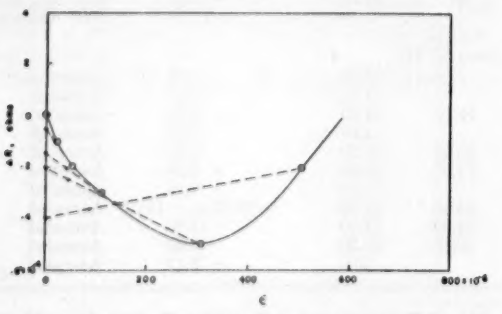

FIG. 2. Change in electrical resistance *versus* strain ϵ, for nickel, illustrating hysteresis.

The variation of the strain coefficient of electrical resistivity with the concentration of Ni in Cu-Ni alloys is represented in Fig. 3. In these alloys the absolute value of strain sensitivity decreases with increasing alloy content. The same observation has been made recently by Linde *et al.*[15,16] in the case of copper-silicon, copper-nickel, silver-tin, silver-manganese, and gold-chromium alloys.

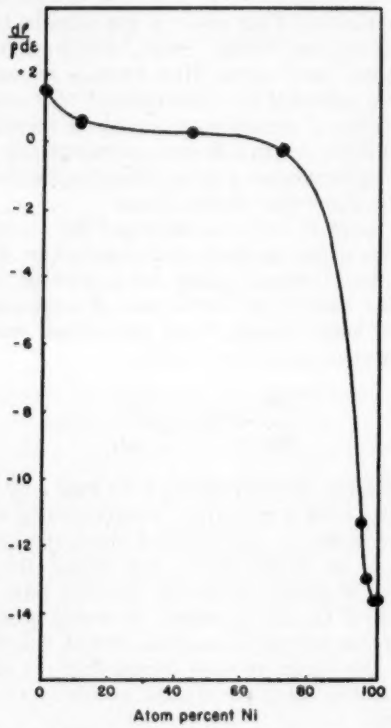

FIG. 3. Strain coefficient of resistivity of Ni-Cu alloys as a function of atomic concentration of nickel.

DISCUSSION OF RESULTS

Many properties of certain groups of metals such as copper, gold, and silver can be semiquantitatively treated as the properties of a hypothetical degenerate electron gas. Thus, in discussing metallic properties, one often assumes that the electrons in a metal can be treated as noninteracting particles moving in some kind of average potential of the periodicity of the lattice. This potential can be considered as being weak in the sense that the distribution of energy levels is

[14] L. W. McKeehan, Phys. Rev. **36**, 948 (1930).
[15] Linde, von Heijne, and von Sabsay, Arkiv Fysik **2**, 81 (1950).
[16] J. O. Linde and C. H. Stade, Arkiv Fysik **2**, 99 (1950).

determined largely by the kinetic rather than the potential energy. The electrical resistivity of a metal can be considered as a function of two variables, the mean free path l of the electrons and the effective number n of free electrons.

$$\rho \sim m/ln.$$

Assuming that the effective mass m of an electron is constant, we shall obtain the following expression for the coefficient of strain sensitivity:

$$\frac{d\rho}{\rho d\epsilon} = -\frac{dl}{ld\epsilon} - \frac{dn}{nd\epsilon}. \tag{2}$$

If a weak potential is assumed, then the energy E of the electrons can be adequately evaluated by the following equation:

$$E = (h^2/2m)k^2, \tag{3}$$

where k is the wave vector. The number of free electrons

$$n = \frac{2}{\pi}\frac{m}{h^2}\left(\frac{\partial E}{\partial k}\right)_{k=k_{\max}}$$

or, using Eq. (3),

$$n = (2\pi)k$$

and

$$dn/nd\epsilon = dk/kd\epsilon.$$

The wave vector $k \sim 1-\beta\epsilon$ where β has different values for different metals but always is of the order of unity, therefore

$$dn/nd\epsilon \sim -1. \tag{4}$$

The change of the mean free path l can be evaluated from the relationship $l \sim 1/\langle X^2\rangle_{Av}$, where $\langle X^2\rangle_{Av}$ denotes the mean square of the displacement of the vibrating atom. It is easy to show[17] that for $T > \theta$, $\langle X^2\rangle_{Av} \sim 1/\theta^2$; therefore $l \sim \theta^2$. On the other hand, the change of the characteristic temperature θ with change of volume V is

$$\frac{d\ln\theta}{d\ln V} = -\gamma,$$

where γ is Grüneisen's constant, conveniently calculated from the following relationship:

$$\gamma = \frac{\alpha C_v}{\chi V_0},$$

where α is the volume coefficient of thermal expansion, C_v the molar specific heat at constant volume, χ compressibility and V_0 the atomic volume. If we assume that electrons in metals are not constrained to any specific path, then, as $d\ln V = (1-2\mu)d\epsilon$,

$$\frac{dl}{ld\epsilon} = \frac{2d\theta}{\theta d\epsilon} = -2\gamma(1-2\mu). \tag{5}$$

[17] N. F. Mott and H. Jones, *The Theory of the Properties of Metals and Alloys* (Oxford University Press, London, 1936).

TABLE II. Strain coefficients of resistivity of metals.

Metal	μ	γ	$\left(\frac{d\rho}{\rho d\epsilon}\right)^a$	$\left(\frac{d\rho}{\rho d\epsilon}\right)^b$	$\left(\frac{d\rho}{\rho d\epsilon}\right)^c$	$\left(\frac{d\rho}{\rho d\epsilon}\right)^d$
Cu	0.35	1.96	1.60	1.60	0.90 to 1.60	2.18
Ag	0.38	2.40	2.16	2.06	...	2.15
Au	0.42	3.03	3.01	2.27	...	1.97
Al	0.34	2.17	2.62	−0.68	1.40	2.39
Pt	0.39	2.54	3.09	3.44	2.60	2.22
Pd	0.39	2.23	1.85	2.70	...	2.00
Pb	0.45	2.73	...	1.12	...	1.55
Sn	0.33	2.14	...	3.65	3.75	2.46
Mo	0.32	1.57	...	1.10	0.80	2.13
W	0.32	1.62	...	1.46	1.16	2.16
Fe	0.28	1.60	0.48	...	0.44	2.42
Co	0.33	1.87	0.37	...	0.84	2.27
Ni	0.30	1.88	−3.40	−9.0	−3.0 to −13.6	2.50
Sb	0.33	0.92	3.90	...	...	1.62
Bi	0.33	1.14	−8.7	−3.52	−11.0 to −11.7	1.775

[a] Refers to Bridgman work, references 5, 6, and 7.
[b] Refers to Rolnick work, reference 8.
[c] Refers to present investigation.
[d] Refers to Eq. (7).

Equations (2), (4), and (5) yield

$$\frac{d\rho}{\rho d\epsilon} = 1 + 2\gamma(1-2\mu). \tag{6}$$

The values of the strain sensitivity coefficient as calculated from Eq. (6) are tabulated in the last column of Table II along with values of μ and γ used in its computation. The agreement is by no means satisfactory but, with a few exceptions, the calculated values are of the right order of magnitude although always too large. It is believed that this is due to the overestimation of effect of free electrons. Also the effect of strains upon the mean free path, as expressed by Eq. (5), is oversimplified. Bridgman[7] rightly states that the difference in longitudinal and transverse coefficients of strain sensitivity seems to indicate that the mean free path of the electrons must be somewhat constrained. However, the assumption of a fully constrained path does give too high longitudinal effects and does not account satisfactorily for the variety of the transverse effects.

The large increments of conductivity induced by elastic strains in nickel and the abnormally low increments of resistivity observed in cobalt and iron have been explained adequately by von Englert.[18] The elastic

TABLE III. Some physical properties of arsenic, antimony, and bismuth.

Property	As ∥	As ⊥	Sb ∥	Sb ⊥	Bi ∥	Bi ⊥
ρ (10^{-6} ohm cm)		28.0	35.6	42.6	143.0	109.0
A cgs units			0.20		−10.00	
C (10^{-6} cgs units) (magnetic susceptibility)			−0.497	1.38	−1.00	−1.50

∥ property measured along trigonal axis
⊥ property measured perpendicular to the trigonal axis

[18] E. von Englert, Ann. Physik **5**, 14, 589 (1932).

field applied to these metals produces appreciable magnetization which in turn increases the conductivity of nickel and decreases that of cobalt and iron. The theoretical treatment of this phenomenon was given by Mott.[19]

It remains to discuss the abnormal strain sensitivity factors exhibited by the metals of the fifth group of the periodic table, antimony and bismuth. These metals as well as arsenic, the third in the same group, crystallize in the rhombohedral system and exhibit peculiar physical properties, placing them on the borderline of the metallic state. Some of their physical properties such as electrical resistivity, Hall constant A, and magnetic susceptibility are listed in Table III. A schematic representation of the unit cell of the bismuth crystal is represented in Fig. 4. All atoms in this cell are equidistant a with the exception of an inside atom. This atom C, is not placed in the middle of the trigonal axis but slightly below its center. As a consequence, the distance b of atom C from its nearest neighbors is shorter than a. This effect is even more pronounced in antimony and arsenic, as can be ascertained from Table IV, where the relative position of this atom on the trigonal axis is listed as u; therefore the bond is stronger in the b than in the a direction and the cell does not deform isotropically under applied stress. The bonds b having greater rigidity will resist deformation more than the bonds a. Therefore, because of transverse contraction accompanying tension in the AB direction, atom C may travel towards the center of the AB axis and the parameter u would approach the value $\frac{1}{2}$.

Jones[20] found that the Brillouin zone for bismuth is bounded by $(1\ \bar{1}\ 0)$, $(2\ 2\ 1)$ and $(\bar{2}\ \bar{2}\ 1)$ planes and contains exactly five electrons per atom, so that it should be completely filled. However, there must be a small number of electrons overlapping because the Hall coefficient for bismuth is large and negative (Table IV),

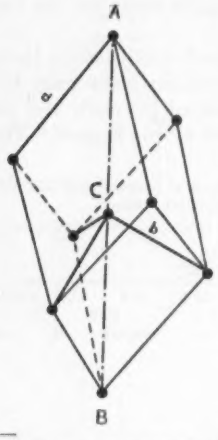

FIG. 4. Unit cell of bismuth.

[19] N. F. Mott, Proc. Roy. Soc. (London) **A156**, 368 (1936).
[20] H. Jones, Proc. Roy. Soc. (London) **A147**, 396 (1939).

TABLE IV. Crystallographic data on the structure of arsenic, antimony, and bismuth.

Metal	As	Sb	Bi
a in A	4.1350	4.4976	4.7356
θ	54° 7′	56° 36′	57° 16′
u	0.452	0.466	0.474
S_{221}	1.369	1.018	0.794

indicating a small number of free electrons. The structure factor, proportional to the energy gap over the plane (hkl), for the rhombohedral system, is

$$S_{hkl}=2\cos\{2\pi u(h+k+l)\}$$

where hkl are Miller indices of a plane and u the ratio CB/AB (see Fig. 4). The values of this structure factor for the (2 2 1) plane, together with the elements of the unit cells of arsenic, antimony and bismuth, are given in Table IV. If u were equal to 0.5, $S_{221}=0$ or there would be no energy discontinuity over this plane. On the other hand, this discontinuity increases sharply with even a slight decrease in u. As mentioned before, the electrical conductivity of bismuth depends chiefly on the overlapping electrons. The number of these electrons, n, is proportional to the probability of an electron jumping over the energy gap, which in turn can be assumed to be a function of the structure factor S. According to Zener[21] this probability is proportional to $\exp(-cS^2)$ where c can be regarded as constant. Therefore, if due to the unequal strength of bonds in the unit cell, anisotropic deformation produces even a slight increase of u, the structure factor S decreases sharply and in consequence the number of overlapping or conducting electrons increases, manifesting itself in a high negative strain sensitivity coefficient. In the case of antimony, the Hall coefficient is large and positive (Table IV), indicating that the zone is not completely filled and in consequence the electric current is largely conducted by holes. Anisotropic deformation does not control the change in number of electrons. However, elastic deformation produces the contraction of the Brillouin zone and appreciable decrease of conducting holes and manifests itself in a large positive coefficient of strain sensitivity. The same is probably true for white tin, whose zone contains 4.24 electrons per atom,[17] hence more electronic states than valency electrons. There should be therefore some overlapping of electrons in some crystallographic direction and holes in others. As the zone is almost filled, deformation will produce a large decrease in $\partial E/\partial k$ or in the number of conducting electrons. Therefore the strain coefficient of sensitivity of tin should be large and positive, as observed.

ACKNOWLEDGMENT

The author is indebted to Baldwin-Lima-Hamilton Corporation in Philadelphia for their generous support of this research.

[21] C. Zener, Proc. Roy. Soc. (London) **A145**, 521 (1934).

Rate of Production of Color Centers in KCl and KBr by X-Rays at 78°K*

WILLIAM H. DUERIG†,‡
Applied Physics Laboratory, The Johns Hopkins University, Silver Spring, Maryland
(Received October 30, 1953)

Growth rates are presented of the F, F', K, V_1, V_2, and V_4 bands occurring when KCl and KBr crystals are x-rayed at 78°K in darkness and under F' light. Under these conditions the concentration of F, F', K, and V_1 centers present at any given time of x-ray exposure is found to have two fixed values, dependent only on whether the crystal is in darkness or under F' light. The rates of production of these centers are reproducible if the crystals are warmed to room temperature under white light after each x-raying at 78°K. This reproducibility indicates that the imperfections responsible for these centers at 78°K are fully removed and the crystals are restored to their initial condition before x-raying, at least as far as these color centers are concerned. A qualitative discussion of the data is presented.

I. INTRODUCTION

SINCE Rose[1] apparently first discovered the phenomena of color centers in 1863, a great deal of research has been conducted in the field of imperfections and coloration in alkali halides. It has been quite well established that the F and F' centers are, respectively, one and two electrons trapped at a negative ion vacancy.[2] A number of new color centers have been discovered and interpretations have been attempted in many cases. One of the experimental techniques that appears likely to contribute to the knowledge and understanding of these imperfections in crystals is the measurement of the rate of growth of the color centers which occurs when a crystal is exposed to penetrating radiation.

A number of such growth-rate measurements made on F centers have been reported in the literature. A review of some of these follows for the purpose of establishing some of the conditions necessary for making the measurements which this paper reports, i.e., the growth-rate curves of various color centers formed in KCl and KBr during x-raying at 78°K (liquid nitrogen temperature).

Belar[3] apparently made the first study by measuring the rates of production of F centers in natural NaCl at room temperature using a shielded radium source (β rays). The coloration reaches a steady state or saturation value which is a function of the intensity of the source. Belar also noted shifts of the steady state value when the rate of irradiation was increased during the experiments.

It should be noted that the source used created F centers at a much slower rate than most present-day sources. Urbach extended the work of Belar to natural KCl, showing the same general results.[4]

Leitner reported extensive room temperature growth-rate data on NaCl[5], (whether the sample was synthetic or natural is not reported). She used β, γ, and 130-kv x-rays. An examination of the data indicates that none of the growth curves show a definite saturation value. For a thin NaCl crystal (0.125 cm), no saturation was indicated with x-rays, although for a thicker sample (0.296 cm), a curvature appears which might result in a saturation. Saturation seems to occur in crystals exposed to β and γ rays.

Schneider reported growth rates in KCl at room temperature using different x-ray intensities.[6] After a rapid initial rise, the density of F centers rises almost linearly.

The most extensive study of the growth-rate problem has been made by Harten for synthetic KCl.[7] He exposed the crystals to x-rays (60 kv) at 60°C, 20°C, −20°C, −75°C, −110°C, and −180°C. The following points should be considered:

(a) The growth-rate curves tend toward saturation at temperatures above −110°C but not at lower temperatures. A definite saturation occurs at 20°C (this does not agree with Schneider's work), and the effects of thermal bleaching appear at 60°C.

(b) If a crystal has an F-center concentration in excess of the saturation (equilibrium) value for a specific temperature, (this can be obtained by changing the temperature after an exposure to x-rays) further exposure decreases the F-center concentration to the saturation value.

Recently, a growth-rate curve obtained by x-rays on synthetic NaCl at 5°K has been reported.[8] The result is a rapid initial rise followed by a linear growth rate. The form of this curve is similar to those found at 78°K in KCl by Harten.

* This research was supported, in part, by the Bureau of Ordnance, Department of the Navy.
† This paper is part of a dissertation presented to the Faculty of the Graduate School of the University of Maryland in partial fulfillment of the degree of Doctor of Philosophy.
‡ Now at Electro-Mechanical Research, Inc., Ridgefield, Connecticut.
[1] H. Rose, Ann. Physik **120**, 1 (1863).
[2] A review of this subject has been given by R. W. Pohl, Proc. Phys. Soc. (London) **49** (extra part) 4 (1937) or Physik. Z. **39**, 36 (1938) and by F. Seitz, Revs. Modern Phys. **18**, 384 (1946).
[3] M. Belar, Wien. Ber. IIA, **132**, 45 (1923), and **135**, 186 (1926).
[4] F. Urbach, Wien. Ber. IIA, **135**, 149 (1926).
[5] I. Leitner, Wein. Ber. IIA, **147**, 407 (1936). A correction to this paper appears in Akad. Wiss. Wien. Anzeiger **74**, 105 (1937).
[6] E. E. Schneider, *Fundamental Mechanisms of Photographic Sensitivity* (Academic Press, Inc., New York, 1951), pp. 13–23.
[7] H. Harten, Z. Physik **126**, 616 (1949).
[8] W. H. Duerig and J. J. Markham, Phys. Rev. **88**, 1043 (1952).

Two studies have been made of F centers formed by ultraviolet light, i.e., excitons. Smakula investigated the growth rates in synthetic KBr at 20°C and −183°C, and synthetic KI, RbBr, and RbCl at room temperature.[9] The data at −183° show a distinct saturation after an exposure of 15 seconds to this radiation. The other curves show only a trend towards saturation. The concentration of F centers per unit exposed area is about two percent of the concentration obtained at low temperatures by means of x-rays. Schröder also reported measurements of the growth of the F band produced by excitons in NaCl at room temperature.[10] Several types of natural and synthetic crystals were used. Further, the crystals were exposed to light during the irradiation so that the F band appears in what is called its "excited" state, i.e., "Errgung."[11] Several points of Schröder's work which should be stressed are:

(a) Some of his synthetic crystals, believed to be of highest purity, are not colored by excitons and in those that can be colored, the coloration reaches a saturation.

(b) No saturation of coloration is observed for natural crystals.

(c) Thermal and mechanical treatments have an important effect on the growth-rate curves.

The effects of impurities on the growth rates have been summarized recently by Schulman[12] and will not be discussed here.

An examination of the above data indicates that the growth rates of color centers are dependent on a large number of variables. Among these are the type and intensity of radiation and the purity and temperature of the crystals. For the experiments described in this paper it was concluded to maintain all the variables constant except the F'-center concentration. The purity of the crystals used has been discussed elsewhere.[8]

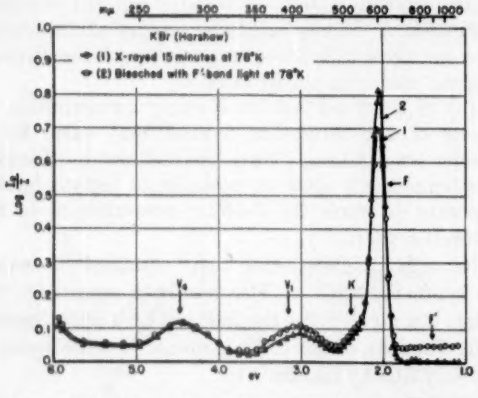

FIG. 1. Effect of x-raying KBr at 78°K and subsequently bleaching at 78°K with F'-band light.

[9] A. Smakula, Z. Physik **63**, 762 (1930).
[10] H. J. Schröder, Z. Physik **76**, 608 (1932).
[11] See, for example, B. Gudden and R. Pohl, Z. Physik **37**, 881 (1926), Fig. 1.
[12] J. H. Schulman, J. Chem. Phys. (to be published).

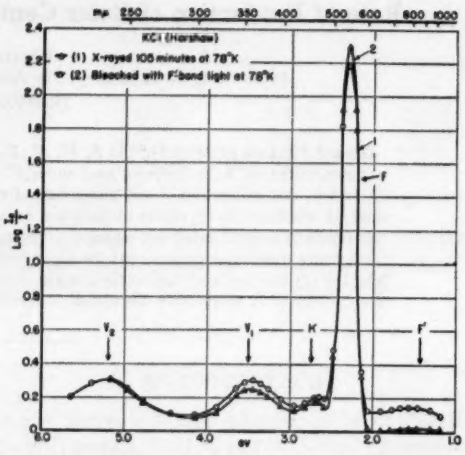

FIG. 2. Effect of x-raying KCl at 78°K and subsequently bleaching at 78°K with F'-band light.

II. GROWTH RATES AT 78°K

Experimental Procedure

Upon x-raying KBr and KCl at 78°K, five bands appear between 210 mμ and 1000 mμ, namely, the F, F', K, V_1, and V_4 bands in KBr, shown in Fig. 1, and the F, F', K, V_1, and V_2 bands in KCl[13] shown in Fig. 2. The structures for the K, V_1, V_2, and V_4 centers have been proposed.[14] In these experiments the V_2 band of KCl behaves like the V_4 band of KBr. The object of these experiments was to obtain growth-rate curves of these bands under two conditions: (1) when the crystal is in darkness and (2) when the crystal is exposed to F' light.

The general experimental technique employed in this study has already been described.[8,15] The crystals, grown by the Harshaw Chemical Company, were x-rayed at 78°K (after being mounted in a low-temperature cell),[15] and an attempt was made to maintain the x-ray intensity constant by careful positioning of the cell and by voltage and current regulation of the x-ray source, a Machlett C-524 molybdenum target tube operated at 50 kv and 28 ma. The crystal was situated about 3 cm from the beryllium window of the tube and the cell had a beryllium window of 0.05 cm thickness.

The crystal absorption is reported in terms of optical measurements made on a Beckman Model Du Spectrophotometer. The data are given in terms of $\log_{10} I_0/I$, where I_0 = fraction of light transmitted before x-raying, and I = fraction of light transmitted after x-raying.

In order to obtain growth-rate curves which might be quantitatively compared, the reproducibility of the

[13] H. Dorendorf, Z. Physik **129**, 317 (1951). The K band appears in this paper, but is not named. Previously the nomenclature V_0-band was used (see reference 8).
[14] F. Seitz, Phys. Rev. **79**, 529 (1950); Revs. Modern Phys. **18**, 384 (1946); Revs. Modern Phys. **26**, No. 1 (1954).
[15] W. H. Duerig and I. L. Mador, Rev. Sci. Instr. **23**, 421 (1952).

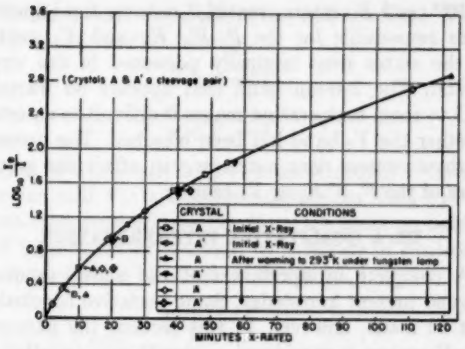

FIG. 3. Reproducibility of the growth of the F band produced in KBr (Harshaw) x-rayed in the dark at 78°K.

curves had to be established. Two techniques were examined.

A crystal about 2 or 3 mm thick was cleaved in half. The resulting pair was mounted in the cell so that each of the faces in contact before cleaving faced the x-ray beam. The crystals were x-rayed at 78°K with the same intensity and the growth of the F band *versus* time was observed. The growth-rate curve shown in Fig. 3 illustrates the close agreement in the rate of production of F centers for both samples of KBr. A similar curve has been obtained for KCl shown in Fig. 4. These experiments were repeated once for both KCl and KBr with the same results.

The second technique involved warming the crystals to room temperature after each x-raying at 78°K and irradiating them with light from an ordinary tungsten lamp for several hours. The reproducibility of the F-band growth curve under repeated x-raying and warming is also shown in Fig. 3. A similar curve has been obtained for KCl and is shown in Fig. 4. A band appears in KCl at 290 mμ on warming to room temperature under the light, but its presence does not affect the growth rates of the other centers. This 290-mμ band bleaches on warming to about 200°C.[16] While both of these techniques permit growth-rate reproduction to within one percent, the second was used since it is more convenient.

The light necessary to bleach the F' band during x-raying was obtained by mounting a 250-watt tungsten projector bulb about 2 inches from a quartz window in the cell which was directly opposite the beryllium window. The proper Corning glass filters[17] were placed against the quartz window so that only F' light could reach the crystal.

[16] H. Harten, reference 7. Harten observed that the growth rate could be reproduced after warming KCl to 350°C for five minutes.

[17] For KCl, a combination of Corning Glass Color Filters 2-58 and 2-64 was used. This procedure insured a very sharp cutoff below 680 mμ and good transmission from 680 mμ to 2.7μ. For KBr, a combination of Filters 2-64 and 7-57 was used, giving a sharp cutoff below 680 mμ and good transmission from 700 mμ to 2.7μ. Under these conditions no bleaching of the F band was noted during periods of F' irradiation to one-half hour.

No significant bleaching of the bands by the light of the spectrophotometer during readings was measured; hence, the number of readings taken during any one run did not influence the shape of the growth curves.

Experimental Results

The bands produced by x-raying KBr and KCl crystals in the dark at 78°K are shown by curves 1 of Figs. 1 and 2. If the F' band is bleached after x-raying, the F band increases, the K and V_1 bands decrease, but the V_2 and V_4 bands are unchanged. These effects are also shown in Figs. 1 and 2 (curve 2).

The growth rates of these bands under the constant x-ray intensity with the crystal in darkness and with the crystal exposed to F' light are presented in Figs. 5 through 11. The growth rate of the K band in KBr was too small to be measured. The following observations can be made.

(1) The shape of the growth curves for the F, F', K, and V_1 bands is similar. In KBr, the initial slope is quite steep, and then falls off slowly after 30 or 40 minutes of x-raying. In KCl a similar effect is noted except that the slope changes much less.

(2) When the crystal is x-rayed in the dark, a lower number of F centers and a higher number of K and V_1 centers are present at any given time compared to the number in a crystal which has simultaneously been exposed to x-ray and F' light.

(3) If the crystal is x-rayed initially in the dark for any number of minutes and the F' light is then turned on, the number of F, F', K, and V_1 centers present after any subsequent x-raying time is the same as if the F' light had been present during the entire time of x-raying.

(4) If the reverse of procedure (3) is followed, i.e., if the crystal is x-rayed initially under F' light and subsequently x-rayed in darkness, the number of F, K and V_1 centers present after a short time in darkness is the same as if the crystal had been x-rayed in darkness throughout the entire period.

(5) The change from F' bleaching to darkness and vice versa may be made any number of times during

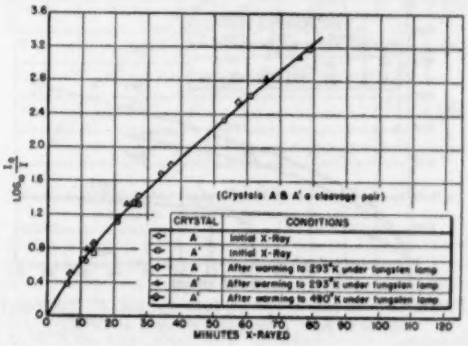
(Crystals A B A' a cleavage pair)
CRYSTAL
CONDITIONS
A Initial X-Ray
A' Initial X-Ray
A After warming to 293°K under tungsten lamp
A' After warming to 293°K under tungsten lamp
A' After warming to 490°K under tungsten lamp
MINUTES X-RAYED

FIG. 4. Reproducibility of the growth rate of the F band produced in KCl (Harshaw) x-rayed in the dark at 78°K.

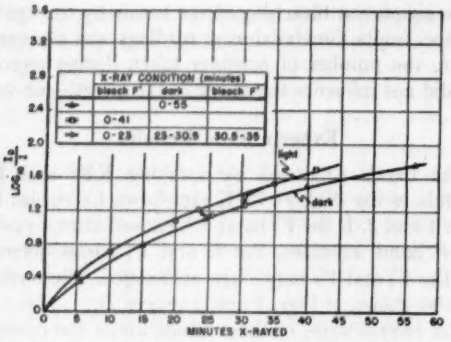

FIG. 5. Growth rate of the F band (605 mμ) in KBr (Harshaw) x-rayed at 78°K.

the x-raying, with the growth-rate curves of the F, F', K, and V_1 bands always quickly changing from one fixed curve to another.

(6) The slope of the V_2 band in KCl and the V_4 band in KBr is nearly linear, independent of whether the crystal is in darkness or not; hence, their growth appears to be independent of the concentration of F, F', K, or V_1 centers present.

Several experimental conclusions may be made from these observations:

(1) Under the condition of the experiments the number of F, F', K, and V_1 centers produced after a specific x-ray exposure at 78°K has two fixed values. These numbers are independent of the number of times the crystal has been in darkness or under F' light; hence, a fixed equilibrium occurs between the production of holes, electrons and vacancies, and the creation and destruction of certain of the color centers with these particles. This effect is similar to one observed by Harten[7] for the F band except that he varied the temperature while here the number of F' centers is varied.

(2) Warming from 78°K to room temperature under white light,[18] after the crystals have had of the order

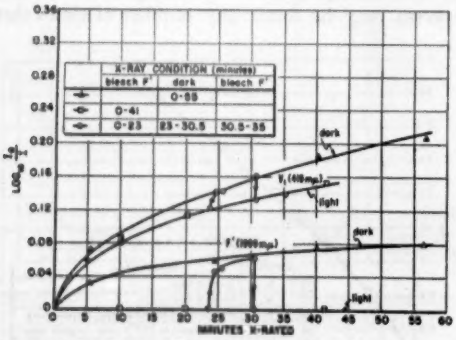

FIG. 6. Growth rate of the V_1 (410 mμ) and F' (1000 mμ) bands in KBr (Harshaw) x-rayed at 78°K.

[18] Actually the light bleaches the F and K bands. The F' and V_1 bands can be bleached by warming alone.

of 10^{18} cm^{-3} F centers created,[19] restores the imperfections responsible for the F, F', K, and V_1 centers to the states they originally possessed in the virgin crystal. The 290-mμ band that appears on warming KCl to room temperature makes it difficult to ascertain whether the V_2 band has been bleached. The presence of these centers does not, however, affect the growth rates of the F, F' K, or V_1 centers.

III. A QUALITATIVE INTERPRETATION

A complete interpretation of the above results is beyond present knowledge. Some tentative conclusions can be made, however. In this section, the nature of the V centers is considered, a growth-rate equation for the F' band is examined, and finally the effects of bleaching the F' band are discussed.

Nature of the V Bands

Four types of color centers[20] or bands have been found, namely, (1) electron centers, e.g., F F' bands; (2) hole centers, e.g., centers which appear in crystals with a stoichiometric excess of halogen; (3) perturbation bands, e.g., the α and β bands of KI and KBr; and (4) colloidal bands. A simple relation exists between group (1) and group (2) in x-rayed crystals, that is, if all the hole bands are bleached, all the electron bands must also disappear (assuming that the lifetimes of the free electron and the free hole are short and that no donor or acceptor impurities are present). An exception in this behavior may occur if all the activation energies for forming a hole center (or an electron center) were very large compared to kT so that free holes have a finite lifetime.

Unfortunately, the fact that the V_1 and K bands decrease when the F' center is bleached does not assure one that they are hole centers. To illustrate the difficulties, consider what might occur when an electron is freed in a crystal containing F centers and negative-ion vacancies. (This case is considered instead of that for a crystal with V centers since the reaction between

[19] After 60 minutes of x-rays (50 kv, 28 ma) at 78°K, the F-center density in KCl reaches about 2.4×10^{18} cm^{-3}. This value is based on Smakula's formula (reference 3), using a depth of coloration d of 0.08 cm; and index of refraction n of 1.46; a half-width W of 0.2 ev; and an oscillator strength f of 0.81. Similarly, for KBr, after 110 minutes of x-rays (50 kv, 28 ma) at 78°K, the F-center density reaches about 2.3×10^{18} cm^{-3}, using the values $d=0.06$ cm, $n=1.52$, $W=0.188$ ev, and $f=1.0$. The depth of coloration d was obtained from measurements made at room temperature by cleaving a very thin slice perpendicular to the surface of an x-rayed crystal and measuring an estimated average depth of coloration with a traveling microscope; hence, these values of d might well be in error by a factor of two or more. The oscillator strength of 0.81 for KCl is taken from F. G. Kleinschrod, Ann. Physik **27**, 97 (1936) and that of 1.0 for KBr from the reasoning that since only one absorption peak is observed, most of the oscillator strength is centered in that band.

[20] This classification is based on the following papers: Delbecq, Pringsheim, and Yuster, J. Chem. Phys. **19**, 574 (1951); A. B. Scott and L. P. Bupp, Phys. Rev. **79**, 341 (1950); A. B. Scott and W. H. Smith, Phys. Rev. **83**, 892 (1951); M. Sawostianowa, Z. Physik **64**, 262 (1930); and E. Mollwo, Ann. Physik **29**, 394 (1937).

an F center and an electron is well known.) Two reactions are possible, namely,

$$F+e_-\rightarrow F', \quad (1)$$

or

$$e_-+V_-\rightarrow F. \quad (2)$$

Here, e_- is a free electron, F is an F center, F' is an F' center, and V_- is a single-negative-ion vacancy. If the reaction expressed by Eq. (1) is the more probable, the F band could be bleached by a release of electrons just as it could be bleached by free holes, i.e.,

$$e_++F\rightarrow V_-, \quad (3)$$

where e_+ is a hole.

Thus, the data presented in Figs. 1 and 2 do not alone prove that V_1 and K bands are hole centers [the by-product corresponding to reaction (1) need not appear in the spectral range examined]. Nevertheless, the bands are probably hole centers. The three properties that this conclusion is based on are (1) the bands

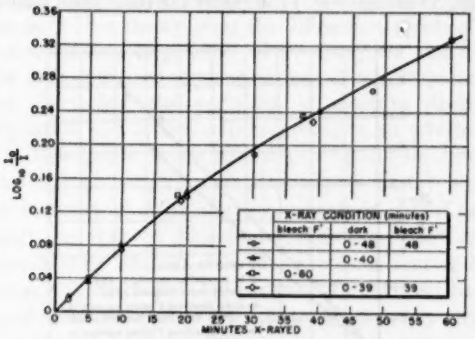

FIG. 7. Growth rate of the V_4 band (280 mμ) in KBr (Harshaw) x-rayed at 78°K.

are bleached by electrons; (2) the bands bleach (thermally) simultaneously with the electron bands (F and F'); and, most important, (3) these V bands have higher growth rates when the number of trapped electrons is large, i.e., the F' band is present.

The V_2 center in KCl (V_4 in KBr) does not seem to be associated with holes or electrons. A simple suggestion regarding the nature of the V_2 center is that it is due to a perturbation of a neutral cluster of vacancies,[21] otherwise one would suppose that its growth rate would be affected by the concentration of the other centers. Being neutral, the cluster does not attract electrons (or holes) at higher temperatures (above 20°K, say), and is not affected directly by the holes and electrons in the crystals.[22]

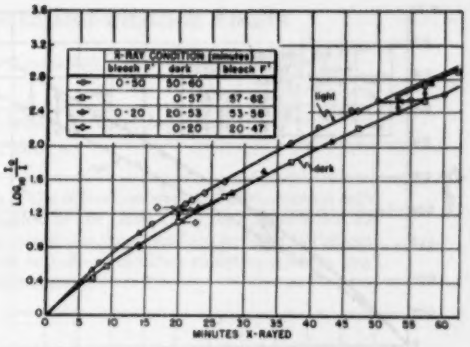

FIG. 8. Growth rate of the F band (540 mμ) in KCl (Harshaw) x-rayed at 78°K.

Growth Rate of F' Band

Factors necessary for the formulation of the growth rate of the F' band are many and include the microscopic cross section for electron capture of the F centers, the cross section for hole capture of the F' centers, the destruction of F' centers by electron or photon collision,[23] and the density of electrons and holes which is dependent on the x-ray intensity and recombination rate of the electrons and holes. Since the recombination of electrons and holes can be assisted by other centers such as the F and V centers, the concentration of these centers will determine in part the electron and hole density. In addition, there may be ways of producing F' centers other than that of the capture of an electron by an F center, e.g., the breaking up of an ion-vacancy

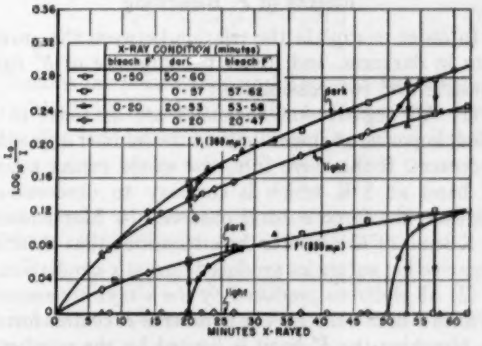

FIG. 9. Growth rate of the V_1 (360 mμ) and F' (830 mμ) bands in KCl (Harshaw) at 78°K.

[21] Recent speculation indicates [J. J. Markham, Phys. Rev. **88**, 500 (1952)] that during x-raying, ion-vacancies are produced. These may cluster to form the V_2 center. This center does not seem to form at 5°K. Indeed, when a KBr crystal with V_4 centers present is exposed to x-rays at 5°K, the V_4 band is suppressed. [See author's thesis, University of Maryland, 1952 (unpublished).] This suggests that the cluster which is responsible for this center attracts an electron or hole and forms a new center, which is stable at 5°K, but not at 78°K. A neutral cluster can be polarized so that it will attract electrons or holes at low temperatures. This model of the V_2 center disagrees with the suggestion proposed by F. Seitz, Phys. Rev. **79**, 529 (1950).

[22] At this point it is assumed that color centers are formed simply by the capture of a hole or electron. In this case an F center would be formed by a negative-ion vacancy capturing an electron. This is not necessarily always true, but it may be assumed for this application, i.e., the formation of F' centers.

[23] At 78°K the mean life of the F' centers is long so that collisions by phonons may be neglected. See H. Pick, Ann. Physik **31**, 365 (1938).

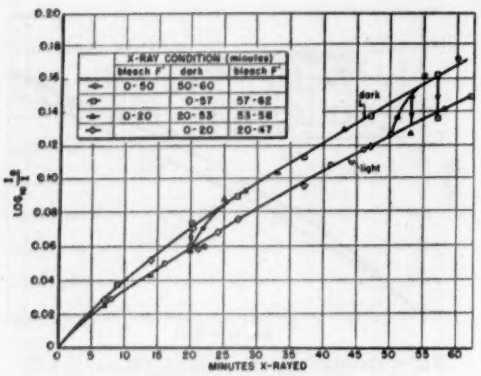

FIG. 10. Growth rate of the K band (465 mμ) in KCl (Harshaw) x-rayed at 78°K.

cluster by a photon. Since the relative density of such clusters is probably very low it may be expected that the F' centers are generated mainly by the capture of electrons by the F centers.

The above factors may be expressed in simplified mathematical form by the equation

$$dn_{F'}/dt = an_F - bn_{F'}. \tag{4}$$

Here, a includes the electron capture cross section of F centers and the density of electrons, and b the hole capture cross section for F' centers, the hole density and the collision cross section of F' centers for photons and electrons. The solution of this equation, however, and similar equations for the growth rate of other color centers, is not possible then until the coefficients a and b can be approximated, both from experimental data and from an understanding of the interactions of all the imperfections that are concerned.

Effects of F' Bleaching

In order to explain the relation between the growth rate in darkness, and under the influence of F' light, consider first two possibilities:

(1) All negative-ion vacancies are assumed to be filled, imposing an upper limit on the number of possible F centers. If this were true, one would expect a large F' band at 5°K which is contrary to observation.[8] Further, the large α band observed by Martienssen[24] in KBr at 20°K supports the assumption that there are negative-ion vacancies produced during x-irradiation.

(2) All electrons produced by the x-rays are assumed to form F or F' centers. The number of F centers formed on bleaching the F' band is limited by the number of free electrons and does not depend on any intermediate state. Thus, this assumption contradicts the fact that electrons released from F' centers bleach V bands, and that holes bleach the F' centers during the x-raying process.

Since both of these hypotheses lead to contradictions they must be rejected. The difference between (1) growing F centers in crystals exposed to F' light, and (2) growing F centers in darkness and then exposing the crystal to F' light, is apparently a question of timing. In the first case, some of the electrons produce F and F' centers. The F' center has a short life, however, and electrons are rejected from these centers to be trapped in various imperfections in the crystals. If it is assumed that the fractions of electrons and holes captured by the centers are independent of time, then the fraction of electrons released from F' centers which terminate in negative-ion vacancies is also independent of time. This hypothesis suggests that the concentration ratio of the various centers is approximately independent of time of x-ray exposure. The number of F centers formed indirectly by bleaching the F' centers is about 10 percent of the total number of F centers. Thus, a variation of ten percent in the capture fractions of the F' centers should be reflected in a change of one percent in the F-center concentration.

Data taken from the growth-rate curves shown in Figs. 5 through Fig. 11, support the conclusion that the

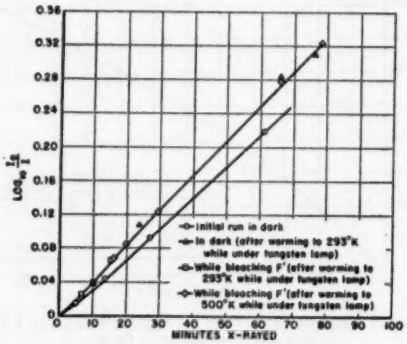
Initial run in dark
In dark (after warming to 293°K while under tungsten lamp)
While bleaching F' (after warming to 293°K while under tungsten lamp)
While bleaching F' (after warming to 500°K while under tungsten lamp)
MINUTES X-RAYED

FIG. 11. Growth rate of the V_2 band (240 mμ) in KCl (Harshaw) x-rayed at 78°K.

concentration ratio does not vary radically; for KCl, the ratios of the K (dark) reading to the F (dark) reading taken in 10-minute intervals (shown in Figs. 8 and 10) are, 0.062, 0.064, 0.063, 0.063, and 0.064. Likewise, for the V_1 and F bands in KBr (dark) one obtains 0.15, 0.13, 0.125, 0.12, and 0.125 (shown in Figs. 5 and 6). The consistency of the ratio V_1 to F in KCl (dark) is not quite as good as the above figures, being 0.145, 0.14, 0.13, 0.12, and 0.11 (shown in Figs. 8 and 9). These ratios indicate, however, that the variation of the fractions of the electrons and holes captured is sufficiently small so that they are not observable in the measurements. Thus, some of the features of the growth-rate curves may be explained qualitatively, although quantitative data at various temperatures are needed.

The author wishes to thank Dr. J. J. Markham and Dr. R. C. Herman for helpful discussions regarding the paper, and Mrs. B. Grisamore for assistance in taking and preparing the data.

[24] W. Martienssen, Z. Physik 131, 488 (1952).

Diffraction Effects of Crystals with Deformation Faults

R. HOSEMANN, *Fritz Haber Institut der Max Planck Gesellschaft, Berlin-Dahlem, Germany**

AND

S. N. BAGCHI, *University College of Science, Calcutta, India*

(Received July 27, 1953)

The theory of ideal paracrystals is applied to the problem of the diffraction effects of face-centered cubic crystals with deformation faults (as distinct from growth faults) in the plane (111). It is shown that the formulas given by Paterson are more easily deduced with the help of this theory and the problem of Paterson is only a special case (e.g., the case of infinitely large crystals and of coordination statistics given by peak functions) of the general deformation effects postulated in this theory.

INTRODUCTION

THE x-ray diffraction effects for face-centered cubic crystals with deformation faults (as distinct from growth faults) has been calculated by Paterson.[1] It will be shown here that such diffraction effects can be calculated much more easily and elegantly with the help of the interference theory of ideal paracrystals.[2,3] This theory gives the diffraction effects of a distorted lattice in general, where distortion and disorder arise due to random variations of lattice parameters (including the variation of electron density distribution in a lattice cell) according to an arbitrary but a definite rule. It has been shown[2,3] that this theory under special circumstances degenerates to the well-known theory of diffraction by crystals by Laue[4] and Bragg[5], to that of liquids by Zernicke-Prins[6] and Debye-Menke[7] and to that of amorphous matter by Guinier,[8] Warren[9] and Hosemann.[10] It has also been shown[2,3] that this theory is better suited than any other above-mentioned single theory to discuss the diffraction effects of matter in intermediate stages of existence and offers much more detailed information about the nature and degree of such disorder and deformation.

Let $\mathbf{a}_k (k=1, 2, 3)$ be the three fundamental vectors of a distorted space lattice, and $H_k(\mathbf{x})$ be the frequency of meeting the vector $\mathbf{a}_k=\mathbf{x}$ in the lattice, so that $\int H_k(\mathbf{x}) \times dv_x = 1$ and $H_k(\mathbf{x})dv_x$ is the probability of finding the vector $\mathbf{a}_k=\mathbf{x}$ ending in the volume element dv_x. $\rho_0(\mathbf{x})$ is the electron density distribution in a lattice cell. It fluctuates from cell to cell but the *a priori* probability of finding a definite ρ_0 is the same for all cells. $s(\mathbf{x})$ is the shape function of the lattice and has the value unity inside the paracrystal but vanishes outside it. Further, let the following functions be defined as Fourier transforms of ρ_0, s, and H_k:

$$f(\mathbf{b})=\mathfrak{F}(\rho_0); \quad S(\mathbf{b})=\mathfrak{F}(s); \quad F_k=\mathfrak{F}(H_k). \quad (1)[11]$$

$f(\mathbf{b})$ is the "structure amplitude," $S(\mathbf{b})$ is the "shape amplitude," and F_k is the "statistical amplitude" of the coordination statistics H_k. $\mathbf{b}$ is the vector reciprocal to $\mathbf{x}$ and is defined by

$$\mathbf{b}=(\boldsymbol{\sigma}-\boldsymbol{\sigma}_0)/\lambda, \quad |\mathbf{b}|=2(\sin\vartheta)/\lambda, \quad (2)$$

where $\boldsymbol{\sigma}$, $\boldsymbol{\sigma}_0$ are the unit vectors in the direction of the scattered and incident beams respectively, λ is the wavelength, and 2ϑ is the scattering angle.

The interference theory of ideal paracrystals[2,3] shows that the mean scattered intensity is given by

$$I(\mathbf{b})=I_0 f_e^2 (I_1+I_2), \quad (3)$$

where

$$I_1=N(\langle f^2\rangle_{\mathbf{w}}-\langle f\rangle_{\mathbf{w}}^2), \quad (4)$$

$$I_2=\frac{1}{v_r}\langle f\rangle_{\mathbf{w}}^2 (Z^{1/v_r} * |S|^2). \quad (5)[12]$$

f_e contains the polarization and Thomson factors; I_0 is the intensity of the primary beam; v_r is the mean volume of the distorted lattice cell in physical space; N denotes the number of lattice cells. $Z^{1/v_r}(\mathbf{b})$ is called the lattice

---

* Formerly: Kaiser-Wilhelm-Institut für physikalische Chemie und Elektrochemie, Berlin-Dahlem, Germany.

[1] M. S. Paterson, J. Appl. Phys. **23**, 805 (1952).
[2] R. Hosemann, Z. Physik **128**, 1, 465 (1950).
[3] R. Hosemann and S. N. Bagchi, Acta Cryst. **5**, 612 (1952).
[4] M. von Laue, Ann. Physik **41**, 989 (1913).
[5] W. H. Bragg and W. L. Bragg, Proc. Roy. Soc. (London) **A88**, 428 (1913).
[6] F. Zernicke and J. A. Prins, Z. Physik. **41**, 184 (1927).
[7] P. Debye and H. Menke, Ergbn. techn. Röntgenk. **2**, 1 (1931).
[8] A. Guinier, thesis, Paris, Series A, Nr. 1854, 2721, 1939.
[9] B. E. Warren, Phys. Rev. **59**, 693 (1941).
[10] R. Hosemann, Z. Physik **113**, 751 (1939).

[11] The symbol $\mathfrak{F}$ represents the Fourier integral. The Fourier transform $G(\mathbf{b})$ of a function $g(\mathbf{x})$ is defined by

$$G(\mathbf{b})=\mathfrak{F}g(\mathbf{x})=\int g(\mathbf{x}) \exp[-2\pi i(\mathbf{b}\cdot\mathbf{x})]dv_x.$$

The inverse transform of $G(\mathbf{b})$ gives back the function $g(\mathbf{x})$:

$$g(\mathbf{x})=\mathfrak{F}^{-1}G(b)=\int G(\mathbf{b}) \exp[+2\pi i(\mathbf{b}\cdot\mathbf{x})]dV_b.$$

dv_x and dv_b are volume elements in physical and reciprocal spaces, respectively. The integrations run over the entire space.

[12] The convolution product (*Faltung* in German) of the functions $g_1(\mathbf{x})$ and $g_2(\mathbf{x})$ is defined by

$$g_1 * g_2(\mathbf{x})=g_2 * g_1(\mathbf{x})=\int g_1(\mathbf{y})g_2(\mathbf{x}-\mathbf{y})dv_y.$$

The integration runs over the entire space.

amplitude of the paracrystal[13,14] and is given by

$$Z^{1/v_r}(\mathbf{b})=\prod_{k=1,2,3}\mathrm{Re}\frac{1+F_k}{1-F_k}=\prod_k\frac{1-|F_k|^2}{1+|F_k|^2-2\,\mathrm{Re}F_k}. \quad (6)$$

In ideal crystals the vectors $\mathbf{a}_k$ show no fluctuations and hence H_k are best represented by peak functions, $P(\mathbf{x}-\mathbf{a}_k)$, such that

$$P(\mathbf{x}-\mathbf{a}_k)=0 \quad \text{for all} \quad \mathbf{x}\neq\mathbf{a}_k, \quad (7)$$

and

$$\int P dv_x=1. \quad (8)$$

The "lattice amplitude" Z^{1/v_r} then describes the well-known peak functions of the reciprocal lattice

$$Z^{1/v_r}(\mathbf{b})\to\frac{1}{v_r}\sum_h P^1(\mathbf{b}-\mathbf{b}_h). \quad (9)$$

Hence the scattered intensity for an ideal crystal is given by

$$I\approx I_2=\frac{1}{v_r^2}\langle f\rangle_{hl}^2\sum_h|S(\mathbf{b}-\mathbf{b}_h)|^2 \text{(crystalline case)}, \quad (3a)$$

since

$$I_1=0.$$

In general $Z^{1/v_r}(\mathbf{b})$ is a "lattice hump function"; individual humps lying at the points $\mathbf{b}_h$ are more and more broadened with increasing $|\mathbf{b}_h|$ till the function Z^{1/v_r} reaches its mean value 1:

$$\lim_{b\to\infty}Z^{1/v_r}(\mathbf{b})=1. \quad (10)$$

In such a region the scattered intensity is given by

$$I\approx Nf_e^2\langle f^2\rangle_{hl} \quad \text{(amorphous case)}.[15] \quad (3b)$$

In the region of diffuse reflections, the humps around the lattice point $\mathbf{b}=\mathbf{b}_h$ are relatively broad compared to the shape factor $|S|^2$, and hence

$$I_2=N\langle f^2\rangle_{hl}Z^{1/v_r}(\mathbf{b}), \quad \text{(diffuse case)} \quad (3c)$$

and

$$I\approx Nf_e^2\{\langle f^2\rangle_{hl}+\langle f\rangle^2_{hl}(Z^{1/v_r}(\mathbf{b})-1)\}. \quad (3d)$$

For special types of fluctuation statistics H_k, it is quite possible (see Hosemann[16]) that a particular hump of the function Z^{1/v_r} lying at $\mathbf{b}=\mathbf{b}_h$ is very narrow compared to $|S|^2$ only in one or two directions of Fourier space. Then Eq. (3a) reproduces the diffraction effects in these directions and Eqs. 3(b), (c), or (d) in the other directions.[17]

The integral width[18] of a diffuse or a partially diffuse reflection in the direction $\mathbf{h}_k$ of Fourier space is given by (see Hosemann[19]):

$$\Delta\mathbf{h}_k=\frac{1-|F_k|}{1+|F_k|}. \quad (11)$$

$\mathbf{h}_k$ is a dimensionless vector obtained from the usual crystallographic vectors by affine transformation.

It is known that a suitable affine transformation of the crystallographic vectors simplifies the calculation to a large extent (see Padurow[20]). It is defined by the dimensionless numbers (p_1, p_2, p_3), and (h_1, h_2, h_3) such that

$$\begin{aligned}\mathbf{x}&=p_1\mathbf{a}_1+p_2\mathbf{a}_2+p_3\mathbf{a}_3,\\ \mathbf{b}&=h_1\mathbf{b}_1+h_2\mathbf{b}_2+h_3\mathbf{b}_3,\end{aligned} \quad (12)$$

and

$$\mathbf{b}_1=\mathbf{a}_2\times\mathbf{a}_3/v_r;\ \mathbf{b}_2=\mathbf{a}_3\times\mathbf{a}_1/v_r;\ \mathbf{b}_3=\mathbf{a}_1\times\mathbf{a}_2/v_r. \quad (13)$$

$\mathbf{b}_k$ are the fundamental vectors of the reciprocal lattice. In the special case of p_k, h_k being whole numbers (positive, negative, or zero); $\mathbf{x}=\mathbf{x}_p$ and $\mathbf{b}=\mathbf{b}_h$ represent the positions of the lattice points in the two spaces, respectively. Now, since

$$(\mathbf{x}\cdot\mathbf{b})=p_1h_1+p_2h_2+p_3h_3=(\mathbf{p}.\mathbf{h}), \quad (14)$$

one can define p_k, h_k as orthogonal components of the dimensionless vectors $\mathbf{p}$ and $\mathbf{h}$. Every type of crystal is thus transformed in $\mathbf{p}$ space as a cubic crystal with $v_r=1$.

In the following section the above-discussed general conclusions of the interference theory of ideal paracrystals will be applied to the special problem of face-centered cubic crystals with deformation faults treated by Paterson.

Paterson[1] considers an infinitely large face-centered cubic lattice in the direction normal to the faulting plane (111). The vectors $\mathbf{a}_x$, $\mathbf{a}_y$, $\mathbf{a}_z$ drawn from the atom 0 and ending in the atoms X, Y, Z lying on the plane (111) build up the unit cell of this cubic face-centered lattice (see Fig. 1). The atoms A, B, C having the coordinates $(\mathbf{a}_x+\mathbf{a}_y)$, $(\mathbf{a}_y+\mathbf{a}_z)$, $(\mathbf{a}_z+\mathbf{a}_x)$ lie on the next

[13] $1/v_r$ denotes an index and not a power of Z (see reference 14) where

$$\int_{\text{lattice cell}} Z^{1/v_r}dv_r=1/v_r$$

and dv_r is the volume element in Fourier space.

[14] P. P. Ewald, Proc. Phys. Soc. (London) **52**, 167 (1940).

[15] The amorphous case is also given by crystalline substances, e.g., polydisperse colloidal substances, specially in the region of small-angle scattering [see Hosemann (reference 10)].

[16] R. Hosemann, Acta Cryst. 4, 520 (1951).

[17] Such reflections are partially crystalline, partially diffuse or partially amorphous and are classified as crystalline-diffuse, crystalline-amorphous, diffuse-amorphous, or crystalline-diffuse-amorphous reflections.

[18] Integral width in the direction $\mathbf{h}_k=\mathbf{h}_1$ is defined by

$$\Delta\mathbf{h}_1=\frac{I(\mathbf{h}_1\mathbf{h}_{2m}\mathbf{h}_{3m})d\mathbf{h}_1}{I(\mathbf{h}_{1m}\mathbf{h}_{2m}\mathbf{h}_{3m})} \quad (11a)$$

where $\mathbf{h}_{km}$ represent the coordinates of the reflection maximum in $\mathbf{h}$ space.

[19] R. Hosemann, Zur struktur und Materie der Festköper (Springer, Berlin, 1951).

[20] A. Padurow, Acta Cryst. 3, 200 (1950).

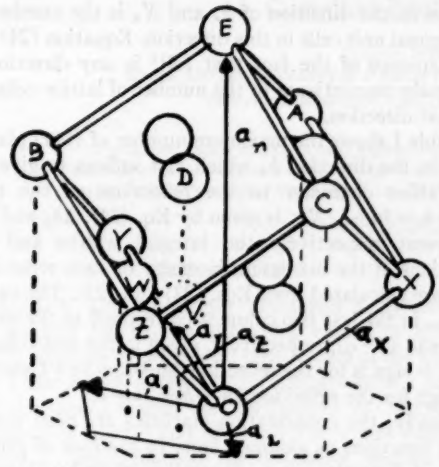

FIG. 1. A cubic face-centered lattice cell with the corner atoms O,X,Y,Z,A,B,C,E. $\mathbf{a}_1$, $\mathbf{a}_2$, and $\mathbf{a}_n$ are the fundamental vectors of a three-fold primitive hexagonal lattice cell. W and D denote the atoms within the cell. The atom W may be displaced to the site V due to deformation faults.

higher (111) plane. Two atoms on the lower (111) plane, i.e., the (111) plane passing through the origin 0, adjacent to the atom 0 lie at

$$\mathbf{a}_1=\tfrac{1}{2}(-\mathbf{a}_x+\mathbf{a}_y) \tag{15}$$

and

$$\mathbf{a}_2=\tfrac{1}{2}(-\mathbf{a}_y+\mathbf{a}_z).$$

The atom W lies at $\frac{1}{2}(\mathbf{a}_y+\mathbf{a}_z)$ and the atom D at $\frac{1}{2}(\mathbf{a}_x+\mathbf{a}_y+2\mathbf{a}_z)$. For convenience an hexagonal three-fold primitive cell is chosen with vectors $\mathbf{a}_1$, $\mathbf{a}_2$ including an angle $2\pi/3$ in the plane (111) passing through the origin 0, and the vector

$$\mathbf{a}_n=\mathbf{a}_x+\mathbf{a}_y+\mathbf{a}_z \tag{15a}$$

normal to this plane. The affine coordinates of the 3 atoms in terms of the hexagonal lattice cell are

$$\left.\begin{array}{lll} P_0 & (000) & \text{for the atom } 0 \\ P_W & (\frac{2}{3}\frac{1}{3}\frac{1}{3}) & \text{for the atom } W \\ P_D & (\frac{1}{3}\frac{2}{3}\frac{2}{3}) & \text{for the atom } D \end{array}\right\}. \tag{15b}$$

In plastic deformation Paterson assumes that the (111) planes remain parallel to one another throughout the crystal, only they are shifted not regularly but randomly against one another in such a way that the atoms always find their places in the hollows of adjacent sheets. For example, if the lower sheet with the atom 0 is kept fixed, the atom W may be shifted to the position $P_V=(\frac{1}{3}\frac{2}{3}\frac{1}{3})$ with a probability $1-\alpha\leq 1$ and the sheets, e.g., the (111) plane passing through the atom W, which remain undeformed are as a whole displaced accordingly. α is the probability that the atom W possesses the coordinate $(\frac{2}{3}\frac{1}{3}\frac{1}{3})$.

In the language of ideal paracrystals the coordination statistics are given by

$$\begin{aligned} H_1(\mathbf{x})&=P(\mathbf{x}-\mathbf{a}_1), \\ H_2(\mathbf{x})&=P(\mathbf{x}-\mathbf{a}_2), \\ H_3(\mathbf{x})&=\alpha P(\mathbf{x}-\mathbf{a}_W)+(1-\alpha)P(\mathbf{x}-\mathbf{a}_V) \end{aligned} \tag{16}$$

$$\mathbf{a}_W=\tfrac{2}{3}\mathbf{a}_1+\tfrac{1}{3}\mathbf{a}_2+\tfrac{1}{3}\mathbf{a}_n; \quad \mathbf{a}_V=\tfrac{1}{3}\mathbf{a}_1+\tfrac{2}{3}\mathbf{a}_2+\tfrac{1}{3}\mathbf{a}_n. \tag{16a}$$

The lattice cell built up by the 3 fundamental vectors $\mathbf{a}_1$, $\mathbf{a}_2$, $\mathbf{a}_W$ (or $\mathbf{a}_V$) of the coordination statistics (16) is contrary to the lattice cell built up by the vectors $\mathbf{a}_1$, $\mathbf{a}_2$, $\mathbf{a}_n$ given in Eqs. (15) and (15a), simple primitive and triclinic.

For infinitely large crystals described by Paterson the shape amplitudes are peak functions. Hence the reflections are characterized by Eqs. 3(c) and (d) and the character and distribution of the reflections are determined by the function $Z^{1/\nu r}$. Equation (6) shows that this function is dependent on the values of the statistical amplitudes F_k. Now,

$$\begin{aligned} F_1=\mathfrak{F}(H_1)&=\int P(x-a_1)\exp[-2\pi i(\mathbf{b}\cdot x)]dv_x \\ &=\exp[-2\pi i(\mathbf{b}\cdot\mathbf{a}_1)]\int P(x-a_1)dv_x \\ &=\exp[-2\pi i(\mathbf{b}\cdot\mathbf{a}_1)], \\ F_2=\mathfrak{F}(H_2)&=\exp[-2\pi i(\mathbf{b}\cdot\mathbf{a}_2)], \\ F_3=\mathfrak{F}(H_3)&=\alpha\exp[-2\pi i(\mathbf{b}\cdot\mathbf{a}_W)]+(1-\alpha) \\ &\quad\times\exp[-2\pi i(\mathbf{b}\cdot\mathbf{a}_V)]. \end{aligned} \tag{17}$$

In hexagonal affine coordinates $\mathbf{h}$, i.e., h_1, h_2, h_n,

$$F_3=[\alpha e^{-\frac{1}{3}\pi i(2h_1+h_2)}+(1-\alpha)e^{\frac{1}{3}\pi i(2h_1+h_2)}]e^{-\frac{1}{3}\pi i h_n}. \tag{17a}$$

Hence,

$$F_3F_3^*=\begin{cases} 1 & \text{for } 2h_1+h_2=3n \\ 1-3\alpha(1-\alpha) & \text{for } 2h_1+h_2=3n\pm 1, \end{cases} \tag{18}$$

where n is a whole number. Further,

$$\mathrm{Re}F_3=\begin{cases} \cos(\frac{2}{3}\pi h_n) & \text{for } 2h_1+h_2=3n \\ \alpha\cos[\frac{2}{3}\pi(h_n\pm 1)]+(1-\alpha)\cos[\frac{2}{3}\pi(h_n\pm 1)], & \\ \qquad\text{for } 2h_1+h_2=3n\pm 1. & \end{cases} \tag{19}$$

The last equation can be rewritten in the form

$$\begin{aligned} \mathrm{Re}F_3&=-\tfrac{1}{2}\cos(\tfrac{2}{3}\pi h_n)\pm(\tfrac{1}{2}-\alpha)\sqrt{3}\sin(\tfrac{2}{3}\pi h_n) \\ &=-[1-3\alpha(1-\alpha)]^{\frac{1}{2}}\cos(\tfrac{2}{3}\pi h_n\pm\varphi), \end{aligned}$$

where

$$\varphi=\arctan(\sqrt{3}(1-2\alpha)). \tag{20}$$

Hence, for $2h_1+h_2=3n\pm 1$, it follows from Eq. (6) that,

$$\mathrm{Re}\frac{1+F_3}{1-F_3}=\frac{3\alpha(1-\alpha)}{2-3\alpha(1-\alpha)+2[1-3\alpha(1-\alpha)]^{\frac{1}{2}}\cos(\frac{2}{3}\pi h_n\pm\varphi)}. \tag{21}$$

TABLE I. Relation between the degree of disorder α, the positions h_{nm} of reflection maxima, the integral widths Δh_n of reflections (for infinitely large crystals), and the maximum numbers of (111) planes N_{3m} necessary to show at least one crystalline reflection.

α(or $1-\alpha$)	Δh_n	N_{3m}	h_{nm}	
0	0	∞	$3m\pm1$	$3m\pm0.5$
0.01	0.023	132	$3m\pm1.004$	$3m\pm0.496$
0.02	0.046	66	$3m\pm1.008$	$3m\pm0.488$
0.05	0.118	25	$3m\pm1.022$	$3m\pm0.478$
0.10	0.234	13	$3m\pm1.048$	$3m\pm0.384$
0.50	1.000	3	$3m\pm1.500$	$3m\pm0.000$

Equation (21) multiplied by the factor

$$N\langle f\rangle_{hr}^2 \operatorname{Re}\frac{1+F_1}{1-F_1}\operatorname{Re}\frac{1+F_2}{1+F_2},$$

gives the intensity distribution of infinitely large crystals.

Equations (11), (17), (18), and (19) show that the integral width of all reflections except of those given by $2h_1+h_2=3n\pm1$ are vanishingly small. (Widths of crystalline reflections are inversely proportional to the number of lattice cells in the particular direction.) For reflections $2h_1+h_2=3n\pm1$, the integral widths in the directions h_1 and h_2 are also vanishingly small but in the direction h_n, it is given by [see Eq. (11)]

$$\Delta h_n=3\frac{1-[1-3\alpha(1-\alpha)]^{\frac{1}{2}}}{1+[(1-3\alpha(1-\alpha))]^{\frac{1}{2}}}. \tag{22}$$

The factor 3 comes in because the lattice cell described by $\mathbf{a}_1$, $\mathbf{a}_2$, $\mathbf{a}_n$ is 3 times as large as that described by $\mathbf{a}_1$, $\mathbf{a}_2$, $\mathbf{a}_W$ or $\mathbf{a}_V$. The position of the maximum of the diffuse reflection, h_{nm}, in the direction of h_n is given by [see Eq. (21)]:

$$\tfrac{1}{3}h_{nm}\pm\varphi/2\pi+\tfrac{1}{2}=m, \tag{23}$$

(m being a whole number). Equations (21), (22), and (23) are identical with Eqs. (7), (9), and (8), respectively of Paterson.[1] As indicated in the next section, the interference theory of ideal paracrystals offers further information regarding the diffraction effects.

The size of the crystal determines the distribution of scattered intensity only when the shape factor $|S|^2$ is much broader than the hump of the $Z^{1/\sigma r}$ function. Reflections of the type $2h_1+h_2=3n$ are always crystalline. Their integral widths are inversely proportional to the number of lattice cells and they are, in general, characterized by the Eq. (3a). Reflections of the type $2h_1+h_2=3n\pm1$ are always crystalline in the direction h_1 and h_2, but in the direction h_n it is crystalline as long as

$$N_3<\frac{3}{\Delta h_n}; \tag{24}$$

otherwise it is diffuse. $N_3(=3N_n)$ is the number of (111) planes in the direction of h_n and N_n is the number of hexagonal unit cells in this direction. Equation (24) is a consequence of the fact that $|S|^2$ in any direction is inversely proportional to the number of lattice cells N_n in that direction.

Table I shows the maximum number of (111) planes, N_{3m} in the direction h_n which just suffices to give the crystalline character to the reflections of the type $2h_1+h_2=3n\pm1$. N_{3m} is given by Eq. (24). Δh_n and h_{nm} represent respectively the integral widths and the positions of the maximum intensity of such reflections and are calculated from Eqs. (22) and (23). The values of h_{nm} in the last two columns correspond to the values of α and $(1-\alpha)$, respectively, given in the first column. The + sign is for the reflection $2h_1+h_2=3n+1$ and the − sign for the reflection $2h_1+h_2=3n-1$.

Finally, the coordination statistics H_k need not be peak functions as assumed here. In the case of general type of distortions, e.g., distortions given by Gaussian functions, the magnitude of F_k, the Fourier transform of H_k, is always less than unity except for $\mathbf{b}=0$ where it has the value of unity:

$$0\leq|F_k|<1. \tag{25}$$

Now, Eq. (11) shows that for all reflections [except the (000) reflection] $\Delta h_k\neq0$. Hence all reflections [except the (000) reflection which is always crystalline] of infinitely large crystals would be always diffuse in all the three directions. For bounded crystals they would be entirely crystalline or partially crystalline in a particular direction when [see Eq. (24)]

$$N_k<1/\Delta h_k. \tag{26}$$

N_k is the number of lattice cells in the direction h_k. Outside the range of validity of Eq. (26) the reflections would be characterized mainly by the nature of the $Z^{1/\sigma r}$ function. As already mentioned, the (000) reflection is always crystalline and its integral width gives the size of the crystal. The reflections would be more and more diffuse with increasing $|b_k|$; ultimately they would cease to appear and would merge into the background. It would be erroneous to estimate the size of the crystallite from such diffuse reflections since the widths of such reflections are characterized not by the shape factor $|S|^2$ but by the corresponding hump of the $Z^{1/\sigma r}$ function [see Eq. (3b–d)]. Moreover, there will always be a definite background scattering determined by this $Z^{1/\sigma r}$ function even if the crystal is perfectly homogeneous and without holes. Here $I_1=0$ and the background is entirely given by the component I_2. In the case of mixed crystals or in the case of existence of holes, the background scattering is determined both by the functions I_1 and I_2 [see Eqs. (3)–(5)]. In fact, I_2 is never zero, since there is always a diffuse background due to thermal motion of scattering centers.

A Complete Bacher and Goudsmit Method

SYDNEY MESHKOV AND C. W. UFFORD
Randal Morgan Laboratory of Physics, University of Pennsylvania, Philadelphia, Pennsylvania
(Received October 23, 1953; revised manuscript received November 9, 1953)

A complete Bacher and Goudsmit method for the calculation of atomic energy states in terms of the experimentally observed energies of ions of higher ionization is developed. The method has been extended to include configurations containing electrons of any angular momentum. A term in d^4 is calculated as an example.

I. INTRODUCTION

BACHER and Goudsmit[1] developed a theoretical method for finding the term values in atomic spectra from the experimental term values of the higher ions. Their results applied to configurations of s and p electrons only. Using the coefficients of fractional parentage of Racah[2] and Meshkov,[3] it is now possible to give a direct method for obtaining Bacher and Goudsmit's results and to extend these results to configurations containing electrons of higher angular momentum than $l=1$.

II. CONFIGURATION CONTRIBUTIONS TO TOTAL ENERGY

A term in a given configuration is expressed as a linear combination of the terms of the configurations of the ions on which it is built. Our problem is to find the coefficients of this linear combination. First, we remove one electron from the original configuration and obtain the configurations of the next higher ion. The contribution of each of these configurations is proportional to the number of ways of forming it from the original configuration. If the original configuration has only equivalent electrons, then we get only one ion configuration; the number of ways of forming this higher ion configuration is $\binom{n}{n-1}=n$. If the original configuration is of the form $l^{n-1}l'$, then there are $\binom{n-1}{n-2}=n-1$ ways of forming the configuration, $l^{n-2}l'$, and there is but one way to form the configuration l^{n-1}. Again, we obtain $\binom{n}{n-1}=n$ ways of forming configurations of the ion. In general, for any configuration of n electrons, there are n ways of choosing configurations, and the sum of the coefficients of the terms of any configuration will be equal to the number of times this configuration occurs.

Each higher ion is broken up into its higher ions in a similar way. The number of ways of obtaining configurations for the ion with $n-2$ electrons is $\binom{n}{n-2}$, and the coefficient of each configuration is equal to the number of times the configuration occurs. This process is continued until the ion consists of a single electron outside closed shells. In general, there are $\binom{n}{r}$ ways of choosing configurations of r electrons, and the coefficient of each configuration will be equal to the number of times this configuration occurs. The energies contributed by the different stages of ionization are in the ratio of the number of ways of obtaining configurations for each ion, i.e., in the ratio

$$\binom{n}{n-1}:\binom{n}{n-2}:\cdots:\binom{n}{r}:\cdots:n.$$

When the configurations of each successive ion are added to obtain the total energy of the term of the original configuration, each ion occurs with alternating signs. The alternation happens because it is necessary to transpose terms to obtain the energy in terms of the observed values of the energies of the successive ions, as was done in (15) of Bacher and Goudsmit.

As an example of the procedure so far, consider a d^4 configuration. The energy of a term may be written in terms of the experimentally observed energies of d^3, d^2, and d. The $d^3:d^2:d$ energy ratios are determined by the coefficients of the binomial expansion. There are four ways to group four electrons, three at a time; six, to group four electrons, two at a time; and four, to group four electrons, one at a time. Therefore, we write in the approximation used by Bacher and Goudsmit

$$W(d^4)=4W(d^3)-6W(d^2)+4W(d). \quad (1)$$

Similarly, for five electrons,

$$W(d^5)=5W(d^4)-10W(d^3)+10W(d^2)-5W(d). \quad (2)$$

III. INDIVIDUAL TERM CONTRIBUTIONS TO TOTAL ENERGY

Having obtained the contributions of the electron configurations of all the ions to the energy, the next step is to express the energy of each configuration as a linear combination of the observed energies of its terms. The coefficients of this linear combination are obtained by using coefficients of fractional parentage together with (16) of M-I. We denote by $1R$ the energy of the term we are computing as given by (16) of M-I.

[1] R. F. Bacher and S. Goudsmit, Phys. Rev. **46**, 948 (1934).
[2] G. Racah, Phys. Rev. **63**, 367 (1943), referred to as R-III.
[3] S. Meshkov, Phys. Rev. **91**, 871 (1953), referred to as M-I. The fractional parentage coefficients are normalized such that the sum of the squares of all the coefficients in any row of a table equals one.

We must find how many R's of energy there are in each stage of ionization.

In the first stage of ionization, we found that the sum of the coefficients of the terms of the configurations with $n-1$ electrons is n. The energy of n electrons is made up of the sum of the energies of $\binom{n}{n-2}=n(n-1)/2$ electron pairs. The energy of $n-1$ electrons is made up of the sum of the energies of $\binom{n-1}{n-3}=(n-1)(n-2)/2$ electron pairs. The energy of n electrons is thus $n/(n-2)$ times the energy of $n-1$ electrons. Therefore, in one R of energy the sum of the coefficients of the terms of the $n-1$ configuration is $n/(n-2)$. We now require x R's of energy to obtain n, the sum of the coefficients of the terms of the $n-1$ configuration. Therefore,

$$xn/(n-2)=n, \tag{3}$$

and

$$x=n-2. \tag{4}$$

In all our discussion, except in special examples, we assume we are considering n electrons, with no specification of equivalence or nonequivalence.

For the second stage of ionization, we require y R's to yield $n(n-1)/2$ terms. To find y, the number of R's, which, when converted to the energies of $n-2$ electrons, are subtracted, we change the energy of n electrons to the energy of $n-1$ electrons and finally to the energy of $n-2$ electrons. To express an n electron energy in terms of the $n-2$ electron energies, we write

$$y\binom{n}{n-2}\binom{n-1}{n-3}=\frac{n(n-1)}{2}, \tag{5}$$

where $n/(n-2)$ is obtained in going from n to $n-1$ electrons and $(n-1)/(n-3)$ is obtained in going from $n-1$ to $n-2$ electrons. Therefore,

$$y=(n-2)(n-3)/2. \tag{6}$$

In general, the number of R's to be added or subtracted is given by $\binom{n-2}{r-2}$, where r is the number of n electrons considered at a time.

For example, in the d^4 configuration, we first find how many R's of energy, expressing d^4 in terms of d^3, we must have. From (1) there are four d^3 energies. From (4), $x=n-2=2$ for $n=4$. Therefore, we must have two R's of d^4 energy expressed in terms of d^3 energies.

To find the number of R's, which, when converted to d^2 energies, are subtracted, we change d^4 energies to d^3 energies and finally to d^2 energies. From (6),

$$y=(n-2)(n-3)/2 \\ =1 \text{ for } n=4. \tag{7}$$

Therefore, one R of d^4 energy expressed in terms of d^2 energy must be subtracted. The final result is

$$W(d^4)=2R(d^3)-R(d^2)+4d. \tag{8}$$

IV. ENERGY OF $(d^4\ {}^1I)$

A specific illustration of the general Bacher and Goudsmit method is the calculation of the term energy $W(d^4\ {}^1I)$. From (8), we need two R's of energy expressed in terms of d^3 energies. Using Tables II and III of R-III and (16) of M-I we get

$$2R(d^3;d^4\ {}^1I)=2\cdot 2\cdot[(3/10)W(d^3\ {}^2G) \\ +(7/10)W(d^3\ {}^2H)] \\ =(6/5)W(d^3\ {}^2G)+(14/5)W(d^3\ {}^2H). \tag{9}$$

To obtain $1R(d^2;d^4\ {}^1I)$, we first take $1R(d^3;d^4\ {}^1I)$ from (9) and transform each d^3 energy into d^2 energies

$$W(d^3\ {}^2G)=(3/42)[10W(d^2\ {}^1D)+21W(d^2\ {}^3F) \\ +11W(d^2\ {}^1G)], \tag{10}$$

$$W(d^3\ {}^2H)=(3/2)[W(d^2\ {}^3F)+W(d^2\ {}^1G)]. \tag{11}$$

Substituting (10) and (11) into $R(d^3;d^4\ {}^1I)$ which is obtained in (9), we find

$$1R(d^2;d^4\ {}^1I)=(3/7)W(d^2\ {}^1D)+3W(d^2\ {}^3F) \\ +(18/7)W(d^2\ {}^1G). \tag{12}$$

Substituting (9) and (12) into (8), we find

$$W(d^4\ {}^1I)=(6/5)W(d^3\ {}^2G)+(14/5)W(d^3\ {}^2H) \\ -(3/7)W(d^2\ {}^1D)-3W(d^2\ {}^3F) \\ -(18/7)W(d^2\ {}^1G)+4W(d\ {}^2D). \tag{13}$$

Although we have illustrated the method for configurations of equivalent electrons, configurations of nonequivalent electrons can be treated in similar fashion.

V. COMMENTS

When terms of the same kind appear, the method gives the elements of the energy matrix rather than the term values themselves. It is therefore necessary to devise a scheme to calculate the values of the matrix elements in terms of the observed energies. A possible method for the calculation of these matrix elements has been applied to the d^3 and d^4 configurations of vanadium.[4]

One drawback to calculating absolute energies by the Bacher and Goudsmit method is the lack of precise experimental values for the ionization potentials of many atoms. However, the method will give the separations of the terms of the same ions, since the separations are independent of ionization potentials.

Some of these ideas have been developed independently by Trees.[5]

[4] S. Meshkov, Phys. Rev. 93, 270 (1954).
[5] R. E. Trees (private communication).

Application of the Rayleigh-Schrödinger Perturbation Theory to the Hydrogen Atom

EUGENE P. WIGNER
Palmer Physical Laboratory, Princeton University, Princeton, New Jersey
(Received November 27, 1953)

The motion of a single electron in the electrostatic field of a nucleus is treated by the Rayleigh-Schrödinger perturbation method, the whole electrostatic potential being considered as the "perturbation." The contribution of the first approximation to the energy vanishes. The second approximation gives a finite ionization energy which is, however, incorrect numerically. The first approximation also vanishes for potentials $\sim r^{-n}$ with $0<n<3$ but the second approximation is finite only for $n=1$: it vanishes for $n>1$, and is infinite for $n<1$.

THERE are several instances in which simple approximation methods yield correct results even though the conditions for the applicability of those methods are not fulfilled. The best known example is the calculation of the Rutherford scattering by Born's approximation.[1] The calculation of the interaction of a large number of particles[2] by the Rayleigh-Schrödinger method is another example. In all these cases, the wave function given by the approximation method is quite meaningless. Thus, in the case of the interaction of many particles, the wave function obtained by the Rayleigh-Schrödinger perturbation calculation's second approximation represents a state in which, at most, two particles are in excited states while, actually, the average number of particles in excited states is, if the number of particles is large, a constant fraction of the number of particles. Nevertheless, the energy given by the second approximation of the Rayleigh-Schrödinger theory appears to be meaningful. One may gain the impression, from these examples, that the second approximation is always correct if it gives a finite result and that this applies particularly to the electrostatic interaction.

It may be of some interest to note, in this connection, that the aforementioned perturbation method yields, in second approximation, a finite result if applied to the problem of an electron moving in the attractive field of a nucleus. In fact, among all the potentials cr^{-n}, this applies only in the case of $n=1$. The starting point, in every case, is a free electron moving in a very large "box." Nevertheless, the numerical result of the perturbation calculation gives a grossly inaccurate result for the Coulomb potential. The wave function is not only inaccurate but virtually meaningless, but this fact does not entail an inaccurate energy value in the cases discussed in the first paragraph.

As the starting point we choose a spherical "box" with a radius R. The unperturbed spherically symmetric wave functions are, then,

$$\psi_n=(\sin\alpha_n r)/C_n r, \tag{1}$$

with the normalization constant C_n being equal to

$$C_n^2=(2\pi/\alpha_n)(\alpha_n R-\sin\alpha_n R\cos\alpha_n R). \tag{1a}$$

The α_n are determined by the boundary condition to be used at the surface of the box. The first approximation to the energy, because of an e^2/r potential, goes to zero with increasing R because the average distance of the particle from the origin is of the order R in the state ψ_1. The second approximation becomes

$$-E=\sum_2^\infty \frac{\left(\int\psi_1(e^2/r)\psi_n 4\pi r^2 dr\right)^2}{(\hbar^2/2m)(\alpha_n^2-\alpha_1^2)}. \tag{2}$$

The denominator contains the energy difference between the states ψ_n and ψ_1. Inserting (1) into (2),

$$-E=\sum_2^\infty \frac{32\pi^2e^4m}{C_1^2C_2^2(\alpha_n^2-\alpha_1^2)\hbar^2}\left(\int_0^R \sin\alpha_1 r\sin\alpha_n r dr/r\right)^2$$

$$=\sum_2^\infty \frac{8\pi^2e^4m}{C_1^2C_2^2(\alpha_n^2-\alpha_1^2)\hbar^2}\left(\int_0^R [\cos(\alpha_n-\alpha_1)r - \cos(\alpha_n+\alpha_1)r]dr/r\right)^2. \tag{2a}$$

The integrals can be transformed by substituting $x=(\alpha_n-\alpha_1)r$ and $x=(\alpha_n+\alpha_1)r$, respectively.

$$-E=\sum_2^\infty \frac{8\pi^2e^4m}{C_1^2C_2^2(\alpha_n^2-\alpha_1^2)\hbar^2} \times\left(\int_{(\alpha_n-\alpha_1)R}^{(\alpha_n+\alpha_1)R}(\cos x-1)\frac{dx}{x}\right)^2. \tag{2b}$$

In order to define the unperturbed system completely, one has to give the value of the logarithmic derivative of the unperturbed wave functions (1) for $r=R$. We set $\rho\psi'(R)=\psi(R)$, which gives

$$\cot\alpha_n R=\frac{1}{\alpha_n\rho}+\frac{1}{\alpha_n R}. \tag{3}$$

This equation determines the values of α_n. We have two cases to distinguish: ρ is either infinite or finite. In the latter case, we assume that ρ remains the same as we increase the size of the "box," i.e., increase R to

[1] See G. Wentzel, *Geiger-Scheel's Handbuch der Physik* (Springer, Berlin, 1933), Vol. 24, Part 1, p. 703.
[2] S. Watanabe, Z. Physik **112**, 159 (1939); **113**, 482 (1939); W. Macke, Z. Naturforsch. **A5**, 192 (1950).

infinity. If this is the case, $\alpha_n R \to n\pi$ as $R \to \infty$, no matter what the value of ρ is. In other words, the value of the expression (2b) converges to the same value as $R \to \infty$, no matter what the value of ρ is as long as ρ remains finite as $R \to \infty$. In this case, then, $C^2 = 2\pi R$, and

$$-E = \sum_2^\infty \frac{2e^4m}{R^2(\alpha_n^2-\alpha_1^2)\hbar^2}\left(\int_{(n-1)\pi}^{(n+1)\pi}(1-\cos x)\frac{dx}{x}\right)^2$$

$$= \sum_2^\infty \frac{2e^4m}{\pi^2\hbar^2(n^2-1)}(\mathrm{Ci}(n+1)\pi - \mathrm{Ci}(n-1)\pi)^2, \qquad (4)$$

where Ci is the cosine integral

$$\mathrm{Ci}x = \int_0^x \frac{\cos x - 1}{x}dx. \qquad (4a)$$

As we anticipated, the second approximation (2) gives a finite value in this case. The sum (4) was evaluated numerically and gave

$$-E = 0.1093e^4m/\hbar^2, \qquad (5)$$

as contrasted with the correct value of $0.5\ e^4m/\hbar^2$. As a matter of fact, it is not surprising that the value (5) is so far from being correct. Although the first approximation correction to the nth characteristic value of the problem,

$$-\int_0^R \psi_n^2(e^2/r)4\pi r^2 dr = \frac{e^2}{R}\,\mathrm{Ci}(2n\pi), \qquad (6)$$

vanishes for very large R, it vanishes only as $1/R$. Furthermore, it increases with n roughly like $\gamma + \ln 2\pi n$. The unperturbed energy differences, on the other hand, go to zero as R^{-2}. Hence, in first approximation, the energy of ψ_2 is actually lower than that of ψ_1 if R is large enough, and the same holds for a large number of other ψ_n. This reversal of the order of the first-order energy values shows again that the perturbation calculation cannot be given a direct physical interpretation in this case.

It remains to be seen whether the other boundary condition, $\psi'(R) = 0$, gives more satisfactory results. In this case ψ_1 is a constant,

$$\psi_1 = (3/4\pi R^3)^{\frac{1}{2}}, \qquad (7)$$

while the other ψ are still given by (1). The equation defining α_n becomes

$$\alpha_n R = \tan\alpha_n R; \quad \alpha_1 = 0. \qquad (8)$$

Denoting the solutions of this equation with $q_n = \alpha_n R = \tan q_n$, the integral

$$\int_0^R \psi_1(e^2/r)\psi_n 4\pi r^2 dr = 6^{\frac{1}{2}}\frac{e^2}{R}\frac{(1+q_n^2)^{\frac{1}{2}}+(-)^n}{q_n^2} \qquad (9)$$

can be expressed in closed form. For the ionization energy $-E$ one obtains

$$-E = \frac{12e^4m}{\hbar^2}\sum_2^\infty \frac{[(1+q_n^2)^{\frac{1}{2}}+(-)^n]^2}{q_n^6} \sim 0.05\frac{e^4m}{\hbar^2}, \qquad (10)$$

i.e., a substantially smaller value than (5).

The reason it was at all possible to expect that the Rayleigh-Schrödinger perturbation method yield a correct expression for the energy is that this approximation method gives a power series expansion for the energy in terms of the perturbation parameter. A power series expansion in terms of the perturbation parameter $\lambda = e^2$ in fact does exist for the energy values of a particle in a Coulomb field: the coefficients of all powers of λ are zero, excepting that of the second power which is $m/2\hbar^2$ for the normal state. The reason that the perturbation method nevertheless gives an incorrect value in second approximation is that the energy is a function of the size R of the "box" which underlies the perturbation calculation. This function could well be of a form similar to

$$(e^4m/2\hbar^2)[1 - c\exp(-me^2R/\hbar^2)].$$

This expression gives the correct energy value for $R = \infty$ and has a convergent power series expansion in terms of e^2. However, this power series expansion does not converge term by term to the power series expansion of the energy for $R = \infty$ and, in particular, the coefficient of the e^4 term is too small by a factor $1-c$.

The fact that the Rayleigh-Schrödinger second approximation gives a definite value for the potential λ/r, but for no other potential of the form λr^{-n}, can be seen already by means of a dimensional argument. The dimension of λ is [energy][length]^n. Since the dimension of the matrix elements of the perturbation energy have the dimension of energy, they are proportional to R^{-n}. The square of the matrix element, divided by a typical difference of the unperturbed energy $\hbar^2/2mR^2$, is therefore proportional to R^{2-2n}. This gives a definite value only for $n = 1$ but tends to infinity as R increases for $n < 1$. It tends to zero if $n > 1$.

The square integral of the first approximation to the wave function tends to infinity with increasing R for all $n < 2$. In order to calculate it we have to divide the square of the matrix element with the square of a quantity of the order $\hbar^2/2mR^2$. Hence, the square integral will be proportional to R^{4-2n} and increase beyond all bounds also in the case of the Coulomb potential $n = 1$. In fact, the first order wave function in our case is closely approximated by ψ_2 multiplied with a very large factor and is almost as poor an approximation to the real wave function as the unperturbed wave function ψ_1. The second approximation to the energy can be finite because it is not the expectation value of the first order wave function.

Mean Excitation Potentials*

DAVID O. CALDWELL† AND J. REGINALD RICHARDSON
Department of Physics, University of California, Los Angles, California

(Received May 11, 1953)

Previous experimental data of Sachs and Richardson on the most probable energy loss of 18-Mev protons on passing through thin foils have been used in connection with the theory of Symon to calculate the mean excitation potential I. The result for aluminum is $I=164\pm3$ electron volts.

IN the work of Sachs and Richardson[1] on the energy loss of 18-Mev protons in passing through thin foils of various materials, the quantity measured by their apparatus was the most probable energy loss. When calculating the mean excitation potentials they assumed that the most probable energy loss and the mean energy loss were the same for their measurements within their expected error. It has recently become possible, however, to evaluate I directly from the most probable energy loss as the result of the work of K. R. Symon quoted by Rossi.[2]

The values of the physical constants used in the calculations are those of DuMond and Cohen.[3] Values of C_k were obtained from the work of Walske,[4] and the atomic weights were obtained from the 1952 Revision of International Atomic Weights.

Table I presents the results of these calculations for the case of aluminum. The difference between the most probably energy loss and the mean energy loss is seen to vary with the foil thickness in the expected way, namely from 2.6 percent for the thinnest foil to 0.23 percent for the thickest foil. The weighted average of these results is $I_{Al}=164\pm3$ electron volts[5] compared to 168 ev from the previous approximate calculations.

Similar calculations were carried through for the experimental results on other materials as shown in Table II. No corrections for nonparticipating electrons are available (to our knowledge) for these materials. Such corrections would tend to lower the values of the mean excitation potentials.

TABLE I. Mean excitation potential of aluminum.

Surface density (mg/cm²)	Most probable energy loss (Mev)	Mean energy loss (Mev)	Mean excitation potential (ev) (with probable error)
7.153	0.153	0.157	156.2±18.8
14.054	0.301	0.305	169.0±12.7
21.432	0.465	0.469	164.7± 8.2
21.532	0.470	0.474	159.6± 9.1
33.875	0.737	0.741	170.7± 6.8
38.395	0.839	0.843	169.4± 4.9
47.457	1.048	1.052	165.1± 8.1
57.493	1.276	1.280	165.8± 5.8
67.294	1.515	1.519	158.6± 5.3
76.849	1.737	1.741	159.9± 4.0

TABLE II. Weighted averages of the mean excitation potentials (uncorrected for nonparticipating electrons).

Element	Weighted average uncorrected mean excitation potential (ev)
Ni	398
Cu	419
Rh	778
Ag	760
Cd	753
Sn	818
Ta	1100
Au	1306

* This work was supported in part by the joint program of the U. S. Office of Naval Research and the U. S. Atomic Energy Commission.

† Fellow, National Science Foundation.

[1] D. C. Sachs and J. R. Richardson, Phys. Rev. **83**, 839 (1951) and **89**, 1163 (1953).

[2] B. Rossi, *High Energy Particles* (Prentice Hall Publishing Company, Inc., New York, 1952).

[3] J. W. M. DuMond and E. R. Cohen, American Scientist **40**, 447 (1952).

[4] M. C. Walske, Phys. Rev. **88**, 1283 (1952).

[5] *Note added in proof.*—The measurement of the range of 18-Mev protons in Al reported by E. L. Hubbard and K. R. MacKenzie in Phys. Rev. **85**, 107 (1952), when corrected for multiple scattering, yields a value of $I_{Al}=165$ from the more accurate relation given by D. H. Simmons in Proc. Phys. Soc. (London) **A65**, 454 (1952).

The $Mg^{24}(\gamma,3p3n)F^{18}$ Reaction Induced by 70-Mev Bremsstrahlung*

FRITZ D. SCHUPP AND DON S. MARTIN, JR.
Institute for Atomic Research and Department of Chemistry, Iowa State College, Ames, Iowa

(Received November 19, 1953)

F^{18} was identified among the products of an irradiation of Mg by 70-Mev bremsstrahlung by means of its chemical and radioactive properties. Considering the F^{18} to be formed solely by the loss of six nucleons from Mg^{24}, the yield of the process $Mg^{24}+\gamma\rightarrow F^{18}$ was 0.042 on the basis of unity for $N^{14}+\gamma\rightarrow N^{13}+n$. Preliminary experiments have indicated that 70-Mev bremsstrahlung gives the processes $Ca^{40}+\gamma\rightarrow Cl^{34}$ and $Cl^{35,37}+\gamma\rightarrow Si^{31}$.

MAGNESIUM metal has been irradiated by the 70-Mev bremsstrahlung beam of the Iowa State College synchrotron. After dissolving, the magnesium fraction was precipitated as a basic carbonate in the presence of sodium ion hold-back carrier to remove the 15.1-hr Na^{24} activity. Only one activity, half-life 110–115 min, was detected in the magnesium within the range of 10 min to 15 hr. This activity was concentrated in a fractional precipitation of MgF_2. Subsequently, its identity as the well-known 112-min F^{18} was established by its absorption characteristics and by a chemical procedure in which it followed fluoride carrier through a steam distillation as SiF_4, hydrolysis of the SiF_4, precipitation of a $Zn(OH)_2$ scavenger, and precipitation as PbClF.

To determine the relative yields for this process, a number of targets were irradiated by the 70-Mev bremsstrahlung. In each case the yield of two radioactivities prepared in the same target were compared. Corrections for air, window and cover absorption, sample self-absorption, and self-scattering were applied.[1–3] The experimental yield comparisons are in Table I. The ratios given are averages of 3 to 6 determinations. In Table II relative yields have been expressed on an isotopic basis and relative to the $N^{14}(\gamma,n)N^{13}$ yield following the convention of other workers[4–6] whose values are given for comparison.

TABLE I. Experimental relative yield determinations for 70-Mev bremsstrahlung.

Target	Reactions compared	Yield ratio per target atom
NH_4HF_2	$\frac{F^{19}(\gamma,n)F^{18}-112\text{ min}}{N^{14}(\gamma,n)N^{13}-10\text{ min}}$	2.8
MgF_2	$\frac{Mg(\gamma,-)Na^{24}-15.1\text{ hr}}{F^{19}(\gamma,n)F^{18}}$	0.19
Mg	$\frac{Mg(\gamma,-)F^{18}}{Mg(\gamma,-)Na^{24}}$	0.062
Na_2CO_3	$\frac{Na^{23}(\gamma,2p3n)F^{18}}{C^{12}(\gamma,n)C^{11}-20.5\text{ min}}$	0.092

The upper limit of possible fluoride content of the magnesium metal, which was not detected in a chemical analysis, precludes the possibility of the formation of F^{18} by a (γ,n) reaction of a fluoride impurity. Experiments are planned to determine the activation by this process as a function of the maximum photon energy. The formation of F^{18} by either a $(\gamma,\alpha d)$ process or by a $(\gamma,\alpha 2n)$ process followed by rapid beta decay has a threshold of 36–40 Mev for reasonable Coulomb barriers.

The slightly higher yield value for the $Na^{23}(\gamma,3p2n)F^{18}$ process than that obtained by Holtzman and Sugarman is to be expected for the higher irradiation energies. In these cases our yields have been in satisfactory agreement with those of Perlman and Friedlander rather than the considerably different values presented by Edwards and MacMillan.

Exploratory work has shown activation at 70 Mev for other elements involving the loss of a number of nucleons. An irradiation of Ca has yielded Cl^{33} which requires the loss of at least 6 nucleons. Si^{31}, formed by either $Cl^{35}(\gamma,3pn)$ or $Cl^{35}(\gamma,3p3n)$, has been found in irradiated LiCl.

We are indebted to Dr. D. J. Zaffarano, Dr. A. G. W. Cameron, and the synchrotron group for their assistance and for providing the synchrotron irradiations.

TABLE II. Relative yields of photonuclear processes for 70-Mev bremsstrahlung on the basis $N^{14}(\gamma,n)N^{13}=1$.

Reaction	This work	Relative yields
$F^{19}(\gamma,n)F^{18}$	2.8	2.8(50 Mev),[a] 10.9(70 Mev)[b]
$Mg^{25}(\gamma,p)Na^{24}$	5.3[c]	13.9 or greater (70 Mev)[b]
$Mg^{24}(\gamma,3p3n)F^{18}$	0.042[c]	
$Na^{23}(\gamma,2p3n)F^{18}$	0.22[d]	0.17(50 Mev)[d,e]

[a] See reference 4.
[b] See reference 5.
[c] Assuming all the activity to be formed by this reaction.
[d] Using the $C^{12}(\gamma,n)C^{11}$ value of Perlman and Friedlander (see reference 4).
[e] See reference 6.

* Work was performed in the Ames Laboratory of the U. S. Atomic Energy Commission. This work was described for the Division of Physical and Inorganic Chemistry at the 124th National Meeting of the American Chemical Society in Chicago, Illinois, September 11, 1953.

[1] L. R. Zumwalt, U.S. Atomic Energy Commission Report AECU-567, 1950 (unpublished).
[2] Engelkemeir, Seiler, Steinberg, and Winsberg, *Radiochemical Studies: The Fission Products* (McGraw-Hill Book Company, Inc., New York, 1951), National Nuclear Energy Series, Plutonium Project Record, Vol. 9, Div. IV, pp 56–65.
[3] R. G. Baker and L. Katz, Nucleonics 11, No. 2, 14 (1953).
[4] M. L. Perlman and G. Friedlander, Phys. Rev. 74, 442 (1948).
[5] L. S. Edwards and F. A. MacMillan, Phys. Rev. 87, 377 (1952).
[6] R. B. Holtzman and N. Sugarman, Phys. Rev. 87, 633 (1952).

Elastic Scattering of Protons by Nuclei*

D. M. CHASE AND F. ROHRLICH†
Palmer Physical Laboratory, Princeton University, Princeton, New Jersey

(Received December 9, 1953)

Exact calculations are carried out for the optical model in the 20-Mev region. A complex potential of spherical well shape is assumed in addition to the Coulomb potential. Results for the elastic scattering of protons by Al, Cu, and Ag are compared with experiments. Though all relevant parameters are varied over large domains, no satisfactory agreement is obtained. Various possible alternatives are discussed. It is also shown that the "boundary condition model" offers a good approximation to the optical model within its range of validity.

1. INTRODUCTION

THE optical model for the scattering of mesons and nucleons by nuclei has enjoyed considerable success. In this model the interaction of the incident particle with the individual constituents of the scattering nucleus is represented by an effective potential which enables one to reduce the problem to an equivalent one-body problem. The effective potential is in general complex, thus making a rather close analogy with the scattering of an electromagnetic wave by a medium of complex index of refraction.

The first success of the optical model was in high-energy neutron scattering.[1] Later, meson reactions were analyzed,[2] and, most recently, low-energy neutron scattering data were very successfully explained by this model.[3] Though the eventual theoretical justifications for the model may be of very different nature at high and low energies, respectively, it is reasonable to expect satisfactory results also at intermediate energies. Indeed, Le Levier and Saxon[4] obtained fairly good agreement with the elastic proton scattering experiments on Al at 18.6 Mev.[5] However, further experiments[6] soon showed that the calculated differential cross section is too large near 180° and in general too flat. For these reasons it was felt that further investigation of the 20-Mev region is appropriate.

Unfortunately, all recent experimental differential cross sections at that energy are for protons rather than for neutrons. Since the Coulomb and nuclear potentials are here of equal importance, this fact implies a considerable complication of the calculations. We have carried out exact calculations for several elements on the basis of the optical model but were limited by the lack of tables of Coulomb functions for parameters corresponding to proton scattering by elements of $Z>50$. Results are presented for Al, Cu, and Ag.

In addition to allowing a comparison with experiments, the exact calculations also enable one to check on approximate theoretical treatments. In particular, the boundary condition model is here investigated.[7] In this model it is assumed that the logarithmic derivative of the wave function ψ_l at the boundary R of the nucleus is independent of the angular momentum l of the incident particle, and that inside the nucleus ψ_l is of the form of an ingoing wave only:

$$u_l=r\psi_l\sim\exp(-ik'r). \tag{1}$$

k' is an average wave number of the incident particle inside the nucleus. This assumption is expected to be valid when the energy of incidence is sufficiently high so that exit through the entrance channel after penetration into the nucleus is very improbable. The logarithmic derivative at the boundary is

$$f_l=(d\ln u_l/d\ln r)_{r=R}=-ik'R. \tag{2}$$

This relation provides an approximate treatment of the optical model. The results of this treatment will be compared with those of the exact calculation.

In the next section we shall outline the method of calculation and in Sec. 3 we shall present the results for a variety of parameters. These are compared with the results of several experimenters and lead to the conclusions stated in the final section.

2. METHOD OF CALCULATION

A nonrelativistic particle in a complex potential satisfies in a stationary state the Schrödinger equation

$$\nabla^2\psi+(2M/\hbar^2)[E-V(r)-iW(r)]\psi=0, \tag{3}$$

where V and W are the real and imaginary part of the potential. In the usual way one finds an equation of continuity,

$$\partial\rho/\partial t+\nabla\cdot\mathbf{j}=(2\rho/\hbar)W, \tag{4}$$

* Supported in part by the U. S. Atomic Energy Commission and the Higgins Scientific Trust Fund.

† Now at the Department of Physics, State University of Iowa, Iowa City, Iowa.

[1] Fernbach, Serber, and Taylor, Phys. Rev. **75**, 1352 (1949).

[2] H. A. Bethe and R. R. Wilson, Phys. Rev. **83**, 690 (1951); Brueckner, Serber, and Watson, Phys. Rev. **84**, 258 (1951).

[3] Feshbach, Porter, and Weisskopf, Phys. Rev. **91**, 453 (1953); **90**, 166 (1953).

[4] R. E. Le Levier and D. S. Saxon, Phys. Rev. **87**, 40 (1952).

[5] J. W. Burkig and B. T. Wright, Phys. Rev. **82**, 451 (1951).

[6] P. C. Gugelot, Phys. Rev. **87**, 525 (1952), and unpublished work. I. E. Dayton (private communication). Dr. Dayton has kindly allowed us to quote some of his preliminary results. The qualitative features of his work are confirmed by relative cross section measurements at 21.5 Mev reported by B. L. Cohen and R. V. Neidigh, Phys. Rev. **93**, 282 (1954). We are grateful to Dr. Cohen for a prepublication copy of this paper.

[7] H. Feshbach and V. F. Weisskopf, Phys. Rev. **76**, 1550 (1949).

with $\rho=\psi^*\psi$ and $\mathbf{j}=(\hbar/2Mi)(\psi^*\nabla\psi-\psi\nabla\psi^*)$. It follows that the nucleus absorbs the incident beam of particles at a rate $(2\rho/\hbar)|W|$, $(W<0)$. We shall assume

$$V(r)=\begin{cases}-V_0 & (r<R)\\ Ze^2/r & (r>R)\end{cases},\quad W(r)=\begin{cases}-W_0 & (r<R)\\ 0 & (r>R)\end{cases}, \tag{5}$$

where R is the radius of the nucleus. The potential (5) corresponds to the assumption that the charge of the nucleus is distributed uniformly over its *surface*. If the nucleus had a uniform charge density throughout its *volume* a correction would have to be added for $r<R$ which is small compared to V_0. Also, the large absorption—the experimental absorption cross section is approximately geometrical—would prevent the incident particle from penetrating deep enough to detect such variations of the potential. The parameters Z, R, V_0, W_0 completely characterize the nucleus in this model.

The solutions u_l of the radial equation for each orbital angular momentum l are nonrelativistic Coulomb wave functions: $F_l(kr)$ and $G_l(kr)$ for $r>R$, and $k'rj_l(k'r)$ for $r<R$. Here,

$$k^2=2ME/\hbar^2,\quad k'^2=k^2+(2M/\hbar^2)(V_0+iW_0), \tag{6}$$

and j_l is the regular spherical Bessel function of order l. The phase shifts are obtained from the requirement of smoothness of the wave function. We define the logarithmic derivative at $r=R$ as in Eq. (2):

$$f_l=a_l+ib_l. \tag{7}$$

The calculation now proceeds in the usual way,[8] except that k'^2 is a complex number. Therefore, the solution u_l will also be complex and the phase shifts will be of the form

$$\delta_l+i\epsilon_l. \tag{8}$$

For the comparison of f_l on both sides of the discontinuity we find

$$f_l=\frac{k'Rj_l'(k'R)}{j_l(k'R)}+1=\frac{kR[F_l'(kR)+\tan(\delta_l+i\epsilon_l)G_l'(kR)]}{F_l(kR)+\tan(\delta_l+i\epsilon_l)G_l(kR)}. \tag{9}$$

An easy calculation yields from this:

$$\exp(-4\epsilon_l)=1-4r_l/[t_l^2+(r_l+1)^2], \tag{10}$$

$$\delta_l=-\arg(G_l+iF_l)+\tfrac{1}{2}\arg[t_l+i(r_l-1)]-\tfrac{1}{2}\arg[t_l+i(r_l+1)], \tag{11}$$

where

$$t_l=G_lG_l'+F_lF_l'-(F_l^2+G_l^2)a_l/kR, \tag{12}$$

$$r_l=(F_l^2+G_l^2)|b_l|/kR; \tag{13}$$

the differentiation is with respect to kr, and all functions are to be taken at $r=R$.

[8] See, e.g., J. M. Blatt and V. F. Weisskopf, *Theoretical Nuclear Physics* (John Wiley and Sons, Inc., New York, 1952).

In order to evaluate the phase shifts from Eqs. (10) and (11) the Coulomb functions must be known and the functions $j_l(k'R)$ and $j_l'(k'R)$ in Eq. (9) must be separated into their real and imaginary parts. For the determination of the Coulomb functions F_l and G_l the tables by Breit and collaborators proved most helpful.[9] However, four and five point interpolation and extrapolation is necessary in some cases, since the tables list only functions for angular momenta $l\leq 4$ and these must be known very accurately so that recursion formulas can be used to obtain functions for higher values of l. For a given argument $\rho=kR$ and parameter $\eta=Ze^2/\hbar v$ the four functions F_l, F_l', G_l, and G_l' are connected by the following relations:[10]

$$F_l'G_l-G_l'F_l=1, \tag{14}$$

$$F_{l-1}G_l-F_lG_{l-1}=l/[l^2+\eta^2]^{\frac{1}{2}}, \tag{15}$$

$$(l+1)[l^2+\eta^2]^{\frac{1}{2}}Y_{l-1}-(2l+1)(\eta+l(l+1)/\rho)Y_l+l[(l+1)^2+\eta^2]^{\frac{1}{2}}Y_{l+1}=0, \tag{16}$$

$$(l+1)Y_l'-((l+1)^2/\rho+\eta)Y_l+[(l+1)^2+\eta^2]^{\frac{1}{2}}Y_{l+1}=0, \tag{17}$$

$$lY_l'+(\eta+l/\rho)Y_l-[l^2+\eta^2]^{\frac{1}{2}}Y_{l-1}=0, \tag{18}$$

where

$$Y_l=G_l+iF_l.$$

These relations are not all independent. In particular, Eqs. (14) and (15) follow from (17) and (18). If, for a definite l, any three of the set of four values (F_l, F_l', G_l, G_l') are known, this set can be calculated for all values of l. For example, all F_l, F_l', G_l, G_l' can be calculated from F_0', F_0, and G_0. However, as one proceeds to larger l the accuracy decreases rapidly. In this connection those of relations (14) to (18) which seem superfluous can be used advantageously in checking the numerical work. Unfortunately, the range of the argument of the aforementioned tables is not sufficient for heavy elements at 20 Mev. Indeed, for 18.3 Mev and the usual nuclear radius [see Eq. (22)] one finds for Ag: $kR=6.36$, which is just outside the range of the tables but can be reached by extrapolation.

The separation of $j_l(k'R)$ into its real and imaginary part can be accomplished either by the series

$$j_l(x+il x)=(1+it)^l\sum_{n=0}^{\infty}j_{l+n}(x)(tx)^n(\tfrac{1}{2}t-i)^n/n!, \tag{19}$$

or by expressing j_l in terms of sine and cosine functions of complex argument. The separation j_l' can be reduced to that of j_l and j_{l-1} by well-known relations among Bessel functions. The spherical Bessel functions j_l of real argument are tabulated.[11]

[9] Bloch, Hull, Broyles, Bouricius, Freeman, and Breit, Revs. Modern Phys. **23**, 147 (1953).

[10] J. L. Powell, Phys. Rev. **72**, 626 (1947).

[11] National Bureau of Standards, Mathematical Tables Project, *Tables of Spherical Bessel Functions* (Columbia University Press, New York, 1947).

After these somewhat laborious auxiliary calculations the phase shifts can be obtained from Eqs. (10) and (11). The differential cross section is found to be

$$d\sigma/d\Omega=(S^2+T^2)/4k^2, \tag{20a}$$

$$S(\vartheta)=\sum_{l=0}^{\infty}(2l+1)[\exp(-2\epsilon_l)\cos(2\delta_l+2\sigma_l) -\cos 2\sigma_l]P_l(\cos\vartheta)+(\eta/\sin^2\tfrac{1}{2}\vartheta) \times\sin(2\sigma_0-2\eta\ln\sin\tfrac{1}{2}\vartheta), \tag{20b}$$

$$T(\vartheta)=\sum_{l=0}^{\infty}(2l+1)[\exp(-2\epsilon_l)\sin(2\delta_l+2\sigma_l) -\sin 2\sigma_l]P_l(\cos\vartheta)-(\eta/\sin^2\tfrac{1}{2}\vartheta) \times\cos(2\sigma_0-2\eta\ln\sin\tfrac{1}{2}\vartheta). \tag{20c}$$

The Coulomb phase shifts σ_0 can also be found in tables.[12]

The absorption cross section is

$$\sigma_a=(\pi/k^2)\sum_{l=0}^{\infty}(2l+1)[1-\exp(-4\epsilon_l)]. \tag{21}$$

It is not explicitly dependent on the Coulomb potential. The formulas (20) express clearly the coherent effect of the Coulomb and nuclear scattering. It is clear from these equations that the amplitudes cannot be written as the sum of an exclusively Coulomb and another, exclusively nuclear, contribution. This fact makes the strict concept of interference between two scattering effects inapplicable for the case of Coulomb and nuclear scattering. Nevertheless, we shall refer to such interference in the sense of comparison of this scattering with pure Coulomb scattering. For simplicity we shall take the pure Coulomb scattering for a point nucleus (Rutherford scattering).

The summation in the first term of $S(\vartheta)$ and $T(\vartheta)$ in (20) extends up to the highest angular momentum l_1 which contributes to the nuclear scattering. For Al, l_1 is about 5 or 6, whereas for Ag, $l_1=7$.

3. RESULTS[13]

We choose for the nuclear radius

$$R=1.42A^{\frac{1}{3}}\times10^{-13}\text{ cm}, \tag{22}$$

and for the energy 18.3 Mev, the energy at which Gugelot's experiments are carried out. The results are not very sensitive to the choice of R as will be shown below. The choice of V_0 and W_0 is somewhat arbitrary. A reasonable value would perhaps be $V_0=30$ Mev, corresponding to the usual Fermi gas well, where for light elements (Al) one may expect that the Coulomb barrier of a few Mev should be subtracted; Le Levier and Saxon claim best results with $V_0=45$ Mev. The value of W_0 for a given V_0 depends, of course, on the energy. The optical model gives the relation

$$W_0=2[V_2(E+V_0)+V_2^2]^{\frac{1}{2}}, \tag{23}$$

where $V_2=\hbar k_2^2/2M$, $k_2=\mathrm{Im}k'$. We can introduce the penetration depth Λ which is the distance a nucleon beam travels in nuclear matter before its intensity is reduced by $1/e$. It follows that $2\Lambda=1/k_2$. For practical purposes V_2 can be neglected compared to $E+V_0$ such that Eq. (23) may be written conveniently

$$W_0=4.5(E+V_0)^{\frac{1}{2}}/\Lambda, \tag{24}$$

where the energies are in Mev and Λ is in units of 10^{-13} cm. We can obtain an estimate of W_0 at 20 Mev by a somewhat daring extrapolation from the 90-Mev neutron data. The penetration depth Λ may be taken approximately equal to the mean free path in nuclear matter. The latter increases at most proportionally to $E+V_0$, but at lower energies the exclusion principle will reduce this dependence considerably. With these assumptions we find from[1] Λ(90 Mev)$\sim4\times10^{-13}$ cm, $V_0\sim30$ Mev, a value Λ(20 Mev)$\sim1.7\times10^{-13}$ cm. Equation (24) now gives $W_0\sim20$ Mev. The potential $-V=30+20i$ Mev thus seems to be a reasonable first approximation near $E=20$ Mev.

The most important results of our calculations are shown in Figs. 1 to 6, together with experimental

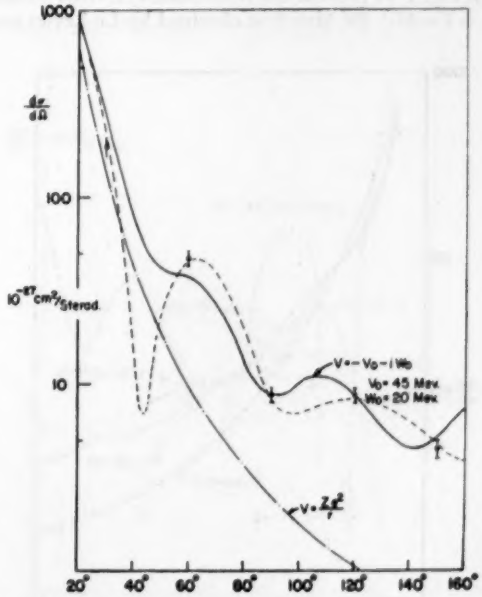

FIG. 1. Elastic scattering of protons by aluminum. The solid curve is the result of an exact calculation at 18.3 Mev. The dashed curve represents the experimental results of Dayton at 19.1±0.2 Mev. The experimental points in this and the following figures are those of Gugelot at 18.3 Mev.

[12] See, for example: National Bureau of Standards, *Tables of Coulomb Functions* (U. S. Government Printing Office, Washington, D. C., 1952), Vol. 1.

[13] Most of the results discussed in this section were first reported at the Washington Meeting of the American Physical Society, May, 1953; see F. Rohrlich and D. M. Chase, Phys. Rev. 91, 454 (1953).

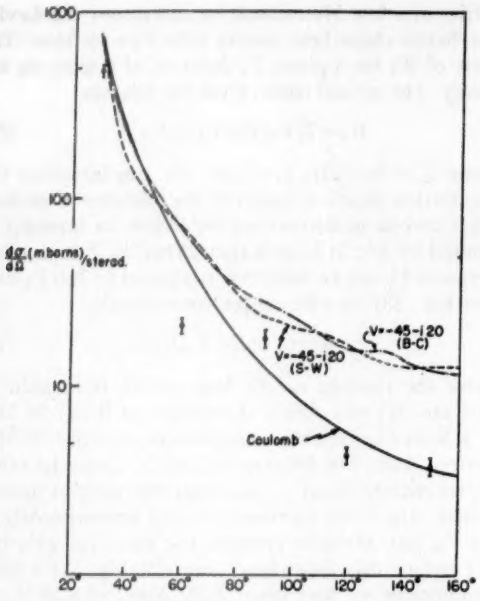

FIG. 2. 18.3-Mev protons on Cu. The good approximation offered by the boundary condition model is compared with the exact calculation (square well shape).

results of Gugelot and of Dayton.[6] These are the only experiments at the present time which give absolute values of the cross section.

In Fig. 1 we present the recalculated Al cross section for $-V=45+20i$ Mev first obtained by Le Levier and Saxon.[4] The calculations agree with the general trend of the measured differential cross section but certainly do not reproduce the pronounced maxima and minima. We notice that nuclear and Coulomb scattering interfere constructively for Al in the sense that the measured cross section over most of the angular range is greater than that for pure Coulomb scattering from a point nucleus.

On the other hand, there is no constructive interference for Cu (Fig. 2). The experimental points indicate that the total scattering cross section is about equal to that for Coulomb scattering. The two theoretical curves for $-V=45+20i$ Mev represent the exact optical model and the boundary-condition model, respectively.

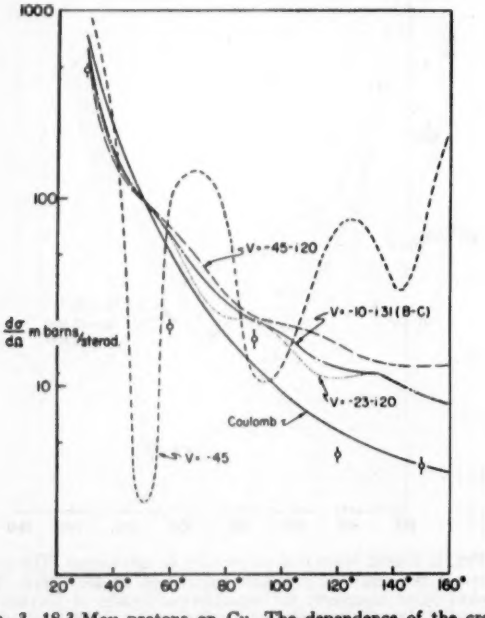

FIG. 3. 18.3-Mev protons on Cu. The dependence of the cross section on V_0 and W_0 is exhibited.

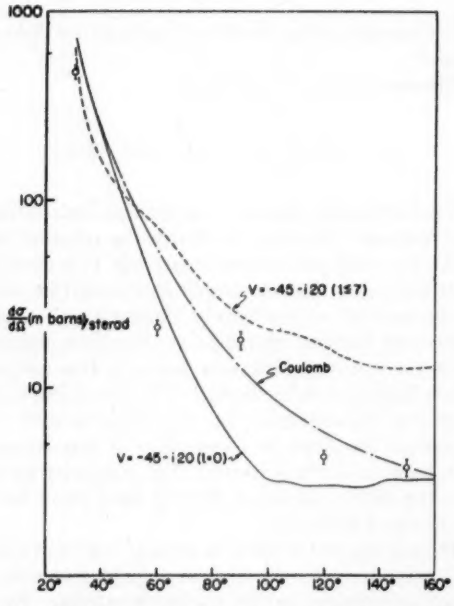

FIG. 4. 18.3-Mev protons on Cu. At large angles the cross section is about four times s-wave scattering in a Coulomb field.

The latter is seen to give a fairly good approximation to the former, but is in general smoother, i.e., it shows less pronounced minima and maxima. Both curves are far above the experimental data.

In order to study the dependence of the theoretical cross section on V_0 and W_0, in Fig. 3 several extreme assumptions are compared with the results of Fig. 2. The effect of a relatively too small absorptive part, W_0, is seen in the extreme case, $-V=45$ Mev. The angular variations are much too large and the cross section is orders of magnitude too large for angles above 90°. (This result is of special interest in connection with the potential $-V=20+i$ Mev recently proposed by Weisskopf[3] which explains the total neutron cross sections below 3 Mev.) However, a reduction of the real part

of V by a factor of two or even four has relatively little effect as long as the imaginary part is kept large.

One might be inclined to think that for large angles the scattering is primarily due to s waves. That this is not at all the case is shown in Fig. 4, where s scattering is compared with previous results. Indeed, s scattering accounts for only one-fourth of the cross section at large angles. (The Coulomb scattering is, of course, always *fully* taken into account.)

For larger Z, nuclear and Coulomb scattering interfere destructively (in the above sense). The actual cross section is only a fraction of Coulomb scattering. Figure 5 shows the results for Ag. A reasonable potential, $-V=35+20i$ Mev, gives about six times more scattering than is observed. Even a rather extreme case, $-V=5+5i$ Mev, gives much too much scattering between 70° and 150°.

Finally, in Fig. 6 we show the effect of a variation of the nuclear force range. Conveniently, only the first five phase shifts were calculated. For Cu, $kR=5.33$ if we use Eq. (22). The corresponding cross section (in the boundary condition approximation for $-V=45+20i$ Mev) is shown, first with all contributing partial waves ($l\leq 7$) included, and again with only the first five included. Also shown are the cross sections for two different radii corresponding to $kR=5.0$ and 5.8 ($l\leq 4$). We see that even a variation of almost ±10 percent leaves the theoretical curves several times higher than the measured values.

A number of further results will be mentioned in the following section.

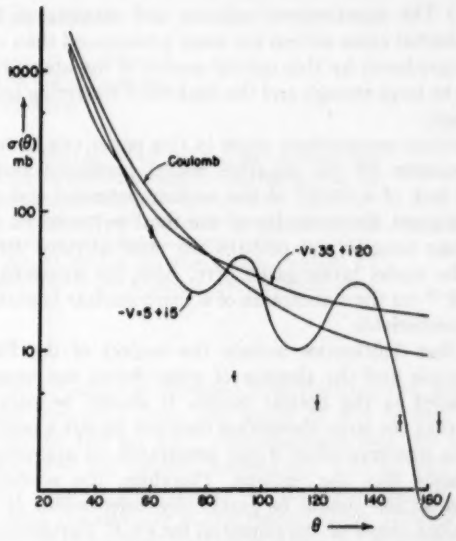

FIG. 5. 18.3-Mev protons on Ag.

4. CONCLUSIONS AND DISCUSSION

(1) Comparison of the differential cross section in the approximation of the boundary-condition model with that from exact calculations shows that this approximation yields very good results, but gives somewhat less pronounced structure. A typical instance is shown in Fig. 2.

(2) When the experimental results are compared with pure Coulomb scattering by a point nucleus, a marked dependence on Z appears: For small Z the nuclear forces contribute constructively to the scattering; for $Z\sim 29$ (Cu) they do not change the total scattering cross section, but cause maxima and minima in the differential cross section; for larger Z they contribute destructively. This Z dependence is most pronounced at large angles, as can be seen from the following four cases at 150°:

Z	13	29	47	78
$\sigma_{\text{exp}}(150°)/\sigma_{\text{Coul}}(150°)$	6.1	1.0	0.31	0.16

(3) The optical model with a square well shape and with the accepted nuclear radii [Eq. (22)] gives considerably more scattering than an equally large point charge, so that reasonable agreement with experiments can be attained only for small Z. This result is valid over a very large range of both V_0 and W_0 and over considerable variations of the nuclear range.

(4) The absorption cross section is found to be between 60 and 90 percent of the geometric cross section for $W_0\sim 20$ Mev in qualitative agreement with experiments.

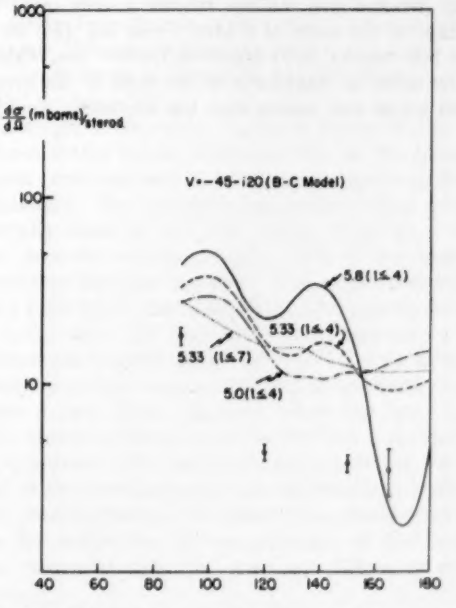

FIG. 6. 18.3-Mev protons on Cu, dependence of the cross section on the nuclear radius. The accepted radius ($kR=5.33$) gives an approximate cross section ($l\leq 4$) which is compared with cross sections for larger and smaller radii in the same approximation.

(5) The experimental minima and maxima of the differential cross section are more pronounced than can be reproduced by this optical model, if the absorption is to be large enough and the backward scattering small enough.

Several assumptions made in this paper can be held responsible for the negative results presented above. The lack of a "tail" of the nuclear potential and the consequent discontinuity of the total potential on the nuclear boundary is perhaps the most obvious defect of the model investigated here. Also, for wavelengths of 10^{-13} cm the assumption of a sharp nuclear boundary is questionable.

Other deficiencies include the neglect of the Pauli principle and the absence of other forces not usually included in the optical model. It should be pointed out that the large absorption does not permit a particle to be scattered after it has penetrated an appreciable distance into the nucleus. Therefore, the scattering cross section should be practically independent of the detailed shape of the potential for $r<R$. Furthermore, the experiments show no dependence on magic numbers or spins of the target nuclei. Spin-dependent forces, therefore, should not be of importance.

However, there seem to be at least two strong arguments in favor of a small absorption potential W_0. One is the excellent agreement of the potential[3] $-V=19(1+0.05i)$ Mev with the neutron scattering data up to 3 Mev; the other is the strong angular dependence of the 20-Mev proton scattering data observed by Cohen and Neidigh[6] and by Dayton (see Fig. 1). The steep maxima and minima require a very small W_0, perhaps of the order of 5 Mev. From Eq. (24) we see that this implies $\Lambda(20\text{ Mev})\sim 6.5\times 10^{-13}$ cm, which is of the order of magnitude of the radii of the investigated nuclei and means that the scattering would be much more sensitive to the shape of the potential well. In this case, it also follows that the extrapolation from the 90-Mev data with the accepted energy dependence of the mean free path [see the argument following Eq. (24)] is completely wrong and that Λ is actually a *decreasing* function of energy, at least for $E\lesssim 50$ Mev. This situation is in very nice agreement with the great success of the shell model at very low energies: the more independently the particles move, the larger is their mean free path. If we accept these arguments and use a potential $-V=30+20i$ Mev, say, then our calculations show that it may indeed be possible to fit the observed angular distribution for not too large angles (up to 90°, say), but that for larger angles this potential gives much too much scattering. The latter effect may then be blamed on the spherical well shape whose large discontinuity causes too much reflection. Thus, with these arguments we are led to believe that a potential of approximate magnitude $-V=30+5i$ Mev *which has a sufficiently long tail* may fit the observed angular distributions. However, such a model would probably give a rather small absorption cross section. Calculations along these lines are in progress.

It will be extremely interesting to study the scattering of neutrons by nuclei in this energy region. If the model presented here can account for neutron scattering, our results show that the optical model can give the correct nuclear scattering amplitude except for a phase factor. This phase factor is of no interest for neutron scattering, but is essential for proton scattering.

In conclusion, we wish to thank Professor P. C. Gugelot and Dr. I. E. Dayton for discussing their experimental results with us and Mrs. Ruth Shoemaker for her able help in the early stages of the numerical work.

The He^3+He^3 Reactions

W. M. Good, W. E. Kunz, and C. D. Moak
Oak Ridge National Laboratory, Oak Ridge, Tennessee
(Received December 21, 1953)

A study has been made in the energy range up to 800 kev of He^3 capture on He^3 and the reactions that accompany this capture. The proton energy spectrum was found to confirm an earlier observation that the capture is followed by two modes of disintegration, *viz.*, into two protons and an α particle, and into a proton and Li^5. Improved resolution and statistics give no evidence of well-defined groups of protons of energy less than the Li^5 ground-state group. The total reaction cross section was observed to rise monotonically in a manner suggesting partial waves of l greater than one. At 200 kev the cross section is at least 2.5 microbarns, substantiating the fact that the capture of He^3 on He^3 is the dominant reaction terminating the $p-p$ cycle for stellar production of energy.

INTRODUCTION

RESULTS have been published to indicate that when He^3 captures He^3 the following processes occur:[1,2]

$$He^3+He^3\rightarrow Be^{6*}\rightarrow Li^5+p+11 \text{ Mev} \quad (1)$$

$$He^4+2p+12.83 \text{ Mev}. \quad (2)$$

The characteristic features of the reactions, such as cross section *vs* energy, energy spectrum of particles, etc., might reasonably be expected to resemble the corresponding features of the $H^3(t;n,n)He^4$ and $H^3(He^3;n,p)He^4$ reactions. Results from the studies of the latter two reactions have been published. The $H^3(t;n,n)He^4$ reaction gives inconclusive evidence of the dineutron.[3,4] The neutron spectrum shows[4,5] beyond much doubt a mode of decay of He^6 in which He^5 is left in its ground state. The presence of a group of neutrons of energy less than the He^5 ground state group but having an approximately equal energy spread is not unequivocal.[4,5] Certainly the cross section *vs* energy does not give any very concrete information on the high-lying states in He^6.[6]

The cross section *vs* energy characteristic of the $H^3(He^3;n,p)He^4$ reaction resembles that of the $H^3(t;n,n)He^4$ reaction.[6,7] The proton energy spectrum from $H^3(He^3;n,p)He^4$ shows a group of protons corresponding to the mode of Li^5 decay which leaves He^5 in its ground state.[7,2] At the same time, a careful examination of the proton energy spectrum does not show evidence for any group of protons of energy less than the He^5 ground-state group. If such a group exists, it is either much less probable than the ground state group, or of much greater spread in energy, or both.

It is reasonable to suppose that additional information on Li^5 could be obtained from studying the proton energy spectrum from the decay of Be^6 formed by capture of He^3 on He^3. This spectrum was the first objective of the present experiment. The second objective was to place limits on the cross section for reactions (1) and (2) in the energy range 100-kev to 800-kev He^3 bombarding energy. The capture of He^3 by He^3 has been suggested as the probable termination of the proton-proton cycle in stellar production of energy.[8,9]

EXPERIMENTAL TECHNIQUE

The results, which are presented in this paper, were obtained using a He^3 target made by the bombardment technique and a NaI crystal spectrometer identical to the one discussed in reference 7. The additional information, beyond that already published on the reaction, results from the use of pure He^3. The accelerator, ion source, He^3 gas-handling equipment, and target are the same as those employed in previous studies with the He^3 ion beam.[7,10,11]

The target arrangement, which is shown in Fig. 1, has been shown before, excepting that in the present instance provision had to be made for water-cooling, as indicated. The necessity for water-cooling arises principally from the fact that helium build-up in the target does not appear to take place if the target-temperature becomes too great. The target was built up in a 2-mil foil of clean aluminum. The appearance of such a foil after He^3 bombardment is noteworthy in relation to the question of He^3 distribution in the target. Whereas aluminum bombarded with protons will show at most a very slight coloration where the beam has struck, aluminum bombarded by He^3 has a decidedly flaky appearance after bombardment, suggesting a rupturing of the aluminum and loss of aluminum surface layers. Such a process, if it takes place, would tend to make for uniformity of concentration of He^3 with depth. Assuming that He^3 does not diffuse in cold

[1] Good, Kunz, and Moak, Phys. Rev. **83**, 845 (1951).
[2] Almqvist, Allen, Dewan, and Pepper, Phys. Rev. **91**, 1022 (1953).
[3] Los Alamos Scientific Laboratory, Phys. Rev. **79**, 238 (1950).
[4] Allen, Almqvist, Dewan, Pepper, and Sanders, Phys. Rev. **82**, 262 (1951).
[5] W. T. Leland and H. M. Agnew, Phys. Rev. **82**, 559 (1951).
[6] Agnew, Leland, Argo, Crews, Hemmindinger, Scott, and Taschek, Phys. Rev. **84**, 262 (1951).
[7] C. D. Moak, Phys. Rev. **92**, 383 (1954).
[8] W. A. Fowler, Phys. Rev. **81**, 655 (1951).
[9] E. Schatzman, Compt. rend. **232**, 1740 (1951).
[10] Kunz, Moak, and Good, Phys. Rev. **91**, 676 (1953).
[11] W. E. Kunz, thesis (to be published).

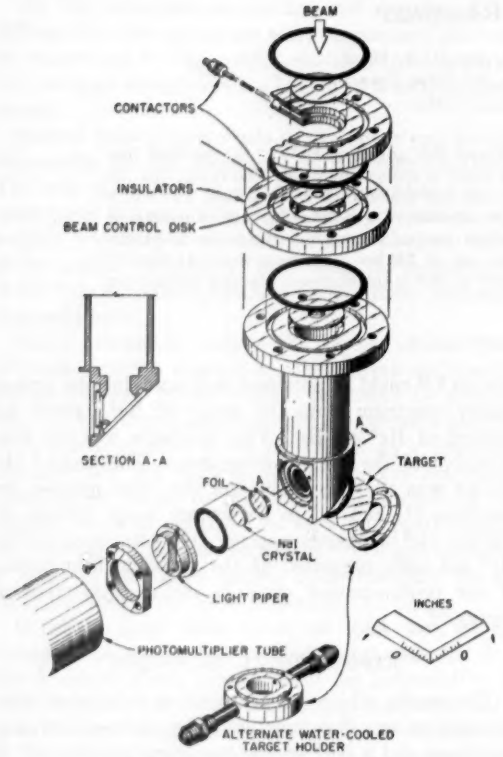

FIG. 1. Target arrangement.

aluminum, the bombarding technique permits making a target whose thickness is known in terms of kilovolts range at one specified energy, *viz.*, the buildup bombarding energy. What is not known is the He^3 distribution with thickness from the maximum depth of the target to the surface.

When a 40 μa beam, 2 mm in diameter, of He^{3+} at 360 kev is placed upon a clean aluminum foil, a counting rate immediately appears, which energy analysis shows to be 14.72-Mev protons from the $He^3(d,p)He^4$ reaction. Because the maximum energy release from reactions (1) and (2) is 12.86 Mev, protons from these reactions do not appear beyond 11 Mev. The energy resolution of the NaI crystal used was a few percent in the energy range 11 to 15 Mev, and, hence, the 14.72-Mev contamination protons, and their recoil α particles as well, could easily be removed by the use of two pulse-height discriminators. In order to do this one pulse-height discriminator was set to count all pulses larger than, say, 3 Mev; the other pulse-height discriminator was set to count all pulses larger than 12 Mev. The difference between these two pulse-height counting rates will hereafter be called the "integral He^3+He^3 rate." This "integral He^3+He^3 rate" did not include the entire proton spectrum from the reactions being studied, but it did exclude both protons and α particles from the contamination $He^3(d,p)He^4$ reaction. Employing a 40 μa beam of about 0.1 cm^2 at 360 kev, this "integral He^3+He^3 rate" was initially zero. However, it rose under the conditions just specified to an equilibrium value of several thousand counts/min in about thirty minutes.

The proton energy spectrum and the cross section with energy were both obtained in the same target apparatus with the NaI spectrometer at 90° to the beam. In determining the proton spectrum the "integral He^3+He^3 rate" served to monitor the number of He^3+He^3 disintegrations against which the relative number of protons in various energy intervals were compared. The measured cross section was for all protons in the "integral He^3+He^3 rate" range of energies.

For the study of the proton spectrum a maximum counting rate is desired. The maximum counting rate would be achieved by bombarding with as large a current density as possible at as high voltage as possible. Actually since many hours of continuous counting were required by the single-channel differential pulse-height selector used to measure the pulse spectrum, less than maximum currents and voltage were employed. The 40 μa of He^{3+} at 360 kev, quoted previously, could easily be maintained for long periods, and, hence, represents the conditions under which the spectrum was obtained.

For obtaining the total reaction cross section, Kunz's method[11] of measuring a relative cross section was employed. That is to say, the "integral He^3+He^3 rate" per microcoulomb against He^3 bombarding energy was compared with the $He^3(d,p)He^4$ rate per microcoulomb against deuteron bombarding energy on the same He^3 target. Since dE/dx for helium is uncertain in the energy range up to 800 kev, it is particularly desirable that the target be thin. This requirement of a thin target was not very well met because the lowest convenient energy available for target buildup at sizeable beams was 84 kev.

A clean aluminum foil was introduced into the target apparatus and bombarded with a 40 μa beam at 84 kev until equilibrium "integral He^3+He^3 rate" was achieved. Three precautions were taken to minimize uncertainties due to target nonuniformity across the area of the target. The beam was made to fill the collimator hole, the beam was carefully positioned over the last collimator hole by means of a quartz viewer, and the count rate per microcoulomb at 800 kev was taken alternately with the count rate per microcoulomb at the other energies. The 800 kev was obtained from the He^{3++} component of the He^3 ion beam. Current measurement employed the same equipment and precautions as previously employed for the $H^2(He^3,p)He^4$ and $H^3(He^3,d)He^4$ and $H^3(He^3;n,p)He^4$ cross-section measurements. For the purpose of assuring that the He^3 beam did not disturb the He^3 target, the currents subsequent to target buildup were kept small and the

total number of particles used to measure cross sections was an insignificant fraction of those used to make the target.

Following the determination of the "integral He^3+He^3 rate" per microcoulomb with energy, the He^3 ion source and gas supply were quickly removed and a deuterium ion source and gas supply introduced. Using the deuteron beam, the $He^3(d,p)He^4$ rate per microcoulomb was obtained for deuterons up to 400-kev or 600-kev equivalent He^3 energy. The ratio of the "integral He^3+He^3 rate" per microcoulomb to the $He^3(d,p)He^4$ rate per microcoulomb at the same He^3 bombarding energy is numerically equal to the ratio of corresponding differential cross sections. From the fact that the $He^3(d,p)He^4$ cross section is known to a few percent, the cross section for reactions (1) and (2) can be obtained.

EXPERIMENTAL RESULTS

The energy spectrum of the protons from the reactions being studied is shown in Fig. 2. Comparing the energy spectrum of the $He^3(He^3;p,p)He^4$ protons with the energy spectrum of the $H^3(He^3;p,n)He^4$ protons,[2,7] a conspicuous difference appears in the relative intensity of the Li^5, He^5 ground-state proton groups. In the case of the $H^3(He^3;p,n)He^4$ reaction there is one proton in the three-body breakup process whose energy distribution appears with the group of He^5 ground-state protons. In the case of the $He^3(He^3;p,p)He^4$ reaction there are two protons in the three-body breakup process whose energy distributions appear with the group of Li^5 ground-state protons. In consideration of the number of protons in the three-body breakups, the proton spectra of the $H^3(He^3;p,n)He^4$ and $He^3(He^3;p,p)He^4$ reactions appear consistent with there being for both the reactions approximately the same ratio of two-body to three-body decays. The proton energy spectra from both reactions give no evidence for groups of protons of energy lower than the Li^5, He^5 ground-state groups. The energy of the proton group in Fig. 2 is insufficiently well-determined to improve upon the present precision of the mass of Li^5. The reasons for a large uncertainty in the energy of the proton group are that the proton energy spectrum from the three-body breakup process is not known and that the crystal employed to obtain the spectrum had only a single calibration point at 14.72 Mev.

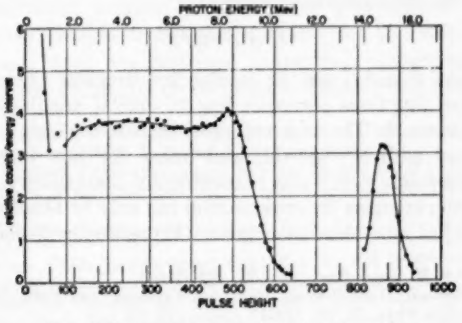

FIG. 2. Energy spectrum of protons from the $He^3(He^3;p,p)He^4$ reaction.

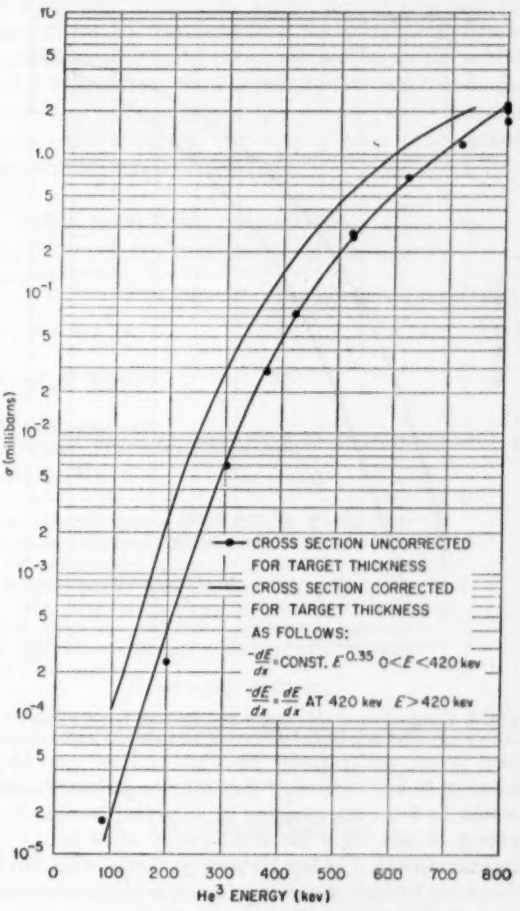

FIG. 3. He^3+He^3 total reaction cross section assuming isotropy of disintegration products.

The cross section of reactions (1) and (2) *vs* bombarding energy obtained with a target whose thickness at 84 kev was 84 kev is shown in Fig. 3. The interpretation of this yield curve is subject to the uncertainty of how the loss of energy of He^3 ions varies with energy in the energy range 100 kev to 800 kev, and in addition to the uncertainty of how the He^3 is distributed in depth. With regard to the distribution of He^3 with depth, the three simplest assumptions are that all the He^3 atoms lie at the end of bombarding energy range, that they all lie on the surface, or that they are uniformly distributed with depth between these two limits. The following argument will show that the last of the above simplest assumptions is most nearly correct. The He^3 atoms cannot all lie at a depth corresponding to the

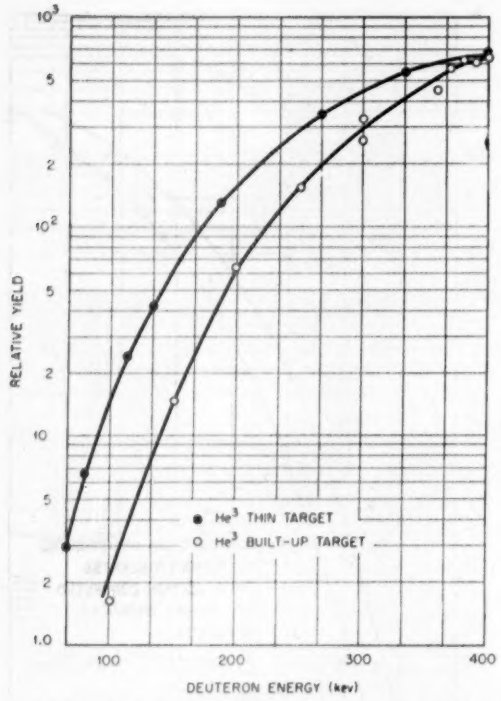

FIG. 4. Comparison of thin target and built-up target yields with bombarding energy of the reaction $He^3(d,p)He^4$.

range of 84 kev because, if they did, the yield at 84 kev would be low corresponding to an actual bombarding energy of zero for a measured energy of 84 kev. The measured yield at 84 kev He^3 energy, on the other hand, was actually high. From this fact, it is safe to conclude that the He^3 did not all reside at a depth corresponding to the range at 84 kev. The information that the He^3 did not all reside at the surface is contained in the shape of the $He^3(d,p)He^4$ yield curve obtained with the He^3 target. Figure 4 shows the $He^3(d,p)He^4$ yield curve as obtained by deuteron bombardment of the He^3 target used for the reactions under investigation. Figure 4 also shows the $He^3(d,p)He^4$ thin target yield.[11] Comparing the two yield curves in Fig. 4, it will be seen that the yield of the "buildup" He^3 target falls more rapidly with energy than does the thin target yield. Hence, it follows that the He^3 cannot all reside on the surface of the target.

It was pointed out earlier in the description of the experiment that the "build-up" He^3 target gave evidence of continuous flaking away at the surface and that such a process would likely tend to make the target uniform with depth. In the following interpretation of the yield curve of Fig. 3, the He^3 target will be assumed to be uniformly distributed to a depth of 84 kev for He^3 of 84-kev energy.

Having made an assumption about the He^3 target distribution with depth, it remains to attach a scale of cross sections to the yield curve of Fig. 3, and finally to correct each energy point for target thickness. The scale of cross sections is obtained as follows: for bombardment with deuterons of 400-kev or 600-kev equivalent He^3 energy, the $He^3(d,p)He^4$ cross section is almost at its maximum and is varying slowly with energy. The ratio of the "integral He^3+He^3 rate" per microcoulomb to the $He^3(d,p)He^4$ rate per microcoulomb will, therefore, be insensitive to target thickness and equal to the ratio of respective differential cross sections. The ratio of cross sections obtained, assuming isotropy, together with the $He^3(d,p)He^4$ cross section of 695 millibarns at 600-kev equivalent He^3 energy, serves to place the scale of cross sections shown on Fig. 3.

There is little information on the stopping of He in the energy range below 1 Mev with which to make a correction for target thickness. A correction is shown in Fig. 3 which is based upon the stopping of low-energy α particles in helium, air and argon.[12] This correction makes the assumption, based upon the helium-air-argon data of reference 12, that

$$dE/dx = \text{constant } E^{0.35}, \qquad 0<E<400 \text{ kev}$$
$$dE/dx = (dE/dx) \text{ at } 400 \text{ kev}, \qquad E>400 \text{ kev}.$$

In calculating the energy loss at the various bombarding energies by means of the above assumptions, the average energy loss in the target has been taken to be 84 kev at 84-kev He^3 energy. Since dE/dx is increasing with energy, the rate of energy loss in the target at 84 kev is greater than the 84 kev lost in coming to rest. This means that the energy corrections applied to the observed cross section with energy are under-estimated, resulting in a corrected curve, Fig. 3, which represents at each He^3 energy a value of cross section which is too low.

At sufficiently low bombarding energies it is reasonable to suppose that the cross section should depend upon energy as

$$\frac{e^{-\frac{2\pi Z_1 Z e^2}{hv}}}{E}.$$

This expression is the form at low bombarding energies of the more general expression[13,14]

$$\lambda/(F_l^2+G_l^2),$$

where F and G are the regular and irregular Coulomb wave functions corresponding to orbital angular momentum lh. The observed cross section has been compared with $\lambda/(F_l^2+G_l^2)$ and below 350 kev there is agreement within the experimental uncertainty. At higher energies the cross section can only be fitted with the just mentioned more general expression by including

[12] P. K. Weyl, Phys. Rev. 91, 289 (1953).
[13] Bloch, Hull, Broyles, Bouricius, Freeman, and Breit, Revs. Modern Phys. 23, 147 (1951).
[14] J. M. Blatt and V. F. Weisskopf, *Theoretical Nuclear Physics* (John Wiley and Sons, Inc., New York, 1952), p. 395.

partial waves of angular momentum of at least two units of $\hbar$.

No attempt has been made to compare the observed cross section with single level resonance theory because a sufficiently high bombarding energy was not achieved for good comparison and also because the level widths and level shifts have not been developed for three-body breakup.[15]

From Fig. 3 the cross section for the reactions (1) and (2) at 200 kev is at least 2.5 microbarns. Fowler and Lauritsen[16] found that for an assumed cross section of 4 microbarns, the $He^3(He^3,2p)He^4$ reaction is the dominant reaction terminating the $p-p$ cycle in stellar production of energy. The essential correctness of their assumption seems established.

[15] E. P. Wigner and L. Eisenbud, Phys. Rev. 72, 29 (1947).

[16] W. A. Fowler (private communication).

PHYSICAL REVIEW VOLUME 94, NUMBER 1 APRIL 1, 1954

The Disintegration of Mo^{99}†

JAGDISH VARMA* AND C. E. MANDEVILLE
Bartol Research Foundation of the Franklin Institute, Swarthmore, Pennsylvania

(Received November 16, 1953)

The radiations of Mo^{99} and Tc^{99m} have been reinvestigated by means of scintillation spectroscopy. Employing single-channel pulse-height analyzers in coincidence, it has been established that a triple cascade of gamma rays, 741 kev→41 kev→140 kev occurs. The 741-kev radiation is also coincident with a gamma ray at 181 kev by an alternate branch of de-excitation which is equally probable. Radiation at 780 kev is present but is non-coincident with other gamma rays. From these data, a disintegration scheme can be constructed. A gamma ray of energy 372 kev was also detected, and, although it appeared to have the proper half-period to be associated with Mo^{99}, was found to be not in immediate coincidence with beta rays or other gamma rays, suggesting that it might be related to an impurity.

INTRODUCTION

EARLIER coincidence studies[1] showed the disintegration scheme of Mo^{99} to be rather complex. Subsequent measurements[2–6] have led to the conclusion that Mo^{99} decays with the emission of two, or possibly three, groups of beta rays, and gamma rays having energies of 1.8, 40, 140, 142, 181, 367, 741, and 780 kev. A careful study[5,6] of the disintegration of the 6-hour isomer of Tc^{99} has revealed that it decays with cascade emission of the 1.8-kev and 140-kev quanta, and that the 142-kev gamma ray is the associated cross-over transition. The disintegration scheme of Mo^{99}, as advanced by Medicus *et al.*,[5] is based upon coincidence measurements between spectrometrically selected beta rays and gamma rays detected in an anthracene scintillation counter. However, the problem of the precise location in the scheme of the 181- and 367-kev gamma rays has remained unresolved. Accordingly, with the utilization of two single-channel pulse-height analyzers in coincidence, the gamma-ray spectrum and the various cascade relationships have been reinvestigated.

THE MEASUREMENTS

For the purposes of the present investigations, a source of Mo^{99} was obtained when a quantity of MoO_3 was irradiated by slow neutrons in the Oak Ridge pile. Because no gamma rays other than those already reported were observed, extensive chemical purification was deemed unnecessary. On occasion, however, Tc^{99m} was separated from its parent element by the method of Coryell and Sugarman.[7]

In Fig. 1 is shown the pulse-height distribution generated by the gamma rays of Mo^{99} in a crystal of thallium-activated sodium iodide which is three centimeters thick. In the case of the particular curve of Fig. 1, the radiation incident upon the detecting crystal had been filtered by a lead absorber of thickness about 2 g/cm² to reduce in intensity the 140–142 kev radiation relative to the harder gamma rays. The radiation at 78 kev arises from the emission from the absorber of the K line of lead, following photoelectric absorption of the intense 140-kev gamma ray. For the purpose of observing carefully the region of lower

† Assisted by the joint program of the U. S. Office of Naval Research and the U. S. Atomic Energy Commission.

* Research Fellow. Permanent address: Morena (M.B.) India.

[1] C. E. Mandeville and M. V. Scherb, Phys. Rev. 73, 848 (1948).

[2] Medicus, Maeder, and Schneider, Helv. Phys. Acta 22, 603 (1949).

[3] Cork, Keller, and Stoddard, Phys. Rev. 76, 986 (1949).

[4] M. E. Bunker and R. Canada, Phys. Rev. 80, 951 (1950).

[5] Medicus, Maeder, and Schneider, Helv. Phys. Acta 24, 72 (1951); Phys. Rev. 81, 652 (1951).

[6] Mihelich, Goldhaber, and Wilson, Phys. Rev. 82, 972 (1951).

[7] L. E. Glendenin in *Radiochemical Studies: The Fission Products*, edited by C. D. Coryell and N. Sugarman (McGraw-Hill Book Company, New York, 1951), Paper No. 98, National Nuclear Energy Series, Plutonium Project Record, Vol. 9, Div. IV, Part 5, Book 2.

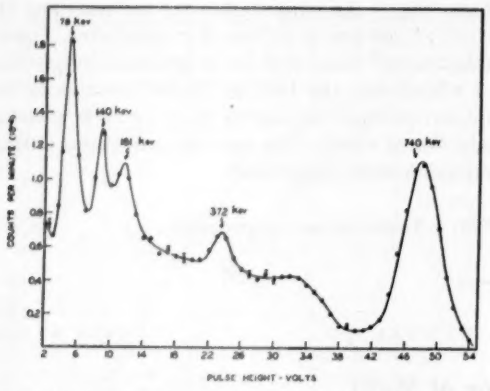

FIG. 1. Pulse-height distribution from NaI(Tl) irradiated by gamma rays emitted in the disintegration of Mo^{99} in equilibrium with Tc^{99m}. The radiations have been filtered by lead (2 g/cm²) to reduce the intensity of the 140-kev radiation.

energies and to detect the 41-kev radiation, without lead absorber and without interference from the K line, an additional curve, not illustrated in this paper, was obtained. In this case, to reduce the intensity of the 140-kev line, approximately two-thirds of the 6-hour Tc activity was removed from the molybdenum by chemical separation. Unless the intensity of the 140-kev line is reduced somewhat, a source of Mo^{99} strong enough to give a clear picture of the spectral region below 140 kev will at the same time give rise to a piling up of 140-kev pulses at the linear amplifier, distorting the spectral region above 140 kev. From the pulse-height spectrogram of Fig. 1, it is clear that only those gamma-rays which have been previously reported are present in the sample of Mo^{99} under study. These gamma rays were observed many times during twelve half-periods of decay and were found to decay with the same half-period.

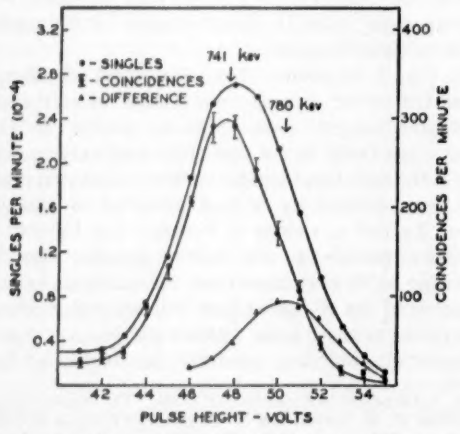

FIG. 2. Coincidence study of the 741-kev–140-kev cascade. The data show that the 780-kev line is noncoincident with any 140-kev radiation.

To study the disintegration scheme of Mo^{99}, gamma-gamma coincidence rates were measured between the two members of all possible pairs of gamma rays.

To ascertain the relation between the 140-kev radiation and the harder gamma rays, the data of the curves of Fig. 2 were collected. The single counting rate in the vicinity of 760 kev is plotted along with a coincidence rate which was obtained with two pulse-height analyzers in coincidence by setting one analyzer at the photopeak of the 140-kev radiation and moving the window of the second through the region of 760 kev. On comparing the half-widths and locations in the energy of the two two peaks, it is seen that the 140-kev radiation is coincident only with the 741-kev line. The difference curve, also shown in Fig. 2, is peaked at 780 kev, showing that the 780-kev radiation is noncoincident with the 140-kev line. A similar curve is shown in Fig. 3 in which coincidences have been recorded between the 741-kev gamma ray and the 181-kev line. A third set of curves, not shown as a figure, was obtained

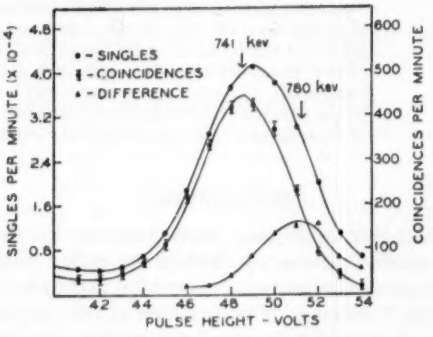

FIG. 3. Coincidence study of the 741-kev–181-kev cascade. The data show that the 780-kev line is noncoincident with any 181-kev radiation.

relative to coincidences between the 41-kev gamma ray and the hard radiations. Again it was found that coincidences were present only between the 741-kev radiation and the softer quantum. To avoid difficulties growing from the presence of the intense 140-kev radiation associated with the decay of the 6-hr metastable level, a partial separation of Tc from Mo was performed before obtaining the data of the curves of Figs. 2 and 3. The soft gamma ray at 41 kev was also found to be coincident with the 140-kev quantum. In performing coincidence measurements between the gamma rays of energies 140 and 41 kev, care was taken that the backscattered quanta from one crystal did not enter the other crystal. A proper choice of absorbers placed between the two crystals eliminated any back scattering effects.

No coincidences were detected between the 372-kev gamma ray and any other gamma rays in the spectrum. A search was also carried out to find two 372-kev quanta in coincidence, but none were found. The

resolving time of the coincidence circuit was 10^{-7} sec. Absence of coincidences may, therefore, be interpreted as evidence that the 372-kev transition terminates at a metastable level of lifetime long compared with 10^{-7} sec or that the 372-kev line arises from the presence of a radioactive impurity.‡

The foregoing coincidence data are consistent with the interpretation that the 780-kev gamma ray terminates at the 6-hr metastable level in Tc^{99}, 142 kev above the ground state, and that the 741-kev gamma ray leads to a level 181 kev above the ground state of Tc^{99}. The level at 181-kev decays with the emission of the 181-kev quantum or with cascade emission of the gamma rays of energy 41 and 140 kev. The cascade relation among the various gamma rays is depicted in the disintegration scheme of Fig. 4. To determine the percent of the total beta-ray emission which leads to the level at 922 kev in Tc^{99}, beta-gamma coincidences were measured. The beta-ray counter was an anthracene crystal and phototube biased to count pulses generated

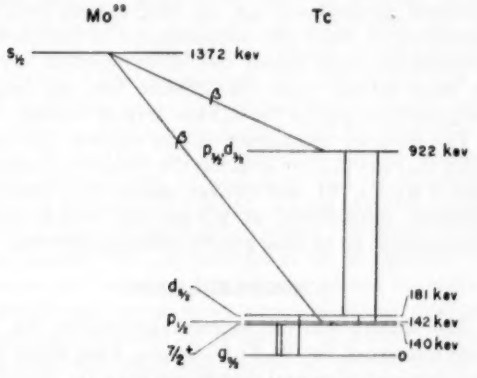

FIG. 4. Term scheme for Mo^{99} and Tc^{99m}.

by beta rays of energy greater than 50 kev. It should also be mentioned that the harder beta-spectrum was found to be non-coincident with gamma rays, in agreement with earlier findings.[1,5] From the gamma-ray counter, all pulses corresponding to a gamma-ray energy greater than 400 kev were accepted. From a carefully calculated solid angle and the counting efficiency of the gamma-ray counter, the 0.5-Mev beta rays were found to constitute 14.5 percent of the total beta emission. This result is in close agreement with the data obtained by Medicus *et al.*[5]

The level at 181 kev can deexcite by way of either of two modes of gamma-ray emission: by the emission of a

‡ *Note added in proof.*—Since this paper was submitted for publication, a second source of Mo^{99} has been obtained from Oak Ridge. Coincidences have been observed between the 372-kev gamma ray and a beta-ray spectrum of maximum energy ~0.87 Mev. The 372-kev gamma transition terminates at the 6-hour level of orbital $p_{1/2}$, indicating an additional level in Tc^{99} at 514 kev. The relative abundance of the 0.87-Mev beta-ray group is of the order of one percent.

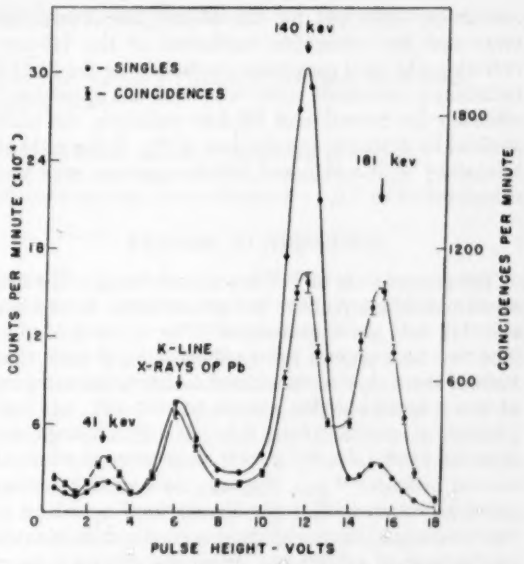

FIG. 5. Gamma-ray spectrum in the region of lower energies of Mo^{99} and Tc^{99m} (Tc^{99m} partially removed by chemical separation). The spectrum of "singles" is to be compared with the spectrum of soft gamma rays in coincidence with the 741-kev radiation.

single gamma ray of energy 181 kev or the 41- and 140-kev quanta in cascade. To determine the probability of deexcitation of the 180-kev level by either mode, coincidences were measured between the 741-kev gamma ray and the entire low-energy spectrum. The pulse-height distribution of single counts in the region of low energy is plotted along with the coincidences between the low-energy gamma rays and those of energy 741 kev as shown in Fig. 5. In actuality, all pulse heights corresponding to energies greater than 400 kev were accepted in the high energy gamma-ray counter. The low-energy gamma-ray counter was shielded from recoil quanta by a lead absorber of thickness 3 g/cm². The aluminum-magnesium oxide jacket in which the crystal of the low-energy gamma-ray counter was encased was estimated to reduce the intensity of the 41-kev gamma ray by 30 percent. If the conversion coefficients of the 140-kev and 181-kev radiations are neglected, it is evident from a consideration of the areas under the peaks of the coincidence curve that the number of disintegrations proceeding by way of the 181-kev branch is about equal to the number in which deexcitation occurs by way of the 41-kev–140-kev transitions. If the conversion coefficient $[\alpha = N(e^-)/N(\gamma)]$ of the 140-kev gamma ray is taken to be 10 percent,[5] the branching ratio of the 41-kev–140-kev and 181-kev transitions is 1.2/1. A one-to-one ratio should exist for the areas under the 41-kev and 140-kev peaks of the coincidence curve. The actual area of the 41-kev peak recorded in Fig. 5 is considerably smaller, indicating a relatively large

conversion coefficient for the 41-kev line. From the areas and the conversion coefficient of the 140-kev radiation, the total conversion coefficient for the 41-kev radiation is calculated to be ~ 5. From the determined efficiency for detection of 181-kev radiation, the solid angle of its detector, and the data of Fig. 5, the ratio of intensities of the 741- and 780-kev gamma rays was calculated to be 2.6.

DISCUSSION OF RESULTS

The ground state of Tc^{99} has the orbital $g_{9/2}$. The two levels immediately above the ground state at 140 kev and 142 kev are characterized[5,8] by $7/2+$ and $p_{1/2}$. The two beta spectra have values of log ft such that both of them may be considered to fall in the category of either first-forbidden spectra ($\Delta I=0, \pm 1$; yes!) or l-forbidden spectra ($\Delta I=\pm 1$, no! $\Delta I=\pm 2$). The ground state of Mo^{99} ($N=57$, $Z=42$) may have any one of several orbitals:[9,10] $g_{7/2}$, $d_{5/2}$, $d_{3/2}$, or $s_{1/2}$. It has been previously shown that the harder beta spectrum of Mo^{99} is noncoincident with gamma rays[1] and terminates[5] at the level of orbital $p_{1/2}$. Were the ground state of Mo^{99} a $d_{5/2}$ configuration, an allowed beta transition, $d_{5/2}\rightarrow 7/2+$ would be present rather than the forbidden transition $d_{5/2}\rightarrow p_{1/2}$. Similarly, if the ground state of Mo^{99} be assumed to be a $g_{7/2}$ level, transitions to $7/2+$ or $g_{9/2}$ would be dominant. None of the above-mentioned allowed transitions are observed; therefore, $d_{5/2}$ and $g_{7/2}$ are rejected as possible orbital designations for the ground state of Mo^{99}. The orbital assignment of $d_{3/2}$ can also be eliminated. It is, however, first necessary to establish the characteristics of the 181-kev level in Tc^{99}. The conversion coefficient of the 41-kev gamma ray identifies it as magnetic dipole radiation ($\Delta I=0$, ± 1; no!). Since this transition terminates at $7/2+$, possible orbital values for the 181-kev level are $d_{5/2}$, $7/2+$, and $9/2+$. Assignment of $7/2+$ or $9/2+$ to the 181-kev level is ruled out by the absence of a gamma-ray transition from the 922-kev level to either the ground state or the level at 140 kev leaving the orbital of the 181-kev level to be $d_{5/2}$. If the ground state of Mo^{99} were of orbital $d_{3/2}$, an allowed beta transition terminating at the 181-kev level would be present. This spectrum is not observed.

The remaining possible orbital assignment for the ground state of Mo^{99} is $s_{1/2}$. If the softer beta spectrum were given a first-forbidden classification, the level at 922 kev in Tc^{99} would have orbitals of $p_{1/2}$ or $p_{3/2}$. If the spectrum is interpreted as l forbidden, the assignment of the 922-kev level would be $d_{3/2}$. The measurements of the present investigation show that the 741-kev and 780-kev gamma-ray transitions to levels of orbitals $d_{5/2}$ and $p_{1/2}$ have the same order of magnitude of probability of occurrence. If the 922-kev level is described as $p_{3/2}$, the multipolarities of the 741- and 780-kev gamma rays are, respectively, $E1$ and $M1$. If, instead of $p_{3/2}$, the level assignment is taken as $d_{3/2}$, the multipole properties of the two hard gamma rays are interchanged. Since the measurements of the present investigation have shown the 741-kev gamma ray to be more intense than the 780-kev line, an orbital assignment of $p_{3/2}$ for the 922-kev level is favored.

The intensity measurements also exclude the possibility that the 922-kev level has the orbital $p_{1/2}$, because were it so, the 741- and 780-kev gamma rays would be classified, respectively, as $M2$ and $M1$, which transitions are known to have greatly differing lifetimes.

ACKNOWLEDGMENT

The writers wish to express appreciation for the kind interest of Dr. W. F. G. Swann. They desire also to acknowledge several discussions with Dr. Franz R. Metzger relative to the measurements of this paper. One of the authors is indebted to the Bartol Research Foundation for a fellowship, making possible his stay in the United States.

[8] M. Goldhaber and R. D. Hill, Revs. Modern Phys. **24**, 179 (1952).
[9] Mayer, Moszkowski, and Nordheim, Revs. Modern Phys. **23**, 315 (1951).
[10] M. G. Mayer, Phys. Rev. **78**, 16 (1950).

The Ground States of Odd-Odd Nuclei

C. SCHWARTZ
Department of Physics and Laboratory of Nuclear Science, Massachusetts Institute of Technology, Cambridge, Massachusetts
(Received December 23, 1953)

Applications of techniques already developed for the study of atomic spectra to calculations on odd-odd nuclei give some particularly simple results. The spins of the ground states of nearly all odd-odd nuclei measured can be accounted for, and the validity of Nordheim's empirical rules is discussed.

INTRODUCTION

IT was found by Nordheim[1] that the total spin J of the ground state of odd-odd nuclei could be given by the rules:

$$J=|j_p-j_n|, \quad \text{if } l_p+j_p+l_n+j_n \text{ is even},$$
$$|j_p-j_n|<J\lesssim j_p+j_n, \quad \text{if } l_p+j_p+l_n+j_n \text{ is odd},$$

where j_p, j_n are the individual spins of the odd proton and odd neutron involved, and l_p, l_n their respective orbital quantum numbers as determined from the shell model most successful in the study of odd-even nuclei. The calculation of de-Shalit[2] on nuclei with one odd proton and one odd neutron outside closed subshells has given a theoretical basis for Nordheim's rule in this restricted case. Other calculations in special cases have been carried out by Kurath[3] and by Flowers.[4]

To discuss the general odd-odd nucleus with n_1 equivalent particles of one kind and n_2 equivalent particles of the other kind all outside closed subshells, we shall adopt the "odd group model." In this approach it is assumed that the particles in the two groups, i.e., protons and neutrons, first interact among themselves to give in their lowest states some well-defined resultant group angular momenta J_1 and J_2. It is expected that this approach, neglecting all but the ground configurations of the separate groups, should be valid for the determination of only the very lowest levels of the combined configuration.[2]

THE INTERACTION MATRIX

We shall start with the zeroth-order wave function of the Mayer-Jensen j-j coupled independent particle scheme with the two groups separately coupled to well-defined resultant angular momenta. The configuration of the n_1 particles of the first group is characterized by the quantum numbers l_1, j_1, J_1; that of the n_2 particles of the second group by l_2, j_2, J_2.

The wave function for the combined configuration with total spin J and magnetic quantum number M is then written:

$$\psi(j_1^{n_1}J_1,j_2^{n_2}J_2,JM)=\sum_{M_1M_2}\psi_1(j_1^{n_1}J_1M_1)\psi_2(j_2^{n_2}J_2M_2)\times(J_1M_1J_2M_2|J_1J_2JM).$$

Here we write the sequence $j_1^{n_1}J_1$ as meaning n_1 equivalent particles each of spin j_1 coupled to a resultant spin J_1; $j_2^{n_2}J_2$ is similarly read. This form has no special symmetries regarding interchange of protons and neutrons, which are thus considered as two distinct particles. Whatever the actual relation between proton and neutron may be, our approximation is certainly valid for heavier nuclei where the total isotopic spin is not a good quantum number.

At this point all the different levels of the total spin J are degenerate. Now introducing an attractive short-range interaction between particles of group one and those of group two, we shall calculate by perturbation theory the first-order energy shifts and see which state of total J is pushed deepest.

Taking the interaction between protons and neutrons as a sum of two-body static potentials, we have

$$V_{12}=\sum_{i=1}^{n_1}\sum_{j=1}^{n_2}V_{ij}, \tag{1}$$

where the indices i and j count particles in the first and second groups, respectively. Now, according to the techniques developed by Racah,[5] the two-particle interaction may be decomposed as

$$V_{ij}=-\sum_k f_k(r_i,r_j)t_i^{(k)}\cdot t_j^{(k)}. \tag{2}$$

Here $t_i^{(k)}$ is a tensor operator with respect to j_1 (thus also with respect to J_1 and J), of rank k, which operates only on the angle and spin coordinates of particle i. $t_j^{(k)}$ is similarly defined with respect to particle j, and $t_i^{(k)}\cdot t_j^{(k)}$ is the scalar product of the two tensors.

Since both groups contain equivalent particles, the radial part of the matrix element of every term in the double sum (1) and (2) will have the same value for a given k, namely

$$F_k=\int_0^\infty\int_0^\infty |R_1|^2|R_2|^2 f_k(r_1,r_2)r_1^2r_2^2dr_1dr_2, \tag{3}$$

where R_1 is the total radial part of the wave function characterized by l_1 and the principal quantum number of the state in question.

[1] L. W. Nordheim, Phys. Rev. **78**, 294 (1950).
[2] A. de-Shalit, Phys. Rev. **91**, 1479 (1953).
[3] D. Kurath, Phys. Rev. **87**, 218 (1952) and **91**, 1430 (1953).
[4] B. H. Flowers, Proc. Roy. Soc. (London) **A212**, 248 (1952).
[5] G. Racah, Phys. Rev. **62**, 438 (1942).

If we now set

$$T_1^{(k)}=\sum_{i=1}^{n_1} t_i^{(k)} \quad \text{and} \quad T_2^{(k)}=\sum_{j=1}^{n_2} t_j^{(k)}, \tag{4}$$

Eqs. (1), (2), (3) combine to give

$$V_{12}=-\sum_k f_k(r_1,r_2)T_1^{(k)}\cdot T_2^{(k)}. \tag{5}$$

For the first-order energy shifts we take the diagonal matrix element of (5). Using (3) we obtain:

$$E(j_1^{n_1}J_1,j_2^{n_2}J_2,J)=-\sum_k F_k(j_1^{n_1}J_1,j_2^{n_2}J_2,JM \times|T_1^{(k)}\cdot T_2^{(k)}|j_1^{n_1}J_1,j_2^{n_2}J_2,JM). \tag{6}$$

Now since $T_1^{(k)}$ operates only on particles of group one and $T_2^{(k)}$ only on particles of group two, we can use a well-known theorem of Racah[6] to decompose this matrix element (6) of $T_1^{(k)}\cdot T_2^{(k)}$ into the reduced matrix elements:

$$(-1)^{J_1+J_2-J}(j_1^{n_1}J_1\|T_1^{(k)}\|j_1^{n_1}J_1)(j_2^{n_2}J_2\|T_2^{(k)}\| \times j_2^{n_2}J_2)W(J_1J_2J_1J_2;Jk), \tag{7}$$

where W is a Racah coefficient.[6]

If, for the j-j coupled[6] configuration j^nJ, we define the Q operator and seniority number v in a manner completely analogous to that done for LS coupling,[7] it is not difficult to derive the pertinent equivalent of Racah's Eq. (69)III:

$$(j^nvJ\|T^{(k)}\|j^nvJ')=(j^vvJ\|T^{(k)}\|j^vvJ') \times\frac{(2j+1-n-v)-(-1)^k(n-v)}{2j+1-2v}, \tag{8}$$

except for $k=0$.

This equation gives for any irreducible tensor operator $T^{(k)}$ the matrix element in a configuration of n particles with seniority v in terms of the matrix element in the configuration of only v particles. For example, if we take $T^{(k)}$ to be the quadrupole moment operator $Q=(16\pi/5)^{\frac{1}{2}}Y_0^2$ (the normalized spherical harmonic is here written as Y_m^l) and v happens to be one ($J=j$), Eq. (8) tells us that the quadrupole moment for the configuration $j^n(J=j)$ is $(2j+1-2n)/(2j-1)$ times the quadrupole moment for a single particle in that state with the same orientation.

Now it has been shown by Edmonds and Flowers[8] and also by Racah[9] that for a wide variety of attractive interactions among like particles the ground state of the configuration j^n for n odd has seniority $v=1$. This gives rise to Mayer's rule that an odd number of equivalent protons or neutrons couple to a resultant J equal to the j of the individual particles. With $v=1$, Eq. (8) reads

$$(j^nJ=j\|T^{(k)}\|j^nJ=j)=(j\|T^{(k)}\|j), \quad \text{for } k \text{ odd}; \tag{9a}$$

$$(j^nJ=j\|T^{(k)}\|j^nJ=j)=(j\|T^{(k)}\|j)\frac{2j+1-2n}{2j-1}, \quad \text{for } k \text{ even}, \tag{9b}$$

except for $k=0$. With an interaction of the Wigner type, i.e., V_{ij} a function of $\mathbf{r}_i-\mathbf{r}_j$ only, it is well known that[5]

$$t_i^{(k)}=(4\pi)^{\frac{1}{2}}Y_i^{(k)}. \tag{10}$$

If we have a spin force of the form

$$V_{ij}=\boldsymbol{\sigma}_i\cdot\boldsymbol{\sigma}_jV(\mathbf{r}_i-\mathbf{r}_j), \tag{11}$$

then

$$t_i^{(k')}=(4\pi)^{\frac{1}{2}}Y_i^{(k)}\sigma_i^{(1)}$$

($\boldsymbol{\sigma}$ is a tensor of rank one) is not an irreducible tensor, but it may be expressed as a sum of irreducible tensors of ranks:

$$k'=k-1,\ k,\ k+1.$$

It can be shown[2,6] that only terms for which k and also $k'+k+1$ are even numbers, contribute in the evaluation of the necessary matrix elements.

Thus for a $\boldsymbol{\sigma}\cdot\boldsymbol{\sigma}$ force the tensors T_1 and T_2 in (7) are of odd rank only. Equation (9a) then tells us that

$$E_\sigma(j_1^{n_1}J_1=j_1,\ j_2^{n_2}J_2=j_2,\ J)=E_\sigma(j_1j_2J) \quad \text{for } \boldsymbol{\sigma}\cdot\boldsymbol{\sigma} \text{ force}. \tag{12}$$

But $E_\sigma(j_1j_2J)$ was just the term calculated by de-Shalit.[2] In the limit of zero range force,

$$E_\sigma(j_1^{n_1}J_1=j_1,\ j_2^{n_2}J_2=j_2,\ J)=E_\sigma(j_1j_2J) =-\tfrac{1}{2}F_0(2j_1+1)(2j_2+1)(j_1\tfrac{1}{2}j_2-\tfrac{1}{2}|j_1j_2J0)^2\frac{1}{2J+1} \times\left\{\frac{[(2j_1+1)+(-1)^{j_1+j_2+J}(2j_2+1)]^2}{4J(J+1)} -[1+2(-1)^{j_1+j_2+J}]\right\}. \tag{13}$$

For Wigner force T_1 and T_2 are of even rank. Noting[5] that T_1^0 is the scalar n_1 and

$$(j_1^{n_1}J_1=j_1\|T_1^0\|j_1^{n_1}J_1=j_1)=n_1(2j_1+1)^{\frac{1}{2}},$$

and similarly for T_2^0, and also with

$$(-1)^{j_1+j_2-J}W(j_1j_2j_1j_2;J0)=[(2j_1+1)(2j_2+1)]^{-\frac{1}{2}},$$

we have finally

$$E_W(j_1^{n_1}J_1=j_1,\ j_2^{n_2}J_2=j_2,\ J) =\frac{2j_1+1-2n_1}{2j_1-1}\frac{2j_2+1-2n_2}{2j_2-1}E_W(j_1j_2J) -F_0\left[n_1n_2-\frac{2j_1+1-2n_1}{2j_1-1}\frac{2j_2+1-2n_2}{2j_2-1}\right]. \tag{14}$$

[6] G. Racah and I. Talmi, Physica 18, 1097 (1952).
[7] G. Racah, Phys. Rev. 63, 367 (1943).
[8] A. R. Edmonds and B. H. Flowers, Proc. Roy. Soc. (London) A214, 515 (1952).
[9] G. Racah, *L. Farkas Memorial Volume*. (Research Council of Israel, Interscience Publishers, New York, Agents, 1952), p. 294.

TABLE I. $-E(j_1j_2J)/F_0$ for zero range forces.

j_1	1/2			3/2			5/2			7/2			9/2			$J-j_1$	j_2
	W	σ^+	σ^-	W	σ^+	σ^-	W	σ^+	σ^-	W	σ^+	σ^-	W	σ^+	σ^-		
	1	−3	1	1	1	−1.67	1	−1.40	1	1	1	−1.28	1	−1.22	1	−1/2	1/2
	1	1	−0.33	1	−0.60	1	1	1	−0.71	1	−0.78	1	1	1	−0.82	+1/2	
				2	−6	2	1.8	1.8	−3	1.72	−2.40	1.72	1.67	1.67	−2.14	−3/2	
				1.20	1.20	0.67	0.89	0.20	0.89	0.76	0.76	0	0.70	−0.11	0.70	−1/2	3/2
				0.40	−1.20	0.40	0.37	0.37	−1	0.38	−0.89	0.38	0.39	0.39	−0.82	+1/2	
				1.20	1.20	−0.86	1.29	−1	1.29	1.33	1.33	−1.09	1.36	−1.15	1.36	+3/2	
							3	−9	3	2.57	2.57	−4.29	2.38	−3.33	2.38	−5/2	
							1.63	1.63	1.29	1.05	0.59	1.05	0.82	0.82	0.30	−3/2	
							0.69	−2.06	0.69	0.62	0.62	−1.67	0.62	−1.45	0.62	−1/2	5/2
							0.91	0.91	0	0.90	−0.14	0.90	0.88	0.88	−0.24	+1/2	
							0.29	−0.86	0.29	0.27	0.27	−0.77	0.27	−0.71	0.27	+3/2	
							1.43	1.43	−1.17	1.52	−1.28	1.52	1.57	1.57	−1.36	+5/2	
										4	−12	4	3.33	3.33	−5.56	−7/2	
										2.10	2.10	1.84	1.25	0.91	1.25	−5/2	
										0.95	−2.86	0.95	0.84	0.84	−2.27	−3/2	
										0.99	0.99	0.36	0.91	0.19	0.91	−1/2	7/2
										0.47	−1.40	0.47	0.43	0.43	−1.24	+1/2	
										0.94	0.94	−0.26	0.95	−0.35	0.95	+3/2	
										0.23	−0.70	0.23	0.22	0.22	−0.65	+5/2	
										1.63	1.63	−1.42	1.71	−1.51	1.71	+7/2	

Again, for zero range forces,[2]

$$E_W(j_1j_2J) = -\tfrac{1}{2}F_0(2j_1+1)(2j_2+1)(j_1\tfrac{1}{2}j_2-\tfrac{1}{2}|\,j_1j_2J0)^2\frac{1}{2J+1} \times\left\{1+\frac{[(2j_1+1)+(-1)^{j_1+j_2+J}(2j_2+1)]^2}{4J(J+1)}\right\}. \quad (15)$$

In Table I are given values of $-E(j_1j_2J)/F_0$ computed from Eqs. (13), (15) with columns headed W for Wigner force and $\sigma\pm$ for spin force in states of positive and negative parity, respectively.

DISCUSSION

Wigner forces alone will not give the desired distinction between configurations of various l's, so we shall investigate the usefulness of a mixture of Wigner and Bartlett forces. If we take the interaction as

$$V_{ij}=-[(1-\alpha)+\alpha\sigma_i\cdot\sigma_j]\delta(\mathbf{r}_i-\mathbf{r}_j), \quad (16)$$

it is interesting to plot against α the energy levels characterized by the different ways in which J_1 and J_2 can combine to the resultant J. In Fig. 1 are a typical set of such graphs for various values of n_1 and n_2 when we have chosen $j_1=5/2$, $j_2=7/2$ and l_1+l_2 is even. de-Shalit gives a number of such graphs for several values of j_1 and j_2 when $n_1=n_2=1$.

From Eqs. (12), (14) we can easily see how these graphs change as we put more particles in each shell:

For a pure $\sigma_1\cdot\sigma_2$ force, $\alpha=1$, the level structure is independent of n_1 and n_2.

for a pure Wigner force, $\alpha=0$, increasing n_1 and n_2 both lowers and compresses the level structure. The former effect, due to the second term in Eq. (14), and, in fact, any translation of the energy scale can be ignored here since it does not affect the level spacing at any mixture. As n_1 and n_2 increase through the first halves of their respective shells, the levels are bilinearly compressed. When either group is exactly half of a filled shell, all the levels (on the Wigner side) are degenerate. As one group only passes through the second half of its shell the levels are inverted and dilated: n_1 holes and n_2 particles give exactly the inverted level structure of n_1 particles and n_2 particles. n_1 holes and n_2 holes are again equivalent to n_1 particles and n_2 particles.

Surveying the data on odd-odd nuclei of Nordheim[10] and of Goldhaber and Hill,[11] and the recent note of

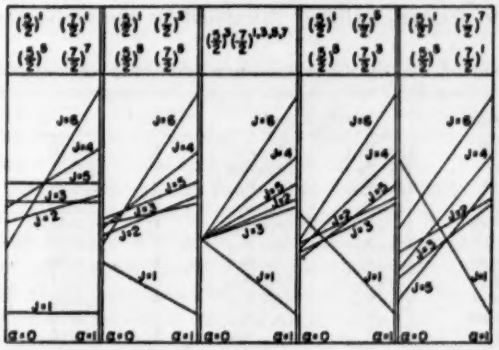

FIG. 1. Energy levels of configurations $(5/2)^{n_1}(7/2)^{n_2}$ with positive parity under interaction $V_{12}=-[(1-\alpha)+\alpha\sigma_1\cdot\sigma_2]\delta(\mathbf{r}_1-\mathbf{r}_2)$. Both subgroups have seniority one.

[10] L. W. Nordheim, Revs. Modern Phys. 23, 322 (1951).
[11] M. Goldhaber and R. D. Hill, Revs. Modern Phys. 24, 179 (1952).

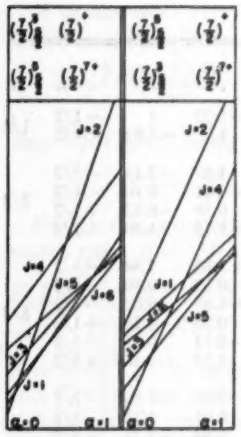

FIG. 2. Energy levels of configurations $(7/2)^{n_1}{}_{5/2}(7/2)^{n_2}{}_{7/2}$ with positive parity under interaction $V_{12}=-[(1-\alpha)+\alpha\sigma_1\cdot\sigma_2]\delta(\mathbf{r}_1-\mathbf{r}_2)$.

King and Peaslee,[12] we find that the above considerations furnish an excellent accounting of the measured and indicated ground state spins. Except for a few nuclei with the configurations $(3d_{5/2})^3$ and $(4f_{7/2})$,[3,5] there were no cases which could not be fitted to our graphs. However, it is known from the spins and magnetic moments of the odd-even nuclei Na^{23} and Mn^{55} that these exceptional configurations are probably not of seniority one and must be treated separately (see next section).

In many cases where the spin was known the configurations could be unambiguously assigned. In cases where measurements were incomplete, some certainty about the configurations involved allowed prediction of the most probable spin.

EXCEPTIONAL CONFIGURATIONS

In some cases it is desirable to calculate the level schemes involving configurations of seniority other than one. For such work we need a general relation between the perturbation energy in the state $(j_1^{n_1}J_1, j_2^{n_2}J_2, J)$ and the terms already calculated for the simple case $n_1=n_2=1$. Such a relation is

$$E(j_1^{n_1}J_1, j_2^{n_2}J_2, J) = n\sum_{J_1'J'}(2J_1+1)(2J'+1)W^2(J_1'j_1JJ_2;J_1J')\times(j_1^{n_1-1}(J_1'),j_1J_1\|j_1^{n_1}J_1)^2E(j_1,j_2^{n_2}J_2,J'),$$

$$E(j_1,j_2^{n_2}J_2,J) = n_2\sum_{J_2'J''}(2J_2+1)(2J''+1)W^2(J_2'j_2J'j_1;J_2J'')\times(j_2^{n_2-1}(J_2'),j_2J_2\|j_2^{n_2}J_2)^2E(j_1j_2J''),$$

where $(j_1^{n_1-1}(J_1'),j_1J_1\|j_1^{n_1}J_1)$ is the fractional parentage coefficient for the configuration $j_1^{n_1}J_1$ as computed by Edmonds and Flowers.[8] Of use in checking numerical work is the sum rule

$$\sum_J(2J+1)E(j_1^{n_1}J_1,j_2^{n_2}J_2,J) = -n_1n_2(2J_1+1)(2J_2+1)F_0. \quad (18)$$

Using Eq. (17) and Table I, we have computed the energy levels for the configuration $(7/2)^3{}_{5/2}(7/2)$ with positive parity under the perturbing potential (16). Since (8) still gives the correct relation between particles and holes for any seniority, we have the several cases shown in Fig. 2.

The spin 4 for Sc^{46} is well accounted for, and we would predict spin 6 for Mn^{52} and 4 or 5 for V^{50}. Recent work[13] gives spin 6 for V^{50}, which is best accounted for by assigning seniority one to the $(7/2)^3$ proton configuration.[14] For Sc^{44} the indicated spin 2 can be fitted only with an extremely small value of α. The correct configuration here is most likely a mixture of $(7/2)^3{}_{5/2}$ and $(7/2)^3{}_{7/2}$; this may also be the case in Mn^{52}.

For F^{20} the configuration $(s_{1/2})[(d_{5/2})^3{}_{5/2}]$ would have $J=3$ lowest whereas $(s_{1/2})[(d_{5/2})^3{}_{3/2}]$ would have $J=2$ lowest. The measurements do not yet indicate which of these two is correct.

Calculations for the nuclei Na^{22} and V^{48} with both neutron and proton configurations having seniority different from one require performing both sums of (17) and have not been carried out. However, for the latter nucleus, letting only one group have seniority one would lead to spin 4 or 5, which are the most probable indicated values.

TABLE II. Effective n-p force mixtures indicated by observed spins

Nucleus	Configurations		Spin	α
Li^6	$(p_{3/2})^1{}_{3/2}$	$(p_{3/2})^1{}_{3/2}$	1	$\geqslant 0.10$
Li^8	$(p_{3/2})^1{}_{3/2}$	$(p_{3/2})^2{}_{3/2}$	2	$\leqslant 0.25$
B^8	$(p_{3/2})^3{}_{3/2}$	$(p_{3/2})^1{}_{3/2}$	2	$\leqslant 0.25$
B^{10}	$(p_{3/2})^3{}_{3/2}$	$(p_{3/2})^3{}_{3/2}$	3	$\geqslant 0.10$
Na^{24}	$(d_{5/2})^1{}_{3/2}$	$(d_{5/2})^3{}_{3/2}$	4	$\leqslant 0.42$
Cl^{36}	$(d_{3/2})^1{}_{3/2}$	$(d_{3/2})^2{}_{3/2}$	2	$\leqslant 0.25$
K^{40}	$(d_{3/2})^3{}_{3/2}$	$(f_{7/2})^1{}_{7/2}$	4	$\leqslant 0.50$
K^{42}	$(d_{3/2})^3{}_{3/2}$	$(f_{7/2})^3{}_{7/2}$	2	$\geqslant 0.17$
Sc^{46}	$(f_{7/2})^1{}_{7/2}$	$(f_{7/2})^5{}_{7/2}$	4	$\leqslant 0.30$
Co^{58}	$(f_{7/2})^7{}_{7/2}$	$(p_{3/2})^2{}_{3/2}$	2	$\leqslant 0.10$
Co^{60}	$(f_{7/2})^7{}_{7/2}$	$(p_{3/2})^3{}_{3/2}$	5	$\geqslant 0.10$
	or			
		$(f_{5/2})^1{}_{5/2}$		$\leqslant 0.50$
Rb^{88}	$(p_{3/2})^3{}_{3/2}$	$(d_{5/2})^1{}_{5/2}$	2	$\geqslant 0.17$; $\leqslant 0.50$
Sb^{122}	$(g_{7/2})^7{}_{7/2}$	$(h_{11/2})^7{}_{11/2}$	2	$\geqslant 0.10$

CONCLUSIONS

In Table II are listed a number of nuclei from which we may infer something about the necessary amount of mixture of the two forces considered. It should be remarked that the two-body interaction taken as a perturbation here is not the total neutron-proton force but is supposed to be the residual of an averaging over all interparticle forces which gives the central potential well of the shell model. Especially since none

[12] R. W. King and D. C. Peaslee, Phys. Rev. **90**, 1001 (1953).

[13] Kikuchi, Sirvetz, and Cohen, Phys. Rev. **88**, 142 (1952).

[14] A. Hitchcock, Phys. Rev. **87**, 664 (1952).

but a scalar potential survives between outer particles and any subgroup coupled to zero total spin, there is no simple reason to expect the mixture of forces in the perturbation to be independent of A. However, with the exception of Co^{58} all of the nuclei can be fitted with a value of α between $\frac{1}{8}$ and $\frac{1}{4}$.

With regard to Nordheim's rules, we now see that their validity is not as general as was first indicated in the case of one odd proton and one odd neutron. Certainly for one less than a filled shell of both neutrons and protons they are equally valid; and the "strong" rule,

$$J=|j_p-j_n|, \quad \text{for } j_p+j_n+l_p+l_n \text{ even},$$

is still good when n_1 and n_2 are both more or both less than half of a filled shell. However, in general, the situation is more complicated, especially as it is unsafe to rely on the constancy of the mixture of forces.

The writer wishes to acknowledge the assistance of Dr. A. de-Shalit, who instigated this work and gave extensive advice throughout its development.

PHYSICAL REVIEW VOLUME 94, NUMBER 1 APRIL 1, 1954

The Decay Scheme of Zr^{95}†*

PHILLIP S. MITTELMAN‡
Rensselaer Polytechnic Institute, Troy, New York
(Received September 8, 1953)

The decay scheme of Zr^{95} has been studied using the techniques of beta-ray spectroscopy and beta-gamma angular correlation. The decay of Zr^{95} is found to proceed by three beta gamma cascades. Two of the beta transitions are allowed and proceed to Nb^{95} levels at 722.0 kev and 754.4-kev. The third beta transition is to a 235-kev level in Nb^{95}. From K-conversion coefficient determinations and shell theory the 722-kev and 754.4-kev levels are both assigned even parity and a spin of 5/2 or 7/2.

THE radiations originating from the decay of Zr^{95} have been studied by a number of investigators with somewhat divergent results. A recent paper by Cork *et al.*,[1] published after the completion of this study, contains an excellent survey of the previous work.

In the present investigation, beta-ray spectrometer studies were made of the Zr^{95} spectra and gamma ray conversion lines. In addition, the angular correlation between the Zr^{95} beta and gamma rays in cascade to the ground state of Nb^{95} was measured.

BETA-RAY SPECTROMETER STUDIES

The beta-ray spectrometer used in this investigation was a double-focusing, high-resolution spectrometer patterned after that of Kurie, Slack, and Osaba.[2] In most of the runs reported here it was operated at a resolution of 0.2 percent. The electron detector used for studies of the shape of the beta spectrum was an end-window Geiger counter with a 0.6-mg/cm² rubber hydrochloride window. Later studies of conversion lines and of the high-energy end of the beta spectrum employed an end-window counter with a 3-mg/cm² mica window.

The magnetic field in the spectrometer was measured using a double-coil monitor with a temperature-stabilized permanent magnet supplying the reference field. The magnetic field could be kept constant to within 1 part in 20,000 for extended periods of time.

The source material used in all of the experiments consisted of a $Zr^{95}-Nb^{95}$ oxalate mixture obtained from Oak Ridge National Laboratory. The Oak Ridge analysis indicated that the radiochemical purity of the source material was better than 99 percent and that the source initially consisted of 40 percent Zr^{95} and 60 percent Nb^{95}.

The source for the spectrometer study of the spectrum shape was prepared by laying down the source material in the form of a line 3 mm wide by 1 inch high on a thin formvar film on which a film of gold had been vacuum evaporated. The areal density of the source backing was less than 125 μg/cm². The areal density of the source material was approximately 50 μg/cm².

Figure 1 shows the Kurie plot obtained with this source. It will be noted that the plot has an "allowed" shape from the end point of the Nb^{95} spectrum at 160 kev out to approximately 360 kev. At the high-energy end of the spectrum the 900-kev branch of the Zr^{95} decay is in evidence but the source was too weak to make significant measurements on it. The K conversion line resulting from the 235-kev isomeric transition in Nb^{95} is also in evidence in this figure.

The conversion lines from the gamma ray transitions in Nb^{95} and Mo^{95} were examined with a stronger source. This source was prepared by ruling a line 1 mm wide and

† This work was carried out in partial fulfillment of the requirements for the Ph.D. degree at Rensselaer Polytechnic Institute. It was supported by the U. S. Atomic Energy Commission.
* This work was reported at the 1953 Washington meeting of the American Physical Society.
‡ Now at Nuclear Development Associates, Inc., White Plains, New York.
[1] Cork, LeBlanc, Martin, Nester, and Brice, Phys. Rev. 90, 579 (1953).
[2] Kurie, Osaba, and Slack, Rev. Sci. Instr. 19, 771-6 (1948).

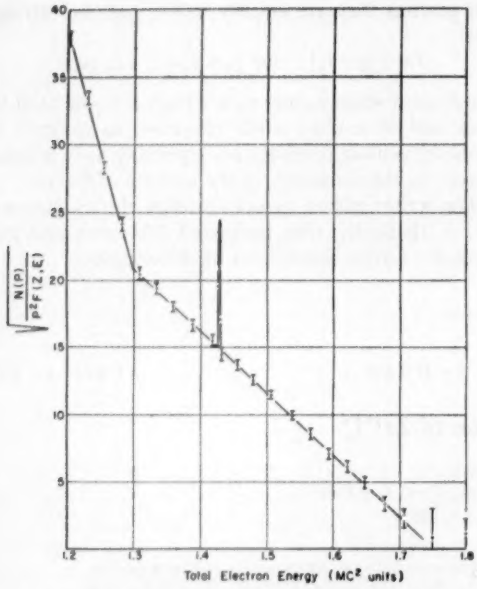

FIG. 1. Fermi plot of the beta spectrum from a mixed $Zr^{95}-Nb^{95}$ source.

1 inch high on 2.7-mg/cm² aluminum foil. The areal density of the source material was approximately 300 μg/cm². Preliminary examinations of the conversion lines indicated the presence of three gamma rays in the 700-kev region. Previous investigations had indicated that only two gamma rays were to be expected in this region, one from an excited state of Nb^{95} at 708 kev and a second from an excited state of Mo^{95} at 760 kev. To determine the origin of the third conversion line, careful studies were made of the *K* and *L* conversion lines with the result shown in Fig. 2. In this figure can be seen the three *K* lines with their associated *L* and *M* lines. The energy differences between the *K* and *L* lines for each of the three sets

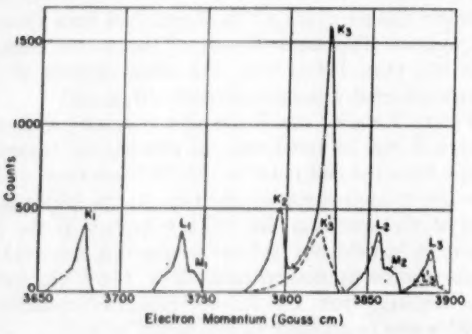

FIG. 2. High-energy internal conversion lines from a mixed $Zr^{95}-Nb^{95}$ source. Counting times for K_1, K_2, and K_3 were three minutes per point; for L_1, L_2, M_1, and M_2, twenty minutes; for L_3, four minutes.

of conversion lines are compared in Table I to the energy differences possible for conversion in Nb^{95} and for conversion in Mo^{95}. It can be seen that gamma rays No. 1 and No. 2 are to be associated with conversion in Nb^{95} and gamma ray No. 3 with conversion in Mo^{95}.

To verify the element assignments, a source rich in Nb^{95} was made. This source was prepared by precipitating Nb^{95} from a solution of $Zr^{95}-Nb^{95}$ oxalate in *10N* HNO_3 by $KMnO_4$ following the method of Connick and McVey.[3] The precipitate containing the Nb^{95} was dissolved in H_2O_2 and laid down as a line source on 2.7-mg/cm² aluminum. The conversion lines obtained with this source are labelled K_3' and L_3' on Fig. 2. It will be noted that the position of K_3' coincides with K_3 in agreement with the previous element assignment of the three gamma rays.

The energies of the gamma rays were determined by making up a mixed $Cs^{137}-Zr^{95}-Nb^{95}$ source on aluminum. Assuming that $H\rho=3380.5\pm3$ gauss-cm for the Ba^{137} conversion line, according to Langer and Moffat,[4] the energies of the three gamma rays are $\gamma_1=722.0\pm1.4$ kev, $\gamma_2=754.4\pm1.4$ kev, $\gamma_3=764.0\pm1.4$ kev.

The presence of two high-energy gamma rays in the decay scheme of Zr^{95} suggested the possibility that there might be two beta branches in the Zr^{95} decay differing in end-point energy by approximately 32 kev. To examine this possibility, a study was made of the high-energy portion of the Zr^{95} beta spectrum using the source prepared for the conversion line studies.

Figure 3 shows the total Zr^{95} beta spectrum near its end point with the 900-kev beta branch subtracted. The total spectrum of Fig. 3 clearly indicates the presence of two partial spectra. Since the energy difference between the two Zr^{95} gamma rays could be determined more precisely than the difference in beta energies from a partial spectrum analysis of the data, the 32-kev energy difference between γ_1 and γ_2 was used as a criterion for drawing the best partial spectra lines to fit the beta spectrum data. These two lines are designated *B* and *C* in Fig. 3 with end points at 364 and 396 kev, respectively. Extrapolating the resolved spectra back to zero electron kinetic energy the branching ratio could be determined. The average of two such determinations yielded a value 1.38 ± 0.1 for the ratio of the intensity of the low-energy branch to that of the high-energy branch.

The conversion line studies yielded the number of conversion electrons for each gamma ray. Associating the 754-kev gamma ray with the low-energy beta branch and the 722-kev gamma ray with the high-energy beta branch, the *K*-conversion coefficient for the 722-kev gamma ray is $1.38\pm0.2\times10^{-3}$ and that of the 754-kev gamma ray is $1.14\pm0.17\times10^{-3}$. According

[3] R. E. Connick and W. H. McVey, J. Am. Chem. Soc. **71**, 3182 (1949).

[4] L. M. Langer and R. Moffat, Phys. Rev. **78**, 74 (1950).

to the tables of Rose, Goertzel, and Perry,[5] these values for the K conversion coefficient are consistent with either $E2$ or $M1$ transition for each of the gamma rays.

BETA-GAMMA ANGULAR CORRELATION MEASUREMENTS

Preliminary to the spectrometer studies of the Zr^{95} beta spectrum, the beta-gamma angular correlation of the beta-gamma cascades in Zr^{95} had been studied.

The radioactive source was mounted in the center of a brass vacuum chamber 5 in. in diameter, 5 in. high and $\frac{1}{8}$ in. thick. A 2 in.-diameter brass tube opening into the vacuum chamber contained the beta detector which consisted of an RCA 5819 photomultiplier with a $\frac{1}{8}$ in. thick anthracene crystal mounted on its photocathode. The crystal was set 5 in. from the source. An 80-mil aluminum disk with a 1 in. diameter hole in its center, mounted in the tube between the source and the crystal, served to prevent electrons, scattered from the main vacuum tank and from the tube wall, from reaching the beta detector. A second 5819 photomultiplier fitted with a $\frac{3}{4}$ in. thick anthracene crystal was mounted outside the vacuum chamber and served as the movable gamma detector. The crystal of this detector was shielded with at least 1 in. of lead on all sides and with 0.1 in. of lead in the direction of the source. The output of each photomultiplier was fed to a cathode follower pre-amplifier and then to a Hewlett-Packard wide band amplifier and finally into a fast coincidence circuit (resolving time 5×10^{-8} sec). Coincidence pulses from the coincidence circuit were amplified in a Model 100 amplifier and recorded on a binary scalar.

Preliminary studies of the angular correlations of the beta-gamma cascades in Co^{60} and Rb^{86} were made with this apparatus. Assuming that the counting rate as a function of the angle θ between the beta and gamma detectors is given by

$$\omega(\theta)=a+b\cos^2\theta,$$

the value of b/a was determined to be 0.00 ± 0.02 for Co^{60} and 0.13 ± 0.05 for Rb^{86}. These values are in good agreement with the work of many investigators for Co^{60},[6-9] and with the work of Stevenson and Deutsch for Rb^{86}.[9]

For the study of the Zr^{95} angular correlation a source composed of 40 percent Zr^{95} and 60 percent Nb^{95} was used. The source consisted of a drop of the $Zr^{95}-Nb^{95}$ oxalate mixture evaporated to dryness on a thin, gold plated, formvar film (mass density 100 $\mu g/cm^2$). The source strength was approximately 70 microcuries and the source density about 300 $\mu g/cm^2$. To eliminate the effect of the Nb^{95} beta-gamma cascade 12 mg/cm^2 aluminum was placed in front of the beta detector.

The value of b/a resulting from this investigation was 0.005 ± 0.03. In the light of the later spectrometer studies, it should be noted that two distinct beta-gamma cascades were being detected and therefore the value of this measurement is open to question.

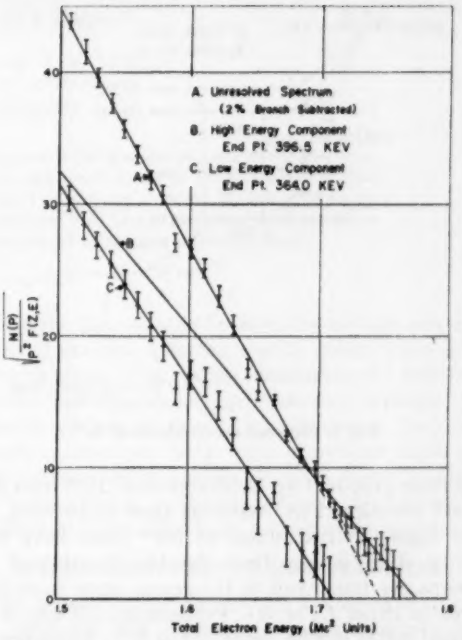

FIG. 3. Fermi plot of the high-energy end of the Zr^{95} beta spectrum.

DISCUSSION AND CONCLUSION

In the light of the above experimental results, the decay scheme of Fig. 4 is proposed for Zr^{95}. This decay scheme is in good agreement with that proposed by Cork *et al.*[1]

The spin and parity assignments of the ground states of Zr^{95} and Nb^{95} and of the first excited state of Nb^{95}

TABLE I. Comparison of experimentally determined $K-L$ energy differences with values determined from critical x-ray absorption energies.[a]

Experimental ($K-L$) energy differences (kev)	Possible $K-L$ differences (kev) Conversion in Nb^{95}	Conversion in Mo^{95}
Gamma No. 1 16.38±0.4	$(K-L_1)$ 16.286	$K-L_1$ 17.134
Gamma No. 2 16.20±0.4	$K-L_2$ 16.519	$K-L_2$ 17.373
Gamma No. 3 17.13±0.4	$K-L_3$ 16.614	$K-L_3$ 17.478

[a] Hill, Church and Mihelich, Rev. Sci. Instr 23, 523 (1952).

[5] Rose, Goertzel, and Perry, Oak Ridge National Laboratory Report ORNL 1023, 1951 (unpublished).
[6] J. R. Beyster and M. L. Wiedenbeck, Phys. Rev. **79**, 728 (1950).
[7] R. L. Garwin, Phys. Rev. **76**, 1876 (1949).
[8] Grace, Allen, and Halban, Nature **164**, 538 (1949).
[9] D. T. Stevenson and M. Deutsch, Phys. Rev. **83**, 1202 (1951).

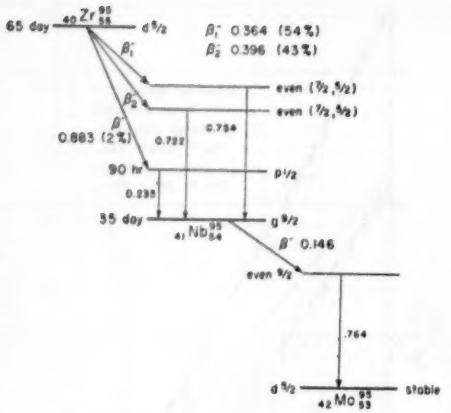

FIG. 4. Proposed decay scheme of Zr^{95}.

are those proposed by Goldhaber and Hill[10] from shell model considerations. Assuming these to be valid, the two highly excited states of Nb^{95} must have even parity. This follows from the identification of the gamma ray transitions to the ground state from these levels as either $E2$ or $M1$. Furthermore the spin of the excited states can be either 7/2 or 5/2. Assignment of 9/2, 11/2, or 13/2 to these levels is ruled out since the Zr^{95} beta transition would be second or higher forbidden in contradiction to the experimental evidence. Using the tables of Feenberg and Trigg,[11] the ft value for the 396-kev branch is 6.9 and that for the 364-kev branch is 6.7. These can at most be associated with once forbidden transitions. Actually the proposed spin and parity assignments indicate that both beta transitions are allowed. Such high ft values for $\Delta I=0,1$ (no) transitions have been reported for Y^{87}, Zr^{89} and other isotropes by Goldhaber and Hill,[10] and are discussed in detail by de-Shalit and Goldhaber.[12]

The proposed spin and parity assignments are in agreement with the fact that the gamma ray transition to the 235-kev level of Nb^{95} is weak or nonexistent. They also lead to the conclusion that the 32.4-kev transition between the two Nb^{95} levels should be very weak.

Since the 754-kev and 722-kev levels of Nb^{95} may be many particle states, no specific orbitals have been assigned. However, the shell model[13] predicts that the next excited levels above $g_{9/2}$ should be $g_{7/2}$ and $d_{5/2}$ and that these should differ only slightly in energy. This prediction is in very good agreement with the proposed level assignment.

The beta-gamma angular correlation work is not in disagreement with the proposed level assignments. The lack of angular correlation implies an allowed shape for the beta spectra[14] and, as noted above, this is predicted by the level assignment and observed in the experiments.

The author wishes to thank the members of his thesis committee, Drs. G. N. Glasoe, W. A. McKinley, and H. A. Landon for their advice and encouragement during the course of this work, and Dr. R. King of Nuclear Development Associates for many informative discussions on nuclear shell theory. Special thanks are also due to Dr. B. Hildebrand and Mr. R. A. Liedtke for their aid in connection with the operation of the spectrometer.

[10] M. Goldhaber and R. D. Hill, Revs. Modern Phys. **24**, 179 (1952).
[11] E. Feenberg and G. L. Trigg, Revs. Modern Phys. **22**, 399 (1950).
[12] A. de-Shalit and M. Goldhaber, Phys. Rev. **92**, 1211 (1953).
[13] M. G. Mayer, Phys. Rev. **78**, 16 (1950).
[14] D. L. Falkoff and G. E. Uhlenbeck, Phys. Rev. **79**, 323, 334 (1950).

Decay of $_{65}Tb^{160}$ (71 Day)

S. B. Burson, W. C. Jordan, and J. M. LeBlanc
Argonne National Laboratory, Lemont, Illinois
(Received December 28, 1953)

By means of 180° internal-conversion electron spectrometers and the scintillation coincidence spectrometer, the radiations of $_{65}Tb^{160}$ (71 day) have been studied. In addition to many of the previously reported transitions in Dy^{160}, three new gamma rays of 0.759, 1.17, and 1.26 Mev are observed. By using the energy values determined from the internal conversion studies together with beta-gamma and gamma-gamma coincidence results a decay scheme is deduced which is consistent with the experiments discussed.

INTRODUCTION

NEUTRON capture in terbium produces a long-lived activity first observed by Bothe[1] who assigned to it a half-life of 73.5 days. The value determined at this laboratory[2] was 71±1 days. In addition to gamma rays Bothe's absorption measurements indicated the presence of several beta rays, the one of highest energy being about 0.75 Mev. From the fact that Tb exists in nature only as stable Tb^{159}, it was deduced that the activity belonged to Tb^{160}. This assignment was confirmed by mass spectrometer measurements.[3] The beta spectrum was resolved by Cork *et al.*[4] into two components of 546 and 882 kev and the presence of numerous gamma rays was ascertained by internal conversion electron measurements. Burson *et al.*[2] resolved the beta spectrum into three components with end-point energies of 860, 521, and 396 kev. Internal conversion lines corresponding to five gamma rays were also observed. Salmi's measurement[5] of the beta spectrum with a double-focusing spectrometer indicated only two components with end-point energies of 886 and 546 kev. Shavtvalov[6] reports a 40 percent beta-ray branch of 850 kev and a 60 percent component referred to as "540, 590 kev." His measurements also indicate that internal conversion electrons representing the 86.3-kev transition are in coincidence predominantly with the lower-energy beta group. McGowan[7] reports that the gamma ray of about 85 kev is to be associated with decay from a metastable state whose half-life is 1.8×10^{-9} second. The delayed coincidence measurements indicate that this state follows the highest-energy beta ray. His measurement of the *K*-shell conversion coefficient is in agreement with the theoretical value for an *E2* transition.

The present study was commenced in an effort to resolve the discrepancies between the various measurements of the beta spectrum and to arrive at a tenable decay scheme. The earliest measurements with our scintillation coincidence spectrometer revealed the presence of gamma rays of higher energy than any heretofore reported. Since these transitions could not be fitted into the previously proposed energy levels of Dy^{160}, coincidence measurements were undertaken in an effort to arrive at a more consistent decay scheme.

INTERNAL CONVERSION MEASUREMENTS

The internal conversion electron studies were carried out using the 180° photographic spectrometers previously described.[8]

The most comprehensive measurements on the internal conversion electron groups are those reported by Cork *et al.*[4] They report 26 conversion lines and 13 photo lines (using a lead radiator) and from these deduce the presence of 12 gamma rays. Our study of the internal conversion spectrum indicates the presence of three additional gamma rays. Our plates, however, do not show lines representing several of the gamma rays reported in the Michigan study. Evidently, the magnetic fields of the spectrometers were adjusted so that different portions of the spectrum were included in the region of maximum sensitivity. Our exposures in the neighborhood of 400 kev were relatively weak, and could have been examined more extensively by longer exposures and stronger sources. Probably the same considerations explain why the high-energy gamma rays were overlooked by the other investigators.

The results of our study of the internal conversion spectrum are tabulated in Tables I and II. To provide a complete presentation of the available information, the gamma rays found by Cork *et al.* are also listed in Table II.

SCINTILLATION EXPERIMENTS

The scintillation studies were made using the scintillation coincidence spectrometer.[9] This instrument consists of two scintillation spectrometers, one equipped with a ten-channel pulse-height analyzer, and the other with a single-channel analyzer. Either may be operated independently, or the single channel may be operated

[1] W. Bothe, Naturwiss. **31**, 551 (1943); Z. Naturforsch. **1**, 179 (1946).
[2] Burson, Blair, and Saxon, Phys. Rev. **77**, 403 (1950).
[3] Inghram, Hayden, and Hess, Phys. Rev. **71**, 643 (1947).
[4] Cork, Shreffler, and Fowler, Phys. Rev. **74**, 240 (1948); Cork, Branyan, Rutledge, Stoddard, and LeBlanc, Phys. Rev. **78**, 304 (1950).
[5] E. Salmi, thesis, University of Michigan, 1950 (unpublished).
[6] L. J. Shavtvalov, Izvestia Akad. Nauk SSSR Ser. Fiz. **17**, No. 4, 503 (1953).
[7] F. K. McGowan, Phys. Rev. **85**, 142, 151 (1952).
[8] Rutledge, Cork, and Burson, Phys. Rev. **86**, 775 (1952).
[9] S. B. Burson and W. C. Jordan, Phys. Rev. **91**, 498 (1953).

TABLE I. Internal conversion electrons associated with $_{65}Tb^{160}$ (71 day).

Electron energy (kev)	Relative intensity	Interpretation	Transition energy (kev)
32.6	9	K	86.4
36.8		Auger (K-L-L)	
39.6		K	93.4
42.2		Auger (K-L-M)	
43.6		Auger (K-L-M)	
77.6	10[a]	L_2	86.2
78.5		L_3	86.3
84.4	2	$M_{2,3}$	86.2
85.8		$N_{2,3}$	86.1
142.3		K	196.1
160.5		K	214.3
187.5		L	196.1
193.8		M	195.6
195.5		N	195.8
206.7		L	215.3
243.8		K	297.6
288.9		L	297.5
337.5		K	391.3
705		K	759
819		K	873
865		L	874
906		K	960
952		L	960
1120		K	1174
1211		K	1265

[a] $L_1 \ll L_2 \approx L_3$.

to gate a coincidence circuit (resolving time ~ 2 microseconds) built into the ten-channel analyzer. The RCA 5819 probe assemblies and detecting crystals were provided by Swank and Moenich of this laboratory, and patterned after their designs.[10] For gamma-ray detection, NaI(Tl) crystals (0.375 in. thick$\times$1.25 in. in diameter) were used. For beta-ray detection, an anthracene crystal (0.5 in. thick$\times$1.5 in. in diameter) provided with a thin aluminum window (2.8 mg/cm^2) was used. The ten-channel analyzer is provided with a window amplifier. By adjusting the photomultiplier voltage, and the gains of the linear amplifier and the window amplifier, any portion of the spectrum can be examined in as much detail as desired. (This apparatus is to be described in greater detail in a separate publication.)

The Normal Photon Spectrum

Using the NaI(Tl) crystal, together with an aluminum absorber sufficiently thick to remove all charged radiation, the pulse-height distribution was determined with the ten-channel analyzer. (Such a single crystal analysis shall hereinafter be referred to as a "normal distribution" as opposed to a "coincidence distribution.")

The normal spectrum for Tb is shown in Fig. 1. To obtain this curve, the single-channel probe of the coincidence circuit was removed from the proximity of the source to reduce scattering effects. The source was placed about ten inches from the detecting crystal to eliminate "sum-lines" (spurious peaks appearing in the spectrum caused by simultaneous detection of two different gamma rays). The resolution of the spectrometer (full-width at half-maximum) was measured to be 13 percent for the 662-kev gamma ray of Cs^{137} and varied from 22 percent at 86.3 kev to approximately 10 percent at about 1.0 Mev. The window width and gain of the analyzer were adjusted so that in the highest energy region the windows were about 28 kev wide. The 1.17, 1.26-Mev peak is thus defined by about ten experimental points. Each time the differential analyzer was readjusted, from three to five channels were allowed to overlap the previous setting to insure accurate fitting together of the adjacent regions of the spectrum. In the lower-energy regions of the spectrum narrower channels were used, being about 5 kev wide for the region containing the 86.3-kev gamma ray and below. In all cases, the counting was continued to obtain statistical accuracy of about 1 percent at each point.

Ten peaks are clearly resolved. The peak with the highest energy represents two gamma rays to be identified with the 1.17- and 1.26-Mev transitions observed in the internal conversion studies. It is evident from its position relative to the Co^{60} calibration lines that the 1.17-Mev radiation predominates, the 1.26-Mev photopeak appearing only as a slight broadening of the high-energy side. The peak at about 900 kev is seen to be broad and clearly due to two radiations close together in energy. These are identified as the two gamma rays of 873 and 960 kev. From the low amplitude of the 1.17 and 1.26-Mev photopeak, it may be safely concluded that the Compton distribution associated with it makes a relatively small contribution to the background underlying the 900-kev peak. The broad peak centered at about 650 kev can be primarily attributed to the Compton distribution due to the 873 and 960-kev gamma rays. It is impossible to ascertain from the shape of this distribution to what extent the 759-kev gamma ray (detected by internal conversion) contributes. A small peak appears at about 400 kev. This peak is interpreted as representing either the 391

TABLE II. Gamma transitions in Dy^{160}.

Cork *et al.* Energy (kev)	Present Energy (kev)	K/L
86.5	86.3±0.3	0.9±0.3
92.6	93.4±0.5	
176.2		
196.4	196.1±0.6	~3
214.7	214.8±0.6	>2
282.0		
297.8	297.6±0.8	>5
375.2		
391.0	391.3±2.0	
410.3		
	759 ±3	
876	873 ±4	~5
962	960 ±4	~5
	1174 ±8	
	1265 ±8	

[10] R. K. Swank and J. S. Moenich, Rev. Sci. Instr. **23**, 502, 503 (1952).

or 410-kev gamma rays, or both. Two strong peaks are resolved at about 296 and 206 kev, using the 279-kev gamma ray of Hg^{203} for calibration. The 296-kev peak is associated with the 298-kev transition. While the peak at 206 kev appears to be a single peak, it is somewhat broader than is to be expected from the resolution of the instrument. This, together with the fact that its energy lies between the 196- and 215-kev gamma rays, would indicate that the peak probably represents this pair. The lowest-energy gamma ray which was detected is assigned an energy of 86 kev using the 85-kev peak of Tm^{170} for calibration. This is identified as the 86.3-kev radiation. The two remaining peaks are interpreted as the K x-ray of Dy^{160} and its associated escape peak, produced when the x-rays of iodine escape from the detecting crystal.

Coincidence Experiments

Because of the many transitions associated with the excited states of Dy^{160}, it is difficult to arrive at a unique arrangement of the energy levels. The experimental errors present in energy measurements alone allow various possible decay schemes such as those previously proposed.[2,4] The most feasible method by which the number of such possible combinations can be reduced is by means of coincidence experiments.

All of the coincidence experiments were performed with the probes placed coaxially inside a cylindrical lead shield whose inside diameter was 4 in. The beta-gamma coincidence measurements were made using the anthracene crystal for the beta detector in the probe of the single-channel analyzer. The analyzer was set in the integral position, and the bias adjusted to reject most of the noise pulses of low amplitude. The ten-channel analyzer was set successively on each of the photopeaks and aluminum absorption curves run on the beta rays in coincidence with each peak. During the gamma-gamma measurements, the crystal faces were about 1.5 cm apart and aluminum filters (350 mg/cm²) placed in front of each crystal holder to prevent charged radiation from being detected.

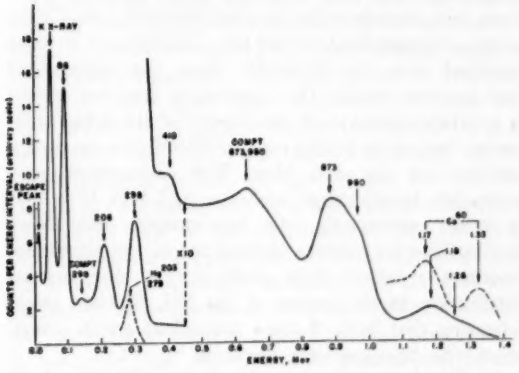

FIG. 1. Gamma-ray spectrum of $_{65}Tb^{160}$ (71 day). NaI(Tl) pulse-height distribution.

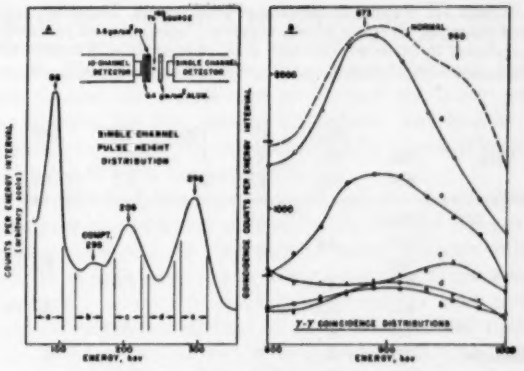

FIG. 2. Coincidence pulse-height distributions for $_{65}Tb^{160}$ (71 day). In B five coincidence distributions are plotted corresponding to the single-channel settings indicated in A. The dashed curve in B represents the normal pulse-height distribution for the region in which the coincidence distributions are recorded.

Figure 2 presents the results of a typical set of gamma-gamma coincidence measurements. Figure 2A shows a normal distribution obtained with the single-channel analyzer using a 5-kev window. After the single-channel normal distribution is so obtained, the ten-channel analyzer is adjusted so that it shows the normal distribution shown by the dashed curve of Fig. 2B. The window of the single-channel analyzer is then opened wide enough to accept most of the pulses contained in a given peak and the corresponding ten-channel coincidence distribution recorded. The curves in "B" represent the coincidence distributions corresponding to the various settings of the single-channel analyzer indicated as "a" through "e" in "A". It is readily apparent from curve "a" that the 86.3-kev gamma ray is predominately in coincidence with the 873-kev radiation. Curve "c" shows that most, if not all, of the coincidences associated with the 206-kev peak are with the 960-kev radiation. Curve "e" is very similar to the normal distribution, from which it may be inferred that the 298-kev gamma ray is in coincidence with both the 873 and 960-kev transitions. Curves "b" and "d" show that the coincidence rates fall off markedly in the valleys between the peaks represented in the single-channel distribution. Figure 2 is representative of a large number of such experiments.

One major advantage of this technique is that rapid comparisons can be made between the normal and coincidence spectra, so that very small peak shifts in the coincidence spectrum can be detected which might otherwise be rejected as being due to drift of the instrument or to statistical uncertainty if the same comparison were to be obtained by a single-channel analyzer.

Interpretation of many of the coincidence experiments is confused by the complex manner in which high-energy gamma rays are detected by the NaI crystals. Since in this study the gamma ray of maximum

TABLE III. Results of coincidence experiments. Transition energies are designated in kev. *A*—Coincidence observed, interpretation unambiguous. *B*—Coincidence observed, interpretation probably correct. *X*—Coincidence required by decay scheme of Fig. 4 but concluded to be below detection limit of apparatus. Numbers refer to paragraphs presenting related experimental details.

		Gamma												
		86.3	93	196	215	298	375	391	410	759	873	960 957[a]	1170	1260
Beta	860	*B*3	*X*	*X*	*X*		*X*		*X*		*A*1	*A*1		
	520	*B*3	*X*	*A*2	*A*2	*A*2	*X*	*X*	*X*	*X*	*B*1	*B*1	*A*2	*X*2
	1260													
	1170	*A*4												
	960					*B*7								
	957[a]	*X*[a]			*B*10[a]									
	873	*A*5				*A*7								
	759	*X*		*B*11	*B*11				*X*					
Gamma	410	*X*	*X*			*X*	*X*	*X*						
	391	*X*		*X*	*X*		*X*							
	375	*X*	*X*	*X*	*X*	*X*								
	298	*A*6		*X*9	*X*9									
	215	*A*6	*X*	*A*8										
	196	*A*6	*X*											
	93	*X*												

[a] The 957-kev transition is grouped with the 960 since they are experimentally indistinguishable.

energy is only slightly in excess of the threshold for pair production, this process presents no serious problem. In coincidence experiments, in which the two detecting crystals are in close juxtaposition, the geometry is excellent for detecting in one crystal a large fraction of the backscattered quanta resulting from Compton scattering in the opposite crystal. For incident gamma rays ranging from 0.7 to 1.3 Mev, the energy of the secondary radiation scattered at 180 degrees increases from 180 kev to only about 210 kev, and approaches approximately 250 kev as the energy of the primary radiation increases without limit. For any given primary gamma ray, the energy of the secondary photons increases slowly as the scattering angle is decreased from 180 degrees. Thus, unless precautions are taken when either spectrometer is set in the neighborhood of 200 kev, copious coincidences may be observed between the Compton recoil pulses and the backscattered photon peak.

In the measurements in which this phenomenon was considered to be a possible source of error, an effort was made to obviate the effect by placing a lead filter between the source and the crystal in which the high energy gamma-ray was being detected, as indicated in the inset in Fig. 2. For example, a $\frac{1}{8}$-in. lead filter attenuates the 960-kev gamma ray by only about 20 percent but reduces the 200-kev secondary radiation by about 98 percent so that in searching for coincidences between the 960-kev gamma ray and the 206-kev photopeak, spurious coincidences which might be caused by Compton scattering of the 1.17 and 1.26-Mev radiations are greatly reduced.

Results of Coincidence Experiments

The results of the coincidence experiments are summarized in Table III. The letters "*A*", "*B*", and "*X*" represent the combinations where coincidences might be observed if the decay scheme proposed in Fig. 4 is correct. Where no coincidences should appear, and in fact were not observed, the spaces in the table are left blank. For those combinations marked "*A*", coincidences were observed which could be unambiguously interpreted as coincidences between the two transitions indicated. The designation "*B*" indicates that coincidences were in fact observed, but interpretation other than as indicated in the table is possible. The designation "*X*" indicates that coincidences were unobservable because of low intensity or inadequate resolution.

The paragraphs below, indicated numerically in the table, present related experimental details.

Beta-Gamma Coincidence Measurements

(1) The beta-ray spectrum in coincidence with the 873, 960-kev peak is clearly complex. The high-energy component has a half-thickness in *A*1 of from 28 to 30 mg/cm^2, corresponding to a beta ray with a maximum energy of approximately 900 kev. This branch is to be identified with the 0.86-Mev beta ray determined from previous work.[2] The experiment does not permit an accurate estimate of the energy of the other component, but its half-thickness could indicate an energy between 0.4 and 0.6 Mev. This component may reasonably be identified with the 0.52-Mev beta ray. In these experiments, the beta-gamma coincidence distributions for various thicknesses of the aluminum absorbers retained their similarity to the normal distribution in the region of the 873, 960-kev peak, indicating that both of these transitions are in coincidence with the same beta spectrum.

(2) The beta rays in coincidence with the 1.17, 1.26-Mev peak show a half-thickness in aluminum of

18–20 mg/cm² corresponding to a beta ray of about 0.6-Mev maximum energy. Within experimental error, this can be identified as the 0.52-Mev beta ray. It is clear from the shape of the coincidence distribution that the 1.17-Mev gamma ray is represented. The statistics of the coincidence measurements are not good enough to establish definitely that the 1.26-Mev radiation is also present, but since it did not stand out as the thicker absorbers were inserted, it seems safe to conclude that it is also fed by the low-energy beta branch. Similar results are obtained for the gamma rays represented in the 298 and 206-kev peaks. In none of these cases did the absorption curve appear to be complex.

(3) The absorption curve for the beta rays in coincidence with the 86.3-kev gamma ray shows an average half-thickness of about 24 mg/cm². The curve may be interpreted as an average derived through a mixture of both components, with the lower energy one predominating. Such an interpretation is consistent with the statistics of the experiment.

(The measurement of the beta-ray spectrum carried out earlier at this laboratory indicated the presence of a third component of 396 kev not found present by any of the other investigators. This contradiction, together with the fact that the decay scheme based on the present measurements permits of only two branches, has lead us to conclude that the 396-kev beta ray is not present. The earlier result may be attributable to some unknown instrumental error.)

Gamma-Gamma Coincidence Measurements

(4) When the ten-channel analyzer was set to cover the 90-kev region, coincidences were observed in the vicinity of all other peaks as the single-channel arm of the coincidence circuit was swept across the spectrum. By careful calibration with the 85-kev gamma ray from Tm^{170} and the 94-kev gamma ray from Dy^{165}, these coincidences were found to be primarily associated with the 86-kev transition rather than the 93-kev gamma ray.

To examine more carefully with the ten-channel analyzer the regions of the spectrum in which these coincidences were observed, the single-channel analyzer was adjusted to accept primarily those pulses contained in the 86.3-kev peak. The ten-channel analyzer was set to observe the highest-energy photopeak. It is to be recalled that this peak consists primarily of the photopeak from the 1.17-Mev gamma ray, the 1.26-Mev gamma ray appearing only as a slight broadening of the high-energy side of the distribution (Fig. 1). While the coincidence distribution between this peak and the 86.3-kev peak clearly indicated that the 1.17-Mev gamma ray is in coincidence with the 86.3-kev radiation, the statistics of the experiment are not good enough to conclude that the 1.26-Mev gamma ray is not. While the ten-channel analyzer was still on the high-energy peak, the single channel was moved upward across the remainder of the spectrum and no coincidences were detected with any other radiation.

(5) The ½-in. lead filter was inserted between the source and the ten-channel probe, and the latter set to observe the 873, 960-kev photopeak. The 86.3-kev gamma ray is seen to be predominantly in coincidence with the 873-kev radiation (Fig. 2).

(6) The lead filter was removed and the ten-channel analyzer was adjusted to observe the 200 and 300-kev regions, respectively (the single channel analyzer still set on the 86.3-kev peak). No conclusive change was apparent between the coincidence spectra and the normal distributions. Thus, it could be concluded that the 86.3-kev gamma ray is in cascade with both the 196 and the 215, as well as the 298-kev radiations.

(7) When the single channel was set to accept the intense portion of the 298-kev photopeak, and the 873 and 960-kev pair observed with the ten-channel spectrometer, the coincidence spectrum is seen to be similar to the normal distribution in that region (Fig. 2), indicating that the 298-kev gamma ray is in coincidence with both components of the peak.

(8) The fact that the peak at about 206 kev (Fig. 1) lies between 196 and 215 kev indicates that this peak probably represents both of these radiations. That the 206-kev peak is composed of more than one component is further indicated by the fact that coincidences are observed when the single channel is also accepting pulses in the 200-kev region. The presence of these coincidences not only supports the assumption that the 206-kev peak is comprised of two or more components, the 196 and 215-kev gamma rays, but further that they are in cascade. Using a 10-kev window, several successive observations of the coincidence distribution were made with the single channel set on adjacent energy intervals in the same region. As the channel was advanced upward in energy, the coincidence distribution seemed to shift slightly downward, however, the evidence for this energy shift is not conclusive.

(9) While still observing the 206-kev peak with the ten-channel analyzer, the single channel was moved in successive steps across the 298-kev peak. The coincidence distribution was ascertained for each setting. Analysis of these data showed that most, if not all, of these coincidences were attributable to background effects, and not due to coincidences between the radiations represented in the two peaks. From this it may be concluded that very few, if any, of the 298-kev transitions are in cascade with either the 196- or 215-kev gamma ray.

(10) With the ½-in. lead filter between the source and the single-channel probe, the single-channel analyzer was set with a 50-kev window on the broad 873, 960-kev peak, as indicated by the dotted lines in Fig. 3*A*. Figure 3*B* shows that the coincidence distribution in the neighborhood of the 206-kev peak clearly shifts upward from the normal distribution, in fact, coinciding with the 214-kev calibration peak

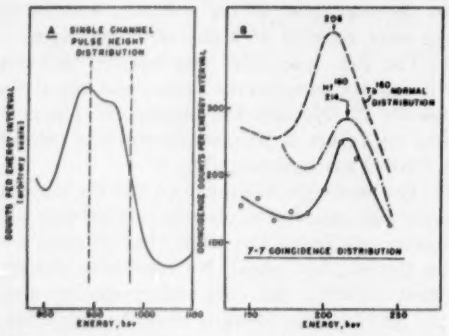

FIG. 3. Coincidence pulse-height distribution for $_{65}Tb^{160}$ (71 day). For the single-channel setting represented in *A*, the coincidence distribution is plotted in *B* for the region whose normal distribution is represented by the dashed curve. To aid in estimating the energy represented by the coincidence curve, the normal distribution of $_{72}Hf^{180}$ is also plotted providing a 214-kev calibration peak.

from Hf^{180}. In the corresponding experiment, the single channel was set on the 206-kev peak and the ten-channel on the 873, 960-kev peak with the lead filter between the source and the ten-channel probe. As discussed above, the coincidence distribution is seen to manifest a single peak at about 960 kev (Fig. 2*B-c*). It would thus be concluded that the 215-kev gamma ray is in coincidence with the 960-kev gamma ray. However, as will be seen in the discussion of the decay scheme, the result may better be interpreted as evidence of a transition of about 957 kev which is experimentally indistinguishable from the 960-kev gamma ray.

(11) The search for coincidences between the 759-kev gamma ray and the 206-kev peak was made with the lead filter in place to reduce spurious counts due to Compton scattering of the 873 and 960-kev gamma rays. The single channel was set on the 206-kev peak and the ten-channel analyzer adjusted to where the 759-kev peak (not resolved in the normal spectrum) should appear. The coincidence distribution manifested a peak, but its poorly defined character does not warrant considering it as reliable evidence.

DECAY SCHEME

From the results of the foregoing experiments, the decay scheme proposed in Fig. 4 is deduced as follows:

Consider the two groups of gamma rays, 86.3, 873, 960 kev, and 86.3 kev, 1.17, 1.26 Mev. In each of these groups, the energy of the 86.3-kev transition adds to that of the second gamma ray to be experimentally equal to that of the third. From internal conversion data, the difference between the 873- and the 960-kev transitions is 87 kev, in excellent agreement with the energy measurement of the 86.3-kev transition. Likewise, for the higher-energy pair, the difference between the 1.17- and the 1.26-Mev transitions is about 90 kev, but still equal within experimental error to 86.3 kev. In both cases, the assumption of these groupings is supported by the coincidence measurements, since the 86.3-kev gamma ray is clearly in coincidence with both the 873 and the 1.17-Mev gamma rays (4,5).

Since the 86.3-kev transition is the only element common to these two triads, the association of these five transitions (indicated by heavy lines in the decay scheme) follows logically. It is immediately seen that the energy difference between 960 kev and 1.26 Mev is equal to the 298-kev transition well within experimental limits. Assignment of the 298-kev transition to this position is substantiated by the coincidence measurement which shows the 298-kev gamma ray to be in coincidence with both the 873 and 960-kev as well as the 86.3-kev transition (6,7). Thus, except for the sequential orientation, these six transitions form a closed system which is unique and consistent with both energy differences and coincidence experiments. Without other considerations, one might place either the 298 or the 86.3-kev transition next to the ground state.

The beta-gamma coincidence measurements support the arrangement as shown, considering the 86.3-kev transition as the ground state transition. The conclusion that the highest-energy state in Dy^{160} is 1.26 Mev is supported by the following experiments: (*a*) The scintillation spectrometer detected no pulses of amplitude greater than those to be associated with the high-energy photopeak representing the 1.17 and 1.26-Mev gamma rays. (*b*) No internal conversion lines were detected for any transition of energy greater than 1.26 Mev. (*c*) No gamma rays were found in coincidence with the high-energy peak, except the 86.3 which could definitely be associated with the 1.17-Mev

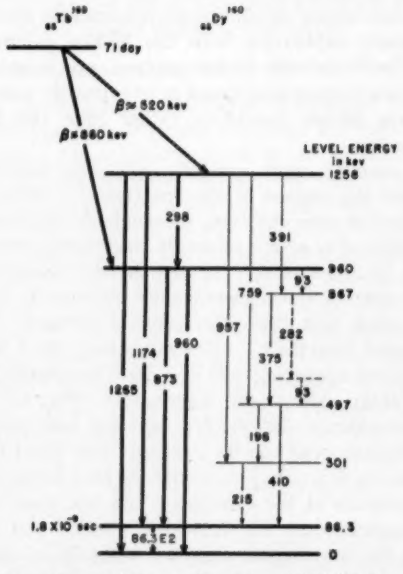

FIG. 4. Proposed decay scheme for $_{65}Tb^{160}$ (71 day).

gamma ray (4). (*d*) The aluminum absorption curve for the beta rays in coincidence with the 1.17, 1.26-Mev peak is simple, showing only the lower-energy component of about 520 kev (2).

The energy difference between the two beta rays, while about 340 kev from the previous measurements of the beta-ray spectrum, is considered close enough to 298 kev to be equal within experimental limits. Thus, these beta-gamma coincidence data, i.e., the 520-kev beta ray in coincidence with the 1.17 and 1.26-Mev gamma rays (2), and the 860-kev beta ray in coincidence with the 873 and 960-kev gamma rays (1) favors placing the 298-kev transition on top with the 86.3-kev at the bottom.

Other considerations favor assigning the 86.3-kev transition to the ground-state position. The 86.3-kev gamma ray is the strongest in the spectrum (Fig. 1) and it also has the most intense internal conversion lines. This indicates that it must be fed by several other transitions, necessitating its being low in the level scheme. From densitometry of the internal conversion lines, the K/L ratio of the transition is 0.9 ± 0.3 indicating that the character of the radiation may be $E2$.[11] This is in confirmation of McGowan's conclusion based on measurements of the K-shell conversion coefficient and of the lifetime of that state; and empirically, ground-state transitions of even-even nuclei are $E2$ transitions. Finally, the energy of 86.3 kev is consistent with that which would be expected from energy systematics of ground-state transitions of even-even nuclei.[12]

The experiments supporting the partial decay scheme just discussed are convincing, but the arrangement disposes of only six of the transitions. If the deductions are correct, and the partial level scheme accepted, then it is readily apparent that there is no way in which the 215-kev transition can be fitted in so that it is in cascade with only the 960- and 86.3-kev transitions. But the experiments do indicate that the 215-kev transition is in coincidence with the 960-kev transition and not the 873 (10). A plausible explanation for this inconsistency is apparent if an energy state is placed at 301 kev, 215 kev above the 86.3-kev level. The coincidences between the 215-kev gamma-ray and what is apparently the 960-kev gamma ray can then be attributed to another radiation of about 957 kev, which represents a transition from the 1.258-Mev level to the 301-kev level. The 957-kev radiation could be strong enough to account for the coincidences without being detected by internal conversion. More evidence for concluding that it is a weak transition is derived from the coincidence experiments between the 298-kev gamma ray and the 873, 960-kev peak (7) (Fig. 2*e*). If the 957-kev radiation were of substantial intensity, the normal distribution might indicate a slightly higher intensity near 960 kev relative to 873 kev than does the coincidence distribution taken with the 298-kev radiation, but no significant difference is apparent. The experiments indicate nothing with respect to the sequence of the 215, 957-kev cascade, but the transition with the lower energy is preferentially placed nearest the ground-state transition.

The coincidence experiments indicate that the 196-kev transition is in cascade with both the 86.3 and the 215-kev radiations (6,8). The presence of the 410-kev transition is taken as evidence that the 196 and 215-kev transitions are adjacent. From these observations, the existence of the level at 497 kev is deduced.

The 759-kev transition is then interpreted as the transition between the 1.258-Mev state and the 497-kev level. The coincidence measurements between the 206-kev peak and the 759-kev region of the spectrum support this arrangement (11), but as has been mentioned, these experiments are not sufficiently unambiguous to be pointed to as primary evidence. The fact that the only beta-ray component found in coincidence with the 206-kev peak was the 520-kev branch does indicate (2), however, that the 196- and 215-kev transitions must be fed predominantly from the 1.258-Mev state, which agrees with the arrangement proposed.

The only reason for placing the 93-kev transition in the position indicated is the energy fit. If it is properly placed here, it must represent a very weak branch, for neither were there any coincidences observed between it and any of the other gamma rays (4), nor were any of the coincidences observed which would support its placement, such as coincidences between the 298-kev and either the 196 or the 215-kev gamma-rays (9). Also, were it a substantial branch, one would expect to find evidence of the high-energy beta-ray branch in coincidence with the 206-kev peak.

The only gamma ray reported by Cork *et al.* which cannot be fitted into the level scheme is the one of 176 kev. We find no evidence for this transition either by internal conversion or by scintillation spectrometer, thus, its association with Tb^{160} is concluded to be doubtful and it is, therefore, disregarded.

We have made an effort to arrive at a decay scheme which is not only consistent with our own data, but which incorporates as much of the previously reported information as possible. Internal conversion lines for the transitions of 282, 375, and 410 kev were not observed in this study, however, more extensive exposures may have led to their detection. The 375- and 410-kev transitions fit into the scheme readily, and the 282-kev transition can be included by placing the 93-kev transition in the alternate position indicated by the dotted lines.

[11] M. Goldhaber and A. Sunyar, Phys. Rev. **83**, 906 (1951).
[12] G. Scharff-Goldhaber, Phys. Rev. **90**, 587 (1953).

The Nuclear Spectra of Ce^{144} and Pr^{144}

W. S. Emmerich, W. J. Auth, and J. D. Kurbatov
Department of Physics, The Ohio State University, Columbus, Ohio
(Received December 18, 1953)

The nuclear spectra of Ce^{144} and Pr^{144} have been studied with magnetic and scintillation spectrometers. The 304-kev beta transition of Ce^{144} was found to be 70.5 percent abundant from a Kurie plot analysis. For the beta spectra leading to the 134-kev and 81-kev levels, intensities of 22 percent and three percent were obtained, respectively, from internal conversion and gamma-ray data. An energy level of 175 kev in Pr^{144} was inferred from energy balance considerations. The relative intensities of the Pr^{144} beta transitions were determined from the abundance of the 695-kev gamma transition in Nd^{144} which was found to be 1.25±0.2 percent. A spin of one and odd parity appears plausible for the 2185-kev level in Nd^{144}.

I. INTRODUCTION

THE nuclear radiations of the Ce-Pr-Nd-144 disintegration have been of interest in the field of nuclear spectroscopy. The most recent information is collected in the table of Hollander, Perlman, and Seaborg[1] whose decay schemes are largely an extension of the one proposed by Porter and Cook.[2] Emmerich, John, and Kurbatov,[3] and Keller and Cork[4] have reported internal conversion electrons which indicate several low excited states in Pr^{144}. Alburger and Kraushaar[5] have shown from angular correlation studies that the 2185-kev, 695-kev, and ground states of Nd^{144} have spins of 1–2–0.

One of the purposes of the present investigation is to clarify the empirical results by remeasuring the beta spectra and evaluating the branching ratios. A further aim has been to check the internal conversion line intensities and attempt to confirm level assignments by means of a scintillation spectrometer.

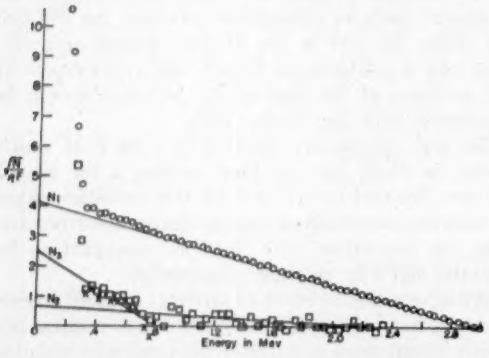

FIG. 1. Kurie plot of the beta-ray spectra of Ce^{144} and Pr^{144}. The circles represent experimental data. The squares represent the first subtraction, and the crosses represent the second subtraction. A subtraction for the 304-kev transition of Ce^{144} is not shown. The components of the Pr^{144} disintegration are labeled *N*1, *N*2, and *N*3.

[1] Hollander, Perlman, and Seaborg, Revs. Modern Phys. **25**, 469 (1953).
[2] F. Porter and C. Cook, Phys. Rev. **87**, 464 (1952).
[3] Emmerich, John, and Kurbatov, Phys. Rev. **82**, 968 (1951).
[4] H. Keller and J. Cork, Phys. Rev. **84**, 1079 (1951).
[5] D. Alburger and J. Kraushaar, Phys. Rev. **87**, 448 (1952).

II. EXPERIMENTAL PROCEDURE AND RESULTS

Carrier-free Ce^{144} obtained from the Oak Ridge National Laboratory was stored for one year to allow disintegration of short-lived impurities. Chemical purification was performed mainly to remove Sr^{90} and rare earth elements other than cerium. The procedure for purification consisted of oxidation of cerium to the tetravalent state with potassium permanganate. The *p*H of the solution was then adjusted to 2.5 and the solution filtered. The cerium retained on the filter paper was dissolved in 6*N* hydrochloric acid and the process repeated four times. The carrier-free Ce^{144} samples were prepared by evaporation of the final solution on rubber hydrochloride films.

The beta-ray spectra of Ce^{144} and Pr^{144} were measured in a magnetic lens spectrometer equipped with a 2-mg/cm² mica window G.M. tube. The momentum resolution of the instrument was 3.5 percent for the internal conversion electrons of Cs^{137}. Phosphorus[32] was used in the adjustment and calibration of the spectrometer. A Kurie plot of the Ce-Pr spectra is shown in Fig. 1. The end-point energy is 2.98±0.02 Mev in close agreement with previously published values.[1] Subtractions are shown which indicate the 2.28-Mev and 0.8-Mev spectra of Pr^{144}, and the 0.30-Mev spectrum of Ce^{144}. The relative intensities as obtained from the Kurie plot may be found in Table I expressed in percent of total disintegration per isobar.

The interval conversion lines were measured between 15 kev and 150 kev in a photographic spectrometer. The line intensities were determined with a photodensitometer and analyzed according to the method

TABLE I. Experimental beta-ray intensities of Ce^{144} and Pr^{144}.

Parent element	Energy in Mev	Intensity from Kurie plot[a]	Intensity from gamma-ray data[a]
Ce	0.304±0.004	70.5±5.0	...
Ce	0.223±0.005	...	≤3.0
Ce	0.170±0.005	...	22.0±5.0
Pr	2.98±0.02	95.5±2.0	97.4±0.8
Pr	2.28±0.2	1.7±1.0	0.8±0.3
Pr	0.80±0.1	2.8±1.0	1.9±0.5

[a] Expressed in percent of total disintegration per isobar.

TABLE II. Internal conversion lines in the disintegration of Ce^{144} and Pr^{144}.

Line energy in kev	Relative[a] intensity	Assignment element	Assignment shell	Gamma energy in kev	Shell ratios K/L	Shell ratios L/M	Multipole radiation
92.2	100	Pr	K	134	8	$\geqslant 4$	$M1$
127.8	12		L				
133.1	$\leqslant 3$		M				
38.5	49	Pr	K	81	5	9	$M2$
74.0	9		L				
79.2	~ 1		M				
27.0	11	Pr	L	34		3	
32.5	4		M				
58.7	4	Pr	K	100			
99.0	1		M				
46.6	3	Pr	L	53			
34.2	11	Pr	L	41		11	
39.6	~ 1		M				
52.7	7	Pr	K	94			
16.8	4	Nd	K	60	1		
53.3	4		L				
29.2	12	Pr	L	Auger		2	
34.2	6		M				

[a] The intensity of an internal conversion line is expressed in percent of the 92-kev line.

of Rutledge, Cork, and Burson.[6] A trace of the photographic plate is shown in Fig. 2. Energies and relative intensities of the lines are found in Table II, where the intensity of the 92-kev K line of the 134-kev gamma transition is taken as 100. Also shown are the associated gamma-ray energies and shell ratios where available.

The values of the Ce^{144} branching ratios were obtained through a comparison of the 134-kev gamma rays with the intensity of other transitions in a scintillation spectrometer, and through a comparison of internal conversion lines. The results are listed in column four of Table I. A more reliable determination of the branching ratio in Pr^{144} than from our Kurie plot was obtained by measuring the relative intensity of the 695-kev gamma transition and the 2.98-Mev beta transition. Calibration was carried out with Cs^{137}. The data were corrected for internal conversion and difference in photoelectric cross section between 662 kev and 695 kev. Three independent determinations gave an average intensity of 1.25 ± 0.2 percent for the 695-kev gamma ray. To compute the branching ratios listed in Table I, this information was combined with the relative intensities of the 695-kev, 1480-kev, and 2185-kev gamma transitions given by Alburger and Kraushaar.[5]

III. DISCUSSION

The K/L ratios which are obtained for the 134-kev and the 81-kev transitions are in agreement with the assignment of $M1$ and $M2$, respectively, made previously by Porter and Cook.[2] The scintillation spectrometer observations, though restricted because of limited resolution attainable in this energy range, indicate an intensity ratio between ten and twenty for free gamma emission of these two transitions. With the relative intensity of the K conversion peaks being 100/40, the ratio for the total transition intensity is about four, assuming a K conversion coefficient of 0.5 for the 134-kev gamma ray. No other gamma rays of the Ce^{144} disintegration were noted in the scintillation spectrum with appreciable intensity. This observation and the fact that the conversion electrons of the 134-kev and

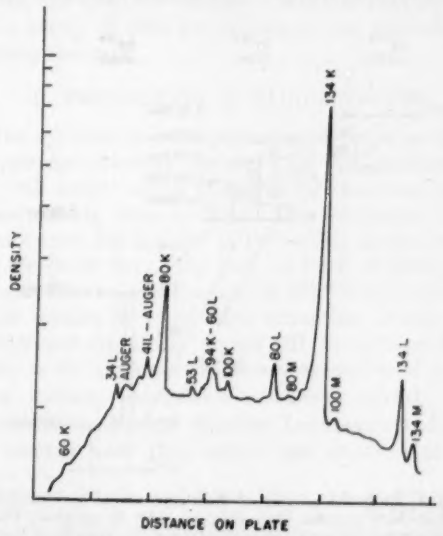

FIG. 2. Photodensitometer trace of the internal conversion lines in the electron spectrum of Ce^{144} and Pr^{144} as recorded on a photographic plate. The principal peaks are identified by the transition energy and atomic shell in which the conversion has occurred.

[6] Rutledge, Cork, and Burson, Phys. Rev. 86, 775 (1952).

the 81-kev transitions represent two thirds of the total conversion intensity, lead to an assignment of relative intensities for the Ce^{144} beta transitions shown in the last column of Table I.

The observed intensity of the 29-kev internal conversion line is 12 in the notation of Table II. The Auger intensity for the LK,L line is 10 as calculated from the fluorescent yield in praseodymium and the L/M ratio for Auger electrons given by Burhop.[7] The agreement is sufficiently close to assume that the 29-kev line is entirely due to Auger electrons. This is not so for the 34-kev line. The observed intensity is 17 whereas the calculated value for the LK,M Auger line is six. The excess is interpreted as L line of a 41-kev gamma ray as previously suggested.[3,4]

The existence of a 175-kev level assumed from 134 kev and 41 kev in cascade is supported by the observation that 81 kev and 94 kev add up to the same value. A direct transition to the ground state was not observed with the scintillation spectrometer. The K conversion line of such a transition almost equals the 134-kev M line in energy. Since the 133-kev line is not excessively intense, a direct transition of 175 kev does not appear abundant through internal conversion. If an admixture of 175-kev K-conversion electrons exists, the L/M ratio for the 134-kev transition will be higher than given in Table II.

The position of the 60-kev transition inferred from internal conversion in Nd^{144} remains unresolved in the present measurements. No evidence was detected with the scintillation spectrometer for free gamma radiation of 60 kev in praseodymium which had been separated chemically from the Ce^{144}. No gamma rays were found with energies of ± 60 kev from the known values of 695 kev, 1480 kev, and 2185 kev with an intensity greater than ten percent of any of these. Internal conversion lines were observed, however, in Ce^{144} and Pr^{144} in equilibrium which agree with previous values.[2,4]

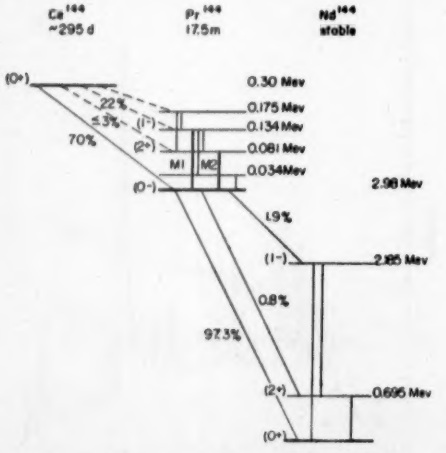

FIG. 3. Proposed scheme of disintegration of Ce^{144} and Pr^{144}. The 0.06-Mev gamma transition in Nd^{144} is omitted. Present results are not inconsistent with placing this transition between a (4+) state of 0.755 Mev and the 0.695-Mev level.

[7] E. H. S. Burhop, *The Auger Effect* (Cambridge University Press, Cambridge, 1948), p. 48.

TABLE III. Summary of beta transition values.

Parent nucleus	Energy in Mev	Initial state	Final state	Spin, parity change	Log ft value
Ce^{144}	0.30	(0+)	(0−)	$\Delta I=0$, yes	7.5
Ce^{144}	0.22	(0+)	(2+)	$\Delta I=2$, no	$\geqslant 8.3$
Ce^{144}	0.17	(0+)	(1−)	$\Delta I=1$, yes	7.2
Pr^{144}	2.98	(0−)	(0+)	$\Delta I=0$, yes	6.5
Pr^{144}	2.28	(0−)	(2+)	$\Delta I=2$, yes	8.1
Pr^{144}	0.80	(0−)	(1−)	$\Delta I=1$, no	6.0

A tabulation is presented in Table III of the results for the transitions obtained by making use of the data from Tables I and II. The difference in the log ft values between the 2.98-Mev and the 0.30-Mev transitions observed by Porter and Cook[2] is confirmed here. The ft values of the inner spectra of Ce^{144} are given without direct experimental evidence for existence of these transitions. They are based on the requirements imposed by internal conversion and gamma-ray intensities.

The log ft value of 6.0 obtained for the 0.80-Mev transition occurs just at the traditional border line between allowed and first forbidden transitions. It may be allowed considering that the ft values observed for first forbidden transitions in this region of the isotopic table are generally high. The assignment of odd parity for the 2185-kev level then agrees with a rule recently suggested by Glaubman[8] for spins and parities of excited states in even-even nuclei. This level may be third or higher among the excited states in Nd^{144} since second excited states of even-even nuclei occur usually as (2+) or (4+) states according to a survey of Scharff-Goldhaber.[9] A single additional state of spin four and even parity in the energy range between 695 kev and 2185 kev could well exist in Nd^{144} but remain undetected in the present measurements due to insufficient feeding either through beta or gamma transitions. The presently unassigned 60-kev gamma transition may be connected with such a level. A disintegration scheme summarizing these results is shown in Fig. 3.

The grant of a fellowship from the Industrial Research Foundation of The Ohio State University received through the Graduate School is greatly appreciated. Acknowledgment is made to Mr. M. Sakai for assistance in beta-ray measurements and to Dr. George John for the chemical separation of praseodymium. It is a pleasure to express our thanks to The Ohio State University Development Fund which secured fundamental research instruments.

[8] M. Glaubman, Phys. Rev. 90, 1000 (1953).
[9] G. Scharff-Goldhaber, Phys. Rev. 90, 587 (1953).

Radiative Electron Capture of Fe^{55}, A^{37}, and Ni^{59}

W. S. Emmerich, S. E. Singer, and J. D. Kurbatov
Department of Physics, The Ohio State University, Columbus, Ohio
(Received December 18, 1953)

The radiative electron capture spectra of Fe^{55}, A^{37}, and Ni^{59} were studied with a scintillation spectrometer. The end-point energies were found to be 226±10 kev, 815±20 kev, and 1065±30 kev, respectively. A method was devised to correct the experimental intensity distributions for distortions due to the Compton effect in the scintillation crystal. This was applied to the spectra of A^{37} and Ni^{59} above 320 kev. In this energy range, the experimental spectrum of A^{37} was found to agree with the calculated spectral shape. In the case of Ni^{59}, a dependence of the spectral shape on the type of transition could not be detected within present experimental limits.

I. INTRODUCTION

THE occurrence of radiative orbital electron capture provides a means of determining directly the transition energy associated with the disintegration. The shape of the spectrum may in some cases give information regarding the type of transition involved. Morrison and Schiff[1] have given an expression for the relative probability of photon emission per unit time, dP, with respect to the total K-capture probability per unit time, P_K. For allowed transitions, this ratio is given, except at low energies, by

$$dP/P_K=(\alpha/\pi)(1-E/E_0)^2EdE, \quad (1)$$

where α is the fine structure constant, E is the energy of the photon in units of mc^2, and E_0 is the energy available for the transition. Jauch[2] has shown that E_0 is obtained by plotting $(N/E)^{\frac{1}{2}}$ against E, where N is the observed activity per unit energy interval. If the experiments are in accordance with the derived distribution, the plot should be linear and intersect the axis at E_0, in analogy to a Kurie plot in beta-ray analysis. The total radiation probability per K capture is approximately given by

$$\int dP/P_K=(\alpha/12\pi)(E_0)^2. \quad (2)$$

Experimental studies of radiative electron capture have been reported by a number of groups. The earliest measurements were carried out with Fe^{55} by Bradt *et al.*,[3] using absorption technique. Later results obtained by Maeder and Preiswerk[4] with scintillation counters showed that the end-point energy of the radiative capture spectrum is within experimental error with the value calculated from the $Mn^{55}(p,n)Fe^{55}$ reaction threshold.[5] It was also shown that the experimental intensity distribution corresponds to the calculations. Bell, Jauch, and Cassidy[6] have reinvestigated the spectrum with a scintillation spectrometer and analyzed their data in the form of a linear plot.

The radiative capture spectrum of A^{37} has been measured by Anderson, Wheeler, and Watson.[7] These authors applied the linear plot analysis to their scintillation spectrometer results and obtained an end-point energy in agreement with that calculated from the $Cl^{37}(p,n)A^{37}$ reaction threshold.[8] The data were corrected by calculating the efficiency of the scintillation crystal for detection of electromagnetic radiation, but not for the effect of Compton scattering.

The possibility of studying radiative electron capture in a forbidden transition presents itself in the case of Ni^{59}. Up to the present time, no investigation has been reported for radiative electron capture in a forbidden transition except Tl^{204}, for which the end-point energy has been determined.[9] Nickel[59] decays by orbital electron capture to the ground state of Co^{59} with a half-life of about 7×10^4 years.[10] The threshold energy of the $Co^{59}(p,n)Ni^{59}$ reaction[11] indicates that an end-point energy of 1066 kev is expected for the radiative capture spectrum.

II. PREPARATION OF RADIOACTIVITIES

The activities for the present study were produced by neutron reactions. Natural iron was irradiated in the Oak Ridge reactor and aged for five years before measurements were initiated. This eliminated interference from the activity of Fe^{59} which decays with a half-life of 46 days. The iron, as ferric chloride, was separated from a small amount of Mn^{54} activity present in the sample, by ethyl ether extraction. It was then precipitated repeatedly at low pH as hydrous ferric oxide, in the presence of carriers consisting of potassium, sodium, manganous, cobaltous, nickel, zinc, strontium, and barium chlorides. Lanthanum and ceric ion carriers were then added and removed as the

[1] P. Morrison and L. I. Schiff, Phys. Rev. **58**, 24 (1940).
[2] J. M. Jauch, Oak Ridge National Laboratory Report ORNL-1102, 1951 (unpublished).
[3] H. Bradt *et al.*, Helv. Phys. Acta **19**, 222 (1946).
[4] D. Maeder and P. Preiswerk, Phys. Rev. **84**, 595 (1951).
[5] P. H. Stelson and W. M. Preston, Phys. Rev. **83**, 469 (1951).
[6] Bell, Jauch, and Cassidy, Science **115**, 12 (1952).
[7] Anderson, Wheeler, and Watson, Phys. Rev. **90**, 606 (1953).
[8] Richards, Smith, and Browne, Phys. Rev. **80**, 524 (1950); Schoenfeld, Duborg, Preston, and Goodman, Phys. Rev. **85**, 873 (1952).
[9] E. der Mateosian and A. Smith, Phys. Rev. **88**, 1186 (1952).
[10] Brosi, Borkowski, Conn, and Griess, Phys. Rev. **81**, 391 (1951); H. W. Wilson (private communication).
[11] J. J. McCue and W. M. Preston, Phys. Rev. **84**, 384 (1951).

oxalates. This was followed by final precipitation of the iron as the hydrous oxide.

The A^{37} activity was obtained by irradiation of 30 grams of calcium oxide in the Brookhaven reactor for a period of two months. The argon, formed by (n,α) reaction, was extracted by reacting the calcium oxide with water in an atmosphere of common argon and collecting the gaseous products in an evacuated vessel. A half-life measurement of electromagnetic radiation emitted by the sample gave a half-life of 35 days.

Nickel[59] was obtained by neutron irradiation of 39 grams of nickel metal for a period of 28 days in position *A* of the NRX reactor. The material was aged for one year before measurements were started. The active impurities present in the nickel sample included millicurie quantities of Co^{58} and Co^{60}, and microcurie amounts of Fe^{55} and Mn^{54}. The Ni^{59} yield, in terms of ordinary electron capture, was calculated to be about 200 microcuries. Iron was removed by precipitation of the hydrous oxide at low pH. The sample was then treated repeatedly with alpha-nitroso-beta-naphthol,

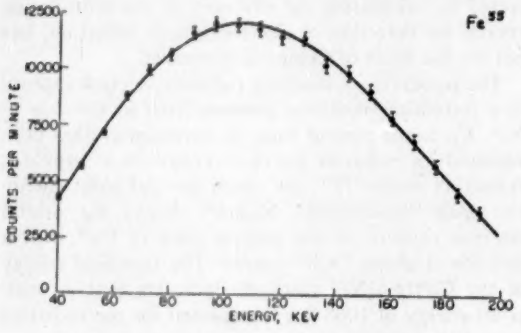

FIG. 1. Uncorrected scintillation spectrogram of the radiative electron capture spectrum in Fe^{55}.

with the addition of cobalt carrier, to remove active cobalt species. The nickel was then separated from Mn^{54} and other contaminants by precipitation of the nickel dimethylglyoxime complex from homogeneous solution using a method devised especially for this investigation.[12] The final sample was obtained by converting the nickel dimethylglyoxime to the oxide. The presence of Ni^{63} did not interfere with the measurement of the radiative capture because no gamma radiation is emitted in the decay and the beta spectrum has a transition energy of only 67 kev.

III. EXPERIMENTAL PROCEDURE

Measurements were made with a scintillation spectrometer consisting of a thallium activated sodium iodide crystal, one inch long and 1.5 inch in diameter, coupled to a RCA type 5819 photomultiplier tube, followed by a linear amplifier, and a Johnstone-type

[12] Singer, Kurbatov, and Kurbatov (to be published).

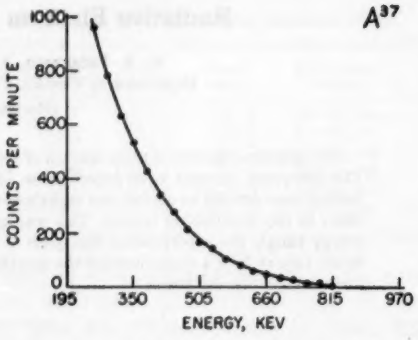

FIG. 2. Uncorrected scintillation spectrogram of the radiative electron capture spectrum in A^{37}. Only the energy region above 300 kev was utilized for analysis of the spectral shape.

single-channel pulse-height analyzer.[13] The experimentally obtained radiative capture spectrum of Fe^{55} is shown in Fig. 1. The spectra for A^{37} and Ni^{59} above energies of 300 kev are shown in Figs. 2 and 3, respectively. In the energy range from 300 kev to 1300 kev, the detection efficiency of the crystal for electromagnetic radiation and the effect of instrumental change in resolution were determined empirically with the gamma rays of Hg^{203}, I^{131}, Au^{198}, Cs^{137}, Zn^{65}, and Co^{60}. The absolute activity of the Co^{60} sample was known and served as a calibration standard. The other samples were standardized by comparison of their beta-ray spectra with that of Co^{60} using absorption technique.

In order to account for the distortion introduced by the Compton scattering into the intensity distribution of the radiative electron capture spectra, the Compton distributions were measured for a number of gamma rays in the energy region of interest. In addition to some of the above mentioned standards, Be^{7} and Mn^{54} gamma rays were utilized. An empirical correction was attained by dividing the radiative capture spectrum into a number of sections, each corresponding in width to the experimentally observed half-width of a gamma-

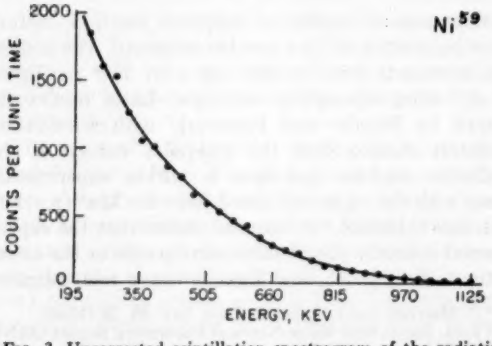

FIG. 3. Uncorrected scintillation spectrogram of the radiative electron capture spectrum in Ni^{59}. Only the energy region above 300 kev was utilized for analysis of the spectral shape.

[13] C. W. Johnstone (private communication).

ray peak in the instrument. Starting with the highest energy section, the corresponding gamma-ray peak was then normalized to the intensity of that section of the radiative capture spectrum, and the contribution due to the Compton scattering subtracted out at the lower energies. This procedure was repeated always for the highest energy section which remained uncorrected, as shown in Fig. 4 for A^{37}, and in Fig. 5 for Ni^{59}. The resultant net intensity of the radiative capture spectrum was then subjected to further correction for crystal efficiency as outlined above.

IV. RESULTS

After the empirical corrections were applied to the radiative capture spectra, they were plotted in linear

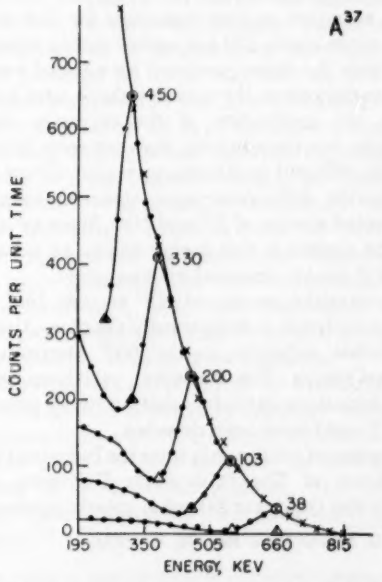

FIG. 4. Correction procedure for the Compton effect applied to the radiative electron capture spectrum of A^{37}. The × 's indicate experimental points of the spectrum. The dots show instrumental gamma-ray distributions which are superimposed on each other to approximate the continuous energy spectrum. The numbers next to the circles show the relative intensities of the gamma rays used in the analysis.

form according to the method of Jauch. The linear plot of Fe^{55} is shown in Fig. 6. In this energy range, the distortion of the spectrum due to Compton effect is negligible with the crystal used in this work. The spectrum is corrected only for the change in resolution of the instrument. The end-point energy of the plot is 226±10 kev. This is within experimental error of the recent nuclear reaction data of Trail and Johnson,[14] which give an energy value of 230±5 kev for this figures

The end-point energy for the spectrum of A^{37} it 815±20 kev as shown in Fig. 7, which is in agreemen.

[14] C. C. Trail and C. H. Johnson, Phys. Rev. 91, 474 (1953).

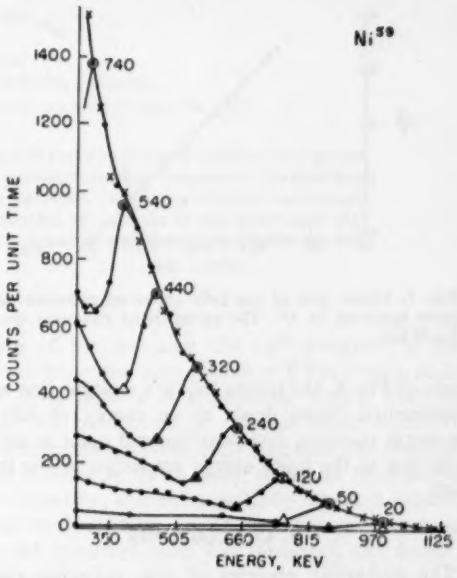

FIG. 5. Correction procedure for the Compton effect applied to the radiative electron capture spectrum of Ni^{59}. The × 's indicate experimental points of the spectrum. The dots show instrumental gamma-ray distributions which are superimposed on each other to approximate the continuous energy spectrum. The numbers next to the circles give the relative intensities of the gamma rays used in the analysis.

with the previously published value.[7] The plot follows a straight line from its end point to an energy of 320 kev, which is the lower limit to which the correction procedure was carried out in this investigation. The Ni^{59} spectrum was analyzed in the same manner as the A^{37} spectrum and the linear plot is shown in Fig. 8. The experimental end-point energy of this spectrum is 1065±30 kev, which is in agreement with $Co^{59}(p,n)Ni^{59}$ threshold measurement.[11] The uncorrected spectrum of Ni^{59}, shown in Fig. 3, appears to be different in shape from that of A^{37}. This difference is neutralized almost completely by the application of the Compton correction procedure to both cases. In the corrected linear

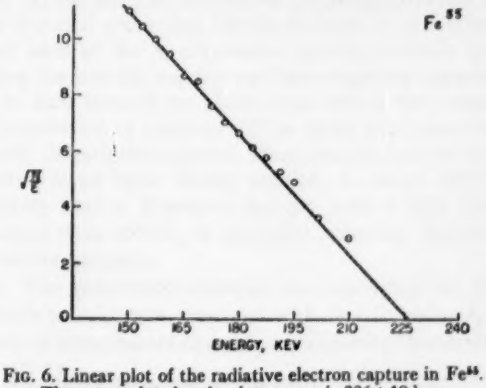

FIG. 6. Linear plot of the radiative electron capture in Fe^{55}. The extrapolated end-point energy is 226±10 kev.

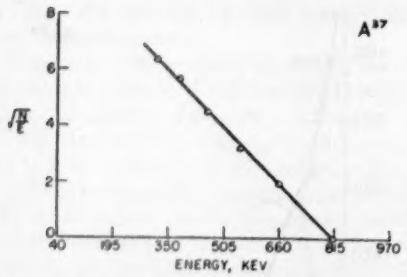

FIG. 7. Linear plot of the fully corrected radiative electron capture spectrum in A^{37}. The extrapolated end-point energy is 815±20 kev.

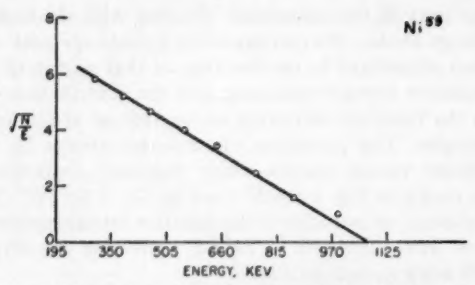

FIG. 8. Linear plot of the fully corrected radiative electron capture spectrum in Ni^{59}. The extrapolated end-point energy is 1065±30 kev.

graph of Fig. 8, the points follow a straight line within experimental limits down to an energy of 320 kev. An excess counting rate near the end point is believed to be due to the finite energy resolution of the instrument.

V. CONCLUSIONS

The end-point energies of the radiative capture spectra of the three examples studied in this work were found to be in agreement with the energies calculated from the nuclear reaction data. The method can be used, therefore, to determine the transition energy involved in the electron capture disintegration directly by means of nuclear spectroscopy. The experimental spectral shapes agree with the predicted intensity distributions for allowed transitions at least in the region between the end-point energy and 40 percent of that value. For Fe^{55} and A^{37}, the agreement is expected to exist since the transitions are probably allowed. In Ni^{59}, it appears from the transition energy and half-life that a second forbidden transition may be involved in the observed decay. A spin change of two is inferred from the measured spin 7/2 of Co^{59}, and a spin 3/2 of the 31st neutron in Ni^{59} as expected from the shell model theory.[16]

The radiative capture spectrum for this transition in the range above 320 kev agrees within experimental limits with the shape predicted for allowed transitions. Small variations in the spectral shape may have been lost in the application of the necessary correction technique, but the spectrum does not seem to be fundamentally different in this energy region. Below 320 kev, considerable differences were observed between the uncorrected spectra of A^{37} and Ni^{59}. Since no correction could be applied in this energy region, an actual difference, if it exists, remained undetermined.

The transition energy of Ni^{59} exceeds $2mc^2$, so that positron emission is energetically possible. A search for annihilation radiation in the Ni^{59} spectrum yielded negative results. The statistical variations were such that a branching ratio for positron decay greater than 2×10^{-5} could have been detected.

The grant of a fellowship from the Industrial Research Foundation of The Ohio State University received through the Graduate School is greatly appreciated.

[16] M. G. Mayer, Phys. Rev. 78, 16 (1950).

Potassium-44

BERNARD L. COHEN
Oak Ridge National Laboratory, Oak Ridge, Tennessee

(Received September 18, 1953; revised manuscript received October 26, 1953)

Potassium-44 was produced by an (n,p) reaction on calcium and found to decay by negatron and gamma emission with a 22.0±0.5 minute half-life. The identification was ascertained by comparison of yields from normal and isotopically enriched calcium, cross section measurements, chemical processing, and investigation of impurity effects. The beta-ray spectrum is quite complex but includes strong components with maximum energies of about 4.9 and 1.5 Mev. The gamma-ray spectrum includes strong gammas at 1.13, 2.07, and 2.48 Mev, and a probable 3.6-Mev gamma.

IN 1937 Walke,[1] while irradiating calcium with fast neutrons to produce 12.4-hour potassium-42 by an (n,p) reaction, detected a short-lived activity that followed the potassium chemistry. He measured the half-life as 18±1 minutes and surmised that it must be either potassium-43 or potassium-44 since only these could be produced by (n,p) reactions on the stable calcium isotopes known at that time. Potassium-43 has since been produced by an (α,p) reaction on argon[2] and found to decay with 22.4-hour half-life. The mass number for this activity, hitherto[3] considered "probable," was confirmed by bombarding isotopically enriched Ca^{43} with high-energy neutrons from the Oak Ridge National Laboratory 86-inch cyclotron. However, since Walke's paper appeared, two new stable calcium isotopes, Ca^{46} and Ca^{48}, have been discovered. Recent isotope tables[3,4] report Walke's 18-minute activity as "element probable, mass number unknown."

Potassium-44 has been produced by irradiating both natural calcium and isotopically enriched[5] calcium-44 with neutrons from a beryllium target bombarded with about 1000 μa of 22-Mev protons; its half-life was determined to be 22.0±0.5 minutes. The following tests were made to ascertain the element and the mass assignment:

1. The ratio of the 22-minute activities produced per unit mass by bombarding enriched (98 percent) Ca^{44} and natural calcium (2.1 percent Ca^{44}) was found to be 60±15 which is roughly proportional to the relative amounts of Ca^{44} present. Since the enriched sample contains a smaller percentage of all other calcium isotopes than normal calcium, there is no possibility that the 22-minute activity is produced by any of these.

2. The cross section for production of the 22-minute activity [assuming it to be produced by $Ca^{44}(n,p)$] was determined to be about nine percent of the cross section for $Ca^{42}(n,p)$. This is roughly what is expected in view of the fact that the Ca^{42} threshold is lower (i.e., the maximum beta energy of K^{42} is lower), and its (n,p) cross section is abnormally large.[6] The cross section for production of the 22-minute activity is sufficiently large to completely eliminate the possibility that it is produced by an (n,p), $(n,2n)$, or (n,α) reaction on an impurity; and the possibility that it is produced by an (n,γ) reaction on an impurity seems obscure since the cadmium ratio was measured and found to be near unity.

3. The 22-minute activity was chemically identified as potassium to the extent that it does not precipitate with scavengers as a hydroxide, carbonate, or sulfide in basic solution. The fact that it was recovered from the solution with nearly 100 percent efficiency by evaporating to dryness eliminates the possibility that the 22-minute activity is produced by an (n,α) reaction since that reaction would result in an isotope of argon.

4. To check the possibility that the 22-minute activity may be due to an impurity, a survey was made of all known isotopes with half-lives between 20 and 25 minutes to determine if any of them exhibit the properties of the isotope here being identified as K^{44}, as follows (a) It is produced by neutron bombardment; (b) it is a beta emitter but not a positron emitter; (c) no other activity of less than one-day half-life is produced simultaneously with an intensity as large as 0.2 percent of the 22-minute; (d) its decay scheme includes strong gamma rays at 1.13, 2.07, and 2.48 Mev; and (e) the activity follows the potassium fraction in the chemical processing described above. It was found that each of the twenty-seven known activities fulfilling the half-life requirement has properties contrary to at least *three* of the above even with a very broad interpretation of property (d) to make allowances for poorly investigated spectra. Since neutron-induced activities have been widely studied, it seems highly unlikely that a 22-minute activity with a high production cross section in naturally occurring material would be unknown.

5. The gamma-ray spectrum accompanying the 22-minute activity was compared with that following the decay of scandium-44 since, if our assignment is correct,

[1] H. Walke, Phys. Rev. **52**, 663 (1937).
[2] Overstreet, Jacobson, and Stout, Phys. Rev. **75**, 231 (1949).
[3] Hollander, Perlman, and Seaborg, Revs. Modern Phys. **25**, 469 (1953).
[4] K. Way *et al.*, *Nuclear Data*, Natl. Bur. Standards Circ. No. 499 (U. S. Government Printing Office, Washington, D. C., 1950).
[5] Enriched stable isotopes were obtained from Isotope Research and Production Division, Oak Ridge National Laboratory.
[6] B. L. Cohen, Phys. Rev. **81**, 184 (1951).

both are due to transitions between excited states of calcium-44. The Sc^{44} decay is accompanied by only one gamma, with an energy 1.16 Mev.[3] This agrees well with the very intense 1.13-Mev gamma found with the 22-minute activity. The other gammas found with the 22-minute activity are probably due to transitions between states of too high an excitation energy to be reached by the Sc^{44} decay.

The best half-life determination was obtained by using the enriched sample, employing chemical processing, and counting under a thick ($\frac{1}{4}$-in.) lead absorber. The decay was followed through nine half-lives (maximum counting rate of chart recording equipment to 25 percent of cosmic ray background) without noticeable deviation from the reported half-life.

The beta-ray spectrum of 22-minute K^{44} was studied with an anthracene scintillation spectrometer and by absorption techniques. The spectrum is quite complex,

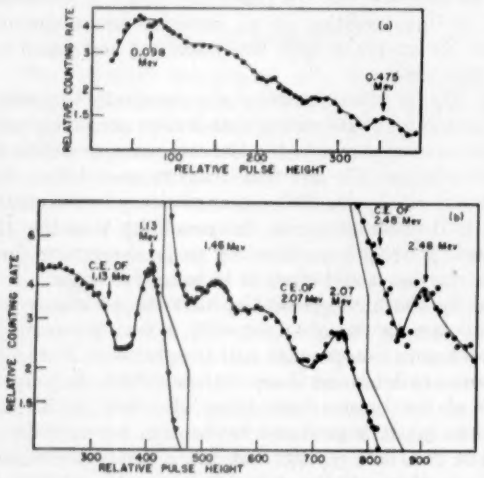

FIG. 1. Gamma-ray spectrum of K^{44} as measured with NaI scintillation spectrometer. The sample was placed about $\frac{1}{2}$ in. above a NaI(Tl) crystal $1\frac{1}{2}$ in. in diameter and 1 in. high. Background was never more than a few percent. "C.E." denotes the theoretical position of the Compton edge for the specified gamma ray. (a) Low-energy portion; (b) high-energy portion.

but seems to include strong components with maximum energy about 4.9 and 1.5 Mev.

The gamma-ray spectrum, as measured with a NaI(Tl) scintillation spectrometer is shown in Fig. 1. The various portions of that figure were obtained with different amplifier settings. Each portion of the spectrum was measured at least three separate times, and each major feature was evident on every run.

From Fig. 1 it is apparent that there are strong gamma rays at 1.13 Mev, 2.07 Mev, and 2.48 Mev. Each is evidenced by a well resolved photoelectric peak and a Compton edge at the calculated position. The 1.46-Mev pair-production peak for the 2.48-Mev gamma is also well resolved, and there are obvious reasons why the pair peaks for the other two gammas are not resolved. The high-energy part of the spectrum, not shown in the figure, exhibits a relatively slow fall-off to about 3.3 Mev followed by a much more rapid decrease with barely discernible peaks at about 3.1 and 3.6 Mev. Tests in which the sample to crystal distance was varied and various absorbers were interposed indicate that this is not due to addition pulses from coincident gammas; it is probably due to a 3.6-Mev gamma as evidenced by the positions of the aforementioned peaks, the rapid fall-off at the energy calculated for the Compton edge of a 3.6-Mev gamma, and the fact that the energies of the 1.13- and 2.48-Mev gammas add up to 3.6 Mev.

The low-energy portion of the spectrum is very difficult to interpret, although the general rise indicates that there are probably several low energy gammas. The peak at 0.475 Mev is not accompanied by the proper Compton edge, and the maximum at 0.098 Mev does not have the proper shape for a photoelectric peak at that energy, although both of these lackings could be accounted for by the presence of other low energy gammas. There is no evidence for 0.511-Mev annihilation gammas; this proves that the 22-minute activity is not a positron emitter and that it must therefore be a negatron emitter as expected.

In summary, gammas at 1.13, 2.07, and 2.48 Mev seem quite certain, a 3.6-Mev gamma seems probable, and there is evidence for several gammas below 0.5 Mev.

A β-Decay Energy Systematics

KATHARINE WAY* AND MARION WOOD*
National Bureau of Standards, Washington, D. C.
(Received September 25, 1953)

A β-decay energy systematics is presented which exhibits linear relations for disintegration energies between atoms (Z,N) and $(Z+1, N-1)$ when plotted as a function of N keeping Z constant. Separate plots are necessary for odd and even values of A. The disintegration energy lines show marked discontinuities for $N=50$, 82, and 126. There is also considerable indication of a discontinuity at $N=28$, and in the *region* of $N=20$ sharp changes in slope are observed. Proton magic numbers at 50, 82, and possibly 28 are indicated by gaps in the spacing of the disintegration energy lines. No definite submagic numbers are at present identifiable. Changes in the even-odd differences of neutron and proton binding energies show up as changes in the line separation pattern. The most striking pattern changes can be interpreted as due to decreases in the even-odd differences for both neutrons and protons after their respective magic numbers. The systematics is useful in estimating disintegration energies in cases where measurements have not yet been made. Part of a systematics for double β decay is also shown.

1. INTRODUCTION

THE continued study in many laboratories of β disintegration decay schemes by means of spectrometers and coincidence techniques has resulted in the fairly accurate determination of total disintegration energies for about 450 radioactive nuclei. It is therefore now possible to give a general presentation of the results, to make an over-all comparison of the experimental values with those given by the semiempirical mass formula,[1] and to discuss implications for nuclear structure.

Although the semiempirical formula has proved helpful in portraying the general features of the mass surface, it has been known for some time that it does not represent the experimental facts in detail. Nevertheless, in searching for over-all regularities in the data, it is natural to look to this familiar generalization for guidance and suggestions.

The semiempirical formula implies three simple relations between total β disintegration energies[2] and nuclear parameters. These relations, one linear and the other two approximately so, are illustrated in Fig. 1 where mass differences between *atoms* (Z,N) and $(Z+1, N-1)$ are plotted as a function of the neutron number of (Z,N) for A odd. Z is as usual the proton number, N the neutron number, and A or $N+Z$ the total number of nucleons in the nucleus. The values used were taken from the table of Metropolis and Reitwiesner.[3] In such a plot mass differences corresponding to β^- emission appear as positive quantities and those corresponding to electron capture or β^+ emission as negative quantities. The energy zero is that for zero kinetic energy of a β^- particle. (Z,A) will be called hereafter the "disintegrating atom" no matter whether the disintegration actually proceeds from (Z,N) to $(Z+1, N-1)$ or *vice versa*.

The most familiar of the three relationships is probably the strictly linear one which follows from the parabolic expression for the mass surface which the semiempirical formula gives for constant A [Eq. (8); Appendix]. If such parabolas actually exist, the disintegration energies for constant values of odd A will give precisely straight lines when plotted against the neutron number, as shown by the dashed lines of Fig. 1.

A second relationship, almost linear, is implied between disintegration energies for which the disintegrating atoms have constant values of $I=N-Z$. Such energies are seen in Fig. 1 to lie on lines which are only slightly convex toward the N axis.

Still a third relation is to be found for decay energies of disintegrating atoms of the same Z. These energies lie along lines of positive slope which are just slightly concave toward the N axis. Other approximately

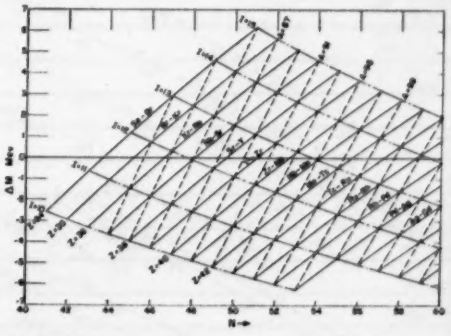

FIG. 1. Odd-A atomic mass differences or total disintegration energies between (Z,N) and $(Z+1, N-1)$ as predicted by the semiempirical mass formula (see reference 1). Values for integral N and Z from the calculations of Metropolis and Reitwiesner (see reference 3) have been connected by three sets of lines: dashed lines for constant A, full lines for constant Z, and long and short dashes for constant $I=N-Z$.

* Present address: National Research Council, 2101 Constitution Avenue, Washington 25, D. C.

[1] See Appendix for expression and references.

[2] The term "β disintegration" is used here to cover disintegration by emission of β^- and β^+ particles and by capture of electrons. By "total disintegration energy" is meant the energy released in transitions from ground state to ground state of the *atoms* involved.

[3] N. Metropolis and G. Reitwiesner, *Table of Atomic Masses*, reproduced by Argonne National Laboratory through the courtesy of the authors, March, 1950 (unpublished).

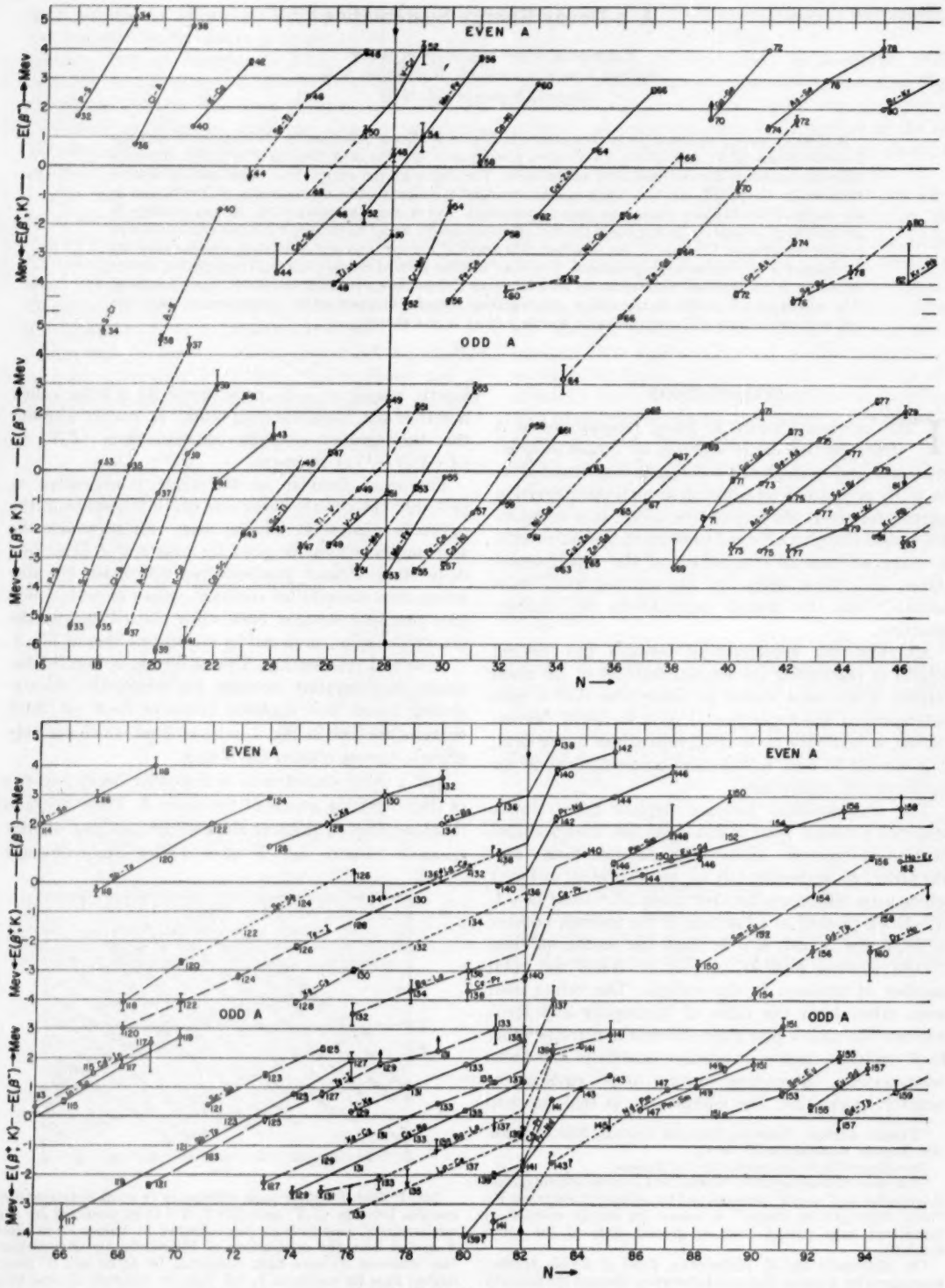

FIG. 2. (Legend on page 122.)

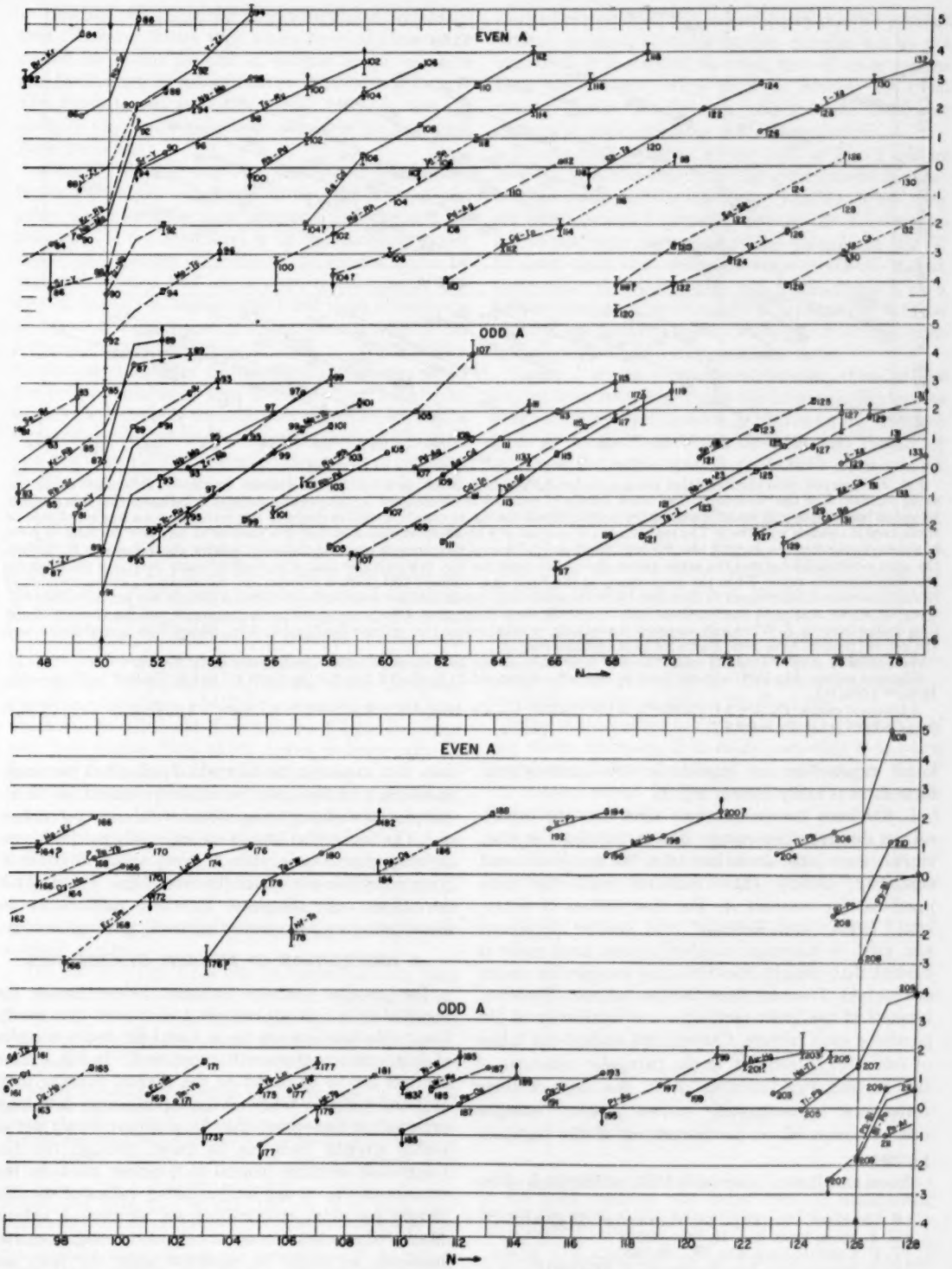

FIG. 2. (Legend on page 122.)

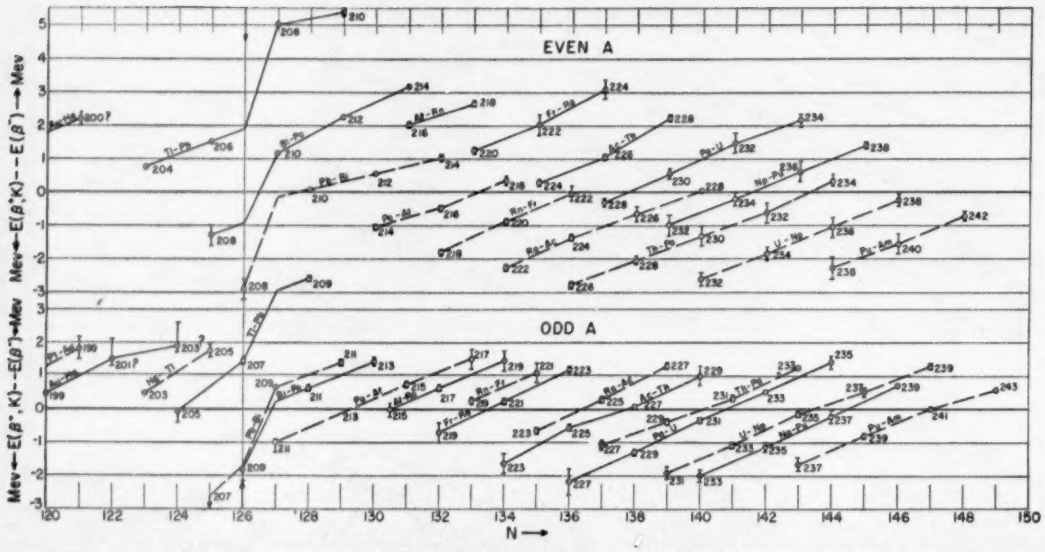

FIG. 2. Observed total disintegration energy, E, for $Z,N \rightleftarrows (Z+1, N-1)$ as a function of neutron number N. Points are connected along constant Z of the "disintegrating" atom. Limits of error are those assigned by the present authors. Φ indicates that it is possible to assign both upper and lower limits. Large asymmetry in the limits usually indicates doubt as to whether or not a single γ should be considered in cascade with the β. The replacement of one bar of Φ by an arrow indicates that it is possible to estimate the limit of error of a point in one direction but not another (e.g., there may be several γ rays whose places in the decay scheme are unknown). If, further, the open circle is deleted and the arrow points downward from the bar, this indicates that it is possible to say only that the energy is less than a certain value. When the arrow starts at the $E=0$ line, it means that there is evidence for the instability of one member of the pair concerned with respect to the other. Question marks near points indicate doubt as to whether a β particle was actually observed. Question marks near mass number show doubt about the mass assignment. Points are joined by line segments, full lines for odd Z and long dashes for even Z. When only an arrow is available, or other reasons for extreme doubt exist, short dashed lines in conformity with the general pattern have been drawn for both odd and even Z.

Note added in proof.—Drafting errors: Ca-Sc[44] error limits should be reversed; Cr-Mn[48] abscissa should be $N=28$.

Changed values: Mn-Fe[48] -1.6 to $\gtrsim -2.0$; Ni-Cu[60] -4.3 to -6.2; Zn-Ga[71] 2.1 to 2.9; Ag-Cd[108] 1.5 to 1.8; Cd-In[113] -2.7 to -2.5; In-Sn[113] 1.0 to 0.7.

Additional values: Ca-Sc[47] 2.1; Co-Ni[56] <-1.8; Ga-Ge[67] ~ -4.4; Br-Kr[87] 8.0; Kr-Rb[86] 0.7; Ru-Rh[95]? -5.0; Sn-Sb[116] -4.7; Cs-Ba[130] 0.4; Ce-Pr[145] ≥ 2.0; Pr-Nd[145] 1.7.

linear regularities are implicit in the semiempirical formula as is easily seen in Fig. 1.

It has been known for some time that the experimental disintegration energy data in the magic number regions show large deviations from the first-mentioned regularity, namely that connected with the mass parabolas for constant A. The observations of Glueckauf,[4] Suess,[5] and Kohman[6] that smaller deviations also exist in nonmagic number regions have made it evident that straight lines for decay energies for values of constant A are far from the general rule. However, because of the great usefulness and familiarity of the parabolic mass picture, Coryell[7] has worked out tables of empirical corrections to the parabolic constants of the semiempirical formula. With the help of these corrections approximately correct β-decay energies can be computed in the framework of the parabolic picture.

Suess and Jensen[8] showed in 1951, on the basis of the data then available, that for odd A, except at the magic numbers, a nearly linear relationship existed for decay energies of disintegrating atoms with constant values of I. The linear relationship was especially good between disintegrating atoms with Z even, values for odd Z lying either below or above the even-Z line. These odd-Z deviations were discussed by these authors in an illuminating way in connection with "pairing" energy.

2. DESCRIPTION OF PRESENT SYSTEMATICS

The present authors searched independently for regularities in β-decay energies and noticed that nearly linear relationships are to be found for decay energies of disintegrating atoms with constant Z. (In Fig. 1 these energies are to be found on the slightly concave lines of positive slope.) When all the experimental data were reviewed, it turned out that for constant Z two sets of nearly straight lines can be drawn through the disintegration energies plotted as function of N in the manner of Fig. 1, one set for odd-A values of the disintegrating atom and another set for even-A values. Marked discontinuities occur only at the magic neutron numbers, as might be expected since the lines are functions of only one kind of nucleon.

[4] E. Glueckauf, Proc. Phys. Soc. (London) **61**, 25 (1948).
[5] H. E. Suess, Phys. Rev. **81**, 1071 (1951).
[6] T. P. Kohman, Phys. Rev. **85**, 530 (1952).
[7] C. D. Coryell, Ann. Rev. Nuclear Sci. **2**, 305 (1953).
[8] H. E. Suess and J. H. D. Jensen, Arkiv Fysik **3**, 577 (1952).

This fact gives the present systematics an advantage over the Suess-Jensen type where irregularities can be caused by proton as well as neutron magic numbers and by changes in pairing energy with both Z and N. The Suess-Jensen systematics has, however, the advantage that more experimental points are available for a given line.

Actually, if only one of the three approximately linear regularities mentioned is to hold without the other two, the shell model suggests that the one fos constant Z is the most likely to do so. According to thir model the greatest smoothness in masses is to be expected between shell edges when the number of one kind of nucleon is kept constant and pairs of nucleons of the other kind are added. The near-linearity of the β-decay energies plotted as function of N is evidence for the smoothness of neutron binding energies when the proton number is kept constant. One would also expect the converse to hold and therefore to find a similar linear pattern in disintegration energies if plotted as a function of Z and connected along lines of constant N. However, there are not enough data to make more than a cursory check of this expectation.

The present "best" values[9] of decay energies plotted as function of N and connected along lines of constant Z are presented in Fig. 2. In this figure the results for odd and even A have been separated to avoid crowding. The same abscissa, N, the neutron number of the disintegrating atom, is used in both cases so the two sets of lines are drawn one just above the other, each with a separate set of ordinates. Points for which the disintegrating atoms have odd Z are connected by full lines which will be called odd-Z lines. Even-Z lines are drawn with long dashes. Very short dashes indicate extreme doubt as to the line pattern in either case.

In Fig. 2 limits of error as estimated by the present authors are indicated. Although single straight lines could in most cases be drawn within these limits, it was decided to connect the "best" value points with line segments in order to show clearly the existing state of the data. This treatment emphasizes the possible real deviations from linearity and suggests in some cases subshell effects.

The points in Fig. 2 can also be connected along lines of constant A or constant I of the disintegrating atoms. However, when this is done, less regularity is found than that resulting from connections along constant Z. It is believed, therefore, that interpolation or extrapolation in the pattern of Fig. 2 should give the best possible present estimate of disintegration energies not as yet measured. It is obvious, however, that in many regions there are not yet enough data to indicate the trend clearly. Future results may also indicate breaks or changes of slope which are not now suggested.

It may turn out that all the lines of Fig. 2 will be found to bend down slightly. The experimental data are still too inaccurate for one to say whether or not they exhibit in general a concavity toward the N axis as do the values from the semiempirical formula in Fig. 1. In some cases they definitely seem to do so, but in these cases the results can also be interpreted as a sudden change in the line slope at a particular neutron number, due possibly to the closing of subshells or even to configuration differences within a shell.

Figure 3 shows comparisons between three of the longest lines from Fig. 2 and the corresponding curves of the semiempirical formula. It illustrates the different types of disagreement which exist between the actual data and the semiempirical predictions in nonmagic number regions.

3. STABILITY PREDICTIONS FOR SPECIFIC NUCLEI

In the systematics of Fig. 2 the criterion for β stability is that the same nucleus should appear as daughter product in both a positive and negative disintegration, i.e., as the end product of both a β^- and K capture disintegration. Thus the fact that Te^{125} is stable is shown by a positive disintegration energy at 125 on the Sb–Te line and a negative disintegration energy at 125 on the Te–I line.

Using this criterion and interpolating and extrapolating where necessary, it is easily seen that it is quite improbable that there should be any β-stable Tc or Pm isotopes except for Tc^{97} and Pm^{145}. For both these nuclei the present line pattern suggests instability, but very slight changes in the data would alter the prediction. Evidence for long-lived electron capture in Pm^{145} has recently been found by Butement.[10] At^{215} is another

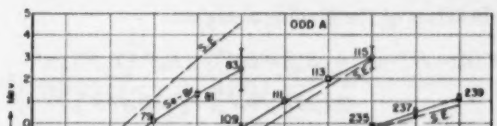

FIG. 3. Observed total disintegration energies (points connected by full lines) compared with values from the semiempirical formula (dashed lines) for three different values of the Z of the "disintegrating" atom.

[9] Values selected were based on data summarized in National Bureau of Standards Circular 499 (U. S. Government Printing Office, Washington, D. C., 1950), its three supplements, and the New Nuclear Data lists of Nuclear Science Abstracts. In the heavy element region a number of values, not directly measured, were estimated with the help of the α systematics of Perlman, Ghiorso, and Seaborg, Phys. Rev. **77**, 26 (1950) and Meinke, Ghiorso, and Seaborg, Phys. Rev. **81**, 782 (1951). A check which these authors were kind enough to make with us showed almost identical interpretations of the data. Considerable help in the construction of many decay schemes was derived from R. W. King's "Beta Decay Schemes and Nuclear Structure Assignments" (unpublished).

[10] F. D. S. Butement, Nature **167**, 400 (1951); M. L. Pool and D. N. Kundu, Phys. Rev. **88**, 171 (1952), assign a 16-day positron activity to Pm^{148} which does not fit the systematics at all.

borderline case but Fr^{219} seems certainly β stable. The short α half-lives of the nuclei which would be the β parents of Fr^{219} undoubtedly have prevented the observation of their β decay. Po^{215} and Po^{218} are clearly β-unstable in agreement with the experimental evidence of Karlik and Bernert,[11] but Po^{216} seems almost certainly β-stable contrary to the observations of these authors.

The evidence from the decay scheme[12] of the 113 chain that Cd^{113} is unstable with respect to In^{113} is so convincing that a positive point was put on the Cd—In line at 113. However, even without this datum the line pattern strongly suggests that Cd^{113} is unstable with respect to In^{113} by 250–350 kev.

Another interesting case is that of Sb^{123}. According to the present pattern, this nucleus is stable with respect to Te^{123}. There should be K capture from Te^{123} to Sb^{123} with a disintegration energy of 250–350 kev. The spin change between the ground states is known to be 3 and according to the shell model there is no change of parity. If the half-life is $>2\times10^{14}$ years[13] the lower limit of log ft is $\sim$21. This value seems large in comparison with the Rb^{87} log ft of 17.6[14] which is presumably for a $\Delta I=3$, yes transition, but the effect of the appropriate forbidden correction factors to f_0 may reduce the difference. A good number for the disintegration energy of Sb^{127} would help to make the systematics prediction for the Sb^{123}—Te^{123} disintegration energy more precise.

4. CONNECTION OF SYSTEMATICS WITH NEUTRON AND PROTON BINDING ENERGIES

Consideration of the relation of neutron and proton binding energies to the slopes and separations of the lines of Fig. 2 gives insight into the implications of the present systematics. Let B_n^{ij}, B_p^{ij} represent the neutron or proton binding energy *to* a nucleus with $Z+i$ protons and $N+j$ neutrons and E^{ij} the β-decay energy between $(Z+i, N+j+1)$ and $(Z+i+1, N+j)$ as indicated in Fig. 4. Then as is seen from this figure, the slope, $K(Z)$, of one of the constant Z lines of Fig. 2 is equal to $(E^{02}-E^{00})/2$.

In terms of the binding energies:

$$\left.\begin{aligned} 2K(Z)=E^{02}-E^{00}&=(B_p^{02}-B_p^{00})-(B_n^{02}-B_n^{00})\\ &\cong[2\partial B_p/\partial N]_s-[2\partial B_n/\partial N]_s\end{aligned}\right\}, \quad (1a)$$

$$\left.\begin{aligned} &=(B_n^{10}+B_n^{11})-(B_n^{01}+B_n^{02})\\ &\cong[\partial B_{2n}/\partial Z]_N-[2\partial B_n/\partial N]_s\end{aligned}\right\}. \quad (1b)$$

[11] B. Karlik and T. Bernert, Naturwiss. **31**, 298 (1943); Z. Physik **123**, 51 (1944); Naturwiss. **32**, 44 (1944).

[12] Apparently there is no observable γ ray from the 3.5-year isomeric state to the ground state of Cd^{113} in agreement with the original report of Gum, Thompson, and Pool, Phys. Rev. **76**, 184 (1949). The γ transition should be an $E5$. According to the empirical $E5$ energy-lifetime relationship of M. Goldhaber and A. W. Sunyar, Phys. Rev. **83**, 906 (1951), if the partial half-life is greater than 10^{10} sec, the energy must be less than 300 kev.

[13] L. I. Rousinow and J. M. Igelnitzky, Compt. rend. acad. sci. U.R.S.S. **49**, 343 (1945).

[14] Curran, Dixon, and Wilson, Phys. Rev. **84**, 151 (1951).

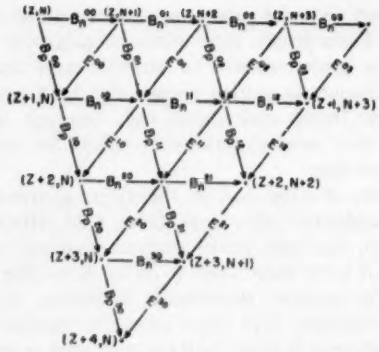

FIG. 4. Schematic diagram showing relations between total beta disintegration energies E, neutron binding energies B_n, and proton binding energies B_p. Any closed loop is an "energy cycle" for which the sum of the vector quantities around the path must vanish if the neutron-proton mass difference is subtracted from E. Examples:

Loop (Z,N), $(Z, N+1)$, $(Z+1, N)$, (Z,N) requires:

$$B_p^{00}+E^{00}-B_p^{00}-(n-p)=0;$$

Loop $(Z, N+1)$, $(Z, N+2)$, $(Z+1, N+1)$, $(Z+1, N)$, $(Z, N+1)$ requires:

$$B_n^{01}+E^{01}-B_n^{10}-E^{00}=0.$$

According to Eq. (1a) there will be a sudden increase in line slope if either the binding energy of the last proton is markedly increased by the addition of two neutrons or the binding energy of the last neutron is markedly decreased by such addition. Such marked changes are found in Fig. 2 at the magic neutron numbers for all values of Z and so are presumably due predominantly to the latter effect. Equation (1b) expresses the slope in an alternative way in terms of changes in B_n only.

The "separation" of two consecutive lines in Fig. 2, e.g., As—Se and Se—Br (such lines are adjacent on the odd-A plot but not on that for even A), will be defined as $E^{00}-E^{11}$ in the notation of Fig. 4 and denoted by $D(Z+1)$ where $Z+1$ is the charge of the atom common to both lines, i.e., Se in the example above. Thus on the odd-A plot the "separation" between the As—Se and Se—Br lines is equal to the difference between the β-disintegration energy of As^{77} and that of Se^{79} or 0.5 Mev, and is designated as $D(34)$. Obviously a slightly different value for the separation results if another pair of points, such as the disintegration energies of As^{79} and Se^{81}, is chosen for its evaluation. However, in spite of this ambiguity it turns out that the definition is adequate for the discussion of general trends.

The advantage of the definition is that it makes it possible immediately to relate the line pattern of Fig. 2 to neutron and proton binding energies. In the notation of Fig. 4,

$$D(Z+1)=E^{00}-E^{11}=(B_n^{11}-B_n^{10})-(B_p^{11}-B_p^{01}). \quad (2)$$

Clearly the magnitude and even the sign of D depend upon which of the two neutrons and protons is odd and

which even. The four different possible cases are easily distinguished with the help of subscripts e and o to denote even and odd particles, respectively, and primes to indicate that the even particle of one of the pairs designated in Eq. (2) has entered the nucelus before the odd one and so is not its "partner." They are:

for odd-A lines:

$$D_1 \equiv E[(Z)_e, (N)_o] - E[(Z+1)_o, (N+1)_e] = (B_{ne} - B_{no}) - (B_{pe} - B_{po}),$$

$$D_3 \equiv E[(Z)_o, (N)_e] - E[(Z+1)_e, (N+1)_o] = (B_{pe}' - B_{po}) - (B_{ne}' - B_{no}); \quad (2a)$$

for even-A lines:

$$D_2 \equiv E[(Z)_e, (N)_e] - E[(Z+1)_o, (N+1)_o] = -(B_{ne}' - B_{no}) - (B_{pe} - B_{po}),$$

$$D_4 \equiv E[(Z)_o, (N)_o] - E[(Z+1)_e, (N+1)_e] = (B_{ne} - B_{no}) + (B_{pe}' - B_{po}). \quad (2b)$$

$B_{ne} - B_{no}$ and $B_{pe} - B_{po}$ will hereafter be called briefly the even-odd neutron and proton differences. A study of the line separations, or D's, then gives information about the relative magnitudes of these differences.

Values of the line separation, D, as found from differences between the most reliable points near the zero-energy line in Fig. 2 are shown in Fig. 5. Care was taken not to use values on opposite sides of magic neutron numbers, so "direct" effects of such numbers are eliminated. "Direct" effects of proton magic numbers, that is, effects due to sudden changes in the general magnitude of the proton binding energies would, however, be expected to show up in D_4 and D_3. These D's involve proton pairs which are not "partners" and thus particles which can be on either side of a magic number. Marked peaks in the plots for these D's are indeed observed at $Z=50$ and $Z=82$ while a small peak is to be seen at $Z=28$ on D_4 but not on D_3.

Discontinuities in the D's are found in a number of places. The most striking ones can be interpreted consistently by assuming that there is a decrease in the even-odd difference for neutrons (or protons) after a neutron (or proton) magic number (with 28 considered as magic). Just such a decrease is to be expected from the calculations of M. G. Mayer[15] on the interaction energy of a number of identical nucleons in the same shell, assuming jj coupling and short-range attractive forces. These calculations give:

$$E(\text{even}) - E(\text{odd}) = C(2j+1)/A, \quad (3)$$

where C depends on the strength of the interaction. This difference is not expected to be identical with the even-odd binding energy difference since the calculation took no account of interaction with unlike nucleons in the same shell or with the whole nuclear "core." Nevertheless, from (3) one would expect decreases in the even-odd differences with decreases in j.

[15] M. G. Mayer, Phys. Rev. 78, 22 (1950).

It seems odd at first that such decreases occur chiefly at the magic numbers where according to the shell model the decrease in j is not so large as in other regions. The explanation may be in the suggestion made by Mayer that in regions where high- and low-j levels are close together an odd nucleon may go into the low-j state while a pair enters the high-j state because of the higher pairing energy predicted by (3). A further note on the data on pairing is in preparation.

The difference expressed in Eq. (3) should be more nearly equal to the quantities 2ν and 2π, now generally called the neutron and proton pairing energies, respectively. Following Coryell,[7] we define ν and π through the mass expressions:

$$M(Z_e, N_o) = f(Z,A) + \nu, \quad M(Z_o, N_e) = f(Z,A) + \pi, \quad (4)$$

where $f(Z,A)$ is the function of Eq. (5) in the Appendix. If $\nu = \pi$, there is a single mass parabola for a given odd A. This is also the condition for approximately equal line separations on the odd-A plot of Fig. 2. If the separation between an even-Z line and the following odd-$(Z+1)$ line is greater than that between the odd-$(Z+1)$ line and the next even-$(Z+2)$ one, ν is greater than π. If the reverse is true, π is greater than ν. Coryell[7] has used changes in line spacing to estimate values of $\pi - \nu$.

The line spacing pattern gives clear-cut results about the relative values of ν and π. However, no simple relationship exists between the π, ν picture and the even-odd difference picture as can be seen at once from

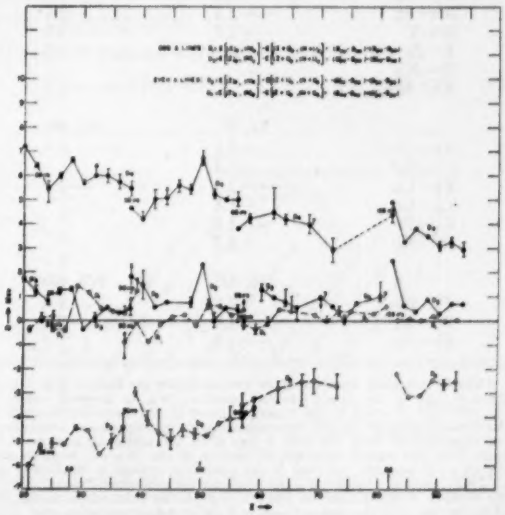

FIG. 5. Line separations, D, as defined by Eqs. (2a) and (2b), evaluated from best points of Fig. 2 near $E=0$. Example:

$D_1(Z=29) = E(\text{Ni}^{60}) - E(\text{Cu}^{64}) = 0.07 + 1.34 = 1.41$
$= [B(36\text{th}n) - B(35\text{th}n)]_{Z=29}$
$- [B(30\text{th}p) - B(29\text{th}p)]_{N=35}.$

Odd—A line separations: D_1 lower middle, D_3 upper middle. Even—A line separations: D_2 bottom, D_4 top curve.

Eqs. (2a) and (2b). If $D_1=D_3$, $\nu=\pi$, but the corresponding relation between the binding energies is quite complicated.

5. CONCLUSIONS ABOUT NUCLEAR STRUCTURE

1. *There are sudden large decreases in neutron binding energies just after neutron numbers 50, 82, 126, and probably 28.* The sharp discontinuities in the disintegration lines of Fig. 2 could be attributed either to changes in neutron or proton binding energies according to Eq. (1). However, for several Z values direct evidence for decreases in neutron binding energies after magic neutron numbers 28, 50, and 126 has already been found by means of Q values for (d,p),[16] (γ,n),[17] and (n,γ)[18] processes. Information has been lacking at $N=82$. The systematics of Fig. 2 indicates that such discontinuities exist for all appropriate proton numbers at $N=50$, 82, and 126. At $N=28$ sudden jumps occur on the V−Cr even-A line and the Ti−V odd-A line and apparently not on the Mn−Fe even-A and the Cr−Mn odd-A lines. However, the data are still rather meager in this region.

TABLE I. Magnitudes in Mev of discontinuities at magic neutron numbers.[a]

Disintegration line	Odd N ΔB_n	Even N $\Delta B_n+\Delta B_p$
	27, 29	*28, 30*
Ti−V	−1.0	
Cr−Mn	−0.0?	
Mn−Fe	−0.9	
	49, 51	*50, 52*
Kr−Rb	−1.5	∼−2.9
Rb−Sr	∼−2.3	−2.9
Sr−Y	−1.7	∼−3.8
Y−Zr		−3.7
Zr−Nb		
Nb−Mo		∼−3.5
	81, 83	*82, 84*
Xe−Cs	−2.1	
Cs−Ba	−1.3	
Ba−La	∼−2.2	∼−2.1
La−Ce	−1.8	
Ce−Pr	∼−1.8	
Pr−Nd	−1.4	
	125, 127	*126, 128*
Tl−Pb	−2.8	∼−1.0
Pb−Bi	−1.9	∼−2.4
Bi−Po	∼−1.8	

[a] Values tabulated were found by extrapolating the lines of Fig. 2 from the low sides of the magic neutron numbers, N_m, to abscissa values of (N_m+1) and (N_m+2) in the respective cases of odd and even neutrons in the disintegrating nuclei and then subtracting the extrapolated values from the experimental ones. For odd N this gives the abnormal change, ΔB_n, apart from the regular decrease, in binding of the (N_m+1) neutron over the (N_m-1) neutron, for even N the abnormal change in binding of the (N_m+2) neutron over the N_m neutron plus the abnormal change, ΔB_p, in the binding of the last proton when a neutron has been added to the new shell. Decreases in the even-odd neutron differences on crossing shell edges make ΔB_n larger for even than for odd N. The magnitudes of such decreases are not sufficiently well known to allow estimates of ΔB_p.

[16] J. A. Harvey, Phys. Rev. 81, 353 (1951); G. F. Pieper, Phys. Rev. 88, 1299 (1952).

[17] Sher, Halpern, and Mann, Phys. Rev. 84, 387 (1951). In addition to their own results, these authors list the results of earlier experiments with references.

[18] Kinsey, Bartholomew, and Walker, Phys. Rev. 82, 380 (1951).

Estimates of the magnitudes of the neutron binding energy changes implied by the present systematics are given in Table I. They are of the same general magnitude as those found in other ways. No effect similar to that seen for the above-mentioned neutron numbers is found at $N=20$.

2. *There are sudden large decreases in proton binding energies just after proton numbers 50, 82, and possibly 28.* The evidence for these discontinuities is from the separations of the lines of Fig. 2 which are plotted in Fig. 5. As mentioned above, the sharp peaks in D_3 and D_4 for $Z=50$ and $Z=82$ are to be attributed to sudden decreases in the binding of the 51st and 83rd protons. At $Z=28$ there is a small peak on D_4 but not D_3. There are not sufficient data to draw conclusions about effects at $Z=20$.

One would expect the heights above background of the D_3 and D_4 peaks at the proton magic numbers to be approximately equal to the values of the discontinuities in the proton binding energies at these points. These values, ∼1.5 Mev at $Z=50$ and $Z=82$ are in agreement with what is known directly about these discontinuities from actual proton binding energies. In the Pb region, which is that of 82 protons and 126 neutrons, a number of binding energies in addition to those directly measured can easily be found with the help of α- and β-decay energies so that here the picture of both neutron and proton binding energies is quite clear.[19]

3. *Very little, if any, effects attributable to sudden binding energy changes at possible "submagic" numbers such as 40, 58, 64 are evident at present.* Figure 2 shows possible breaks in some but not all of the disintegration energy lines in the neighborhood of $N=58$ and $N=64$. However, as the disintegration energy data become more accurate they may prove very helpful in showing how neutron shells are filled for different values of Z.

4. *The difference between the binding energies of neighboring even and odd like nucleons decreases after a magic number.* Figure 5 shows graphs of the D's on which this statement is based. In this plot one sees, for example, that after $N=50$, D_1 and D_4 suddenly decrease while D_2 and D_3 take sudden jumps upward. These changes can be accounted for only if it is assumed that the even-odd neutron difference after $N=50$ is smaller than before $N=50$ by about 1 Mev.

At $Z=50$, peaks in D_3 and D_4 are observed due to the proton magic number. It is seen that in addition both D_3 and D_4 are lower after $Z=50$ than before, while D_1 and D_2 are slightly higher, a phenomenon which can be accounted for only by a drop of about 0.5 Mev in the even-odd proton difference after the magic proton number. Similar and even greater changes in the D's are observed in the region of $Z=28$ although this

[19] N. Feather, Phil. Mag. 2, 141 (1953); A. H. Wapstra, thesis, Amsterdam, 1953 (unpublished); K. Way and M. Wood, Phys. Rev. 86, 608 (1952).

proton number is not shown up very clearly as magic by means of a peak.

5. *The slopes of the β disintegration energy lines of Fig. 2 do not agree with those given by the semiempirical formula.* Figure 6 shows a comparison of the observed slopes and those calculated from the semiempirical formula values of Metropolis and Reitwiesner. The observed slopes were taken from the best (by eye) straight lines given by points near $E=0$ and the semiempirical formula slopes were evaluated at the bottom of the potential valley. The observed slopes are greater than these semiempirical slopes for the very heavy elements ($Z>70$) and markedly less for elements in the regions $Z=20$, $Z=34$, and $Z=54$.

6. *N_Z, the value of N for which a given β disintegration energy line crosses the axis, shows large positive and negative deviations from the N_Z given by the semiempirical formula.* This value of N, in general a nonintegral one, is that for which $M(Z,N_Z)$ is just equal to $M(Z+1, N_Z-1)$. Figure 7 compares the experimental values of

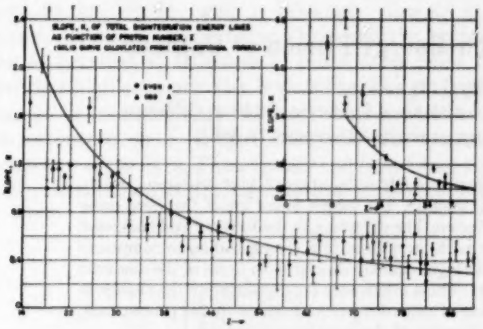

FIG. 6. Comparison of slopes of disintegration energy lines of Fig. 2 in the vicinity of $E=0$ with slopes of analogous lines as given by the semiempirical formula.

N_Z with those calculated from the semiempirical formula. The experimental values jump from one side of the calculated curve to the other showing that the semiempirical formula gives only the general location of the bottom of the valley. Coryell, Brightsen, and Pappas[20] have noted a similar discontinuous behavior for Z_A, the most stable charge for a given A [see Eq. (8)].

7. *The energy release to be expected in double β decay shows even greater regularity than that of single β decay as shown by Fig. 8.* Here odd-A and even-A values lie approximately on the same lines. The condition that they do so for a line such as Zr—Mo is that the even-odd neutron difference in Zr should be equal to the even-odd neutron difference in Mo. Such an equality can exist but is not general as implied by Fig. 8. Nevertheless the over-all simplicity of the double β-decay energy pattern may point the way to a convenient empirical mass formula. The double β-decay regularity was first pointed out by H. E. Duckworth.

[20] Coryell, Brightsen, and Pappas, Phys. Rev. **85**, 732 (1952).

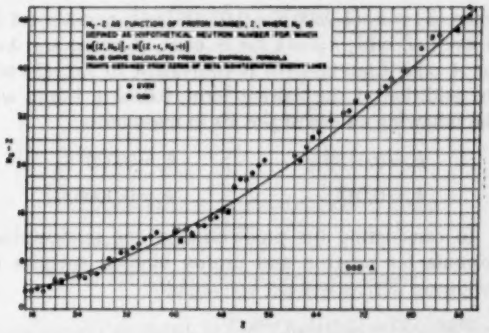

FIG. 7. Comparison of observed values of N_Z-Z with those found from semiempirical formula. N_Z is the generally nonintegral value of N for which $M(Z,N_Z)=M(Z+1, N_Z-1)$.

The authors are indebted to Gladys H. Fuller for assistance in the comparison with the semiempirical formula. They have profited greatly from discussions with Professor Charles D. Coryell and Dr. C. L. McGinnis.

APPENDIX

A simplified form of the original Weizsäcker[21] semiempirical mass formula, proposed by Bethe and Bacher[22] in 1936, has been in general use since that time. It is:

$$M(Z,N)=NM_n+ZM_p-k_v(N+Z)+k_s(N+Z)^{\frac{2}{3}}+[k_p(N-Z)^2/(N+Z)]+[k_cZ^2/(N+Z)^{\frac{1}{3}}]. \quad (5)$$

Metropolis and Reitwiesner[3] have expressed $M(Z,N)$ in the following form:

$$M(Z,A)=1.01464A+0.014A^{\frac{2}{3}}-0.041905Z_A+0.041905(Z-Z_A)^2/Z_A+0.036\lambda A^{-\frac{1}{2}}, \quad (6)$$

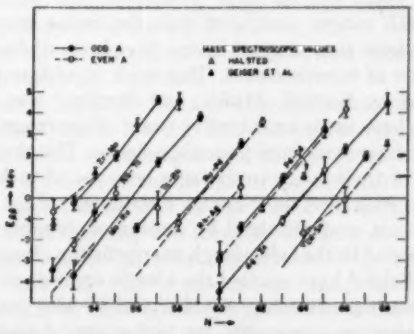

FIG. 8. Energies of two successive disintegrations, or energy differences in double β decay, plotted in the manner of Fig. 2. Points shown are from sums of appropriate points on Fig. 2. Where no points are indicated, values have been read from lines on Fig. 2. Mass spectroscopic values are from Geiger, Hogg, Duckworth, and Dewdney, Phys. Rev. **89**, 621 (1953) and R. E. Halsted, Phys. Rev. **86**, 408 (1952).

[21] C. von Weizsäcker, Z. Physik **96**, 431 (1935).

[22] H. A. Bethe and R. F. Bacher, Revs. Modern Phys. **8**, 165 (1936).

where $Z_A = A/(1.980670+0.0149624A^{\frac{1}{3}})$ and $\lambda=+1$ for A even, Z odd; $\lambda=-1$ for A even, Z even; and $\lambda=0$ for A odd. Equation (6) is equivalent to Eq. (5) with the addition of the pairing term, $0.036\lambda A^{-\frac{1}{2}}$, and with the following values of the k's in mass units:

$$k_v=0.01507, \qquad k_p=0.02075,$$
$$k_s=0.014, \qquad k_c=0.000627.$$

In considering the predictions of the semiempirical formula for neutron and proton binding energies the following derivatives are convenient:

$$\partial^2M/\partial N^2=(2/9)k_sA^{-4/3}-8k_pZ^2A^{-3}-(4/9)k_cA^{-7/3},$$
$$\partial^2M/\partial Z^2=(2/9)k_sA^{-4/3}-8k_pN^2A^{-3}-\tfrac{2}{3}k_c[3A^{-1/3}-2ZA^{-4/3}+\tfrac{2}{3}Z^2A^{-7/3}], \quad (7)$$
$$\partial^2M/\partial N\partial Z=(2/9)k_sA^{-4/3}+8k_pNZA^{-3}+\tfrac{2}{3}k_c[ZA^{-4/3}-\tfrac{2}{3}Z^2A^{-7/3}].$$

Bohr and Wheeler[23] expressed the semiempirical formula in the form:

$$M(Z,A)=A(1+f_A)+\tfrac{1}{2}B_A(Z-Z_A)^2+\lambda\delta_A, \quad (8)$$

where f_A is the packing fraction at the bottom of the mass valley, Z_A is a generally nonintegral value of Z for the "most stable" nucleus of given A, B_A is analogous to k_p/A and $\lambda\delta_A$ is again a pairing term. Empirical values for B_A, Z_A, and δ_A have been given by Bohr and Wheeler,[23] Coryell,[7] Suess,[8] Kohman,[6] and others.

[23] N. Bohr and J. A. Wheeler, Phys. Rev. 56, 426 (1939).

PHYSICAL REVIEW VOLUME 94, NUMBER 1 APRIL 1, 1954

The Ranges of Fragments from High-Energy Fission of Uranium*

E. M. Douthett † and D. H. Templeton
Radiation Laboratory and Department of Chemistry, University of California, Berkeley, California
(Received October 26, 1953; revised manuscript received December 15, 1953)

The ranges in aluminum of several fragments from the fission of U^{238} induced by 18-Mev deuterons and by 335-Mev protons have been measured by a radiochemical method. The ranges found are of the same order of magnitude as those reported for slow-neutron-induced fission. The difference in the forward and backward recoil ranges in the deuteron (18-Mev) case is consistent with the momentum corresponding to compound nucleus formation. The ranges found in the proton (high-energy) case are shorter than those of the deuteron case, the differences being greater for the lighter fragments. These differences are explained by the change in mass of the complementary fragments due to evaporation of neutrons prior to fission in the proton case, which causes the observed fragment to receive a smaller fraction of the total kinetic energy.

I. INTRODUCTION

THE ranges associated with the fission fragments from slow-neutron fission have been studied by a number of experimenters. This work is adequately reviewed by Katcoff, Miskel, and Stanley,[1] who themselves have made an extensive study of the ranges in air of the fragments from plutonium fission. The characteristics of their range study have been found to be consistent with the kinetic-energy distribution of the fission fragments as determined by ionization-chamber measurements.[2] In the field of high-energy fission, Jungerman and Wright[3] have studied the kinetic energies of fission fragments produced by 45-Mev and 90-Mev neutrons. No range measurements for high-energy fission have been reported. Such range measurements were undertaken by a radiochemical method because it makes possible the independent study of fragments of various identities. Because the production of sufficient radioactivity was a problem, the experiments were restricted to fission induced by charged particles. Originally 18-Mev deuterons were used, because of the high beam currents available. An improved technique made possible experiments with 335-Mev protons.

II. EXPERIMENTAL METHOD

Fission was induced in a thin uranium source by 18-Mev deuterons and 335-Mev protons in the 60-in. and 184-in. Berkeley cyclotrons. Adjacent to this source during the irradiation was a stack of aluminum foils. After the irradiation, the relative amount of a certain radioactive fission product in each foil was determined by radiochemical methods. From these data and the known thicknesses of the foils, the mean range of that particular kind of fission fragment was calculated.

The geometrical arrangement is indicated in Fig. 1. If the fission recoils are isotorpic, half of them will enter

* This work was performed under the auspices of the U. S. Atomic Energy Commission.
† Lt. Col., U. S. Air Force, now in HQ, USAF, Washington, D.C.; assigned to the Radiation Laboratory under the auspices of the U. S. Air Force Institute of Technology, Civilian Institutions program.
[1] Katcoff, Miskel, and Stanley, Phys. Rev. 74, 631 (1948).
[2] D. C. Bruton and W. B. Thompson, Phys. Rev. 76, 848 (1949); Can. J. Research A28, 498 (1950).
[3] J. Jungerman and S. C. Wright, Phys. Rev. 76, 1112 (1949).

the stack of aluminum foils. Those which a given range R leaving any one point of the source will be deposited on a hemispherical surface of radius R. A foil of thickness t in the stack will then contain recoils deposited on a zone of the sphere, and since the zone has an area of $2\pi Rt$, the activity from a given recoil fragment of range R in the foil will be proportional to the thickness of that foil. This will be true for each foil out to a distance from the source equal to the range. It follows that the same will be true for all points of the source, and, therefore, for the whole source, if the absorbers are sufficiently larger than the area of the source. Because of straggling and the finite thickness of the source, the observed curve of activity per unit foil thickness plotted against distance from the source is of the type shown in Fig. 1 rather than a perfect step function.

The first experiments were made with stacks of many very thin foils as had been done previously (for low-energy neutron fission) by Joliot,[4] Suzor,[5] and Finkle and co-workers.[6] The aluminum foils were a commercial grade of hammered aluminum, purchased in sheets $5\frac{1}{2}$ in.$\times 5\frac{1}{2}$ in. with a thickness close to 0.2 mg/cm^2. However, it was found that even the best of these foils varied in thickness so much from point to point that high accuracy was impossible. The probable errors of the ranges calculated from these experiments were estimated as 5 percent based on the internal consistency of the data. These results confirmed that the activity distribution in this experimental arrangement is

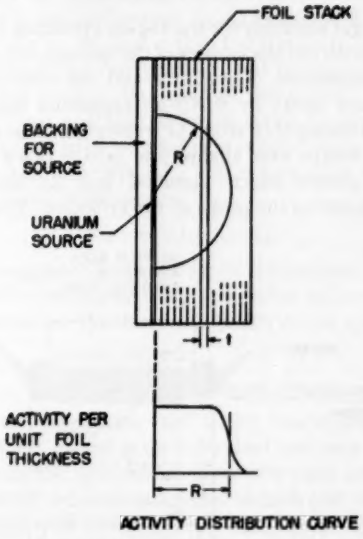

FIG. 1. Schematic arrangement.

[4] F. Joliot, Compt. rend. 218, 488 (1944).
[5] F. Suzor, Compt. rend. 224, 1155 (1947); 226, 1081 (1948); Ann. Phys. 4, 269 (1949).
[6] Finkle, Hoagland, Katcoff, and Sugarmann, *Radio-Chemical Studies: The Fission Products* (McGraw-Hill Book Company, Inc., New York, 1951), Paper No. 46, National Nuclear Energy Series Plutonium Project Record, Vol. 9, Div. IV, p. 471.

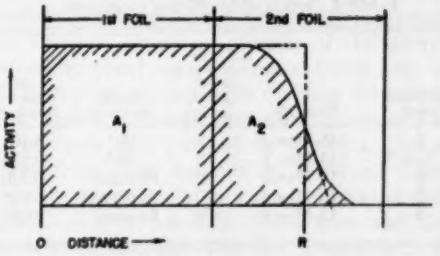

FIG. 2. Activity distribution—two-foil scheme.

approximately as shown in Fig. 1, in agreement with the results of the previous workers.[4–6]

More consistent results were obtained with a thick-foil technique. One can select the foil thickness so that the given fission recoil is completely stopped in just two foils, as indicated in Fig. 2. Let A_n and t_n be the activity and thickness of the nth foil and a and a_0 the activities per unit thickness of absorber at distances x and 0. The arithmetic mean range is

$$R=\int_0^{\infty} Xda \Big/ a_0.$$

If the region of straggling does not extend into the first foil (the control foil), then a_0 is equal to A_1/t_1; the integral is the total activity A_1 plus A_2; and

$$R=(1+A_2/A_1)t_1.$$

This result is independent of the shape of the activity distribution in the second foil. If the activity extends to a third foil, A_3 is added to A_2 in the above expression.

In the above discussion, it has been assumed that the foils are in contact with each other during the irradiation. However, the results are valid so long as the foils are parallel and sufficiently large so that every recoil particle remains in the stack.

Eight experiments, listed in Table I, were carried out by the "thick-foil" method.

Because the projectile has appreciable momentum, the fission recoils are not isotropic in the laboratory system, if they are isotropic with respect to the excited nuclues. However, it can be shown by geometrical arguments that the method of calculation introduces no error at all if the range of a fragment of a particular mass is proportional to its initial velocity and if the velocity of the recoil is sufficiently greater than that of the fissioning nucleus so that there is appreciable recoil in all directions in the laboratory. Experimental measurements[1] and the formula of Bohr[7] are both consistent with the interpretation that the range of fission fragments in gases is indeed proportional to the initial velocity. We might expect that this would also be true in aluminum. However, to investigate how exactly this condition must be satisfied, we calculated examples

[7] N. Bohr, Phys. Rev. 59, 270 (1941).

TABLE I. Details of irradiation conditions.

Bombardment	Projectile	Quantity of irradiation (μa hr)	Recoil direction*	Source thickness (mg/cm²)
1	335-Mev p	2	90°	1.101
2, 3, 4, 5	335-Mev p	2	90°	0.920
6	18-Mev d	20	forward	0.920
7	18-Mev d	20	backward	0.920
8	18-Mev d	150	forward	0.055

* With respect to the beam direction.

using the difference between the forward and backward ranges actually observed in the deuteron experiments and the extreme assumption that the ranges were proportional to the zero and first powers of the energy. The errors introduced in such cases were of the order of only one percent for forward and backward recoils and insignificant for perpendicular recoils. Thus we are confident that no appreciable error is introduced into the present results by the asymmetry of recoil.

A. Source Preparation

The sources were prepared by sputtering natural uranium onto a two-mil aluminum sheet.[8] The aluminum sheet, cut to the desired shape for target mounting, was masked by a thin bronze masking plate during the sputtering process so as to define accurately the source area. The sputtering was accomplished in a low-pressure argon atmosphere with an applied potential of 1500 volts. The average source thickness was determined by weighing the cleaned aluminum sheet before and after the sputtering process. It was necessary once or twice to stop the sputtering process and weigh the aluminum in order to determine the amount of progress made. During these intervals and after completion of the sputtering process, the uranium was in contact with the air and some UO_3 undoubtedly formed. It must, therefore, be considered that each source contained unspecified amounts of the oxide.

The sources were thick enough to introduce some uncertainty into the results. The correction for source thickness is discussed in a later section of this paper. It was not convenient to use thinner sources because, even with the thick foil technique, the 335-Mev proton experiments yielded relatively modest amounts of radioactivity in the bombardment times which were available.

B. Foil Thickness Measurements

The "thick" foils were commercial, rolled aluminum sheet of nominal thickness 0.00033 in. in bombardments 1 through 3 and 0.00025 in. in the subsequent experiments. The thickness of each foil used was calculated from the weight and the area. In the first three bombardments, the areas were determined from dimensions observed under a calibrated graph paper over an illuminated viewing plate. In subsequent experiments a foil was placed on a plate-glass surface under a special hardened steel tool with a ground flat surface of accurately known shape and with perpendicular sides. The foil was then cut to size with a scalpel. After weighing, the procedure was repeated with a slightly smaller tool to give a second measurement as a check. For over 60 foils, the differences between the pairs of thickness measurements averaged 0.07 percent.

To check the error due to macroscopic non-uniformity of the foils, a third tool was used to cut smaller areas similar to those actually exposed to the recoil fragments. These areas were cut from a large number of foils, from the same supply as those used in the bombardments, after their thicknesses had been determined as described above. The average difference between these results and those obtained by the graph paper technique was 0.3 percent, with a maximum difference of 0.53 percent. The average difference from the results of the improved method was 0.2 percent.

Very thin foils with a nominal thickness of 0.2 mg/cm² were used adjacent to the source in some cases. The thickness of these foils was determined after the bombardment by cutting to shape in a similar way. If the error were no more than one percent, a safe estimate, the contribution to the error in range would be 0.002 mg/cm², which is negligible.

C. Target Assembly

The target assembly for the 184-in. cyclotron is shown in Fig. 3, with the thicknesses of the various components greatly exagerated. The source and the collector foils were spaced apart by 0.002-in. aluminum spacers to facilitate disassembly after the irradiation. The spacers, foils, and source were aligned and held in place by four machine screws which threaded into an aluminum block adapted to the probe of the cyclotron. Vent holes

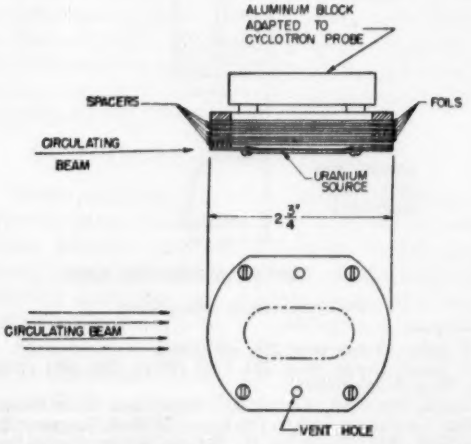

FIG. 3. Target assembly for 184-inch cyclotron experiments.

[8] J. Strong, *Procedures in Experimental Physics* (Prentice-Hall, Inc., New York, 1938), p. 159.

were provided so that the air between the foils could escape when the target was let down to the cyclotron tank pressure. The supporting foil for the source was dished slightly so that the uranium source extended into the circulating beam of the cyclotron, which struck the target almost parallel to the foils. In this arrangement, the range measured corresponds approximately to that of recoils at right angles to the beam. The uranium is disposed so that it is a thick target with respect to the beam and thin with respect to the collected recoils. The effective energy spectrum of the protons therefore extends from 335 Mev down to some lower energy, and the detail of this spectrum is unknown. This target arrangement was necessary because otherwise insufficient activity would have been obtained in reasonable bombardment times.

The target assembly for the 60-in. cyclotron was substantially the same except that it was mounted with the foils perpendicular to the deflected beam. The foils and source were so thin that they absorbed little power from the deuteron beam. The aluminum backing block, which absorbed most of the power, was water cooled. In this case the target was thin with respect to the beam, and the effective energy of the deuterons was about 18 Mev.

Those recoils which are ejected at an angle sufficiently small with respect to the plane of the source can be stopped in the spacer between the source and the first foil, and presumably there are some which spend only part of their range in this first spacer, being collected in the foil beyond. So that an error due to this cause might be avoided, a thin foil (about 0.2 mg/cm^2) was placed in the first position, and the second foil, of the thicker variety, was used as the control foil. The geometry was such that no fission recoil could reach the second spacer without having traversed more than its range in the first thin foil. The ranges were then calculated from the expression

$$R=t_1+t_2(1+A_3/A_2).$$

This arrangement was used for bombardments 2–5, the results of which showed this precaution to be unnecessary. Thereafter the thin foil adjacent to the source was not used.

D. Chemical Procedure

After the irradiation, the target was disassembled. Each foil was placed in an individual test tube and dissolved with 6*M* hydrochloric acid. The same amount of mixed carrier solution was added to each test tube, and the samples were divided into two nearly equal parts for chemical analysis. When silver carrier was added, it was added separately after the other carriers. The exchange between silver ion and freshly formed silver chloride has been shown to be reasonably fast,[9] and the solutions were thoroughly stirred and heated to effect this exchange. The silver chloride was then separated by centrifuging, and the filtrate was divided into two nearly equal aliquots. Duplicate samples of the silver were obtained by dissolving the silver chloride with ammonium hydroxide solution, then dividing the solution.

The carriers were separated using qualitative analytical methods and purified by chemical procedures adapted from those outlined by Newton.[10] The final precipitate was mounted in a small aluminum dish and weighed (glass or porcelain dishes were used for the silver chloride samples). The dish, covered with a thin piece of Cellophane, was counted with an end-windowed chlorine-argon-filled Geiger tube. Since only relative values of the specific activities are required, no attempt was made to determine absolute disintegration rates.

E. Identification of the Radioactivities

Barium 140 was identified by its half-life of 12.8 days and distinguished from 12-day Ba^{131} by the growth of its daughter La^{140}. This growth showed that not enough Ba^{131} was counted under the conditions used to cause any serious error. In bombardments 1, 2, 4, and 5, the barium separation was effected after eight days after the bombardment so that the decay of the 39-hour Ba^{139m} and 29-hour Ba^{135m} would not mask the La^{140} growth. In bombardment 3, this precaution was not taken and the lanthanum growth was obscured, but it was inferred from the other results that the 12.8-day activity was Ba^{140}. In the 18-Mev deuteron experiments, not enough of the short-lived barium activities was produced to be of any concern.

The radium spallation products[11] which contaminated the barium samples in the high-energy bombardments were taken into account in several ways. In bombardment 1, which utilized the first foil as the control foil, alpha activity was detected only in the two samples from the first foil. The beta activity due to the radium was corrected for by converting the observed alpha counting rate to the equivalent beta counting rate, the equivalence being determined by a suitable radium standard counted in both counters. Radium was separated from the barium samples during the chemistry in bombardment 2 by the use of Dowex resin columns eluted with citrate.[12] In bombardment 3, alpha activity measurements showed that the ranges of the radium spallation products were less than the thickness of the "very thin" foil adjacent to the source. Radium contamination in the samples of the thin foil caused no error, because the activities of these samples were not used in the range calculations. Radium spallation products were of no concern in the lower-energy deuteron bombardments.

Resolution of the decay curves for the tin samples showed the three half-lives of the 27.5-hour Sn^{121}, 9.5-day Sn^{125}, and 130-day Sn^{123} isotopes.[13]

[9] A. Langer, J. Chem. Phys. **10**, 321 (1942).

[10] A. S. Newton, Phys. Rev. **75**, 17 (1949).

[11] P. R. O'Connor and G. T. Seaborg, Phys. Rev. **74**, 1189 (1948).

[12] E. R. Tompkins, J. Am. Chem. Soc. **70**, 3520 (1948).

[13] Hollander, Perlman, and Seaborg, Revs. Modern Phys. **25**, 469 (1953).

TABLE II. Data from bombardment No. 4.

	Target detail				
	Source	0.920 mg U/cm²			
	Foil No. 1	0.218 mg Al/cm²±1.0%			
	Foil No. 2 (control foil)	1.7100 mg Al/cm²±0.2%			
	Foil No. 3	1.7099 mg Al/cm²±0.2%			
	Foil No. 4	1.7150 mg Al/cm²±0.2%			
	Foil No. 5	1.7078 mg Al/cm²±0.2%			
	Observed mean normalized specific activity (counts min^{-1} mg^{-1})				
Isotope studied	Foil No. 1	Foil No. 2	Foil No. 3	Foil No. 4	Foil No. 5
Ba^{140}	0.1200±0.0015	1.000±0.0017	0.4078±0.0035	0.0008±0.0007	0.0008±0.0007
$Sn^{123,125}$	0.1052±0.0031	1.000±0.024	0.4877±0.0094	0.0021±0.0005	0.0002±0.0001
Cd^{115}	0.1254±0.0023	1.000±0.0024	0.6231±0.0041	0.0045±0.0007	0.0004±0.0001
Ag^{111}	0.1382±0.0027	1.000±0.0089	0.659±0.010	0.0074±0.0004	0.0001±0.0000
Sr^{91}	0.1219±0.0007	1.000±0.014	0.9066±0.0046	0.0972±0.0013	0.0047±0.0005*
Sr^{89}	0.1296±0.0008	1.000±0.0027	0.8899±0.0035	0.1038±0.0012	0.0013±0.0013

* Na^{24} contamination probable.

All cadmium samples gave decay curves of the same shape, which could be resolved into two components for the isomers of Cd^{115}. The half-lives observed were 43 days and 53 hours. The latter value agrees with the observations of Wahl and Bonner[14] and of Folger, Stevenson, and Seaborg,[15] but is slightly lower than the previously accepted values.

Silver-111 was identified by the 7.5-day half-life. In addition, one absorption curve was taken for each proton bombardment, using the most active sample from the control foil, to differentiate it from the 8.2-day Ag^{106}. The absorption curves showed that the radiation counted was predominantly a beta spectrum with a range of 400 mg/cm² of beryllium, which corresponds to the radiation of Ag^{111}. The level of radiation counted that could be associated with Ag^{106}, which has an abnormally high ratio of gamma-ray counts to electron counts,[16] was of the order of 0.2 percent.

When the 9.7-hour Sr^{91} activity was sought, the final strontium separation was made after 13.5 hours after the end of the bombardment. so that the 2.7-hour Sr^{92} and its 3.6-hour daughter would not interfere. The isotope was identified by the 9.7-hour half-life which tailed into the long half-life of from 54 to 61 days. Corrections for the activity of the 53-day Sr^{89} were negligible for the observations used for the range calculations.

The strontium samples were chemically repurified after the Sr^{91} had decayed to a low level. This permitted counting the 54-day Sr^{89} activity without interference from Y^{91}. However this repurification was not accomplished in bombardments 6 and 7. In these two instances the difference between the ranges of Sr^{89} and Sr^{91} was calculated from the observed shift in the relative activities caused by the change in the abundance of the isotopes with time.

The activity in the samples from the foils beyond the range of the fragments was so near background level that its decay was confused by statistical fluctuations. However, a low level of Na^{24} contamination was indicated in some of the Sr^{91} samples.

III. EXPERIMENTAL RESULTS

The observed specific activities of the samples, i.e., counts per minute per milligram of sample, could be used directly for range calculations since, for a given bombardment, the same amount of inactive carrier had been added to each of the dissolved foils. For a given sample pair, i.e., both from the same foil, half the percentage difference between the two specific activities was recorded each time the pair was counted, and an average of this quantity was taken to be the observed experimental uncertainty, independent of the statistical counting error. Included in this were errors due to chemistry, differences in self-absorption, self-scattering and backscattering, and small differences in counting geometry.

The sum of the two specific activities of an identical pair was divided by that of the control foil each time the samples were counted and recorded as the normalized specific activity of that foil. For a given isotope investigation, the samples from all foils decayed with the same half-life so that this normalized specific activity remained a constant figure except for the statistical variation. The error due to fluctuations in counter sensitivity and to statistics was estimated from this variation. Small corrections were made whenever necessary for the decay in the time between the counting of the various samples.

Table II lists the mean normalized specific activities determined as described above for one experiment. The error shown in each case is the combined observed uncertainty, estimated from the data, due to the errors mentioned above. As shown, each isotope investigation included an examination of at least one foil beyond the end of the range. The normalized specific activity found in this foil was in *every* case less than one percent. In some cases, however, its magnitude was comparable to the observed error in the other foils. For the sake of consistency, this correction was subtracted in all cases before substitution into the equation, although generally

[14] A. C. Wahl and N. A. Bonner, Phys. Rev. 85, 570 (1952).
[15] Folger, Stevenson, and Seaborg (private communication).
[16] N. Feather and J. V. Dunworth, Proc. Roy. Soc. (London) A168, 566 (1938).

TABLE III. Experiments with 335-Mev protons. Ranges are given in mg/cm² Al.

Bombardment	Sr^{89}	Sr^{91}	Ag^{111}	Cd^{115}	$Sn^{123,125}$	Ba^{140}
1		3.52±0.03				2.67±0.04
2	3.66±0.03	3.63±0.04	3.11±0.04			2.80±0.03[a]
3	3.66±0.06	3.72±0.23[b]	3.12±0.02			2.82±0.01[a]
4	3.62±0.02	3.65±0.03	3.07±0.03	3.00±0.01	2.76±0.05	2.62±0.01
5	3.63±0.02		3.04±0.03	2.99±0.04	2.85±0.04	2.64±0.03
			Mean range corrected for straggling			
1						2.53±0.04
2			3.08±0.04			
3			3.08±0.02			
			Weighted averages, bombardments 2–5[c]			
	3.63±0.01	3.63±0.02	3.07±0.01	3.00±0.01	2.82±0.03	2.63±0.01

[a] Used to estimate straggling and not included in weighted average.
[b] Larger error due to chemistry.
[c] Uncorrected for source thickness.

this manipulation contributed little to the accuracy of the measurement.

The mean ranges calculated from these data using the formulas already developed are listed in Tables III and IV. The formulas are not valid if the straggling effect extends into the control foil. This condition exists for the shorter ranges in experiments 1, 2, and 3, since foil thicknesses near 2.3 mg/cm² were used. In addition, the "very thin" foils (near 0.2 mg/cm²) were used adjacent to the source in experiments 2 and 3, which further aggravated this condition. This explains, for example, why the calculated ranges for Ba^{140} from experiments 2 and 3 are longer than those calculated from experiments 4 and 5. In all of these four bombardments, the same source was used.

It is possible to make some deductions concerning the magnitude of the straggling from these data. If a tangent is drawn to the activity distribution curve (Fig. 2) at its steepest point, it intersects the distance axis at the *extrapolated range*. We define the *straggling parameter* as the difference between the mean range and the extrapolated range. If it is assumed that the shape of the activity distribution curve is that of an integrated Gauss error curve, then a straggling parameter can be selected to fit the observed data. In the case of Ba^{140}, the parameter was selected to make the data of bombardments 2 and 3 consistent with the weighted average of the ranges from bombardments 4 and 5. Similar estimates were made using the data from bombardments 4 and 5 for those longer ranged fragments (Sr^{89} and Sr^{91}) which penetrated appreciably into the fourth foil. The activity distributions in the deuteron experiments allowed a single estimate of the straggling parameter of Ag^{111}. The resulting parameters, listed in Table V, are rather sensitive to errors in range and observed activity ratios. For example, a one-percent uncertainty in the mean range combined with a one-percent uncertainty in the ratio of observed activities results in an eight-percent uncertainty in the estimated straggling. The assumption that the shape of the activity distribution curve is Gaussian is not critical. These parameters include the effect of the source (0.920 mg/cm² thick in all cases) and are not to be confused with the straggling of recoils from a thin source.

The data for barium and strontium show that for the conditions of bombardments 2–5 the straggling parameter is 15±1 percent of the uncorrected mean range for both heavy and light fragments. If this is true for all fragments, then reversed calculations show that the ranges for Ag^{111} from bombardments 2 and 3 are high by about one percent. The only other case which requires this correction is that of Ba^{140} in bombardment 1. A parameter of 0.47 mg/cm² Al was used, on the basis that the thickness of the source was largely responsible for the straggling. The values for Ba^{140} from bombardments 2 and 3 are not corrected, nor are they included in the average, because they were used to estimate the straggling parameters.

A difference between the range of Sn^{123} and Sn^{125} was not distinguishable. Since both isotopes are present in the same samples, a difference in range would be indicated by a gradual shifting with time of the value for the normalized specific activity of those samples taken from the foils beyond the control foil, coincident with the change in the relative abundance of the two isotopes. No such trend was distinguishable. Unfortunately, the low activity level of the 130-day Sn^{123} isotope gave rise to statistical fluctuations larger than the magnitude of the expected shift.

It has been mentioned that the observed decay of the tin samples showed the presence of the 27.5-hour Sn^{121} isotope. The range calculations referred to above were made using the activities observed after the 27.5-hour activity had decayed to a low level. No range is reported for Sn^{121} because the associated soft β^- radiation

TABLE IV. Experiments with 18-Mev deuterons.

Bombardment	Uncorrected mean range (mg/cm² Al)			
	Sr^{89}	Sr^{91}	Ag^{111}	Ba^{140}
6	4.05±0.03	3.99±0.02	3.38±0.04	2.91±0.02
7	3.71±0.03	3.66±0.02	3.06±0.05	2.54±0.01
8	4.40±0.04		3.76±0.04	3.26±0.02

TABLE V. Straggling parameters.

Bombardment	Fragment	Straggling parameter (mg/cm² Al)	(percent*)
2	Ba^{140}	0.38	14
3	Ba^{140}	0.41	16
4	Sr^{91}	0.50	14
4	Sr^{89}	0.57	16
5	Sr^{89}	0.56	15
6	Ag^{111}	0.43	13

* Percent of the uncorrected mean range.

(0.38 Mev)[17] led to large errors due to differences in self-absorption between the various samples.

A. Corrections for Source Thickness

Experimental evidence of the effect of the source thickness was obtained from bombardments 6 and 8, both made under identical conditions except that the two uranium sources differed considerably in thickness. The differences between the observed ranges for the two bombardments are

Fragment	ΔR (mg/cm² Al)
Ba^{140}	0.350±0.028
Ag^{111}	0.374±0.058
Sr^{89}	0.353±0.050
Weighted mean	0.354±0.023

The three are in agreement within the limits of the experimental error, and the weighted average was taken to be equivalent to 0.865 mg/cm² of source thickness, the difference between the measured thicknesses of the two sources. Corrections were then made on the assumption that the effect of the source upon the mean range was proportional to the measured source thickness.

For a uniform source the source correction should be equal to the aluminum equivalent of half the source thickness. On this basis, one mg/cm² of aluminum was equivalent to 1.22 mg/cm² of our source material. This relative stopping power is in disagreement with that calculated from the results of Segrè and Wiegand.[18] They reported that for fission products one mg/cm² of aluminum is equivalent to 3.4 of uranium or 2.7 of U_3O_8. The discrepancy is in the direction corresponding to uneven thickness of our source. A thickness variation, because of the geometry of sputtering, roughness of the aluminum surface, diffusion of the uranium into the aluminum under the conditions of the sputtering, or chemical reaction of the uranium with the aluminum, may be the cause of this effect. Suzor[5] suggested similar explanations for wide discrepancies observed in his work concerning slow-neutron-induced fission. He also observed quite an appreciable difference in the relative stopping power of an uranium source electroplated onto copper and one electroplated onto nickel. The observations concerning the straggling described above are in line with the magnitude of the source corrections used.

In bombardments 2–5, each range was measured two or more times under comparable conditions, and the agreement found is evidence of the consistency of the experimental method. The results of bombardment 1, when corrected for the source thickness, are in good agreement with the other high-energy results. Listed in Table VI are the final averages of the corrected results, obtained by weighting the various determinations inversely as the squares of their probable errors. The errors listed include that introduced by the source correction.

The forward and backward recoil ranges measured in the deuteron experiments 6 and 7 were averaged and listed in the last column in Table VI as the recoil ranges at right angles to the beam. The averaging process cancels out the effect of the momentum exchange with the incident deuteron so that they can be compared with the ranges measured in bombardments 1–5.

IV. DISCUSSION OF RESULTS

The differences between the forward and backward ranges of fragments from the deuteron-induced fission are related to the momentum imparted to the uranium nucleus by the deuteron. These differences, from bombardments 6 and 7, are

Fragment	ΔR (mg/cm² Al)
Sr^{89}	0.339±0.047
Sr^{91}	0.326±0.027
Ag^{111}	0.322±0.066
Ba^{140}	0.372±0.021
Weighted average	0.351±0.015

The probable errors do not include contributions from the source correction because the same source was used in these two experiments. Within these errors, the differences agree, and to simplify the discussion the average value will be considered.

The excitation energy of 27 Mev (corresponding to capture of an 18-Mev deuteron) is in the region where compound nucleus formation is probable. If a compound nucleus of mass A is formed with a forward kinetic energy E_0 and the total kinetic energy of the two fragments in the center-of-mass system is E, then it can be shown that for a fragment of mass M the difference in kinetic energy between the forward and backward

TABLE VI. Corrected mean ranges.

Fragment	Range in mg/cm² aluminum: 335-Mev p 90°	18-Mev d forward	18-Mev d backward	18-Mev d 90°
Sr^{89}	4.01±0.03	4.43±0.03	4.09±0.04	4.26±0.03
Sr^{91}	4.00±0.03	4.36±0.03	4.04±0.03	4.20±0.03
Ag^{111}	3.44±0.03	3.77±0.03	3.44±0.06	3.60±0.04
Cd^{115}	3.37±0.03	...	...	...
$Sn^{125,126}$	3.19±0.04	...	...	...
Ba^{140}	3.00±0.02	3.29±0.02	2.92±0.03	3.10±0.02

[17] R. B. Duffield and L. M. Langer, Phys. Rev. **76**, 1272 (1949).
[18] E. Segrè and C. Wiegand, Phys. Rev. **70**, 808 (1946).

directions will be

$$\Delta E = 4[EE_0M(A-M)]^{\frac{1}{2}}/A.$$

The effect of the loss of a few neutrons has been neglected, but it amounts to less than one percent. Using 168 Mev for E, similar to the values found for slow-neutron-induced fission[2] as corrected by Leachman,[19] and 18(2/240) for E_0, the following differences were calculated:

M	ΔE (Mev)
89	9.7
91	9.7
111	10.0
140	9.9

An average of 9.8 Mev was selected as representative of the region studied. The uncertainty in the correct value of E is unimportant in the following discussion.

Since the observed differences in range and the estimated differences in energy are both nearly independent of M, then the stopping power of aluminum for fission fragments must be nearly independent of M near the beginning of the range. The average value of this stopping power is estimated to be 28 Mev cm²/mg, based on the above data.

Nuclei which are excited by "stripping" reactions in which only one nucleon is captured or by "hit-and-run" reactions in which neither is captured would gain considerably less momentum than those forming true compound nuclei. If such reactions were important, then the stopping power calculated above would be too large.

The variation of ionization along the recoil paths has been studied in various gases by Lassen.[20] If it is assumed that the rate of energy loss in aluminum varies in the same way, normalization of his curves to the ranges in aluminum yield estimates of the stopping power. Such estimates (for the first tenth of the range) yield values ranging from 40 to 50 Mev cm²/mg for the rate of energy loss in aluminum. Since the average energy loss over the whole path must be about 20 Mev cm²/mg, our estimate of 28 is not likely to be high but may rather be low. In the absence of a theory of the stopping mechanism for fission fragments in metals, it is difficult to say whether the disagreement of the values converted from the gas measurements with that which we calculated is reasonable.

Since calculation on the basis of the alternate modes of reaction described above leads to values of the rate of energy loss which are less than the average over the whole range, which is impossible, these data support the assumption that compound nucleus formation is, in fact, the predominant mode of reaction leading to fission when uranium is bombarded with 18-Mev deuterons.

The ranges reported here are substantially the same as those from low-energy fission, as they must be if the recoil energy is due simply to the Coulomb repulsion of the two fragments according to the liquid drop-model of fission. Small differences are expected according to the mass and charge of the fissioning nucleus and according to the speed of the reaction, as discussed below. Accurate comparison of the ranges reported here with previous work is difficult for several reasons. Most of the previous measurements were made on fragments from the fission of U^{235} or of Pu^{239} induced by slow neutrons, whereas we used U^{238} and charged particles. Our fissioning nucleus is likely an isotope of neptunium, at least in the deuteron case. The accuracy of much of the previous work is in doubt, and considerable disagreement exists between various results. In those cases where the ranges were measured in substances other than aluminum, the conversion to aluminum introduces additional uncertainty. The distinction between *mean* and *extrapolated* ranges confuses some of the comparisons Our own corrections for source effects are not as reliable as we would prefer.

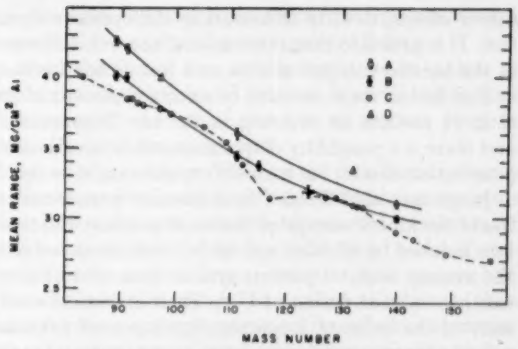

FIG. 4. Mean ranges of fragments from fission induced by: A, 18-Mev deuterons; B, 335-Mev protons; C, slow neutrons, Katcoff *et al.* (reference 1); D, slow neutrons, Suzor (reference 5).

The most significant comparison can be made with the ranges reported by Katcoff, Miskel, and Stanley[1] from their extensive study of slow-neutron-induced fission of Pu^{239}. Their values, corrected to aluminum, are compared with our results in Fig. 4. The pronounced dip in the center of their curve indicates the lower kinetic energies that prevail when the fission is nearly symmetrical, an effect that has been verified by Brunton and Thompson.[2] There is no evidence for a similar dip in our curve for fission induced by 335-Mev protons. Our points for the 18-Mev deuteron case are too few to give evidence concerning a dip.

According to these curves and our stopping power estimate of 28 Mev cm²/mg, the average kinetic energy of uranium fission induced by 18-Mev deuterons is 5 or 10 Mev greater (considering both fragments) than that of Pu^{239} induced by slow neutrons, whereas the difference in nuclear charge should cause a small difference in the opposite direction. On the other hand, the results obtained by Suzor[5] for ranges in aluminum of fragments from low-energy fission of U^{235}, after correction for

[19] R. B. Leachman, Phys. Rev. **83**, 235 (1951).
[20] N. O. Lassen, Phys. Rev. **70**, 577 (1946); **75**, 1762 (1949); Kgl. Danske Videnskab. Selskab, Mat.-fys. Medd. **25**, No. 11 (1949); **26**, No. 5 and 12 (1951).

source effects, deviate from ours in the opposite direction. It is probable that there should be some difference in the kinetic energies of slow and fast fission because in slow fission there seems to be some adjustment of the ratio of protons to neutrons in the two fragments[21,22] and there is a possibility of quantum-mechanical barrier penetration effects, but such differences should be small.

Jungerman and Wright[3] by ionization measurements found the kinetic energy of fission of uranium and thorium induced by 45-Mev and 90-Mev neutrons to be on the average about 5 percent greater than that of slow-neutron-induced fission of U^{235}. Their statistical errors were of the order of 2 percent. Spallation of neutrons prior to fission may increase the kinetic energy by decreasing the nuclear dimensions; according to the simple model described by Jungerman and Wright, this effect amounts to 1 percent in the energy for each seven neutrons lost. Each proton lost decreases the energy about 2 percent, but loss of several protons is unlikely.[23] This decrease might be compensated by measurement of the ionization caused by the protons. This work confirms the idea that there is little difference in kinetic energy between fast and slow fission, apart from changes due to the identity of the particular nucleus which fissions, but because of the difficulties mentioned above the magnitude of the difference is not well established.

The comparison of our 335-Mev proton and 18-Mev deuteron experiments is more satisfactory than the comparison with low-energy work because the similarity of the experimental conditions allows us to place greater confidence in the significances of the differences. Numerical values for the differences calculated from the data of bombardments 2–7 only (to avoid the additional uncertainty caused by the source correction) are

Fragment	ΔR (mg/cm²)	ΔE (Mev)
Sr^{89}	0.249±0.028	7.0
Sr^{91}	0.192±0.029	5.4
Ag^{111}	0.153±0.036	4.3
Ba^{140}	0.099±0.016	2.8

The range differences have been converted to approximate energy differences by use of the stopping power (28 Mev cm²/mg) estimated above.

These data can be explained very well by a model similar to those discussed by Goeckermann and Perlman[24] and by Jungerman and Wright.[3] To simplify the discussion we shall make certain approximations. The kinetic energy of fission will be assumed to be 168 Mev, as before, and in accordance with the preceding discussion will be considered as independent of the excitation induced within the fissioning nucleus. In calculating the momentum distribution between the two fragments, the mass of the complementary fragment will be calculated neglecting the two or three (or more?) neutrons lost after fission from the fragments in flight.[25,26]

Our model for the high-energy proton-induced fission is as follows. The initial event is the excitation of the uranium by the proton by one or more nucleon-nucleon collisions. The proton may escape with some fraction of its original energy. It may have undergone charge exchange and escape as a fast neutron. In rare cases it may be captured to form a compound nucleus. Some of the nucleons struck by the proton may also escape with very high energies. Mesons may be produced in these initial events and escape the nucleus. Whatever the details of these initial events, there remains a more or less highly excited nucleus of mass about 238 and charge about 92. The excitation energy is dissipated by spallation, mostly of neutrons. When the nucleus is relatively unexcited, fast fission, with no preferential distribution of charge competes effectively with the other processes, especially after many neutrons have been lost. In those cases where many protons have been lost, the fissionability parameter Z^2/A is relatively less favorable. Thus the distribution of fissioning nuclei is principally among nuclides more deficient in neutrons than is the distribution of spallation products which will be found by radiochemical studies.[11]

Because the mass of the fissioning nucleus is less than in the low-energy case, a particular fragment, say Ba^{140} is associated with a smaller complementary fragment and therefore receives a smaller fraction of the total kinetic energy. If E is the total kinetic energy of fission, A the mass of the uranium nucleus before spallation, M the mass of the fission fragment being considered, and N the number of neutrons lost prior to fission, then the difference in recoil energy ΔE_M between deuteron and proton fission is given by the expression

$$\Delta E_M = EMN/A(A-N),$$

if the effect of spallation on the value of E is neglected. From this approximate expression it follows that if the fission takes place predominantly at a single nuclide (or a few very close together) so that N is practically a constant, the observed differences in recoil energy would be approximately proportional to the masses of the fragments, whereas the observed differences are almost inversely as the masses. This expression was used to calculate the value of N corresponding in each case to the observed difference in recoil energies. The results are

Fragment	ΔE_M (Mev)	N
Sr^{89}	7.0	25
Sr^{91}	5.4	19
Ag^{111}	4.3	13
Ba^{140}	2.8	8

One unit has been substracted from N to allow for the difference in mass of the proton and deuteron, and two

[21] Coryell, Glendenin, and Edwards, Phys. Rev. **75**, 337 (1949).
[22] D. C. Brunton, Phys. Rev. **76**, 1798 (1949).
[23] Y. Yamaguchi, Progr. Theoret. Phys. (Japan) **5**, 142 (1950).
[24] R. H. Goeckermann and I. Perlman, Phys. Rev. **73**, 1127 (1948); **76**, 628 (1949).
[25] R. R. Wilson, Phys. Rev. **72**, 189 (1947).
[26] J. S. Fraser, Phys. Rev. **88**, 536 (1952).

units have been added to compensate for the probable loss of one to three neutrons prior to fission in the deuteron case. No great accuracy can be attributed to these numbers of neutrons lost because of the approximations made in the calculation.

The results of high energy, proton-induced fission study by Folger, Stevenson, and Seaborg[15] allow one to deduce that the strontium and barium fragments from 335-Mev proton-induced fission studied in the present work are largely produced as primary yields; that is, relatively little of these activities result from beta decay of other primary products. Probably the Ag^{111} is formed principally as Pd^{111} or Rh^{111}. On the basis of the assumption that there is no time in fast fission for preferential charge distribution, one can estimate the identity of the principal fissioning nucleus responsible for each observed fragment. The results of such estimates are

Fragment	Fissioning nucleus	N
Sr^{89}	U^{214} or Np^{215}	21–22
Sr^{91}	U^{220} or Np^{222}	16–18
Pd^{111}	U^{232} or Np^{234}	15–16
Rh^{111}	U^{227} or Np^{229}	10–11
Ba^{140}	U^{230} or Np^{232}	6–8

The agreement of these values of N with those calculated from the observed differences in energy is probably better than can be expected of so crude a treatment, but it indicates that the trend of results is consistent with our model of the fission process.

The differences in recoil energy can be explained in each case by various arbitrary numbers of protons together with some corresponding numbers of neutrons, but no single "average" fissioning nucleus can explain all the data. Thus we are forced to conclude that a considerable variety of nuclei undergo fission.

Since the loss of two or three protons is enough to explain all of the observed decrease in recoil energy, it it demonstrated that extensive loss of protons prior to fission is not a frequent event.

Another possible mechanism is that fission occurs while the nucleus is still highly excited and that neutrons escape from the remaining highly excited fragments. If it is assumed that the excitation energy is shared between the fragments in proportion to their masses and that the neutrons escape in random directions, then with the same approximations as made before it results that about half as many neutrons are required to be lost (from both fragments) as in the case when they are lost prior to fission in order to explain the observed differences in recoil energy. We consider it unlikely that fission precedes very much of the spallation, but this calculation showed that loss of a few of the neutrons after fission does not affect our treatment very seriously.

A consequence of these data is that the observed curve of yield of fission products as a function of mass number, which for high-energy fission of uranium has a broad maximum,[11,15] is a weighted superposition of individual curves, one for each of the various species which undergo fission. It is possible that these individual curves are peaked much more sharply.

This problem was suggested by Professor Glenn T. Seaborg, whose encouragement and advice aided us throughout the work. We are indebted also to Dr. A. S. Newton for many helpful suggestions and to Dr. W. R. McDonell for assistance in the experiments. These experiments would have been impossible without the cooperation of the crews of the 60-in. and 184-in. cyclotrons.

The Third Forbidden Beta Spectrum of Rubidium-87†

M. H. MacGregor* and M. L. Wiedenbeck
Randall Laboratory of Physics, University of Michigan, Ann Arbor, Michigan
(Received November 16, 1953)

The use of thin-lens beta spectrometers has been extended to the measurement of an isotope of extremely low specific activity, rubidium 87. The Rb^{87} beta spectrum is third forbidden and not "unique." The spectrum gave a linear Kurie plot when the third forbidden tensor (or vector) correction factor was applied. The extrapolated value $E_{max}=275$ kev agreed well with the results of recent investigations.

An extension of a recent measurement of the Rb^{87} half-life was carried out with an enriched sample of Rb^{87}, and a value $T_{\frac{1}{2}}=6.2\pm0.3\times10^{10}$ years was obtained.

I. INTRODUCTION

THE radioactive decay of rubidium-87 into strontium-87 has been studied by many investigators. The long half-life of the decay and the low energy of the emitted beta particle combine to make accurate measurements of the decay constants extremely difficult. Although absorption measurements indicated that no gamma rays are present in the decay,[1] some investigations[2–6] seemed to point to a complex beta spectrum, containing one or more conversion electrons. Other experiments[1,7,8] indicated that the beta decay is directly to the ground state of Sr^{87}. In a previously reported paper by the present authors,[9] a coincidence measurement was described which showed that the presence of any conversion electrons in the decay is highly unlikely.

Measurements of the half-life of the decay that have been made[1,7,8,10] must be carefully evaluated. Often large corrections were necessary for the solid angle subtended, self-absorption in the source, back-scattering from the support, and assumptions concerning the decay scheme. Corrections of this nature can lead to a considerable uncertainty in the final result.[11,12] In the paper mentioned above,[9] the present authors reported a half-life measurement that depended on only one correction factor, the extrapolation to zero source-plus-backing thickness. A value for the specific activity of 478 counts per gram of natural RbCl per second was obtained. Subsequent to this report, an electromagnetically-enriched sample of RbCl was obtained from the Carbon and Carbide Chemicals Division at Oak Ridge, Tennessee. This sample contained 89.62 percent Rb^{87} as compared with 27.85 percent Rb^{87} in natural rubidium.[13] Three very thin enriched RbCl sources were prepared and counted in the manner previously described. The data for the enriched sources yield a value of the half-life, $T_{\frac{1}{2}}=6.2\pm0.3\times10^{10}$ years. The thinnest source-plus-backing thickness was 0.05 mg/cm², which corresponds to a zero-thickness extrapolation from about 5 kev to zero.

Measurements of the maximum energy of the beta spectrum range from 130 kev to 560 kev.[5,14–16] The two most recent spectra reported, those of Curran[7] and Lewis,[8] both give maximum energies of about 275 kev, a result also confirmed by Bell.[17] Curran used a RbCl source placed on the cathode of a proportional counter. Lewis used a rubidium iodide crystal mounted on the end of a photomultiplier tube.

II. PRELIMINARY MEASUREMENTS WITH A THIN-LENS SPECTROMETER

In an attempt to determine if a magnetic measurement of the rubidium-87 beta spectrum would be feasible, a conventional thin-lens beta spectrometer was used to test the effect of large-area sources. On the basis of the results obtained, a special thin-lens spectrometer 16 inches in diameter and 42 inches in length was constructed. Sources and counters in a variety of sizes were investigated. With a source and counter each 4 inches in diameter, an optimum resolution of 10 percent was obtained, using the Cs^{137} conversion line for the measurement. In order to minimize the background counting rate, the final arrangement chosen was a source 4 inches in diameter and a counter 2 inches in diameter.

For the sake of beam intensity, the spectrometer baffles were placed to give a resolution of 14 percent. The effect of this rather poor resolution on the shape of the beta spectrum can be readily calculated. To a good approximation, the shape of a conversion line can

† This research was supported in part by the Michigan Memorial Phoenix Project.
* U. S. Atomic Energy Commission Predoctoral Fellow. Now at the University of California Radiation Laboratory, Livermore, California.
[1] S. Eklund, Arkiv Mat. Astron. Fysik **A33**, No. 14 (1946).
[2] G. Hoffman, Z. Physik **25**, 177 (1924).
[3] W. Mühlhoff, Ann. Physik **7**, 205 (1930).
[4] G. Orban, Akad. Wiss. Wien, 2a, **140**, 121 (1930).
[5] Z. Ollano, Nuovo cimento **18**, 11 (1941).
[6] O. Haxel and F. G. Houtermans, Z. Physik **124**, 705 (1948).
[7] Curran, Dixon, and Wilson, Phys. Rev. **84**, 151 (1951).
[8] G. M. Lewis, Phil. Mag. **43**, 1070 (1952).
[9] M. H. MacGregor and M. L. Wiedenbeck, Phys. Rev. **86**, 420 (1952).
[10] Haxel, Houtermans, and Kemmerich, Phys. Rev. **74**, 1886 (1948).
[11] Bähnisch, Huster, and Walcher, Naturwiss. **39**, 16, 379 (1952).
[12] C. Charpak and F. Suzer, Compt. rend. **233**, 1356 (1951).
[13] A. O. Nier, Phys. Rev. **79**, 450 (1950).
[14] W. F. Libby and D. D. Lee, Phys. Rev. **55**, 245 (1939).
[15] A. K. Saha, Proc. Natl. Inst. Sci. India **12**, 159 (1946).
[16] T. Fazzini and S. Franchotti, Nuovo cimento **5**, 311 (1948).
[17] Bell, Cassidy, and Davis, *Nuclear Data*, National Bureau of Standards Circular 499, Supplement 1 (U. S. Government Printing Office, Washington, D. C., 1951), p. 20.

be represented by an isosceles triangle. The ratio of the half-width of the triangle to the momentum of the line is defined as the resolution W. If we let $K(p,p')$ represent the shape of the conversion line, where p' is the momentum of the conversion electrons and p is the momentum corresponding to the current flowing through the spectrometer coil, the equation for the observed spectrum $n(p)$ in terms of the true spectrum $N(p)$ is:

$$n(p)=\int_0^\infty K(p,p')N(p')dp'.$$

Since $K(p,p')$ is a function only of the ratio of p to p', a Fourier expansion is feasible. The equation for the true spectrum in terms of the observed spectrum is then

$$N(p)\simeq\frac{n(p)}{p}-\frac{W^2}{12}\left(\frac{n(p)}{p}+4\frac{dn(p)}{dp}+\frac{d^2n(p)}{dp^2}\right).$$

For $W=0.14$, this correction amounts to less than 2 percent over most of the spectrum.

The spectrometer was calibrated with the 623.8-kev conversion line from Cs^{137}. As a check on the operation of the instrument, the S^{35} beta spectrum was run. With the source mounted on a thin Zapon film and with a counter window of 0.25-mil Mylar (0.6 mg/cm²), the Kurie plot was linear down to about 70 kev. When the S^{35} source was sandwiched between two RbCl films having a combined thickness of 0.44 mg/cm², this simulated thick source gave a S^{35} Kurie plot that began to tail up at about 110 kev. (The RbCl, of course, contributed a negligible number of electrons.) The ratio of these two Kurie plots was used to apply a low-energy correction to the data obtained with a "thin" RbCl source (0.44 mg/cm²), as described in the next section. The end-point energy of the S^{35} Kurie plot was 166 kev, which gave a good check on the calibration of the spectrometer.[18]

III. MEASUREMENT OF THE RUBIDIUM BETA SPECTRUM

In order to measure the rubidium spectrum, two enriched RbCl sources were prepared, each 4 inches in diameter. The RbCl was deposited on the backing by the process of sublimation from a hot crucible in a vacuum. This method insures microscopic uniformity. In order to obtain macroscopic uniformity, each source was put on in a series of four carefully-spaced evaporations. The "thin" source had a thickness of 0.44 mg/cm² and was deposited on an aluminized Zapon backing (0.05 mg/cm²). The "thick" source had a thickness of 1.6 mg/cm² and was deposited on an aluminized Mylar backing (0.6 mg/cm²).

Since the specific activity of RbCl is so low, the problem of reducing the background counting rate was extremely important. The spectrometer cell counter was made of copper and had a minimum volume consistent with good counter characteristics—2 inches in diameter and ½ inch in length. An anticoincidence counter was placed immediately beneath the spectrometer counter to eliminate cosmic ray counts. (The spectrometer was mounted vertically, with the source at the top.) The counter assembly and the inside of the spectrometer at the counter end were shielded with one inch of copper inside of two inches of lead. With external quench circuits on each counter, the spectrometer operation was stable enough so that reproducible results could be obtained.

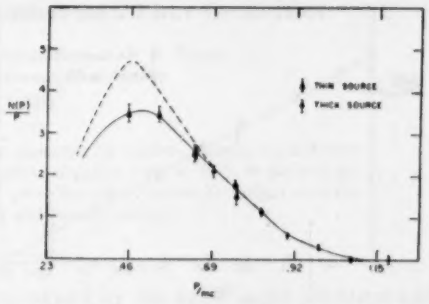

FIG. 1. Rubidium-87 momentum spectrum. The dotted line represents the spectrum before correcting for source thickness.

The rubidium-87 beta spectrum that was measured is shown in Fig. 1. Each error flag represents an 84 percent probability that the point lies within the limits indicated. The correction for finite resolution has been applied, and the source-thickness correction derived from the S^{35} measurements has also been made. This spectrum agrees well with the spectrum obtained by Lewis[8] down to about 70 kev, at which point the spectrometer counter window absorption becomes important.

IV. ANALYSIS OF THE BETA SPECTRUM

The "allowed" Kurie plot of the Rb^{87} beta spectrum is nonlinear, as shown in Fig. 2. The spin change of

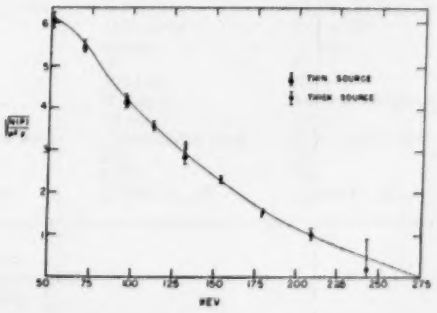

FIG. 2. Allowed Kurie plot of the rubidium-87 spectrum.

[18] Hollander, Perlman, and Seaborg, Revs. Modern Phys. 25, 469 (1953).

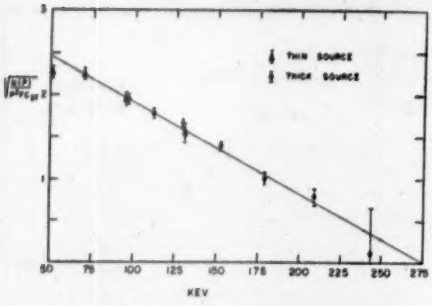

FIG. 3. Corrected Kurie plot of the rubidium-87 spectrum.

the nucleus is 3,[19,20] and the shell model predicts a parity change.[21] When the third forbidden tensor correction term is applied, the Kurie plot becomes linear, at least insofar as can be determined by the statistics (Fig. 3), and it indicates an upper energy limit of 275 kev, in good agreement with recent experiments.[7,8,17]

In the calculation of the third-forbidden correction factor, C_{3T} (Fig. 4), the expressions derived by Greuling[22] were evaluated with the assistance of the tables for L_ν, M_ν, N_ν, P_ν, Q_ν, R_ν computed by Rose *et al.*[23] In the terminology of Tomozawa, Umezawa, and Nakamura,[24]

$$C_{3T}=\left|\frac{Q_3(\beta\sigma\times\mathbf{r},\mathbf{r})}{3!}\right|^2(f-2g\rho+\rho^2h),$$

where

$$\rho=Q_3(\beta\alpha,\mathbf{r})/Q_3(\beta\sigma\times\mathbf{r},\mathbf{r}).$$

The values for f, g, and h published by Tomozawa *et al.*[24] are not correct,[25] and consequently the value

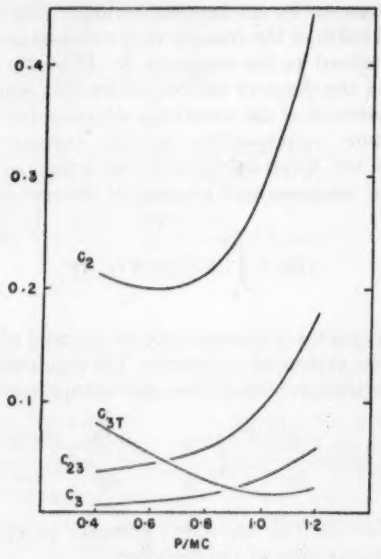

FIG. 4. Correction factor C_{3T} using $\rho=2.37$.

$\rho=4.2$, obtained empirically, is also incorrect. Yamada[26] gives a theoretical value of $\rho=2.37$. This value does give the linear Kurie plot shown in Fig. 3. Since the cancellation of terms of nearly equal size is involved, C_{3T} is a very sensitive function of ρ.

It is interesting to note that in all the known cases of second and third forbidden beta spectra of the "nonunique" type,[27] the tensor (or vector) correction factor is sufficient to linearize the Kurie plot. At the present time it is difficult to draw conclusions as to the relative magnitudes of the scalar and tensor interactions for Rb^{87}.

[19] S. Millman and M. Fox, Phys. Rev. **50**, 220 (1936).
[20] M. Heyden and H. Kopfermann, Z. Physik **108**, 232 (1938).
[21] P. F. A. Klinkenborg, Revs. Modern Phys. **24**, 63 (1952).
[22] E. Greuling, Phys. Rev. **61**, 568 (1942).
[23] Rose, Perry, and Dismuke, Oak Ridge National Laboratory Report ORNL-1459 (unpublished).
[24] Tomozawa, Umezawa, and Nakamura, Phys. Rev. **86**, 791 (1952).
[25] S. Nakamura (private communication).
[26] M. Yamada, Progr. Theoret. Phys. Japan **9**, 268 (1953).
[27] E. J. Konopinski and L. M. Langer, Ann. Rev. Nuclear Sci. **2**, 301 (1953).

Total Neutron Cross Section for Uranium from 20 kev to 20 Mev

R. L. Henkel, L. Cranberg, G. A. Jarvis, R. Nobles, and J. E. Perry, Jr.
Los Alamos Scientific Laboratory, Los Alamos, New Mexico

(Received November 30, 1953)

The total neutron cross section of normal uranium has been measured for neutron energies from 20 kev to 7.6 Mev and at 17, 19, and 20 Mev. When combined with other published work in the 7–14 Mev range, the result is a smooth cross-section curve up to 20 Mev. The curve fits smoothly on the surface showing total neutron cross section as a function of both atomic weight and neutron energy.

INTRODUCTION

ALTHOUGH there had been made some early measurements of the total neutron cross section for uranium,[1–4] the results were mutually in disagreement well beyond the quoted statistical errors, and it therefore seemed desirable to repeat the work. The first recent measurements were made at Wisconsin[5] and covered the neutron energy region up to 1.6 Mev. The present work repeated these measurements in better geometry, and considerably extended the energy range

PROCEDURE

The measurements were made at the large electrostatic accelerator at Los Alamos. The experimental area at this generator is located 20 feet above the ground and has a minimum amount of neutron scattering material nearby. This makes the room-scattered background smaller than is usually found at other laboratories. The experiment consisted of a good geometry transmission measurement in which samples of normal uranium were placed midway between the source of neutrons and a neutron detector. The samples were 1-inch diameter metallic uranium cylinders whose lengths were adjusted to give a neutron transmission of about 60 percent. The cross sections were calculated by assuming the usual exponential decrease of neutron intensity in the sample. Neutrons were obtained from the reactions $Li^7(p,n)Be^7$, $T(p,n)He^3$ and $D(d,n)He^3$, and $T(d,n)He^4$. Since there was a spread in neutron energies caused by the finite target thickness and by straggling in the entrance foil of the gas targets, the effective neutron energy was taken to be the average neutron energy. The neutron energies were calculated from the known Q values and dynamics of the various reactions.

The techniques and geometries varied considerably for the different neutron energy ranges. Many of the experimental details are given in Table I, wherein all items should be self-explanatory except the definition of the background. The room-scattered background is caused by those neutrons which are scattered back into the detector by the floor, apparatus, etc. This background is measured by replacing the sample by an opaque shadow cone. The extraneous background is caused by neutrons released by deuterons which strike control slits, beam collimators, and target foils. It is measured by replacing the target gas by hydrogen and repeating all measurements. Miscellaneous additional details are given below.

Lithium layers were evaporated in high vacuum onto a 0.010-inch tantalum backing while in position on the proton beam tube. The evaporation was from a stainless steel furnace heated by an external radio-frequency induction coil. Mirror-like lithium layers of controlled thickness were easily obtained. The target was designed so that it could be made to gyrate about the beam axis without the use of a rotating vacuum seal, and was cooled with air. Under these conditions both the neutron yield and the target thickness were stable with time.

Table I. Experimental conditions.

Neutron energy range	20 kev–160 kev	160 kev–3.8 Mev	4–7.6 Mev	17, 19, 20 Mev
Source reaction	$Li^7(p,n)Be^7$	$T(p,n)He^3$	$D(d,n)He^3$	$T(d,n)He^4$
Target	Evap. Li	T_2 gas	D_2 gas	T_2 gas
Neutron angle	115°	0°	0°	0°
Neutron energy spread	15 kev	40–20 kev	200 kev	200 kev
Neutron detector	BF_3	H_2 recoil	H_2 recoil	Anthracene scintillator
Source detector separation	36 cm	58 cm	58 cm	144 cm
Shadow cone	CH_2, B_4C cone	Polyethylene cone	Polyethylene cone	18-in. copper bar
Room-scattered background correction	40%	1%	2%	1%
Extraneous background correction	0	0	0.1%	2%
Gas target entrance foil		0.0001 in. Al	0.00005 in. Ni	0.00005 in. Ni

[1] J. H. Williams, University of Minnesota, 1943 (private communication).
[2] H. H. Barschall and V. F. Weisskopf, 1944 (Los Alamos private communication).
[3] W. H. Zinn, Argonne National Laboratory, 1945 (private communication).
[4] D. H. Frisch, Los Alamos Report LA-256, 1945 (unpublished).
[5] Barschall, Adair, Bockelman, Graves, Henkel, and Peterson, Los Alamos Report LA-1060, 1950 (unpublished).

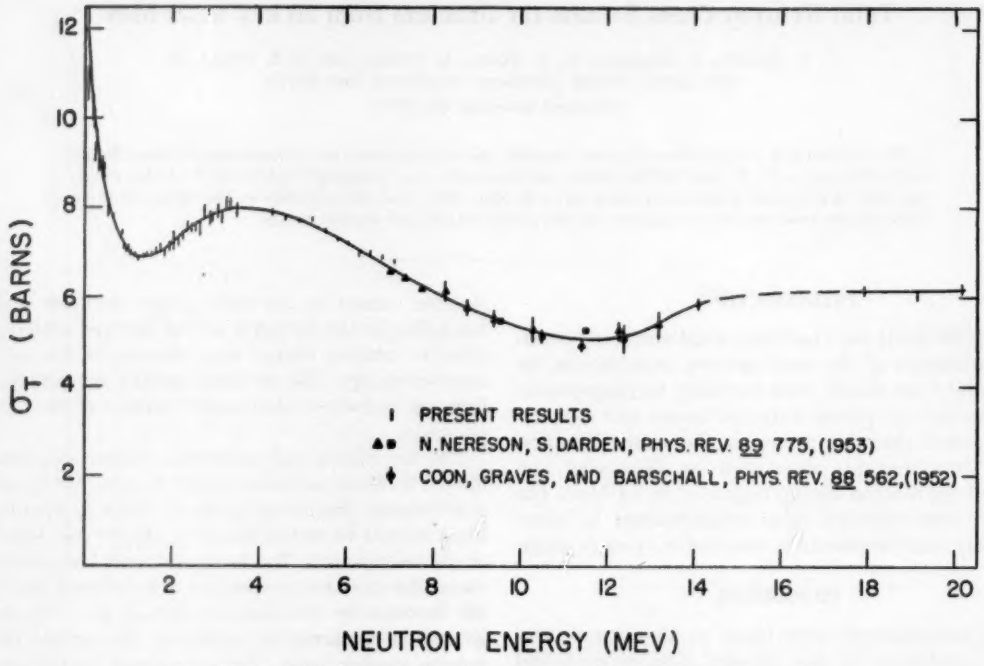

FIG. 1. Total neutron cross section for uranium as a function of neutron energy.

The target arrangement produced a point neutron source having a long life without the disadvantages of oil and carbon deposits on the lithium experienced with the earlier targets employing rotating seals.

The gas targets were contained in a cell 3 cm long. Protons for the T(p,n) reaction entered the cell through a 0.0001-in. aluminum foil, but, because of the large Al(d,n) yield, it was necessary to change to 0.00005-in. nickel foil for the *DD* and *DT* reactions. The boron trifluoride counter was similar to that described by Seagondollar.[6] It was essentially a scaled-down version of a long counter,[7] but with increased efficiency at low neutron energies. This counter was 2 in. in diameter by 5 in. long and was filled with about 32 psi of $B^{10}F_3$. The recoil counters had an active volume of $\frac{7}{8}$-in. diameter by 3 in. long and were filled with purified hydrogen or helium at pressures up to 700 psi. For the 17-, 19-, and 20-Mev points, the counting system utilizing anthracene scintillation counters was that developed by Coon *et al.*,[8] for their total cross-section measurements at 14 Mev. The total cross-section values obtained were independent of the type of counter used.

RESULTS

The data are presented in Figs. 1 and 2. They show a smooth variation of cross section with energy. Although data were taken at 30-kev intervals between 200 kev and 3.8 Mev, these data shown in Fig. 1 are averaged over 100-kev intervals since within statistical errors they were in agreement with the curve shown. The statistical errors for most points are less than ± 0.2 barn. The points plotted between 7 and 12 Mev are from the work of Nereson and Darden[9] and the point at 14 Mev is from the work of Coon *et al.*[8] The squares in Fig. 2 are the averaged data taken from the Wisconsin work.[5] We have applied to all the present data an inscattering correction of the form[10] $\Delta\sigma/\sigma=\frac{1}{2}[(D/L)(kr+1)]^2$, where L is the distance between the neutron source and the detector, D is the diameter of sample, k is the neutron wave number, and r is the nuclear radius given by $1.4A^{\frac{1}{3}}\times 10^{-13}$ cm. The correction was appreciable (2–3.5 percent) only from 4 to 7 Mev.

DISCUSSION

The present results do not agree with the early work[1–4] but do agree quite well with the work done by Barschall *et al.*[5] The poorer geometry used in reference 5[11] led to a 3-percent inscattering correction

[6] L. W. Seagondollar and H. H. Barschall, Phys. Rev. **72**, 439 (1947).
[7] A. O. Hanson and J. L. McKibben, Phys. Rev. **72**, 673 (1947).
[8] Coon, Graves, and Barschall, Phys. Rev. **88**, 562 (1952).
[9] N. Nereson and S. Darden, Phys. Rev. **89**, 775 (1953).
[10] R. B. Day and R. L. Henkel, Phys. Rev. **92**, 358 (1953). [This formula is an approximate relation derived from Feld *et al.* in Final Report of the Fast Neutron Data Project NYO-636, 1951 (unpublished).]
[11] The Wisconsin measurements (see reference 5) were performed in the same manner as those described by Adair, Barschall, Bockelman, and Sala, Phys. Rev. **75**, 1124 (1949). The $Li^7(p,n)Be^7$ reaction was used as the source of neutrons, and a $B^{10}F_3$ counter served

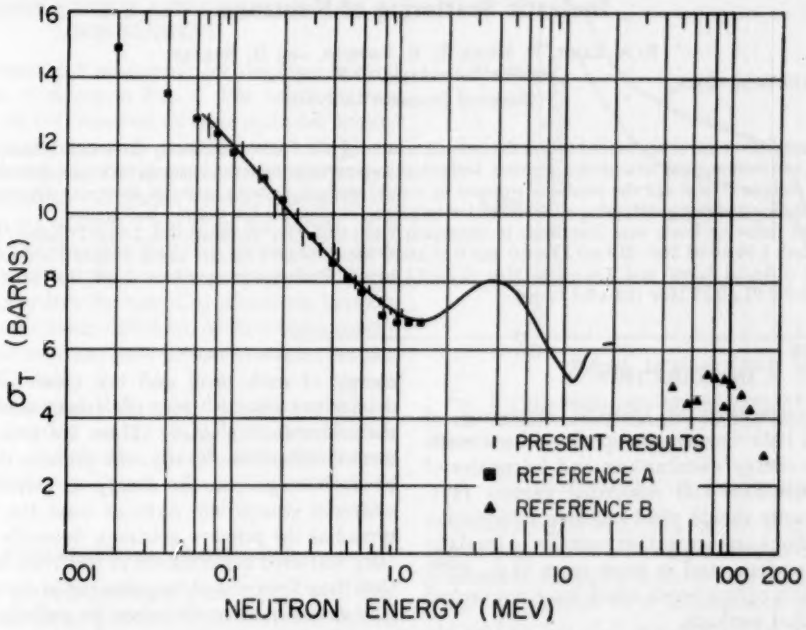

FIG. 2. Total neutron cross section for uranium as a function of neutron energy. Reference A: H. H. Barschall *et al.* (see reference 5). Reference B: W. I. Linlor and B. Ragent, Phys. Rev. **92**, 835 (1953).

which was made on the assumption of isotropic scattering. If neutron diffraction had been used as the basis for the inscattering correction, the agreement with the present data would have been better for energies above 1 Mev.

Barschall[13] has shown that up to 3 Mev there is a regular pattern followed by the curves of total neutron cross section with neutron energy as one considers heavy nuclei of different atomic weight. Nereson[9] finds a similar smooth variation with atomic weight for neutron energies up to 12 Mev. The present data for uranium seem to fit smoothly into this general pattern. Feshbach, Porter, and Weisskopf[14] have been able to describe this behavior by their "cloudy crystal ball" theory which replaces the nucleus by a complex potential well. This simple model reproduces the main features of the cross-section curves for neutron energies below 3 Mev. Higher energy calculations have not yet been published.

The authors are indebted to M. Walt for the design and construction of the high-pressure proportional counters and the oscillating lithium target assembly used in the work. We wish also to thank J. H. Coon for the use of the neutron detecting system used for the high-energy measurements.

as the neutron detector. Cylindrical samples of uranium, of 1¾-in. diameter, were placed in a geometry such that the cross section for neutrons scattered through angles greater than 20° was measured. The statistical errors of the data varied from ±0.7 barn at lower energies to about ±0.2 barn above 1 Mev. However, these data were subject to two appreciable systematic errors. First, an inscattering correction assuming isotropic scattering was applied to the data of this relatively poor geometry experiment, whereas diffraction scattering should have been considered at higher energies. This error resulted in lowering the value of the reported cross section. Second, because of the 430-kev excited state in Be^7, there is a second group of low-energy neutrons for proton energies above 2.31 Mev (or ground-state neutron energies greater than 650 kev). The intensity of the second group is only about 5 percent of the main group (see reference 12). However, the presence of the low-energy group reduced the effective neutron energy and made the observed cross sections too large. These two systematic errors are in opposite directions, and the reported cross sections are probably accurate to 5 percent.

[12] F. Ajzenberg and T. Lauritsen, Revs. Modern Phys. **24**, 321 (1952).

[13] H. H. Barschall, Phys. Rev. **86**, 431 (1952).

[14] Feshbach, Porter, and Weisskopf, Phys. Rev. **90**, 166 (1953).

Inelastic Scattering of Neutrons

E. A. Eliot, D. Hicks, L. E. Beghian, and H. Halban
Clarendon Laboratory, Oxford, England

(Received December 15, 1953)

Experiments have been carried out on the inelastic scattering of 2.5 Mev neutrons by chromium, bismuth, iron, and indium, using scintillation counters. Inelastically scattered neutrons and gamma rays were observed in a stilbene crystal and the results interpreted by a ratio method. Gamma radiation alone was observed in a sodium iodide crystal, using a normalization technique to eliminate the neutron background.

The following levels were identified: in chromium 1.42±0.05 Mev (cross-section 1.0±0.2 barns); in bismuth 1.58±0.05 Mev (0.6±0.2 barns) and 0.85±0.02 Mev (1.2±0.3 barns); and in indium 0.92±0.04 Mev (0.4±0.1 barns) and 0.61±0.06 Mev (0.2±0.1 barns). Preliminary experiments with iron gave a level of 0.91±0.15 Mev (1.0±0.3 barns).

1. INTRODUCTION

SINCE the discovery of inelastic scattering of neutrons in 1935[1,2] many attempts have been made to measure the energy distributions and intensities of the scattered neutrons and associated gamma rays. Such measurements should yield valuable information about cross sections and excitation energies of levels in the scattering nucleus, and in some cases (e.g., Bi^{209}) the process excites energy levels which have not proved accessible by other methods.

Studies of the process have been made[3] by examination of gamma rays,[4–6] the residual activity of isomeric states,[7] and neutrons.[8–13]

The energy distributions of the gamma rays have been observed for several nuclei[4–6] and the cross sections for inelastic scattering estimated. The disadvantage in observing only gamma radiation is that the excited levels may decay by cascade. This means that the level energies cannot be determined without additional intensity measurements.

In some cases (e.g., In^{115}, Au^{197})[7] the levels excited by inelastic scattering may decay into an isomeric state. If the energy of the primary neutrons is gradually increased, there are discontinuities in the intensity of excitation of the isomeric level. Each of these discontinuities corresponds to the excitation of a new level which decays into this isomeric state.

In principle, the most complete information can be derived from the study of neutron groups, since the energy of each level and the cross section can be determined directly from the energy and intensity of the corresponding group. There are two main experimental difficulties. Firstly, the primary neutrons must be as homogeneous in energy as possible since the scattered groups will have at least the same energy spread as the primary neutrons. Secondly, the inelastically scattered neutrons are of relatively low intensities (less than 5 percent of the primaries in our experiments). The detector must therefore be sufficiently sensitive and at the same time have sufficient resolution to separate the groups. Cloud chambers,[9] proportional counters,[10] photographic plates,[11,12] and organic scintillators[13] have been used as detectors, but the resolution in most cases was not comparable with that of the gamma-ray experiments previously quoted.

In the work described below both neutrons and gamma rays have been observed. The energies of the neutron groups were determined with nearly the same precision as those of the gamma rays. The intensities of the neutron groups were measured with sufficient accuracy to give the cross sections for excitation of each level to between 0.1 and 0.3 barn.

In order to obtain sufficient homogeneity in neutron energy a d-D neutron source was used with a beam energy of 30 kev. With the bad geometry employed this gives a maximum spread of 0.2 Mev in neutron energy.

Since no convenient neutron detector is available which is completely insensitive to gamma radiation, two complementary types of experiment were performed. In the first, both neutrons and gamma rays were observed with a stilbene crystal and photomultiplier. Then the gamma-ray spectrum only was determined with a sodium iodide crystal in place of the stilbene. This made it possible to distinguish the gamma rays from the neutron groups in the spectrum from the stilbene crystal and thus obtain the energy distribution of the inelastically scattered neutrons.

With this technique neutron groups corresponding to the excitation of levels between 0.10 and 2.0 Mev could be observed. Over most of this range resolution of levels more than 0.15 Mev apart appeared to be possible.

[1] D. E. Lea, Proc. Roy. Soc. (London) **A150**, 637 (1935).
[2] Amaldi, D'Agostino, Fermi, Pontecorvo, Rasetti, and Segrè, Proc. Roy. Soc. (London) A149, 522 (1935).
[3] H. Goldstein, Nucleonics 11, 7, 39 (1953).
[4] Beghian, Grace, Preston, and Halban, Phys. Rev. **77**, 286 (1950).
[5] Grace, Beghian, Preston, and Halban, Phys. Rev. **82**, 969 (1951).
[6] R. B. Day, Phys. Rev. **89**, 908 (1953).
[7] A. A. Ebel and C. Goodman, Phys. Rev. **72**, 130 (1951).
[8] B. T. Feld, Phys. Rev. **75**, 115 (1949).
[9] Little, Long, and Mandeville, Phys. Rev. **69**, 414 (1946).
[10] Barschall, Battat, Bright, Graves, Jorgensen, and Manley, Phys. Rev. **72**, 881 (1947).
[11] P. H. Stelson and W. N. Preston, Phys. Rev. **86**, 132 (1952).
[12] Mandeville, Swann, and Seymour, Phys. Rev. **86**, 861 (1952).
[13] M. J. Poole, Phil. Mag. 43, 1060 (1952).

2. NEUTRON SOURCE AND EXPERIMENTAL ARRANGEMENT

The experimental arrangement for the first series of measurements is shown in Fig. 1. The neutrons were produced by the d-D reaction using an occluded target.[4] Disk-shaped scatterers of 5 cm diameter 1 or 1½ cm thick were placed directly in contact with the target. The photomultiplier was placed vertically beneath the scatterer with its window 3 cm from the target. It is evident from the diagram that the inelastically scattered neutrons which could be detected by the stilbene crystal originally left the target in directions between 0° and 90° to the beam direction. With a beam energy of 30 kev these neutrons have primary energies ranging from 2.46–2.67 Mev.

The stilbene crystal (1.5 cm in diameter and 0.5 cm thick) was mounted on an E.M.I. photomultiplier Type VX.5047. Pulses from the photomultiplier were amplified and then analyzed with a 25-channel kicksorter.

3. EXPERIMENTAL PROCEDURE

A number of measurements were made with and without scatterers in position. 20 000–70 000 counts per kicksorter channel were recorded in each case. The pulse height stability was better than 2 percent. Typical results obtained with chromium are shown in Fig. 2. Although there is evidence of inelastically scattered neutrons, the interpretation of the spectrum is not at all clear. However on taking the ratio for each channel:

$$R=\frac{\text{counts per channel with scatterer}}{\text{counts per channel without scatterer}}, \quad (1)$$

the existence of the group becomes quite clear (see Fig. 6) and its intensity and energy may be calculated as follows.

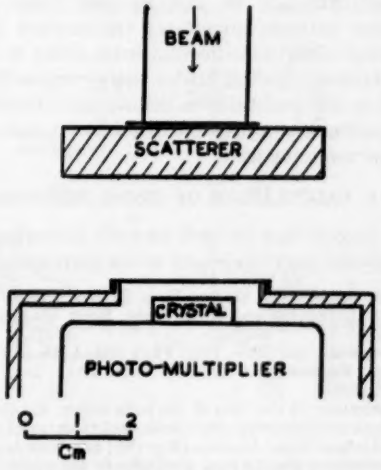

FIG. 1. Experimental arrangement.

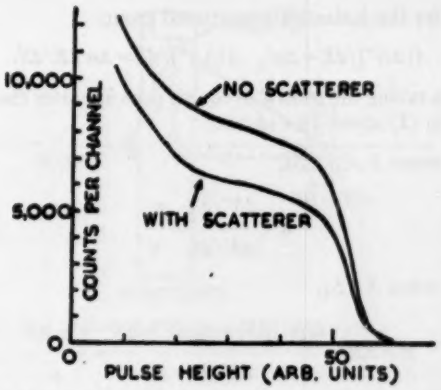

FIG. 2. Pulse-height distributions produced by d-D neutrons in the stilbene crystal taken with and without a chromium scatterer.

4. DISCUSSION OF RATIO METHOD

Monoenergetic neutrons in the energy region concerned give rise to a recoil proton spectrum with equal numbers of protons in equal energy intervals. The pulse height S produced by a recoil proton of energy E is a unique function of E (see next paragraph).

Consider the pulse spectrum produced by monoenergetic neutrons. Let E_0 = neutron energy, E = proton recoil energy ($E \leqslant E_0$), N = number of recoil protons produced with energy $\leqslant E$, S = pulse height produced by a proton of energy E. Then,

$$\frac{dN}{dE}=n \quad \text{(where } n \text{ is a constant of the group)}$$

[see Fig. 3(a)]; (2)

$$\frac{dN}{dS}=\frac{dN}{dE}\cdot\frac{dE}{dS}=n\frac{dE}{dS}, \quad (3)$$

and dN/dS is proportional to the counts per channel recorded by the kicksorter.

With the scatterer in position three types of neutrons enter the crystal, primary, elastically scattered, and inelastically scattered. Since all the materials used were of fairly high atomic mass, elastic scattering produced only a small change in the energy of the neutrons (2 percent for iron and chromium, 1 percent for indium and ½ percent for bismuth). With the resolution available, the recoil spectrum produced by elastically scattered neutrons was indistinguishable from that due to primary neutrons. We shall therefore refer to both these types as "neutrons of full energy."

Suppose for simplicity that a scatterer is used which produces only one group of inelastically scattered neutrons of energy E_1; see Fig. 3(b), (c). By analogy with (2) and (3) we have, using primes to denote the presence of the scatterer, for the neutrons of full energy

$$dN'/dE=n', \quad dN'/dS=n'dE/dS; \quad (4)$$

and for the inelastically scattered group

$$d(\Delta N')/dE=\Delta n', \quad d(\Delta N')/dS=\Delta n' dE/dS. \quad (5)$$

Thus taking the ratio R of counts per kicksorter channel [as in (1) above] we obtain:

(a) when $S_1<S<S_0$,

$$R=\frac{dN'/dS}{dN/dS}=\frac{n'}{n}; \quad (6)$$

(b) when $S<S_1$,

$$R+\Delta R=\frac{(dN'/dS)+d(\Delta N')/dS}{dN/dS}=\frac{n'+\Delta n'}{n}. \quad (7)$$

A plot of R against S will have the form shown in Fig. 3(d).

The pulse height S_1 at the step corresponds to a proton recoil energy equal to that of the inelastically scattered neutrons. The sharpness of the step depends on the homogeneity in energy of the primary neutrons and on the resolution of the photomultiplier. Experimentally obtained ratio plots are shown in Figs. 6, 7. The calculation of cross-sections from these plots depends on the quantity $\Delta R/R$ (see paragraph 9). This is independent of the actual value of the ratio R. It was therefore not necessary to normalize the pulse-height distributions taken with and without the scatterer to equal neutron emissions from the source.

The advantages of the ratio method over methods involving subtraction may be summarized as follows: (a) the steps are separated by plateaux; (b) the positions of the plateaux can be fixed with much greater precision than the statistical uncertainty on a single point; (c) it is not necessary to introduce any normalization to reveal the groups; (d) the cross-section calculation is comparatively straightforward though some normalization is needed here (see paragraph 6).

5. CALCULATION OF LEVEL ENERGIES

According to Birks[14] the pulse height S produced in stilbene by a recoil proton of energy E may be obtained from the following formula

$$\frac{dS}{dr}=\frac{AdE/dr}{1+kBdE/dr}, \quad (8)$$

where r=range (centimeters of air) of a proton of energy E, A=a constant of the crystal and electronics, and kB is a constant obtained in reference (2) from experimental data. Its value is 7.15 Mev/cm air equivalent for anthracene and similar crystals (in particular stilbene).

This formula has been verified for protons of up to 16 Mev.[14] From Eq. (8),

$$S=A\int_0^r \frac{dE/dr}{1+kBdE/dr}\cdot dr. \quad (9)$$

The integral was evaluated numerically as a function of E using the range-energy data for protons in air given by Bethe[15] and Bethe and Livingston.[16] Following Birks in reference 2, the variation in stopping power of the crystal with proton energy was neglected. We then have:

$$S=Af(E), \quad (10)$$

where $f(E)$ is known.

The constant A was found from the pulse-height distribution measured without scatterer (due to primary neutrons traveling in the beam direction). The pulse height half-way down the fall (see Fig. 2) is taken to correspond to the maximum recoil proton energy of 2.67 Mev. An energy scale is thus established from which the proton recoil energy at any step on the ratio plot may be deduced. This is equal to the energy of the corresponding inelastically scattered neutron group.

The energy of each excited level is calculated by subtracting the energy of the appropriate group from the average primary energy $\bar{E}_0$ of the inelastically scattered neutrons. $\bar{E}_0$ is less than the maximum neutron energy of 2.67 Mev because of the variation in energy of the primary neutrons with direction. It was calculated from the geometry of the apparatus and the angular distribution of the d−D neutrons,[17] taking into account only those neutrons which undergo a single inelastic collision. The value of $\bar{E}_0$ was 2.54 Mev for the 1-cm thick scatterers, and 2.55 Mev for the 1.5-cm thick scatterer. (The upper limit on the error, due to double scattering, was estimated at 0.02 Mev in all cases.)

Gamma rays corresponding to ground state transitions from the levels excited by neutrons have been observed from Cr, Bi, and Fe (see Table I). The agreement between gamma-ray and neutron measurements was within experimental error, which shows that Birks' formula[8] is valid in this energy region.[18,19] However, it is still preferable to deduce excitation energies from gamma-ray measurements, where possible, since these are more precise.

6. CALCULATION OF CROSS SECTIONS

The cross section for each inelastic scattering process is calculated from the height of the corresponding step

[14] J. B. Birks, Proc. Phys. Soc. (London) **A64, 874** (1951).

[15] H. A. Bethe, Revs. Modern Phys. **22**, 213 (1950).

[16] M. S. Livingston and H. A. Bethe, Revs. Modern Phys. **9**, 261 (1937).

[17] Eliot, Roaf, and Shaw, Proc. Phys. Soc. **A216**, 57 (1953).

[18] Allen, Beghian, and Calvert, Proc. Phys. Soc. (London) **A65**, 295 (1952).

[19] In reference 18 the form of the pulse-height distribution was interpreted as indicating that pulse height is proportional to energy. In fact Birks' formula [Eq. (8)] accounts satisfactorily for the observed distribution, especially in the region of proton recoil energy below 1 Mev.

on the ratio plot. Consider the case of the single step represented in Fig. 3.

From Eqs. (6) and (7),

$$\Delta R/R=\Delta n'/n'. \tag{9}$$

Let P=total number of recoil protons due to neutrons of full energy, ΔP=total number of recoil protons due to inelastically scattered neutrons, E_0=energy of primary neutrons, E_1=energy of inelastically scattered neutrons, M=number of neutrons of full energy entering the crystal with scatterer, ΔM=number of inelastically scattered neutrons entering the crystal, $s_0=n$-p scattering cross section for the primary neutrons, and $s_1=n$-p scattering cross section for the inelastically scattered group. Then

$$\frac{\Delta P}{P}=\frac{\Delta n'}{n'}\times\frac{E_1}{E_0}=\frac{\Delta R}{R}\times\frac{E_1}{E_0},$$

$$\frac{\Delta M}{M}=\frac{s_0}{s_1}\times\frac{\Delta P}{P};$$

therefore

$$\frac{\Delta M}{M}=\frac{\Delta R}{R}\times\frac{E_1}{E_0}\times\frac{s_0}{s_1}. \tag{10}$$

Let M_0 be the number of primary neutrons which would have entered the crystal in the absence of the scatterer (for the same total emission from the source). The ratio $\Delta M/M$ must be converted to $\Delta M/M_0$. To find the conversion factor $F_1=M/M_0$, a series of 1-minute measurements were made alternately with and without scatterer. The total count was recorded above a discriminator bias level set sufficiently high to cut out all pulses due to inelastically scattered neutrons (i.e., pulses were recorded with pulse height greater than S_1). Thus, apart from a negligible contribution from high-energy gamma rays (see paragraph 7), all the counts recorded were due to neutrons of full energy.

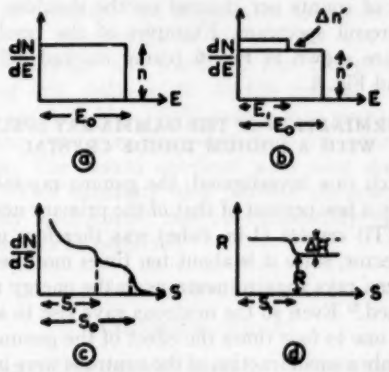

FIG. 3. (a) Energy distribution of recoil protons (no scatterer); (b) energy distribution of recoil protons (with scatterer); (c) idealized pulse-height distribution with scatterer; (d) idealized ratio plot.

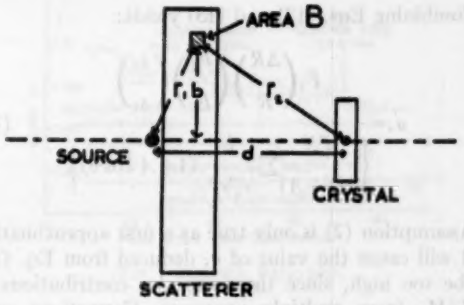

FIG. 4. Notation for cross-section calculation.

Then

$$F_1=\left(\frac{\text{total count recorded with scatterer}}{\text{total count recorded without scatterer}}\right). \tag{11}$$

For the chromium scatterer $F_1=0.91\pm0.01$, for bismuth $F_1=0.89\pm0.01$, and for indium $F_1=0.98\pm0.01$. Then

$$\frac{\Delta M}{M_0}=F_1\left(\frac{\Delta M}{M}\right)=F_1\left(\frac{\Delta R}{R}\right)\left(\frac{E_1}{E_0}\right)\left(\frac{s_0}{s_1}\right). \tag{12}$$

The relation between the inelastic scattering cross section and $\Delta M/M_0$ is calculated by dividing the scatterer into a number of rings of square cross section (see Fig. 4). In assessing the contribution by inelastic scattering of each ring to $\Delta M/M_0$, the following assumptions were made:

(1) The neutron flux emitted from the target has an angular distribution of the form $(1+A\cos^2\theta)$, where $A=0.5\pm0.1$ at 30 kev,[17] and θ is the angle between the neutron path and the beam direction.

(2) Only those neutrons which undergo a single inelastic collision (and no other processes) need to be considered; i.e., the effect of multiple processes can be ignored.

(3) The angular distribution of inelastically scattered neutrons is isotropic.

On this basis,

$$\frac{\Delta M}{M_0}=\sigma_i\frac{d^2NB}{2(1+A)}\sum T\frac{b}{r_1^2r_2^2}(1+A\cos^2\theta), \tag{13}$$

where the summation is made over all elements in the scatterer and N=number of scattering nuclei per unit volume, $A=0.5$ (see assumption 1), B=area of cross section of ring, σ_i=inelastic scattering cross section of scatterer, and dr_1r_2b are distances marked in Fig. 4.

T is the probability that a neutron will undergo no process in its passage through the scatterer other than a single inelastic collision in the volume element concerned. It was calculated from total neutron cross sections of the scattering material.

Combining Eqs. (12) and (13) yields:

$$\sigma_i = \frac{F_1\left(\frac{\Delta R}{R}\right)\left(\frac{E_1}{E_0}\right)\left(\frac{s_0}{s_1}\right)}{\left\{\frac{d^2N}{2(1+A)}\sum T\frac{b}{r_1^2 r_2^2}(1+A\cos^2\theta)\right\}}. \quad (14)$$

Assumption (2) is only true as a first approximation and will cause the value of σ_i deduced from Eq. (14) to be too high, since there are also contributions to $\Delta M/M_0$ from multiple processes. Corrections were estimated from the total neutron cross sections and the value of F_1. The increases in σ_i were found to be

(12±10) percent for bismuth,
(8± 7) percent for chromium,
(2± 2) percent for indium.

The total neutron cross section for chromium at 2.5 Mev is not known. A value of 3 to 5 barns seems reasonable for an element of this atomic mass. The extreme values of the correction are then (4±4) percent and (12±10) percent. The value quoted above corresponds to a cross section of 4 barns. No correction has yet been calculated for iron since the measurements are still in the preliminary stage.

Even if assumption (3) is not valid and the angular distribution of scattered neutrons is markedly anisotropic, the value calculated for the cross section will not be much in error because of the poor geometry. Consider for example the hypothetical case:[20]

Target nucleus	$I=\frac{1}{2}$,
Compound nucleus	$J=3$,
Product nucleus	$I'=\frac{3}{2}$,
Incident neutron	$l=2$,
Scattered neutron	$l'=1$,

where the angular distribution is

$$W(\phi)=1+\frac{36}{23}\cos^2\phi.$$

(ϕ is the angle between the paths of the incident and scattered neutrons.)

In this case calculation of the cross section on the assumption that the distribution is isotropic leads to a value which is 4 percent too low.

7. RESPONSE OF THE STILBENE CRYSTAL TO GAMMA RAYS

The detection efficiency of the crystal for gamma rays of mean energy 1.25 Mev from a standard Co^{60} source was measured and found to be 4 percent. This is comparable to the 5 percent efficiency for 2.5-Mev neutrons calculated from the n-p cross section. Moreover, Compton electrons and recoil protons give rise to similarly shaped pulse-height distributions (compare Figs. 2 and 5), so that gamma rays as well as neutrons can produce steps on the ratio plot. The pulse height at the Compton edge of a 0.9-Mev gamma ray is equal to that of a 2.5-Mev recoil proton. Thus each step may be provisionally interpreted either as a neutron group corresponding to a certain level excitation or as a gamma ray of some definite energy less than 0.9 Mev. So that a final interpretation of the ratio plot might be obtained, the gamma-ray energies were investigated in a second series of experiments (see paragraph 8).

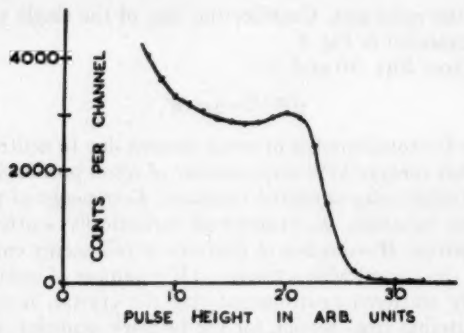

FIG. 5. Pulse-height distribution produced in the stilbene crystal by the 810-kev gamma rays from Mn^{54}.

Gamma rays of energy greater than 1.1 Mev produce Compton edges beyond the steep fall of the proton recoil spectrum. When a pulse-height distribution is taken with scatterer, these edges can be seen superimposed on a background provided by the high-energy tail of the proton recoil spectrum. This background is predominantly due to the neutrons of full energy. Hence it can be determined from a pulse-height distribution made without scatterer, normalized to the same number of neutrons of full energy, i.e., to the same number of counts per channel on the shoulder of the proton recoil spectrum. Examples of the results obtained are shown in Fig. 6 (curve marked difference plot) and Fig. 8.

8. DETERMINATION OF THE GAMMA-RAY SPECTRUM WITH A SODIUM IODIDE CRYSTAL

In each case investigated, the gamma-ray intensity was only a few percent of that of the primary neutrons. A NaI(Tl) crystal (1-in. cube) was therefore used as the detector, since it is about ten times more sensitive to gamma rays than to neutrons in the energy regions concerned.[21] Even so the neutrons gave rise to a background one to four times the effect of the gamma rays. Since only a small fraction of the neutrons were inelastically scattered, this background was predominantly due to neutrons of full energy. Accordingly it could be

[20] E. Segrè, *Experimental Nuclear Physics* (John Wiley and Sons, Inc., New York, 1953), Vol. II, p. 300.

[21] M. A. Grace (private communication).

calculated from a primary neutron pulse-height distribution taken without the scatterer.

Two pulse-height distributions were recorded, A with and B without the scatterer. These were normalized to the same total neutron emission from the source. Then the ratio F_3 of the numbers of neutrons of full energy detected with and without the scatterer was found with a stilbene crystal, by a method similar to that used for F_1 (see paragraph 6). The background in the gamma-ray measurement (A) could now be found by multiplying the counts in each channel of (B) by the factor F_3.

When measuring F_3, in order to approximate to the geometry of the sodium iodide crystal, a stilbene crystal 2.5 cm in diameter and 0.5 cm thick was placed successively in positions corresponding to the top and bottom of the one-inch cube. A value of F_3 was found for each position, and the mean value weighted with respect to counting rate was calculated. For the bismuth scatterer $F_3=0.88\pm0.01$ and for indium $F_3=0.98\pm0.01$. No sodium iodide measurements have been made with chromium or as yet with iron (see "Discussion of Results").

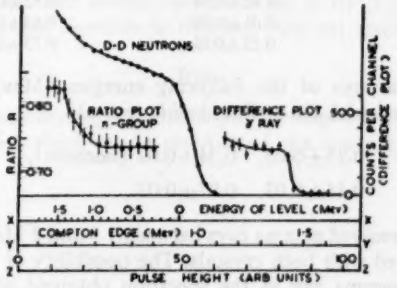

FIG. 6. Chromium. Neutron group and associated gamma ray observed with the stilbene crystal.

A gamma-ray spectrum obtained after subtracting the neutron background is shown in Fig. 9, which refers to bismuth. The apparently poor resolution is due to the degradation of the gamma rays in their passage through the scatterer. For the purpose of checking this, pulse-height distributions of 0.81-Mev (Mn^{54}) and 1.28-Mev (Na^{22}) gamma rays were recorded with the scatterer interposed between source and detector. The results obtained were very similar to Fig. 9. This similarity also justifies the assumption that any background due to inelastically scattered neutrons can be neglected.

9. DISCUSSION OF RESULTS

Chromium (Fig. 6)

The scattering material consisted of chromium filings contained in a cylindrical can of aluminium 5 cm diameter×1 cm deep and 0.03 cm thick. The results obtained are shown in Fig. 6. The curve marked D-D neutrons shows the pulse-height distribution due to primary neutrons on an arbitrary vertical scale. The single step found on the ratio plot represents a scattered neutron group associated with a level of 1.3 ± 0.1 Mev or, alternatively, gamma radiation of 0.4 Mev. The Compton edge of a gamma ray of 1.42 ± 0.05 Mev was found beyond the neutron spectrum (see curve marked difference plot) in agreement with the work of Grace *et al.* using a sodium iodide crystal.[22] It was therefore not considered necessary to make sodium iodide measurements in this case. Since there were no other steps on the ratio plot and since some level must have been excited to give the 1.4-Mev gamma ray, we interpreted the step found as a neutron group. The cross section was calculated from the height of the step and was 1.0 ± 0.2 barns.

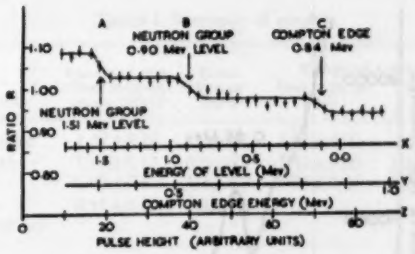

FIG. 7. Bismuth. Ratio plot.

Bismuth (Figs. 7, 8, 9)

The scatterer was a cylindrical block 5 cm diameter by $1\frac{1}{2}$ cm thick. Three steps A, B, and C were observed on the ratio plot (Fig. 7). The following alternative interpretations could be made:

Step	Energy of level if a neutron group	Energy if gamma radiation
A	1.51 ± 0.10 Mev	0.31 ± 0.03 Mev
B	0.90 ± 0.07 Mev	0.53 ± 0.04 Mev
C	0.11 ± 0.05 Mev	0.84 ± 0.03 Mev

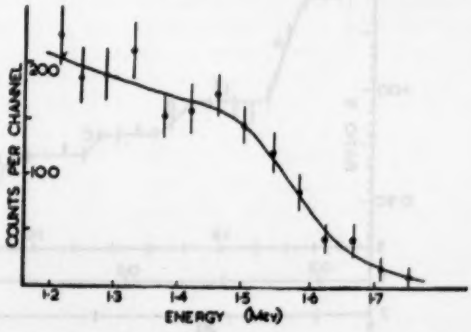

FIG. 8. Bismuth. Compton edge of 1.58-Mev gamma ray observed with the stilbene crystal.

[22] Grace, Lemmer, and Halban, Proc. Phys. Soc. (London) A65, 456 (1952).

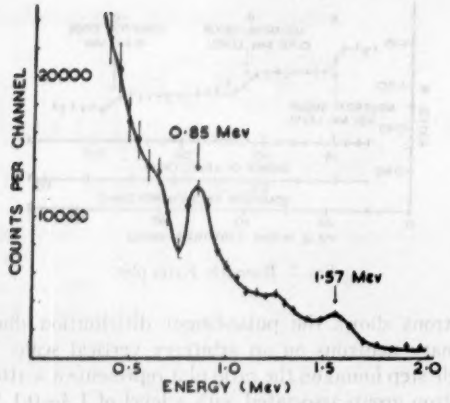

FIG. 9. Bismuth. Gamma rays observed with sodium iodide crystal.

The Compton edge of a gamma ray of 1.59±0.05 Mev was also observed with the stilbene crystal (Fig. 8).

With the sodium iodide crystal two gamma rays were observed (Fig. 9):

0.85±0.03 Mev and 1.57±0.07 Mev.

The results were interpreted as follows. Step *C* corresponds to the 0.85-Mev gamma ray observed with the sodium iodide crystal. The presence of this radiation and the absence of a 0.53-Mev gamma ray in the sodium iodide measurements shows that step *B* must be a neutron group. Considering step *A*, the possibility of a 0.31-Mev gamma ray cannot be ruled out on the evidence of Fig. 9 alone. If *A* is due to gamma radiation, then it must correspond to a transition to the ground state or to the 0.85-Mev level. Thus a neutron group would be required to feed a 0.31-Mev or a 1.19-Mev level. No steps of the necessary intensity are observed at either energy (see Fig. 7). Therefore *A* must represent a neutron group. This conclusion is supported by the presence of the 1.58-Mev gamma ray.

Our final interpretation is that two levels of energies 1.58±0.05 Mev and 0.85±0.02 Mev are excited with cross sections of 0.6±0.2 and 1.2±0.3 barns, respectively, and each decays directly to the ground state.

The possibility that the 1.58-Mev level also decays by cascade through the 0.85-Mev level with the emission of 0.73-Mev gamma ray cannot be excluded. (Upper limit to intensity 30 percent of the 1.58 Mev ground-state transition.)

Indium

Six steps were observed on the ratio plot (Fig. 10). The following alternative interpretations could be made:

Step	Energy of level (Mev) if a neutron group	Energy (Mev) if a gamma ray
A	1.70±0.05	0.23±0.03
B	1.36±0.05	0.35±0.03
C	1.14±0.05	0.43±0.03
D	0.92±0.04	0.52±0.03
E	0.61±0.06	0.64±0.04
F	0.25±0.07	0.75±0.05

Gamma rays of the following energies (Mev) were observed with the sodium iodide crystal:

0.25±0.03, 0.34±0.02 (isomeric),

0.44±0.03, 0.87±0.03.

Unresolved gamma rays between 1.1 and 2 Mev were observed with both crystals. The possibility of a 0.75-Mev gamma ray in the spectrum obtained with the sodium iodide crystal cannot be excluded. The decay of the isomeric state was observed after the neutron bombardment had ceased

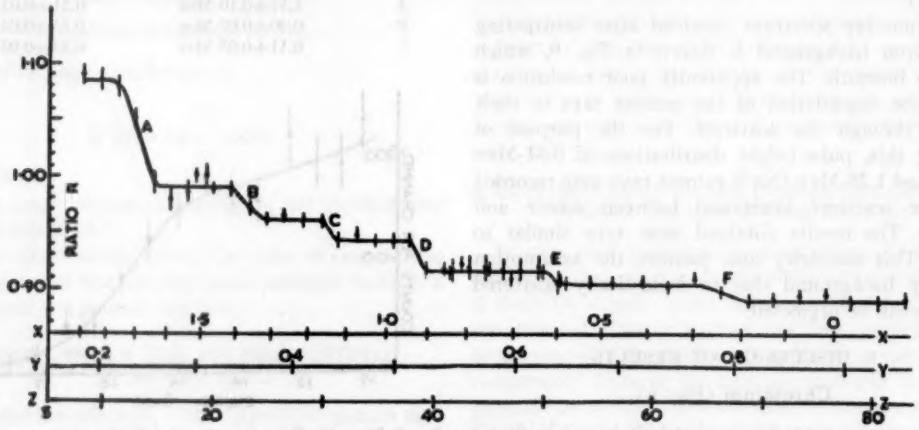

FIG. 10. Indium. Ratio plot.

Scale *X*—Energy of level excited by neutrons (Mev).
Scale *Y*—Gamma ray Compton edge (Mev).
Scale *Z*—Pulse height (arbitrary units).

Our tentative interpretation of these results is

Step A: γ ray.
Step B: γ ray (but see below).
Step C: γ ray.
Step D: Neutron group—level excited 0.92 ± 0.04 Mev; cross section $0.4\ \pm0.1$ barn.
Step E: Neutron group—level excited 0.61 ± 0.06 Mev; cross section $0.2\ \pm0.1$ barn.
Step F: Probably a weak γ ray.

There was no trace of direct excitation of the 360-kev isomeric level; from the ratio plot the upper limit to this cross section is 0.1 barn.

These results are in agreement with those of Ebel and Goodman[7] from excitation of the isomeric state. They found levels in In^{115} at

0.60 ± 0.04 Mev, 0.96 ± 0.04 Mev, 1.37 ± 0.04 Mev.

The neutron group corresponding to a 1.37-Mev level would produce a step on the ratio plot which could not be resolved from that due to the isomeric gamma ray. The cross section for excitation of the 1.37-Mev level cannot therefore be deduced from our results.

Iron

Preliminary experiments showed a single step on the ratio plot which can be interpreted as a neutron group from a level of 0.91 ± 0.15 Mev, in agreement with previous work.[4,6]

The results for chromium, bismuth, iron, and indium are summarized in Table I.

TABLE I. Summary of results.

Nucleus	Energy of level from neutron group (Mev)	Cross-section barns	Energy of gamma ray from stilbene Mev	Energy of gamma ray from NaI Mev
Chromium	1.30 ± 0.10	1.0 ± 0.2	1.42 ± 0.05	
Bismuth	1.51 ± 0.15	0.6 ± 0.2	1.59 ± 0.05	1.57 ± 0.07
	0.90 ± 0.10	1.2 ± 0.3	0.84 ± 0.03	0.85 ± 0.03
Iron (preliminary result)	0.91 ± 0.15	1.0 ± 0.3		
Indium	0.61 ± 0.06	0.2 ± 0.1	No ground state γ observed	No ground state γ observed
	0.92 ± 0.04	0.4 ± 0.1	No ground state γ observed	No ground state γ observed
			0.23 ± 0.03	0.25 ± 0.03
			0.35 ± 0.03	0.34 ± 0.02
			0.43 ± 0.03	0.44 ± 0.03
				0.87 ± 0.03

We would like to thank Dr. D. Roaf and Dr. P. F. D. Shaw for the use of the high-tension set and Dr. D. J. Hughes for his helpful criticism of the manuscript. We also wish to thank Lord Cherwell for extending to us the facilities of this laboratory.

Long-Lived Isomer of RaE (Bi^{210})†

HARRIS B. LEVY AND I. PERLMAN
Radiation Laboratory and Department of Chemistry, University of California, Berkeley, California
(Received November 17, 1953)

The mass assignment of a long-lived bismuth alpha activity previously reported as being an isomer of Bi^{210} has been confirmed by means of electromagnetic mass separation. The half-life of the Bi^{210} (long) is now reported to be 2.6×10^6 years. The alpha-decay energy of Bi^{210} (long) has been redetermined and found to be 5.031 ± 0.020 Mev. Comparison with the alpha-decay energy of RaE places the Bi^{210} (long) 25 kev below RaE with, however, an uncertainty of the same order of magnitude. Bi^{210} (long) has measurable β^- branching (1 part in 270) to give Po^{210}, and this gives a partial half-life of 7.0×10^8 years for this mode of decay. An unsuccessful search was made for Bi^{210} (long) as a decay product of RaD (Pb^{210}), resulting in a lower limit of 2×10^7 years for the decay of RaD to this isomer. Also, an upper limit of 1.4×10^4 years was set on the half-life for the transition from RaE to Bi^{210} (long). On the basis of decay data now available, the most probable designation for the Bi^{210} (long) state is deduced to be 4− although a somewhat higher spin number could be possible.

A. INTRODUCTION

WHEN bismuth (Bi^{209}) is irradiated with slow neutrons, a long-lived bismuth alpha emitter is noted after the 5.0-day RaE (Bi^{210}) has decayed and its alpha-emitting daughter Po^{210} has been removed.[1] For a number of reasons it was thought to be Bi^{210} and, therefore, an isomer of RaE: (1) the radioactivity was produced by slow neutrons on bismuth; (2) the alpha-particle energy (5.1 Mev) was about that expected for Bi^{210} and not for Bi^{208} or Bi^{211}; (3) the alpha emitter proved to be the parent of a 4.2 ± 0.5-min thallium beta emitter which seemed to be Tl^{206} as well as could be discerned with the weak source available. No decay could be observed over an extended period of time and a lower limit of 25 years for the half-life could be set on the basis of this information. Actually a half-life of the order of 10^6 years can be deduced from other considerations to be discussed.

It was deduced in the earlier report[1] on the basis of available decay data that the long-lived alpha emitter was the upper isomeric state of Bi^{210}. It will be seen that this conclusion must now be revised and that RaE is most likely the upper state although the uncertainties of the decay data upon which the decision is based are about the same as the energy difference. We shall designate the long-lived isomer simply as Bi^{210} (long).

The present report also deals with a measurement of the β^- branching of Bi^{210} (long) and experiments which set lower limits of the decay periods for the isomeric transition and for the β^- decay of RaD to Bi^{210} (long). From these data it is possible to deduce that the probable spectroscopic state for Bi^{210} (long) is 4−.

B. CONFIRMATION OF THE MASS ASSIGNMENT OF Bi^{210} (LONG)

A sample of neutron-irradiated bismuth was stored until the RaE had decayed and then was purified rigorously. The specific alpha activity was 4 disintegrations per minute per milligram of bismuth. This material was subjected to calutron isotope separation,[2] collecting the bismuth ions at positions corresponding to mass numbers 208, 209, and 210.

Samples were taken from each fraction and weighed after electrodeposition onto tared platinum disks. The disks then served as sources for alpha disintegration rate determinations. The results are shown in Table I where it is seen that the bismuth caught at mass number 210 is considerably enhanced in alpha activity while that at positions 208 and 209 is depleted. The finding of higher specific activity at mass number 208 than at 209 is not considered as indicating alpha activity as mass 208 and could result from the pattern of "spillover" of an isotope into successive mass number positions.

C. ALPHA-DECAY ENERGY OF Bi^{210} (LONG)

In the absence of the observation of an isomeric transition between RaE and Bi^{210} (long) the way remains for deciding which is the higher energy state by comparing their alpha- or beta-decay energies. The alpha-decay energy of RaE can be calculated from other decay data and that for Bi^{210} (long) can be measured. The beta-decay energies cannot be compared because the specific activity of Bi^{210} (long) is far too low for beta-ray spectroscopy and the preponderance of the

TABLE I. Specific alpha activity of calutron separated neutron-irradiated bismuth.

Mass fraction	Alpha disintegrations per minute per milligram of bismuth Sample 1	Sample 2
Unseparated 4		
208	1.2±0.6	1.8±0.6
209	0.6±0.6	<0.2
210	128±10	142±10

† This work was performed under the auspices of the U. S. Atomic Energy Commission.

[1] Neumann, Howland, and Perlman, Phys. Rev. 77, 720 (1950).

[2] We are indebted to Dr. R. S. Livingston and members of the Electromagnetic Research Division, Oak Ridge National Laboratory, and to Dr. C. P. Keim and the Stable Isotopes Research and Production Division for performing this separation.

alpha-decay daughter, Tl^{206}, would make measurement impossible in any case.

Using the calutron-enriched Bi^{210} (long), thin samples were prepared by electroplating onto platinum disks. The alpha-particle energy distribution was then measured in an ionization chamber connected to a 48-channel differential pulse height analyzer. The results of five determinations gave values of 4.92, 4.94, 4.94, 4.93, and 4.945 Mev; and, although the last one cited is probably more reliable than the others, we shall take the average 4.935±0.020 Mev. For the first three runs, Ra^{226} and daughters were used for energy calibration, and for the last two, Po^{208} and Po^{210} were run simultaneously with the Bi^{210} (long) to provide an internal standard. The pulse-analysis curve for the last determination is shown in Fig. 1. There was no evidence for more than a single alpha group for Bi^{210} (long); the greater width of the peak compared with those of the polonium isotopes can be explained by the sample thickness.

Despite the absence of complex alpha structure, the possibility would still exist that the observed group does not lead directly to the ground state of Tl^{206} and therefore would not define the decay energy. If so, there should be conversion electrons or gamma-rays present in abundance comparable to the alpha group. Dr. D. C. Dunlavey of this laboratory looked for low-energy conversion electrons by impregnating an Ilford G5 photographic plate with some of the bismuth and counting the coincidences between alpha-particle and electron tracks. The number of electrons of <150 kev in coincidence with alpha particles was much too small to satisfy the above supposition, and the few observed probably could be accounted for by the low energy tail of the Tl^{206} beta spectrum. The sample of Bi^{210} (long) was also examined with a scintillation spectrometer, and no gamma rays were observed.

From these experiments it is fairly certain that the 4.935-Mev alpha group represents the ground-state transition, and, when correction for recoil energy is made, the decay energy becomes 5.031±0.020 Mev.

The alpha-decay energy for RaE is calculated from the measured β^--decay energies of RaE and Tl^{206} and

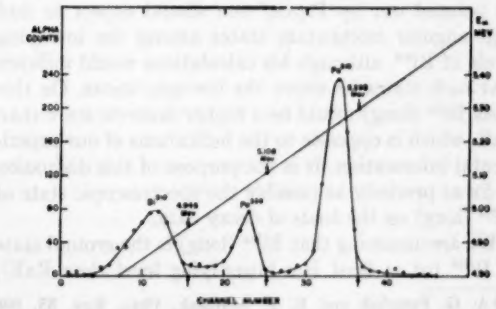

FIG. 1. Alpha pulse analysis of long-lived Bi^{210} with Po^{208} and Po^{210} as standards.

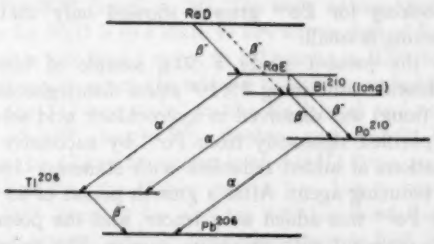

FIG. 2. Decay cycles involving RaE and Bi^{210} (long). (Broken lines indicate modes of decay which are possible but which have not been observed directly or indirectly.)

the alpha energy of Po^{210}, as may be visualized from the decay cycle, Fig. 2. For this purpose the following decay energies are adopted:[3] RaE β^- decay—1.165 Mev, Po^{210} α decay—5.401 Mev, Tl^{206} β^- decay—1.51 Mev. The alpha-decay energy of RaE, therefore, becomes 5.056 Mev, which has an uncertainty of perhaps 20 kev. From these figures it would appear that RaE is heavier than Bi^{210} (long) by 25 kev, but the uncertainties of the data are of the same order.

If the beta-decay energy of RaD to RaE is taken to be 65 kev,[3] then RaD is unstable with respect to Bi^{210} (long) by 90 kev. This difference is probably outside of the uncertainties of the data and the attempt to observe this decay will be mentioned below.

D. ALPHA-DECAY HALF-LIFE OF Bi^{210} (LONG)

Two groups[4–6] have reported a discrepancy between the neutron activation cross section of bismuth to give RaE and the total absorption cross section. Hughes and Palevsky[5] have adopted the value[7] 19 millibarns (mb) for the RaE activation cross section and have determined the total absorption cross section to be 33 mb. The difference, 14 mb, presumably goes into the formation of Bi^{210} (long). Littler and Lockett[6] have found the RaE activation and absorption cross sections to be 20.5 and 30.8 mb, respectively, leaving 10 mb for the Bi^{210} (long) activation.

Using the amount of Po^{210} as an internal standard of neutron exposure and the specific activity of Bi^{210} (long) found in this laboratory, Hughes and Palevsky have calculated the alpha-decay half-life for Bi^{210} (long) to be 2.6×10^6 yr.

E. BETA-DECAY HALF-LIFE FOR Bi^{210} (LONG)

Since Bi^{210} (long) has the same mass as RaE within about 25 kev, it must be beta-unstable. A previous attempt[1] to observe the beta branching of Bi^{210} (long)

[3] References to these data may be found in the "Table of Isotopes," Hollander, Perlman, and Seaborg, Revs. Modern Phys. 25, 469 (1953).

[4] Palevsky, Hughes, and Eggler, Phys. Rev. 83, 234 (1951).

[5] D. J. Hughes and H. Palevsky, Phys. Rev. 92, 1206 (1953).

[6] D. J. Littler and E. E. Lockett, Proc. Phys. Soc. (London) A66, 700 (1953).

[7] *Neutron Cross Sections*, U. S. Atomic Energy Commission Report AECU-2040, Supplement 2 (Office of Technical Services, Department of Commerce, Washington, D. C., 1952).

by looking for Po^{210} growth showed only that the branching is small.

In the present study a 50-g sample of bismuth oxychloride containing 2×10^5 alpha disintegrations of Bi^{210} (long) was dissolved in hydrochloric acid solution and purified rigorously from Po^{210} by successive precipitations of added tellurium with stannous chloride as a reducing agent. After a growth period of 83 days some Po^{208} was added as a tracer, and the polonium again removed with tellurium carrier. The tellurium was separated from polonium by dissolving the mixture and precipitating the tellurium alone with sulfur dioxide. The polonium was next extracted with 20 percent tributyl phosphate in dibutyl ether, back extracted into concentrated nitric acid and finally electroplated onto a platinum disk after the nitric acid had been removed by evaporation and the polonium taken up in dilute sulfuric acid.

The bismuth sample was allowed to remain for another period of 82 days, and a second polonium removal was carried out. The yields of Po^{210} were determined by total alpha-particle counting in a standard alpha counter and Po^{210}/Po^{208} ratio measurement with the pulse analyzer. After correcting for chemical yield (from Po^{208} recovery) and growth of Po^{210} to saturation, the equilibrium value of Po^{210} in the two experiments was 685 and 661 disintegrations per minute. The bismuth contained 1.8×10^5 alpha disintegrations per minute. From this the β^- branching of Bi^{210} (long) is seen to be 3.7×10^{-3} and the β^--decay half-life is accordingly 7.0×10^8 yr.

It is of course not completely out of the question that Bi^{210} (long) is the upper isomer and that the growth of Po^{210} resulted primarily through the isomeric transition to RaE. In this case, the value 7.0×10^8 yr would apply to the isomeric transition, and the β^- half-life would then be even longer. Since the evidence does point to Bi^{210} (long) as the ground state, we shall assume that the growth of Po^{210} arose directly from the beta decay.

F. SEARCH FOR Bi^{210} (LONG) IN NATURE

As already mentioned, RaD is undoubtedly unstable with respect to Bi^{210} (long). Based on the energy relationship of the Bi^{210} isomers and the 65-kev decay energy of RaD to RaE, the decay energy of RaD to Bi^{210} (long) is 90 kev.

The most sensitive means of looking for this transition is by the examination of uranium ores in which the Bi^{210} (long) would be at its equilibrium concentration. The bismuth fraction was removed from a sample of pitchblende and purified. Over a period of several weeks it showed only the decay period of RaE, and the amount at the time of separation was 5.5×10^6 disintegrations per minute. After complete decay of the RaE, the Po^{210} was removed and the sample examined for the alpha activity of Bi^{210} (long). None was found, and the limits of detection corresponded to a maximum of 5 disintegrations per minute.

The fraction of RaD which decays to Bi^{210} (long) is, therefore, $<10^{-6}$, and its partial half-life is $>2\times10^7$ yr. Bi^{210} (long) could also arise from the isomeric transition from RaE. By use of the same data, the half-life for this transition is $>10^4$ yr.

G. DISCUSSION

In discussing the nuclear configuration for Bi^{210} (long), we shall adopt the following properties for it and neighboring nuclei, most of which have been discussed in this paper:

(1) Bi^{210} (long) is the ground state of Bi^{210}, and it is 25 kev lighter than RaE. The half-life for the isomeric transition is $>10^4$ yr.
(2) The alpha-decay half-life for Bi^{210} (long) is 2.6×10^6 yr and its decay energy is 5.03 Mev.
(3) The corresponding values for RaE are 3×10^6 yr and 5.06 Mev.
(4) The β^--decay half-life for Bi^{210} (long) is 7.0×10^8 yr, and its decay energy is 1.14 Mev.
(5) The corresponding values for RaE are 5.0 days and 1.17 Mev.
(6) The half-life for the decay process RaD$\rightarrow Bi^{210}$ (long) is $>2\times10^7$ yr and the decay energy is 90 kev.

According to the independent particle model, Bi^{210} with one proton beyond the 82-proton shell and one neutron beyond the 126-neutron shell should have odd parity low-lying states. With this assumption, Petschek and Marshak[8] have assigned RaE to a 0− state on the basis of the shape of its beta spectrum. The other possibilities, 2− and 1−, gave a poorer fit. Detailed calculations on the possible low-lying states of Bi^{210}, according to the independent-particle model, have been made by Pryce[9] and his results are not at variance with this assignment for RaE.

Since the beta-decay transitions involving Bi^{210} (long) differ so radically from those of RaE, it is fairly certain that Bi^{210} (long) possesses a large spin number. This would also be borne out by the long lifetime for the isomeric transition between the two isomers of Bi^{210}. As pointed out by Pryce,[9] one should expect to find high angular momentum states among the low-lying levels of Bi^{210}, although his calculations would indicate that such states lie above the low-spin states. On this basis Bi^{210} (long) would be a higher isomeric state than RaE, which is opposite to the indications of our experimental information. It is the purpose of this discussion to fix as precisely as possible the spectroscopic state of Bi^{210} (long) on the basis of decay data.

We are assuming that Bi^{210} (long) is the ground state of Bi^{210} (or at least is a lower-lying level than RaE),

[8] A. G. Petschek and R. E. Marshak, Phys. Rev. **85**, 698 (1952).
[9] M. H. L. Pryce, Proc. Phys. Soc. (London) **65**, 773 (1952).

and therefore the observed growth of Po^{210}, governed by a half-life of 7.0×10^8 yr, comes directly through beta emission. The log *ft* value for this transition is ~19 which is similar to that for the K^{40} beta decay. Since both Bi^{210} (long) and K^{40} probably decay directly to the ground states of even-even nuclei,[10-12] it is possible that Bi^{210} (long), like K^{40}, has spin 4. Similarly, the failure to find Bi^{210} (long) from the decay of RaD (partial half-life $>2\times10^7$ yr) means that the log *ft* value is >13.6 and that the spin for Bi^{210} (long) is at least 3.

From the same measurement it could be concluded that the half-life for the 25-kev isomeric transition from RaE to Bi^{210} (long) is $>1.4\times10^4$ yr. By use of the Weisskopf formula[13] the lifetimes for 25-kev transitions of multipole order may be calculated: $\tau_\gamma(E3)\sim9\times10^{-4}$ yr, $\tau_\gamma(M3)\sim0.2$ yr, $\tau_\gamma(E4)\sim8\times10^4$ yr, and $\tau_\gamma(M4)\sim2\times10^7$ yr. These lifetimes refer only to radiative transitions and internal conversion would make the transition half-lives shorter. It would seem, therefore, that spin changes of three or less for the isomeric transition are ruled out unless the energy difference is 5 kev or less rather than the indicated 25 kev. Therefore, if the spin for RaE is 0, that for Bi^{210} (long) must be at least 4.

From the absence of Bi^{210} (long) in the beta decay of RaD (decay energy 90 kev, half-life $>2\times10^7$ yr) the log *ft* value is >13.6. This large log *ft* value is consistent with the other information indicating that the spin for Bi^{210} (long) is >3. The only known mode of decay for RaD is to a state 47 kev above that of RaE,[14] and since less than 1 event in 10^6 results in Bi^{210} (long), a limit can be set on the relative transition probabilities from the "47-kev state" to the RaE level and to the level of Bi^{210} (long). Wu, Boehm, and Nagel[14] have shown the 47-kev transition is of the *M*1 type, so that if RaE is 0−, the 47-kev level is 1−. Let us suppose that Bi^{210} (long) is 4− and see whether the failure to observe transitions from the 47-kev state to Bi^{210} (long) is consistent. This would be an *M*3 transition of 72 kev (47+25) for which the lifetime would be of the order of 10^2 sec. The lifetime for the 47-kev *M*1 transition should be about 10^{-9} sec, so that the failure to observe Bi^{210} (long) in the decay of RaD through this pathway is understandable. An assignment of 4− for Bi^{210} (long) is seen to be consistent with the data presented here.

Mention should be made of the alpha-decay half-lives of the two isomers, although alpha-decay theory for such nuclei is not very helpful at present for assigning spectroscopic states. The two isomers have almost the same decay energy, but the partial alpha half-life of Bi^{210} (long) is about 100-fold that of RaE. RaE itself is highly hindered as are other bismuth alpha emitters.[15] A large spin change for the decay of Bi^{210} (long) could well be a factor, but also the rearrangement necessary in creating the alpha particle is probably involved when nucleons having such large spins are involved and when two closed shells are broken open as is the case here.

[10] The first excited state of Po^{210} is probably at 1.19 Mev in accordance with a gamma ray observed by Hoff (see reference 11) in the electron capture decay of At^{210}. Neither RaE nor Bi^{210} (long) could decay to this state. A level at this energy is also expected from the systematics of the first excited states of even-even nuclei (see reference 12).

[11] R. W. Hoff, Ph.D. thesis, University of California Radiation Laboratory Unclassified Report UCRL-2325, September, 1953 (unpublished).

[12] F. Asaro and I. Perlman, Phys. Rev. 87, 393 (1952).

[13] J. M. Blatt and V. F. Weisskopf, *Theoretical Nuclear Physics* (John Wiley and Sons, Inc., New York, 1952).

[14] Wu, Boehm, and Nagel, Phys. Rev. 91, 319 (1953).

[15] Perlman, Ghiorso, and Seaborg, Phys. Rev. 77, 26 (1950).

H. ACKNOWLEDGMENT

We wish to acknowledge the part played by Dr. Henry Neumann (now at Northwestern University) in some of the early phases of this work.

$_{94}Pu^{240}$ and Its Spontaneous Fission*

O. CHAMBERLAIN, G. W. FARWELL,† AND E. SEGRÈ
Department of Physics, University of California, Berkeley, California

(Received November 10, 1953)

Measurements of spontaneous fission of $_{94}Pu^{239}$ show that neutron irradiation of this substance forms a body with a high spontaneous-fission rate. This substance is with practical certainty $_{94}Pu^{240}$ and has a spontaneous-fission rate of approximately 1.6×10^{6} fissions/g hr. $_{94}Pu^{239}$ itself has a spontaneous-fission rate of the order of 40 fissions/g hr.

SPONTANEOUS fission of samples of element 94 has been under study for the last year, and it now seems desirable to give a short review of the present status of the experiments. It is to be understood that this is not a final report and many quantitative points are still under study, although the qualitative features are rather sure.

The significant experimental results are summarized in the following table which gives the spontaneous fission observed in various samples of element 94.

Sample	$94^{240}/94^{239}$	Counts	Fissions/g hr
C6	0.6×10^{-6}	8	40
C10	65×10^{-6}	131	180
C16	1000×10^{-6}	154	1580

Sample *C6* is material produced by irradiation with the Berkeley cyclotron, *C10* is material produced in the Oak Ridge pile, and *C16* is material reirradiated at Oak Ridge. The third column gives the number of fissions observed on which the number of the fourth column is based. When samples *C6* and *C10* were observed, it was thought that the difference in the spontaneous-fission rate was significant, and the hypothesis was put forward in a discussion between E. Fermi and the writers that its increase may be due to 94^{240} having a very high spontaneous-fission rate and being present in different amounts in the two samples. In order to check this hypothesis, sample *C16* of reirradiated material was investigated.

The figures in column two have been estimated with use of all available data upon the irradiation conditions and the following constants at thermal energies: $\sigma_f(94^{239})=664\times10^{-24}$ cm^2; $\sigma_\gamma(U^{238})=2.8\times10^{-24}$; $\alpha(94^{239})=0.54$.[1] A correction was also made for resonance absorption in U^{238}, and a reasonable hypothesis for the neutron density along a string in the pile was used. It is felt, however, that this part of the data is the most uncertain one, errors of a factor 2 being possible.

The data of the table, however, fit very well with the assumption that 94^{239} has a spontaneous fission rate of 40 fissions/g hr and 94^{240} has a spontaneous fission rate of 1.6×10^{6} fissions/g hr.

A discussion of the possibility that the observed spontaneous fission may be due to isotopes of uranium or 93 leads to untenable conclusions on the basis of the fact that slow-neutron irradiation of 94^{239} produces the highly-fissioning materials. Now the possible reactions conceivably, although not very probably, produced by slow neutrons are as follows:

(1) 94^{239} could go to U^{236} by an (n,α) reaction, but the spontaneous fission of U^{236} has been investigated by us and is at least 10 times too small, if present at all, to account for the observed fission rate of reirradiated 94^{239}.

(2) An (n,p) reaction would produce 93^{239}, a well-known substance with a period of 2.3 days. Our observations on spontaneous fission do not show any decay with such a period; and it is also known from the growth of 94^{239} or to 93^{239} that there is no long-lived isomeric state of 93^{239}. If we consider the possibility of elements 95 or 96 being responsible for the spontaneous fission we have the following difficulties: (a) 94^{239} by neutron capture should not give a beta emitter which could decay to 95 and 96. This fact would be very exceptional and against known semiempirical rules of nuclear systematics. (b) Experiments by R. Wilson using Edwin McMillan's recoil method have not shown the existence of a nonrecoiling beta activity of short life. (c) Long-lifed beta activities have been extracted from the reirradiated sample, at least to a great extent.

These points will be investigated also by chemical methods in cooperation with Mr. A. C. Wahl.

Note added in preparing the manuscript for publication: The spontaneous fission rate of Pu^{240} was subsequently measured at Los Alamos by the methods described by E. Segrè [Phys. Rev. 86, 21 (1952)] and found to be 4.61×10^{3} fissions/g sec based on 10^{4} fissions observed. This number should be added to Table II of that paper.

* This paper is, with minor literary changes, a report dated September 8, 1944, of work done at the Los Alamos Scientific Laboratory of the University of California. It has recently been declassified.

† Department of Physics, University of Washington, Seattle, Washington.

[1] α is the ratio of radiative-capture probability to fission probability when a neutron is absorbed.

Energy Spectrum of Spontaneous Fission Fragments*

EMILIO SEGRÈ AND CLYDE WEIGAND
Department of Physics, Radiation Laboratory, University of California, Berkeley, California
(Received November 10, 1953)

The energy spectrum of spontaneous fission fragments of Pu^{240} is compared with the same spectrum for slow-neutron fission of Pu^{239}. No significant difference was found, and the interpretation of this result is discussed.

THE energy spectrum of fission fragments for fission induced in Pu^{239} by slow neutrons has been investigated recently by Deutsch,[1] who measured the ionization produced by the fission fragments. There is also detailed information of the yield of the various chains based upon chemical evidence.

It is of considerable interest to compare the energy spectrum of spontaneous fission of Pu^{240} with that of the slow-neutron-induced fission of Pu^{239}. The nucleus undergoing fission is in both cases Pu^{240}, the only difference being that in the case of spontaneous fission it is in the fundamental state, whereas in the case of slow-neutron-induced fission it has an excitation of about 5 Mev. This excitation reduces the "half-life" for fission from 1.25×10^{11} years to an estimated 10^{-15} second, i.e., by a factor 10^{34}. Now one could think that in the case of spontaneous fission, only a very special type of nuclear motion may be conductive to fission and that only one or very few types of fragments would be emitted. If this were true, the energy spectrum would contain one pair or very few pairs of lines (pairs because there are always one line due to the heavy fragment and one line due to the light fragment).

It can be remarked, however, that even if only one type of motion ends in spontaneous fission, the two fragments, *after* having passed the potential barrier so that their destiny of coming apart is fixed, may interchange nuclear matter and hence change their relative mass and energy.

In order to settle these problems experimentally, we have investigated the energy spectrum of spontaneous fission of Pu^{240} and compared it with that of slow-neutron fission of Pu^{239}. The results of the investigation do not show any very great difference between the two spectra, a fact which could be interpreted by the assumption that several types of motion lead to spontaneous fission—in other words, that there are several passes through which the potential barrier can be crossed by the fragments. Another possible interpretation would be a reshuffling of nuclear matter after the crossing of the barrier as mentioned above.

It must be pointed out, however, that the experiments are not completely conclusive because the resolution of the apparatus used has turned out to be relatively poor, as one can see by comparing, e.g., the spectrum of the slow-neutron fission fragments of Pu^{239} measured by Deutsch with ours. It does not appear to us that it would be expedient to try to improve our technique by a large margin, and we would rather suggest a chemical approach to the problem, namely, observation of the yields of the various chains in spontaneous fission. This procedure seems feasible if one operates with about 50 grams of Pu containing about 2 percent Pu^{240}. Special precautions should, of course, be taken to prevent the multiplication effects from playing an important part in determining the rate of fission in the material. This can be obtained, e.g., by working with very small batches or by using some protective substance, such as boron or cadmium, in the solutions.

In our experiment the ionization produced by the spontaneous fission fragments emerging from a thin layer of Pu was measured with a linear pulse amplifier and recorded photographically. With the same apparatus and samples, we recorded also the ionization produced by slow-neutron fission fragments.

The chamber used contained purified argon and operated on electron collection. The collecting electrode had a screen grid shield in order to make the pulse size independent of the place at which the ions originated.

The data from a resolution test using alpha particles from natural uranium showed the two groups resolved and their energies in the correct ratio.

The sample used in the fission-fragment energy experiment was a deposit of plutonium one cm in diameter electroplated on 0.005-inch thick platinum. The sample weighed about 17×10^{-6} gram, the measurement being made by counting the alpha activity (7 percent of the Pu was Pu^{240}). The sample gave 1.91 spontaneous fissions per hour. Seven hundred and fifty spontaneous and 839 slow-neutron-induced fissions were used in our histograms.

The linear amplifier used had a time of rise of 0.2 microsecond. The time of collection of the electrons in the chamber was about one microsecond and the decay time of the amplifier was 5 microseconds. This resistance-capacitance decay time resulted in considerable loss of pulse height but was necessary because of the fluctuating background of the alpha-particle ionization when the apparatus was adjusted to record

* This paper is, with minor literary changes, a report dated December 19, 1949, of work done at the Los Alamos Scientific Laboratory and at the Radiation Laboratory of the University of California. It has recently been declassified.

[1] M. Deutsch and M. Ramsey, U. S. Atomic Energy Commission Report MDDC-945 (unpublished).

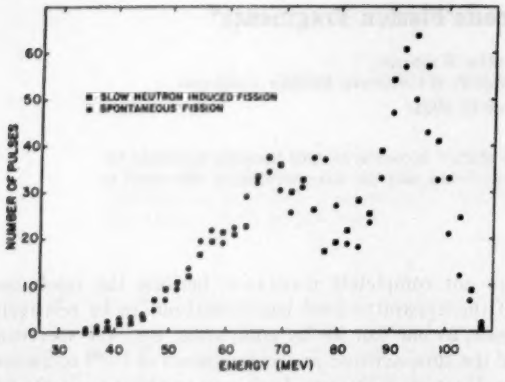

FIG. 1. Histograms of the ionization produced by spontaneous fission pulses of Pu^{240} and by slow-neutron fission pulses of Pu^{239}.

fission pulses. However, an absolute determination of the energy of the fission fragments was not needed since a comparison was made with fragments produced by slow neutrons. The recording was done by feeding the output of the amplifier to an oscilloscope and photographing the screen.

In order that drifts in gain of the amplifying equipment could be detected and corrected for, a series of pulses from a standard pulse generator was impressed on the film at the beginning and end of each run. For this calibration the pulse generator was connected directly to the screen electrode of the chamber and, by capacitance coupling to the collecting electrode, the pulse was fed through the entire apparatus.

Figure 1 presents a histogram of the spontaneous-fission pulses recorded. For comparison the pulse-height distribution of slow-neutron-induced fissions is shown on the same graph. The induced-fission curve was obtained with the same apparatus and sample. The slow neutrons were obtained from a radium-plus-beryllium source with water as the slowing-down medium.

The abscissa scale is a scale of deflections of the oscilloscope, in arbitrary units. We assume that the energy of the fragment is proportional to the organization produced. Under this assumption we have calibrated the abscissa scale in such a way that the energy corresponding to the light fragment peak is 93 Mev as measured by Deutsch.[1] In the ordinates we have the number of pulses giving an ionization between definite limits.

PHYSICAL REVIEW VOLUME 94, NUMBER 1 APRIL 1, 1954

Spontaneous Fission Systematics

JOHN R. HUIZENGA
Argonne National Laboratory, Lemont, Illinois
(Received October 30, 1953)

Previous correlations of spontaneous fission half-lives *vs* Z^2/A predict that the half-lives of even-even isotopes increase with A. A deviation from the above correlation is discussed, and it is shown that the spontaneous fission half-lives of the even-even isotopes go through a maximum with increasing A. The shorter spontaneous fission half-lives beyond the maximum may be a result of the greater deformations of the larger-A nuclides. Some comments are made on fission thresholds.

THE most successful correlations of spontaneous fission half-lives to date are those of Seaborg[1] and Whitehouse and Galbraith.[2] These authors plotted the logarithm of the spontaneous fission half-lives of several nuclides as a function of the parameter Z^2/A, and observed that the logarithm of the spontaneous fission half-lives of even-even nuclides decrease with increasing Z^2/A values in a linear manner. Whitehouse and Galbraith point out that the exception of U^{234} is so striking that the question of experimental error cannot be dismissed.[2] Ghiorso *et al.*[3] remeasured the spontaneous fission half-life of U^{234} and confirmed the earlier results.

The purpose of this note is to call attention to a consistent deviation from the Z^2/A relationship suggested by the above authors,[1,2] and in addition to point out a new relation, namely, that each group of even-even isotopes exhibits a maximum stability toward spontaneous fission. The latter phenomenon suggests the possibility of obtaining information on nuclear deformation and nuclear configuration from spontaneous fission half-lives.

At constant Z, the Z^2/A parameter predicts that the spontaneous fission half-lives of even-even nuclides increase with increasing values of A. For example, at constant Z an increase of two mass units in the heavy region of the periodic table should produce a tenfold increase in spontaneous fission half-life. This can be readily calculated using the slope of the spontaneous

[1] G. T. Seaborg, Phys. Rev. **85**, 157 (1952).
[2] W. J. Whitehouse and W. Galbraith, Nature **169**, 494 (1952).
[3] Ghiorso, Higgins, Larsh, Seaborg, and Thompson, Phys. Rev. **87**, 163 (1952).

fission half-life *vs* Z^2/A line of Seaborg plotted in Fig. 1. The predicted spontaneous fission half-life of U^{238} is one hundred times longer than that of U^{234}. The experimental half-life of U^{238} is shorter than that of U^{234} by a factor of two. The spontaneous fission half-lives of the even-A uranium isotopes therefore do not obey the $(1/A)$ parameter.

Previously reported spontaneous fission rates of the plutonium and curium nuclides have not included the neutron excess isotopes since they are more difficult to prepare. Uranium data give one the first indication of the effect of neutron excess on spontaneous-fission rate. From Fig. 1, it can be seen that the uranium data suggest, at constant Z, a maximum in the spontaneous fission half-lives of even-even nuclides analogous to beta stability.

The latter model of spontaneous fission predicts that the half-lives of the neutron-excess even-A plutonium isotopes will not continue to increase. Assuming the spontaneous fission half-life of Pu^{242} to be equal or less than that of Pu^{240}, calculations showed the possibility of detecting a spontaneous fission contribution from Pu^{242} in a plutonium sample containing a small amount of this isotope. The measured spontaneous fission half-life of Pu^{242} was 7×10^{10} years,[4] a value twofold less than that of Pu^{240}.[5] These data show that the even-A plutonium isotopes deviate from the Z^2/A parameter and have a maximum stability for spontaneous fission analogous to the behavior of the even-A uranium isotopes. The maximum stability can be seen in Fig. 2 where the logarithm of the spontaneous fission half-lives of the even-A isotopes of even Z elements are plotted as a function of A (Z/N, A-$2Z$, N, etc., are just as effective as A).

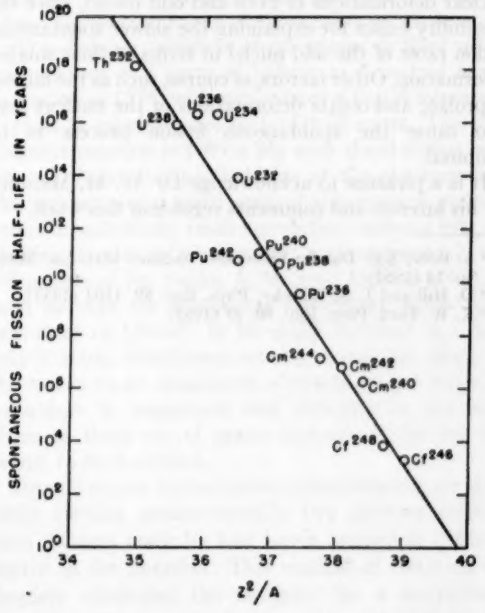

FIG. 1. Plot of spontaneous fission rates as a function of Z^2/A. Spontaneous fission half-lives and references to the data are summarized in the chapter referred to in reference 12 of this paper.

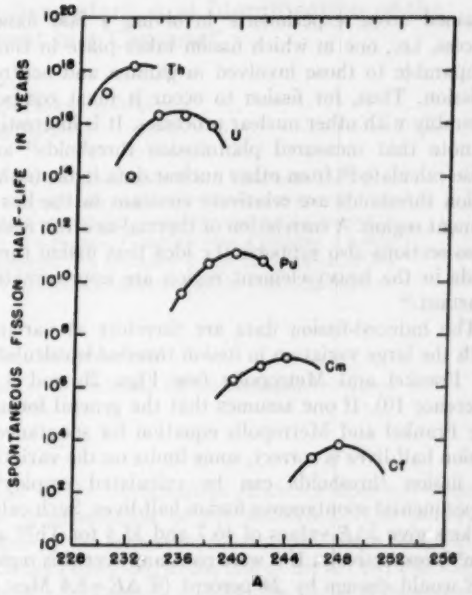

FIG. 2. Plot of spontaneous fission rates as a function of A and Z. Spontaneous fission half-lives and references to the data are summarized in the chapter referred to in reference 12 of this paper.

It is apparent from the above discussion that in predicting the spontaneous fission half-lives of even-even nuclides an error of several factors of ten can be introduced by extrapolating with the Z^2/A parameter. The larger even-A isotopes become more unstable and their spontaneous fission half-lives become shorter. This effect can be seen in Fig. 2.

Bohr and Wheeler[6] in a natural extension of the well-known theory of alpha decay calculated the probability per unit time for a spontaneous fission event. Flügge[7] and Turner[8] have also attempted to evaluate spontaneous fission half-lives with slight modifications of the Bohr-Wheeler formula, but as Segrè[9] points out, neither was successful. Frankel and Metropolis[10] have derived an equation of the following form for the spontaneous-fission half-life in seconds

$$T=10^{-21+k\Delta E},$$

where ΔE is the energy deficit at the saddle point in Mev and k is a constant for a particular nuclide.

Some information on fission thresholds has been

[4] M. H. Studier and A. Hirsch (private communication).
[5] Chamberlain, Farwell, and Segrè, this issue [Phys. Rev. 93, 156 (1954)].
[6] N. Bohr and J. A. Wheeler, Phys. Rev. 56, 426 (1939).
[7] S. Flügge, Z. Physik 121, 294 (1943).
[8] L. Turner, Revs. Modern Phys. 17, 292 (1945).
[9] E. Segrè, Phys. Rev. 86, 21 (1952).
[10] S. Frankel and N. Metropolis, Phys. Rev. 72, 914 (1947).

obtained from experiments involving a fast fission process, i.e., one in which fission takes place in times comparable to those involved in gamma and neutron emission. Thus, for fission to occur it must compete favorably with other nuclear processes. It is interesting to note that measured photofission thresholds[11] and those calculated[12] from other nuclear data indicate that fission thresholds are relatively constant in the heavy element region. A correlation of thermal-neutron fission cross sections also supports the idea that fission thresholds in the heavy-element region are approximately constant.[13]

The induced-fission data are therefore at variance with the large variation in fission thresholds calculated by Frankel and Metropolis (see Figs. 2b and 3 in reference 10). If one assumes that the general form of the Frankel and Metropolis equation for spontaneous fission half-lives is correct, some limits on the variation of fission thresholds can be calculated employing experimental spontaneous fission half-lives. Such calculations give $k\Delta E$ values of 46.7 and 35.4 for Th^{232} and Cm^{242}, respectively. If k were constant over this region, ΔE would change by 24 percent (if $\Delta E = 5.4$ Mev for Th^{232}, then $\Delta E = 4.1$ for Cm^{242}; these two nuclides represent the range over which information is available for photofission and neutron fission). The value of k decreases[10] in going from Th^{232} to Cm^{242}, so that the actual change in ΔE may be small enough to be within the experimental error of the experiments mentioned above. The longer spontaneous fission half-lives of the odd isotopes can possibly be explained by a small increase in their fission threshold. An increase in $k\Delta E$ of 10 percent (change in $\Delta E \lesssim 0.5$ Mev) in going from Pu^{238} to Pu^{239} would account for the increase in spontaneous fission half-life and not be inconsistent with other data. Thus, within experimental error the variations in fission thresholds calculated from spontaneous fission data are possibly in agreement with neutron fission and photofission thresholds.

The collective model[14,15] predicts that the energy of the first excited state of even-even nuclei depends principally on the equilibrium value of the nuclear distortion. The large changes in the energies of the first excited states at major shell closures have been explained in terms of nuclear distortion. [16] The energy of the first excited state of even-even nuclei in the region thorium to curium is not decreasing very fast, and thus it is assumed that the change in deformation is not large in this region. At constant Z, the Coulomb energy decreases with increase in radius (at constant Z, the radius may not increase proportionally to $A^{\frac{1}{3}}$). The spontaneous fission half-lives of the even-even isotopes, however, do not continue to increase with A. The shorter spontaneous fission half-lives beyond the maximum are possibly a result of the greater deformations of the larger-A nuclides. The ellipsoidal deformation may increase the decay rate due to the improvement in penetration through the thinner barrier.[15] Therefore spontaneous fission half-lives may be a sensitive measure of the deformation of a nucleus and thus yield some information on nuclear configuration.

It would be interesting to have data on the relative nuclear deformations of even and odd nuclei, since the possibility exists for explaining the slower spontaneous fission rates of the odd nuclei in terms of their smaller deformation. Other factors, of course, such as the mixing of prolate and oblate deformations of the nucleus may also cause the spontaneous fission process to be inhibited.

It is a pleasure to acknowledge Dr. W. M. Manning for his interest and comments regarding this work.

[11] Koch, McElhinney, and Gasteiger, Phys. Rev. **77**, 329 (1950).
[12] J. R. Huizenga, unpublished data discussed in Chapter 20 of *The Transuranium Elements: Survey* (McGraw-Hill Book Company, Inc., New York, 1954), National Nuclear Energy Series, Plutonium Project Record, Vol. 14A, Div. IV.
[13] J. R. Huizenga and R. B. Duffield, Phys. Rev. **88**, 959 (1952).
[14] A. Bohr, Kgl. Danske Vibenskab. Selskab Mat.-fys. Medd. **26**, No. 14 (1952).
[15] D. Hill and J. A. Wheeler, Phys. Rev. **89**, 1102 (1953).
[16] K. W. Ford, Phys. Rev. **90**, 29 (1953).

A V-Decay Event with a Heavy Negative Secondary, and Identification of the Secondary V-Decay Event in a Cascade*

E. W. COWAN
California Institute of Technology, Pasadena, California
(Received December 31, 1953)

Two cosmic-ray decay events have been photographed in a cloud chamber under conditions that yield mass values from combined magnetic-field momentum measurements and ionization measurements from droplet counting. A method has been developed for assigning meaningful probable errors to the ionization measurements. The first event is interpreted as the decay of a neutral V particle into a positive π meson and a negative particle of mass $1850\pm250m_e$. On the assumption of a two-body decay, the Q value for the decay is 11.7 ± 4 Mev. The second event is a cascade decay that can be summarized by the following reaction:

$$V^-\rightarrow 67\pm12\text{ Mev}+\pi^-+\Lambda^0$$
$$\Lambda^0\rightarrow 40\pm13\text{ Mev}+\pi^-+p.$$

The proton of the Λ^0 decay is identified by a measured mass of $2050\pm350m_e$. On the assumption of a two-body decay, the mass of the primary V particle is $2600\pm34m_e$.

INTRODUCTION

THE two events to be described were photographed in an expansion-type cloud chamber that has been operated in a 4200-gauss magnetic field for the purpose of obtaining good momentum measurements combined with ionization measurements made by droplet counting. A penetrating-shower selection system requiring a multiple coincidence from counters embedded in lead above and below the chamber was used to take the two photographs, which occurred in a series of about 10 000 cosmic-ray pictures taken at sea level.

The chamber, which is 48 cm square, is filled with a gas mixture of 2 parts of helium to 1 part of argon, saturated at 27°C with vapor from a liquid mixture of 2 parts of ethyl alcohol to 1 part of water. The total absolute pressure is 100 cm Hg with the chamber compressed. Good thermal isolation of the chamber from the magnet plus a small vertical temperature gradient result in sufficiently small convection currents that the limiting factor in momentum measurements is the diffuseness of the tracks. A "delayed expansion" is not used so that the tracks are sufficiently sharp for a curvature of 100 m^{-1} to be easily detected in a full-length track. Multiple-scattering errors are small for the tracks to be considered. Corrections are made for variations in magnitude and direction of the field, although these are of minor importance for the two events to be described.

Droplet counts for ionization measurements are made while viewing stereoscopically two pictures selected from pictures made by four lenses focused at different depths in the chamber. This method of counting the droplets eliminates the necessity for a background correction. Each expansion is calibrated individually for minimum ionization by means of electron tracks of known momenta appearing in the picture so that the value of the condensation efficiency does not enter in the determination of the ionization. The statistical errors in the ionization measurements are assigned by a method discussed at the end of the article, that makes use of a probability distribution curve determined experimentally. An allowance is made for counting errors on the basis of the reproducibility of the counts and the consistency of the ionization values for electron tracks in different regions of the chamber. The errors in ionization, and all other errors listed, are probable errors.

EVENT I

The stereoscopic pictures in Fig. 1 of the first decay event show tracks in the shape of a V with an included angle of $23\pm2°$ opening downward from a point in the upper left corner of the picture near the origin of a penetrating shower that occurred in a lead block above the chamber. The right leg undergoes a sharp deflection of $16\pm5°$ about $\frac{1}{4}$ of the way downward from the apex. Since the particle deflected almost directly away from the camera, the angle is difficult to measure and also difficult to observe unless the pictures are viewed stereoscopically. The momenta and angle are consistent within experimental error with the interpretation that a $\pi-\mu$ decay event occurred at the deflection. The momentum of the π meson measured directly from the curvature is 135 Mev/c, but this measurement is rough since the track is short and has a scarcity of droplets near the center. However, a better value of momentum can be obtained if the momentum of the μ meson, 130 ± 10 Mev/c, and the known Q value of a $\pi-\mu$ decay are used. The resulting momentum of the π meson, 165 ± 25 Mev/c, also checks with the observed ionization.

A line drawn from the apex of the V to an origin indicated by the intersection in three-dimensional space of two tracks in the shower is coplanar with lines tangent to the tracks at the apex of the V, within ex-

* Supported in part by the joint program of the U. S. Office of Naval Research and the U. S. Atomic Energy Commission.

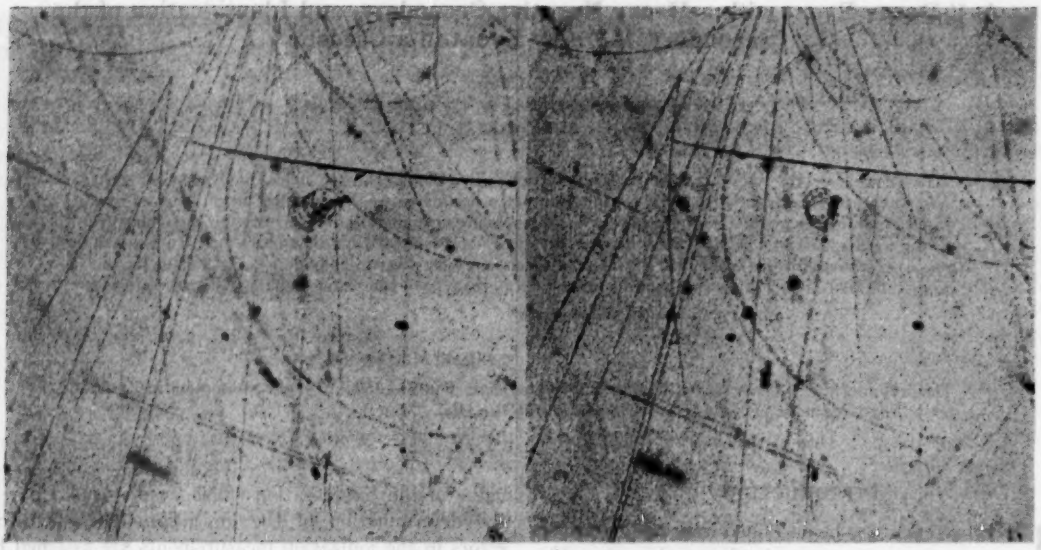

FIG. 1. A V-decay event with a heavy negative secondary.

perimental error. The transverse momenta of the two legs of the V also balance about this line, within experimental error. These facts indicate that the event is the decay of a neutral V particle that originated in the lead above the chamber into a positive π meson and a negative charged particle.

The alternative interpretation that the left leg of the V is a positive charged V particle traveling upward toward the origin of the shower and decaying into a π meson moving downward requires not only a very unlikely direction for the motion of the V particle and a direction for the decay almost exactly in the line of motion but also is inconsistent dynamically with any decay scheme known at present.

The momentum of the left leg of the V, which is negative for motion downward, is 875 ± 70 Mev/c and the ionization is 1.70 ± 0.19 times minimum ionization. These values correspond to a mass of 1850 ± 250 electron masses.

In light of the errors of measurement, the mass of this particle is near or equal to that of a proton and is not consistent with the mass of any negative particle that has been identified, e.g., the hyperon of cascade events ($\sim 2600m_e$) or the κ or τ mesons ($\sim 1000m_e$). There is no clear evidence that the particle is actually an antiparticle to the proton. No annihilation phenomenon is observed, and the Q value for the decay is definitely below the accepted range of values for the Q of the $\Lambda^0(V_1^0)$ decay, which yields a π meson and a proton.

The Q value calculated on the basis of a two-body decay and using the momentum of the π meson from direct curvature measurement is 8.6 Mev. A somewhat better value is obtained if the momentum of the π meson calculated from the $\pi-\mu$ decay is used, and this value of the Q is 11.7 ± 4 Mev.

If the negative decay product of the V particle is neither a negative proton nor a particle that decays into a negative proton, then it presumably decays into lighter particles, but no information is furnished concerning such a decay other than the fact that the particle observed lived longer than 10^{-9} sec.

Still other possibilities, although unlikely, must be considered. On the basis of calculated values of ionization for velocities above the minimum ionization value, the ionization of the negative particle is consistent within the probable error with that of an electron of the observed momentum. (All known mesons with this momentum and mass less than $1000m_e$ have an ionization less than 1.1.) The probability that the event is an electron pair with the observed 23° angle is exceedingly small, and in addition the production of a pair with this angle and the observed momenta requires the transfer of sufficient momentum to a nucleus so that a blob of droplets should be observed. Also the 16° deflection in the positive track must then be explained as an unlikely radiative collision. However, the decay products could be an electron and a π meson. The Q value on the assumption of a two-body decay with these decay products is 225 ± 20 Mev.

EVENT II

Photographs of the second event, a V-particle cascade, are shown in Fig. 2. A negatively charged V particle entered the chamber at the upper left and decayed into a meson, which produced a track nearly at right angles to the charged V particle, and a neutral V particle,

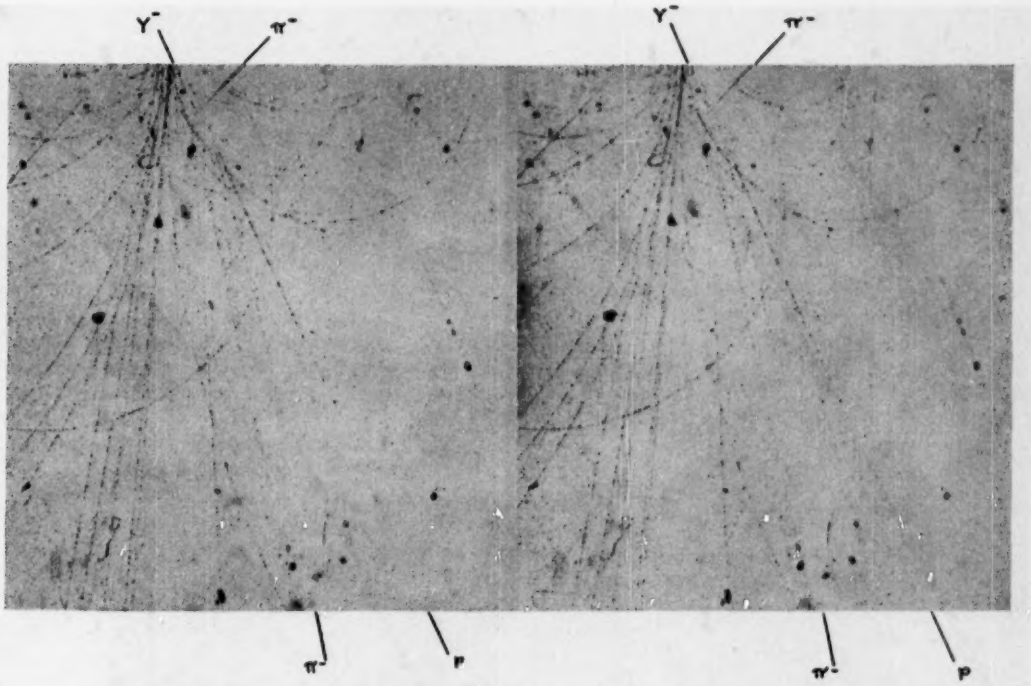

FIG. 2. A cascade event in which a negative charged V particle decays into a π meson and a neutral V particle that in turn decays into a π meson and a proton.

which traveled only 1.6 cm before decaying into two charged particles.

A number of such cascade events have been reported.[1,2] A single picture containing a charged and neutral V particle cannot be proven with certainty to be a cascade since the path of the neutral V particle can never be retraced with certainty. However, the event described here presents an unusual amount of evidence in favor of its being a cascade, and the identification of the neutral V particle is possible.

Only two origins are indicated by the intersection in three dimensions of the extensions of the tracks of penetrating particles in the chamber. One of these origins was a source of four charged particles and a neutral V particle, which decayed near the top of the chamber and is not connected with the cascade. The second origin, a short distance below and to the left of the first, was the source of a proton and the charged V particle of the cascade. A line drawn from either of these origins through the point of decay of the secondary V particle passes outside of the angle included between the tangents to the tracks at the apex of the V. If the secondary V decay event is a two-body decay, which is indicated by the identification of the V particle, the neutral V particle must have originated at the decay point of the charged V particle or else have come from some origin not indicated by the presence of other charged particles in the chamber. The fact that the charged and neutral V particles cannot have come from the same origin is of considerable importance, since other cascade events have not ruled out the possibility that "cascades" are the production of neutral and charged V particles in pairs, with a strong angular correlation.

In addition, if the neutral V particle is assumed to originate from the decay of the charged V particle, the following properties to be expected of a cascade event check well within experimental error: (1) coplanarity of the decay products of the secondary V particle with its origin, (2) transverse momentum balance of the decay products about the line of flight of the neutral V particle, (3) coplanarity of the lines of flight of the primary charged V particle, the meson resulting from the first decay, and the secondary neutral V particle, (4) transverse momentum balance of the decay products of the primary V particle about its line of flight.

Items (3) and (4) cannot be measured with sufficient accuracy to establish that the primary decay event gives rise to only two particles, since the directions of flight of the primary and secondary V particles differ by only about 4°, and the latter direction is determined by two points close together.

[1] Armenteros, Barker, Butler, Cachon, and York, Phil. Mag. **43**, 597 (1952).
[2] Anderson, Cowan, Leighton, and van Lint, Phys. Rev. **92**, 1089 (1953).

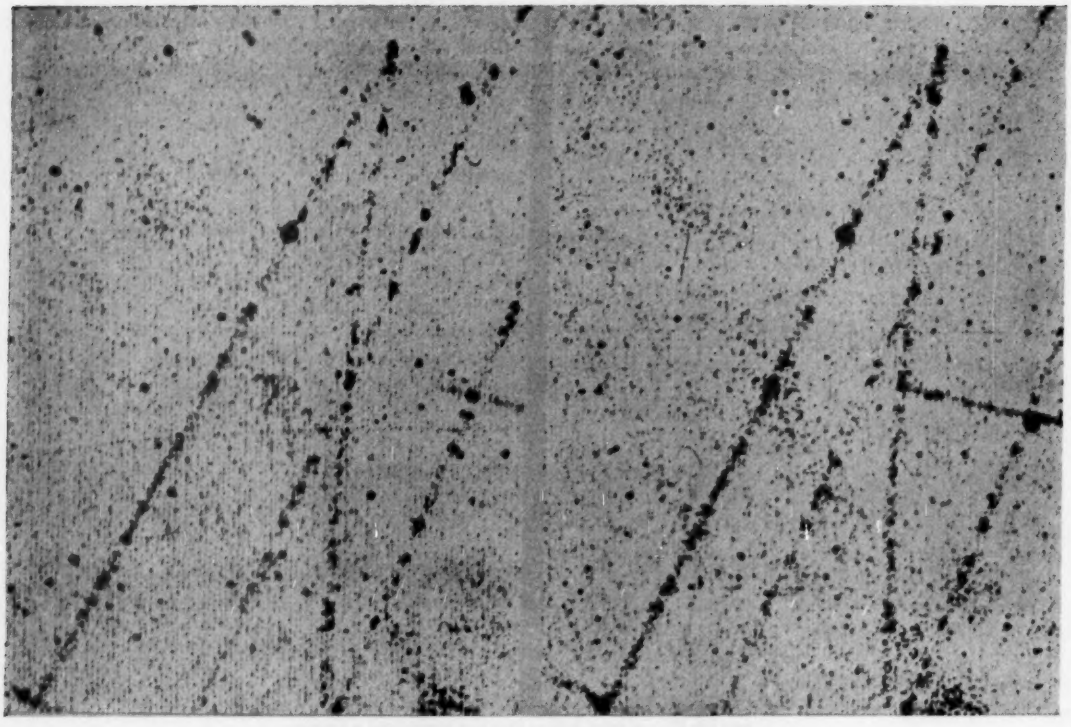

FIG. 3. Enlarged view of region near apex of V in Event I.

The momentum of the positive decay product of the secondary V particle is 730 ± 100 Mev/c and the ionization is 2.35 ± 0.26 times minimum ionization. These values correspond to a mass of 2050 ± 350 electron masses, and this particle is assumed to be a proton. The momentum of the negative decay product is 295 ± 40 Mev/c, the ionization 1.21 ± 0.14, and the included angle of the V is $6.5\pm1°$, giving a Q value of 40 ± 13 Mev. These characteristics check with the properties of a Λ^0 particle.

The meson decay product of the charged V particle has a momentum of 69 ± 10 Mev/c and an ionization 3.4 times minimum ionization. The method developed for determining ionization probable errors has not been extended to values of ionization this large, but experience with other similar tracks has shown that the values of ionization obtained from droplet counting in such cases are usually too small. Since a μ meson of the above momentum is ionizing only 2.6 times minimum ionization, whereas the corresponding ionization of a π meson is 3.7, the first meson of the cascade is probably a π meson. The included angle between the lines of flight of the primary decay products is $95\pm3°$.

On the assumption of a two-body decay, the Q value of the primary decay is 67 ± 12 Mev, and the complete reaction of the cascade is as follows:

$$Y^-\rightarrow 67\text{ Mev}+\pi^-+\Lambda^0$$
$$\searrow$$
$$p+\pi^-+40\text{ Mev}.$$

With the above assumption, the mass of the primary V particle is 2600 ± 34 electron masses.

ERRORS IN IONIZATION MEASUREMENTS

The problem of assigning statistical errors to ionization comparisons made by droplet counting for tracks of nearly equal ionization has been approached in the following manner. A track is divided into cells of length about equal to the width of the track by means of a transparent scale placed over the picture, with the starting point of the scale taken at random. The number of droplets in each cell is recorded, with the exception that all numbers exceeding 25 are discarded. From the numbers for a large group of cells, a probability curve is plotted giving the probability of finding a given number in a cell as a function of that number, and the average and mean square deviation are determined from this curve.

The central limit theorem of probability theory then permits the evaluation of the probable error in the droplet count of a track consisting of cells that have

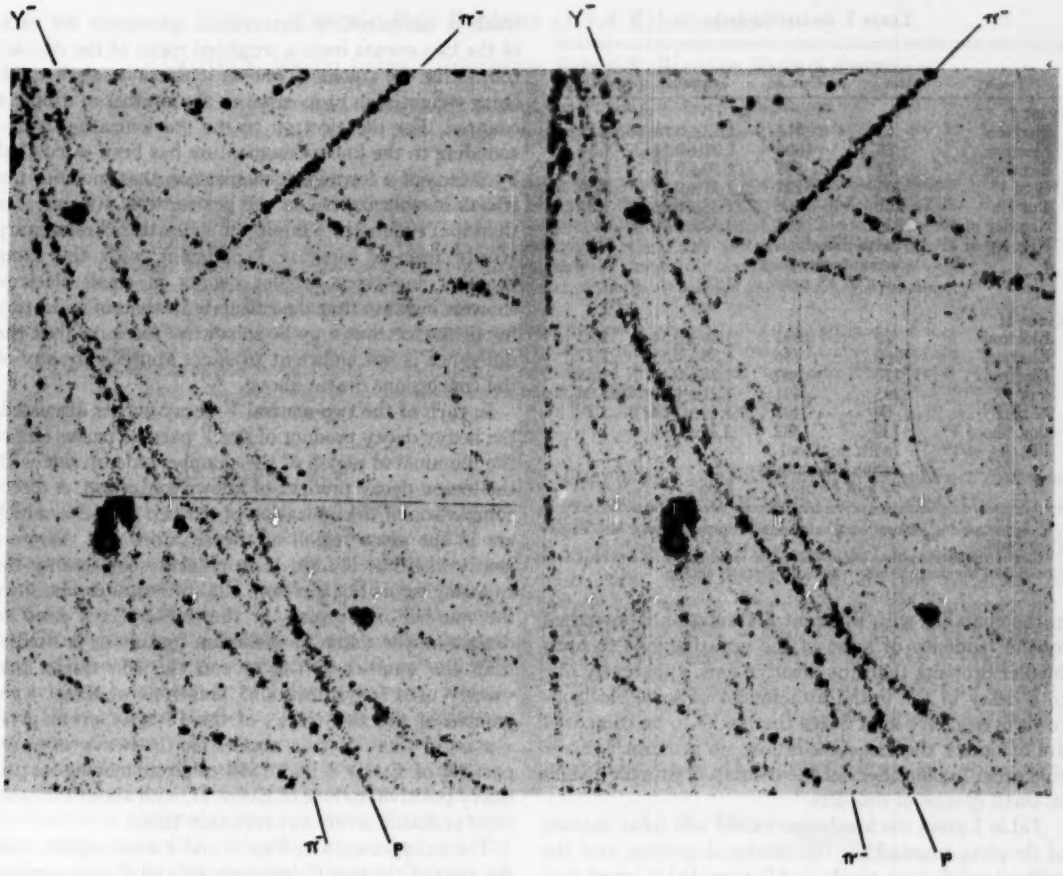

FIG. 4. Enlarged view of region near apex of *V* in Event II.

this same probability curve. This result is independent of whether or not the probability distribution is a Gaussian distribution as long as the number of cells in each track is large, but the result applies only to the comparison of tracks of the same ionization.

For tracks of about 1.5 times minimum ionization, the average of the probability curve mentioned above is about 9 droplets, and the square root of the second moment or root-mean-square deviation is 5.

Approximately 1.5 percent of the cells exceed the limit of 25 and are discarded. Since the tracks compared in this article all lie in the range of ionization between 1.1 and 2.4, the general shape of the probability curve for all is the same with small shifts in the average value.

For this range of ionization, the average for the probability distribution is assumed to be proportional to the ionization calculated on the basis of a maximum energy transfer corresponding roughly to the production of 25 droplets by a single ionizing event. Although the number of droplets in a cell can exceed the limit of 25 either because of the production of a large number of droplets in one event, or because of statistical fluctuations in the position of ionizing events along the track, only a small proportion of the cells is discarded, and the shape of the ionization curve as a function of velocity in the region of interest is relatively insensitive to the assumed value of the maximum energy transfer.

On the basis of the analysis outlined above, the probable error arising from statistical fluctuations in the ionization of tracks in the range mentioned has been found to be 1.7 times the probable error calculated on the basis of a Gaussian distribution involving the total number of droplets. This is the same as the probable error that would be calculated on the basis of a Gaussian distribution of primary ionizing events with each event producing 3 ions, which is about the average number actually produced.

A second source of error, about equal in magnitude to the statistical error, arises in counting the droplets. This error is introduced by the necessity of estimating the number of droplets in small clumps that contain a few droplets too close together to be resolved. The difficulty in making this type of estimate for regions

TABLE I. Ionization data.

Track	Momentum (Mev/c)	Nos. droplets counted	Experimental ionization	Calculated ionization
Event I				
Electron	13	414	1.12±0.14	1.23
Electron	25	1006	1.27±0.14	1.34
Electron	21	595	1.50±0.17	1.31
[a]π of V^0	165	227	1.31±0.17	1.39
μ of V^0	130	406	1.38±0.16	1.37
Neg. leg of V^0	875	631	1.70±0.19	···
Neg. leg of V^0	(with min. ionization determined by μ of V^0 only)		1.68	···
Event II				
Electron	22	1045	1.46±0.16	1.32
Electron	69	886	1.38±0.15	1.47
Electron	120	889	1.25±0.14	1.53
π of V^0	295	491	1.21±0.14	1.06
[b]π of V^-	69	497	3.45±(0.4?)	3.7
Pos. leg of V^0	730	582	2.35±0.26	···
Pos. leg of V^0	(with min. ionization determined by π of V^0 only)		2.06	···

[a] Not included in calibration of minimum ionization because momentum is uncertain.
[b] Not included in calibration of minimum ionization because ionization is outside of the range to which analysis of errors applies.

in the chamber with different illumination is increased by the tendency of some of the negative ions to form smaller droplets than the positive ions, apparently due to a delay in the initial attachment of some electrons to form negative ions. Since the tracks to be compared are of nearly the same ionization, no attempt is made to correct for the effect of the overlap of droplet images in small groups of droplets.

Table I gives the ionization values and total number of droplets counted for the tracks of interest and the calibration electron tracks and lists probable errors that include an estimated 10 percent error in counting. This estimated counting error is considerably larger than the differences obtained in successive droplet counts of the same track. The values of ionization for the known tracks, which are taken from several different parts of the picture, show internal consistency within the limits of the listed errors.

The value of minimum ionization, with which each track is compared, is determined separately for each of the two events from a weighted mean of the droplet counts for the tracks of known ionizations, each track being weighted in proportion to the number of droplets counted. For the electron tracks the ionization corresponding to the known momentum has been calculated by means of a formula for ionization that includes the effects of polarization in the gas for velocities greater than that required for minimum ionization. Preliminary results from a separate experiment with the same chamber involving droplet counts in small electron showers indicate that the calculated values of ionization for these electrons may be somewhat too large, but the difference is not sufficient to affect appreciably any of the conclusions drawn above.

In each of the two neutral V-decay events discussed, the heavy decay product of the V particle passes out of the illuminated region of the chamber side by side with the meson decay product of known ionization. A direct comparison of the ionization of the two particles, which are in the same region of the chamber and therefore nearly identical illumination, reduces considerably the counting errors but increases the statistical errors, since the number of droplets in the meson track used to determine the value of minimum ionization is smaller than the number in the several electron tracks previously used for calibration. This type of direct comparison of the two tracks of the V-decay event gives a mass of 1800 electron masses for the heavy negative particle of Event I and 1850 electron masses for the heavy positive particle of Event II, with about the same total probable errors as previously listed.

The enlargements in Figs. 3 and 4 show regions near the apex of the two V-decay events and gives some idea of the spacing of the droplets in the tracks. With only a visual estimate of the ionization, it is possible to establish with reasonable certainty that the heavy particle in both of the events has a mass greater than 1000 electron masses.

I would like to acknowledge many helpful suggestions concerning this work from Dr. C. D. Anderson, Dr. R. F. Christy, and Dr. R. B. Leighton.

Cosmic-Ray Protons at 3.4 Kilometers*

CHARLES E. MILLER, JOSEPH E. HENDERSON, GERALD R. GARRISON, DAVID S. POTTER, WAYNE M. SANDSTROM, AND JAY TODD, JR.
Applied Physics Laboratory,† University of Washington, Seattle, Washington
(Received July 29, 1953; revised manuscript received December 21, 1953)

A magnetic cloud chamber and an appropriate arrangement of coincidence and anticoincidence Geiger counters were used to photograph tracks of charged particles with ranges of 0.4 to 15 cm and 0.4 to 30 cm of lead. The momentum intervals corresponding to these range intervals are sufficiently different for protons and mesons that there resulted a large momentum interval in which only protons were stopped due to ionization losses. At higher momenta, most of the protons were stopped by nuclear interaction because of the large thicknesses of absorber used. At lower momenta, where both protons and mesons were stopped, the protons were distinguished by track density.

The result is an accurate proton momentum spectrum for the interval 0.7 to 2.0 Bev/c, in which it is found that protons form 20±2 percent of all ionizing nonelectronic particles. From the number of protons stopped in 15 and 30 cm of lead the path length for removal of protons in lead by nuclear interaction is calculated to be 206±30 g/cm² in the momentum interval 0.9 to 2.5 Bev/c.

I. INTRODUCTION

ALTHOUGH protons are considered to constitute the major part of the primary cosmic radiation, measurement of their intensity and energy distribution is difficult because of their similarity to other charged particles. Previous work of this laboratory[1–4] has shown that the magnetic cloud chamber, along with an arrangement of absorbers to give range selection, is especially suited to the separation of singly occurring protons from other charged particles. Although the earlier experiments demonstrated the feasibility of the method, it was immediately clear that for an accurate determination of the proton momentum spectrum certain improvements in equipment were necessary. Large corrections were previously required to account for the protons lost from the counter telescope because of scattering and nuclear interaction. The basic objective of the present work is to eliminate these losses and thus obtain a reliable momentum spectrum over the entire interval from 0.7 to 2.0 Bev/c. In addition, information is obtained on the nuclear interaction path length of protons in lead.

II. EXPERIMENTAL ARRANGEMENT

Figure 1 shows schematically the arrangement used. Although most of the equipment is the same as that used in previous work,[1–4] the arrangement differs considerably. The principal changes are the use of a 2-fold rather than a 3-fold coincidence in the counter telescope and a greatly improved anticoincidence tray.

Counters $C1$ and $C2$ are used in coincidence to define a beam of particles through the chamber. The six $A1$ counters all lie just outside the coverage defined by counters $C1$ and $C2$ and are used in anticoincidence with these. They serve to reduce the recording of shower-type events. The counters $A2$ completely surround a large block of lead absorber so that a charged particle traversing $C1$ and $C2$ will not be recorded if it, or one of its charged secondaries, penetrates this absorber. The 2.5 cm of lead absorber above the equipment serves to multiply the density of electron showers penetrating it and thus aids in their recognition through

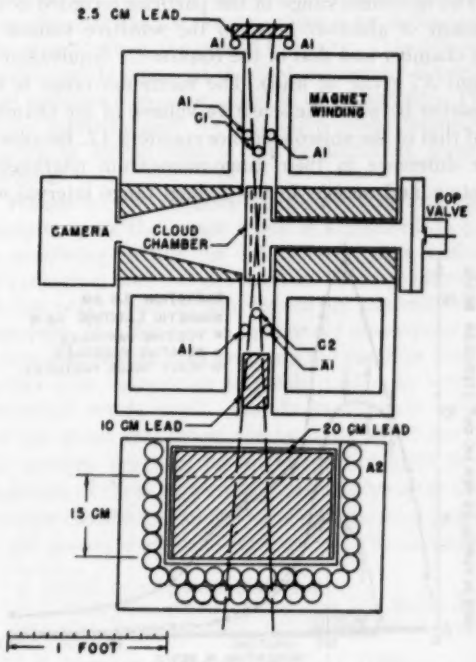

FIG. 1. Experimental arrangement.

* This work was supported by contract with the U. S. Office of Naval Research.
† A division of the Department of Physics.
[1] Miller, Henderson, Potter, and Todd, Phys. Rev. **79**, 459 (1950).
[2] Miller, Henderson, Potter, and Todd, Phys. Rev. **84**, 981 (1951).
[3] D. S. Potter, Ph.D. dissertation, University of Washington, 1951 (unpublished).
[4] Jay Todd, Jr., Ph.D. dissertation, University of Washington, 1952 (unpublished).

actuation of one of the $A1$ counters (in which case they are not recorded), or by the appearance of more than one track in the chamber.

The $A2$ counters are arranged to prevent particle leakage between counters. These are metal-walled counters arranged with adjacent counters in contact. Below the absorber an extra row of counters is used to cover the small dead spaces between counters. Along the sides the single rows are considered adequate as very few particles will be so scattered as to traverse these counters and, in addition, they would have to be traveling almost horizontally to pass through the small dead space between adjacent counters.

The corrections for loss of protons by scattering and nuclear interaction within the counter telescope have, with the present arrangement, been made negligible. This is primarily due to the use of a 2-fold coincidence. The chamber and counter walls are the only absorber in the C train that may cause scattering or nuclear interaction. Scattering in this material may be into or out of the coverage of $C2$ and thus the scattering error is nearly compensated. Since the material is only about 2 percent of the proton nuclear removal path length, the loss in the C train due to nuclear interaction is negligible. Scattering out of the $A2$ coverage has been nearly eliminated by extending the $A2$ coverage so that particles must be scattered 50 degrees or more in the absorber layer below $C2$ in order to miss the $A2$ counters.

III. MESON-PROTON SEPARATION

The minimum range of the particles recorded is the amount of absorber between the sensitive volume of the chamber and that of the counter $C2$ (equivalent to about 3.7 g/cm² of lead). The maximum range is the absorber between the sensitive volume of the chamber and that of the anticoincidence counters $A2$. Because of the difference in their range-momentum relationship protons and mesons in the defined range interval will appear in displaced momentum intervals. Measuring the momentum of all particles thus separates the protons from the mesons, except at momenta where the intervals overlap. Using various thicknesses of absorber, the proton intensity is obtained over a large momentum interval.

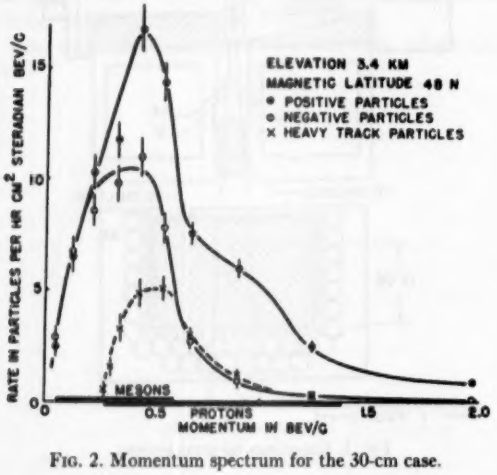

FIG. 2. Momentum spectrum for the 30-cm case.

At momenta above the proton ionization cutoff, large numbers of protons are also included due to nuclear interactions in the absorber between $C2$ and $A2$. By using an absorber whose thickness is nearly twice the removal path length, approximately 80 percent of the protons are included at the highest momentum measured (2.5 Bev/c). At momenta where both protons and mesons are recorded, the track density of protons is considerably greater so that the protons can be selected by examination of the tracks of the particles in the photographs.

IV. THE EXPERIMENT

Two sets of observations were made which differed only in the thickness of lead absorber between $C2$ and the anticoincidence tubes; 30 cm in one case and 15 cm in the other. They are referred to here as the 30-cm case and the 15-cm case, respectively. For the 15-cm case, the absorber was placed in the lower position as shown in Fig. 1.

The equipment was oriented with the chamber axis in a north-south direction. The maximum entrance angle from the vertical for the particles was four degrees to the north and south and 26 degrees to the east and west, resulting in a longer path through the absorber for some of the particles. The effective path length for the measured particles has been calculated to be 3 percent greater than the thickness of the absorber.

The observations were made at Climax, Colorado at an elevation of 3.4 kilometers and magnetic latitude 48 degrees north during the summer and fall of 1950. Approximately 6500 cloud-chamber expansions were photographed for the 30-cm case and 6300 for the 15-cm case.

V. MEASURING TRACK CURVATURE

In general the method consisted of enlarging the photographs and comparing the tracks directly with a circular arc of known radius. Thus, from a number of prepared arcs, the one that fitted the track best was selected. The method, described in detail in an earlier paper,[1] was capable of measuring tracks with radii between 0.3 and 10 meters. For each track, the sign of the charge and the momentum corresponding to the measured radius were recorded.

Only single tracks with length at least 88 percent of the chamber diameter were measured. Shorter tracks were not used because they cannot be measured as accurately and their position nearer the chamber wall leads to greater track distortion. With the exception of the few tracks whose widths indicated that they

were not time coincident with the triggering pulse, all single tracks of the necessary length were included regardless of quality or track density.

VI. RESULTS AND DISCUSSION

A. Momentum Distribution

Measurement of the track curvatures gives the momentum distribution of all particles recorded by the counter telescope. The absolute rate is determined from the *C-A* counting rate in the manner described in reference 2, part D. In Figs. 2 and 3 are given the rates, as a function of momentum, of singly occurring particles selected by the experimental arrangement used. From the design of the experiment these should represent the momentum spectra of charged particles other than electrons at an altitude of 3.4 kilometers and magnetic latitude 48 degrees north which have ranges in lead from 3.7 to 388 g/cm² and from 3.7 to 210 g/cm², respectively. These, of course, do not include all charged particles at this altitude. Indeed, the vast majority of mesons at this altitude have ranges in excess of the upper limits imposed here, as shown by previous work[1,3] in which the total spectrum was obtained. For protons, however, the 30-cm case should include almost all of those present in the radiation and having momenta above 0.3 Bev/*c*. The determination of this proton intensity is the primary objective of this experiment.

At the bottom of each figure is indicated the momentum interval for mesons and protons corresponding to the ranges in lead as imposed by the experiment. These have been taken from the range values given by Gross.[5] The ranges are based on energy loss through ionization only and are not expected to be correct for protons which undergo occasional catastrophic losses through nuclear interaction. Mu mesons are known to have nuclear interaction path lengths in lead many times longer than the absorber thicknesses used here so that the indicated ranges for these particles are expected to be correct.

From the standpoint of the present experiment, it is important to show that the probability of obtaining a single electron track of energy greater than 100 Mev which could not then be distinguished from a meson is very small. The small frequency of occurrence of single tracks of angle beyond the counter-telescope acceptance limits, and absence of tracks below the absorption cutoff in other experiments with this equipment,[3,4,6] show the number of single electron tracks photographed to be small even compared to the statistical uncertainty of the meson intensities. It may seem odd that showers often show up as either multiple tracks or blank photographs but rarely as single tracks. However, appearance of at least one electron track of energy greater than

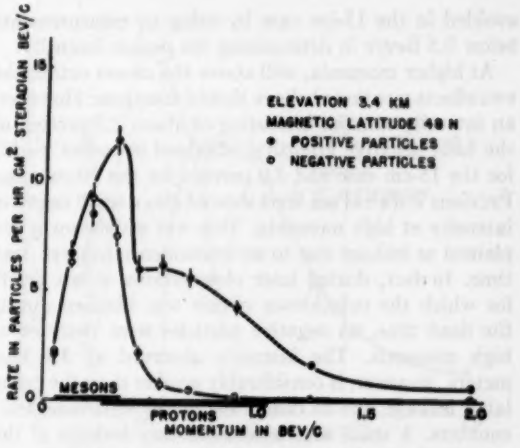

FIG. 3. Momentum spectrum for the 15-cm case.

100 Mev almost assures, according to fairly well-established shower theory, that it will be accompanied by other tracks, thus the data probably include very few electrons.

The particles included in the distribution are thus believed to be only mu mesons and protons with the exception (at low momenta) of a small number of electrons that would not affect the observed values within statistics. Assuming this to be true, the spectra of negative particles are for mesons only while the positive spectra are for positive mesons plus protons. The decided difference between the positive and negative distributions for the two cases is an indication of the magnitude of the proton intensity. This difference would exactly represent the proton intensity if positive and negative mesons occurred in equal numbers. From many investigations[6–11] the positive meson intensity is known to exceed that of the negatives by some 20 percent.

Failure of the negative distribution to drop more sharply above the meson cutoff is attributed, in part, to scattering outside the *A*2 coverage since sufficient *A* protection was not provided in the long dimension of the beam cross section defined by the coincidence telescope. It is due also to the limited momentum resolution that results from grouping the particles into the rather wide momentum intervals needed to keep the statistical errors small. This is particularly evident for the 30-cm case where the intensity at 0.7 Bev/*c* is the average intensity for an interval of 0.165 Bev/*c*. Inclusion of these high-energy mesons above the cutoff has only the effect of adding some statistical uncertainty to the proton intensity determination. The difficulty is

[5] D. J. X. Montgomery, *Cosmic Ray Physics* (Princeton University Press, Princeton, 1949).
[6] F. M. Charbonnier, Ph.D. dissertation, University of Washington, 1952 (unpublished).
[7] M. Correll, Phys. Rev. **72**, 1055 (1947).
[8] W. L. Whittemore and R. P. Shutt, Phys. Rev. **86**, 940 (1952).
[9] Bernardini, Pancini, Conversi, Scrocco, and Wick, Phys. Rev. **68**, 109 (1945).
[10] I. F. Quercia *et al.*, Nuovo cimento **7**, 277 (1950).
[11] R. B. Brode, Phys. Rev. **76**, 468 (1949).

avoided in the 15-cm case by using no measurements below 0.5 Bev/c in determining the proton intensity.

At higher momenta, well above the meson cutoff, the two effects mentioned above should disappear. However, an intensity remains consisting of about 2.5 percent of the total negative intensity (obtained in earlier work[3]) for the 15-cm case and 3.0 percent for the 30-cm case. Previous work[12] at sea level showed also a small negative intensity at high momenta. This was satisfactorily explained as leakage due to anticoincidence counter dead time. In fact, during later observations at sea level[13] for which the coincidence circuit was blanked during the dead time, no negative particles were detected at high momenta. The intensity observed at 3.4 kilometers, however, is considerably greater than the calculated leakage due to dead time of the anticoincidence counters. A small anticoincidence tray leakage of this magnitude would not have been objectionable for the present work; thus this measured negative flux at high momenta is not presented as positive evidence of some high-momentum particle with range less than the thickness of absorber used.

Figure 2 shows, in addition to the distribution of total positives and negatives, the momenta of those tracks selected as having greater than minimum density. These tracks were selected without regard to sign of curvature. Of the 351 tracks so selected for the 30-cm case, one with momentum 0.54 Bev/c showed negative curvature. Of the corresponding 395 tracks for the 15-cm case, two with momenta 0.35 Bev/c were of negative curvature. Among all tracks judged as heavily ionizing, this 0.4 percent showing negative curvature probably represents protons backscattered from the absorber below the C train. A similar small percentage of such tracks was found in earlier work.[1,3] The intensities shown for these heavily ionizing tracks may not represent true proton intensities as their determination is based, in part, on one's ability to recognize these tracks. At a momentum of 0.5 Bev/c, protons have an ionization density of three times minimum; and this density increases rapidly at lower momentum where it is probable that most protons have been found in this way. Indeed, here the intensity of heavily ionizing tracks accounts for most of the difference in intensity between total positives and negatives. At 0.75 Bev/c, protons have an ionization density of two times minimum. At this and higher momenta few of the protons present are recognized through track density as will be seen by comparison with the total proton intensity, discussed in the following section.

As is expected from the experimental arrangement, the distribution of heavy tracks shows a sharp cutoff on the low-momentum side. For the 30-cm case, three heavy tracks were found with momentum near 0.28 Bev/c while none were found at lower momenta. The distribution of Fig. 2 is drawn to zero at this value. Similarly for the 15-cm case, a heavy track was found at both 0.25 and 0.28 Bev/c with none at lower momenta. These experimental cutoffs correspond satisfactorily with that for protons as computed from the minimum range for the experiment.

B. Proton Spectrum

The problem now is to combine all available data to give a best estimate of the proton spectrum at Climax. This is obtained in part from the difference between the positive and negative intensities, and in part (at momenta below 0.5 Bev/c) from the intensity of heavily ionizing tracks. At momenta above 1.0 Mev/c, a small correction involving a knowledge of the nuclear removal path length is necessary. This path length is estimated and discussed in the next section. For comparison, data from earlier work,[4] in which particles stopping in 5 cm of lead were studied, are included.

The difference between the positive and negative rates for each interval have been plotted in Fig. 4 separately for the 15- and 30-cm cases. For the 15-cm case, only those positive-negative differences above 0.5 Bev/c are included. At lower momenta the increasing meson intensity makes the magnitude of the difference uncertain, and a correction would have had to be made for the positive meson excess. Similarly, for the 30-cm case, only differences above 0.65 Bev/c are included. The intensities plotted at 0.33 and 0.45 Bev/c are taken from the heavy track distributions which probably give a better estimate of the proton intensity at these momenta than is given by the positive-negative difference. Also included in Fig. 4 are similar values from earlier work with 5 cm of absorber.

The agreement in Fig. 4 between the maximum intensities for the various cases is considered satisfactory. For the 15- and 30-cm cases the peak intensities agree well within the indicated statistics. For the 5-cm case, the peak intensity is somewhat low. Here the sharp maximum (corresponding to the small absorption range

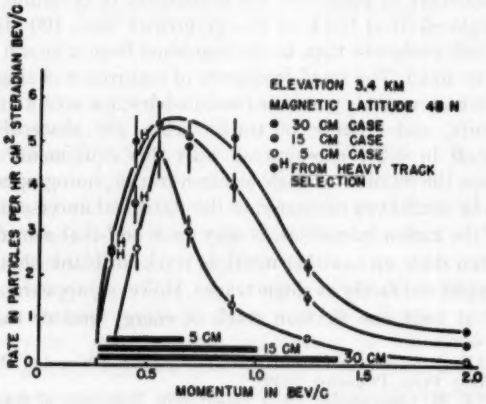

FIG. 4. Momentum spectrum of protons stopped in the absorber.

[12] Jay Todd *et al.* (unpublished).
[13] W. R. Davis, Phys. Rev. 92, 406 (1953).

used) cannot be expected to be properly resolved without obtaining intensities at more closely spaced intervals. Also, the arrangement of counters and absorbers used here led to errors of scattering not present in the present observations. For all three cases in Fig. 4, the low-momentum cutoff is an instrumental effect and occurs at the same momentum since the minimum ranges selected were the same.

Figure 5 gives total proton intensities as computed from the three distributions of Fig. 4. To some extent the intensities of Fig. 5 need to be discussed point by point. The intensities for each case lying well within the interval where protons stop due to ionization have been transcribed without change. For the 5-cm case, the intensities at 0.45 and 0.70 Bev/c have been omitted as uncertain due to scattering. For each case, intensities well above the ionization cutoff have been corrected to total intensities assuming a nuclear removal path length of 206 g/cm². The method of doing this will be

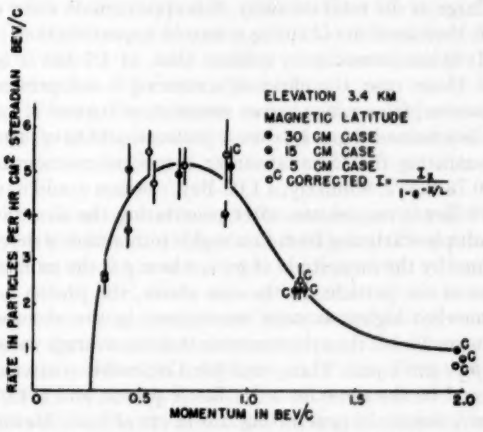

FIG. 5. Momentum spectrum of protons under 2.5 cm of lead.

explained in the next section. The points in Fig. 5 show some spread, but since they come from different sets of observations and have rather large statistical uncertainties, the agreement among the various estimates is considered quite good.

In Fig. 6 the various estimates of intensity have been combined to give a single value at each momentum. The intensities of Fig. 5 are all for the radiation as observed under the 2.5-cm lead absorber used above the chamber. In Fig. 6 a correction has been made for this absorber and, in addition, for the counter $C1$, the top of the chamber, and the roof of the trailer, assuming the path length as previously mentioned. This amounts to multiplying each intensity of Fig. 5 by 1.21 and plotting the result at the momentum the protons would have had before entering the lead. The difference in shape, as well as the higher-momentum cutoff, of Fig. 6 as compared to Fig. 5 is due to this correction. Figure 6, then, is expected to give the atmospheric intensities of

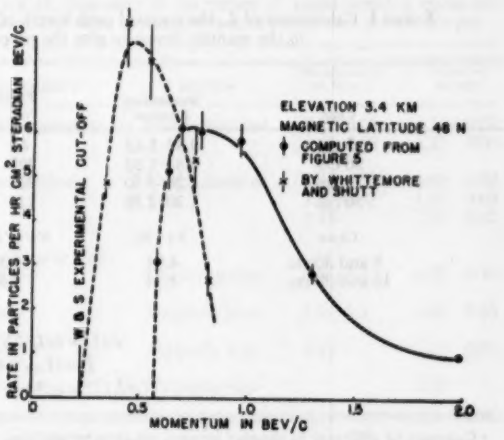
RATE IN PARTICLES PER HR CM² STERADIAN BEV/C
W. & S. EXPERIMENTAL CUT-OFF
ELEVATION 3.4 KM
MAGNETIC LATITUDE 48 N
COMPUTED FROM FIGURE 5
BY WHITTEMORE AND SHUTT
MOMENTUM IN BEV/C

FIG. 6. Momentum spectrum of protons at 3.4 kilometers.

protons at the altitude 3.4 kilometers between momenta of 0.7 and 2.0 Bev/c. The rapid decrease in intensity below 0.7 Bev/c is, of course, instrumental. In any case, the actual intensity must fall rapidly at low momentum as protons of momenta 0.2 Bev/c, for example, have a range in air at this altitude of only two meters.

Whittemore and Shutt[3] obtained information on the proton momentum spectra at 3.4 kilometers by using two cloud chambers with a magnetic field between. In the lower chamber were placed lead absorbers to aid in the energy determination and a threefold coincidence telescope selected particles in a vertical direction. All particles with heavy tracks stopping in a 6-cm absorber in the lower chamber were considered to be protons. The proton intensities thus determined have been plotted in Fig. 6. The use of very thin-walled coincidence counters resulted in a much lower momentum cutoff. Their intensities near 0.5 Bev/c are higher than any intensity found in the present investigation, but occur below the absorption cutoff of the present work. At higher momenta their intensities are low, as protons cannot be recognized by track density at such high momenta. Also, protons with momentum greater than 0.7 Bev/c would not be stopped by ionization losses in 6 cm of lead. The results obtained by Whittemore and Shutt complement the present work by extending the proton momentum spectrum down to 0.5 Bev/c.

Whittemore and Shutt have also calculated the proton intensity at higher momenta from their measurements of the total positive component and the total negative component. They assumed that the positive excess of mesons remains constant as these mesons travel from 3.4-kilometers altitude to sea level and that the meson positive excess is equal to the positive excess for all particles at sea level. Their calculated results show no disagreement, considering their rather large statistical error, with the curve of Fig. 6.

TABLE I. Calculation of L, the removal path length of protons in lead. The average L and the errors were calculated in the manner shown to give the proper weight to each of the two calculations of L.

Case	Momentum interval	Particles Pos.	Particles Neg.	Difference	Normalization factor	Rate
5 cm	0.82–1.33	61	4	57	0.0318	1.87[a]
30 cm	0.82–1.33	297	37	255	0.0267	6.81
15 cm	1.20–2.50	207	22	185	0.0195	3.61
30 cm	1.20–2.50	226	29	219[b]	0.0267	5.85
Cases	N_0-N_s	$N_0/(N_0-N_s)$	$\ln[N_0/(N_0-N_s)]$	x	L	
5 and 30 cm	4.94	1.38	0.322	62.4	194±37	
15 and 30 cm	2.24	2.61	0.960	207	221±41	
				Average	206±30	

$$e^2(L)=(\partial L/\partial N_0)^2e^2(N_0)+(\partial L/\partial N_s)^2e^2(N_s)$$
$$L=(L_1e_1^{-2}+L_2e_2^{-2})/(e_1^{-2}+e_2^{-2})$$
$$[e(L)]^{-2}=e_1^{-2}+e_2^{-2}$$

[a] Corrected for difference in absorber between the chamber and final coincidence counter for the two cases.
[b] Corrected for the protons passing through 30 cm of lead without nuclear interaction.

C. Nuclear Interactions of Protons in Lead

In addition to the loss of energy due to ionization' protons occasionally suffer catastrophic losses by collisions with nuclei. The result of the collision may be a scattering of the proton or a disruption of the nucleus with the emission of a number of secondary particles. The removal of protons as a result of such collisions is usually described by assuming that the intensity at x cm of absorber is given by

$$N_0-N_s=N_0e^{-x/L}, \qquad (1)$$

where N_0 is the number of protons incident on the absorber, N_s is the number stopping in x cm of absorber due to nuclear interactions, and L is the mean free path for removal of the protons. L, of course, differs from the nuclear-interaction mean free path only because of an occasional interaction that either causes so little change in the direction and energy of the incident proton that the proton continues through the absorber or else produces a secondary that penetrates the remaining absorber.

Calculation of L can be conveniently made from a measurement of the protons stopped by nuclear interaction along with a corresponding measurement of the total intensity of protons incident on the absorber. Examination of Fig. 4 shows that, for the 30-cm case, there is a large momentum interval where protons would be stopped by ionization losses. Since 30 cm is expected to be considerably greater than L, most of the protons at higher momenta will be stopped due to nuclear interaction. Thus, the interval 0.8 to 2.5 Bev/c contains nearly all the protons incident on the absorber.

For the 15-cm case the region from 1.2 to 2.5 Bev/c was selected as one in which the intensity represents protons stopped only by nuclear interaction. This intensity is compared to the corresponding intensity for the 30-cm case, which is assumed to give the total intensity, in arriving at an approximate value for L. Since the 30-cm intensity at high momenta is not quite as large as the total intensity, this approximate value of L is then used in obtaining a second approximation.

It is not immediately evident that, at 1.2 Bev/c for the 15-cm case, the effect of scattering is not present. However, from range *versus* momentum curves[5] it can be determined that a 1.2-Bev/c proton would have, after penetrating the 15-cm absorber, a residual momentum of 0.78 Bev/c. Similarly, a 1.05-Bev/c meson would have 0.78-Bev/c momentum after penetrating the absorber. Multiple scattering from Coulombic interaction is determined by the magnitude of pv/c, where p is the momentum of the particle. In the case above, the proton has somewhat higher average momentum in the absorber but smaller v/c than the meson so that the average values of pv/c are equal. Thus, multiple Coulombic scattering should be the same for a 1.2-Bev/c proton and a 1.05-Bev/c meson in penetrating the 15 cm of lead. Mesons are known to show Coulombic interaction only. The negative meson intensity at 1.0 Bev/c for the 15-cm case (see Fig. 3) is only 2 percent of the total negative intensity at this momentum. Actually the appearance of even this small number of mesons at this momentum has later been shown to be due more to A counter dead time than to scattering. Thus, no appreciable fraction of protons of 1.2-Bev/c momentum are expected to be photographed as a result of Coulombic scattering. Of course, large angle single scattering from nuclear interaction may result in a longer path length so that the proton will stop or be scattered outside the A coverage. The effects of such nuclear scattering are included in the definition of L.

For the 5-cm case a similar computation shows that, at 0.8 Bev/c, the effect of scattering is negligible. The interval chosen for the computation of L is 0.8 to 1.3 Bev/c. The intensity here is compared with the total intensity for this interval as given by the 30-cm case. Extending the interval to higher momenta would have increased the number of particles included in the

protons stopped in 5 cm of absorber, but at higher momenta a correction to the 30-cm intensity would have to be made to obtain the total intensity, thus no advantage would be gained. Also, the use of 30-cm data in an interval other than that used in the previous calculation makes the two calculations independent.

Table I contains the two separate calculations of L, along with statistical errors, and the average of the two results. Since the 5-cm case involved a 3-fold coincidence, it was necessary to correct for the protons lost between $C2$ and $C3$. This was done by using an estimated value for L to compute the number lost. The result obtained for L is 206 ± 30 g/cm^2.

Calculation of L from a comparison of the 5- and 15-cm cases cannot be made with an accuracy comparable to those of Table I. This results from the inability to determine the shape of an exponential curve from two points on the fairly straight part of the curve.

In Fig. 4 the values at higher momenta for the 5- and 15-cm cases represent the number that are removed by nuclear interactions in the absorber. By using the value of L computed above, Eq. (1) can be solved for N_0 to obtain the total number of protons incident on the absorber. The two highest-momentum values for the 15- and 30-cm cases and the three highest momentum values for the 5-cm case were corrected in this manner in arriving at the total proton intensities in Fig. 5.

The value for L obtained here can be compared with a result obtained by Mylroi and Wilson.[14] They measured the momenta at sea level of all particles stopping in 5, 10, 15, and 20 cm of lead by means of a counter-absorber arrangement placed below a magnetic spectrograph. Protons and mesons were separated by nearly the same method as used by the authors. Their result of 160 ± 40 g/cm^2 is in fair agreement with ours.

Froehlich, Harth, and Sitte,[15] using a multiple-plate cloud chamber with a counter-absorber hodoscope below to measure the range, obtained a value for L of 190 ± 15 g/cm^2 for nuclear interacting particles with momentum less than 2.85 Bev/c. The events recorded as nuclear interactions were: (1) penetrating showers with ionizing primary and two or more secondaries, (2) stars with one or more heavy prongs, and (3) large showers containing heavy prongs.

D. Positive Excess for Mesons

With the foregoing determination of the proton component, it is possible to compute the positive excess for mesons alone. Use is made of the work of Potter[1,3] which gives the spectra of all positive and negative particles at 3.4 km. The positive excess is assumed to be due to the presence of protons and to a positive excess of mesons. Therefore, subtraction of the protons from the positive particles leaves only positive mesons. Dividing the intensity of the positive mesons by that of the negative mesons gives the positive excess for mesons.

TABLE II. Summary of the values of meson positive excess obtained by other investigators at altitudes near 3.4 kilometers.

Investigator	Method	Momentum in Bev/c	Positive excess
This experiment	Cloud chamber	0.17–0.60	1.14 ± 0.07
		0.60–2.00	1.17 0.06
Charbonnier[a]	Cloud chamber	0.34–1.0	1.09 0.06
		1.0 –1.67	1.21 0.08
		1.67–	1.22 0.07
Whittemore and Shutt[b]	Cloud chamber	0.3 –0.7	1.35 0.10
Brode[c]	Magnetic lens	1.0 –2.5	1.30 0.03
Quercia[d]	Magnetic lens	0.23–	1.13 0.01
Bernardini[e]	Magnetic lens		1.20

[a] See reference 6.
[b] See reference 8.
[c] See reference 11.
[d] See reference 10
[e] See reference 9.

One value for the meson positive excess can be obtained in the interval 0.17 to 0.60 Bev/c from the 30-cm case. In this interval both mesons and protons were stopped by ionization losses. The observed heavy track intensity was subtracted from the intensity of positive particles to give, in the manner stated above, a meson positive excess of 1.14 ± 0.07. Another determination can be made in the momentum interval 0.60 to 2.0 Bev/c. Here the total proton intensity, which was obtained in Sec. B, was used to calculate a positive excess of 1.17 ± 0.06.

Table II is a comparison of the values of the meson positive excess obtained here with values obtained by others at nearly the same altitude. A careful study of the experiments yields no explanation for the discrepancy between the high values of Whittemore and Shutt and of Brode and the lower values obtained by the authors, by Quercia, and by Bernardini *et al.*

The authors wish to thank the Climax Molybdenum Company for their generous cooperation. The contributions of Mr. Don Eng, electronic technician, and Mr. Elmer Wright, instrument maker, are deeply appreciated.

[14] M. G. Mylroi and J. G. Wilson, Proc. Phys. Soc. (London) **A64**, 417 (1951).
[15] Froehlich, Harth, and Sitte, Phys. Rev. **87**, 504 (1952).

Total Cross Sections for 410-Mev Neutrons*

V. ALEXANDER NEDZEL†
Physics Department and Institute for Nuclear Studies, University of Chicago, Chicago, Illinois
(Received December 21, 1953)

Good geometry transmission measurements were conducted in the high-energy neutron beam of the University of Chicago synchrocyclotron. Total cross sections of fourteen elements, measured at an effective neutron energy of 410 Mev, were determined as follows (units of millibarns):

Hydrogen	33.7±1.3	Chlorine	742±10
Deuterium	62.0±4	Iron	1073±12
Beryllium	231±4	Copper	1187±14
Carbon	297±3	Cadmium	1848±21
Oxygen	378±5	Lead	2890±30
Aluminum	587±8	Thorium	3210±40
Sulfur	672±9	Uranium	3230±40

It was found that the following two-parameter empirical formula was consistent with the measured cross sections to within the accuracy of their determination:

$$\sigma = 2\pi R^2[1-\exp(-KR)],$$

where $R=r_0A^{\frac{1}{3}}$, and the two constants were chosen as $r_0=1.20\times10^{-13}$ cm, and $K=0.360\times10^{13}$ cm^{-1}. The sole exception was hydrogen, for which the prediction by the formula was 5 percent below the measured value.

The results are compared with neutron cross sections at lower energies, with proton cross sections at the same energy, and are discussed from the point of view of the transparent optical model.

I. INTRODUCTION

THE measurement of the total cross sections of nuclei for fast neutrons provides one of the best bases for the determination of nuclear radii. Knowledge of the dependence of these cross sections on energy and on mass number allows tests of various nuclear models.

For neutrons of greater energy than those at which resonances occur, the total cross sections would be expected to show a smooth dependence on mass number and on energy. Provided the energy of the neutrons is not so high that nuclei begin to show transparency effects, the theory of nuclear cross sections of Feshbach and Weisskopf[1] predicts asymptotically, for high energy and large R,

$$\sigma_t = 2\pi(R+\lambda)^2, \tag{1}$$

where R is the nuclear radius and λ the de Broglie wavelength of the incident neutron. In this limit, and assuming constant nuclear density, one would expect

$$(\sigma_t/2\pi)^{\frac{1}{2}} = a + r_0A^{\frac{1}{3}}, \tag{2}$$

where r_0 is the nucleon radius and a is independent of A but a function of the energy. The agreement with experimentally determined cross sections at 14 Mev[2-5] and at 25 Mev[9] is fair, at least as to over-all trend. Some of these data have been interpreted[1,7,10] to yield a value of about 1.5×10^{-13} cm for r_0.

Striking deviations from (1) and (2) were observed in measurements at 42 Mev,[11] at 83 Mev,[12,13] and at 95 Mev.[14] The transparent optical model of Fernbach, Serber, and Taylor[15] successfully interpreted the cross sections at 83 Mev, the best fit to the data occurring when the three parameters of the theory were chosen as follows: the nucleon radius, $r_0=1.38A^{\frac{1}{3}}\times10^{13}$ cm^{-1}; the increase in wave number of the neutron wave upon entering the nucleus, $k_1=0.285\times10^{13}$ cm^{-1}; and the absorption coefficient of the neutron wave in nuclear matter, $K=0.30\times10^{13}$ cm^{-1}.

At the still higher energy of 153 Mev,[16] and particularly at 270 Mev[17] and 280 Mev,[18] the character of the dependence of the cross sections on mass number was found to change again. In order to apply the optical model to the latter two observations the constant k_1 had to be taken as zero, implying that the index of

* Assisted by a joint program of the U. S. Office of Naval Research and of the U. S. Atomic Energy Commission.
† Now at Lincoln Laboratory, Massachusetts Institute of Technology, Cambridge, Massachusetts.

[1] H. Feshbach and V. F. Weisskopf, Phys. Rev. **76**, 1550 (1949).
[2] Amaldi, Bocciarelli, Cacciapuoti, and Trabacchi, Nuovo cimento **3**, 203 (1946).
[3] A. H. Lasday, Phys. Rev. **81**, 139 (1951).
[4] D. I. Meyer and W. Nyer, Los Alamos Report LA-1279, 1951 (unpublished).
[5] Poss, Salant, and Yuan, Phys. Rev. **85**, 703 (1952).
[6] Ageno, Cortellessa, and Querzoli, Rend. reale accad. nazl. Lincei **13**, 253 (1952).
[7] Coon, Graves, and Barschall, Phys. Rev. **88**, 562 (1952).
[8] L. S. Goodman, Phys. Rev. **88**, 686 (1952).
[9] R. Sherr, Phys. Rev. **68**, 240 (1945).
[10] E. Amaldi and B. N. Cacciapuoti, Phys. Rev. **71**, 739 (1947).
[11] R. H. Hildebrand and C. E. Leith, Phys. Rev. **80**, 842 (1950).
[12] Cook, McMillan, Peterson, and Sewell, Phys. Rev. **75**, 7 (1949).
[13] Bratenahl, Fernbach, Hildebrand, Leith, and Moyer, Phys. Rev. **77**, 597 (1950).
[14] J. DeJuren and N. Knable, Phys. Rev. **77**, 606 (1950).
[15] Fernbach, Serber, and Taylor, Phys. Rev. **75**, 1352 (1949).
[16] Taylor, Pickavance, Cassels, and Randle, Phil. Mag. **42**, 20, 751 (1951).
[17] J. DeJuren, Phys. Rev. **80**, 27 (1950).
[18] Fox, Leith, Wouters, and MacKenzie, Phys. Rev. **80**, 23 (1950).

refraction of nuclear matter had become one for neutrons of these energies.

The dependence of the cross sections on the mass number A at these various energies is illustrated in Fig. 1. The variation of $(\sigma_t/2\pi)^{\frac{1}{2}}$, the effective nuclear radius, with $A^{\frac{1}{3}}$ is shown in Fig. 2.

Observations have also been made[19–21] of the cross sections of certain elements as functions of energy in the 30–200 Mev range. Taylor and Wood[22,23] discovered maxima in this energy range of the cross sections of several elements. This phenomenon has been interpreted by Lawson[24] as a diffraction effect demonstrating the transparency of nuclei to high-energy neutrons.

The rapid drop in cross sections between about 100 and 150 Mev can be understood in terms of the optical model if the index of refraction of nuclear matter is postulated to drop rapidly to one at these energies. This variation of the index is not predicted by the Fermi gas model (a discussion of this point, and of the optical

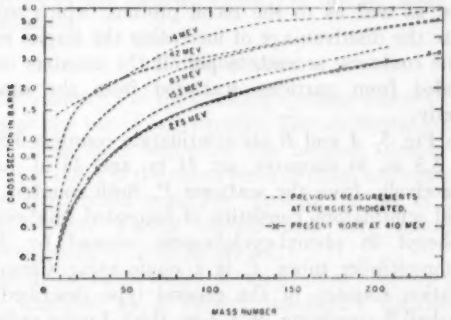

FIG. 1. Total cross sections are plotted as functions of the mass number for neutrons of the energies indicated. Except in the case of several of the lighter elements at 14 Mev, the actual experimental values fall within the estimated errors of the smooth curves drawn. The 14-Mev data used was that of reference 7.

model more generally, is given in Memmert).[25] This theoretical postulate, which implies that it is the coherent or elastic contribution to the total cross section that drops rapidly in this energy range, is supported by comparison of the observations of the elastic and inelastic cross sections at 95 Mev[14] with those at 300 Mev.[26] A theory more in accord with the observed variation of the index of refraction was proposed by Jastrow,[27] who calculated the index in terms of the forward scattering amplitudes of the nucleon-nucleon interactions using his "hard core" model.[28] Jastrow

[19] J. DeJuren and B. J. Moyer, Phys. Rev. **81**, 919 (1951).
[20] Taylor, Pickavance, Cassels, and Randle, Phil. Mag. **42**, 328 (1951).
[21] Mott, Guernsey, and Nelson, Phys. Rev. **88**, 9 (1952).
[22] A. E. Taylor and E. Wood, Phys. Rev. **87**, 907 (1952).
[23] A. E. Taylor and E. Wood, Phil. Mag. **44**, 95 (1953).
[24] J. D. Lawson, Phil. Mag. **44**, 102 (1953).
[25] G. Memmert, Z. Physik **134**, 42 (1952).
[26] W. P. Ball, University of California Radiation Laboratory Report UCRL-1938 (unpublished).
[27] R. Jastrow, Phys. Rev. **82**, 261 (1951).
[28] R. Jastrow, Phys. Rev. **81**, 636 (1951).

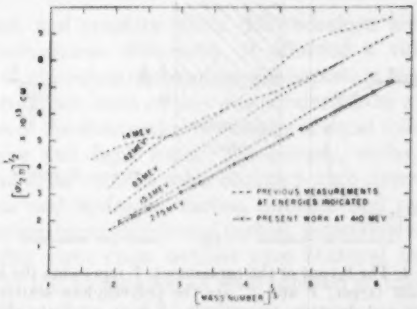

FIG. 2. Effective radii, $(\sigma/2\pi)^{\frac{1}{2}}$, are plotted as functions of $A^{\frac{1}{3}}$ for neutrons of the energies indicated. Except in the case of several of the lighter elements at 14 Mev, the actual experimental values fall within the estimated errors of the smooth curves drawn.

and Roberts[29] have proposed a nuclear model with a nonuniform density in order to better account for the variation of the neutron cross sections over the whole 14–270 Mev range. These various features of the energy dependence of total cross sections are shown in Fig. 3. In this compilation use was made of a previous summary.[30]

Since 280 Mev represents the highest energy at which total neutron cross sections have heretofore been measured, it was thought of importance to undertake the present study at the University of Chicago cyclotron where neutrons of over 400 Mev are available in considerable intensity. It appeared of especial interest to investigate whether the leveling off of the cross sections observed between 150 and 300 Mev extended

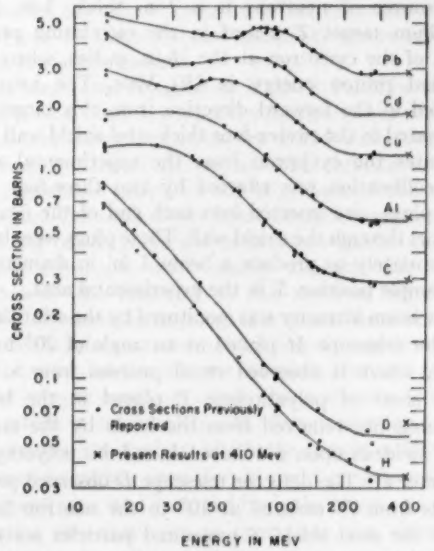

FIG. 3. Total cross sections of several elements as functions of neutron energy.

[29] R. Jastrow and J. E. Roberts, Phys. Rev. **85**, 757 (1952).
[30] Hildebrand, Hicks, and Harker, University of California Radiation Laboratory Report UCRL-1305, 1951 (unpublished).

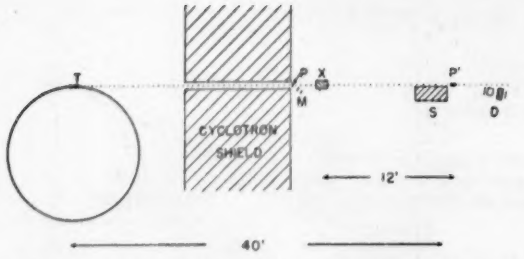

FIG. 4. The layout of the experiment. T represents the internal beryllium target; P and P' are the polyethylene scatterers for monitor and detector, respectively; S is an auxiliary shield for the detector; X is the sample (in beam attenuating position); and M and D represent monitor and detector telescopes.

to higher energies, and to compare the mass number dependence of the cross sections at 400 Mev with that at lower energies. To this end, fourteen elements were selected for study, as follows: hydrogen, deuterium, beryllium, carbon, oxygen, aluminum, sulfur, chlorine, iron, copper, cadmium, lead, thorium, and uranium. The cross sections of these elements were determined by good geometry transmission measurements, with the width of the effective neutron energy spectrum limited by the use of a proton recoil threshold detector.

Some of the results of this work have already been reported in preliminary form.[31,32]

II. APPARATUS AND PROCEDURE

A. Layout

The arrangement of the experiment is shown in Fig. 4. The source of neutrons is a 2-in. thick, 1-in. high beryllium target T placed in the circulating proton beam of the cyclotron at the 76-in. radius, where the nominal proton energy is 450 Mev. The neutrons emitted in the forward direction from this target are collimated in the twelve-foot thick steel shield wall that separates the cyclotron from the experimental area. The collimation was effected by two three-foot long steel plugs, one inserted into each end of the neutron channel through the shield wall. These plugs were bored appropriately to produce a beam 1 in. in diameter at the sample position X in the experimental area.

The beam intensity was monitored by the scintillation counter telescope M placed at an angle of 20° to the beam, where it observed recoil protons from a 1-in. thick sheet of polyethylene P placed in the beam. Neutrons not removed from the beam by the sample were incident upon a 1 in.×1 in.×5 in. polyethylene scatterer P'. The detector telescope D observed proton recoils from P' emitted at 10° to the neutron beam, while the steel shield S prevented particles scattered from the sample from reaching the counters of D directly.

The distance from the Be target to the sample was twenty-eight feet, while that from sample to detector scatterer was twelve feet. The detector scatterer subtended a solid angle of 4.8×10^{-5} steradian at the sample position.

B. Counters

The principal requirements of the counter systems were strict linearity and stability, maximum sensitivity to high-energy proton recoils from the polyethylene scatterers, and minimum sensitivity to radiation reaching the counters from other directions. In the case of the detector, it was also desired to have an absolute energy threshold for the counting of proton recoils.

The arrangement of the detector and monitor counters is shown in Fig. 5. The counters of the detector telescope are set along a line 10° off the direction of the neutron beam. This was done for two reasons: First, to get the counters out of the direct beam where they would be subject to neutrons, gamma rays, and electrons, as well as to the recoil protons, which would create the disadvantage of increasing the singles rates in the counters; second, to permit the counters to be shielded from particles scattered from the sample directly.

In Fig. 5, A and B are scintillation counters 3.5 in. and 5.5 in. in diameter, set 24 in. and 38 in. back, respectively, from the scatterer P. Both counters use liquid scintillators, consisting of saturated solutions of terphenyl in phenyl-cyclohexane, viewed by 5819 photomultiplier tubes. C is a nonfocusing Čerenkov radiation counter, of the general type described by Marshall,[33] consisting of a 4-in. thick Lucite radiator mounted in the axis of the telescope and covering the 4.25 in.×3.125 in. photocathode of the RCA developmental type C7157 photomultiplier tube against which it is fastened.

A Čerenkov radiation counter was selected for use in the detector because it has a natural threshold (the

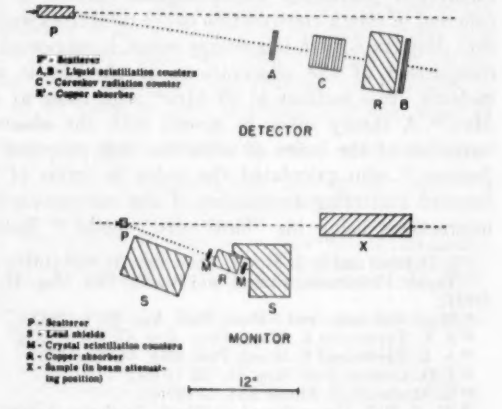

FIG. 5. The detector and monitor telescope arrangement.

[31] V. A. Nedzel and J. Marshall, Phys. Rev. 86, 604 (1952).
[32] V. A. Nedzel, Phys. Rev. 90, 169 (1952); 91, 440 (1953).
[33] J. Marshall, Phys. Rev. 86, 685 (1952).

limiting β with a Lucite radiator is 0.67) and because of its inherent low background properties. In operating this counter with the photomultiplier cathode in the proton recoil beam, it was found that it had a slight sensitivity for protons below the Čerenkov threshold. This was reduced below measurable limits by a 3-in. thick Cu absorber, R' in Fig. 5.

The monitor telescope was set to observe proton recoils at 20° to the neutron beam. The counters M in Fig. 5 are 1 in.$\times$1 in.$\times\frac{1}{4}$ in. diphenyl-acetylene crystals optically coupled to 1P28 photomultiplier tubes, set 9 in. and 13 in. from the scatterer. R is a 2.5-in. thick copper absorber that limits the sensitivity of the telescope to high-energy recoils. This was done so that the monitor actually monitored the neutron beam used in the experiment, and not stray radiations from the cyclotron that might not be strictly proportional to the neutron intensity. The lead shields S served to reduce singles rates in the counters and also to prevent any influence of the sample, which was not far away, on the monitor.

C. Electronics

Strict linearity of the counting systems was achieved through the use of fast circuits. The accidental coincidence rates were negligibly low because of the fast resolving times of the coincidence circuits, and counting losses were made negligible through the use of high speed, 10-Mc scaling circuits and very moderate counting rates of 15 to 30 per sec.

The signal pulses from the two monitor counters were each amplified by a 200-Mc bandwidth distributed amplifier of voltage gain 10, clipped to 4×10^{-9} sec by shorted cables, and fed into a two-channel, 6BN6 tube coincidence circuit of the type described by Fischer and Marshall.[34] The output of the coincidence circuit was connected directly to a Hewlett-Packard 10-Mc scaling circuit for counting. Since the average counting rate was low, a slow scaler was not needed, and the output of the Hewlett-Packard was connected directly to the mechanical register circuit.

Similarly, the signals from the photomultiplier tubes of the detector telescope were amplified, limited, clipped to 6×10^{-9} sec and connected to a multichannel diode coincidence circuit. The voltage gain used in the two liquid scintillator channels was 10, while that in the Čerenkov counter channel was 300. This fast coincidence circuit, similar to one described by Chen,[35] was designed and built by Fischer of this laboratory. The coincidence output was amplified by two 200-Mc distributed amplifiers, each with a gain of 10, and connected to a 10-Mc scaler.

D. Samples

The hydrogen cross section was obtained from measurements of the attenuation of cyclohexane, benzene, and graphite. Since this technique involved two independent differences, it afforded a valuable check on the values obtained for this important element. The deuterium cross section was obtained from a comparison of the attenuation of samples of equal thickness of heavy and light water. The oxygen, sulfur, and chlorine cross sections were obtained from differences of water and hydrogen, carbon disulfide and carbon, and carbon tetrachloride and carbon, respectively. The remaining eight cross sections were obtained from a study of the attenuation of solid samples of the pure elements.

Great purity of samples is not necessary for even very accurate cross-section determinations, particularly those of medium weight elements, provided actual measured densities are used in the calculations, for since the cross section per nucleon does not change rapidly with mass number, a given weight impurity will not have a greatly different contribution to the cross section than the principal element. Accordingly, commercial purities were considered adequate for the metals studied, though the uranium and thorium samples, loaned by Argonne National Laboratory, happened to be of very high purity, as were the samples of pile graphite used. The liquid samples were all of reagent grade purity, since their use involved differences in the calculation of desired cross sections.

E. Procedure

The chief concerns in the actual running of the experiment were the geometrical alignment of the apparatus, the proper operation of the electronic equipment, and the statistical and systematic errors inherent in the procedure chosen.

The target was designed such that it could be placed in the proton beam reproducibly by remote control; the collimators, being welded to the shield wall, formed a permanently aligned system, and also constituted good visual reference points for the alignment of the entire apparatus. Before each day's run, the detector assembly, consisting of the polyethylene scatterer holder and the counter telescope, was visually aligned. The exact position of the scatterer in the neutron beam was checked by exposing an x-ray film to the beam immediately behind the scatterer holder. Any necessary adjustments having been made, the sample holder was placed in the proper position using the scatterer and the collimators as reference points. A special rolling platform was constructed on which the sample holder was mounted in such a way that it could conveniently be interposed into, and removed from the beam.

During the above set-up operations, the electronic circuits were turned on and allowed to come up to their ambient temperatures, and the photomultiplier voltages were adjusted to assure operation of the scintillation counters on plateaus. Delay curves were taken in the two channels of the monitor and in the three channels

[34] J. Fischer and J. Marshall, Rev. Sci. Instr. 23, 417 (1952).
[35] T. C. Chen, Proc. Inst. Radio Engrs. 38, 511 (1950).

of the detector, in the first place to assure that the counters were aligned in time, and in the second place to judge, by the extent to which the curves were of the expected shape and width, that the over-all system, including the coincidence circuit, was operating properly.

Concerning the statistical errors of counting, the over-all accuracy was limited by the total number of counts obtained in the intensity measurements, the errors being minimized by the appropriate apportionment of counting times between observing attenuated and unattenuated intensities, and by the use of optimal thicknesses of sample whenever feasible.[36]

With regard to systematic errors, the chief concerns are with (a) the variations in the relative counting efficiency of the monitor and detector systems and (b) the linearity of these two systems. The adverse effect of the first of these can be held down by counting attenuated and unattenuated beams for short periods alternately. Then, for any steady drift in the efficiencies over a period of hours, the effect on one complete cycle of I and I_0 is minimized, and for any random fluctuations in the efficiencies the effects will tend to average out when the values of many cycles are combined. Thus, possible systematic error from these causes can be converted into a random error which can be reduced by simply taking more data.

Possible deviations from linearity in either of the counting systems are extremely important, though more serious in the case of the detector than the monitor, since any nonlinearity in the detector would lead directly to a misleading estimate of cross section, whereas errors in the monitor would tend to be more random in nature, particularly since data were taken only when the cyclotron beam intensity was quite steady. Over-all linearity of the detector was checked by comparing ratios of I to I_0 obtained with the same sample at different beam intensities. For this purpose the cyclotron intensity was reduced by adjusting only the ion source conditions, leaving the rf system unaltered in order to reduce the possibility of changing the duty cycle factor and thus invalidating this test. No nonlinearities were observed to within the precision of the tests.

III. VALIDITY CONSIDERATIONS

A. Neutron Energy

If the cross sections determined are to be characteristic of a definite neutron energy, it is evident that the beam used should be reasonably monoenergetic, and that its average effective energy should be known. The precise extent of the energy spread allowable can be gauged from the rapidity with which the cross sections appear to vary with energy. Inasmuch as comparison of the present results with those at 280 Mev indicates that the cross sections appear nearly independent of energy in this energy range, the requirements in the direction of a monoenergetic beam are not very stringent for the present experiment.

The energy spectrum of the neutrons from the beryllium target was deduced from range measurements of recoil protons,[37] basing the energies on the range values of Aron.[38] The resulting neutron spectrum is shown as curve A in Fig. 6. A fairly sharp peak is evident at about 400 Mev. However, in view of the uncertainty of the corrections for loss of protons in the absorbers due to nuclear processes, as well as other inherent difficulties in the deduction of high-energy neutron spectra from range measurements, curve A is to be considered of limited reliability in its details, particularly that of the low-energy tail. The relative narrowness of the distribution is similar to that reported for the Carnegie cyclotron,[39] but apparently quite different from the very broad distributions observed at Columbia[40] and at Berkeley.[41]

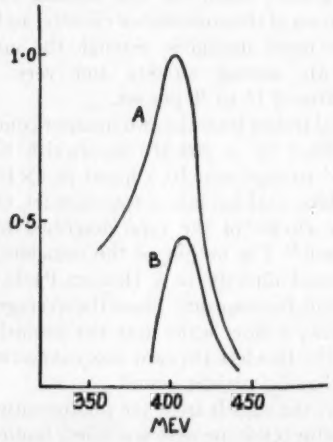

FIG. 6. Neutron energy spectra: A—produced by 450-Mev protons on a 2-in. beryllium target; and B—effective energy spectrum of the neutron beam used in the experiment.

[36] It can be shown, for the case of low background, that the optimal thickness of sample in a transmission measurement is about two mean free paths. Also, the statistical errors can be minimized (for a total time spent counting) if the counting times are apportioned as

$$t/t_0=(I_0/I)^{\frac{1}{2}} \quad \text{and} \quad t_B/t=(I_B/I)^{\frac{1}{2}},$$

where t, t_0, and t_B are the counting times of the attenuated, the unattenuated, and background intensities, I, I_0, and I_B, respectively.

[37] The neutron spectrum shown here is a composite of the results of three independent unpublished measurements at this laboratory: Marshall and Nedzel, range in Pb, and Nedzel, range in Cu, both observations made at 10° to the neutron beam on recoils from polyethylene; G. Yodh, range in Cu using recoils at 20° from a liquid hydrogen target. The three neutron spectra deduced from these range measurements agreed within 10 Mev on the energy of the maximum and of the end point of the distribution, but yielded relatively poor agreement on the low-energy tail.

[38] W. A. Aron, University of California Radiation Laboratory Report UCRL-1325, 1951 (unpublished).

[39] A. J. Hartzler and R. T. Siegel, Phys. Rev. **90**, 362 (1953).

[40] Goodall, Loar, Durbin, and Havens, Phys. Rev. **89**, 724 (1953).

[41] Cladis, Hadley, and Hess, Phys. Rev. **86**, 110 (1952).

The neutron spectrum having a fairly well defined high-energy limit, the spread of the effective beam can be set by cutoff at the low energy and through the action of a threshold detector. The effective spectrum for the present experiment was determined empirically by measuring the range of the protons actuating the detector, making suitable corrections for the stopping power of the counter itself. In addition, the residual range of the recoils above the threshold of the detector was measured by interposing absorbers between the first two of the three counters of the telescope. These measurements yielded the effective energy spectrum *B* of Fig. 6. Although this is not a very precise determination, inasmuch as the entire extent of the distribution was only 60 Mev, it permitted an entirely adequate estimate of the mean effective neutron energy for the purposes of this experiment. This mean effective neutron energy was determined as 410±20 Mev.

B. Tests of Exponential Attenuation

The significance of a definition of cross section independent of the amount of attenuating material rests on the exponential nature of attenuation. There is little question that a beam of neutrons of a given energy will exhibit pure exponential attenuation in an ideal good geometry experiment. Therefore, one good check on the validity of the experiment would be a measurement of the attenuation over a wide range of thicknesses of absorber. The presence of a background counting rate or any nonlinearity in the detector system would show up as a deviation from the expected exponential attenuation.

TABLE I. Deviations of the observed attenuations from those expected on the basis of measurements made with absorbers of about two mean free paths thickness.

Thickness in mean free paths	Deviation of I/I_0	Precision of I/I_0
0.456	− 0.3%	0.5%
0.458	− 0.7%	1.2%
0.762	+ 0.6%	1.6%
0.890	+ 0.9%	1.1%
0.916	− 0.7%	1.7%
1.030	− 1.0%	1.2%
1.118	− 0.6%	1.5%
1.190	+ 0.8%	1.0%
4.27	+ 6%	10%
6.46	−10%	20%

Most of the elements were studied in samples of several thicknesses, the largest being about two mean free paths in each case. The observed attenuations for the thinner samples are the points plotted at the upper left of Fig. 7. The straight line drawn is the expected attenuation on the basis of measurements with two mean free path thick samples. In order to extend this test of exponentiality into a region of greater thicknesses, two measurements of attenuations, at four and at six mean free paths, were made with lead absorbers especially for this purpose. Table I gives the deviations and the precision of determination (the statistical error) of each point. No systematic deviation beyond the accuracy of measurement is evident.

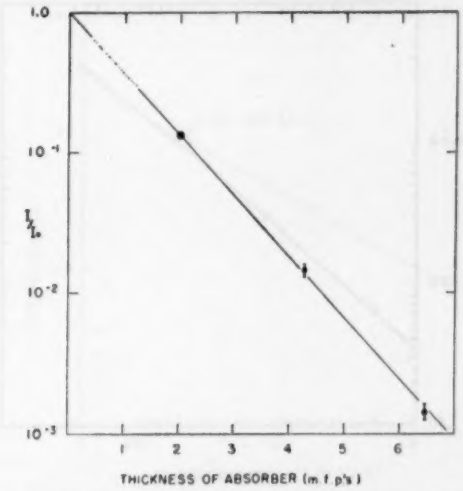

FIG. 7. Transmission of the neutron beam *vs* number of mean free paths thickness of absorber. Points are plotted for the attenuation of samples of all elements for which more than one thickness was studied. Normalization was in terms of the two mean free path thick samples. No background rates were subtracted, whence the strict exponential nature of the attenuation apparent is an indication of the negligibly low background achieved in this experiment.

C. Corrections

Few and only small corrections had to be applied to the observed rates. The accidental coincidence rates were always negligible, and hence no corrections were required for this factor.

A correction was applied for finite geometry, taking into account the scattering of neutrons into the detector by the sample in the same general fashion as described by Cook *et al.*[12] Tests conducted provided an approximate verification, at least in the upper limit, of this correction factor. In the present experiment, this correction for finite geometry amounted to only 1 percent in cross section for uranium, and less for other elements, being proportional to the cross section for the same geometry.

In the case of the liquid samples a correction had to be applied for the attenuation by the aluminum windows of the sample holders. This was calculated from the measured aluminum cross section, and amounted to 1.1 percent in attenuation.

D. Errors

The statistical errors of counting were the predominant source of uncertainty in the case of all cross sections measured. However, the deviations of individual counts were not observed to be significantly outside of the expected standard deviations. Accidental coinci-

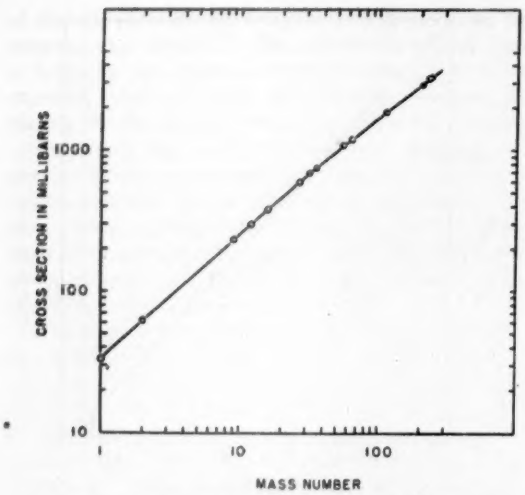

FIG. 8. The total cross sections observed in this experiment.

dence rates were negligible, no counting losses were detected, and over-all linearity tests always indicated linearity within the statistical accuracy of these observations, which was better than 0.3 percent in I/I_0 ratio. No short term variations, outside of statistics, were observed in the relative detector-monitor efficiencies. Slow drifts as great as 5 percent in twelve hours did occur, which were not important for the present experiment, since the amount of change during the relatively short interval of one cycle of observations was entirely negligible. The physical dimensions and weights of the samples were measured accurately, the densities and thicknesses of the solid samples being known to better than 0.3 percent in all cases, and those of the liquid samples to be better than 0.1 percent. The densities of the liquids were determined at the same temperature as that at which they were used.

IV. RESULTS AND CONCLUSIONS

The results of the cross-section measurements of the present experiment are shown as a function of mass number in Fig. 8. The numerical values are presented in Table II, with adjacent columns listing the published cross sections at 280 Mev[18] and 270 Mev,[17] the highest energies previously reported. Comparison reveals that for the heavy elements, the cross sections do not appear to be significantly different at 410 Mev from the values at the lower energies; for the lighter elements, except for the hydrogen cross section, the present work yields somewhat higher cross sections.

A. Hydrogen and Deuterium

The hydrogen cross section was deduced from measurements of the attenuation of samples of cyclohexane, benzene, and graphite, containing approximately the same number of carbon atoms per cm². These attenuations were self-consistent, as evidenced in Fig. 9, where they are plotted against moles of hydrogen per cm². The straight line drawn corresponds to a hydrogen cross section of 33.7 mb. Observations with these liquid samples also yielded a carbon cross section of 297±3 mb, in good agreement with the 297.5±2 mb value obtained from measurements on graphite.

The *n-p* total cross section at 410 Mev appears somewhat lower, while the deuterium cross section appears higher, than the weighted averages of these same cross sections measured at 270 and 280 Mev; the two sets of values, however, can almost be considered the same within their estimated accuracies. If one

TABLE II. Summary of results. The fourth column represents the results of the present study, at 410 Mev. The published cross sections at 280 Mev and 270 Mev, the highest energies previously reported, are given for comparison in the fifth and sixth columns. The third column gives the radius of the opaque nucleus $(\sigma/2\pi)^{\frac{1}{2}}$ that would give the observed cross section in each case, while the two sets of R, F, and σ columns give the radii, the opacity ($F=\sigma/\pi R^2$), and the cross sections predicted by the two formulas discussed in the text.

Element	$A^{\frac{1}{3}}$	$(\sigma/2\pi)^{\frac{1}{2}}$ (cm×10⁻¹³)	σ(410 Mev) mb	σ(280 Mev) mb	σ(270 Mev) mb	Formula (3) R (cm×10⁻¹³)	Formula (3) F	Formula (3) σ mb	Formula (7) R (cm×10⁻¹³)	Formula (7) F	Formula (7) σ mb
H	1.00	0.73	33.7±1.3	33±3	38±1.5	1.20	0.70	32	1.23−	0.68	32
D	1.26	0.99	62±4	49±5	57±3	1.51	0.84	60	1.55	0.80	60
Be	2.08	1.92	231±4	225±4	229±3	2.50	1.18	231	2.56	1.12	230
C	2.29	2.17	297±3	279±4	288±3	2.75	1.25	298	2.82	1.18	296
O	2.52	2.45	378±5	380±8	372±7	3.02	1.33	381	3.10	1.25	377
Al	3.00	3.06	587±7	566±18	555±8	3.60	1.45	591	3.69	1.37	584
S	3.18	3.27	672±9			3.81	1.49	682	3.91	1.40	672
Cl	3.29	3.44	742±9			3.94	1.51	740	4.05	1.42	734
Fe	3.82	4.13	1073±12			4.60	1.62	1071	4.70	1.52	1056
Cu	3.99	4.34	1187±14	1190±20	1145±15	4.79	1.64	1182	4.90	1.54	1165
Cd	4.83	5.42	1848±21			5.79	1.75	1841	5.94	1.65	1822
Pb	5.92	6.78	2890±30	2890±30	2840±30	7.10	1.85	2915	7.29	1.74	2910
Th	6.14	7.16	3210±40			7.36	1.86	3170	7.55	1.76	3150
U	6.20	7.18	3230−40	3140±50	3290±30	7.44	1.86	3240	7.63	1.76	3220

assumes that the deuterium cross sections at these energies can be considered simply as the sum of the n-p and n-n cross sections, then the 410-Mev data give $\sigma(n\text{-}n)=28\pm4$ mb while the lower energy data yield 19 ± 3 mb.

B. Comparison with Proton Cross Sections

The total neutron cross sections may be compared with the total (nuclear) proton cross sections measured at 408 Mev.[42] These are given in Table III. [The value of the neutron cross section listed for lithium was interpolated by calculation from the empirical formula (3) given below, fitted to the neutron cross sections.] The comparison shows evidence for support of the charge symmetry hypothesis.

C. Empirical Formula

It was suggested by Fermi in a private communication that the formula

$$\sigma=2\pi R^2[1-\exp(-KR)], \tag{3}$$

where $R=r_0A^{\frac{1}{3}}$, be fitted to the data, in order to allow approximately for the transparency of nuclei for neutrons. A best fit was obtained for

$$r_0=1.20\times10^{-13}\text{ cm}, \quad K=0.360\times10^{13}\text{ cm}^{-1}. \tag{4}$$

Using the above values of the parameters, the cross sections of all the elements studied were calculated, the results being given in Table II in the column labeled "σ" under the formula (3) heading. The values of R shown under this same heading were calculated from $r_0A^{\frac{1}{3}}$; the F values are the ratios of these cross sections to the "geometrical cross section," i.e., $F=\sigma/\pi R^2$, which might be termed the nuclear opacity and has the value two for an opaque nucleus. Comparing the cross sections computed from this formula with the measured values, surprisingly close agreement is evident, the formula values being identical to the measured values within the accuracy of determination of the latter, except in the case of hydrogen.

The function (3) is plotted as curve A in Fig. 10, the points shown on it being the experimentally observed cross sections plotted according to the choice of parameters (4).

TABLE III. Comparison of total nuclear cross sections of various light elements for neutrons and for protons.

Neutron cross sections (mb)			Proton cross sections (mb)		
n-p	(H)	33.7±1.3	p-n	(D-H)	31.6+2
n-n	(D-H)	28±4	p-p	(H)	24±1
	Li[a]	186		Li	194±8
	Be	231±4			242±6
	C	297±3			285±14
	O	378±5			406±3

[a] Interpolated from empirical formula.

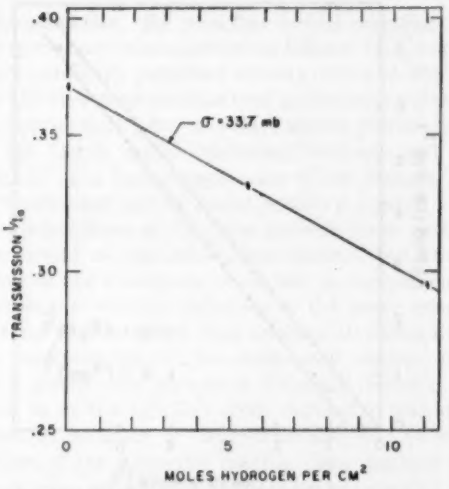

FIG. 9. Attenuation of the neutron beam by hydrogen. The plotted points are the observed transmissions of samples of graphite, benzene, and cyclohexane, respectively, all samples containing the same surface density of carbon.

D. Nuclear Radii

The cross-section data can be used to compute the radii on the basis of the opaque nucleus model, as given by Eq. (2). The values of the radius, $(\sigma/2\pi)^{\frac{1}{2}}$, and of $A^{\frac{1}{3}}$ are shown in Table II, and a plot of these data is given in Fig. 11. It is seen that, except for

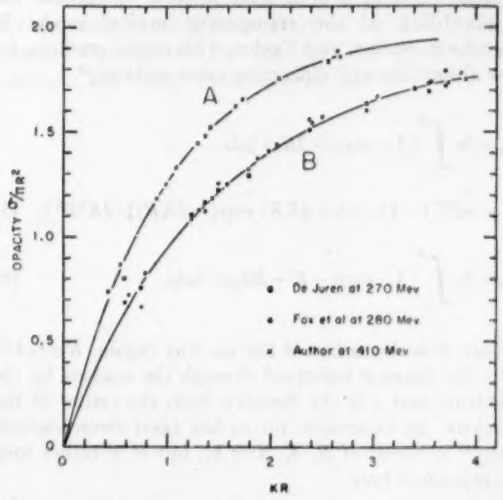

FIG. 10. The opacity of nuclei to neutrons *vs* the product of the nuclear radius R and the absorption coefficient K of neutrons in nuclear matter—curve A, as predicted by the empirical formula (3), and curve B, as predicted by the transparent optical model when $k_1=0$. The plotted points are the experimental data to which these functions were fitted.

[42] Marshall, Marshall, and Nedzel, Phys. Rev. 91, 767 (1953).

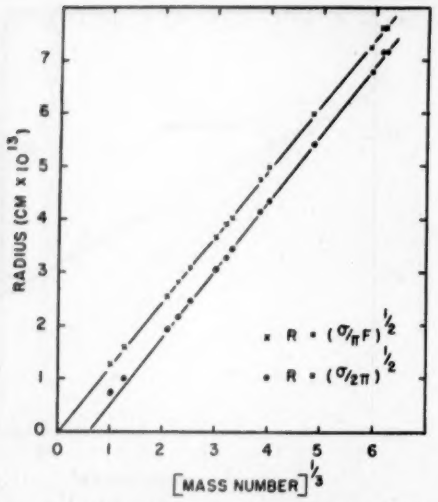

FIG. 11. The points along the lower straight line are the radii of the equivalent opaque nucleus; *viz.*, $R=(\sigma/2\pi)^{\frac{1}{2}}$; the points along the upper straight line are the radii calculated from the observed cross sections on the basis of the fit (8) to the transparent optical model; *viz.*, $R=(\sigma/\pi F)^{\frac{1}{2}}$, where F is the nuclear opacity.

hydrogen and deuterium, the points fall quite closely on a straight line in the form of (2), where $r_0=1.27\times10^{-13}$ cm and $a=-0.73\times10^{-13}$ cm. These values at 410 Mev can be compared with those reported for 280 Mev,[18] *viz.*, $r_0=1.27\times10^{-13}$ cm and $a=-0.82\times10^{-13}$ cm, and with those which can be fitted to the 153-Mev data, $r_0=1.39\times10^{-13}$ cm and $a=-0.86\times10^{-13}$ cm.

Since the phenomenon of negative intercepts of (2) revealed above is not readily explainable in terms of an opaque nucleus, it is of some interest to examine the applicability of the transparent optical model of Fernbach, Serber, and Taylor. This model predicts, for the absorption and diffraction cross sections,[43]

$$\sigma_a=2\pi\int_0^R[1-\exp(-2Ks)]sds$$

$$=\pi R^2[1-\{1-(1+2KR)\exp(-2KR)\}/2K^2R^2]; \quad (5)$$

$$\sigma_d=2\pi\int_0^R|1-\exp(-K+2ik_1)s|^2\rho d\rho, \quad (6)$$

where R is the radius of the nucleus (again, $R=r_0A^{\frac{1}{3}}$), s is the distance traversed through the nucleus by the neutron, and ρ is the distance from the center of the nucleus. An expression for σ_d has been given analytically[16] in terms of R, K, and k_1, but it is rather long to reproduce here.

[43] It is to be noted that the absorption cross section σ_a as used here refers to all inelastic processes; the diffraction cross section σ_d then refers to all elastic processes.

[44] S. Fernbach, University of California Radiation Laboratory Report UCRL-1382 (unpublished).

As was the case at 280 Mev,[44] it was found that observed cross sections were best fit when $k_1=0$. For this case the expression for the total cross section reduces considerably; *viz.*, the sum of σ_a and σ_d from (5) and (6) becomes

$$\sigma=\sigma_a+\sigma_d$$
$$=2\pi R^2\{1-2[1-(1+KR)\exp(-KR)]/K^2R^2\}, \quad (7)$$

shown as curve B in Fig. 10. This equation was fitted to the data assuming r_0 and K independent of mass number, a best fit being obtained for

$$r_0=1.23\times10^{-13}\text{ cm} \quad \text{and} \quad K=0.51\times10^{13}\text{ cm}^{-1}. \quad (8)$$

The cross sections calculated from formula (7) are shown in Table II, and the agreement of the formula with the experimental values is indicated in Fig. 10. Nuclear radii calculated from the measured cross sections on the basis of (7) are plotted in Fig. 11, where they are seen to fall closely on a straight line, passing through the origin when plotted against $A^{\frac{1}{3}}$, as is required for constant nuclear density.

However, this particular choice of values of the parameters, though it gives the correct A dependence of the cross sections, is not entirely satisfactory from the point of view of the transparent optical model. K is presumably the absorption coefficient of neutrons in nuclear matter and should be given in terms of the nucleon interactions by

$$K=\frac{3}{4\pi r_0^3A}[Z\sigma_{np}+(A-Z)\sigma_{nn}]. \quad (9)$$

If one uses the aforementioned choice of r_0, the value of σ_{np} of 34 mb observed from this work, and $\sigma_{nn}=\sigma_{pp}=24$ mb from the measurements at 408 Mev, and further assumes that these cross sections for free nucleons apply fully to bound nucleons, then (9) gives $K=0.36\times10^{13}$ cm^{-1}, a value considerably less than that required to fit the A dependence of the cross sections. This particular difficulty could be related to the assumption of nuclear density independent of A and would be less serious if the density were larger for heavier nuclei.

One would expect the optical model to apply more rigorously to the heaviest nuclei. K can be calculated according to (9) and then r_0 determined by fitting to measured cross sections. Using the cross sections of Pb, Th, and U, one obtains $r_0=1.35\times10^{-13}$ cm and $K=0.274\times10^{13}$ cm^{-1}. This choice of parameters, however, predicts cross sections 10–15 percent too low for light elements.

Thus, if one requires nuclear radii to be strictly proportional to $A^{\frac{1}{3}}$, the transparent optical model can be made to fit the observed dependence of the total cross sections on mass number very well, but not for values of the absorption coefficient expected on the basis of its definition.

E. Comparison to Cross Sections at 270–280 Mev

The cross sections at 410 Mev can be compared in a systematic way with those at 270–280 Mev by fitting the latter to (7) in the same manner as was done with the former, and comparing the parameters in the two cases. This comparison may be of interest even if the interpretation of the parameters themselves is in question. A fit is obtained[45] for

$$r_0 = 1.23 \times 10^{-13}\,\text{cm} \quad \text{and} \quad K = 0.485 \times 10^{13}\,\text{cm}^{-1}. \quad (11)$$

The 270- and 280-Mev cross sections[17,18] are plotted in Fig. 10 to illustrate the quality of the fit. By comparing (11) with (8), it is to be noted that K is about 5 percent larger at 410 Mev. On the basis of the definition (9) of K, this systematic difference could be explained by an average increase of the nucleon-nucleon cross sections in that amount. There is evidence for this in the higher value obtained for the deuterium cross section at 410 Mev, but the probable errors are too large to make the comparison completely convincing. The neutron cross sections already discussed seem to deny that the n-p cross section is rising, but again there is an appreciable probable error. As to the n-n cross section, one can again assume equality with the nuclear part of the p-p cross section. Comparison of the total cross sections at the two energies is difficult because of the present ambiguous status of the available data. However, there there is some evidence[46] that the elastic part of the nuclear p-p cross section remains constant in this energy range, while the meson production rises to about 2–3 mb at the higher energy.

[45] This choice is different from that of Fernbach, reference 44 (*viz.*, $r_0 = 1.39 \times 10^{-13}$ cm and $k = 0.25 \times 10^{13}$ cm^{-1}) because here the formula of the optical model is fitted as an empirical formula, whereas in the other, both theoretical and experimental considerations influenced the choice of the parameters.

[46] Marshall, Marshall, and Nedzel, Phys. Rev. **91**, 767 (1953); **92**, 834 (1953).

In conclusion, the principal results emerging from this study may be summarized as follows: (1) Compared to the previously published values at 270 and 280 Mev, the 410-Mev cross sections tend to the same values for the heavier nuclei, but to values several percent higher for the lighter nuclei (excluding hydrogen and deuterium); (2) a formal application of the formula from the transparent optical model permits a good fit to the mass dependence of the cross sections (even with the requirement of constant nuclear density), but leads to values of the absorption coefficient in nuclear matter inconsistent with the definition of the latter quantity in terms of this model, thus creating an ambiguity in the interpretation of the determined nuclear radii; (3) a simple two parameter empirical formula was found to fit the 410-Mev cross sections to within the estimated accuracy of their determination; (4) comparison of the measured neutron cross sections with proton cross sections supports charge symmetry.

The author wishes to express his appreciation to Professor John Marshall for his suggestion of the work and for his guidance and help during the course of the experiment; to Professors S. K. Allison and H. L. Anderson for their encouragement of the work; and to Professor R. H. Hildebrand for many valuable discussions and for his help in procuring special materials for the experiment. Thanks are also given to Mr. Joachim Fischer for his assistance with the electronics, particularly for his construction of the multichannel coincidence circuit used, and to Mr. Lester Kornblith and the members of the cyclotron crew for their friendly cooperation during the many hours of running required for this study. Grateful acknowledgment is made to the Argonne National Laboratory of the U. S. Atomic Energy Commission for the loan of the thorium, uranium, and heavy water samples used.

Production of K Mesons*

U. HABER-SCHAIM,† *Weizmann Institute of Science, Rehovoth, Israel*

AND

Y. YEIVIN AND G. YEKUTIELI, *Cosmic-Ray Section, Israel Atomic Energy Commission, Tel Aviv, Israel*

(Received September 23, 1953)

Calculations reported in an earlier paper are extended to lower energies using Fermi's explicit statistical method. A few pertinent details of the calculation are given, and the results compared with the observations of the Bristol group.

I. INTRODUCTION

ABOUT a year ago two of us (U.H. and G.Y.) applied Fermi's theory of pion production[1] to the production of K mesons.[2] One of the objects of that paper was to find out whether the characteristic volume in which the K mesons would be produced, according to the Fermi model, is of the order of $(4\pi/3)\lambda\!\!\!^{-}{}_K{}^3$ or $(4\pi/3)\lambda\!\!\!^{-}{}_\pi{}^3$, where $\lambda\!\!\!^{-}{}_K$ and $\lambda\!\!\!^{-}{}_\pi$ are the Compton wavelengths of the K meson and pion, respectively. The few experimental data available at that time were sufficient to show that both kinds of mesons are produced in the same volume.

In the meantime, more experimental data have been obtained. It seemed, therefore, worthwhile to extend the former calculation which was limited to high energies ($>20Mc^2$) to energies in the vicinity of the threshold.

II. METHOD OF CALCULATION

Following Fermi,[1] we consider the two colliding nucleons and the K mesons as nonrelativistic and the pions as extreme-relativistic particles in the cm system. We restrict the conservation of momentum to the two nucleons; this condition reduces somewhat the injustice done to the K mesons in taking them as nonrelativistic particles. The production of K mesons and pions in a nucleon-nucleon collision has then the statistical weight S_{rs} given by

$$S_{rs}=\frac{2^\alpha \mathfrak{M}^{\frac{1}{2}}}{3^\beta \pi^\gamma \mu^{2\beta}\alpha!}\times\frac{(W-2-rm)^\alpha}{W^\beta(W-2)^{\frac{1}{2}}}, \tag{1}$$

$$\alpha=3s+\tfrac{3}{2}r+\tfrac{1}{2};\quad \beta=r+s;\quad \gamma=s+\tfrac{1}{2}(r-1).$$

W is the total energy in the cm system in units of Mc^2, and m is the mass of the K meson in units of M. Further, $\mathfrak{M}=\frac{1}{2}m'$ and μ is the mass of the pion.

So far we have taken into account only the density of states in momentum space. We still have to sum over the various possibilities of the distribution of the electric charge among the nucleons and mesons, each of which has a specific statistical weight.[3] Consider, for example, a collision between a proton and a neutron in which four pions are produced. There are seven different charge states which obey the conservation of charge:

$$p+n\rightarrow\begin{cases}2p+\pi^++\pi^0+2\pi^-\\ 2p+\quad 3\pi^0+\pi^-\\ p+n+2\pi^++2\pi^-\end{cases}$$
etc.

The first of these has a statistical weight $\frac{1}{4}$ because there are two pairs of identical particles; the second state gives $\frac{1}{12}$, etc. The spin of the nucleons has been neglected—to include it would cause only minor changes. Now, if instead of four pions one K meson and three pions are produced, the statistical weight factor is increased since we now have fewer identical particles. In other words, the price one has to pay in momentum space in order to produce a heavy meson is reduced by the increase of the statistical weight of the charge states. This point has been overlooked in a recent paper by Kothari,[4] who finds a decrease with energy of the ratio of K mesons to pions. The values of the factors a_{rs} multiplying the S_{rs} are given in Table I.

The average number of K mesons n_K' and the average number of pions n' are given by:

$$n'_K=\Sigma_{rs}ra_{rs}S_{rs}/\Sigma_{rs}a_{rs}S_{rs},$$
$$n'_\pi=\Sigma_{rs}sa_{rs}S_{rs}/\Sigma_{rs}a_{rs}S_{rs}. \tag{2}$$

TABLE I. The statistical weight factors a_{rs} for pn and pp collisions.

r \ s	pn 0	pn 1	pn 2	pp 0	pp 1	pp 2
0	1	2	2.5	1	3	4
1	2	5	6.5	3	8	9.2
2	2.5	6.5	8.76	4	9.2	10.8
3	2.67	5.84	8.0	3.07	7.2	14.2
4	1.46	4.0	5.55	1.8	7.1	10
5	0.8	2.22	...	1.42	4.0	...
6	0.37	1.08	...	0.67	2.05	...

* The results of this paper were briefly reported at the Cosmic Ray Conference at Bagnères-de-Bigorre, July, 1953 (unpublished).

† Now at the Department of Physics, University of Berne, Berne, Switzerland.

[1] E. Fermi, Progr. Theoret. Phys. Japan **5**, 570 (1950); Phys. Rev. **81**, 683 (1951).

[2] U. Haber-Schaim and G. Yekutieli, Phil. Mag. **43**, 997 (1952).

[3] U. Haber-Schaim, "Tables Related to Fermi's Theory of Pion Production," University of Chicago, Department of Physics, 1951 (unpublished).

[4] L. S. Kothari, Nature **171**, 309 (1953); Phys. Rev. **90**, 1087 (1953).

We finally introduce an approximate correction for the conservation of angular momentum $g(W)$:

$$n=g(W)n' \tag{3}$$

for both K mesons and pions, where $g(W)$ decreases from 0.67 at the threshold for pion production to 0.51 at extremely high energies.[1] Within these limits the correction is somewhat arbitrary.

III. RESULTS AND DISCUSSION

The results of these calculations for pn collisions are given in Table II. They are only slightly different for pp collisions. For the mass of the K meson, $m=0.69$ has been used. The values at high energies are taken from our previous paper,[2] and the experimental values were found by the Bristol group.[5]

For the comparison of our results with experiment, one should keep in mind that, although the calculated values are for nucleon-nucleon collisions, the observed values are for nucleon-nucleus collisions. It is difficult to state the effect of the nucleus quantitatively, but, qualitatively, it should reduce the ratio for two reasons (a) the energy available in secondary collisions inside the nucleus is only a fraction of the primary energy, hence the production of K mesons becomes less probable; and (b) there is a chance for a K meson to be reabsorbed in the same nucleus in which it was created, and a pion may even be emitted on this occasion.[6] We would expect this process to occur more frequently at low energies where the K particle is slow than at high energies. In view of these arguments the agreement with experiment does not look unreasonable. One should also note that the whole theory contains only one parameter, the characteristic volume.

TABLE II. Comparison with experiment.

Energy in Mc^2 in lab. system	Calculated			Observed	Kothari (calculated)
	n_K	n_π	n_K/n_π	n_K/n_π	n_K/n_π
4	0.08	0.93	0.09		0.52
6	0.17	1.14	0.14	0.09±0.03	0.040
10	0.30	1.40	0.22		0.036
15	0.47	1.62	0.29	0.20±0.02	0.034
20	0.63	1.78	0.35		
50	1.17	2.34	0.50		
100	1.64	2.85	0.57		
200	2.25	3.43	0.66	0.5±0.2	

[5] D. H. Perkins, Rochester Conference, Dec. 1952 (Interscience Publishers, New York, 1953) and private communication.

[6] B. Peters, Cosmic Ray Conference, Bagnères-de-Bigorre, 1953 (unpublished).

PHYSICAL REVIEW VOLUME 94, NUMBER 1 APRIL 1, 1954

Renormalization

P. T. MATTHEWS, *Department of Mathematical Physics, The University, Birmingham, England*

AND

ABDUS SALAM, *Government College, Lahore, Pakistan*

(Received October 7, 1953)

A theoretical justification for the infinite subtractions, which have to be made in the renormalization of the S matrix, is given along the lines suggested by Gupta and developed by Takeda. It is shown that this is equivalent to working with the renormalized field variables of Dyson, and that the method deals very simply with overlapping divergences and the "wave function" renormalization associated with external lines. It also gives directly Ward's identities and brings out their essential dependence on gauge invariance. The method is applied to free and bound electrons in electrodynamics and all renormalizable meson theories.

In the later sections the new method is related to the original method of Dyson; the Bethe-Salpeter equation is renormalized and closed forms are derived for the renormalization constants.

INTRODUCTION

THE general proof of the renormalization of the charge expansion of the S matrix of interacting fields[1] falls into three distinct parts. Firstly the number of types of infinity (primitive divergents) in the theory is determined. (If this number is finite the theory is renormalizable.) The second step is to define a subtraction procedure which removes these infinities. The third step is to provide a theoretical justification for these subtractions. A general outline of this proof, applied to electrodynamics and various meson theories, has already been given by us.[2] The purpose of the present review is to assume the results of the first two parts of the proof for any renormalizable theory, and to give, in detail, a treatment of the third part, which has previously presented the greatest difficulty. The central idea is to treat all divergences of the theory by means of infinite counter terms, as has always been done for the mass renormalization. This was first suggested by

[1] F. J. Dyson, Phys. Rev. **75**, 1736 (1949).

[2] P. T. Matthews and Abdus Salam, Revs. Modern Phys. **23**, 311 (1951).

Gupta[3] and the idea was developed along the lines presented here by Takeda.[4] The derivation of the required counter terms was given by Dyson.[5]

The great advantage of the present method is that it reduces to trivialities the two main problems of Dyson's original approach,[1] concerning the treatment of overlapping divergencies and of external lines.

This program occupies the first five sections. In Secs. VI and VII the present approach is related to the point of view adopted originally by Dyson[1] and followed in our general review.[2]

In the final sections the theory of the renormalization of the Bethe-Salpeter equation is given and closed forms are derived for the renormalization constants.

We would like to stress that this paper is intended mainly as a review and contributes little that is essentially new to the general theory. We feel that the subject matter is sufficiently important to justify its repetition in a complete and relatively simple form.

I. ELECTRODYNAMICS

The usual treatment starts with the Lagrangian:

$$\mathbf{L}=\mathbf{L}_0+\mathbf{L}_I, \tag{1.1}$$

$$\mathbf{L}_0(x)=-\tfrac{1}{4}\mathbf{F}_{\mu\nu}(x)\mathbf{F}_{\mu\nu}(x)-\tfrac{1}{2}[\nabla_\mu\mathbf{A}_\mu(x)]^2 -\psi^*(x)[\gamma_\mu\nabla_\mu+\kappa]\psi(x), \tag{1.2}$$

$$\mathbf{L}_I(x)=-ie\mathbf{A}_\mu(x)\psi^*(x)\gamma_\mu\psi(x)+\delta\kappa\psi^*(x)\psi(x). \tag{1.3}$$

Here κ is the observed mass and is related to the "bare" (or mechanical) mass κ_0 by

$$\kappa=\kappa_0+\delta\kappa. \tag{1.4}$$

However, e is the "bare" charge.[6] The Hamiltonian corresponding to this Lagrangian is

$$\mathbf{H}=\mathbf{H}_0+\mathbf{H}_I.$$

If one transform to the interaction representation (IR) by applying the transformation $U=\exp[i\mathbf{H}_0(t-t')]$ to the Schrödinger representation, defined at some fixed time t', the new equation of motion is

$$i\frac{\partial}{\partial t}\Psi\rangle=\int H_I(\psi^*,\psi,A,e)d^3x\Psi\rangle, \tag{1.5}$$

where ψ^*, ψ, and A are interaction representation operators which annihilate and create bare particles with the observed mass. If one uses the subtraction procedure defined by Dyson, as extended by Salam to deal with overlapping divergences,[6a] one obtains finite matrix elements for the S matrix defined by this equation. The finite part of the theory is defined in such a way that it is both Lorentz and gauge invariant.

It is necessary finally to justify the apparently arbitrary dropping of the divergent terms. This is the part of the proof which will be given here in detail.

The subtraction procedure is defined in terms of infinite constants[7] $A(e)$ and $B(e)$, $C(e)$, and $L(e)$, the sum of the true divergences[6a] from electron, and photon, self-energy parts and vertex parts, respectively. We now take the essential step in the proof.[4] Define renormalized Heisenberg variables and observed charge by the equations

$$\psi=Z_2^{\frac{1}{2}}\psi_1,\quad \psi^*=Z_2^{\frac{1}{2}}\psi_1^*, \tag{1.6}$$

$$\mathbf{A}=Z_3^{\frac{1}{2}}\mathbf{A}_1,$$

$$e=Z_1Z_2^{-1}Z_3^{-\frac{1}{2}}e_1, \tag{1.7}$$

where

$$Z_1=1-L(e_1),\qquad Z_2=1+B(e_1),\quad Z_3=1+C(e_1). \tag{1.8}$$

ψ_1, ψ_1^*, and $\mathbf{A}_1$ are identical with the renormalized Heisenberg variables which have been discussed at length by Dyson,[5] but for our purposes they can be taken as defined by (1.6), (1.7), and (1.8). Expressing $\mathbf{L}$ in terms of renormalized Heisenberg variables, one obtains

$$\mathbf{L}=\mathbf{L}_1=\mathbf{L}_{10}+\mathbf{L}_{1I}, \tag{1.9}$$

where

$$\mathbf{L}_{10}=\mathbf{L}_0(\psi_1,\psi_1^*,\mathbf{A}_1) \tag{1.10}$$

is the same function of the new variables (provided we redefine the ∇A term which has no physical effect) and (see reference 24)

$$\mathbf{L}_{1I}=-ie_1[1-L(e_1)]\mathbf{A}_{1\mu}\psi_1^*\gamma_\mu\psi_1 -B(e_1)\psi_1^*[\gamma_\mu\nabla_\mu+\kappa]\psi_1+Z_2\delta\kappa\psi_1^*\psi_1 -\tfrac{1}{4}C(e_1)\mathbf{F}_{1\mu\nu}\mathbf{F}_{1\mu\nu}. \tag{1.11}$$

The corresponding Hamiltonian is

$$\mathbf{H}_1=\mathbf{H}_{10}+\mathbf{H}_{1I}.$$

Now transform to the renormalized interaction representation[8] (R.I.R.) by the transformation

$$U_1=\exp[i\mathbf{H}_{10}(t-t')]$$

[3] S. N. Gupta, Proc. Phys. Soc. (London) **A64**, 426 (1951).
[4] G. Takeda, Progr. Theoret. Phys. Japan **7**, 359 (1952).
[5] F. J. Dyson, Phys. Rev. **83**, 608 (1951).
[6] We denote by $\psi^*(\Psi^*)$ the quantity which appears elsewhere in the literature as Ψ. $\psi^*=\psi\dagger\gamma_4$. [See J. Schwinger, Phys. Rev. **74**, 1439 (1948)].
[6a] Reference 1, Secs. I–VI; Abdus Salam, Phys. Rev. **82**, 217 (1951), Secs. II and III; and Phys. Rev. **84**, 426 (1951).
[7] We use Dyson's notation, except that factors 2π (or $2\pi i$) have been absorbed in A, B, and C.
[8] Some care is required in deriving the Hamiltonian and the commutation relations in the renormalized interaction representation (R.I.R.). Firstly, all velocities $d\boldsymbol{\phi}/dt$ must be eliminated from the Hamiltonian, which must be expressed in terms of the field variables and their canonical momenta, $\boldsymbol{\phi}_1$ and $\boldsymbol{\pi}_1$, say, where

$$\boldsymbol{\pi}_1=\frac{\partial L_1(\boldsymbol{\phi}_1)}{\partial(d\boldsymbol{\phi}_1/dt)}.$$

After transforming to the R.I.R. the interaction Hamiltonian is the same function of the new canonical variables $H_{1I}(\phi_1,\pi_1)$, where

$$\phi_1=U_1^{-1}\boldsymbol{\phi}_{1s}U_1,$$

$$\pi_1=U_1^{-1}\boldsymbol{\pi}_{1s}U_1,$$

where the suffix s denotes the Schrödinger representation. This shows that π_1 and ϕ_1 satisfy the equations of motion determined by H_{10}. Therefore π_1 is determined by the free Lagrangian only,

on the Schrödinger representation. The resulting equation of motion for the state vector is

$$i\frac{\partial}{\partial t}\Psi\rangle=\int H_{1I}(\psi_1^*,\psi_1,A_1,e_1)d^3x\Psi\rangle, \tag{1.12}$$

where H_{1I} is essentially equal to $-L_{1I}$ apart from 'surface-dependent' terms which can safely be neglected since they cancel exactly with similar terms from the P brackets in the S matrix.[9]

The new field variables ψ_1^*, ψ_1, and A_1 are operators which annihilate and create a new type of bare particles which have not only the observed mass but also the observed charge. They will be referred to as renormalized bare particles. We now show that the new Hamiltonian contains just the right counter terms to cancel all divergences, provided $\delta\kappa$ is chosen so that

$$Z_2\delta\kappa=A(e_1), \tag{1.13}$$

and that it leads directly to the finite results of the subtraction procedure.

It should be noted, firstly, that in this formulation no difficulty arises from self-energy insertions in external lines. If one works with ordinary bare particles in the interaction representation (I.R.) based on (1.3) these give rise to terms of the form [reference 1, Eq. (37)].

$$\begin{aligned}\psi'(p)&=\psi(p)+S_F(p)\Sigma(p)\psi'(p)\\&=\psi(p)+S_F(p)B(e_1)S_F^{-1}(p)\psi(p),\end{aligned} \tag{1.14}$$

where, to obtain the second equality, the linear divergence of $\Sigma^*(p)$ has to be canceled by $\delta\kappa$ and the rest vanishes because it operates on an external particle. The remaining term is ambiguous because

$$S_F(p)\times[S_F^{-1}(p)\psi(p)]=0, \tag{1.15}$$

but

$$[S_F(p)S_F^{-1}(p)]\times\psi(p)=\psi(p). \tag{1.16}$$

The ambiguity is only removed if an adiabatic switching on and off of the charge is introduced to make (1.14) determinate.[10] However, working in the R.I.R. The counter terms are defined so that *all* the radiative corrections to an external line vanish identically. The analog of (1.14) is unambiguously

$$\psi_1'(p)=\psi_1(p). \tag{1.17}$$

No adiabatic switching is required. The renormalized bare particles entering or leaving a scattering process can be identified with true free particles. All graphs containing insertions in external lines can be ignored.

Now consider the separation of internal divergences. When no overlaps occur, all graphs can be built up unambiguously by insertions of vertex and self-energy parts into all the vertices and lines of irreducible graphs. Whenever vertex parts or proper self-energy parts are inserted, one may also insert the appropriate new counter term of H_{1I} which, using (1.13) automatically cancels the infinities and carries out correctly Dyson's[1] subtraction procedure.

When overlaps occur, one must use Salam's prescription.[6] This is equivalent to Dyson's when no overlaps occur. Since this case has already been dealt with, Salam's prescription need only be applied explicitly to graphs involving overlaps, that is to say, in electrodynamics graphs.

Consider any self-energy graph—to be referred to as "the original" graph—of any degree of complexity, but built up of vertices at which only the main interaction term, $ieA_\mu\psi^*\gamma_\mu\psi$, is operating. If there exists a subpart of this graph, which is divergent, Salam's prescription is that one must subtract the infinite part (true divergence) of this subgraph, multiplied by the rest of the graph (reduced integral) obtained by shrinking to a single vertex the divergent subpart in the original graph (to be referred to as the "shrunk" vertex). If the graph has m nonoverlapping divergent subparts, with true divergences $D_1,\cdots,D_m$, then the true divergence of all the subparts together is defined to be $(-1)^mD_1D_2\cdots D_m$, and the reduced integral is the graph obtained by shrinking each of the m divergent subparts to a single vertex. A subtraction must be made for all possible ways of splitting the graph into divergent subparts and a reduced integral, including the case in which the subpart is the whole original graph. Finally, all self-energy graphs and their subtractions (up to some given order in the charge) must be summed.

Consider a particular way of splitting the original graph into a divergent subpart and a reduced integral. When the summation over all graphs is made, there occur a set of graphs all of which have the same reduced integral and the same type of subpart (vertex or self-energy), but in the set this part appears in all possible forms. Adding together the subtractions which must be made for this particular splitting of this set of graphs, one gets the reduced integral multiplied by the sum of all the true divergences (again up to the same given order in the charge) of all possible forms of the divergent subpart. But this is exactly the term which will arise from the Hamiltonian H_{1I} of (1.12) if the appropriate counter term is operating at the "shrunk" vertex of this set of graphs. This argument is readily extended to the case when the splitting of the original graph involves two or more nonoverlapping subparts, and leads to a subtraction term with two or more "shrunk" vertices at which the appropriate counter terms of H_{1I} are operating. Summing over all possible graphs given by H_{1I}, one sees that also when overlaps occur the sub-

---

namely

$$\pi_1=\frac{\partial L_{10}(\phi_1)}{\partial\dot{\phi}_1}.$$

Hence, ψ_1^*, ψ_1, and A_1 satisfy the ordinary free field commutation relations (with no Z factor), and are correctly normalized to annihilate and create particles. The last equation can be used to express H_{1I} in terms of velocities in the R.I.R., to give (1.12).

[9] P. T. Matthews, Phys. Rev. **76**, 684 (1949).

[10] F. J. Dyson, Phys. Rev. **83**, 608 (1951), Sec. X. See particularly the remark following Eq. (178).

traction procedure is automatically carried out by the Hamiltonian H.

The "subtraction procedure" is thus not a mutilation of the original theory by the arbitrary dropping of infinite terms, but a simple reinterpretation brought about by a change of normalization—(infinite) change of scale—of the charge and field variables. This is its justification, and any 'subtractions' which can be interpreted in this way will be referred to as renormalizations.

II. THE BOUND INTERACTION REPRESENTATION

For many problems it is convenient to split the electromagnetic field into the radiation field and an external part, due to external sources, which is assumed to be given classical function. For this purpose we replace A above by $A^{ex}+A$, where A now means the quantized radiation field. Following through exactly the same argument as before one obtains

$$\mathbf{L}_{10}=\mathbf{L}_0(\psi_1^*,\psi_1,\mathbf{A}_1{}^{ex}+\mathbf{A}_1) \tag{2.1}$$

and additional terms in the 'interaction.'

$$\mathbf{L}_{1I}{}^{ex}=-ie_1[1-B(e_1)]A_{1\mu}{}^{ex}\psi_1^*\gamma_\mu\psi_1 -\tfrac{1}{4}C(e_1)[2F_{1\mu\nu}{}^{ex}\mathbf{F}_{1\mu\nu}+F_{1\mu\nu}{}^{ex}F_{1\mu\nu}{}^{ex}]. \tag{2.2}$$

These will be referred to as the external interaction term plus three external counter terms. If the external field is weak, so that an expansion in terms of it is suitable, the renormalization argument goes through just as before. The three external counter terms being just those required to cancel the infinities, which involve the external interaction term. The last one makes finite the vacuum-to-vacuum expectation value of the S matrix which appears as an essential factor in the matrix element of any process if the external field can create pairs.[11]

Of more interest is the case of a strong external field, the outstanding example of which is of course the theory of the Lamb shift in which the electron under consideration is bound in the potential of the nucleus. For these problems we include the external interaction term in H_{10}, and put only the external counter terms in H_{1I}. With this splitting of the Hamiltonian one can pass to the renormalized bound interaction representation (R.B.I.R.). This is similar to that introduced by Furry[12] in that the electron field operators annihilate and create electrons in bound states and the electron propagator $S_F{}^{ex}$ is now the Feynman sum over bound states. It differs from Furry's bound interaction representation in that it contains counter terms with constants defined by the free I.R. Now any divergent graph (self-energy or vertex parts) in the R.B.I.R. will involve $S_F{}^{ex}(p)$ at least once. This can be replaced by the *exact* expression,

$$S_F{}^{ex}(p)=S_F(p)+S_F(p)\gamma A^{ex}(p)S_F(p) +S_F(p)\gamma A^{ex}S_F{}^{ex}(p)\gamma A^{ex}S_F(p). \tag{2.3}$$

In this way any divergent expression involving $S_F{}^{ex}$ may be expressed as a divergent expression involving S_F plus a finite expression involving $S_F{}^{ex}$ [the terms in $S_F{}^{ex}$ are finite since at least two extra external lines have been introduced, corresponding to the two factors A^{ex} in the last term of (2.3)]. But since the first two terms in the right-hand side of (2.3) are the beginning of the expansion of $S_F{}^{ex}$ in terms of the external field, the internal lines of all the divergent parts obtained in this way, are identical with those obtained in the renormalized free interaction representation. Since the infinities were canceled there by the counter terms, they will be canceled here too by the same counter terms to any order in the charge. Thus the R.B.I.R. gives directly finite results for any cross section or energy shift. This is the theoretical basis of the subtraction procedure adopted by Baranger[13] and by Kroll and Pollock.[14]

III. WARD'S IDENTITY

It has been shown above that a theory with divergences of the type which appear in electrodynamics can be renormalized even if no relation exists between the 'true divergences' of self-energy and vertex parts. However, the infinite constants have in fact been defined in such a way that the finite S-matrix elements given by the subtraction procedure are gauge invariant. This implies that if these finite elements can be derived from a new Lagrangian, this new Lagrangian must also be gauge invariant. Therefore the terms involving ψ_1 and either A_1 or ∇ in L_1 must combine to give an expression involving only

$$\nabla+ie_1A_1. \tag{3.1}$$

Since the original Lagrangian was gauge invariant, this is equivalent to the condition

$$e_1A_1=eA. \tag{3.2}$$

It follows that

$$Z_1=Z_2 \tag{3.3}$$

and hence that

$$L(e_1)=-B(e_1). \tag{3.4}$$

This is Ward's identity.[15] The above derivation brings out very clearly its direct dependence on the gauge invarance of the theory. This argument is due to Takeda.[4]

IV. MESON INTERACTIONS

It is clear that exactly the same argument can be applied to any renormalizable meson-nucleon interaction. Consider, for example, the pseudoscalar inter-

[11] R. P. Feynman, Phys. Rev. 76, 749 (1949). Abdus Salam, and P. T. Matthews, Phys. Rev. 90, 690 (1953).
[12] W. H. Furry, Phys. Rev. 81, 115 (1951).
[13] M. Baranger, Phys. Rev. 84, 866 (1951).
[14] N. M. Kroll and F. Pollock, Phys. Rev. 86, 876 (1952).
[15] J. C. Ward, Phys. Rev. 78, 182 (1950).

action of pseudoscalar mesons. All that is required is to replace the free photon terms in the Lagrangian by

$$\mathbf{L}_m=-\tfrac{1}{2}[(\nabla\phi)^2+\mu^2\phi^2], \tag{4.1}$$

and

$$\mathbf{L}_I=-ig\phi\psi^*\gamma_5\psi+\tfrac{1}{2}\delta\mu^2\phi^2+\delta\lambda\phi^4+\delta\kappa\psi^*\psi, \tag{4.2}$$

where the masses are already renormalized and the necessary contact interaction $\delta\lambda\phi^4$ has been introduced. Changing to renormalized variables as in the previous section, produces a Lagrangian which leads directly to the finite theory.

An even greater simplification is brought about by this approach in the interaction of spin-zero mesons with the electromagnetic field, where the overlapping of divergences can be very complicated. Here L consists of the free meson and photon terms, and

$$\mathbf{L}_I=ie'\mathbf{A}_\mu(\phi\nabla_\mu\phi^*-\nabla_\mu\phi\cdot\phi^*)-e^2\mathbf{A}^2\phi\phi^*+\delta\mu^2\phi\phi^*+\delta\lambda\phi^{*2}\phi^2. \tag{4.3}$$

e is supposed equal to e' (so that L is gauge invariant) but we distinguish, for the moment, between charges in the linear and bilinear terms. The S matrix based on this interaction is infinite, but can be made finite by subtractions which are defined in terms of infinite constants L, B, C, R given by Salam.[16] The next step is to define renormalized field variables, which introduce the required counter terms into the theory. It is not hard to see that we must take

$$\phi=Z_2^{\frac{1}{2}}\phi_1 \quad \mathbf{A}=Z_3^{\frac{1}{2}}\mathbf{A}_1 \tag{4.4}$$

where

$$\begin{aligned} Z_2&=1+B(e_1),\\ Z_3&=1+C(e_1). \end{aligned} \tag{4.5}$$

This gives the required self-energy counter terms. To cancel these in the main interaction terms and introduce the required factors in L and R, we must define

$$\begin{aligned} e'&=Z_3^{-\frac{1}{2}}Z_1Z_2^{-1}e_1,\\ e^2&=Z_3^{-1}Z_2^{-1}Z_4e_1^2, \end{aligned} \tag{4.6}$$

where

$$Z_1=1-L(e_1), \quad Z_4=1-R(e_1). \tag{4.7}$$

Then

$$\begin{aligned} L_{1I}=ie_1&[1-L(e_1)]A_{1\mu}(\phi_1\nabla_\mu\phi_1^*-\nabla_\mu\phi_1\cdot\phi_1^*)\\ &-e_1^2[1-R(e_1)]A_1^2\phi_1\phi_1^*+\delta\mu^2Z_2\phi_1\phi_1^*\\ &+\delta\lambda Z_1^2\phi_1^{*2}\phi_1^2-\tfrac{1}{4}C(e_1)F_{1\mu\nu}F_{1\mu\nu}\\ &-B(e_1)(\nabla_\mu\phi_1\nabla_\mu\phi_1^*+\mu^2\phi_1\phi_1^*). \end{aligned} \tag{4.8}$$

The subtractions defined by Salam,[6] whether overlapping divergences are involved or not, take place automatically when the S matrix is based on this Lagrangian, which thus provides the theoretical basis of the finite theory.

By this approach we have avoided all the complicated argument required when the Z factors are introduced and justified by the method of Salam[16] (following Dyson), or the ingenious, but far from perspicuous manipulations involved in the proof due to Ward.[17] Also, as above, no ambiguity arises from external lines.

Further, by the argument given in Sec. III, the renormalized Lagrangian is gauge invariant. Therefore

$$eA=e'A=e_1A_1. \tag{4.9}$$

Hence

$$Z_1=Z_2=Z_4. \tag{4.10}$$

It is clear that these considerations can be extended immediately to the combined interaction of three fields.

This completes our main purpose of providing, in a simple way, a theoretical justification for the infinite subtractions which occur in the renormalization of a divergent S matrix.

V. ALTERNATIVE FORMULATIONS

We have shown that the Lagrangian (1.9) leads to an S matrix in electrodynamics which is finite, term by term, in the charge expansion. The result of course does not depend on the particular split between the "free" and interaction parts. We may, alternatively, write exactly the same Lagrangian in the form

$$\mathbf{L}=\mathbf{L}\dagger=\mathbf{L}_0\dagger+\mathbf{L}_I\dagger, \tag{5.1}$$

where

$$\mathbf{L}_0\dagger=-\tfrac{1}{4}Z_3\mathbf{F}_{1\mu\nu}\mathbf{F}_{1\mu\nu}-\tfrac{1}{2}Z_3(\nabla_\mu\mathbf{A}_{1\mu})^2-Z_2\psi^*(\gamma_\mu\nabla_\mu+\kappa)\psi, \tag{5.2}$$

$$\mathbf{L}_I\dagger=-ie_1Z_1\mathbf{A}_{1\mu}\psi_1^*\gamma_\mu\psi_1+Z_2\delta\kappa\psi_1^*\psi_1, \tag{5.3}$$

and define a new interaction representation[18] in terms of $L_0\dagger$ in which the variables are denoted by $\dagger$. In this representation the complete electron and photon propagators are infinite, that is S_{F1}', not S_F', is generated by making all possible self-energy insertions in a simple line. However, the simple propagator contains infinities coming from the Z factors in $L_0\dagger$. Thus $S_F\dagger(x)=Z_2^{-1}S_F(x)$, $D_F\dagger(x)=Z_3^{-1}D_F(x)$. Again the Z factors in $L_0\dagger$ gives rise to Z factors in the commutation relations of $\psi_1^*\dagger$, $\psi_1\dagger$, and $A_1\dagger$ so they are not correctly normalized for annihilators and creators of bare particles. To avoid this and to get graphs with simple propagators S_F rather than $S_F\dagger$ we express the interaction in terms of $Z_3^{\frac{1}{2}}A_1\dagger$, $Z_2^{\frac{1}{2}}\psi_1^*\dagger$ and $Z_2^{\frac{1}{2}}\psi_1\dagger$. Or equivalently we continue to work with unrenormalized field variables and introduce only the charge renormalization (1.7). This gives the original Lagrangian (1.1) but with the interaction expressed in terms of the renormalized charge

$$L_I=-ie_1Z_3^{-\frac{1}{2}}Z_1Z_2^{-1}A_\mu\psi^*\gamma_\mu\psi+\delta\kappa\psi^*\psi, \tag{5.4}$$

which again must lead to a finite S matrix when expressed as a power series in e_1. This is the formulation

[16] Abdus Salam, Phys. Rev. **86**, 731 (1952).

[17] J. C. Ward, Phys. Rev. **84**, 897 (1951).

[18] S. Kamefuchi and H. Umezawa, Progr. Theoret. Phys. Japan **7**, 399 (1952).

given by Dyson,[1] but established quite differently by him.

VI. DYSON'S RELATIONS

For completeness we now derive from our definitions, the relations by which the Z factors were defined by Dyson.[1]

By definition

$$-\tfrac{1}{2}S_F(y-y^1)=\langle T(\psi(y),\psi^*(y^1))\rangle_0, \tag{6.1}$$

where T is the chronological product as defined by Wick.[19] It follows immediately from the graphical definition of S_F', as the electron propagator modified by all possible self-energy insertions, that

$$-\tfrac{1}{2}S_F'(y-y^1)=\langle T(S,\psi(y),\psi^*(y^1))\rangle_0/\langle S\rangle_0, \tag{6.2}$$

where $\langle\cdots\rangle_0$ is the bare vacuum expectation value and

$$T(S,\psi(y),\psi^*(y^1))=\sum_n\frac{(-i)^n}{n!}\int\cdots\int dz_1\cdots dz_n T(H(z_1)\cdots \times H(z_n),\psi(y),\psi^*(y^1)). \tag{6.3}$$

By the argument given by Low and Gell-Mann[20] and using their definition of the true vacuum $\Psi_0\rangle$, it follows that

$$-\tfrac{1}{2}S_F'(y-y^1)=\langle\Psi_0 T(\psi(y),\psi^*(y^1))\Psi_0\rangle. \tag{6.4}$$

By an exactly similar argument, only replacing all operators by the corresponding renormalized operators, the finite propagator is

$$-\tfrac{1}{2}S_{F1}'(y-y^1)=\langle\Psi_0 T(\psi_1(y),\psi_1^*(y^1))\Psi_0\rangle. \tag{6.5}$$

Using the definitions of ψ_1 and ψ_1^*, it follows that

$$S_F'(e)=Z_2S_{F1}'(e_1). \tag{6.6}$$

Similarly,

$$D_F'(e)=Z_1D_{F1}'(e_1). \tag{6.7}$$

Let $\Lambda_1(e_1)$ be the sum over all vertex parts obtained from H_{1I} in the R.I.R. Consider any vertex part which does not contain any self-energy part. The effect of all self-energy insertions, including their counter terms, is given by writing $S_{F1}'(e_1)$ and $D_{F1}'(e_1)$ for the lines. The vertex counter term is included by multiplying by $1-L(e_1)(=Z_1)$ at each vertex. If the part has $2n+1$ vertices, there are $2n$ electron lines and n photon lines. Using relations (1.7), (6.6), and (6.7), and summing over all such vertex parts, gives

$$Z_1^{-1}\Lambda_1(e_1)=\Lambda(e), \tag{6.8}$$

where $\Lambda(e)$ is the sum over all vertex parts given by H_I in the I.R. Now

$$\begin{aligned}\Gamma(e)&=\gamma+\Lambda(e)\\&=Z_1^{-1}[Z_1\gamma+\Lambda_1(e_1)]\\&=Z_1^{-1}\Gamma_1(e_1).\end{aligned} \tag{6.9}$$

(6.7), (6.8), and (6.9) are the relations which Dyson[1] uses to *define* the Z factors. It should be noted that they are not required for the general proof of renormalization as presented here.

VII. THE BETHE-SALPETER EQUATION

The derivation of the Bethe-Salpeter[21] equation for pseudoscalar coupling given by Low and Gell-Mann[20] can be repeated step by step using renormalized quantities throughout, to derive the renormalized equation, which contains no infinities.

Alternatively, one can start from the unrenormalized form, which can be written symbolically as[22]

$$K=S_F'S_F'-\int S_F'S_F'GK. \tag{7.1}$$

Define the renormalized two-particle propagator

$$K_1(x_1,x_2,x_3,x_4)=\langle\Psi_0 T(\psi_1(x_1),\psi_1(x_2),\psi_1^*(x_3),\psi_1^*(x_4))\Psi_0\rangle. \tag{7.2}$$

Then, immediately from the definitions of ψ_1, etc.,

$$K=Z_2^2K_1. \tag{7.3}$$

The interaction function G can be derived from the sum of all irreducible graphs with just four external nucleon lines, by replacing the lines and vertices by S_F', Δ_F' and Γ_4. A graph with $2n$ vertices has n meson lines and $2n-2$ nucleon lines. Therefore, by (6.7), (6.8), and (6.9),

$$G(e)=Z_2^{-2}G_1(e_1). \tag{7.4}$$

Substituting into (7.1), all the Z factors cancel and

$$K_1=S_{F1}'S_{F1}'-\int S_F'S_F'G_1K_1,$$

which is the finite equation for the renormalized propagator. Similarly, the renormalized "wave function" is

$$\begin{aligned}\chi_{n1}(x_1,x_2)&=\langle\Psi_0 T(\psi_1(x_1),\psi_1^*(x_2))\Psi_n\rangle\\&=Z_2^{-1}\chi_n(x_1,x_2),\end{aligned}$$

and again, on substitution into the B-S equation,[23] all Z factors cancel, leaving the renormalized equation:

$$\chi_1=-\int S_F'S_F'G_1\chi_1.$$

It is important for this argument that no divergences are produced by the iteration of the equation for K.

VIII. CLOSED FORM OF THE THEORY

In this final section the infinite constants introduced in (1.6)–(1.8) are expressed in terms of renormalized field variables.

[19] G. C. Wick, Phys. Rev. **80**, 268 (1950).
[20] M. Gell-Mann and F. E. Low, Phys. Rev. **84**, 350 (1951).
[21] H. A. Bethe and E. E. Salpeter, Phys. Rev. **84**, 1232 (1951).
[22] Reference 20, Eq. (23).
[23] Reference 20, Eq. (37).

Returning to S_F', we have the general relation:

$$S_F'(y-y^1)=S_F(y-y^1)+\int\int dzdz^1 S_F(y-z)\Sigma(z-z^1)S_F(z^1-y^1). \quad (8.1)$$

Compare this with (6.1) and (6.2). The first term on the right-hand side of (8.1) is given by putting $n=0$. The second term is got by combining $\psi(y)$ with any $\psi^*(z)$ and $\psi^*(y^1)$ with any $\psi(z^1)$ $(z^1\neq z)$ in the T bracket, which can be done in $n(n-1)$ ways in the nth term. There are additional nonvanishing terms in which $\psi(y)$ and $\psi^*(y^1)$ are combined with the $\psi^*(z)$ and $\psi(z)$ of a single $\delta\kappa$ term, which may be done in n ways in the nth term. One thus obtains an expression for $\Sigma(z-z^1)$, namely

$$\Sigma(z-z^1)=\langle T(S,f(z),f^*(z^1))\rangle_0/\langle S\rangle_0-\tfrac{1}{2}i\delta\kappa\delta(z-z^1) \quad (8.2)$$

$$=\tfrac{1}{2}[\langle\Psi_0 T(\mathbf{f}(z),\mathbf{f}^*(z^1))\Psi_0\rangle-i\delta\kappa\delta(z-z^1)], \quad (8.3)$$

where

$$\mathbf{f}=ig\boldsymbol{\phi}\gamma_5\boldsymbol{\psi}-\delta\kappa\boldsymbol{\psi},$$
$$\mathbf{f}^*=ig\boldsymbol{\phi}\boldsymbol{\psi}^*\gamma_5-\delta\kappa\boldsymbol{\psi}^*, \quad (8.4)$$

which, for pseudoscalar interaction, is the analog of the current in the equations of motion for $\boldsymbol{\psi}$ and $\boldsymbol{\psi}^*$, respectively. To obtain (7.3) we have again used the argument of Low and Gell-Mann.[20]

Alternatively, working with renormalized variables

$$\Sigma_1(z-z^1)=\tfrac{1}{2}[F_1(z-z^1)+iZ_2\delta\kappa-B(e_1)(\gamma_\mu\nabla_\mu+\kappa))\delta(z-z^1)], \quad (8.5)$$

where

$$F_1(z-z^1)=\langle\Psi_0 T(\mathbf{f}_1(z),\mathbf{f}_1^*(z^1))\Psi_0\rangle, \quad (8.6)$$

and

$$\mathbf{f}_1=igZ_1\boldsymbol{\phi}_1\gamma_5\boldsymbol{\psi}_1+B(e_1)(\gamma_\mu\nabla_\mu+\kappa)\boldsymbol{\psi}_1-Z_2\delta\kappa\boldsymbol{\psi}_1. \quad (8.7)$$

Expressing (8.5) in momentum space,

$$\Sigma_1(p)=\tfrac{1}{2}[F_1(p)+iZ_2\delta\kappa+B(e_1)(p-i\kappa)] \quad (8.8)$$

where

$$p=p_\mu\gamma_\mu. \quad (8.9)$$

But the infinite constants B and $\delta\kappa$ have been defined so that

$$\Sigma_1(i\kappa)=0, \quad (8.10)$$

and

$$[\partial\Sigma_1/\partial p]_{i\kappa}=0. \quad (8.11)$$

Therefore

$$Z_2\delta\kappa=-iF_1(i\kappa), \quad (8.12)$$

and

$$B(e_1)=-[\partial F_1/\partial p]_{i\kappa}. \quad (8.13)$$

Similar expressions can be obtained for $Z_3\delta\mu^2$ and $C(e_1)$ by considering Δ_{F1}'.

Again, from a consideration of the graphs, it can be seen that the finite part of all vertex parts is

$$\Lambda_1(x,y,z)=\langle T(S_1,f_1^1(x)f_1^{*1}(y),\times j_1^1(z))\rangle_0/\langle S_1\rangle_0-\gamma L \quad (8.14)$$

where

$$f_1^1=ig_1Z_1\boldsymbol{\phi}_1\gamma_5\boldsymbol{\psi}_1, \quad (8.15)$$

$$j_1^1=Z_1\boldsymbol{\psi}_1^*\gamma_5\boldsymbol{\psi}_1. \quad (8.16)$$

Thus, adding the term from the single vertex,

$$\Gamma_1(x,y,z)=G_1(x,y,z)+\gamma_5(1-L), \quad (8.17)$$

where

$$G_1(x,y,z)=\langle\Psi_0 T(\mathbf{f}_1^1(x),\mathbf{f}_1^{*1}(y),\mathbf{j}_1^1(z))\Psi_0\rangle.$$

In momentum space,

$$\Gamma_1(p,p^1)=G(p,p^1)+\gamma_5(1-L). \quad (8.18)$$

Also, since

$$\Gamma_1(i\kappa,i\kappa)=\gamma_5, \quad (8.19)$$

$$\gamma_5 L=G_1(i\kappa,i\kappa). \quad (8.20)$$

Relations similar to (8.12) and (8.13) were first obtained by Kallen.[24] With the use of these expressions it is possible to state the renormalized theory, without mention of power series expansions. Thus the Lagrangian is (1.9)–(1.11). The infinite constants appearing in the Lagrangian are defined by the implicit relations (8.12), (8.13), (8.20), etc.

We do not wish to suggest that this is necessarily a finite theory independent of charge expansion. Dyson's analysis[25] of the divergences into primitive divergents depends essentially on the charge expansion. If this expansion is not absolutely convergent, there is no reason to suppose that the S-matrix elements, obtained by some method other than a charge expansion, would have divergences restricted in the same way and removable by the same renormalizations.[26]

One of us (A. S.) would like to thank Prof. R. E. Peierls for the hospitality of Birmingham University extended to him during the summer of 1953. We also acknowledge helpful conversations with Dr. J. G. Valatin.

[24] G. Kallen, Helv. Phys. Acta **25**, 417 (1952). If Σ_1 is defined by the relation,

$$\langle\Psi_0 T(\boldsymbol{\psi},\boldsymbol{\psi}^*)\Psi_0\rangle=-\tfrac{1}{2}(S_F+S_F\Sigma_1 S_F),$$

and the infinite constants B and $\delta\kappa$ are defined by (8.10) and (8.11), then Eqs. (8.12) and (8.13) can be derived without the use of power series by methods employed by P. T. Matthews and Abdus Salam, Proc. Roy. Soc. (London) **A221**, 128, Sec. III.

[25] Reference 1, Sec. V.

[26] See, for example, G. Feldman, Proc. Roy. Soc. (London) (to be published).

Quantized Space-Time

EMIL J. HELLUND AND KATSUMI TANAKA
Argonne National Laboratory, Lemont, Illinois

(Received August 21, 1953; revised manuscript received January 6, 1954)

The operators and commutators of the space-time coordinates and momenta in quantized space-time are formulated. Then the eigenfunctions and eigenvalues of the space-time operators are found. Finally, the time spectrum of the plane-wave solution of the Dirac equation is determined and a convergent perturbation analysis is proposed.

1. INTRODUCTION

SEVERAL attempts have been made to remove divergence difficulties in quantum theory of wave fields by introducing the fundamental radius of elementary particles. Some have predicated continuous and others discrete space-time. It seems plausible that a theory of elementary particles based on a universal constant of the dimensions of length will be free of divergence difficulties, removing one of the most important obstacles to the progress of field theories.

Some have considered the fundamental radius of an elementary particle as a small region in which a point particle is confined, violently in motion. This does not appear attractive, although it may be easier to treat mathematically. We consider the fundamental radius as a real extension of a physical body, itself limiting the the fineness of measurement in discrete space. The fundamental length is expected to play a fundamental role in eliminating divergence difficulties. The situation is very similar to the difficulty appearing in the law of blackbody radiation, which was eliminated by the introduction of the universal constant $\hbar$ into radiation theory.

One is tempted to assume that the development of this concept requires the use of finite-difference equations. Since there exists a Lorentz-invariant space-time in which there is a natural unit of length,[1] it is possible to formulate a theory which describes a particle of finite size, is consistent with relativity, easier to treat mathematically than difference calculus, and also interpretable physically in quantized space. It can be shown that unless quantized space is accepted, one can localize a particle in any infinitesimal region contradicting the concept of a real radius of elementary particles.[2] Now the question arises whether the discreteness of space necessitates the simultaneous discreteness of time. Heisenberg[3] considered discrete space-time and the concept of infinitely small volume in space-time and investigated this supposition. We, however, adopt continuous time for reasons of mathematical simplicity as long as it has not been rigorously proved that the other alternative is more suitable physically.

We begin with a configurational c space which is used to express operators in a q space. q space denotes a space in which the coordinates do not commute among themselves and c space denotes a space with commuting coordinates. The noncommutativity of operators representing configuration space means that simultaneous measurements of space and time are interfering operations. The momentum operators can be taken to commute among themselves, since they may be continuous as the time operator is continuous and thus unchanged. This is consistent with the concept that any arbitrarily small volume is meaningless as there exists an inherent volume of space-time because of the noncommutativity of space and time.

In this paper, the operators and commutators of x_μ, p_μ, M_μ are formulated and the eigenfunctions of the observable space and time coordinates are obtained. It is shown that the plane-wave solutions of the Dirac equation for free particles do not represent states localized on a given space-like surface.

2. FORMULATION OF OPERATORS, COMMUTATORS

The noncommutativity of the space-time operators requires that the coordinate operators be nondiagonal in c space in such a manner that at the limiting case when the fundamental length is put to zero, they become diagonal. Further, the coordinates must be covariant under Lorentz transformation, Hermitian, and mathematically as simple as the physical content permits. The preceding conditions on the new form of the coordinate operators imply that a quadratic Lorentz invariant term with a coefficient proportional to some power of the fundamental length can be added to the ordinary coordinate operator.[4] A simple transformation could be written for free particles, as follows:

$$x_\mu' = x_\mu - l^2 \frac{\partial}{\partial x_\mu} x_\nu \frac{\partial}{\partial x_\nu}; \quad \mu,\nu = 1,2,3,4; \quad x = (x,y,z,ict), \tag{1}$$

where primes always denote the observable q space and unprimed quantities the c space. With the above formulation, one could take momentum and energy to remain covariant under such a transformation.

$$p_\mu' = p_\mu = \frac{\hbar}{i} \frac{\partial}{\partial x_\mu}; \quad p = (p_x,p_y,p_z,iE/c). \tag{2}$$

[1] H. S. Snyder, Phys. Rev. 71, 38 (1947); 72, 68 (1947).
[2] V. F. Weisskopf, Naturwiss. 23, 669 (1935).
[3] W. Heisenberg, Z. Physik 110, 251 (1938).

[4] Or one could take $x_\mu' = x_\mu - l^2(\partial/\partial x_\mu)(\gamma_\nu \partial/\partial x_\nu)$, where γ_ν are the components of the 4-vector introduced by Dirac.

Real part of operator is taken as defined only for that Hilbert space in which it is real.

In classical mechanics, the definition of angular momentum is $\mathbf{M}=\mathbf{r}\times\mathbf{p}$; so, in our new quantum mechanics, we take

$$\begin{aligned} M_x' &= x'p_z' - z'p_y', \\ M_y' &= z'p_x' - x'p_z', \\ M_z' &= x'p_y' - y'p_x'. \end{aligned} \tag{3}$$

Substituting (1) and (2) into (3), we obtain

$$x_\mu p_\nu - x_\nu p_\mu = x_\mu' p_\nu' - x_\nu' p_\mu'. \tag{4}$$

Note that all previous definitions of x' in terms of x have been considered only with respect to a fixed origin. Translation of the origin may be introduced by changing the definition of x' in terms of x to

$$x_\mu'(x_1,x_2) = (x_{\mu 1}-x_{\mu 2}) - l^2 F\left\{\frac{\partial}{\partial(x_{\mu 1}-x_{\mu 2})} \times (x_{\nu 1}-x_{\nu 2})\frac{\partial}{\partial(x_{\nu 1}-x_{\nu 2})}\right\}, \tag{5}$$

where $x_\mu'(x_1,x_2)$ denotes an observable interval and R denotes real or self-adjoint part. This means that the observable geometry is not a function of the coordinate origin, or that a change of origin in the unprimed space does not affect the observable interval. One does not have an affine space for $l\neq 0$.

The commutators for the coordinate operator are as follows:

$$[x_\mu', x_\nu'] = l^2\left\{x_\mu\frac{\partial}{\partial x_\nu} - x_\nu\frac{\partial}{\partial x_\mu}\right\}, \tag{6a}$$

or

$$\begin{aligned} [x',y'] &= i(l^2/\hbar)M_z, \\ [y',z'] &= i(l^2/\hbar)M_x, \\ [z',x'] &= i(l^2/\hbar)M_y, \end{aligned} \tag{6b}$$

$$[t',x_i'] = l^2\left[t\frac{\partial}{\partial x_i} + \frac{x_i}{c^2}\frac{\partial}{\partial t}\right], \quad i=1,2,3.$$

The commutators for the coordinate and momentum operators are as follows:

$$\begin{aligned} [x_\mu', p_\nu'] &= i\hbar(\delta_{\mu\nu} - l^2\partial^2/\partial x_\mu \partial x_\nu) \\ &= i\hbar[\delta_{\mu\nu} + (l^2/\hbar^2)p_\mu p_\nu]. \end{aligned} \tag{7}$$

The commutator for a particular coordinate is

$$[x_\mu', p_\mu'] = i\hbar[1+(l^2/\hbar^2)p_\mu^2], \tag{8}$$

where it is understood that μ is not summed. It is obvious that the commutator is covariant and reduces to the conventional form when l is equal to zero.

Since two physical quantities A and B satisfy the following uncertainty relation

$$\Delta A \Delta B \geq |C|, \tag{9}$$

when

$$[A,B]=C,$$

one immediately finds from (8),

$$\Delta x_\mu' \Delta p_\mu' \geq \hbar[1+(l^2/\hbar^2)p_\mu^2]. \tag{10}$$

This shows that Heisenberg's uncertainty principle holds as a limiting case. Space-time symmetry and properties of angular momentum in (6b) yield directly, using (10),

$$\Delta x' \Delta t' \geq l^2/c. \tag{11}$$

3. EIGENFUNCTIONS AND EIGENVALUES

The eigenvalues and eigenfunctions of the coordinate x for no field in one dimension may be found by substituting

$$u = \frac{1}{\sqrt{2}}\left(\frac{x}{ct}+\frac{ct}{l}\right), \quad v = \frac{i}{\sqrt{2}}\left(\frac{x}{ct}-\frac{ct}{l}\right)$$

into (1), which gives for the eigenvalue equation

$$\left[-\left(\frac{\partial^2}{\partial u^2}+\frac{\partial^2}{\partial v^2}\right)+(u^2+v^2)\right]\psi = 2\frac{\lambda}{l}\psi = (\lambda_n+\lambda_m)\psi. \tag{12}$$

This is the eigenvalue equation for a two-dimensional harmonic oscillator whose eigenfunctions and eigenvalues are given as

$$\begin{aligned} \psi_{nm} &= N_{nm}H_n(u)H_m(v)\exp[-\tfrac{1}{2}(u^2+v^2)], \\ \lambda &= (n+m+1), \end{aligned}$$

where N_{nm} is a normalization factor. The spectrum is discrete.

Let us now obtain the eigenfunctions and eigenvalues of the x coordinate for no field and stationary states. Putting $\partial/\partial t=0$ in (1), we have for the eigenvalue equation

$$\left[x - l^2\frac{\partial}{\partial x}\left(x\frac{\partial}{\partial x}+y\frac{\partial}{\partial y}+z\frac{\partial}{\partial z}\right)\right]\psi = \lambda\psi. \tag{13}$$

Letting $x_\mu = l x_\mu'$, $\lambda = l\lambda'$, and dropping primes, we have

$$\left[x - \frac{\partial}{\partial x}\left(x\frac{\partial}{\partial x}+y\frac{\partial}{\partial y}+z\frac{\partial}{\partial z}\right)\right]\psi = \lambda\psi.$$

Substituting $\psi = y^p z^q e^{-x} F(x)$, then replacing $2x$ by ξ, we obtain

$$\xi\frac{d^2F(\xi)}{d\xi^2} + (p+q+1-\xi)\frac{dF(\xi)}{d\xi} + \tfrac{1}{2}(\lambda-p-q-1)F(\xi) = 0. \tag{14}$$

The solution of (14) is[5]

$$F(\xi)=\frac{d^{p+q}}{d\xi^{p+q}}\frac{L_n(\xi)}{n!}=\frac{L_n^{p+q}(\xi)}{n!},\quad p+q>-1,$$

where $L_n^{p+q}(\xi)$ is the generalized Laguerre polynomial and $\lambda=2n-p-q+1$. Hence, the solution of (13) is

$$\psi_n=\frac{1}{l^{p+q}}y^pz^qe^{-x/l}\frac{L_n^{p+q}}{n!}(2x/l),\quad 0\leqslant 2x/l\leqslant\infty,$$

$$\lambda=l(2n-p-q+1).$$

For the case $p=q=0$,[6] the normalized solution is

$$\psi_n=e^{-x/l}\frac{L_n}{n!}(2x/l),\quad 0\leqslant 2x/l\leqslant\infty,$$

$$=0 \text{ otherwise};$$

$$\psi_n=e^{x/l}\frac{L_n}{n!}(-2x/l),\quad -\infty\leqslant 2x/l\leqslant 0,$$

$$=0 \text{ otherwise};$$

so that finally the solution of (13) is

$$\psi_n=\frac{y^pz^q}{l^{p+q}}\frac{\exp(-|n|x/nl)}{|n+(n-|n|)/2n|!}L^{p+q}_{|n+(n-|n|)/2n|}(2|n|x/nl),$$

$$0\leqslant 2|n|x/nl\leqslant\infty,\quad n\neq 0,$$

$$\psi_0=\frac{y^pz^q}{l^{p+q}}\exp(-x/l)L_0^{p+q}(2x/l),$$

$$0\leqslant 2x/l\leqslant\infty,\quad n=0,$$

$$\lambda_n=(2n-p-q+1),\quad n=\cdots-3,-2,-1,0,1,2,3,\cdots.$$

The time operator according to (1) is

$$t'=t+\frac{l^2}{c^2}\frac{\partial}{\partial t}\left(x_r\frac{\partial}{\partial x_r}\right)\equiv t+\alpha.$$

The positive sign appears before l^2 because the fourth coordinate is *ict*. We are interested in eigenfunctions ψ_a defined by

$$\frac{l^2}{c^2}\frac{\partial}{\partial t}\left(x_r\frac{\partial}{\partial x_r}\right)\psi_a=\frac{l^2}{c^2}\frac{\partial}{\partial t}\left(t\frac{\partial}{\partial t}+r\frac{\partial}{\partial r}\right)\psi_a=a\psi_a,\quad (15)$$

where

$$r=(x^2+y^2+z^2)^{\frac{1}{2}}.$$

Solutions of (15) are found to be[7]

$$\psi_a=J_0\left\{\left[\frac{4c^2\hbar a}{l^2E}\left(\frac{pr}{\hbar}-\frac{Et}{\hbar}\right)\right]^{\frac{1}{2}}\right\}$$

$$=J_0\left\{\left[n\alpha\left(\frac{pr}{\hbar}-\frac{Et}{\hbar}\right)\right]^{\frac{1}{2}}\right\},\quad (16)$$

or

$$J_0\left\{\left[n\alpha\left(\frac{p_xx}{\hbar}-\frac{Et}{\hbar}\right)\right]^{\frac{1}{2}}\right\},$$

and similarly for other components. Note that pr is not a scalar product. Substituting (16) into (15), one finds eigenvalues α.

4. DIRAC EQUATION AND DISCUSSION

It is expected that the problem of particle-plus-field should yield a convergent perturbation analysis. In such a treatment, one prescribes an initial state in the neighborhood of some time, say $t=0$. It is, therefore, relevant to ask whether or not plane-wave solutions of the Dirac equation correspond to time-localized states. Expanding Dirac's solution in one dimension, in terms of ψ_a given by (16), one obtains

$$\psi_D=u\exp[i(px/\hbar-Et/\hbar)]$$

$$=\frac{4}{in}\int_0^\infty uJ_0\left\{\left[n\alpha\left(\frac{px}{\hbar}-\frac{Et}{\hbar}\right)\right]^{\frac{1}{2}}\right\}e^{-ian/4}d\alpha,$$

for $(px-Et)/\hbar>0$ and a negative spectrum for $(px-Et)/\hbar<0$, where u is the spinor part.

The modulus of ψ_a is constant, or the spectrum is flat. This means that the plane-wave solution of the Dirac equation for free particles does not represent states localized in the neighborhood of a given space-like region. The solution of the problem of a particle coupled to a field in which the particle is assumed to be in some definite state in the neighborhood of $t=0$ would be changed as follows:

One replaces $\psi_{\text{Dirac, free}}$ by $U\psi_{\text{Dirac, free}}$, where U is the unitary transformation matrix necessary to obtain time localizability. Under such a transformation the equation of motion,

$$V_{kj}C_j=i\hbar\partial C_k/\partial t,$$

is replaced by

$$\bar{V}_{kj}\bar{C}_j=i\hbar\partial\bar{C}_k/\partial t,\quad (17)$$

where $|C_k|^2$ denotes the probability of finding the system in the state ψ_k and $UVU^{-1}=\bar{V}$, $UC=\bar{C}$. It is now Eq. (17) which may have convergent expansions for $\bar{C}$ in powers of $\bar{V}$.[8]

Observation is made with respect to certain times in a system which has certain measurable variables. That is, we are observing certain properties at *definite times*. The

[5] E. Madelung, *Die Mathematischen Hilfsmittel Des Physikers* (Dover Publications, New York, 1943), p. 58.

[6] H. Bethe, *Handbuch der Physik* (Springer, Berlin, 1943), Vol. 24, No. 1, p. 337.

[7] Calculations involving Bessel functions used in this paper may be found in G. A. Campbell and R. M. Foster, *Fourier Integrals or Practical Applications* (American Telephone and Telegraph Company, 1942); G. N. Watson, *Theory of Bessel Function* (Macmillan Company, New York, 1944), second edition.

[8] N. Arley and V. Borchsenius, Acta Mat. **76**, 261 (1945); H. Salecker, Z. Naturforsch. **5a**, 431, 482 (1950).

states that we see are time-localizable states. The properties are those which we can say belong to quite definite times. The entirety of states which are allowable as solutions of the free Dirac equation span a certain Hilbert space. Then, of that whole space, only a certain part is allowable as representing time localizability. These are the only states that are *observable*. One can see that a portion of it must be excluded as not compatible with the concept of time localizability. It is for this reason that we have shown that the entire plane-wave solutions were not a proper basis for the calculation of certain properties, for instance, the rest mass. This may be further elucidated in the following way. Think of the Dirac plane wave solutions as representing a set of basis vectors in an infinite dimensional space; then only certain combinations of them form time-localizable solutions. This is to be pictured in this previously-mentioned infinite-dimensional space as representing a certain portion of that space formed from those combinations of the Dirac equation which satisfy the above-mentioned criterion of time localizability. The later portion of space is observable and the entire space outside is without meaning, in the sense of observability. We have established a criterion for selection of states which are allowed as solutions of the Dirac equation. These are allowed on the basis that the states have the significance of permitting space and time-localizable properties.

PHYSICAL REVIEW VOLUME 94, NUMBER 1 APRIL 1, 1954

Configuration Space Methods for the Construction of Potentials

ABRAHAM KLEIN
Harvard University, Cambridge, Massachusetts
(Received December 21, 1953)

Methods proposed recently by Lévy and by Brueckner and Watson for the construction of potentials in quantum field theory by superficially dissimilar techniques are rederived on a unified basis, that of the underlying equations in Fock space. It is supposed that certain amplitudes contained in the state vector are of primary physical interest, and it is demonstrated that the two methods differ essentially only in the order of elimination of the remaining amplitudes. The interpretation and practical use of the methods is discussed in a formal way, with emphasis on problems of consistency which limit the utility of the techniques. Elementary examples are discussed in the appendixes.

I. INTRODUCTION

SEVERAL methods have been proposed recently for the construction of potentials for meson-nucleon problems[1,2] which aim at the improvement of the results of perturbation theory. These methods are most closely tied to the Tamm-Dancoff (T.D.) type of procedure[3,4] which limits, at each stage of approximation, the number of free-particle amplitudes required to describe a state of a few real particles, but which attempts to take into account exactly the amplitudes which are retained.

The method of Lévy[1] is framed directly as a generalization of the T.D. approximation. The coupled equations of the field theory are replaced by a single Schrödinger equation for the amplitude of primary interest together with a set of integral equations which must be solved in succession in order to construct the interaction in the former equation. The method of Brueckner and Watson[2] (B.W.) has superficially quite a different aspect, since it employs the Møller wave matrix[5] in the formulation of Lippman and Schwinger.[6] This matrix, which connects all mutually accessible free-particle states, is decomposed by algebraic means into submatrices, and in particular one selects that submatrix which connects the states of primary interest. In this process, the original interaction Hamiltonian is transformed into an effective interaction which connects such states only, and which also requires for its construction the solution of auxiliary integral equations.

One of the purposes of this paper is to give a unified treatment of the two methods which permits one to understand in what sense they exhaust the possibilities of obtaining approximate solutions of the underlying equations in Fock space. It will be seen that the two procedures differ essentially only in the *order* of the elimination of those free-particle amplitudes which are not of primary interest and that other possible methods of elimination are in a sense intermediate between the two.

A second point which is emphasized is that the methods present difficulties of application, perhaps not fully appreciated hitherto. Consider, for example, the

[1] M. M. Lévy, Phys. Rev. **88**, 72 (1952).
[2] K. A. Brueckner and K. M. Watson, Phys. Rev. **90**, 699 (1953).
[3] I. Tamm, J. Phys. (U.S.S.R.) **9**, 449 (1945).
[4] S. M. Dancoff, Phys. Rev. **78**, 382 (1950).
[5] C. Møller, Kgl. Danske Videnskab. Selskab Mat.-fys. Medd. **23**, No. 1 (1954).
[6] B. A. Lippmann and J. Schwinger, Phys. Rev. **79**, 469 (1950).

two-nucleon problem in the adiabatic limit (fixed nucleon sources). The Schrödinger equation for the amplitude for two free nucleons reduces to an equation involving the amplitude for the absence of mesons and provides an eigenvalue equation for the vacuum meson energy, i.e., for the nuclear potential energy. It will be seen that for any of the above methods that goes beyond the one-meson approximation, the mere formulation of the eigenvalue problem requires a knowledge of the solution, i.e., one has a self-consistency problem, and even the one-meson approximation requires strictly the solution of a transcendental equation. A framework for improving the results of perturbation theory is provided, nevertheless, if one is willing to countenance further approximations and the limitations imposed by these on the validity of the results. Some crude approximations are illustrated in the appendixes.

II. METHOD OF LÉVY

We are interested in obtaining the stationary states of interacting meson and nucleon fields by solving the usual Schrödinger equation,

$$(H_0+H')\Psi=E\Psi. \tag{1}$$

For the time being we shall assume for the sake of simplicity that the interaction Hamiltonian H' is linear in meson absorption or creation operators and that there is no nucleon pair production. Thus, H' is the sum of two parts,

$$H'=H^{(+)}+H^{(-)}, \tag{2}$$

referring to the emission and absorption of a meson into or from an eigenstate of H_0, the unperturbed Hamiltonian, which is usually the sum of the free field Hamiltonians.

Let us think of the two-nucleon problem for definiteness and decompose Ψ into parts referring to different numbers of mesons by means of projection operators P_n,

$$\Psi=\sum_{n=0}^{\infty}P_n\Psi=\sum_{n=0}^{\infty}\Psi_n, \tag{3}$$

the number of nucleons being fixed. Equation (1) is then equivalent to the infinite set of coupled equations[7]

$$\begin{aligned}&(E-H_0)\Psi_0=H^{(-)}\Psi_1,\\ &(E-H_0)\Psi_1=H^{(-)}\Psi_2+H^{(+)}\Psi_0,\\ &\quad\cdots\\ &(E-H_0)\Psi_n=H^{(-)}\Psi_{n+1}+H^{(+)}\Psi_{n-1},\\ &\quad\cdots\end{aligned} \tag{4}$$

The Lévy method is based on the assumption that $\Psi_n=0$ for $n>N$, N fixed. One can then attempt to solve the resulting finite set of coupled integral equations. Alternatively, one can eliminate all amplitudes but Ψ_0 and obtain a single Schrödinger equation for it; the interaction is then constructed by solving an auxiliary set of integral equations. It is this latter procedure that will occupy our attention.

Consider first the case $N=2$. By eliminating Ψ_2, we are left in this approximation with the equations[8] $[G_0=(E-H_0)^{-1}]$

$$\begin{aligned}&(E-H_0)\Psi_0=H^{(-)}\Psi_1,\\ &(E-H_0)\Psi_1=H^{(+)}\Psi_0+H^{(-)}G_0H^{(+)}\Psi_1.\end{aligned} \tag{5}$$

If we define $K_{1,0}$ by means of the relation

$$(E-H_0)\Psi_1=K_{1,0}\Psi_0, \tag{6}$$

then the equation for Ψ_0 has the form

$$(E-H_0)\Psi_0=H^{(-)}G_0K_{1,0}\Psi_0, \tag{7}$$

where $K_{1,0}$ is the solution of the integral equation

$$K_{1,0}=H^{(+)}+H^{(-)}G_0H^{(+)}G_0K_{1,0}. \tag{8}$$

We may term $K_{1,0}$ a generalized emission operator. It describes the emission of a meson, when none was previously present. As discussed by Lévy,[1] the case of general N requires the solution of a succession of integral equations for operators $K_{1,0}$, $K_{2,0}$, $\cdots K_{N,N-1}$, where $K_{N,N-1}=(H^{(+)})_{N,N-1}$. The construction of any one of the operators K depends on the solution of the equations for larger values of the subscripts, Eq. (7) remaining unaltered in form.

An alternative formulation is related more immediately to the method of B.W.[2] If we define

$$G_1=(E-H_0-H^{(-)}G_0H^{(+)})^{-1}, \tag{9}$$

then a solution of the second of Eqs. (5) can be given in terms of the Green's function G_1,

$$\Psi_1=G_1H^{(+)}\Psi_0, \tag{10}$$

and Eq. (7) is replaced by

$$(E-H_0)\Psi_0=H^{(-)}G_1H^{(+)}\Psi_0\equiv H^{(-)}WG_0H^{(+)}\Psi_0, \tag{11}$$

where W is the Møller scattering matrix[5,6] determined by the "potential" $H^{(-)}G_0H^{(+)}$,

$$W=1+G_0H^{(-)}G_0H^{(+)}W. \tag{12}$$

Equation (12) follows directly from (9) and the definition $G=WG_0$. Equations (11) and (12) are the basis of the applications made by B.W.,[9] and are deducible less directly from the formulas given in Sec. IV.

We demonstrate next that for a linear Hamiltonian it is possible to obtain, following the lines of Eqs. (9)–(11), a concise formulation that is exact in principle. Consider the procedure of elimination described by Eqs. (9)–(11) as applied to the case of arbitrary N. To

[7] In Eq. (4) and on subsequent occasions throughout this paper the presence of projection operators where required for exactness of expression will be understood. For example, the expression $H^{(+)}\Psi_0$ should be written $P_1H^{(+)}P_0\Psi$, and of course $[P_n,H_0]=0$.

[8] The Green's function G_0 has no singularities, if we suppose that we are dealing with a bound state for which $E<H_0$. The possible occurrence of singularities in the more complex Green's functions defined below will not be considered in our discussion.

[9] K. A. Brueckner and K. M. Watson, Phys. Rev. 92, 1023 (1953).

eliminate the component Ψ_N we require the Green's function G_0, to eliminate Ψ_{N-1} the Green's function G_1, to eliminate Ψ_{N-2} the Green's function

$$G_2=(E-H_0-H^{(-)}G_1H^{(+)})^{-1}, \tag{13}$$

etc. Thus, to eliminate Ψ_1 requires the Green's function

$$G_{N-1}=(E-H_0-H^{(-)}G_{N-2}H^{(+)})^{-1}, \tag{14}$$

whereas the amplitude Ψ_0 is determined by the equation

$$(E-H_0)\Psi_0=H^{(-)}G_{N-1}H^{(+)}\Psi_0. \tag{15}$$

It should be clear that Eqs. (14) and (15) are approximate forms of the equations

$$G=(E-H_0-H^{(-)}GH^{(+)})^{-1}, \tag{16}$$

$$(E-H_0)\Psi_0=H^{(-)}GH^{(+)}\Psi_0, \tag{17}$$

which obtain in the limit $N\to\infty$, assuming the required convergence of the procedure.

III. DISCUSSION OF METHOD

It now becomes necessary to discuss carefully the significance of the formulation represented by Eqs. (16) and (17) or any approximations thereto. The point of view taken in the derivation was that one first constructs the Green's function G from Eq. (16), which in turn determines the interaction in the eigenvalue equation (17). This point of view is illusory for a number of reasons.[10] The Green's function G is itself a function of the energy E, so that one requires a simultaneous solutions of Eqs. (16) and (17). We distinguish here the adiabatic and the nonadiabatic treatment of the nucleons. In the latter case E is a number, which can be considered as a parameter in the solution of (16). However, Eq. (17) does not then yield the conventional eigenvalue problem, since the interaction $H^{(-)}GH^{(+)}$ is a function of E, and it is thus impossible to establish the orthogonality of solutions belonging to different eigenvalues.[11] Indeed, it is in general not consistent with the original Schrödinger equation, Eq. (1), to view Ψ_0 as a normalized wave function for the computation of observables. All the higher amplitudes included in the original approximation must be taken into account dutifully as part of the quantum-mechanical description, the mere process of elimination of the higher amplitudes in the procedures expounded here having in no way *decoupled* the amplitudes.

In the adiabatic limit, which we consider in somewhat greater detail, we remark that Ψ_0 is proportional to the meson vacuum state. We can choose $H_0\Psi_0=0$ and from Eq. (16b) find

$$\begin{aligned} E&=(\Psi_0,H^{(-)}GH^{(+)}\Psi_0)/(\Psi_0,\Psi_0)\\ &=\langle H^{(-)}GH^{(+)}\rangle. \end{aligned} \tag{18}$$

We must view Eq. (18) as a transcendental equation for the energy E, which is then taken as the potential energy of interaction between the nucleons. If we define the scattering matrix Λ (which connects one-meson states) by the relation

$$G=\Lambda(-H_0)^{-1}, \tag{19}$$

then we can rewrite Eq. (16) (after some trivial algebra) and (18) in the forms

$$\Lambda=1+(-H_0)^{-1}[-E+H^{(-)}\Lambda(-H_0)^{-1}H^{(+)}]\Lambda, \tag{20a}$$

$$E=\langle H^{(-)}\Lambda(-H_0)^{-1}H^{(+)}\rangle. \tag{20b}$$

Equations (20) have been established as the forms which are most appropriate for a consistent solution by successive approximations. For example, the second approximation to the potential energy, obtained from these equations,

$$\begin{aligned} E^{(2)}=&\langle H^{(-)}(-H_0)^{-1}H^{(+)}\rangle+\langle H^{(-)}(-H_0)^{-1}\\ &\times H^{(-)}(-H_0)^{-1}H^{(+)}(-H_0)^{-1}H^{(+)}\rangle\\ &-\langle H^{(-)}(-H_0)^{-1}H^{(+)}\rangle\langle H^{(-)}(-H_0)^{-2}H^{(+)}\rangle, \end{aligned} \tag{21}$$

corresponds precisely to the well-known formulas of Rayleigh-Schrödinger perturbation theory, in which the energy of the unperturbed state is zero. The potential of Eq. (21) is Hermitian and energy-independent; it is consistent to insert it into a nonrelativistic Schrödinger equation for the two-nucleon problem in the sense of our previous discussion.[11]

It is instructive to compare the correct perturbation result with other procedures that have been employed. For this purpose, define Λ_1 by the equation

$$G=\Lambda_1(E-H_0)^{-1}. \tag{22}$$

Equations (16) and (17) are replaced by the relations

$$\Lambda_1=1+(E-H_0)^{-1}H^{(-)}\Lambda_1(E-H_0)^{-1}H^{(+)}\Lambda_1, \tag{23a}$$

$$E=\langle H^{(-)}\Lambda_1(E-H_0)^{-1}H^{(+)}\rangle. \tag{23b}$$

By neglecting to approximate E consistently at each stage, the second approximation now takes the form

$$\begin{aligned} E^{(2)}=&\langle H^{(-)}(E-H_0)^{-1}H^{(+)}\rangle+\langle H^{(-)}(E-H_0)^{-1}H^{(-)}\\ &\times(E-H_0)^{-1}H^{(+)}(E-H_0)^{-1}H^{(+)}\rangle, \end{aligned} \tag{24}$$

the usual T.D. kernel obtained by successive elimination. Contrary to a viewpoint taken by the author and others,[12] it is seen by a comparison of (21) and (24) that a consistent treatment of the energy dependence of the first term of (24) (by Taylor expansion) is in no way

[10] Not the least of these is the problem of self-interactions. To a limited extent this problem can be by-passed in the applications by the expedient of omitting the self-interactions. When including them in noncovariant applications, common practice (see references 9, 13) has been to emulate covariant procedures, adding cutoffs where these are still required for convergence.

[11] This point and the ones that follow have been emphasized recently by D. Feldman, Bull. Am. Phys. Soc. **28**, No. 6, 31 (1953) and private communications. Analogous questions arise in the perturbation theory of particle quantum mechanics as has been emphasized by Prof. J. Schwinger in his lectures at Harvard.

[12] Y. Nambu, Progr. Theoret. Phys. Japan **5**, 614 (1950); M. M. Lévy, Phys. Rev. **88**, 725 (1952); A. Klein, Phys. Rev. **90**, 1101 (1953).

related to nonadiabatic effects. Moreover, any procedure which sets $E=0$ in that term while including other higher-order terms is strictly inconsistent.[13]

Suppose, for example, that one could justify both the adiabatic approximation and the statement that the amplitude for finding more than one free meson in the field is negligible. Then the problem of constructing the exact one-meson adiabatic potential would still require the solution of the transcendental equation

$$E=\langle H^{(-)}(E-H_0)^{-1}H^{(+)}\rangle, \tag{25}$$

by no means a trivial task, since E is, in general, a function of spin, isotopic spin, and position variables of the nucleons. On the other hand, the construction of the exact two-meson potential requires the simultaneous solution of Eqs. (23b) and the linear form of (23a) which results from replacing the first Λ_1, appearing on the right-hand side by unity. Further approximations which are required to make any headway, which ignore or approximate the energy when it appears in the form $(E-H_0)^{-1}$, necessarily obscure the quantitative interpretation of the results, although they are useful in a qualitative investigation of the importance of higher-order effects.[9] Two fairly crude approximations of this character are illustrated in Appendixes A and B in application to the symmetric scalar theory.

The point of view taken here requires no revision in the more general case of interactions which are nonlinear in the meson field and/or describe nucleon pair production. As a rule, it is not possible to provide as concise a formulation as is contained in Eqs. (16) and (17), except for the instance of a meson pair term alone. Thus, if H' is a superposition of the form

$$H'=H^{(++)}+H^{(--)}+H^{d}, \tag{26}$$

describing emission of a pair of mesons by $H^{(++)}$, the absorption of a pair of $H^{(--)}$, and mixed emission and absorption by H^{d}, then starting from the equations analogous to Eq. (4), one finds that Eqs. (16) and (17) are replaced by

$$G=(E-H_0-H^{d}-H^{(--)}GH^{(++)})^{-1}, \tag{27a}$$

$$(E-H_0)\Psi_0=(H^{d}+H^{(--)}GH^{(++)})\Psi_0. \tag{27b}$$

In a more general situation, providing a formulation for any pre-assigned approximation is not the difficult problem.

IV. METHOD OF BRUECKNER AND WATSON

Consider first for simplicity an interaction of the form of Eq. (2). The Schrödinger equation, Eq. (1), is then represented by Eqs. (4). Instead of eliminating amplitudes in the manner described in the previous section, a natural procedure that suggests itself is to eliminate *alternate* components. This leaves a set of equations involving the components Ψ_0, Ψ_2, $\cdots$, Ψ_{2n}, $\cdots$, where the equation for the general component Ψ_{2n} is

$$(E-H_0)\Psi_{2n}=(H^{(-)}G_0H^{(+)}+H^{(+)}G_0H^{(-)})\Psi_{2n} +H^{(-)}G_0H^{(-)}\Psi_{2n+2}+H^{(+)}G_0H^{(+)}\Psi_{2n-2}. \tag{28}$$

It is useful with B.W.[2] to define the operators

$$\Delta_0=H'G_0H', \tag{29a}$$

$$V_0=\text{D.P. }\Delta_0, \tag{29b}$$

$$U_0=\text{N.D.P. }\Delta_0, \tag{29c}$$

where D.P. and N.D.P. refer to diagonal and nondiagonal parts respectively, in occupation number space, and to rewrite (28) as

$$(E-H_0)\Psi_{2n}=V_0\Psi_{2n}+U_0^{(-)}\Psi_{2n+2}+U_0^{(+)}\Psi_{2n-2}. \tag{28'}$$

We proceed again to eliminate every second component of the remaining set of coupled equations. At this second stage the general equation is easily found to have the form

$$(E-H_0)\Psi_{4n}=(V_0+V_1)\Psi_{4n} +U_1^{(-)}\Psi_{4n+4}+U_1^{(+)}\Psi_{4n-4}, \tag{30}$$

where, in terms of

$$\Delta_1\equiv U_0(E-H_0-V_0)^{-1}U_0, \tag{31a}$$

the quantities appearing in Eq. (30) are defined by the relations

$$V_1=\text{D.P. }\Delta_1=U_0^{(-)}(E-H_0-V_0)^{-1}U_0^{(+)} +U_0^{(+)}(E-H_0-V_0)^{-1}U_0^{(-)}, \tag{31b}$$

$$U_1=\text{N.D.P. }\Delta_1;\quad U_1^{(\pm)}=U_0^{(\pm)}(E-H_0-V_0)^{-1}U_0^{(\pm)}. \tag{31c}$$

The procedure of elimination of alternate components can be continued interminably. If we define

$$\mathcal{U}_l=\sum_{k=0}^{l}V_k, \tag{32a}$$

$$\Delta_l=U_{l-1}(E-H_0-V_{l-1})^{-1}U_{l-1}, \tag{32b}$$

$$V_l=\text{D.P. }\Delta_l, \tag{32c}$$

$$U_l=\text{N.D.P. }\Delta_l=U_l^{(+)}+U_l^{(-)}, \tag{32d}$$

then after $l+1$ stages of elimination, the equation for Ψ_0, in particular, becomes

$$(E-H_0)\Psi_0=\mathcal{U}_l\Psi_0+U_l^{(-)}\Psi_{2^{l+1}}. \tag{33}$$

In the limit $l\to\infty$, if the procedure converges, we obtain

$$(E-H_0)\Psi_0=\mathcal{U}\Psi_0, \tag{34}$$

where

$$\mathcal{U}=\lim(l\to\infty)\mathcal{U}_l. \tag{35}$$

It is clear that $\mathcal{U}$ and all the successive approximations to it are diagonal operators in occupation number

[13] Similar arguments from a different point of view have been presented by Feldman (reference 11), and by E. M. Henley and M. A. Ruderman, Phys. Rev. 92, 1036 (1953). Brueckner and Watson (reference 9) argue to a different conclusion.

space and that the U_l have matrix elements for either the emission or the absorption of 2^{l+1} mesons *only*. The outstanding characteristic of the method outlined here as distinguished from that of the previous section is that, instead of improving the approximation by adding one meson amplitude at a time, it optimistically jumps by factors of two.

The method of explicit elimination described above does not permit a simple inductive statement of the result analogous to Eq. (32) for a more general interaction than that of Eq. (2). The special simplicity of the linear Hamiltonian results from the fact that a given amplitude is coupled only to adjoining amplitudes, which is not true for any other interaction, barring the meson pair interaction if the latter comprises the entire interaction.[14] Nevertheless, in any "practical" application one stops after a very few stages of elimination, and these can be performed easily for any Hamiltonian.

A consistent application of the method requires the construction of the Green's functions $(E-H_0-\mathcal{V}_l)^{-1}$ or of the associated scattering operators, and one is here beset by the same limitations as discussed in detail in the previous section, in particular the dependence of the Green's functions on the energy.

We conclude this section by presenting a more symbolic derivation of the method under discussion, a derivation which applies formally also to nonlinear interactions. We shall, in fact, treat the more general case, since the linear case has already been discussed in a preliminary account of this work.[15]

Suppose that we decompose our state-vector into two parts,

$$\Psi=\Psi_e+\Psi_o, \tag{36}$$

the even part Ψ_e, comprising the amplitudes for 0, 2, $\cdots 2n\cdots$ mesons, the odd part Ψ_o containing the remaining amplitudes. Concomitantly, we write the interaction H' as the sum

$$H'=H(e1)+H(o1), \tag{37}$$

where $H(e1)$ has matrix elements for the emission (absorption) of an even number (including zero) of mesons, and $H(o1)$ has matrix element for the emission (absorption) of an odd number of mesons. Then the Schrödinger equation, Eq. (1), is replaced by the equations

$$(E-H_0-H(e1))\Psi_e=H(o1)\Psi_o, \tag{38a}$$

$$(E-H_0-H(e1))\Psi_o=H(o1)\Psi_e. \tag{38b}$$

We can now formally eliminate either Ψ_e or Ψ_o. In what follows we shall, for the sake of argument, consistently eliminate the part which is termed odd and thereupon drop the subscript e. From (38) we therefore deduce the equation

$$\begin{aligned}(E-H_0)\Psi&=[H(e1)+H(o1)(E-H_0-H(e1))^{-1}H(o1)]\Psi\\&\equiv[H(e2)+H(o2)]\Psi,\end{aligned} \tag{39}$$

where it has proved convenient, in the second form of (39), to recognize that the operator on the right hand side has matrix elements for the emission (absorption) of an even multiple (including zero) of two mesons, $H(e2)$, and those for the emission (absorption) of an odd multiple of two mesons $H(e1)$.

With this relabeling, we are essentially back where we started, and the process leading from (38) to (39) can be repeated, the next step resulting in the equation

$$\begin{aligned}(E-H_0)\Psi&=[H(e2)+H(o2)(E-H_0-H(e2))^{-1}H(o2)]\Psi\\&\equiv[H(e2^2)+H(o2^2)]\Psi,\end{aligned} \tag{40}$$

where Ψ consists of the amplitude for $4n$ mesons $n=0, 1, 2\cdots$, and the operators defined in Eq. (40) have the obvious meaning after this second stage of elimination. After l stages of elimination, only the amplitudes for $2^l\times n$ mesons remain in a Ψ that satisfies

$$\begin{aligned}(E-H_0)\Psi&=[H(e2^{l-1})+H(o2^{l+1})\\&\quad\times(E-H_0-H(e2^{l-1}))^{-1}H(o2^{l-1})]\Psi\\&\equiv[H(e2^l)+H(o2^l)]\Psi.\end{aligned} \tag{41}$$

At this stage the quantity that corresponds to the potential of the previous discussion is

$$\mathcal{V}_l=\text{D.P. } H(e2^l), \tag{42}$$

since if one ignores the coupling of Ψ_0 to Ψ_{2^l} and to still higher amplitudes, Ψ_0 satisfies

$$(E-H_0)\Psi_0=\text{D.P. } H(e2^l)\Psi_0. \tag{43}$$

The assumption of convergence permits the limit $l\to\infty$ to be taken.

Although this method has aesthetic advantages in the general case, it has none in practice over earlier procedures, since, as pointed out by B.W.,[2] the construction of the potential requires further manipulation of the Green's functions $[E-H_0-H(e2^l)]^{-1}$, which are still nondiagonal in occupation number space.

The work of the preceding sections should make it abundantly clear that the techniques of Lévy and of B.W. are, perhaps, the two most natural ways of *reformulating* the Schrödinger equation, although one can, to no useful end, conjure up combinations of the two.

It is a pleasure to thank Professor David Feldman for several enlightening discussions.

APPENDIX A

We shall illustrate a procedure for applying Lévy's method, Eqs. (5)–(8) of the text, which is particularly convenient for the treatment of higher-order meson exchange effects if one is willing to omit self-interactions. Since H', the interaction, has the form

$$H'=H_1'+H_2', \tag{A.1}$$

referring to the individual nucleon sources, and relabeling the operator K_{L0} as $K^{(+)}$, the expression for

[14] Compare the analogous situation in Sec. III.

[15] A. Klein, Phys. Rev. **91**, 1285 (1953).

the potential (adiabatic limit) is

$$E=\langle H_1^{(-)}(E-H_0)^{-1}K_2^{(+)}\rangle+1\leftrightarrow 2. \qquad (A.2)$$

We limit the discussion further as follows: (1) There are no more than two mesons in the field at any time. (2) We employ the symmetric scalar theory. (3) We temporarily ignore the dependence on E of the right-hand side of (A.2) both in $(E-H_0)^{-1}$ and in $K^{(+)}$. This is the type of limitation discussed in Sec. III. Corrections can be made but will not be discussed here (see Appendix B, however) since our aim is merely to illustrate a procedure for constructing $K^{(+)}$ under the specified approximations. The result will be well defined but not necessarily consistent without additions.

The matrix elements for the emission and absorption of a free meson are essentially[16]

$$H_{i\lambda}^{(\pm)}(k)=g\tau_\lambda^{(i)}(2\omega)^{-\frac{1}{2}}(2\pi)^{-\frac{3}{2}}\exp(\mp i\mathbf{k}\cdot\mathbf{z}_i), \qquad (A.3)$$

$i=1, 2$; $\lambda=1, 2, 3$. With the limitation to finite effects specified above, Eq. (8) of the text, when written fully, takes the form

$$\begin{aligned}K_{i\lambda}^{(+)}(k)=&\,g\tau_\lambda{}^i(2\omega)^{-\frac{1}{2}}(2\pi)^{-\frac{3}{2}}e^{-i\mathbf{k}\cdot\mathbf{z}_i}\\&+\frac{g^2}{(2\pi)^3}\sum_{j\neq i}\int\frac{d\mathbf{k}'\tau^j\cdot\tau^l}{2\omega\omega'(\omega+\omega')}\\&\qquad\times K_{i\lambda}^{(+)}(k)e^{i\mathbf{k}'\cdot(\mathbf{z}_j-\mathbf{z}_l)}\\&+\frac{g^2}{(2\pi)^3}\sum_{j\neq i}\int\frac{d\mathbf{k}'\tau_\rho{}^j\tau_\lambda{}^i}{2\omega^{\frac{1}{2}}(\omega')^{\frac{1}{2}}(\omega+\omega')}\\&\qquad\times K_{l\rho}^{(+)}(k')e^{i(\mathbf{k}'\cdot\mathbf{z}_j-\mathbf{k}\cdot\mathbf{z}_i)}. \qquad (A.4)\end{aligned}$$

The solution of (A.4) by iteration is tantamount to perturbation theory. To obtain a more accurate solution, it is first convenient to introduce the quantity $\mathcal{K}_{i\lambda}$ by means of the equation

$$K_{i\lambda}^{(+)}=g(2\omega)^{-\frac{1}{2}}(2\pi)^{-\frac{3}{2}}e^{-i\mathbf{k}\cdot\mathbf{z}_i}\mathcal{K}_{i\lambda}. \qquad (A.5)$$

Inserting (A.5) into (A.4) and setting $i=1$, for example, we have $(\mathbf{r}=\mathbf{z}_1-\mathbf{z}_2)$

$$\begin{aligned}\mathcal{K}_{1\lambda}(k)=&\,\tau_\lambda^{(1)}+\frac{g^2}{(2\pi)^3}\int\frac{d\mathbf{k}'e^{i\mathbf{k}'\cdot\mathbf{r}}}{\omega\omega'(\omega+\omega')}\mathcal{K}_{1\lambda}(k)\\&+\frac{g^2}{(2\pi)^3}\int\frac{d\mathbf{k}'e^{i\mathbf{k}'\cdot\mathbf{r}}}{2(\omega')^2(\omega+\omega')}\\&\times[\tau_\rho^{(1)}\tau_\lambda^{(1)}\mathcal{K}_{2\rho}(k')+\tau_\rho^{(2)}\tau_\lambda^{(1)}\mathcal{K}_{1\rho}(k')]. \qquad (A.6)\end{aligned}$$

In Eqs. (A.4)–(A.6), the dependence of K and $\mathcal{K}$ on nucleon coordinates has been suppressed.

It is easily established from the invariance properties of the potential and from those of Eq. (A.6) that $\mathcal{K}_{1\lambda}$ and $\mathcal{K}_{2\lambda}$ can differ only by an interchange of isotopic variables. Now $\mathcal{K}_{1\lambda}$, as a vector in isotopic spin space, must have the form

$$\mathcal{K}_{1\lambda}=\tau_\lambda^{(1)}F_1+\tau_\lambda^{(2)}F_2+i(\tau^{(1)}\times\tau^{(2)})_\lambda F_3, \qquad (A.7)$$

where $F_{1,2,3}$ are invariant functions of k and r. Thus

$$\mathcal{K}_{2\lambda}=\tau_\lambda^{(2)}F_1+\tau_\lambda^{(1)}F_2+i(\tau^{(2)}\times\tau^{(1)})_\lambda F_3. \qquad (A.8)$$

Coupled equations for F_1, F_2 and F_3 can be found by inserting (A.7) and (A.8) into (A.6) and computing the three traces, $\mathrm{tr}\tau_\lambda^{(1)}\mathcal{K}_{1\lambda}$, $\mathrm{tr}\tau_\lambda^{(2)}\mathcal{K}_{1\lambda}$ and $\mathrm{tr}(\tau^{(1)}\times\tau^{(2)})_\lambda\mathcal{K}_{1\lambda}$. We thereby find the equations

$$\begin{aligned}\{F_1(k),F_2,F_3\}=&\,\{1,0,0\}+\frac{g^2}{(2\pi)^3}\int\frac{d\mathbf{k}'e^{i\mathbf{k}'\cdot\mathbf{r}}}{\omega\omega'(\omega+\omega')}\\&\times\{F_2(k)+2F_3(k),\,F_1-2F_3,\,F_1-F_2-F_3\}\\&+\frac{g^2}{(2\pi)^3}\int\frac{d\mathbf{k}'e^{i\mathbf{k}'\cdot\mathbf{r}}}{(\omega')^2(\omega+\omega')}\{F_2(k'),\,F_1,\,-F_3\}. \qquad (A.9)\end{aligned}$$

To facilitate further progress, we shall approximate the kernels of Eq. (A.9) by the most simply chosen separable kernels, replacing the denominators of both the second and third terms by $2(\omega')^3$. This provides a very close numerical approximation in the perturbation theory limit (see below). Setting $G=F_1+F_2$, we find that the function G satisfies the uncoupled equation

$$G(k)=1+\tfrac{1}{2}g^2I(r)G(k)+\tfrac{1}{2}g^2\Lambda(r), \qquad (A.10)$$

where

$$\Lambda(r)=(2\pi)^{-3}\int d\mathbf{k}e^{i\mathbf{k}\cdot\mathbf{r}}G(k)\omega^{-3}, \qquad (A.11)$$

$$I(r)=(2\pi)^{-3}\int d\mathbf{k}e^{i\mathbf{k}\cdot\mathbf{r}}\omega^{-3}=(1/4\pi)(2/\pi)K_0(\mu r). \qquad (A.12)$$

By constructing $\Lambda(r)$ from the left hand side of (A.10), we obtain the value of that quantity, which in turn leads immediately to the solution

$$G(r)=[1-g^2I(r)]^{-1}. \qquad (A.13)$$

The solution of the remaining two equations of (A.9) proceeds similarly, and we shall be content with a statement of the final results,

$$F_1+F_2=[1-g^2I]^{-1}, \qquad (A.14)$$

$$\begin{aligned}F_1-F_2=&\,[(1+\tfrac{1}{2}g^2I)(1+\tfrac{3}{2}g^2I-\tfrac{1}{2}g^4I^2)-\tfrac{1}{2}g^6I^3]\\&\times[(1-\tfrac{1}{2}g^2I)(1+\tfrac{3}{2}g^2I)(1+2g^2I)]^{-1}, \qquad (A.15)\end{aligned}$$

$$\begin{aligned}F_3=&\,\tfrac{1}{2}g^2I[1+\tfrac{1}{2}g^2I]^{-1}(F_1-F_2)\\&-\tfrac{1}{4}g^4I^2[(1+\tfrac{1}{2}g^2I)(1+2g^2I)]^{-1}. \qquad (A.16)\end{aligned}$$

For the potential, we find from (A.2), (A.5), (A.7), (A.8), (with $x=\mu r$)

$$\begin{aligned}E=-\mu(g^2/4\pi)\{&\tau^1\cdot\tau^2(e^{-x}/x)(F_1+2F_3)\\&-3(e^{-x}/x)F_2\}. \qquad (A.17)\end{aligned}$$

[16] That is, except for population factors depending upon occupancy of initial and final states. These cancel out in the computation of the potential.

To order g^2 this agrees with the usual static approximation. To order g^4, (A.17) yields

$$E^{(2)}\cong E^{(1)}-\mu(g^2/4\pi)^2(e^{-x}/x)(2/\pi)\times K_0(x)(\tau^1\cdot\tau^2+3). \quad \text{(A.18)}$$

On the other hand, the correct result for the quantity called $E^{(2)}$ is easily found from (A.4),[17]

$$E^{(2)}=E^{(1)}-\mu(g^2/4\pi)^2(e^{-x}/x)(2/\pi)K_0(x)(3-2\tau^1\cdot\tau^2) -4\mu(g^2/4\pi)^2\tau^1\cdot\tau^2(2/\pi)K_0(2x). \quad \text{(A.19)}$$

Numerically (A.18) approximates (A.19) to within a few percent, although this does not necessarily vouch safe the accuracy of (A.14)–(A.16).

The contribution of higher-order effects is determined by the magnitude of $g^2I=(g^2/4\pi)(2/\pi)K_0(x)$ compared to unity. For $(g^2/4\pi)=0.1$, this varies from 3 percent for $x=1$ to 10 percent for $x=0.25$, so that perturbation theory converges quite rapidly for the symmetric scalar theory in the range considered, mainly as a consequence of the fact that higher-order terms are not much more singular than the lowest-order potential. The same conclusion does not obtain, therefore, for the gradient coupling[9] which will be considered in detail in a later publication.

APPENDIX B

In this appendix we shall consider a few crude approximations for the solution of Eq. (24) of the text, considered as an exact eigenvalue equation,

$$E=\langle H^{(-)}(E-H_0)^{-1}H^{(+)}\rangle+\langle H^{(-)}(E-H_0)^{-1} \times H^{(-)}(E-H_0)^{-1}H^{(+)}(E-H_0)^{-1}H^{(+)}\rangle. \quad \text{(B.1)}$$

Perturbation theory corresponds to the expansion of the right-hand side of (B.1) in powers of E and subsequent solution by iteration. Even an exact solution of (B.1) takes the one-meson amplitude into account exactly, the two-meson amplitude, however, only in an approximate manner.

Consider first the one-meson potential. For illustration we choose the symmetric scalar theory and omit self-interactions. Under these circumstances, (B.1) becomes

$$E=\frac{g^2}{(2\pi)^3}\int d\mathbf{k}e^{i\mathbf{k}\cdot\mathbf{r}}\tau^1\cdot\tau^2\frac{1}{\omega(E-\omega)}. \quad \text{(B.2)}$$

Now

$$[\omega(E-\omega)]^{-1}=-(k^2+\mu^2-E^2)^{-1} -E[\omega(k^2+\mu^2-E^2)]^{-1}. \quad \text{(B.3)}$$

[17] The correct perturbation result is obtained by adding to (A.19) the contribution of the last term of Eq. (21). This cancels the second term of the right-hand side of (A.19).

The first term yields a Yukawa interaction of range $(\mu^2-E^2)^{-\frac{1}{2}}$. Bounds on the second term are obtained by the replacements

$$\omega(k^2+\mu^2-E^2)^{-\frac{1}{2}}\to\omega^{-1} \quad \text{or} \quad (k^2+\mu^2-E^2)^{-\frac{1}{2}}. \quad \text{(B.4)}$$

Choosing the first form of (B.4), for example, we find that

$$E=-(g^2/4\pi)\tau^1\cdot\tau^2[\exp(-r(\mu^2-E^2)^{\frac{1}{2}})/r +(2/\pi)K_0(\mu r)E]. \quad \text{(B.5)}$$

(B.5) provides eigenvalue equations for charge singlet and triplet states, separately, by means of which one can investigate the importance of higher-order contributions to the one-meson potential.

Independent of the particular model, it is clear from (B.5) that the adiabatic approximation ceases to have a meaning as soon as the potential (computed) becomes of the order of the meson rest energy. Thus any straightforward perturbation treatment cannot be trusted at internuclear separations which yield potentials of this order of magnitude.

The utility of a formulation such as (B.5) is restricted on several accounts. First, as soon as its implications differ materially from those of the g^2 potential, higher-order terms must be included, and the attempt to cast these in equally useful (and accurate) analytic form becomes prohibitive, although the next term in (B.1) can still be handled. Second, for a model which yields tensor forces, the method is powerless for spin triplet states.

A less pretentious manner of treating (B.1) is to expand the right-hand side to first-order terms in the energy. If we denote the right-hand side by $F(E)$, then to this approximation we find

$$E=F(0)/[1-F'(0)], \quad \text{(B.6)}$$

which may be considered a reasonable improvement on perturbation theory as long as $|F'(0)|$ is less than unity. For example, in this approximation, (B.5) is replaced by

$$E=-(g^2/4\pi)\tau^1\cdot\tau^2[\exp(-\mu r)/r] \times[1+(g^2/4\pi)\tau^1\cdot\tau^2(2/\pi)K_0(\mu r)]^{-1}, \quad \text{(B.7)}$$

which can become singular at a finite internuclear separation. The occurrence and position of such singularities is modified when additional terms of $F(E)$ are included. The situation is qualitatively not dissimilar to that encountered in the previous appendix.

Letters to the Editor

PUBLICATION of brief reports of important discoveries in physics may be secured by addressing them to this department. The closing date for this department is five weeks prior to the date of issue. No proof will be sent to the authors. The Board of Editors does not hold itself responsible for the opinions expressed by the correspondents. Communications should not exceed 600 words in length and should be submitted in duplicate.

Paramagnetic Resonance in Irradiated Ice

BERNARD SMALLER, MAX S. MATHESON, AND EDWARD L. YASAITIS
Chemistry Division, Argonne National Laboratory, Lemont, Illinois
(Received February 5, 1954)

WE have recently detected the presence of paramagnetic resonance in samples of ice previously exposed to ionizing radiation at 77°K. The detection equipment utilized a regenerative 350-Mc one-quarter wave coaxial line oscillator incorporated into a double-wall Dewar. The auxiliary circuits have been described previously.[1] The irradiation source was a 400-curie Co^{60} gamma source[2] with total dosages used in the range $(2\text{–}20)\times10^{20}$ ev/g, yielding signal-to-noise values of 10 to 1000. Irradiations were carried out by using cylinders of ice approximately 5 mm in diameter and 50 mm in length; the resonance-sensitive volume being, however, about 0.1 cc. Measurements were made at temperatures ranging from 4°K (in liquid helium) to 225°K with most of the data taken at 77°K (liquid nitrogen).

At 77°K the H_2O ice displayed a doublet resonance structure at a gyromagnetic ratio of 2.0 with a separation of *ca* 30 gauss and line widths of 6 gauss, each component of equal intensity. Using D_2O ice, a triplet structure was obtained with component separation of 5 gauss and line width of 2 gauss; intensity ratios along the structure were in the ratio 1:2:1.

The results indicated represent substantial evidence for the existence of a free spin (i.e., unpaired electron) existing near an H or D nucleus, with resultant hyperfine structure. Relative line intensities substantiate this assumption, and the line widths are also in the correct ratio if one assumes that neighboring protons or deuterons are the source of the line broadening. The ratio of the hyperfine splitting constants in H_2O ice and D_2O ice, 4.0, is in good agreement with the corresponding atomic beam ratio of $W_H/W_D=4.3$.[3] However, the splitting values (e.g., 85.5 Mc/sec in H_2O ice) are considerably less than the free-atom values (e.g., 1420 Mc/sec for H).[3] One may attribute this reduction in interaction, at least qualitatively, to the polarization effect of the ice. In fact, the required effective dielectric constant is 2.55, approximately equal to the determined high-frequency value.[4]

In measurements at 4°K, a second doublet structure was revealed in H_2O ice with a separation of 10 gauss, while the D_2O ice resonance spectrum showed a distortion attributable to a second close triplet structure.

In the radiation chemistry of aqueous systems the presence of H and OH is deduced by indirect evidence, and it is suggested that the OH free radical may be responsible for this second resonance. The reversible disappearance of this doublet at higher temperatures remains to be explained. On irradiation of H_2O ice containing H_2O_2, a second doublet structure 12 to 15 gauss in separation becomes prominent at 77°K, while the 30-gauss doublet is weakened or disappears. It is plausible to assign this doublet to OH also, and this weakening of the 30-gauss doublet would be expected if the thermodynamically favorable reaction, $H+H_2O_2 \rightarrow H_2O+OH$, occurs. The persistence of the OH doublet at the higher temperatures may be taken to be a manifestation of the stabilization of the resonance of this radical. Annealing experiments indicate a greater stability for this radical than that attributed to the H atom. Results with D_2O_2 in D_2O are in agreement with the effects obtained in $H_2O_2-H_2O$.

We have also investigated the free radical species formed in solid NH_3 and solid HCOOH irradiated at 77°K. These reveal a more complex resonance spectrum with the formation of an intermediate paramagnetic species during annealing. A more complete report of this work will be published shortly.

[1] B. Smaller and E. Yasaitis, Rev. Sci. Instr. **24**, 991 (1953).
[2] Blomgren, Hart, and Markheim, Rev. Sci. Instr. **24**, 298 (1953).
[3] J. E. Nafe and E. B. Nelson, Phys. Rev. **73**, 718 (1948).
[4] N. E. Dorsey, *Properties of Ordinary Water Substance* (Reinhold Publishing Corporation, New York, 1940), pp. 496–500.

The Heat Capacity and Entropy of Liquid He^3 from 0.42°K to 1.06°K

DARRELL W. OSBORNE, BERNARD M. ABRAHAM, AND BERNARD WEINSTOCK
Argonne National Laboratory, Lemont, Illinois
(Received February 8, 1954)

PRELIMINARY measurements have been made on the heat capacity of liquid He^3 between 0.42°K and 1.06°K. These results, when combined with vapor pressure and melting pressure data, show that the entropies of both the liquid and the solid are approximately $R\ln 2$ at 0.42°K, and it is concluded that there is no appreciable alignment of the nuclear spins in either liquid or solid He^3 down to 0.42°K.

The calorimeter consisted of a cylindrical copper container, in the center of which was located a 1.87-cc copper vessel connected to an external He^3 filling line through a small cupronickel tube. Ferric ammonium alum (74 g) was hand-tamped around the He^3 vessel to about 0.7 times the crystal density. Four copper vanes were hard-soldered to the He^3 vessel to provide a large area of contact with the alum, and a strip carbon resistor, which served both as a resistance thermometer and as a heater, was fastened to one of the vanes. The free volume in the container was filled with He^4 gas to about 1 atmos pressure at room temperature in order to improve the heat transfer within the calorimeter.

The temperature scale was obtained by calibrating the resistance thermometer and the susceptibility of the iron alum against the vapor pressure of liquid He^4 from 1.1 to 4.2°K. Below 1.1°K the resistance thermometer was calibrated against the susceptibility of the iron alum. Kistemaker's corrections[1] were applied to the "agreed" helium temperature scale,[2,3] and corrections for the difference between the magnetic temperature and the thermodynamic temperature were made on the basis of the results of Kurti, Simon, and Squire.[4] A smooth table of resistance *versus* thermodynamic temperature was then constructed from the calibration data.

The heat capacity of the empty calorimeter was determined before making the measurements with He^3. The first liquid He^3 experiments were made with 1011 cc (STP) of gas, or approximately 1.7 cc of liquid. It was found that with this quantity of He^3 the available magnetic field was insufficient to cool the calorimeter below about 0.7°K; consequently, for runs at lower temperatures the amount was reduced to 601 cc or 315 cc (STP). The heat capacity of liquid He^3 along the saturation line is expressed by the equation:

$$C_{sat}=0.53+0.487T \text{ cal deg}^{-1}\text{ mole}^{-1}. \quad (0.42\leq T\leq 1.06\text{°K}). \quad (1)$$

Because of a rather large heat leak in these experiments the results may be in error by as much as 5 percent.

The entropy of liquid He^3 at 1°K, including the nuclear spin entropy, has been calculated from vapor pressure measurements to be 2.09 ± 0.14 cal deg^{-1} mole^{-1}.[5,6] From this result and from Eq. (1) it follows that the entropy of the liquid at its saturated vapor pressure is

$$S_{liq}=2.09+0.53\ln T+0.48(T-1) \text{ cal deg}^{-1}\text{ mole}^{-1} \quad (2)$$

in the temperature range 0.42 to 1°K. At the lowest temperature of the measurements, 0.42°K, the entropy of the liquid is 1.35 ± 0.15

cal deg^{-1} mole^{-1}, or very nearly equal to $R\ln 2 = 1.38$ cal deg^{-1} mole^{-1}, the value for random orientation of the nuclear spins. If the reasonable assumption is made that the contribution of phonon excitation to the total entropy is small at this temperature, it can be concluded that the nuclear spins are not appreciably ordered in liquid He^3 at 0.42°K, in agreement with our previous prediction.[6] The results also indicate, contrary to suggestions by others,[7–9] that liquid He^3 cannot be treated as an ideal Fermi-Dirac gas having the same molecular weight and density as liquid He^3; for the entropy of such a gas at 0.42°K would be 0.84 cal deg^{-1} mole^{-1}, instead of the measured value of 1.35 ± 0.15 cal deg^{-1} mole^{-1}.

The present results may also be combined with data on the melting pressure to obtain the entropy of solid He^3. It has been been found[10] that the slope of the melting pressure curve becomes zero near 0.42°K, and hence from the thermodynamic relation,

$$dp/dT = \Delta S/\Delta V, \qquad (3)$$

the difference in entropy between the compressed liquid and the solid becomes zero near this temperature. Provided that the entropy change on compression of the liquid is small, the entropy of solid He^3 at 0.42°K must therefore be 1.35 ± 0.15 cal deg^{-1} mole^{-1}, which corresponds to random orientation of the nuclear spins in the solid. This conclusion substantiates Pomeranchuk's assumption[11] regarding nuclear spin alignment in solid He^3.

[1] J. Kistemaker, Physica **12**, 272, 281 (1946).
[2] H. van Dijk and D. Shoenberg, Nature **164**, 151 (1949).
[3] C. F. Squire, *Low Temperature Physics* (McGraw-Hill Book Company, Inc., New York, 1953), p. 233.
[4] A. H. Cooke, Proc. Phys. Soc. (London) **A62**, 269 (1949).
[5] Abraham, Osborne, and Weinstock, Phys. Rev. **80**, 366 (1950).
[6] Weinstock, Abraham, and Osborne, Phys. Rev. **89**, 787 (1953).
[7] E. M. Lifshitz, J. Exptl. Theoret. Phys. (U.S.S.R.) **21**, 659 (1951).
[8] K. S. Singwi, Phys. Rev. **87**, 540 (1952).
[9] T. C. Chen and F. London, Phys. Rev. **89**, 1038 (1953).
[10] Weinstock, Abraham, and Osborne, Phys. Rev. **85**, 158 (1952), and unpublished results.
[11] I. Pomeranchuk, J. Exptl. Theoret. Phys. (U.S.S.R.) **20**, 919 (1950).

Energy Loss of Electrons in Passage Through Thin Films*

L. Marton and Lewis B. Leder
National Bureau of Standards, Washington, D. C.
(Received February 8, 1954)

THIS is a preliminary report on measurements of the energy loss spectrum of 30-kev electrons passing through thin films of metals and insulators. These losses are of the same type as those measured by Ruthemann,[1] Lang,[2] and Möllenstedt,[3] and as those calculated by Pines and Bohm[4] by means of their "plasma oscillation" theory of metals.

To make these measurements, we modified an electrostatic electron microscope by replacing its two projection lenses with a slit and a "cylindrical" lens. The analysis of the scattered primary beam is accomplished by utilizing the off-axis chromatic aberration of the "cylindrical" lens.[5] The slit has a fixed spacing of approximately 2 microns, and was built into the shell of one of the projection lenses with provision made for rotation and translation from outside the vacuum of the instrument. The "cylindrical" lens was made using the shell and outer electrodes of the other projection lens, and replacing the center electrode by an element with an elongated aperture. These were placed in the former projection lens positions with the slit above the lens. After proper alignment, as described by Möllenstedt, it was found that the projected image of the slit could be shifted parallel to itself when the accelerating potential was changed relative to the lenses. With this arrangement we have obtained an energy resolution of 1 part in 35 000.

The thin films, which were between 50 and 100A thick, were prepared by evaporation onto salt crystal faces, floated off on water, and mounted on 200-mesh screens. These were placed in the normal object position of the microscope so that an enlarged image appeared on the slit. In cases where the material oxidized rapidly in the air, it was evaporated onto another thin film substrate in the vacuum of the analyzer itself.

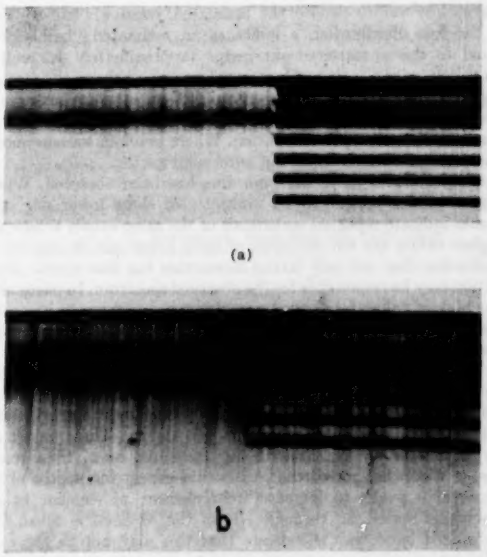

(a)

(b)

FIG. 1. Examples of the type of spectra obtained. Fig. 1(a) is the spectrum of germanium, and Fig. 1(b) is the spectrum of beryllium. The top line in each case represents the primary energy. The diffuse line on the left is the energy spectrum of electrons transmitted through the scatterer, and on the right are calibration markers spaced 6 ev apart.

Figure 1 shows examples of the type of spectra obtained. On the left is the energy spectrum of electrons transmitted through the film, and on the right are calibration markers spaced 6 ev apart. The spectrum contains, besides the undisturbed baseline, one or more lines which in some cases are quite sharp. Table I lists preliminary values of the energy losses corresponding to the maxima of these lines for the materials which we have measured so far. The letters *a*, *b*, *c*, *d*, and *e* shown as subscripts to the

TABLE I. Energy loss values in ev for approximately 30-kev electrons passing through thin films of various materials. The subscripts refer to estimated widths of the lines (see text).

Material	Energy loss values in ev
Beryllium	6.5_a 18.9_c
Na on quartz	5.4_a 10.7_a 13.3_a 17.5_c
Na on collodion	5.1_a 10.8_a 17.5_b 18.6_c
Magnesium	9.7_a 20.3_d
Aluminum	6.2_a 13.9_a 19.2_b 27.8_a 35.0_b
Silicon	5.2_a 16.9_c
K on silicon	7.8_a 11.3_a 15.0_a 18.7_a 22.6_a 27.8_b
K on collodion	8.0_a 11.0_a 14.9_a 19.5_a 22.7_a 25.8_b
Titanium	11.4_a 21.4_b 42.9_b
Chromium	9.7_a 21.8_d 45.0
Manganese	9.9_a 22.1_d
Iron	15.8_b 19.4_b 56.1
Cobalt	5.7_a 18.3_c
Nickel	5.8_a 9.4_a 13.2_a 17.6_a 23.4_c
Copper	6.9_a 11.3_a 19.6_d
Germanium	16.0_b 30.1_b
Palladium	15.7_a 21.5_a
Silver	16.0_c
Cadmium	14.5_a
Tin	4.5_a 12.4_a 18.0_a 23.9_a
Antimony	14.2_a 24.3_a
Gold	16.5_a 21.5_a
Bismuth	13.0_a 25.2_a
Collodion	4.5_a 19.3_d
Quartz	5.5_a 19.4_c
Air (nitrogen)	12.9_a

energy-loss values denote the estimated relative "half-widths" of the loss distribution. *a* indicates an estimated "half-width" equal to the unscattered slit image (approximately 1.2 volts), *b* a width twice *a*, *c* three times, etc. Figure 1(a) shows the scattering in germanium and is an example of the *a*-type distribution, while Fig. 1(b) shows the scattering in beryllium which is an example of the *e*-type distribution. Where previous measurements have been made, the extent of agreement varies.

In most cases more than one line has been observed. Where higher values appear to be multiples of some lower one, this would indicate repeated occurrence of the same event. Where the higher values are not multiples of some lower one, it may be an indication that not only lattice interaction but also atomic interaction may be responsible for the observed spectrum. In particular, the highest values for chromium and iron can perhaps be identified with the $M_{II}M_{III}$ x-ray absorption values while the single value found for cadmium is close to its N_{IV} x-ray absorption value.

Pines and Bohm[4] have calculated some values of energy loss by means of their plasma oscillation theory. They give 15.9 ev for aluminum and 18.8 ev for beryllium. Also, Pines[5] has calculated 10.8 ev for magnesium and ~6 ev for sodium. These values are in reasonable agreement with our measured ones. In a recent paper Wolff[6] has stated that one would expect the widths of the absorption peaks to increase from element to element in the transition series, Sc through Ni, as the 3*d* shell is filled. Our estimated band widths indicate that this may not be the case. However, further careful analysis of the bands is necessary before this can be stated more definitely. Similar losses have also been observed by Rudberg,[7] Haworth,[8] Turnbull and Farnsworth,[9] and Reichertz and Farnsworth[10] by measuring the energy distribution of very low-energy electrons reflected from metallic surfaces. It is highly probable that these were due to the same mechanism as the losses observed in transmission.

* This work was supported by the U. S. Office of Naval Research.

[1] G. Ruthemann, Naturwiss. **29**, 648 (1941); Ann. Physik **2**, 113 (1948).
[2] W. Lang, Optik **3**, 233 (1948).
[3] G. Möllenstedt, Optik **5**, 499 (1949); Zeit. angew. Phys. **3**, 187 (1951); Optik **9**, 473 (1952).
[4] D. Pines and D. Bohm, Phys. Rev. **85**, 338 (1952); D. Pines, Phys. Rev. **92**, 626 (1953).
[5] D. Pines (private communication).
[6] P. A. Wolff, Phys. Rev. **92**, 18 (1953).
[7] E. Rudberg, Kgl. Svenska Vetenskapsakad. Handl. **7**, 1 (1929); Proc. Roy. Soc. (London) **A127**, 111 (1930); Phys. Rev. **50**, 138 (1936).
[8] L. J. Haworth, Phys. Rev. **37**, 93 (1931); **42**, 906 (1932); **48**, 88 (1935).
[9] J. C. Turnbull and H. E. Farnsworth, Phys. Rev. **54**, 509 (1938).
[10] P. P. Reichertz and H. E. Farnsworth, Phys. Rev. **75**, 1902 (1949).

Coulomb Excitation by Means of Bombardment with Various Particles

JØRGEN H. BJERREGAARD AND TORBEN HUUS
Institute for Theoretical Physics, University of Copenhagen, Copenhagen, Denmark
(Received February 10, 1954)

THE production of Coulomb excitation effects by the impact of different types of projectiles, such as protons, deuterons, and α particles, not only gives a very convincing check on the nature of the process, but also provides a simple method for determining the multipole order of the transition in question.[1]

The cross section for Coulomb excitation produced by the electric multipole field of order λ of the impinging particle may be written[2]

$$\sigma = Z_1^2 \frac{B_e(\lambda)}{e^2 a^{2\lambda}} \cdot \left(\frac{a}{v}\frac{e^2}{\hbar}\right)^2 \cdot f_\lambda(\xi), \tag{1}$$

where

$$a = \frac{Z_1 Z_2 e^2}{m v^2}; \quad \xi = \frac{Z_1 Z_2 e^2 \Delta E}{\hbar m v^3}. \tag{2}$$

Here Z_1e is the charge, m the reduced mass, and v the velocity of the bombarding particle, whereas Z_2e is the charge, ΔE the excitation energy, and $B_e(\lambda)$ the reduced transition probability[3] for the target nuclei. The function $f_\lambda(\xi)$ has been evaluated for the case $\lambda=2$ by Alder and Winther.[4] The expression (1), which can be deduced from simple dimensional arguments, is derived by considering the projectile as moving along its classical trajectory, and neglecting the change in the orbit caused by the energy loss ΔE.

Elimination of a and v from (1) and (2) gives

$$\sigma = C_\lambda\{Z_2, \Delta E, B\} Z_1^2 \left(\frac{m}{Z_1}\right)^{2\lambda/3} \xi^{2-4\lambda/3} f_\lambda(\xi), \tag{3}$$

where C_λ is a constant which depends only on λ and the properties of the target nuclei.

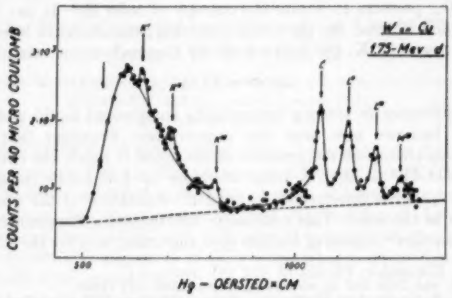

FIG. 1. The β spectrum measured for W bombarded by 1.75-Mev deuterons. The cutoff at small momenta is due to the 0.9-mg/cm² mica window of the counter. The dashed line indicates the general background mainly due to the effect of penetrating radiation from carbon deposits.

One can thus directly determine the multipole order of the excitation process by comparing, for the same value of ξ, the cross sections obtained with particles having different m/Z_1 ratios.

We have tested these conclusions by means of measurements on W bombarded with protons, deuterons, and α particles in the energy range from 1 to 2 Mev.[5] Figure 1 shows the entire β spectrum obtained by bombardment with 1.75-Mev deuterons. For the present purpose we used mainly the L' peak, which corresponds to an excitation energy of 100 kev assigned to the first excited state in W^{182}.[6]

When the background is subtracted, the peak height y of the line can be used as a measure of the corresponding cross section, since the thickness of the target layer was only about $\frac{1}{2}$ mg/cm². Figure 2 shows a plot of $\log_{10}(y/Z_1^2)$ *versus* ξ. The points for deuterons and α particles should be shifted a constant amount

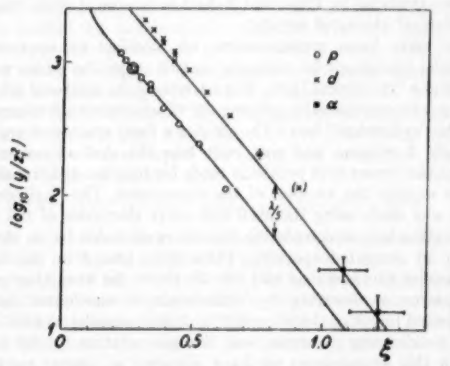

FIG. 2. Relative yields of the L' peak from Fig. 1, measured for protons, deuterons, and α particles of energies between 1 and 2 Mev. The constant distance $\lambda/5$ shows the multipole order of the excitation process. The theoretical curves for $E2$ excitation are normalized at the point marked with a ring. The ξ values have been corrected for the effect of the target thickness, but not for the energy ΔE lost by the excitation.

$\frac{1}{2}\lambda \log_{10}2 = 0.20\lambda$ in the direction of the ordinate axis, as compared to those for protons. The shift determined from the figure has a value of about 0.44, which thus confirms the expected $E2$ character of the excitation. The small difference from the theoretical value 0.40 may well be due to the experimental uncertainties.

Since the function $f_2(\xi)$ is known,[4] one can also compare the experimental ξ-dependence with the theory. The theoretical curves shown in Fig. 2 have been normalized at the experimental point corresponding to 1.75-Mev protons. The measurements are seen to confirm the theoretical calculations of the excitation function. The experimental accuracy is not quite sufficient to test to what extent the bombarding energy should be corrected for the energy loss in the excitation process. The comparison provides, nevertheless, still a relatively critical test on the evaluation of ξ, and can therefore be considered as a check on the value used for $Z_2\Delta E$. This can be an aid in cases where the assignment of a particular peak is not clear.

The kind of particle one should use in a given case in order to get the highest absolute yield is determined by the bombarding energy available. This is illustrated by Fig. 3, where the $E2$ excitation cross sections calculated by means of Eqs. (1) and (2) are compared for the various particles. The use of protons is evidently advantageous for the higher excitation energies. For lower excitation energies the heavier projectiles are the most suitable, and in particular so, because the background radiation found in this region is much smaller for slow particles. This is demonstrated by the appearance of the K lines shown in Fig. 1. In the spectrum obtained with protons[7] these lines were concealed by the background of stopping electrons, which was an order of magnitude larger than in the case of deuterons.

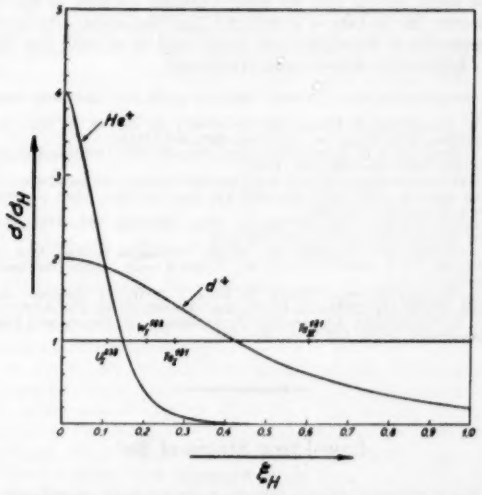

FIG. 3. Ratio of theoretical values for $E2$ excitation cross sections for deuterons and α particles, to those for protons accelerated with the same high voltage, plotted as a function of $\xi_H = Z_2\Delta E/(13U^{\frac{1}{2}})$, where ΔE is the excitation energy in Mev and U the voltage in Mv. $4(\sigma_d/\sigma_H)$ gives the curve for α particles accelerated as He^{++} ions. The marks give the ξ_H values for the first (I) and second (II) excited state corresponding to $U = 2$ Mv.

Similar considerations apply to the γ-ray experiments,[6,8] which are preferable when the conversion coefficients are small. In using Fig. 3, however, it should be remembered that thick-target measurements give relatively larger yields for protons because of their longer range.

The processes responsible for the background radiation from the target atoms are discussed in the following Letter.

[1] We are grateful to A. Bohr and B. Mottelson for bringing this point to our attention.

[3] K. A. Ter-Martirosyan, J. Exptl. Theoret. Phys. U.S.S.R. **22**, 284 (1952).

[4] See A. Bohr and B. Mottelson [Kgl. Danske Videnskab. Selskab, Mat.-fys. Medd. **27**, No. 16 (1953)], whose notation we follow. K. Alder and A. Winther, Phys. Rev. **91**, 1578 (1953). The function $f_2(\xi)$ given by these authors is equal to $25f_2(\xi)/2\pi^2$.

[5] G. M. Temmer and N. P. Heydenburg [Phys. Rev. **93**, 351 (1954)] have produced Coulomb excitation by α particles as well as by protons, and their results are consistent with the $E2$ character of the process, in the cases studied.

[6] A small contribution to the peak should come from the first excited state in W^{183}, the energy of which, however, is only slightly larger than for W^{182}. [C. L. McClelland and C. Goodman, Phys. Rev. **93**, 904 (1954)]. The most precise value for the first excited state of W^{183} seems to be that obtained from the work of Muller, Hoyt, Klein, and DuMond [Phys. Rev. **88**, 775 (1952)].

[7] T. Huus and J. H. Bjerregaard, Phys. Rev. **92**, 1579 (1953).

[8] D. Hill, Phys. Rev. **93**, 923 (1954).

Emission of δ- and X-Rays from Targets Bombarded by Accelerated Ions

ČRTOMIR ZUPANČIČ* AND TORBEN HUUS

Institute for Theoretical Physics, University of Copenhagen, Copenhagen, Denmark

(Received February 10, 1954)

WHEN one bombards elements with protons or heavier ions of such a low energy that they cannot penetrate into the nucleus, then nuclear reactions are confined to Coulomb excitation. In addition one observes other inelastic events, which are due to the ejection of atomic electrons and to bremsstrahlung in the Coulomb field of the nucleus. In the present note we discuss some measurements on these latter radiations, which provide the most important background in Coulomb excitation experiments.

The cross section for the ejection of K electrons from atoms bombarded with heavy charged particles has been calculated by Henneberg.[1] He used plane waves to represent the bombarding particles and nonrelativistic wave functions for the electrons. In this approximation the differential cross section per atom (i.e., per two K electrons) for ejection of a K electron with an energy E_δ, is given by

$$d\sigma_K \simeq 1.4\times10^{-8}Z_1^2e^4(E_1/A_1)^4E_K^3(E_K+E_\delta)^{-10}dE_\delta,$$
$$E_K \gg E_0 \quad \text{or} \quad E_\delta \gg E_0, \quad (1)$$

where Z_1e is the charge, A_1 the mass number, and E_1 the energy of the bombarding particle. The expression is valid if the binding energy E_K is large compared to the maximum energy E_0 which an electron can obtain in a free collision with the bombarding particle. By integrating (1) over E_δ, one can in this case easily obtain the total cross section for ionization of the K shell. However, regardless of the magnitude of E_K, Eq. (1) should hold for the higher energies in the spectra, i.e., for $E_\delta > E_0$.

In this region the yields of electrons found experimentally by bombardment with protons, deuterons, and α particles[2] correspond to cross sections of the order[3]

$$d\sigma \simeq 10^{-16}Z_1^2e^4(E_1/A_1)^4Z_2^4E_\delta^{-3}dE_\delta, \quad (2)$$

for $E_1 \simeq 1$ to 2 Mev, $E_\delta \simeq 40$ to 100 kev, and $Z_2 \simeq 50$ to 80. Z_2 is the atomic number of the target material. The electrons were measured in a broad angular region around 90°, and anisotropy has been disregarded in the evaluation of the total 4π cross section (2). Thick target yields can be estimated from (2) by assuming that the electrons are produced in an effective layer of thickness l, where $l \simeq 2\times10^{-3}E_\delta^2$ mg/cm² for E_δ in kev.

The form of (2) is similar to (1), but the magnitude is much larger. For the heavier elements already the number of electrons in the investigated part of the spectrum is larger than the total number of the ejected K electrons as deduced from x-ray measurements.[4,5] The observed electrons are therefore probably mainly L electrons. For this high-energy region of the spectrum, relativistic effects are important; theoretical estimates indicate that a relativistic treatment may yield cross sections in closer agreement with (2).

The yield of the characteristic K, L, and M x-rays, which are emitted in the de-excitation process, have been studied by a number of investigators. Recent measurements[4,5] of the K x-rays gave cross sections in rough agreement with Henneberg's theory. Deviations were found especially in heavy elements and for high bombarding energies and were attributed to relativistic effects.[4]

Another contribution to the radiation from the targets comes from the bremsstrahlung produced by the bombarding particles.

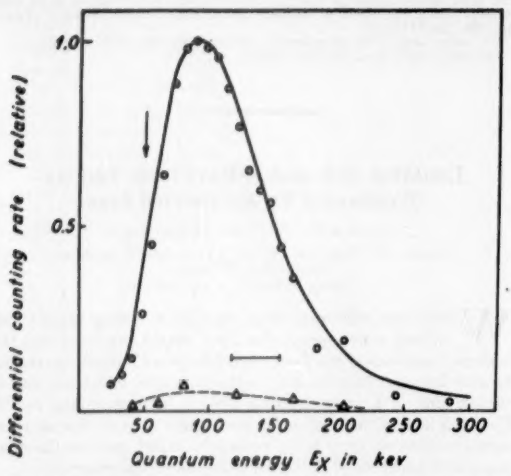

FIG. 1. The experimental points give the spectrum of x-rays from a thick Sn target bombarded with 1.75-Mev protons. Measurements were made at 90°. The theoretical spectrum (solid curve) is normalized at the highest experimental point. The dashed curve shows the background. The arrow indicates the energy at which the absorber (about 2 mm Cu) reduced the intensity by a factor 100. For comparison the experimental half-width of the 137-kev line (see reference 5) in Ta is indicated by the horizontal bar. Under the present conditions this line would have a relative height of about 5.

Sommerfeld and his collaborators[6] have calculated the rate of emission of dipole quanta for the cases in which nonrelativistic particles are deflected in the Coulomb field of the target nuclei. They find for the differential cross section, after integrating over all angles:

$$d\sigma_X = (16\pi/3^4)137 r_0^2 \alpha_i^2 FG dE_X/E_X \quad \text{for } \alpha_i \gg 1, \tag{3}$$

with

$$F = 1 \quad \text{for } \alpha_f - \alpha_i \gg 1, \tag{4a}$$

$$F = (\sqrt{3}/\pi)(\alpha_f/\alpha_i) \log_e\{(\alpha_f+\alpha_i)/(\alpha_f-\alpha_i)\} \quad \text{for } \alpha_f - \alpha_i \ll 1, \tag{4b}$$

where

$$\alpha_{i,f} = Z_1 Z_2 e^2/\hbar v_{i,f}. \tag{5}$$

Here $r_0 = e^2/mc^2$ is the classical radius of the electron, while v_i and v_f are the relative velocities of the bombarding particle before and after the collision, respectively. E_X is the energy of the bremsstrahlung quantum.

In the case of electrons the factor G equals 1, while for positive particles impinging on nuclei with mass number A_2, this factor is given by

$$G = (1836)^{-2}(Z_1/A_1 - Z_2/A_2)^2 \exp\{-2\pi(\alpha_f - \alpha_i)\}. \tag{6}$$

By bombarding heavy elements with protons,[4] we have found continuous x-radiation in approximate agreement with the aforementioned cross sections. It was found for all the elements investigated (e.g., Ag, Sn, Sb, W, Au, Pb), whenever it was not hidden by other phenomena. In most cases the amount of higher-energy γ rays was small, so that no explanation in terms of backscattering or Compton peaks was possible.

Figure 1 shows the x-ray spectrum measured when Sn was bombarded with 1.75-Mev protons. The theoretical curve (solid line) was obtained by computing the thick-target yields by means of Eqs. (3)–(6) and correcting for absorption, crystal sensitivity, and counter resolution. Since $\alpha_f - \alpha_i \lesssim 1$, we computed F from (4b), which gives a value of about 2 in the present region of interest, where it is not sensitive to the energy of either the protons or the x-rays. Anisotropy was disregarded. The curve was normalized at one of the experimental points, but within the experimental uncertainty of 50 percent the absolute theoretical yield also agreed with the measured one. Furthermore, spectra of Sn were taken at different bombarding energies and with various absorbers, and the results were found to be in agreement with theory.

The expressions (3) to (6) are valid for a bare nucleus. Some x-radiation should also be produced by the atomic electrons, partly during the collision with the incident particle, and partly during the subsequent stopping of ejected electrons. However, in the example of Sn considered above, this contribution to the x-radiation can presumably be neglected, since, in the region considered, the cross section given by Eqs. (3) to (6) for emission of proton bremsstrahlung is larger than the experimental cross section (2) for ejection of electrons of corresponding energy. This might not be true for lower quantum energies or heavier elements. In the case of α particles (and deuterons), the factor G appearing in the dipole cross section may be so small [see (6)] that higher-order terms become important.

* On leave from the "J. Stefan" Institute of Physics, Ljubljana, Yugoslavia.

[1] W. Henneberg, Z. Physik **86**, 592 (1933); see also D. R. Bates and G. Griffing, Proc. Phys. Soc. (London) **A66**, 961 (1953).

[2] T. Huus and J. H. Bjerregaard, Phys. Rev. **92**, 1579 (1953) and preceding letter [Phys. Rev. **94**, 204 (1954)].

[3] The powers given are only approximately correct. In particular, the actual electron yields were decreased less than 16 times, when deuterons were used instead of protons.

[4] Lewis, Simmons, and Merzbacher, Phys. Rev. **91**, 943 (1953). This paper includes references to previous work.

[5] T. Huus and Č. Zupančič, Kgl. Danske Videnskab. Selskab, Mat.-fys. Medd. **28**, No. 1 (1953). (N.B. In Sec. 8, line 8, read "larger" instead of "smaller.")

[6] A. Sommerfeld, Ann. Physik (5) **11**, 257 (1931); O. Scherzer, Ann. Physik (5) **13**, 137 (1932); G. Elwert, Ann. Physik (5) **34**, 178 (1939); see also: A. Sommerfeld, *Atombau und Spektrallinien* (F. Vieweg und Sohn, Braunschweig, 1939), Vol. 2, pp. 495–567.

Low-Lying States of Be^8

E. W. TITTERTON
Research School of Physical Sciences, Australian National University, Canberra, Australia

(Received February 15, 1954)

IN a recent letter Malm and Inglis[1] reviewed some of the evidence relating to the low-lying levels of Be^8 and gave new results for the reaction $B^{11}(p,\alpha)Be^8$ leading only to the well-established ground and first excited states. This reaction, like $B^{10}(d,\alpha)Be^8$ recently investigated by Treacy[2] in this laboratory, suffers from the difficulty that the continuum of α particles from the breakup of Be^8 itself tends to obscure α-particle groups corresponding to states which may be weakly excited.

Although, in principle, information on other states can be derived from the shape of the spectrum, the analysis is difficult and, for this reason, these two reactions do not readily give information about levels other than the ground and first excited states.

It is the purpose of this note to outline evidence from other reactions, especially ones studied in this laboratory, which suggest even states of Be^8 at 4.05, 5.3, and 7.5 Mev and provide evidence against a state at 4.9 Mev de-exciting by γ-ray emission.

(a) *The 4.05-Mev Level.* The first evidence for this state came from the work of Gibson and Green[3] in the neutron spectrum from $Li^7(d,n)Be^8$. That it has even properties was indicated by the observation of breakup into α particles by Calcraft and Titterton[4] in the reaction $B^{11}(\gamma,t)Be^8$ and by Brinkworth and Titterton[5] in the reaction $B^{10}(\gamma,d)Be^8$. Recently, in this laboratory,[6] it has

been demonstrated by means of a $\gamma-\alpha$ coincidence experiment that a γ-ray transition from the 17.63-Mev $(1+)$ state of Be^8 occurs to the level concerned. In 1952 Trumpy, Grotdal, and Graue[7] repeated the $Li^7(d,n)Be^8$ experiment, confirmed the presence of a state at 4.1 Mev, and suggested a new state at 2.2 Mev. More recently, the Bristol group,[8] using the same reaction, have clearly resolved a group corresponding to a level at 4.05 Mev and at the same time confirm the presence of a group corresponding to a state at 2.2 Mev. Later, photodisintegration experiments[9,10] on the reactions $B^{11}(\gamma,t)Be^8$ and $B^{10}(\gamma,d)Be^8$ confirm the results mentioned in the foregoing.

(b) *Evidence against a 4.9-Mev γ-Emitting State.* In our photographic plate experiments on $B^{10}(\gamma,d)Be^8$ and $C^{13}(\gamma,\alpha)Be^8$ with γ rays from the $Li^7(p,\gamma)$ 440-kev resonance, we have made a careful search for events which would correspond to formation of a γ-emitting state of Be^8 at 4.9 Mev. Such events would be characterized by an energy deficit of 4.9 Mev, the presence of two low-energy α particles from the ground state of Be^8 (provided the lifetime of the state is shorter than 10^{-12} sec) and, since the γ-ray momentum is negligible, the events should still satisfy momentum balance. Such events have not been observed in the boron experiments. However, "low-energy" events are observed in the $C^{13}(\gamma,\alpha)Be^8$ experiment but, in general, they are not characterized by the presence of the ground state of Be^8.[8] It has been shown[11,12,8] that they correspond to a weak γ-ray line in the $Li^7(p,\gamma)$ spectrum located at 12.3 Mev. These results, while not conclusive, indicate that, if a 4.9-Mev state of Be^8 exists at all, it is either long-lived or does not lead to γ-ray emission.

The original suggestion of the level came from the Rice group[13] who detected γ rays of 4.9-Mev energy in the $Li^7(d,n)Be^8$ reaction. If their interpretation is correct, the γ ray should be in coincidence with a neutron. Such coincidences have been searched for in an an experiment undertaken in the University of Melbourne,[14] the preliminary results of which are against the presence of coincidences.

The conclusions of these experiments are supported by recent work at the Rice Institute,[15] where it is now believed the original results can be explained as due to effects arising from the competing reaction $Li^7(d,p)Li^8(\beta^-)$.

(c) *The 5.3-Mev State of Be^8.* The first evidence for a state in this general vicinity came from the photodisintegration reactions,[4,5] $B^{10}(\gamma,d)Be^8$ and $B^{11}(\gamma,t)Be^8$. Apart from this, several observers noticed the "low-energy" $C^{13}(\gamma,3\alpha)$ events induced by the $Li^7(p,\gamma)$ radiation which were mentioned above. Nabholz, Stoll, and Wäffler[11] suggested that they were caused by a γ ray of 12.7-Mev energy formed in a cascade transition via the reported 4.9-Mev state of Be^8. It was shown by Titterton[12] that this was unlikely and the alternative suggestion was made that the transition took place through the even state of Be^8 at 5.3 Mev observed in the photodisintegration experiments. To elucidate the point, a $(\gamma-\alpha)$ coincidence experiment was undertaken in this laboratory by Inall and Boyle,[6] the results of which confirm the presence of the 5.3-Mev state.

The new work at Bristol[8] on the neutron spectrum from $Li^7(d,n)Be^8$ gives further confirmation of these results—a clearly separated group is found corresponding to a state at 5.2 Mev.

(d) *The 7.5-Mev State of Be^8.* Evidence for this broad level was given by Richards[16] [$Li^7(d,n)Be^8$] and confirmed by Green and Gibson[3] in later experiments. The $(\gamma-\alpha)$ coincidence experiment[6] mentioned above gives direct confirmation of the assignment, and a recent $\alpha-\alpha$ scattering experiment by Steigert and Sampson[17] requires a state at 7.65 Mev, of spin zero, for its interpretation. This spin assignment is compatible with the γ-ray intensity observed in the $Li^7(p,\gamma)$ Canberra experiment[6] which implies a magnetic dipole or electric quadrupole transition.

The body of evidence outlined above strongly indicates the presence of even states of Be^8 at 4.05, 5.3, and 7.5 Mev, and a study of the $(\gamma-\alpha)$ angular correlations in the reaction $Li^7(p,\gamma)Be^8 \times(\alpha)He^4$ currently in progress in this laboratory should enable spin assignments to be made in due course.

In addition to these levels, others have been suggested in the energy region under consideration, namely: 2.2 Mev,[7,8,18] 3.4 Mev,[10] 4.62 Mev,[18] 4.9 Mev (even state; not γ emitter),[10] and 6.8 Mev.[10] As pointed out by Malm and Inglis in their Letter, more experimental evidence is required before these can be regarded as established.

[1] R. Malm and D. R. Inglis, Phys. Rev. **92**, 1326 (1953).
[2] P. B. Treacy, Phil. Mag. **44**, 325 (1953).
[3] L. L. Green and W. M. Gibson, Proc. Phys. Soc. (London) **62**, 407 (1949).
[4] M. E. Cakraft and E. W. Titterton, Phil. Mag. **42**, 666 (1951).
[5] M. J. Brinkworth and E. W. Titterton, Phil. Mag. **42**, 952 (1951).
[6] E. K. Inall and A. J. F. Boyle, Phil. Mag. **44**, 1081 (1953).
[7] Trumpy, Grotdal, and Graue, Nature **170**, 1118 (1952).
[8] W. M. Gibson, (private communication).
[9] R. Müller and P. Stoll, Nuovo cimento (supp.) **9**, 1232 (1952).
[10] Erdös, Scherrer, and Stoll, Helv. Phys. Acta. **26**, 207 (1953).
[11] Nabholz, Stoll, and Wäffler, Phys. Rev. **82**, 963 (1951).
[12] E. W. Titterton, Australian, J. Sci. **15**, 174 (1953).
[13] Bennett, Bonner, Richards, and Watt, Phys. Rev. **59**, 904 (1941); Phys. Rev. **71**, 11 (1947).
[14] L. H. Martin and J. Campbell (private communication).
[15] T. Bonner (private communication).
[16] H. T. Richards, Phys. Rev. **59**, 796 (1941).
[17] F. E. Steigert and M. B. Sampson, Phys. Rev. **92**, 660 (1953).
[18] K. Boyer, Massachusetts Institute of Technology, unpublished report as quoted in F. Ajzenberg and T. Lauritsen, Revs. Modern Phys. **24**, 321 (1952).

Kinematics of Λ^0 Production*

GEORGE T. REYNOLDS AND S. B. TREIMAN
Palmer Physical Laboratory, Princeton University, Princeton, New Jersey

(Received February 15, 1954)

CLOUD-CHAMBER observations by the Princeton Cosmic-Ray Group indicate that an appreciable fraction of Λ^0 particles produced in heavy elements (lead and copper) have low kinetic energies in the laboratory system.[1] At least 10 percent of the observed Λ^0 particles have energies below 70 Mev; whereas chamber bias against the observation of high-energy Λ^0 particles is not serious below a few Bev.

In order to investigate the implications of this result, we have considered the kinematics of several fundamental interactions which might lead to Λ^0 production, of the type

$$m_0+m_1 \rightarrow m+m_2+\cdots, \tag{1}$$

where m_0 is the incident particle (pion or nucleon), m_1 the target nucleon, m the Λ^0 particle, m_2 a secondary particle, and the possibility is allowed that additional particles may be produced in the interaction. The essential assumption is that the interaction occurs with a single nucleon in the nucleus. It is also assumed that the Λ^0 particle suffers no appreciable loss of energy in escaping from the nucleus.

We then find that it is difficult to explain the large fraction of low-energy Λ^0 particles if the production is isotropic in the center-of-mass system. There is of course no *a priori* reason why the production should be isotropic; but the departure from isotropy indicated by our results is so pronounced as to merit quantitative discussion.

Let $P(E_0,<E')$ be the probability that an incident particle of energy E_0 in the target-nucleon rest frame Σ gives rise to a Λ^0 particle of energy $<E'$ in the laboratory frame Σ', taking into account the internal motion of the nucleons in the nucleus. Let $P(E_0,E)dE$ be the probability that the incident particle produce a Λ^0 particle of energy between E and $E+dE$ in the Σ frame; and let $w(E,<E')$ be the probability that this Λ^0 particle have energy $<E'$ in the Σ' frame. Then,

$$P(E_0,<E')=\int P(E_0,E)w(E,<E')dE. \tag{2}$$

To obtain the function $w(E,<E')$—which expresses the effect of the internal motion of the target nucleons—a Fermi gas model of the nucleus was adopted, with maximum nucleon kinetic energy of 20 Mev (our final numerical results are insensitive to this choice

of upper limit). The expression for w is lengthy and will not be written here.

To obtain the function $P(E_0,E)$, it is necessary to specify the details of reaction (1). It turns out that for the particular reactions and energies considered here, the probability of obtaining low-energy Λ^0 particles (<70 Mev) is greatest when no "additional" particles are produced in reaction (1). With the neglect, then, of "additional" particles, the Λ^0 energy E in the Σ frame can be expressed as a unique function of the incident particle energy E_0 and the angle θ^* of the Λ^0 particle in the center-of-mass frame,

$$E=A(E_0)+C(E_0)\cos\theta^*, \tag{3}$$

where the functions $A(E_0)$ and $C(E_0)$ are lengthy, but easily obtained by standard methods of collision kinematics. Then

$$P(E_0,E)=u(\cos\theta^*)/C(E_0), \tag{4}$$

where $u(\cos\theta^*)d(\cos\theta^*)$ gives the angular distribution of Λ^0 production in the center-of-mass system; $\cos\theta^*$ is to be expressed here as a function of E, by means of Eq. (3).

We consider in the first place the case of isotropic Λ^0 production $[u(\cos\theta^*)=\frac{1}{2}]$. The results for four possible reactions are shown in Fig. 1, where the probability for producing Λ^0 particles below 70

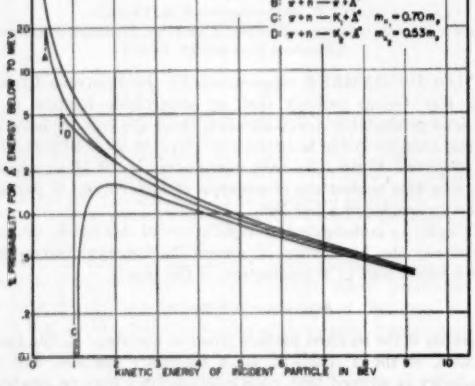
KINEMATICS OF Λ° PRODUCTION
CURVE: A: π⁻+n → n+Λ°
B: π⁺+n → π⁺+Λ°
C: π⁺+n → K⁺+Λ° m_K = 0.70 m_π
D: π⁻+n → K⁰+Λ° m_K = 0.53 m_π
% PROBABILITY FOR Λ° ENERGY BELOW 70 MEV
KINETIC ENERGY OF INCIDENT PARTICLE IN BEV

FIG. 1. Probability for Λ^0 energy less than 70 Mev in the laboratory frame, expressed as a function of the incident particle energy in the target-nucleon rest frame (for the large energies involved, this does not differ appreciably from the incident particle energy in the laboratory frame). These results are for the case of isotropic Λ^0 production. In curve C, the mass of the K meson is taken to be 1300 m_e; in curve D, 970m_e.

Mev in the laboratory frame is plotted against the energy of the incident particle in the target-nucleon rest frame. The curves begin at the respective threshold energies; at large energies they coincide and go as E_0^{-1}. Only for reactions A and B is it possible to obtain probabilities larger than 10 percent and then only very near threshold.

Several explanations may be suggested to account for the large fraction of low-energy Λ^0 particles. Consider an anisotropy of the form

$$u(\cos\theta^*)=\tfrac{1}{2}(n+1)|\cos^n\theta^*|.$$

It can then be shown from Eqs. (2) and (4) that

$$P_n(E_0,<E')<(n+1)P_0(E_0,<E').$$

Thus to explain our observed results, on the basis of anisotropy and assuming Λ^0's to be produced well above threshold in the cosmic-ray beam, we require $n>6$.

Alternately, one might consider Λ^0 production to result from a multiple process, or cascade, in which π's or nucleons produce π's which in turn produce Λ^0's at energies near threshold. However, the Brookhaven results[5] indicate that Λ^0's produced by 1.5-Bev π's (i.e., near threshold energy) also show a strong backward peaking in the center-of-mass system.

* Supported by the U. S. Office of Naval Research and the U. S. Atomic Energy Commission.

[1] Ballam, Harris, Hodson, Rau, Reynolds, Treiman, and Vidale, Phys. Rev. 91, 1019 (1953).

[5] Fowler, Shutt, Thorndike, and Whittemore, Phys. Rev. 91, 1287 (1953).

Small-Angle Neutron-Proton Scattering at 90 Mev*

OWEN CHAMBERLAIN AND JAMES W. EASLEY
Radiation Laboratory, Department of Physics, University of California, Berkeley, California

(Received February 10, 1954)

THE relative neutron-proton differential cross section has been measured for several angles near zero degrees. This range of angles has been difficult to investigate because of the very short range of the recoil protons. Previously published work,[1-5] done by measurement of proton recoils, has not covered these angles. However, some cloud-chamber experiments are currently in progress at this laboratory[6] in which recoil protons are employed in this range.

The neutron beam was obtained by stripping 190-Mev deuterons on a $\frac{1}{2}$-in. beryllium target in the 184-inch Berkeley cyclotron. A steel shielding block 6 ft long$\times$6 in. high$\times$3 in. thick was placed close to the beam on the same side as the counters to reduce background.

The target was of liquid hydrogen contained in a cylindrical vessel of 5.6-in. diameter with axis vertical. The beam dimensions at the target were 3 in. high$\times$1 in. wide. A bismuth fission counter was employed as a beam monitor.

Scattered neutrons were counted at small angles to the neutron beam. Figure 1 shows the neutron counter, which consisted of the

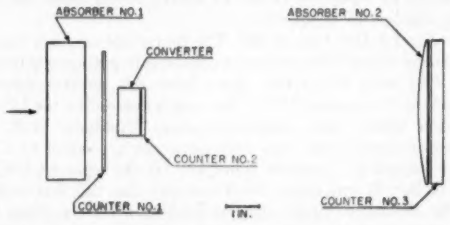

FIG. 1. Arrangement of components of neutron counter.

following components, listed in the order that they would be traversed by a scattered particle: (a) absorber number 1, 25 g cm^{-2} of copper to prevent protons from reaching the scintillation counters directly; (b) scintillation counter number 1, made of plastic scintillant 4.0 in.$\times$3.5 in.$\times$0.080 in. thick; (c) the converter, 1.74 g cm^{-2} of polyethylene; (d) scintillation counter number 2, a liquid counter with active volume 2.2 in.$\times$1.4 in. $\times$0.118 in. thick; (e) absorber number 2, which was from 1.0 to 1.8 g cm^{-2} of copper plus a shaped aluminum absorber of maximum thickness 1.8 g cm^{-2}; (f) scintillation counter number 3, made of plastic scintillant 6.6 in.$\times$4.2 in.$\times$0.4 in. thick. The distance from the center of the target to the center of the converter was 48 in. for the range of the laboratory scattering angle Θ from 18.5° to 5.0° and 70 in. for the range of 5.0° to 2.5°.

The neutrons actually counted were those that were "converted" in the polyethylene converter or in counter number 2. The term "converted neutron" refers to a neutron that yields a high-energy proton by n-p scattering or nuclear interaction. These recoil protons were counted in coincidence in counters 2 and 3. In order to reject charged particles originating in other

TABLE I. Experimental data for neutron-proton scattering at 90 Mev. θ is the scattering angle in the center-of-mass system. Column I gives the ratio of the differential cross section in the center-of-mass system at the angle θ to that at 36°. Column II gives the absolute differential cross section obtained by normalizing to the results of Hadley *et al.* (see reference 1). The errors listed are the standard deviations of the counting statistics.

θ	I Relative cross section	II Absolute cross section (10^{-27} cm²/steradian)
5.1	1.70±0.14	12.9±1.2
10.3	1.58±0.06	12.0±0.7
20.8	1.36±0.05	10.3±0.6
36.0	1.00	7.6±0.4

processes, counter 1 was connected in anticoincidence. Only events detected in counters 2 and 3 but not 1 were counted.

The thickness of absorber 2 determined the minimum energy which a scattered neutron could have and still be counted. In the present work the minimum energy was adjusted at each scattering angle to be $[(60 \text{ Mev}) \cos^{3}\Theta]$. Therefore, a neutron in the beam must have had at least 60 Mev in order to have been counted after scattering, since otherwise the proton yielded at the converter would have had insufficient range to reach counter 3. The shaped portion of absorber number 2 was thickest in the center and was shaped so that to good approximation the minimum neutron energy to count would be independent of the angle with which the recoil proton emerged from the converter. To determine the shape of the absorber we assumed that most of the recoil protons were from n-p scattering processes in the converter. In order to ascertain whether the relative differential cross sections were particularly sensitive to the value of the minimum energy for detection of the scattered neutrons, a measurement was made with this minimum energy increased to 66 Mev. The results were in agreement with those obtained for the 60-Mev minimum within the uncertainty of the counting statistics.

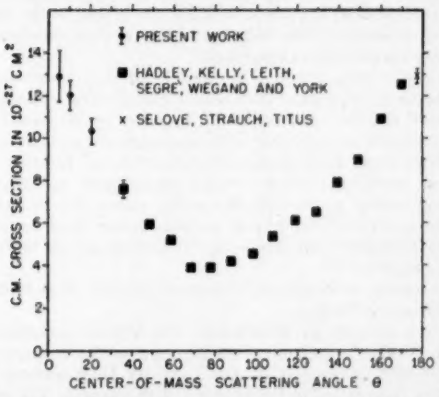
PRESENT WORK
HADLEY, KELLY, LEITH, SEGRÈ, WIEGAND AND YORK
SELOVE, STRAUCH, TITUS
C.M. CROSS SECTION IN 10^{-27} C M^2
CENTER-OF-MASS SCATTERING ANGLE θ

FIG. 2. Differential neutron-proton cross section in the center-of-mass system in 10^{-27} cm²/steradian.

The results are tabulated in Table I. Figure 2 shows the data in their relation to prior work, indicating a marked similarity of the differential cross section in the region of 0° to that in the region of 180°.

Thanks are due Dr. Martin O. Stern for initial studies of background and design of the neutron collimator.

* This work was done under the auspices of the U. S. Atomic Energy Commission.

[1] Hadley, Kelly, Leith, Segrè, Wiegand, and York, Phys. Rev. **75**, 351 (1949).
[2] Brueckner, Hartsough, Hayward, and Powell, Phys. Rev. **75**, 555 (1949).
[3] R. H. Fox, U. S. Atomic Energy Commission Report UCRL-867, 1950 (unpublished).
[4] R. Wallace, Phys. Rev. **81**, 493 (1951).
[5] Selove, Strauch, and Titus, Phys. Rev. **92**, 724 (1953).
[6] C. Y. Chih and W. M. Powell (private communication).

Additional Properties of Isotopes of Elements 99 and 100

P. R. FIELDS, M. H. STUDIER, J. F. MECH, H. DIAMOND, A. M. FRIEDMAN, L. B. MAGNUSSON, AND J. R. HUIZENGA
Argonne National Laboratory, Lemont, Illinois

(Received February 11, 1954)

A SHORT-LIVED alpha activity was previously reported to elute at the element-100 position.[1] This activity was observed, a few hours after column separation, to be in equilibrium[1] with an element-99 parent which decayed with a longer (~2-day) half-life. Preliminary data obtained from irradiations in the Argonne pile indicated that an MTR irradiation of 10^{4} alpha counts/minute of the 6.6-Mev element-99 isotope would produce several hundred 7.2-Mev alpha counts/minute of element 100.

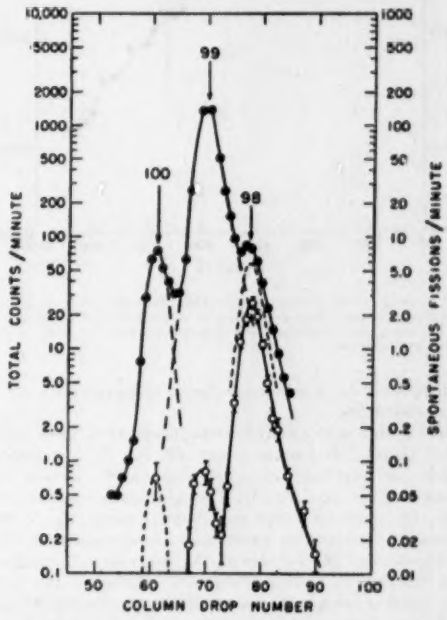

FIG. 1. The solid points represent the total counts/minute (alphas plus spontaneous fissions) from each drop at the time of removal from the cation column. The dashed curves outline the individual element separations as determined by alpha-pulse analysis and spontaneous fission measurements. The open circles represent the spontaneous fission activity as a function of drop number. The value at drop 61 is a result of a spontaneous fission activity measurement immediately after column elution. The other spontaneous fission measurements were made more than 12 hours after column elution, and therefore isotope 100^{254} was in approximate equilibrium with its element-99 parent causing the spontaneous fissions on the element-99 drops.

This note describes the results obtained from a four-day irradiation of an element-99 fraction with californium impurity in the Materials Testing Reactor (MTR) at Arco, Idaho to produce the following reaction:[2]

$$99^{254}(n,\gamma)99^{255} \xrightarrow{\beta^-} 100^{255}.$$

The separation of elements 98, 99, and 100 has been discussed previously and the degree of separation in this experiment is shown in Fig. 1. The peak of the 7.2-Mev alpha activity of element 100 eluted from the cation resin column on drop 61, while the peak of elements 99 and 98 eluted on drops 69–70 and 78, respectively.

The 7.2-Mev alpha-emitting isotope of element 100 decayed with a 3.3±0.2 hour half-life (Fig. 2) measured both by total and by spontaneous fission activity. The ratio of 7.2-Mev alpha

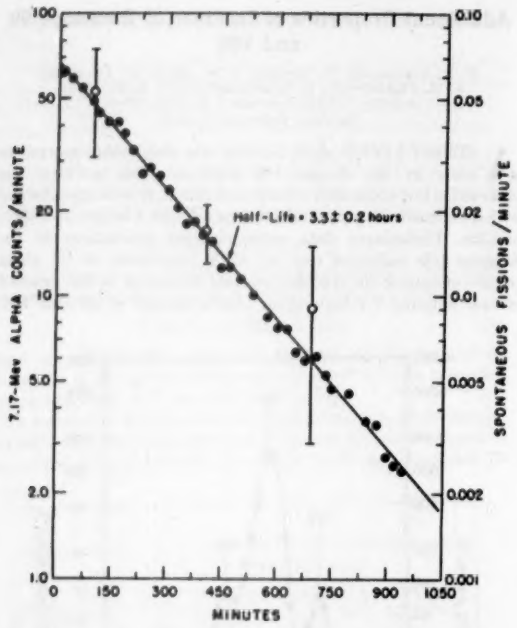

FIG. 2. Decay of the element-100 fraction. The solid points represent the 7.17-Mev alpha counts/minute of drop 60 as a function of the time in minutes. The open circles represent the spontaneous fission activity of drop 61 as a function of time.

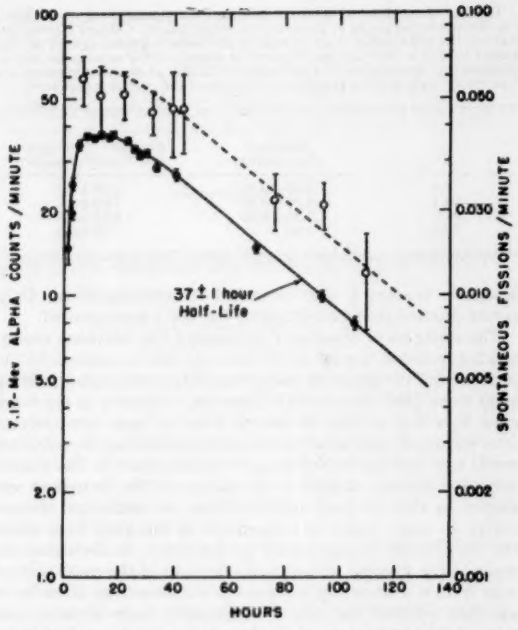

FIG. 3. Growth and decay of element-100 isotope in an initially separated element-99 fraction. The solid circles represent the 7.17-Mev alpha activity on drop 71 as a function of time. The open circles represent the spontaneous fission activity on drop 68 as a function of time. The dashed line is a parallel displacement of the solid line.

disintegrations to spontaneous fission disintegrations on drop 61 was 2000±700.

The 7.2-Mev alpha activity was observed to grow into the purified element 99 fraction (drops 69, 70, 71) by alpha-pulse analysis, and eventually decayed from the 99 fraction with a 37-hour half-life (see Fig. 3). The spontaneous fission activity on drop 68 followed a similar growth-decay curve (Fig. 3). Figure 1 shows the spontaneous fission peak in the element-99 fraction after the element-100 (7.2-Mev alpha) had grown into equilibrium. These experiments confirm the genetic relation of the 7.2-Mev alpha-emitting isotope of element 100 to its element-99 parent. In addition, a measurable spontaneous fission activity is shown to be associated with the element-100 isotope emitting the 7.2-Mev alpha particles.

The ratio of 7.2-Mev alpha disintegrations to spontaneous fission disintegrations was measured more accurately with samples containing element 100 in equilibrium with the element-99 parent. The ratio is 1600±300, in good agreement with the less accurate value from drop 61. The calculated spontaneous fission half-life of the 3.3±0.2 hour element-100 isotope is 220±40 days. This half-life is in agreement with the prediction for an even-A isotope of element 100 with mass 254, and is corroborative evidence for the even-A assignment.[3]

TABLE I. Nuclear properties of some isotopes of elements 99 and 100.

Isotope	Radiation	Half-life	Alpha energy (Mev)	Spontaneous fission half-life
99^{253}	α	19.3±0.3 days	6.61±0.01	$>10^8$ yr
99^{254}	β^-	37 ±1 hr		>10 yr
100^{254}	α	3.3±0.2 hr	7.17±0.01	220±40 days

An equilibrium sample (the specific 7.2-Mev alpha activity four-hundred-fold greater than that in the previous measurement described in reference 1) of 100^{254} supported by its parent 99^{254} was employed for additional alpha-spectrum studies. The energy of the prominent alpha group was measured to be 7.17±0.01 Mev, in close agreement with the initial measurement of 7.20 Mev.[1] More discussion on the 7.03-Mev alpha emitter will be included in a later manuscript. The pile neutron capture cross section of 99^{253} is 240±100 barns, assuming no electron-capture branching in the decay of 99^{254}.

The nuclear properties of isotopes of elements 99 and 100 are summarized in Table I.

It is a pleasure to acknowledge the helpful cooperation of W. H. McCorkle and the operating crew of the Argonne pile. We also wish to thank W. B. Lewis and the MTR staff for their excellent cooperation in the handling of this sample. The experimental assistance given by D. W. Engelkemeir, J. E. Gindler, M. M. Petheram, and R. K. Sjoblom is gratefully acknowledged. We again wish to thank W. M. Manning for his continued interest in these experiments.

[1] Studier, Fields, Diamond, Mech, Friedman, Sellers, Pyle, Stevens, Magnusson, and Huizenga, Phys. Rev. 93, 1428 (1954).
[2] The tentative mass assignments are based on mass yields and heavy-element systematics.
[3] J. R. Huizenga, Phys. Rev. 94, 158 (1954).

CONTENTS

THE PHYSICAL REVIEW — SECOND SERIES, VOLUME 76, NO. 1 — APRIL 1, 1949

Positive Point-to-Plane Corona Studies in Air . . . . . M. Misakian and L. H. Fisher 1

Experimental Measurement of the Gyromagnetic Ratio of the Free Electron . . . . . W. H. Louisell, R. W. Pidd, and H. R. Crane 7

Problem of Multiple Scattering . . . . . E. P. Wigner 17

Calculated Values of the Parameters of Noble Gas Discharges . . . . . Walter J. Graham and Arthur J. Rahlig 23

Ionic Conductivity of Impure Polar Crystals . . . . . A. B. Lidiard 29

Polaron Self-Energy and Bloch-Nordsieck Method . . . . . K. S. Singwi and S. M. Udgaonkar 36

Piezoresistance Effect in Germanium and Silicon . . . . . Charles S. Smith 42

Magnetic Susceptibility of Nd Metal . . . . . J. F. Elliott, S. Legvold, and F. H. Spedding 59

Magnetic Domains by the Longitudinal Kerr Effect . . . . Charles A. Fowler, Jr., and Edward M. Fryer 52

Electrical Conductance of Pressed Powders, in Particular of Zinc Oxide . . . . . J. C. M. Brentano and Colman Goldberg 56

Effect of Elastic Strain on the Electrical Resistance of Metals . . . . . G. C. Kuczynski 61

Rate of Production of Color Centers in KCl and KBr by X-Rays at 78°K . . . . . William H. Duerig 65

Diffraction Effects of Crystals with Deformation Faults . . . . . R. Hosemann and S. N. Bagchi 71

Complete Bacher and Goudsmit Method . . . . . Sydney Mashkevich and C. W. Ufford 73

Application of the Rayleigh-Schrödinger Perturbation Theory to the Hydrogen Atom . . . . . Eugene P. Wigner 77

Mean Excitation Potentials . . . . . David O. Caldwell and J. Reginald Richardson 79

$Mg^{24}(\gamma,\beta\beta 3n)F^{18}$ Reaction Induced by 70-Mev Bremsstrahlung . . . . . Fritz D. Schupp and Tom S. Martin, Jr. 80

Elastic Scattering of Protons by Nuclei . . . . . D. M. Chase and F. Rohrlich 81

He^3+He^3 Reactions . . . . . W. M. Good, W. E. Kunz, and C. D. Moak 87

Disintegration of Mo^{95} . . . . . Jagdish Varma and C. E. Mandeville 91

Ground States of Odd-Odd Nuclei . . . . . C. Schwartz 98

Decay Scheme of Zr^{95} . . . . . Philip S. Mittelman 99

Decay of $_{65}Tb^{149}$ (71 day) . . . . . S. B. Burson, W. C. Jordan, and J. M. Lollinger 103

Nuclear Spectra of Co^{144} and Pr^{144} . . . . . W. S. Emmerich, W. J. Ash, and J. D. Kurbatov 110

Radiative Electron Capture of Fe^{55}, A^{37}, and Hg^{203} . . . . . W. S. Emmerich, S. E. Singer, and J. D. Kurbatov 113

Potassium-44 . . . . . Bernard L. Cohen 117

β-Decay Energy Systematics . . . . . Katharine Way and Marion Wood 119

Ranges of Fragments from High-Energy Fission of Uranium . . . . . E. M. Douthett and D. H. Templeton 126

Third Forbidden Beta Spectrum of Rubidium-87 . . . . . M. H. MacGregor and M. L. Wiedenbeck 136

Total Neutron Cross Section for Uranium from 20 kev to 20 Mev . . . . . R. L. Henkel, L. Cranberg, G. A. Jarvis, R. Nobles, and J. E. Perry, Jr. 141

Inelastic Scattering of Neutrons . . . . . E. A. Eliot, D. Hicks, L. E. Beghian, and M. Halbern 144

Long-Lived Isomer of RaE(Bi^{210}) . . . . . Harris B. Levy and I. Perlman 152

$_{94}Pu^{240}$ and Its Spontaneous Fission . . . . . O. Chamberlain, G. W. Parvell, and E. Segrè 156

Energy Spectrum of Spontaneous Fission Fragments . . . . . Emilio Segrè and Clyde Wiegand 157

Spontaneous Fission Systematics . . . . . John R. Huizenga 158

γ-Decay Event with a Heavy Negative Secondary, and Identification of the Secondary γ-Decay Event in a Cascade . . . . . E. W. Cowan 161

Cosmic-Ray Protons at 3.6 Kilometers . . . . . Charles E. Miller, Joseph E. Henderson, Gerald R. Garrison, David S. Potter, Wayne M. Sandstrom, and Jay Todd, Jr. 167

Total Cross Sections for 418-Mev Neutrons . . . . . V. Alexander Nedzel 174

Production of K Mesons . . . . . U. Haber-Schaim, Y. Yekutieli, and G. Yekutieli 184

Renormalization . . . . . P. T. Matthews and Abdus Salam 185

Quantized Space-Time . . . . . Emil J. Hellund and Kazuo Tanaka 192

Configuration Space Methods for the Construction of Potentials . . . . . Abraham Klein 198

(continued on cover three)

LANCASTER PRESS, INC., LANCASTER, PA.